THE DYNAMICS AND CONTROL OF FLUX-PINNED SPACE SYSTEMS: THEORY AND EXPERIMENT

A Dissertation

Presented to the Faculty of the Graduate School

of Cornell University

In Partial Fulfillment of the Requirements for the Degree of

Doctor of Philosophy

by

Laura Lynne Jones

August 2012

THE DYNAMICS AND CONTROL OF FLUX-PINNED SPACE SYSTEMS: THEORY AND EXPERIMENT

Laura Lynne Jones, Ph. D.

Cornell University 2012

Advanced space systems are increasingly reliant on close-proximity operations to achieve complex mission objectives on orbit. These maneuvers – such as docking and rendezvous, formation flying, and on-orbit assembly, refit, and repair – require spacecraft that can provide robust, stable, and predictable behavior. Flux-pinned interfaces (FPIs) for spacecraft are a developing technology that addresses these growing demands on the capabilities and reliability of space systems by exploiting the physics of magnetic flux pinning.

Flux pinning is a phenomenon in superconducting physics involving type II superconductors cooled below their critical temperature in the presence of a magnetic field. When set up correctly, the superconductor resists changes to the distribution of magnetic flux present during the temperature transition. The resulting physics passively "pins" a magnetic field source in a six-degree-of-freedom equilibrium relative to the superconductor. By using this interaction to influence the dynamics between spacecraft, an FPI can provide stiff, stable, and controllable relative equilibrium points between magnets on one spacecraft and the superconductors on the other.

This dissertation details the extensive research and development work on flux-pinned interfaces for spacecraft. In addition to describing the concepts and literature

relevant to the technology, this document examines the modeling, actuation, and control strategies that provide the theoretical grounding for designing FPIs. Going beyond mathematical foundations, subsequent sections explain the results from FPI technology development efforts in laboratory and microgravity experimental environments. The concluding chapters address the practical considerations an orbital FPI design and the prospects for the technology as a whole.

BIOGRAPHICAL SKETCH

Laura was born in Florida in 1985 to Robin and Michael Jones. She was raised in the traditional military-family way, by moving every four years to exotic places such as Hawaii, Holland, and Alabama. By age four she had decided to become an astronaut, so once she graduated from Mt. Vernon High School in 2003, she moved to the quiet mountain town of Blacksburg, VA to study aerospace engineering at Virginia Tech. While at Tech, she worked in the Space Systems Simulation Lab (SSSL) with Dr. Chris Hall developing a webcam into an attitude determination sensor for the three-degree-of-freedom satellite testbed in the lab. At Dr. Hall's encouragement, in her senior year she applied to the National Science Foundation (NSF) Graduate and the National Defense Science and Engineering Graduate (NDSEG) Fellowship program and was awarded both. She earned her Bachelor of Science in aerospace engineering with a minor in mathematics in 2007.

Laura joined the Space Systems Design Studio at Cornell University in the summer of 2007 to work with Mason Peck in pursuit of her doctoral degree. After spending a year working on CMG steering laws, she settled on the flux-pinned interfaces for spacecraft project, where she has devoted over three years of research. In addition to her research, she spends her time playing flute in the Ithaca Concert Band, volunteering as the Aerospace Education Officer for the local Civil Air Patrol squadron, and hiking mountains. Laura graduated in the summer of 2012 with her Ph.D. in Aerospace Engineering, with a concentration in Dynamics and Controls and a minor in Astronomy.

ACKNOWLEDGMENTS

I owe many thanks to everyone who helped bring me to this point in my career. I'd first like to thank my advisor, Mason Peck, for his direction and insight throughout this process. Mason, thanks for teaching me so much- everything from the intricacies of the aerospace community to the subtleties of navigating a "NaN" budget. I also appreciate the guidance offered by my committee members – Mark Campbell, Terry Herter, and Ephrahim Garcia. I really value the breadth and depth you have all given to my graduate experience.

The members of the Space System Design Studio (both past and present) have also been incredibly helpful in this long journey. To all of the ones who have paved the way ahead – Michele Carpenter, Mike Norman, Joe Shoer, Dan Brown, Justin Atchison, Brett Streetman – thanks for setting a great example about what it means to be on Team Peck and for your insight into the graduation and job search process. To those in the SSDS as I move on – Liran Gazit, Rodrigo Zeledon, Zac Manchester, Ben Reinhardt, and Lorraine Weis – thanks for being incredibly helpful as I wrapped up my work. Don't forget to email me if you need future advice! Liran, thanks especially for your help on those microgravity projects. Rodrigo, thanks for collaborating on the CMG work and for all of your help with machining/testing/other insights!

I'd like to thank my collaborators – Matt Sorgenfrei at the University of California at Davis and Dr. James Forbes at McGill University – for their amazingly talented support of my work. I would also like to thank my undergraduate mentor, Dr. Hall, for his continuing advice and for convincing me to apply to those fellowships!

Everyone in the Mechanical and Aerospace staff deserves credit for making sure I met all of the requirements to graduate, and helping me resolve the nuances of getting things done: Marcia, Patti, Emily, and everyone else.

Throughout my time at Cornell, I've had a veritable army of researchers working on the Flux Pinning Research Team. Their dedication and commitment to the difficult task of making hardware and software actually work made this research happen. In particular, my subsystem leads Chris Jewison, Andrew Kerns, and Sammy Nowierski deserve special recognition – their insight, leadership, and wiliness to find an answer to the most obscure questions on short notice made this project happen. Also, a special thanks to Max Knobel and Jillian Gorsuch, who spent their M.Eng. projects working long hours to make the microgravity flight projects and thorny simulations work. Thanks for being great teammates!

I'd also like to acknowledge the members of the Flux Pinning Research Team: Mason Brody-Carney, Markus Burkhardt, Guo Jie Chin, Ellen Chuang, Justin Churchill, Jason D'Souza, Cameron Glass, Timothy Kim, Steph Kubala, Alexander Lavin, "Leo" Lin, Kevin Lo, Jun Ma, Sarah Mburu, Patrick MacGregor, Rob Moore, Will Moseson, Alexander Rojas, Paras Sanghavi, Calvin Winder, and Frances Zhu.

I wouldn't have come this far without the support of my friends, so thanks to Trish for the cats, Mike Cropper for keeping me grounded, Aimée for keeping in contact through months of silence as I wrote this dissertation, Mary & Melissa for being kindred spirits, Narayana & Chelsea for the adventures, Cesar & Heidi for the insights and kindness, and the rest of the MAE graduate students for their laughs and quirks.

And of course, I'd like to thank my family for their support through this effort. Thanks to my dad for always making a pointed effort to understand my research, my mom for her tactical and strategic suggestions, und Meine Schwester, der große Freund, ich wollte immer in einer Schwester. Thanks to my grandparents for being an amazing inspiration.

William – thanks for literally everything. For getting me into this project, for keeping me sane, and for understanding. You are the best.

TABLE OF CONTENTS

LIST OF FIGURES

LIST OF TABLES

LIST OF ABBREVIATIONS

AC	=	alternating current
AMIM	=	advanced mirror image model
CAD	=	computer-aided design
CMG	=	control moment gyroscope
CO_2	=	carbon dioxide
CORTX	=	Controlled Operations for Reconfigurable Technology eXperiments
DC	=	direct current
DOF	=	degrees of freedom
EINAR	=	Electromagnet Interface for Noncontacting Actuation and Reconfiguration
EM	=	electromagnet
FAST	=	Facilitated access to the Space environment for Technology
FIM	=	frozen-image model
FPI	=	flux-pinned interface
F-PROX	=	Flux-pinned Proximity Rendezvous Operations eXperiment
FPS	=	frames per second
GNC	=	guidance, navigation, and control
HTSC	=	high-temperature superconductor
IMU	=	inertial measurement unit
ISS	=	International Space Station
LED	=	light emitting diode

LN2	=	liquid nitrogen
MMMS	=	multiple-magnet, multiple-superconductor
MMSS	=	multiple-magnet, single-superconductor
PCB	=	printed circuit board
PID	=	proportional-integral-derivative (control)
PLT	=	precision lab translator
PM	=	permanent magnet
RAGNAR	=	Robust, Autonomous Grappler for Non-contacting Actuation and Reconfiguration
SMMS	=	single-magnet, multiple-superconductor
SMSS	=	single-magnet, single-superconductor
SSDS	=	Space Systems Design Studio
TRL	=	technology readiness level
YBCO	=	Yttrium Barium Copper Oxide ($YBa_2Cu_3O_x$)

LIST OF SYMBOLS

$\hat{\boldsymbol{a}}$	=	unit direction vector perpendicular to superconductor
A	=	area enclosed by electromagnet current loop
B	=	magnetic field strength
B_r	=	residual flux density
c	=	damping coefficient
d	=	linear distance
f	=	frequency value
F	=	force
F_{ab}	=	air bearing flow rate
f_k	=	coefficient of kinetic friction
f_s	=	coefficient of static friction
g	=	gravitational acceleration
H	=	Hamiltonian
I	=	inertia
J	=	current density
k	=	stiffness
k_d	=	derivative control gain
k_i	=	integral control gain
k_p	=	proportional control gain
m	=	mass
m_{CO_2}	=	total mass of CO_2 available in the pressure system
n_{ab}	=	number of air bearings in the system

n_{CO_2}	=	molar mass of CO_2
P	=	pressure
q	=	state of interest
$\boldsymbol{q}$	=	quaternion of spacecraft attitude
$Q2$	=	quaternion value
r	=	radius
$\boldsymbol{r}$	=	position vector
R	=	ideal gas constant
R^2	=	coefficient of determination
R_i	=	resistance
t	=	time (also thickness in specific contexts)
T	=	kinetic energy (also temperature in specific contexts)
T_C	=	material-dependent critical temperature
T_i	=	number of turns in an electromagnet
t_{float}	=	floating time of air bearing use in minutes
U	=	potential energy
V	=	voltage value
$V(x(t))$	=	Lyapunov function
x	=	linear distance
x_{mag}	=	position of magnet on x-axis
Y	=	displacement about the y-axis in mm
y_{mag}	=	position of magnet on y-axis
Z	=	displacement about the z-axis in mm

z_{mag}	=	position of magnet on z-axis
$\boldsymbol{\rho}$	=	distance between magnet and its image
τ	=	torque
τ_{fric}	=	friction torque
μ_0	=	permeability of free space
μ_h	=	solution of the *z*-direction magnetic steering law found by adding the numerator terms
μ_i	=	magnetic moment of source magnet *i*
μ_l	=	solution of the *z*-direction magnetic steering law found by subtracting the numerator terms
$\dot{\omega}$	=	angular acceleration
ω_d	=	damped natural frequency
χ	=	real vector space
ζ	=	linear damping ratio

CHAPTER 1

AN INTRODUCTION TO FLUX-PINNED INTERFACES FOR SPACECRAFT

1.1. Close-Proximity Spacecraft Operations

In the 1960s, the ambitious and highly successful Gemini program demonstrated a string of impressive firsts in the field of close-proximity spacecraft operations in preparation for the Apollo lunar program. These achievements such as the first successful on-orbit rendezvous of Gemini 7 and Gemini 6 in 1965 (shown in Figure 1.1) inspired generations of spacecraft designers, who went on to develop new mission designs involving complex sequences of close-proximity maneuvers such as formation flying,[1] autonomous docking,[2] and on-orbit re-servicing.[3] If they can be implemented successfully, such mission architectures have the ability to revolutionize on-orbit operations.

Figure 1.1. Gemini 7 as viewed from the hatch window of Gemini 6 during the 1965 rendezvous maneuver. Source: NASA

However, the Gemini-era proximity operations were fraught with risk to both the mission and the crew. They relied heavily on the judgment and expertise of the highly-trained astronauts in the capsules, and in some cases were operated "by eyeball."[4] This bold approach to close-proximity operations does not lend itself to the low-risk, highly-predictable maneuvering of un-crewed vehicles envisioned in these mission architectures.

Researchers thus spent decades studying new ways to safely and robustly move spacecraft near one another, [5,6] leading to the many successes of the Shuttle program[7] and the development of the International Space Station.[8]

After almost 50 years since the initial Gemini rendezvous, NASA has once again prioritized research in advanced concepts for close-proximity operations. In the 2010 Space Technology Roadmap, proximity navigation, autonomous formation flying, docking and rendezvous, and proximity operations are all cited as essential technologies for future on-orbit endeavors.[9,10] This prioritization reflects the space community's recognition that robust and reliable close-proximity maneuvers are increasingly critical to advancing capabilities for future space systems.

In particular, the ability to operate multiple spacecraft within meters (or less) of one another offers expanded functionality that is difficult to achieve at larger relative distances. When combined with spacecraft modularity, close proximity operations may provide additional lifetime and mission-adaptability for spacecraft in the coming decades. Thus, there is a significant interest in various classes of proximity operations, including autonomous rendezvous and docking,[11,12,13] formation flying,[14] on-orbit reconfiguration and servicing,[15] on-orbit assembly,[16] and satellite grappling.[17] Advancements in these areas are redefining the state-of-the-art where on-orbit repairs or upgrades can be completed remotely from ground stations, satellite components are regularly launched in multiple vehicles to autonomously assemble in orbit, and spacecraft can be resupplied with expendables more effectively and economically than replacing the entire flight vehicle.

However, despite the considerable advancements in close-proximity maneuvers since the advent of the field, software-based approaches to these challenges have their limitations. They were strikingly revealed in 2005 by DART (Demonstration of Autonomous Rendezvous Technology) mishap. In this mission, errors in the autonomous guidance, navigation, and control software caused the spacecraft to collide with its intended rendezvous target.[18] Although the DART collision was relatively benign, this mishap is a sobering reminder that close-proximity maneuvers carry an inherent risk of collision, which can lead to the crippling or destruction of multi-million dollar hardware – or worse. Clearly, it is vital for the system to be robust and the relative position stable in the presence of a variety of control or navigation errors, environmental disturbances, and other factors of uncertainty. Focusing on the issue of robustness represents a path toward fully realizing the promise of close-proximity spacecraft operations.

1.2. The Physics of Magnetic Flux Pinning

One possible solution to these challenges lies in the field of superconducting physics. A phenomenon known as magnetic flux pinning (shown in Figure 1.2)

Figure 1.2. Magnetic flux pinning of a superconductor disk (large dark cylinder) and various magnets (silver/white square or cylinder) after cooling in a bath of liquid nitrogen.

provides a stiff non-contacting, passively stable, and naturally damped[19] connection between type II superconductors and a magnetic field. At a macroscopic level, a superconductor cooled in the presence of a magnet produces a nonlinear potential well that acts to keep the magnet in the relative position and orientation that it has when the superconductor cools below its critical temperature. This effect enables superconductors not only to levitate a magnet in a 1-*g* environment, but also to hold the magnet in that equilibrium when suspended under or next to the superconductor (in up to six degrees of freedom), as shown in Figure 1.2. Figure 1.3 shows a magnet flux pinned in an unusual equilibrium to illustrate the passive stability and versatility of the effect.

This effect, described in more detail in Chapters 2 and 3, occurs because magnetic fields penetrate the superconductor below its material-dependent critical temperature (T_C) and quanta of flux become trapped on defects in the superconductor's material lattice. These trapped magnetic flux lines induce so-called supercurrent vortices in the superconducting material, which then act to resist changes to the trapped or "imprinted" magnetic flux distribution via Lenz's Law.[20,21] The distribution of magnetic flux present at the point when the superconductor crosses below its critical temperature defines the equilibrium that the superconductor maintains.

Figure 1.3. A 58 mm diameter, 18 mm thick YBCO disk (bottom) with a magnet pinned at a position that would otherwise be unstable in gravity.

The end result is that the superconductor effectively pins the magnetic field source in an equilibrium defined by the magnet's position and orientation during the cooling process (referred to here as the "field-cooled" state). Perturbations from this equilibrium are counteracted by a nonlinear restoring forces and torques produced by the superconductor and require no externally applied power or active control.[22] The equilibrium position imprinted in the superconductor remains in place as long as the superconductor is kept below its critical temperature. The effect is erased by heating the superconductor above that temperature, and a new equilibrium can then be set as the superconductor is cooled again.

The superconductor examined in this work is Yttrium Barium Copper Oxide ($YBa_2Cu_3O_x$), or YBCO, which is a ceramic-like material (see Figure 1.3) that was discovered by researchers in the University of Alabama and the University of Houston in 1987.[20,23] YBCO has become one of the most well-studied high-temperature superconductors in literature, making it a convenient baseline for technology development efforts. This superconductor starts its transition to superconductivity at 93 K and generally has the characteristic zero-resistance superconductivity around 88 K.[20] For the purposes of this work (from an engineering perspective), the critical temperature is taken to be 88 K, although many physicists will quote the slightly higher 92 or 93 K.[24] Previous research has established that for a YBCO disk 5.8 cm in diameter and 1.8 cm thick, flux pinning effects can be seen at separation distances up to 10 cm, although the flux-pinning force can support a typical NdFeB permanent magnet's weight in 1-*g* at a field-cooled distance on the order of only centimeters.[19]

Flux pinning exhibits high stiffness and damping over a range determined by the strength of the magnetic field and the field-cooled position and orientation of the magnet. The stiffness, damping, and equilibrium of the flux pinning effect can be tuned for particular applications (for example, by augmenting a permanent magnet's field with that of an electromagnet) or to constrain particular degrees of freedom. A completely asymmetric field exhibits a change in magnetic flux when moved in any degree of freedom; so, the superconductor-magnet system exhibits stiffness in all six rigid-body degrees of freedom. For an axisymmetric field, however, the superconductor does not respond to motion about the axis of symmetry because there is no change in magnetic flux. Thus, this motion does not exhibit any stiffness from the superconductor. This property of flux pinning enables a cylindrical magnet (dipole) to spin freely about its longitudinal axis, while a magnetic field from a square magnet settles into one of the four spin-symmetric equilibrium positions.

1.3. Flux-Pinned Interfaces (FPIs) for Spacecraft

The passively stable, adaptable, and stiffly damped relative motion that flux pinning requires no computation and no power beyond what is necessary for cooling and is therefore an attractive feature for interactions between spacecraft in close proximity to one another. For this reason, a technology known as the flux-pinned interface (FPI) is being developed to enable spacecraft to exploit these natural physics in governing the dynamics between two spacecraft within meters of each other. A flux-pinned interface consists of any system where flux pinning is used to influence the relative dynamics of spacecraft, but it is generally composed of an array of

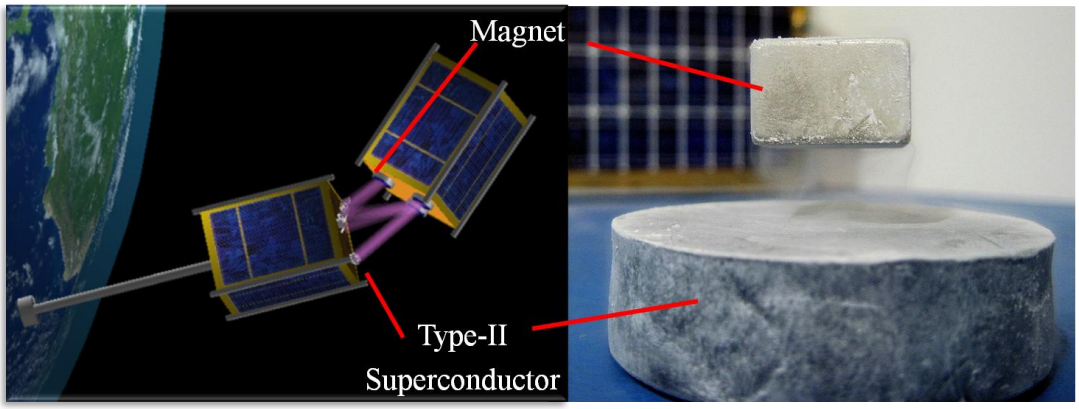

Figure 1.4. A flux-pinned interface for spacecraft (FPI) typically consists of a magnet array and a superconductor array on different satellites that then use flux pinning dynamics to influence their relative motion.

magnets on one spacecraft and a superconductor or array of superconductors on another as shown in Figure 1.4.

With the properties of flux pinning physics, the FPI can maintain a passively stable equilibrium position in all six degrees of freedom, and may be turned off or reversed (to provide undocking capability). The relative equilibrium of the spacecraft can be altered in orbit simply by changing the magnetic field in the FPI (for example, by varying currents in an electromagnet).[25] Flux pinning stiffness is likely sufficient to resist many perturbations commonly found in the space environment.[19] For these many reasons, FPIs offer a robust, flexible solution to proximity operations for spacecraft in a relative distance range that is typically filled with significant risk.

The natural dynamics of the FPI can provide a wide range of benefits to many different close-proximity applications. For example, it can provide impact attenuation for docking maneuvers because a restoring force from the superconductor can resist a collision even in the event of a loss of control. Modular space systems linked with flux pinning have tunable stiffness and damping properties while in a passively stable

formation with inter-module separation distances up to tens of centimeters. In a virtual space structure, spacecraft can be locked together with an FPI connection and later released, safely enabling applications such as repairing or refueling modularized space systems. FPIs can also be uniquely applied to the problem of reconfigurable spacecraft by acting as non-contacting kinematic mechanisms.[26] By controlling the symmetries in the magnetic field, an FPI can act as a hinge joint during one phase of a maneuver, a cylindrical joint during another, and then convert to a fixed connection to hold the satellite formation in its final configuration.[27] These applications and others are illustrated in Section 9.2.

However, in order to be implemented in flight systems, the theoretical and technological development of FPIs must be advanced enough to validate their merit. The theoretical foundation must provide sufficient evidence of the system's stability and must lay the groundwork for appropriate modeling, simulation, and control

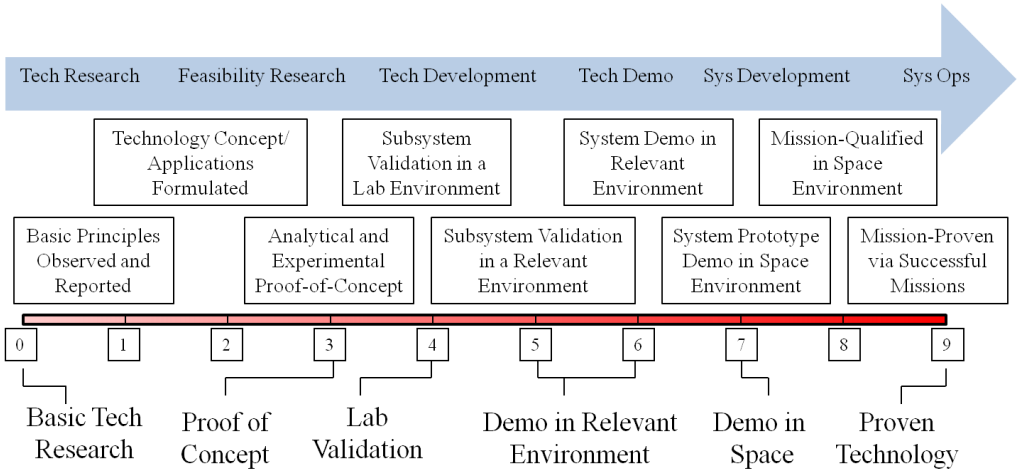

Figure 1.5. The Technology Readiness Levels as defined by NASA, where a technology moves from basic research to system operations. Each level corresponds to a set of guidelines regarding the requirements for a technology to achieve that particular level.

development. On the technological side, the FPIs must advance through the Technology Readiness Levels (TRLs), which are codified stages of the maturity of the technology. Progressing through these levels, which are shown in Figure 1.5, involves demonstrating functionality and performance at increasingly sophisticated and flight-like environments until the system is considered a proven technology at TRL 9.

1.4. Applications of Flux-Pinned Interfaces for Spacecraft

The unique features of flux-pinned interfaces can be leveraged for a wide variety of spacecraft applications. This dissertation sets the stage to explore a number of these different applications, which are described in more detail in Chapter 9. For example, using the stiff, alterable connections of an FPI, a payload segment can be pointed relative to the spacecraft bus though a non-contacting connection that damps vibrations. Using an FPI between separate modules can create a close formation flying system. Because of the easily modified FPI, individual vehicles in the system can be replaced to repair broken subsystems of the formation. This close proximity capability can also be used to assemble larger structures that are prohibitively difficult to launch as a single unit.

The ability of FPIs to passively enforce a specific relative alignment between spacecraft modules allows them to greatly improve docking procedures. An FPI can assist docking by guiding the system to a known position, or augmenting a human-controlled grappling arm to ease the task of capturing another vehicle. Once connected by a flux-pinned interface, a multi-modular system could use the interface to reconfigure, providing task-specific arrangements of modular components. Because flux pinning can be applied on widely varying physical scales, these principles can be

leveraged to construct a particular solar sail, with each small component connected to its neighbors via flux pinning and able to be independently actuated for optimal steering.

1.5. Contributions of this Work and Organization of the Thesis

This paper examines a cross-section of various aspects of both theoretical and technology development work related to flux-pinned interfaces for spacecraft. It highlights the following major contributions of this research:

- Development of design principles for close-proximity spacecraft interactions influenced by flux pinning
- Extension of the frozen image model of flux pinning to include the full nonlinear multi-magnet six-degree-of-freedom equations of motion
- Proof of the stability of a general class of FPIs
- Establishment of FPI actuation principles and control techniques inspired by passivity principles
- Formulation of a magnetic steering law for FPI control
- Experimental validation of FPI architectures in both a laboratory and microgravity environment
- Formulation of FPI-driven mission architectures and flight-operations strategies

The dissertation is organized into nine chapters, of which this introduction is the first. Chapter 2 provides background information on relevant research and previous work related to FPI applications and other magnet-based spacecraft actuation techniques. Chapter 3 details the modeling of the FPIs and sets up the theoretical model and framework within which the FPIs are analyzed. Chapter 4 then details various actuation strategies and design principles based on a series of simulations.

Chapter 5 details the theoretical stability and control synthesis work for FPIs. Chapters 6 and 7 describe the experimental setup and results of various technology-development efforts and associated support activities in the laboratory and in microgravity, respectively. Chapter 8 discusses designs and considerations for orbital FPIs. The last chapter wraps up the dissertation with an assessment of the prospects for FPI as a technology for spacecraft including descriptions of various FPI applications, and summarizes the contributions of this dissertation. Subsequent appendices provide information from additional work that was conducted during the period of this dissertation but does not directly fit into the body of the work.

CHAPTER 2

RELEVANT RESEARCH AND PREVIOUS WORK

2.1 The Path to Flux-Pinned Interfaces

It is important to fully understand the context surrounding flux-pinned interfaces for spacecraft before examining fundamental analytical and technological content related to the concept. Thus, this chapter describes common practices and state-of-the-art research in fields relevant to FPIs, including close-proximity spacecraft applications, magnet-based spacecraft maneuvering techniques, current applications of flux pinning, and past work that has laid the groundwork for the presented FPI research. The more technical and mathematical background material that is necessary for specific analyses or more detailed topics is provided in the beginning of individual chapters.

2.2 Current Approaches to Close-Proximity Spacecraft Maneuvers

The niche that flux-pinned interfaces have the potential to occupy in close-proximity operations is directly related to the industry's current methods for achieving these maneuvers. This section highlights key technologies and methodologies that are relevant to potential FPI applications, focusing when possible on modern techniques that are flight-proven or currently in use.

2.2.1 Autonomous Docking and Rendezvous

Although perhaps not the same as "autonomous," at least one source claims that Russia completed the first "automatic" docking on orbit in 1967 and the first

successful "automatic" flyby during the Mir era.[28] Most other space-faring entities have claimed their own independently success much more recently, including the US and Europe. America demonstrated its first successful autonomous rendezvous in April of 2007 – only two years after the ill-fated DART mission[29] – when the satellites ASTRO and NextSat autonomously rendezvoused and docked on orbit during DARPA's Orbital Express mission.[30] Europe was not far behind; a year later it celebrated the first autonomous docking of its Autonomous Transfer Vehicle (ATV), the Jules Verne, with the International Space Station (ISS).[31] More recently, commercial companies have been making strides in docking (although not yet autonomously) with the successful 2012 docking of the SpaceX Dragon capsule to the ISS.[32]

Although unsuccessful due to an error in the GNC software, DART's general methods for achieving autonomous docking are still valid and effective ways to approach this docking scenario. The DART chaser spacecraft first performed several Clohessy-Whiltshire transfers in order to maneuver within one kilometer of the target spacecraft, MUBLCOM. Once within that range, the spacecraft initiated a series of –V-bar and +R-bar maneuvers to evaluate the sensor and algorithms performance prior to the attempted rendezvous. The spacecraft was intended to use its Advanced Video Guidance Sensor (which featured a GPS receiver, laser range finders and an optical detector to capture returns from the retroreflective arrays on the target) to perform the final approach. The final maneuver was designed with a number of safety precautions as the relative distance between the spacecraft decreased. DART was to approach the target twice to within 5m, and then perform a simulated collision avoidance maneuver

to ensure the system was in working order prior to the final docking.[29] The navigation failure occurred at a relative distance of 200 m, prior to the full implementation of the AVGS, and so the spacecraft moved forward without accurate laser ranging information. DART ended up colliding with its target at a relative velocity of approximately 1.5 m/s, fortunately without any apparent damage to either spacecraft.[18]

Orbital Express, implemented successfully only a year later, used many similar anti-collision procedures and precautions to DART, as well as using the same AVGS sensing packet to perform the final maneuver.[30] After following the DART docking procedure (but with a corrected guidance system), Orbital Express was able to pump fuel to and from the target spacecraft, transfer a battery to the target, and perform an undocking and re-docking maneuver.[30]

The Jules Verne ATV is unique in that its control sequences were designed for an autonomous docking with a manned space station. Thus, it includes a human-in-the-loop failsafe procedure for astronauts to activate in the event of an imminent collision. The ATV approaches from a distance of 250 m for the final maneuver at a speed of 7 cm/s with 1.5 cm precision to the target,[31] using a newly design laser-based videometer with two secondary telegoniometer sensors to govern docking with the ISS.[8]

The Dragon capsule, while again not fully autonomous, performed a fly-by of the ISS prior to the docking attempt in order to validate flight software. Although much of its procedures are too new to have been published in detail, the final phase of the docking maneuver was performed by an astronaut manually grappling the capsule with the Canadarm2.[33]

2.2.2 On-Orbit Reconfiguration

On-orbit reconfiguration is a generic term often used to describe a formation of satellites that alter their relative orientations to achieve some end goal. For example, a formation may launch in one configuration to optimize its dimensions for a launch fairing, but then reconfigure on orbit to better perform its primary mission. One of the most dramatic cases of spacecraft reconfiguration is the International Space Station which, over the course of many years, has been reconfigured multiple times by astronauts manually manipulating the relative orientation of the modules.[29] However, other more theoretical concepts have been researched as a way to fully exploit a multi-module formation of spacecraft.

The problem of spacecraft reconfiguration is particularly challenging because a realistic system includes highly nonlinear dynamics and constraints. For example, several studies have explored formation reconfiguration using optimization methods, with particular attention to the constraints on the attitude and position of the orbital system, [34] performing collision-free maneuvers using minimal energy,[35] and using a heuristic approach to maneuvering planning that avoids collisions.[36] Current work has shown solutions for two-,[35] three-,[36] and four-[34] spacecraft formations that successfully avoid collisions, but only using carefully designed active control algorithms and heavily optimizing over the expended energy of the system. These limitations are in large part because such maneuvers require significant thrusting corrections to work and the fuel costs quickly become a serious issue for these maneuvers.

2.2.3 Satellite Formation Flying

Formation flying is a concept by which multiple spacecraft can maneuver as a system while being physically separate entities. Using multiple satellites to achieve a goal improves mission flexibility because the individual vehicles can be repositioned in the formation to perform different tasks, and the failure of one element in the system does not halt the entire mission. Traditional formation flying techniques that have successfully flown on orbit (many completed as a part of the Gemini missions) have been limited to two spacecraft manually controlled by a human.[37] However, more modern techniques are moving toward optimized controllers that can manage the interaction of far more than two spacecraft in the formation. New capabilities such as pulsed plasma thrusters are revolutionizing how the formation flying concept is implemented and even more sophisticated techniques are being developed by researchers in the field.[37]

For example, Sabol attempted to show the cost-effectiveness of formation flying using the Draper Semianalytic Satellite Theory, where simulations showed that a formation with distances on the order of one kilometer produced additional maneuvering costs of only 0.0001 cm/s per year.[14] Researchers have also attempted to develop general control techniques for the problem of spacecraft formation flying. Hu and Ng, for example, published a robust controller for formation flying purposes in 2007,[5] which considered the effect of time-varying external disturbances from the space environment on a dual-spacecraft formation. They developed a robust control scheme to compensate for these disturbances and found a bounded error for the relative motion of the system.

Several studies have shown the benefits of formation flying for a variety of tasks. For example, ESA launched the Cluster mission in 2000, which involves a tetrahedral formation of satellites that operate on relative distances ranging between 17km and 10,000km depending on the specific task. This mission has successfully operated for over a decade producing a three-dimensional map of the Earth's magnetosphere.[38] The TerraSAR-X satellite mission began flying in formation in 2010 when a sister satellite was launched into orbit. It performs Earth observations using radar imaging and flies in formation to act as a single, larger, SAR for increased imaging capabilities.[39] DARIS is a proposed low frequency (1-10MHz) radio astronomy mission that forms a very large aperture array using 6 small satellites (less than 100kg) in formation with a seventh, larger satellite of approximately 900 kg. The large satellite acts as the central node of the array, as well as the downlink communications hub.[40] Missions such as these illustrate the advantages offered by formation flying and provide a motivation for developing FPI technologies for these applications.

2.2.4 Grapplers and Robotic Arms

Robotic arms have played an increasingly significant role in complex spacecraft operations, especially those in which spacecraft are maneuvered within meters of one another. For example, the Canadarm was used on the Space Shuttle for 30 years as the payload bay's primary manipulator. It can capture a target even with initial misalignments of 10° in roll, 15° in pitch and yaw, and a radial misalignment of 0.1m.[17] Robotic arm technology also plays a key role in many concepts for on-orbit servicing and refueling, such as on the Orbital Express mission. One of the most successful modern robotic arms is Canadarm 2 on the ISS.[41] Installed in 2001, it works

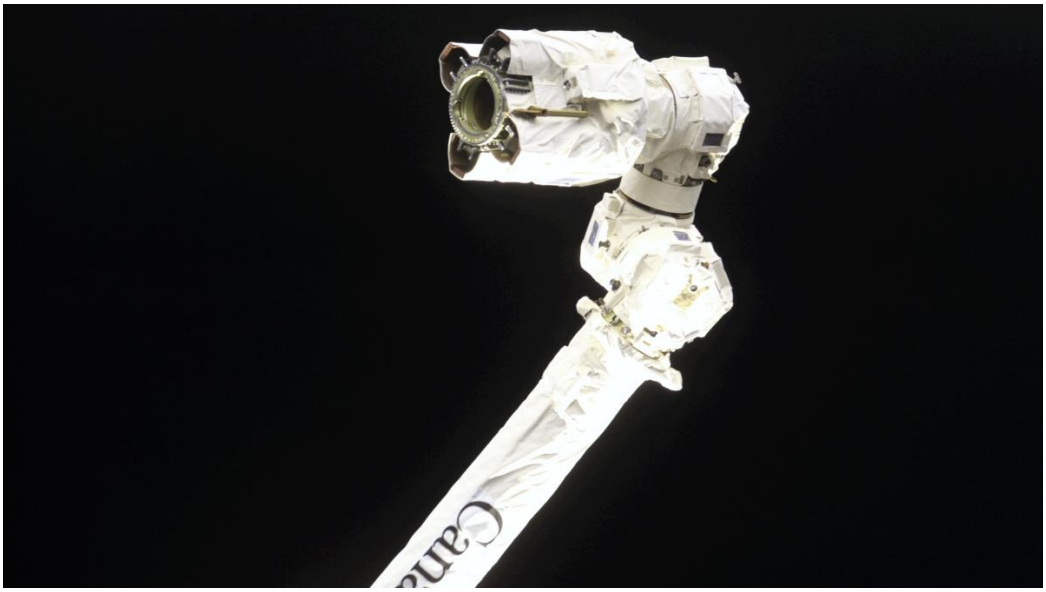

Figure 2.1. The Canadarm end effector used on the Space Shuttle. Image courtesy of NASA.

in tandem with the Dextre 'hand' robot, to use a variety of tools to perform various tasks and partially replace the need for human spacewalks.[42] A flux-pinning grappler would likely use similar technology for the arm itself, giving it similar performance characteristics.

The major difference between an FPI grappler and a normal robotic arm is the end effector. On the Canadarms, the end effector is designed specifically to accept a standard interface used on mission payloads. Candarm can provide power and control to alternative end effectors that can be connected automatically on top of the existing structure.[17] The FPI version of this alternative end effector would involve a small cryocooler with an active thermal control that can be imprinted with a magnet field for manipulating a satellite with on-board magnets without the need for actual contact. A photograph of the Space Shuttle's Canadarm end effector is shown in Figure 2.1.

2.3 Magnetic Control Strategies for Spacecraft

The concept of using magnetic interactions to manipulate spacecraft is not new. Although they do not use flux pinning, many different techniques exist (either in practice or in concept) that use similar forces to manipulate the behavior of a space system. However, if should be noted that techniques that rely purely on r^2 laws cannot be passively stable in all six degrees of freedom (DOF) according to Earnshaw's Theorem.[43] This theorem states that a collection of point charges under the influence of magnetic or other electrostatic forces cannot maintain a stationary stable equilibrium. Flux pinning neatly side steps this restriction, and so FPIs are the first technology to offer these traits to spacecraft.

2.3.1 Magnetorquers

Magnetorquers (also known as torque rods or coils) are one of the most commonly used magnet-based techniques on orbit. These attitude control devices have been used on the Hubble space telescope,[44] commercial communications satellites,[45] and Cornell's own upcoming Violet satellite.[46] They work by powering an electromagnet that then interacts with the Earth's magnetic field to apply a torque on the spacecraft. As a result, they work best in low earth orbit and are subject to the variations in the Earth's magnetic field. Magnetorquers generally cannot produce torques that are parallel to the Earth's magnetic field. However, they can be fairly compact and easy to implement, and so are especially popular on small satellites for de-saturating reaction wheel control systems.[44,45] Although these control devices have been in use for decades, new research is still being conducted to exploit these devices to their fullest capabilities. For example, some research has been conducted on using only

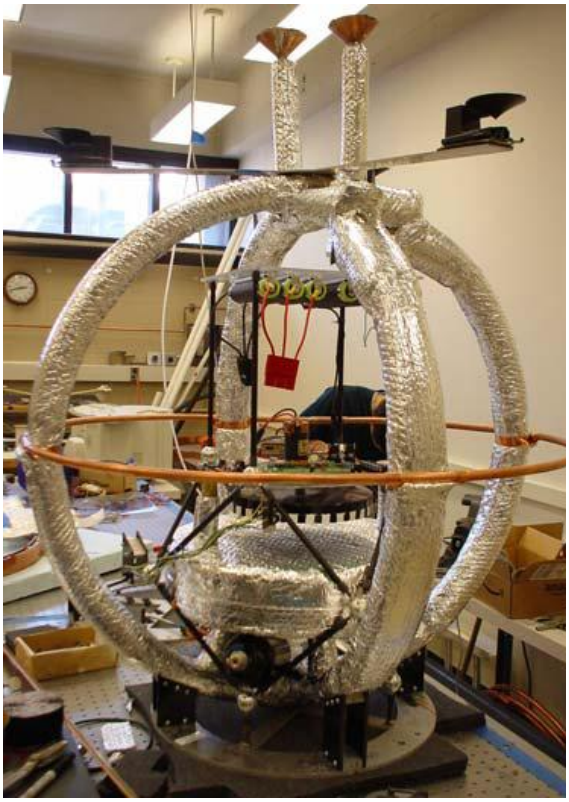

Figure 2.2. MIT's Electromagnetic Formation Flying testbed. [52]

magnetorquers to control all three axes of a spacecraft.[47] In one paper Wang proposes a method to control spacecraft attitude using only magnetic torquers by using a sliding mode controller to impose stability on the passively unstable behavior of the system.

2.3.2 Magnetic Manuevering Techniques for Spacecraft

More advanced research has examined theoretical and experimental concepts related to controlling the charge of a spacecraft in order to manipulate its position relative to other charged spacecraft. Three of these concepts, known as electromagnetic formation flying, Coulomb formation flying, and electromagnetic docking, are particularly noteworthy.

Electromagnetic formation flying uses electromagnets to generate magnetic fields which control the separation between spacecraft modules. Studies have shown that this force is sufficient to control a system on the order of the Terrestrial Planet Finder mission at distances of up to 150 m.[48] In order to control the relative position in the formation, these magnetic fields can be combined in various configurations to produce attraction and repulsion forces to perform a maneuver of the modules. [49] Kwon and Miller have studied applying electromagnetic formation flying to sparse aperture arrays. [50] They found that in combination with reaction wheels, electromagnets can

replace attitude systems which depend on consumables. The Space Systems Laboratory at MIT has built an experimental testbed – the Electromagnetic Formation Flying (EMFF) testbed pictured in Figure 2.2 – for examining these concepts in the laboratory.[51,52]

Another relevant formation flying technique – Coulomb formation flying – was proposed by Schaub at the University of Colorado.[53] This technique allows for relative spacecraft distances on the order of tens of meters with a response time on the order of milliseconds. Although static solutions are unstable, researchers working on this technique have developed a nonlinear orbital element-based feedback control strategy.[54] Other directions for this research include complex, spinning formations and three- and four- satellite formations. This novel approach to formation flying enables proximity distances in a range not generally considered by other techniques. However, implementing the high uniform charges necessary to make the system work (without arcing) is a yet-unaddressed challenge.

Electromagnetic docking techniques are another area of current interest in applying electromagnet control to spacecraft operations.[55] Like flux pinning, this technique (which only uses electromagnets) has the potential to self-dock, although it can theoretically perform these maneuvers at a distance of three meters. This highly nonlinear system has many degrees of freedom and requires a precise control of the electromagnet to within 10^{-3} mA to maintain stability.[55] Current research is focused on developing LQR and tracking control methods to develop a 6DOF controller that can govern the motion of the docking spacecraft to within these constraints.[56]

Figure 2.3. A CubeSat CAD model based on parts from CubeSatKit.com.

2.4 Small Satellites as a Platform for Advanced Research

Much of the research work discussed in this dissertation focuses on scaling appropriate for small satellites below 50 kg. Although most of the major advancements in spacecraft technology have been demonstrated on traditional, large spacecraft, there is a growing recognition that small satellites offer a viable science[57] and technology validation[58] platform, often with shorter development times and more cost-effective launch options. For example, in 2007 a 10kg small satellite in the CTSB1 program measured CubeSat performance in photography on orbit.[59]

Although some orbital concepts for FPIs use 50 kg satellites as a baseline, much of the FPI research work has been developed around the class of small satellites known as CubeSats. The one-unit (or 1-U) CubeSat standard is a 10 cm cube with a 1 kg mass (see Figure 2.3).[60] In the original paper, CubeSats were envisioned to standardize small satellites for low-cost development and deployment. The paper details the CubeSat standard size, capacities, and launch mechanism. The paper also lays out additional guidelines for the standard, such as the prohibition of explosives, designs for external mounting hardware, and compatibility requirements for the standard launch system.

Ultimately, this standard for small satellites has become enormously popular, particularly with universities. Its standard structure and commercial-off-the-shelf parts

make it easy to integrate a viable bus and focus on payload development, while the P-POD launch systems have enabled CubeSats to find launches with relative ease.[61] The P-POD launch system, developed by Cal Poly, was first used for CubeSat deployment in 2003, although it has since been revised for better access to both payload CubeSats and launch vehicles.[62]

Many developers are now exploiting the standard for relatively larger satellites based on the 2-U and 3-U CubeSat standards and larger numbers of those satellites.[61] These expanded standards have enabled CubeSats to contribute to significant research by providing a platform for testing new solar panels,[58] performing imaging missions,[59] and conducting on-orbit technology demonstrations (although the NanoSail-D mission did not make orbit due to a launch failure).[63] The QB50 mission, which is currently in development, calls for a mission using 50 2-U CubeSats.[64] This mission hopes to launch all 50 CubeSats in a single vehicle in 2014 in order to create a satellite network to gather thermosphere Earth-science measurements. Innovations such as these are pushing CubeSats to the forefront of space technology research, and are therefore a promising scale at which to develop FPI technology.

2.5 Flux Pinning Research and Current Applications

The late 1980s throughout the 1990s saw an explosion in research related to applications of high-temperature superconductivity after the discovery of superconducting materials that could be cooled below their critical temperature with liquid nitrogen. Because superconductors are particularly interesting from a physics perspective (particularly those that flux pin, as described in Chapter 3), much of the initial research into flux pinning focused on manufacturing techniques of type II

superconductors,[65,66] the discovery and characteristic comparison of new superconducting alloys,[67,68] and techniques to change the various characteristics of the superconductor's performance (such as strengthening pinning sites).[69,70] While these research efforts greatly contributed to the high-quality superconductors available today, much of this research is not particularly relevant to the spacecraft-dynamics perspective on flux pinning. Thus it is not examined further in this work.

However, some of the basic characterization efforts do have a significant influence on FPI behavior and design. For example, studies of hysteresis in the superconductor[71,72] and the influence of AC currents on pinning strength[73,74] both have an impact on the design parameters for FPIs. Also, the material properties such as the critical temperature or critical fields of YBCO are important to bear in mind for FPIs.[75,76] Each of these topics are discussed in more detail in subsequent sections (hysteresis in Chapter 3, flux degradation due to AC currents in Chapter 8, and YBCO properties in Chapter 3) and so are not repeated here. Another established characteristic of flux pinning that may be relevant but is not discussed in more detail in this work is the flux density as a function of magnetic field.[77]

Beyond basic physics and characterization work, flux pinning is already being applied to many existing technologies.[75] One of the most enduring applications for flux pinning in literature involves levitation in a 1-*g* environment. Studies have shown that flux pinning can be particularly valuable in levitating trains.[78] Mag-lev trains currently use repelling magnets below and alongside the train to support the train-mounted magnets. Flux pinning can offer increased stability with reduced power requirements by mounting the superconductors on the train and permanent magnets on

the rails. This application is so compelling to the community at large that it is often the motivation for a host of related flux pinning research in the stability of the levitated object, [79] the rigidity of non-symmetric magnetic fields pinned to superconductors,[80] improving the lateral stiffness,[22] and comparing the forces affecting magnet tilting and magnet traversal.[81]

Other common applications for these types of superconductors are power transmission,[82] frictionless bearings,[83,84] and vibration-free platforms.[83] In fact, the idea of frictionless flux-pinned bearings exactly follows the concept of a FPI-based kinematic joint, where the non-stiff degree of freedom is exploited to offer several advantages compared to traditional bearings. Non-contacting bearings, of which flux-pinned bearings are the most studied, provide almost zero friction, reduce heat buildup, and prevent mechanical wear. Some drawbacks of these devices, which are currently limited to conceptual designs, are the low stiffnesses in the device and the need for auxiliary parts.

With this extensive background in published characterization and application work, flux pinning has developed the necessary contextual depth in both a theoretical and experimental regimes to be proposed as the basis for a new spacecraft technology. However, the intense focus on Earth-bound applications and the lateral motion and stiffness has left some areas of research incompletely explored. In particular, little attention appears to have been paid to the full six-degree-of-freedom problem with multiple interacting magnets which are necessary to fully describe the dynamics of FPIs. This problem is examined in this work.

2.6 Prior FPI Results and Parallel FPI Research Work

The concept for flux-pinned interfaces was first developed in 2006 as a method to connect fractionated space systems,[85] with Shoer[86] and Norman[87] jointly investigating the concept. In his original work, Shoer characterized the stiffness of a magnet-superconductor pair using a robot arm and a pendulum experimental setup. He reports stiffness at various relative distances, with a stiffness of 100 N/m at a separation distance of 1 cm (the most commonly used initial relative distance in this work). One experiment finds the 6DOF linear restoring forces and torques on a FPI for small (mm-scale) displacements from an equilibrium. A second experiment finds the stiffness and damping for a FPI for a range of zero to three centimeters. He concludes that for this range of separation distance, the examined FPI exhibited useful pinning strength for spacecraft applications. This paper was eventually accepted in its journal form in 2009.[88]

Norman took a slightly different direction in his original paper on flux pinning. In it, he considers the flux-pinning effect as a means of connecting a satellite formation. Modeling the FPIs as a linear system, he uses a series of linearized equations to examine the stability of a formation for a two-body and tetrahedral case.

As this preliminary research began to show promising results, in 2008 the team expanded to examine broad applications-based such as the work by Gersh.[159] Gersh wrote a paper proposing the design of a flux-pinned large-aperture space telescope. In this concept, the mirror segments would use FPI connections to assemble on orbit and then exploit the FPI's passive stability to maintain their relative position. In this paper she discusses a sparse-aperture architecture where identical mirror segments are flux-

pinned together to form a spherical manifold surrounding central detector. Although these mirror segments are not a formation in the traditional sense of the word, the structure would be passively stable and would enable telescopes of a size currently impossible to launch in one vehicle. Her broad conclusions are that FPIs would be an advantageous solution to the assembly of a large space telescope. This work has been developed further in analyses in 2011.[89,90]

Norman continued his theoretical development of FPIs on spacecraft by modeling and simulating the station-keeping of an *n*-body satellite formation connected using FPIs. [91] The motivation for the paper also cited a space telescope with FPI-connected mirror segments. In the paper, which was eventually published in the Journal of Guidance, Control, and Dynamics,[92] Norman uses Kordyuk's frozen-image model (also used in this work, and described in Chapter 3) to develop a mathematical framework for a satellite formation governed by flux-pinned equilibria. He ultimately establishes that a passively stable ring formation telescope can be established without the need for feedback control. Norman also investigates the linearized equations of motion between two spacecraft connected by an FPI.[158] He uses the Kordyuk model to derive a linearized system of the spacecraft formation. This work is also notable because Norman applies feedback control on-orbit, using a linear state-feedback control law and using linearization of the non-linear model to obtain the gains.

During 2008 Shoer published a paper,[19] which ultimately appeared in the Journal of Spacecraft and Rockets,[26] describing the use of FPIs for CubeSats. In this paper he described the mechanism by which FPIs can operate as alterable kinematic mechanisms, particularly for spacecraft reconfiguration. The paper also contains

experimental data on a flux-pinned pendulum system where different modes were excited by varying the current input to an electromagnet pinned to a superconductor. Shoer also employs Kordyuk's results to model the FPI and compare to the experimental findings.

In 2009 Shoer generalized his flux pinning research to discuss his concept of passive spacecraft reconfiguration (enabled by FPI kinematic joints) and a hybrid control technique for achieving this architecture.[19, 93,27]

The first laboratory technology development work was started in 2009 by Wilson[94], who published the results of the first functional prototype of an FPI revolute joint. These results led to the first FPI microgravity project over the summer of 2009. The results of this work were published in the Journal of Spacecraft and Rockets[161] and are discussed in Chapter 7.

In 2010, a significant amount of laboratory development work produced the FloatCube testbed,[95,96] which serves as a 3-degree-of-freedom air-bearing testbed for CubeSat-scale spacecraft. The second FPI microgravity flight took place in the fall of 2010, and so the results of this work were published the following year.[97] These results are presented in Chapter 7.

2.7 Present Work in the Context of FPI Research

This dissertation covers FPI work performed from 2008 to 2012, a period in which many of these parallel FPI efforts were underway. It covers application-based studies drawn from conceptual work detailing the use of FPIs novel solar sailing techniques[162] and docking and rendezvous. [160] Details of this work are included in Appendices A and B.

Although other researchers have used the frozen image model of flux pinning (described in Chapter 3) to analytically study the behavior of an FPI as described above, this dissertation is the first publication of the fully nonlinear multi-magnet implementation of the model in all six degrees of freedom. This work also represents the first Lyapunov[98] proof of FPI stability for passive and active control. The model discussed here is not linearized because other FPI researchers have already examined this approach to the system. Using this expanded model, this dissertation examines actuation techniques for FPIs with multiple magnets.[25] This analysis is the first of its kind; no other FPI researcher has published work relating to the performance of these FPIs under different actuation conditions. This work is discussed in Chapter 4.

The dissertation also covers a number of technological development efforts that are unique contributions in the context of other FPI work. While other researchers have used prototype laboratory experiments to characterize FPIs, this work is the first to analyze FPIs in hardware at a component and system level. As a part of that effort, this work also details the unique CubeSat-scale dynamics testbed developed for FPI hardware. The present work also details the results from the first demonstrations of FPIs in a microgravity environment, which were performed in conjunction with other FPI researchers.

CHAPTER 3

FLUX-PINNING THEORY AND FPI MODELING

3.1 Flux-Pinning Physics and Superconductor Properties

3.1.1 Type I vs. Type II Superconductors

Superconductors were discovered in 1911 when the resistivity of Mercury samples was found to drop to zero when the sample was cooled below about 4 K, its critical temperature.[99] A few decades later, it was found that superconductors interact with magnetic fields in unusual ways. For example, all superconductors exhibit a phenomenon known as Meissner Repulsion, where the superconductor expels the magnetic flux from its interior once it is below its critical temperature, as shown in Figure 3.1. This effect occurs as a result of small superconducting current loops induced into the superconductor, creating a shielding magnetic field that exactly cancels the applied magnetic field.[100] However, if a sufficiently strong magnetic field (the critical field, B_c) is applied to the material, it loses its superconducting state and once again becomes a "normal" material. These early observations about superconductors such as

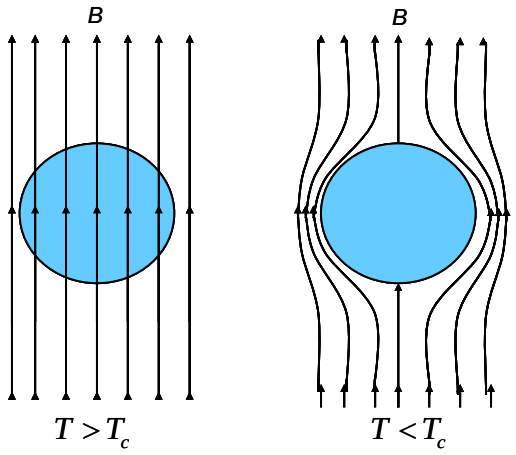

Figure 3.1. (a) Above the critical temperature, the superconductor (shown as a circle) is unaffected by the magnetic field lines. (b) Once below the critical temperature, the superconductor exhibits the Meissner effect and repels the magnetic field lines from its volume .

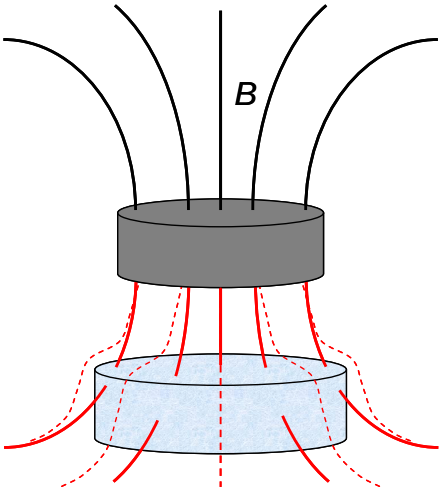

Figure 3.2. The superconductor (shown as the cylinder at the bottom) exhibits Meissner repulsion (dashed flux lines) in the presence of weak magnetic fields, but for sufficiently strong magnets the type-II superconductor reaches its mixed state and the flux lines enter the superconductor's volume.

lead, aluminum, and tin, (all now known to be type I) were the mainstay of superconductivity research until the 1950s.

In 1957, however, researchers discovered that certain types of superconductors (now called type II) exhibited very different magnetic interactions from those documented in earlier studies.[101] In particular, these superconductors have an intermediate phase between superconducting and normal, called the vortex or mixed state, which is defined by a region in between two critical field values (B_{c1} and B_{c2}). When cooled below its critical temperature and exposed to a magnetic field above B_{c1} and below B_{c2}, the superconductor allows magnetic flux to enter its volume via regions of non-superconducting material, as shown in Figure 3.2.[20] These trapped lines of magnetic flux induce supercurrents in the superconducting portion of the material as shown in Figure 3.3. These supercurrent vortices (often called fluxons) resist changes in the magnetic

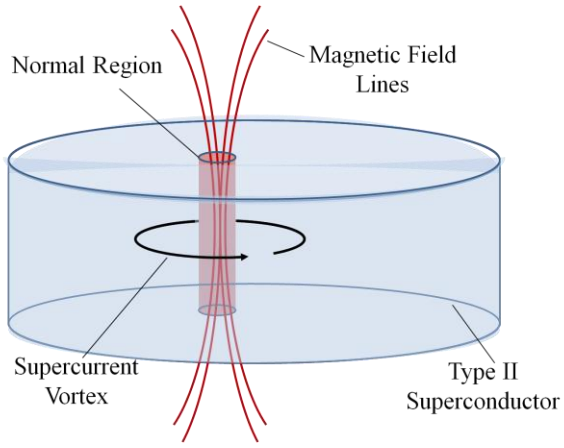

Figure 3.3. A type II superconductor in its mixed state allows flux lines to penetrate its volume through regions of normal (non-superconducting) material, inducing supercurrent vortices. Although only one such region is shown, many exist.

flux via Lenz's Law. Lenz's law states that a change in magnetic field creates an electric potential, and so electrons flow to oppose the change. This action in turn resists the motion of the source magnet, and the resulting non-contacting forces and torques are the macroscopic effects exploited in FPIs.

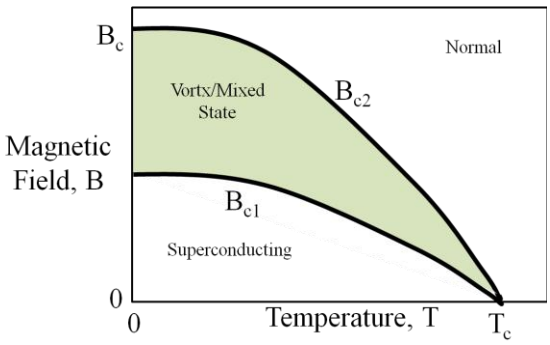

Figure 3.4. Representation of a generic type II superconductor plot of critical magnetic fields as a function of temperature. Above B_{c2}, the material behaves as a normal conductor and below B_{c1}, the material behaves as a type-I superconductor and only exhibits Meissner repulsion. Flux pinning occurs between the two lines. Taken from Serway, et. al. 2005.

The critical fields of type II superconductors are temperature-dependent and show the relationship illustrated in Figure 3.4,[24] (which was remade based on the plot on page 493 of Reference 20). When no magnetic flux is present at the point the superconductor crosses below its critical temperature (a zero-field-cooled state), the superconductor exhibits the Meissner repulsion characteristic of the pure superconducting state. However, if the superconductor is cooled in the presence of a strong enough magnetic field (field-cooled), the superconductor instead enters its vortex state. It is in this state where flux pinning occurs. Any flux trapped within the superconductor's volume during that temperature transition induces supercurrent vortices, setting the equilibrium flux distribution that the superconductor then acts to maintain.

3.1.2 Altering the Flux Distribution and Hysteresis

Certain conditions make it possible to hysteretically alter the flux distribution within the superconductor, and thus change the equilibrium it seeks to enforce.[102] One way to irreversibly change the magnetic flux distribution is warming the

superconductor above its critical temperature. This act erases the imprinted magnetic flux. Thus, if the superconductor is cooled below its critical temperature again, the superconductor imprints with a new magnetic distribution and cannot maintain the original equilibrium. Although unintentionally warming the disk is undesirable for FPIs, this property can be exploited as a technique for re-training new equilibrium positions and orientations into the FPI if the application calls for this capability.

Another way that the flux distribution can be altered is by forcing the fluxons to leave their pinning site. As discussed above, when a superconductor is in its mixed state, some regions of the disk (often impurities or variations in the material's structure) do not reach a superconducting state. These so-called pinning sites lock quanta of magnetic flux tubes (fluxons) in place via an energy barrier. In order to move away from the pinning site, the fluxon must overcome the pinning force, as shown in Figure 3.5.[103] Hysteresis occurs when these fluxons successfully move from their pinning site, and the equilibrium set by field-cooling is no longer enforced. The magnet may still be in an equilibrium with the superconductor, but it is based on the new magnetic flux

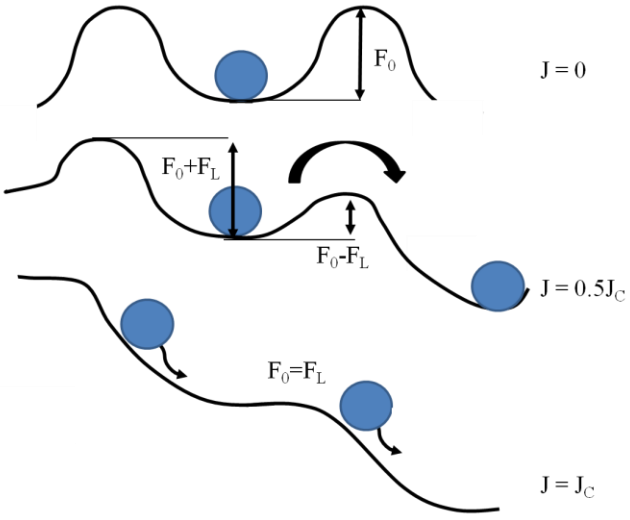

Figure 3.5. A representation of flux-flow, where flux lines (circles) must overcome an energy barrier (pinning strength) to move to a different site. Under a Lorenz force, the energy barriers become easier to overcome. Taken from Sheahan, 1994.

distribution instead of the original field-cooled configuration.

Applying a current through the superconductor can cause this phenomenon to happen more readily because it applies a Lorentz force on each fluxon.[104] The Lorenz force overcomes the flux pinning force at the critical current density (J_C), at which point the superconductor stops flux pinning.[104] The effect is known as flux-flow. Hysteresis can also occur when thermally activated fluxons move to other parts of the lattice due to the Lorentz force in a phenomenon known as flux-creep.[105]

For most FPI applications, hysteresis should be minimized because it reduces the predictability and reliability of the system. Thermal variations over time in the superconductor should also be avoided to minimize risk of the accidental loss of the imprinted flux distribution. Although most FPI designs do not directly apply current through the superconductors, using electromagnetic actuators on a superconductor can have a similar effect (discussed in Chapter 8). Spacecraft designers should be aware of this effect and take steps to avoid inducing currents at or near the critical current.

However, hysteresis properties of the superconductor can be treated as a design parameter for the system. This issue can generally be addressed by selecting a superconductor that has been grown specifically to strengthen the pinning sites and minimize hysteretic effects. The YBCO disks used in this work, for example, are made from a single crystal, which tends to limit hysteresis.

3.1.3 High-Temperature Superconductor Properties

Although a number of type-II superconductors exist, the most important class for this work are the ones known as high-temperature superconductors (HTSC). These superconductors have critical temperatures above 30 K (and ranging as high as 134

K). Of these, the ones that have critical temperatures above the boiling point of liquid nitrogen (77 K) are most popular for practical applications because they are relatively inexpensive to cool in a laboratory environment. For space applications the thermal requirements will relax considerably for a HTSC with higher critical temperatures. Table 3.1 details a subset of various superconductor properties.[20,24]

The choice of the particular high-temperature superconductor used in an FPI influences a number of factors about its behavior; most notably, its critical temperature, current, and magnetic field. The work detailed in this document focuses exclusively on Yttrium Barium Copper Oxide (YBCO), primarily because it has been extensively studied and is thus better characterized than many other superconductor types. It is non-toxic and inert, so it is safe to handle in the lab. It can also be easily produced in single-crystal form to reduce hysteresis and it has very high critical magnetic fields, making it easy to obtain high-stiffness connections. These advantages

Table 3.1. Parameters of High Temperature Superconductors: [i] Reference 24, [ii] Reference 20

Superconductor	Critical Temp., T_c (K)	Upper Critical Field, B_{c2} (T)	Critical Current Density, J_c (A/mm^2)
$YBa_2Cu_3O_x$ [i,ii] (YBCO)	88 – 93	@ 0 K: 160 @ 77 K: > 5	@ 77 K: >100
$Bi_2Sr_2CaCu_2O_x$ [i] (BSCCO)	87	@ 77K: 0.005	@ 77 K: 100
$DyBa_2Cu_3O_7$ [ii]	92.5		
$ErBa_2Cu_3O_9$ [ii]	94	@ 0 K: >28	
$Bi_2Sr_2CaCu_2O_x$ [i] (BSCCO)	110	@ 77K: 3000	@ 77 K: 500
TlBaCaCuO [ii]	125		
$HgBa_2Ca_2Cu_3O_8$ [i]	134		

aside, many different superconductor types capable of achieving flux pinning exist and may have more desirable traits than YBCO for specific mission designs.

As discussed in Chapter 1, the critical temperature of YBCO is 88 K; above this temperature the material is fully in its normal state and cannot flux pin. The upper critical field for YBCO is extremely high, with some sources citing the value at over 300 T in directions parallel to the copper oxide planes[106] (and over 100 T in other directions[107]). The lower critical field is relatively small, with sources citing these values near 0 K as 0.1 T for directions perpendicular to the copper oxide plane and 0.02 T parallel to the planes.[107,108] Below these values (which are lower for higher temperatures), the superconductor exhibits Meissner repulsion. These values collectively set up the thermal, current, and magnetic field strength constraints on a YBCO-based FPI.

3.2 Modeling Flux Pinning

Given the physics and limits of the flux pinning effect, the first step in developing a flux-pinned interface for spacecraft is to develop a model that can be applied to various FPI configurations. A simple linear model can be applied for very small displacements in which no nonlinear modes are excited. However, for more complex motion, a modified image model captures many of the key nonlinearities in the FPI's behavior. This section discusses both models, but focuses on the nonlinear image model in particular.

3.2.1 Linear Model

For small magnet displacements, particularly in transverse direction (parallel to the surface of the superconductor) the interface acts as a non-contacting linear spring-mass-damper system. A simple harmonic oscillator is thus a valid model for small motions that do not significantly excite the nonlinear modes of the system. The linear model incorporates the forces caused by flux pinning simple unforced single-degree-of-freedom harmonic oscillator with the standard equation of motion:

$$m\frac{d^2q}{dt^2} + c\frac{dq}{dt} + kq = 0 \tag{3.1}$$

where q is the state of interest, k is the stiffness, c is the damping coefficient, and m is the magnet mass. Given a damped natural frequency ω_d and a damping ratio ζ, this equation becomes:

$$\frac{d^2q}{dt^2} + \frac{2\zeta\omega_d}{\sqrt{1-\zeta}}\frac{dq}{dt} + \frac{\omega_d^2}{1-\zeta}q = 0 \tag{3.2}$$

The time and frequency response for each degree of freedom can be calculated with the initial conditions q_0 and $\dot{q}_0$. Equivalent equations can be written for the system orientation, using the torsional stiffnesses, damping, and inertia of the system. This model is effective when its assumptions are not violated, but these assumptions are particularly limiting for FPI applications, necessitating a more sophisticated model for flux pinning.

3.2.2 Nonlinear Image Model

Frozen-Image Model Concept

Although the linear model for the system captures the small-displacement dynamics to the first order, modeling the full six-degree-of-freedom nonlinear forces and torques caused by flux pinning is an essential step in the theoretical advancement of FPI research. Fortunately, an analytical model for the transverse behavior of a magnet under the influence of flux pinning already exists and can be expanded to fill these needs. This model, known as the advanced mirror image model (AMIM) or frozen-image model (FIM), was developed by Kordyuk in 1998.[109] The model originally grew out of a strong community interest in understanding lateral levitation forces[22] of flux pinning, but Kordyuk applied the model to the different transverse modes of the magnet's motion as well. Since then, a linearized version of this model has been applied to six degrees of freedom by Norman; however, this work expands the model to include nonlinear multi-magnet interactions.

In order to provide an analytical solution to the forces and torques acting on the system, the model necessarily makes several simplifying assumptions. In particular, the magnets in the system are all modeled as dipoles and the hard superconductor is assumed to be an infinite plane with no hysteretic or edge effects. The model, however, can accommodate any shape of permanent magnet so long as the magnetic moment indicates the direction and magnitude of the volume's magnetization. These assumptions are common in magnetostatic image models,[110] but they do limit the applicability of the image dipole model for FPIs (and these limitations are discussed further in Section 3.4). Kordyuk also assumes that the distance between the magnet

and the superconductor is much greater than the penetration depth of the magnetic field into the superconductor.

The frozen-image model describes the position and strength of a set of virtual dipoles, known as "images," for every magnet interacting with the superconductor. These images are reflected in the superconductor and the sum of the magnetic fields they represent produce the observable forces and torques acting on the flux-pinned magnet.

An illustration of the basic concept of the FIM is shown in Figure 3.6. If the magnetic dipole was present when the superconductor was field-cooled, two images of that dipole are created in the model. The first virtual magnet, known as the mobile image, follows the position and orientation of the true magnet as it moves around and acts like a mirror image. The position of this image is found by taking the reflection of the true magnet's position over the surface of the superconductor. The orientation of the image's dipole is mirrored over the surface of the superconductor, providing a repelling restoring force when the dipole is not at its equilibrium. The dipole strength matches that of the magnet at any given point in time. Thus, this image provides the mechanism by which the equilibrium of a flux-pinned interface can be altered after the field-cooled equilibrium is set.

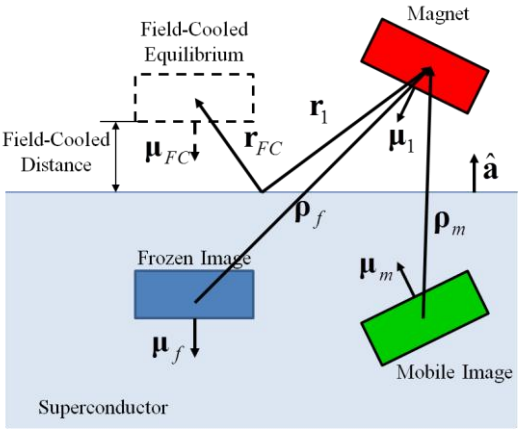

Figure 3.6. Relevant variables and terminology used in the advanced mirror image model.

The position of second virtual magnet, called the frozen image, can be found within the superconductor by calculating the inverse reflection of the field-cooled position of the magnet across the surface of the superconductor. The dipole direction of the inverse mirror image is thus oriented such that it cancels the mobile image at equilibrium and attracts the dipole when it is oriented in its field-cooled attitude. The strength of the frozen image dipole is equivalent to that of the magnet at field cooling. None of these values change as long as the superconductor is kept beneath its critical temperature. The frozen image thus provides a basin of attraction to the magnet, drawing it back to the equilibrium that was set in the field cooling process. At the equilibrium, the mobile and frozen images cancel out, leading to no net force or torque acting on the magnet.

However, for source magnets that are not present during field cooling, the frozen image is reflected to negative infinity and does not offer this same basin of attraction. These magnets only produce mobile images and can thus (independently, at least) only produce repulsion forces, regardless of the polarity of the magnet. (They can, however, be attracted by the frozen image of a different magnet, which can complicate the system as seen in Chapter 4).

It is important to note that Kordyuk originally derived this model to produce an analytical model for the forces on the system (particularly the lateral forces). He makes no mention of the possible extension of this model to include torques, although later papers[91] have suggested its use to do exactly that, but have linearized the system before its full implementation in the dynamics. The representation presented here is generalized for multiple magnets acting in the same superconductor, and the results in

this paper represent the first implementation of the full nonlinear six-degree-of-freedom multi-magnet model.

Modeling the Images

This work uses the terminology and variable assignments shown in Figure 3.6, where a subscript of *m* denotes the mobile image, *f* denotes the frozen image, and *i* denotes the source magnet *i* and bold face represents vectors, a hat represents a unit vector, and italics indicate a scalar variable. The generic solution for the dipole magnetic field of the mobile image produced by source *j* acting on source magnet *i* is:[111]

$$\mathbf{B}_{mi} = \frac{\mu_0}{4\pi\rho_{mj,i}^{\ 3}}\left(3\left[\boldsymbol{\mu}_{mj}\cdot\hat{\boldsymbol{\rho}}_{mj,i}\right]\hat{\boldsymbol{\rho}}_{mj,i} - \boldsymbol{\mu}_{mj}\right) \tag{3.3}$$

and the magnetic field for the frozen image dipole is equivalent, with the subscripts simply denoting the different magnetic moment and distance:

$$\mathbf{B}_{fi} = \frac{\mu_0}{4\pi\rho_{fj,i}^{\ 3}}\left(3\left[\boldsymbol{\mu}_{fj}\cdot\hat{\boldsymbol{\rho}}_{fj,i}\right]\hat{\boldsymbol{\rho}}_{fj,i} - \boldsymbol{\mu}_{fj}\right) \tag{3.4}$$

In these two equations, the $\boldsymbol{\mu}$ term denotes the vector magnet moment of the dipole, the $\hat{\boldsymbol{\rho}}$ term denotes the unit vector direction of the position of the magnet relative to its image, the ρ term denotes the scalar magnitude of the distance between the magnet and its image, and the μ_0 term is the permeability of free space ($4\pi\times10^{-7}$ T·m/A). When *j=i*, the equation is for the source magnet being acted upon by its own images. The relative position vectors from the image to the magnet,[19] as interpreted from Kordyuk's model are:

$$\boldsymbol{\rho}_{mi,i} = 2\left(\hat{\mathbf{a}}\cdot\mathbf{r}_i\right)\hat{\mathbf{a}} \tag{3.5}$$

$$\boldsymbol{\rho}_{fi,i} = \mathbf{r}_i - \mathbf{r}_{FCi} + 2\left(\hat{\mathbf{a}}\cdot\mathbf{r}_{FCi}\right)\hat{\mathbf{a}} \tag{3.6}$$

where $\mathbf{r}_1$ is the position vector of the magnet from a fixed origin, $\mathbf{r}_{FC}$ is the position vector of the magnet during the field cooling process (the equilibrium position), and $\hat{\mathbf{a}}$ is the unit direction vector perpendicular to the surface of the superconductor. These equations reflect the position of the magnet over the surface of the superconductor to find the relative position between the image and its source. For example, note that the mobile relative vector is always parallel to the direction of the superconductor, implying it mirrors the position of the source magnet. When finding the relative position vector between an image *j* and source image *i*, the vector expression becomes:

$$\boldsymbol{\rho}_{mj,i} = \mathbf{r}_i - \left(\mathbf{r}_j - \boldsymbol{\rho}_{mi,i}\right) \tag{3.7}$$

$$\boldsymbol{\rho}_{fj,i} = \mathbf{r}_i - \left(\mathbf{r}_j - \boldsymbol{\rho}_{fi,i}\right) \tag{3.8}$$

The magnetic moments of the images can similarly be found by:[19]

$$\boldsymbol{\mu}_{mi} = \left(\boldsymbol{\mu}_i - 2(\hat{\mathbf{a}} \cdot \boldsymbol{\mu}_i)\hat{\mathbf{a}}\right) \tag{3.9}$$

$$\boldsymbol{\mu}_{fi} = \left(2\left(\hat{\mathbf{a}} \cdot \boldsymbol{\mu}_{FCi}\right)\hat{\mathbf{a}} - \boldsymbol{\mu}_{FCi}\right) \tag{3.10}$$

where $\boldsymbol{\mu}_i$ is the magnetic moment vector of source magnet *i* at a given time, and $\boldsymbol{\mu}_{i,FC}$ is the magnetic moment of the i^{th} magnet at field cooling.

Modeling the Magnets

FPIs generally have a combination of permanent and electromagnets, and so it is necessary to have a model of the magnets for each type. Because the model is simplified by assuming the magnets are dipoles, the magnet model consists simply of estimating the magnetic moment of the various magnets. For a permanent magnet, the estimated magnetic dipole moment magnitude is:

$$\boldsymbol{\mu}_i = \left(\frac{2\pi B_i d_i^{\,3}}{\mu_0} \right) \hat{\boldsymbol{\mu}}_i \tag{3.11}$$

where B_i is the surface strength of the magnetic field of the dipole measured along its dipole axis and d_i is the distance from the center of the magnet to its surface (or half its thickness). This equation is derived from the equation for the strength of the magnetic field along a magnet's dipole axis:

$$B_{axis} = \frac{\mu_0}{4\pi} \left(\frac{2\mu_z}{d_z^{\,3}} \right) \tag{3.12}$$

where B_{axis} is the strength of the magnetic field of the dipole in the direction of its dipole axis at distance d_z from the center of the dipole with a magnetic moment of μ_z. Section 3.3 discusses the selection of the magnetic moment and the errors associated with them in more detail, but it should be noted that this technique chronically under-estimates the magnetic field strength along the axis of symmetry of the cylinder. In order to calculate the magnetic moment for an electromagnet, this expression is instead:

$$\boldsymbol{\mu}_i = \left(\frac{V_i(t) A_i T_i}{R_i} \right) \hat{\boldsymbol{\mu}}_i \tag{3.13}$$

where $V_i(t)$ is the voltage applied across the electromagnet as a function of time, A_i is the area enclosed by the electromagnet's current loop, T_i is the number of turns in the electromagnets, and R_i is the resistance of the electromagnet. This equation does not take into account variations in the enclosed area associated with a winding wire in the electromagnet.

Modeling the Forces and Torques on the Source Magnet

Now that the magnets and the images can be modeled, the forces and torques acting on the source magnet from a single image can be calculated using the standard expressions (of mobile image *j* acting on magnet *i*)[112]:

$$\begin{aligned}\mathbf{F}_{j,m\_i} = &\frac{3\mu_0\mu_{mj}\mu_i}{4\pi\rho_{mj,i}^{\ 4}}\left[\hat{\boldsymbol{\rho}}_{mj,i}\left(\hat{\boldsymbol{\mu}}_{mj}\cdot\hat{\boldsymbol{\mu}}_i\right)+\hat{\boldsymbol{\mu}}_{mj}\left(\hat{\boldsymbol{\rho}}_{mj,i}\cdot\hat{\boldsymbol{\mu}}_i\right)+\hat{\boldsymbol{\mu}}_i\left(\hat{\boldsymbol{\rho}}_{mj,i}\cdot\hat{\boldsymbol{\mu}}_{mj}\right)\right] \\ &-\frac{3\mu_0\mu_{mj}\mu_i}{4\pi\rho_{mj,i}^{\ 4}}\left[5\hat{\boldsymbol{\rho}}_{mj,i}\left(\hat{\boldsymbol{\rho}}_{mj,i}\cdot\hat{\boldsymbol{\mu}}_{mj}\right)\left(\hat{\boldsymbol{\rho}}_{mj,i}\cdot\hat{\boldsymbol{\mu}}_i\right)\right]\end{aligned} \tag{3.14}$$

$$\boldsymbol{\tau}_{mj,i} = \frac{\mu_0\hat{\boldsymbol{\mu}}_{mj}\hat{\boldsymbol{\mu}}_i}{4\pi\rho_m^{\ 3}}\left[3\left(\hat{\boldsymbol{\mu}}_{mj}\cdot\hat{\boldsymbol{\rho}}_{mj,i}\right)\left(\hat{\boldsymbol{\mu}}_i\times\hat{\boldsymbol{\rho}}_{mj,i}\right)+\left(\hat{\boldsymbol{\mu}}_{mj}\times\hat{\boldsymbol{\mu}}_i\right)\right] \tag{3.15}$$

where μ_0 is the permeability of free space, μ is the magnetic dipole moment vector magnitude, $\hat{\boldsymbol{\mu}}$ is the magnetic dipole unit vector, and $\hat{\boldsymbol{\rho}}_{mj,i}$ is the vector from the mobile image *j* to the source magnet *i*. The frozen image is the exact same expression, but with subscripted *f* instead of *m*.

With these expressions, the total force and torque acting on the magnet is simply the sum of the different images acting on it. Each magnet is clearly influenced by its own set of images, but it is important to note that a magnet can also be influenced by the images of other magnets in the array. For example, a bar with two embedded dipoles pinned next to one another with the same strength in the same direction (perpendicular to the bar) has two equilibriums, one in which the magnet is paired with its own frozen image, and one in which the dipoles have swapped potential wells. Thus, in order to sum up the effects acting on a given source magnet *i* magnet, one must sum through the images of all of the other *n* magnets in the system:

$$\mathbf{F}_{tot,i} = \sum_{j=1}^{n}\left(\mathbf{F}_{mj,i}+\mathbf{F}_{fj,i}\right) \tag{3.16}$$

$$\boldsymbol{\tau}_{tot,i} = \boldsymbol{\rho}_i \times \mathbf{F}_{tot,i} + \sum_{j=1}^{n} \left(\boldsymbol{\tau}_{mj,i} + \boldsymbol{\tau}_{fj,i} \right) \tag{3.17}$$

where $\boldsymbol{\rho}_i$ is the vector from the body's center of mass to the dipole's location (in the case where the magnet alone is being studied, this term goes to zero).

Equations of Motion for a Spacecraft with an FPI

In order to apply the frozen-image model to a spacecraft with *n* magnets, the model's basic concept is retained and the dynamics of a spacecraft body in six degrees of freedom are added. Figure 3.7 shows the parameters developed in previous sections as they apply to an FPI on a spacecraft.

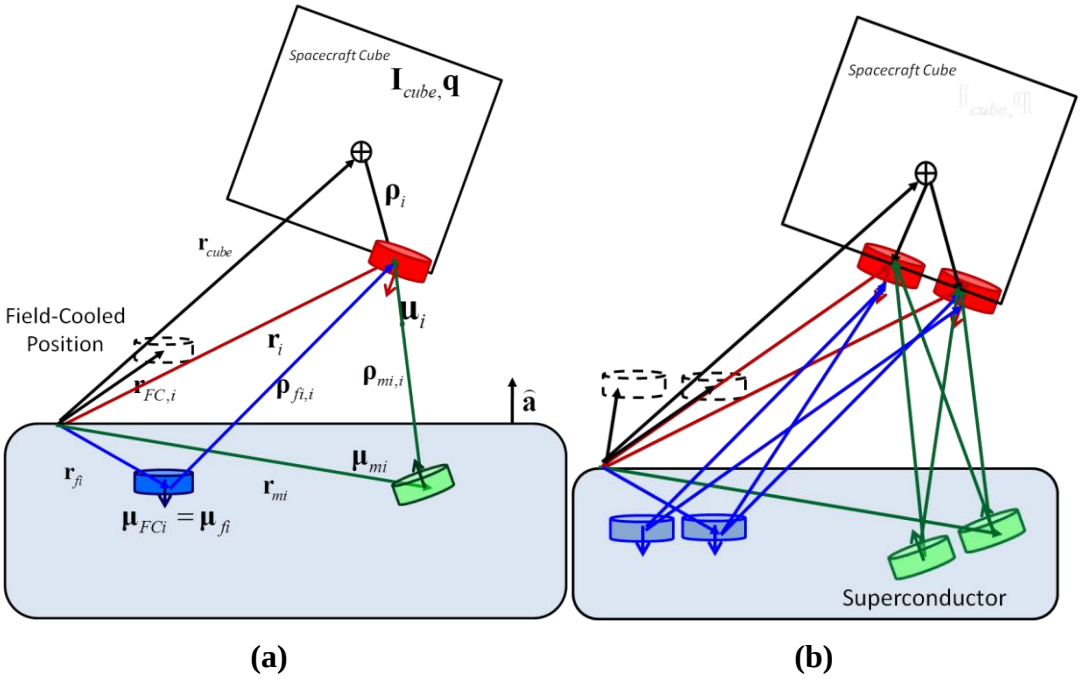

Figure 3.7. (a) Parameters for an FPI implemented on a spacecraft. (b) Concept of multiple magnets on the FPI with images influencing all of the magnets present.

Using these terms, the equations of motion of the spacecraft can be written for a generic *n* number of magnets:

$$\mathbf{M}\ddot{\mathbf{r}}_{cube} + \mathbf{C}_r\dot{\mathbf{r}}_{cube} - \mathbf{F}_{mag}(\mathbf{r}_{cube}, \mathbf{q}) = \mathbf{F}_{applied} \tag{3.18}$$

$$\mathbf{I}\dot{\boldsymbol{\omega}}_{cube} + \mathbf{C}_\theta\boldsymbol{\omega}_{cube} - \boldsymbol{\tau}_{mag}(\mathbf{r}_{cube}, \mathbf{q}) = \boldsymbol{\tau}_{applied} \tag{3.19}$$

where $\mathbf{M}, \mathbf{C},$ and $\mathbf{I}$ are the mass, damping, and inertia matrices respectively, and $\boldsymbol{q}$ is the quaternion representation of the spacecraft's attitude, and the $\mathbf{F}_{mag}$ and $\boldsymbol{\tau}_{mag}$ terms are the summation of the forces acting on all of the magnets in the array:

$$\mathbf{F}_{mag} = \sum_{i=1}^{n} \mathbf{F}_{tot,i} \tag{3.20}$$

$$\boldsymbol{\tau}_{mag} = \sum_{i=1}^{n} \boldsymbol{\tau}_{tot,i} \tag{3.21}$$

It is important that the vectors are all represented in their appropriate frames when implemented in a system. In order to do so, it is important to rotate the vectors defined in the body frame (in particular, the magnetic dipole moment $\hat{\boldsymbol{\mu}}_i$ and the position of the magnet relative to its center of mass $\boldsymbol{\rho}_i$) into the inertial frame before using them in the appropriate expressions.

3.3 Simulated Passive System Dynamics

Using the expanded multi-magnet frozen-image model described here, it is possible to integrate the equations of motion over time to observe the behavior of the system. For this work, the equations were implemented in a Simulink model with various MATLAB functions to set up the appropriate variables. An image of the Simulink model of the highest level of the plant of the FPI-influence spacecraft dynamics is shown in Figure 3.8.

Although the free-response of the system when an electromagnetic actuator perturbs the system is examined in more detail in Chapter 4, it is worth briefly examining the passive response of a multi-magnet system to an initial position displacement. The following simulation was performed using the parameters for a CubeSat-sized spacecraft with two permanent magnets (of the same strength and size as listed in Section 3.4) centered on its face. The system was perturbed with a relatively small initial non-equilibrium condition in *x*, *y*, and *z*, but the system was started at rest. The effects of gravity are not simulated.

Without examining the details of this particular FPI setup or spacecraft (issues that are covered in subsequent chapters), the translational, rotational, and frequency response are shown in Figure 3.9, Figure 3.10, and Figure 3.11.

For these small perturbations, the system behaves very similarly to a linear system,

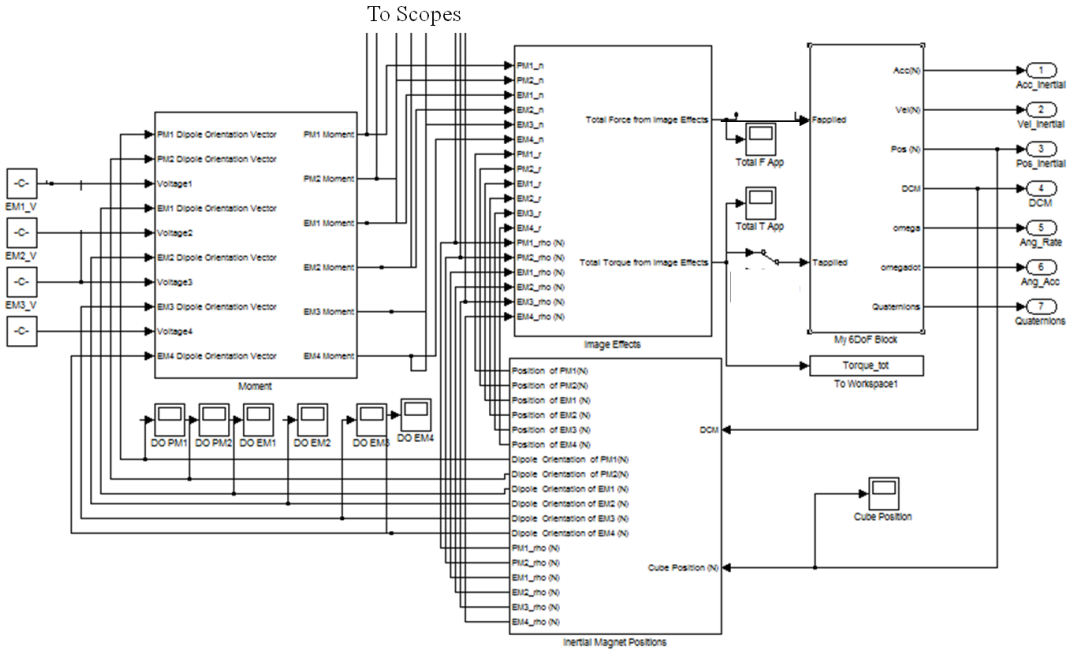

Figure 3.8. The Simulink model of the spacecraft plant with the effects of the FPI influencing the behavior of the system.

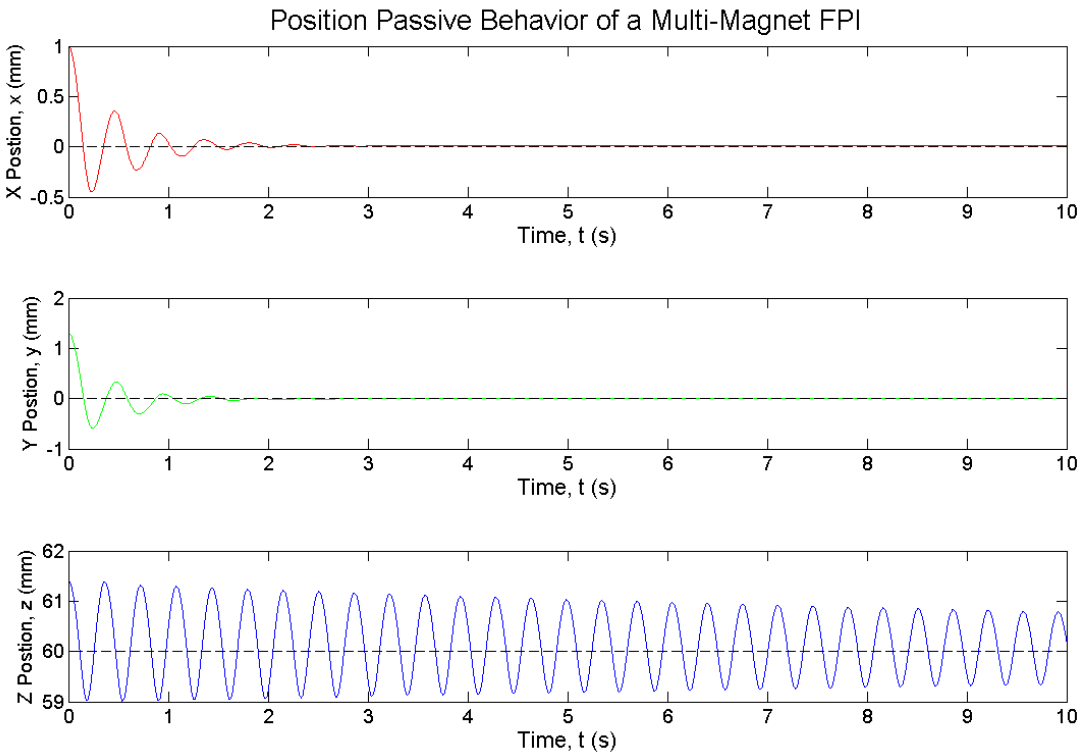

Figure 3.9. The position response of a CubeSat-scale FPI with two permanent magnets with initial displacements in *x*, *y*, and *z*, where *z* is the lateral direction between the superconductor and CubeSat and *x* and *y* are the transverse directions.

although the *z* direction tends to exhibit nonlinear behavior even with this small displacement. The *z* position states also exhibits a strong oscillatory response. At higher perturbations, this degree of freedom exhibits a stiffening-spring behavior when moving closer to the superconductor and a softening-spring behavior when moving away from the superconductor. Another important observation is that, although the position was initially in its equilibrium attitude, rotational modes are excited due to the cross-coupling between the translational states.

These details aside, the most striking behavior here is that the system – using flux pinning alone, without active control – rejects the disturbances relatively quickly, and (aided by the natural damping in the system), the response looks very similar to the

behavior of an actively controlled system. It is this property that makes the concept of the FPI so compelling: the system's physics are actually improving the system's behavior. Although in many nonlinear systems there is a strong desire to mitigate the effects of the nonlinearities in the system, in FPIs the nonlinearities are actually beneficial and should be exploited, not canceled. For example, the superconductor increasingly resists motion that is closer than the set equilibrium. So in the region where the magnet is threatening a collision, the system pushes back with nonlinearly increasing amounts of force to keep the magnet (or the spacecraft with the magnet attached) from impacting the superconductor (or the spacecraft with the

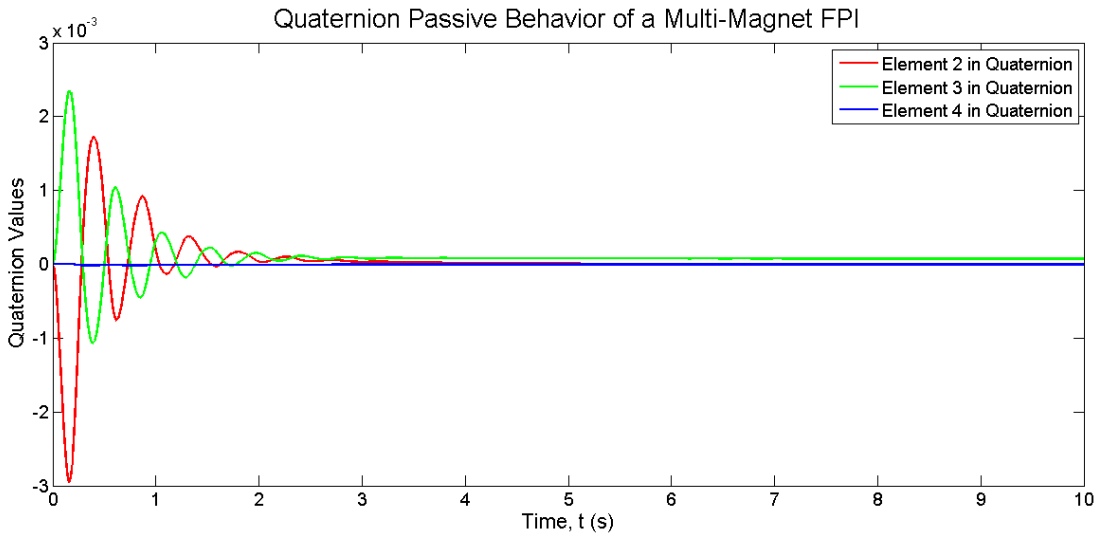

Figure 3.10. The quaternion response of a CubeSat-scale FPI with two permanent magnets with initial displacements in *x*, *y*, and *z*.

superconductor attached). Thus, the goal of FPI control (discussed in Chapter 5) is to exploit and cultivate system's passive behavior as seen in these plots.

3.4 Model Assumptions

The implemented version of this model has a number of assumptions built into its framework, and so it is important to investigate the merits associated with these

assumptions. Of these assumptions, the infinite-plane superconductor is relatively reasonable given the general distances involved. However, the influence of edge effects is not well-studied and should be examined more thoroughly in future work. The assumption that the magnets are dipoles, on the other hand, is a relatively well-studied assumption that has a significant influence on the resulting FPI behavior. Thus, this section examines that assumption more closely.

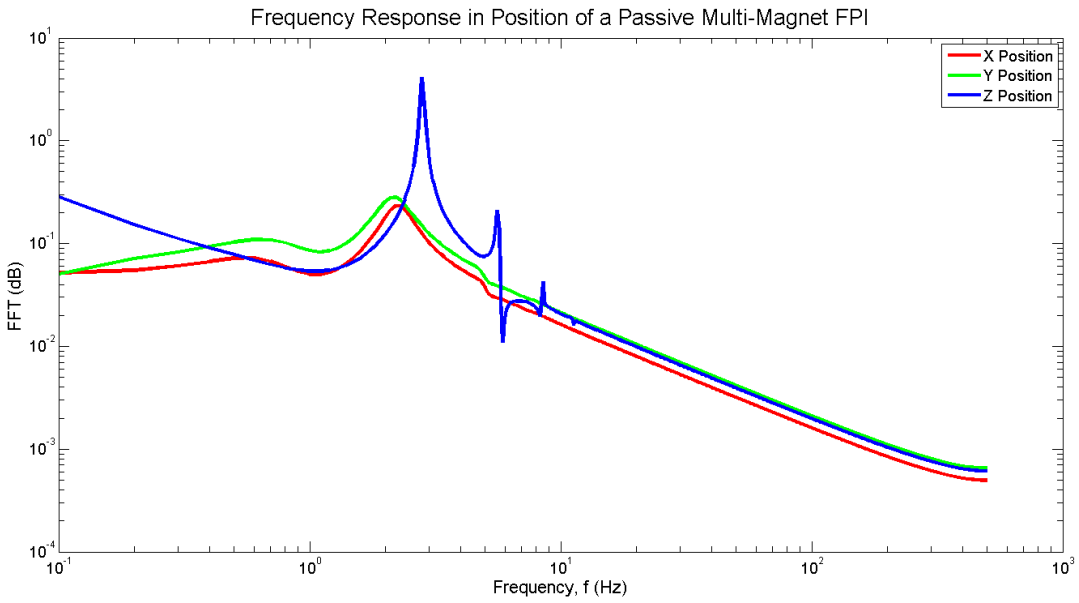

Figure 3.11. The position frequency response of a CubeSat-scale FPI with two permanent magnets with initial displacements in *x*, *y*, and *z*.

Dipole Magnet Assumption

The stipulation that the magnets can be modeled as perfect dipoles is convenient because it enables the use of pre-existing expressions for force, torque, and magnetic field in the model. Although the magnets considered in this work are generally cylinders, they are certainly not ideal dipoles. The FPI applications require modeling the magnet's interactions at relatively close distances, so generic far-field assumptions

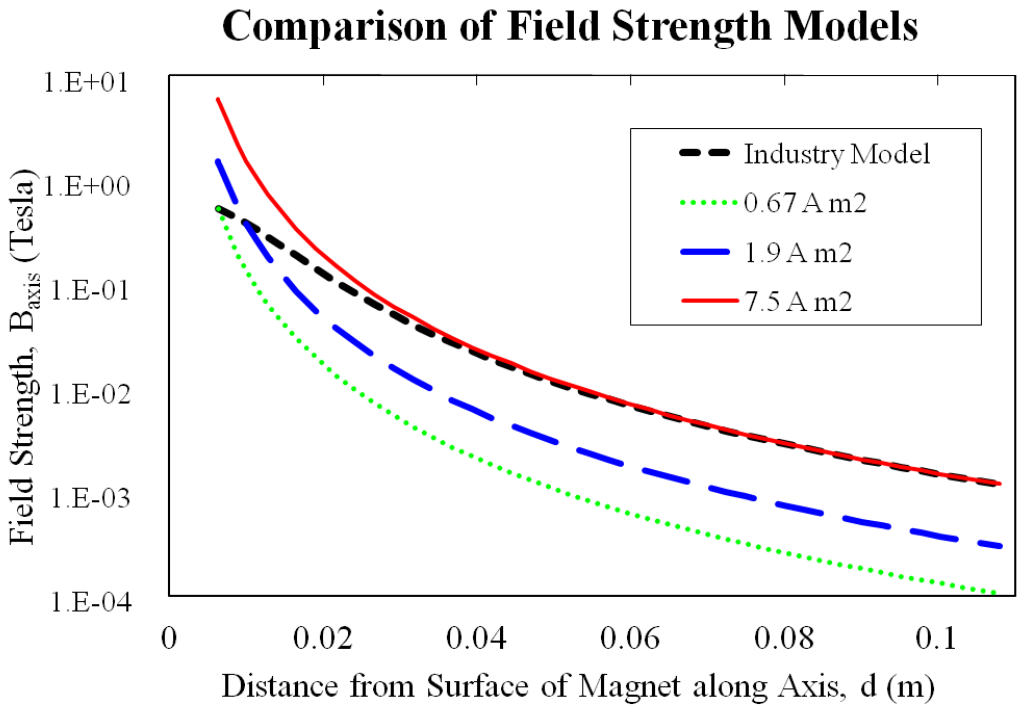

Figure 3.12. A comparison of the field strength on logarithmic scale of an N52 Neodymium cylindrical magnet one inch in diameter and half an inch thick along the dipole axis. The different plots compare the empirical field model to the dipole model at different magnetic moments.

do not work. Although a bulk-magnet model would be the best way to capture the dynamics in this range, it is possible to intelligently select the magnetic moment used to model the system and still use the equations developed earlier.

According to an empirical model used in industry, the magnetic field strength along the axis of the cylindrical magnet is:[113]

$$B_{axis} = \frac{B_r}{2}\left(\frac{(t+x)}{\sqrt{r^2+(t+x)^2}} - \frac{x}{\sqrt{r^2+x^2}} \right) \tag{3.22}$$

where B_{axis} is the strength of the magnetic field in Gauss, B_r is the residual flux density in Guass, r is the radius of the cylinder, t is the thickness of the magnet along the direction of magnetization, and x is the distance from the face of the magnet along its

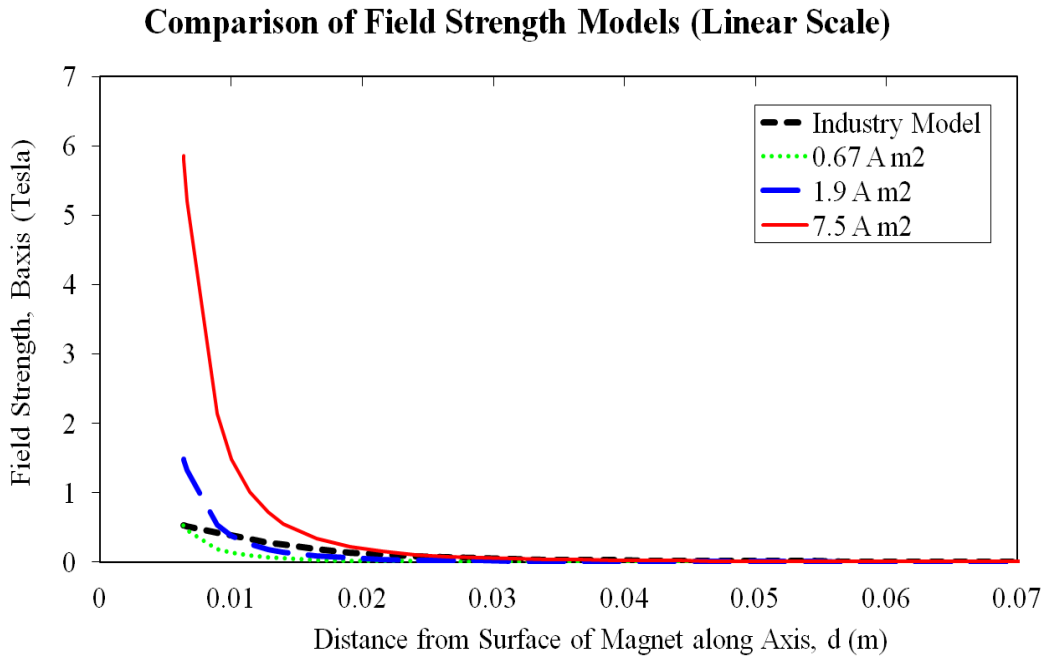

Figure 3.13. A comparison of the field strength in lineasr scale of an N52 Neodymium cylindrical magnet one inch in diameter and half an inch thick along the dipole axis. The different plots compare the empirical field model to the dipole model at different magnetic moments.

axis. In order to see how this expression compares to the dipole model, Figure 3.12 shows the magnetic field in logarithmic scale along the dipole axis for various magnetic moments. Figure 3.13 shows the same plot in linear scale. The values are taken from the N52 Neodymium permanent magnet that is one inch in diameter and half an inch thick.

The figures clearly show the trade-off in the selection of magnetic dipole moment. For larger values of the magnetic moment, the system converges with the empirical model very well. For this magnet (which is used in subsequent analyses), a magnetic moment value of 7.5 Am^2 has an error relative to the empirical model below 10% after about four centimeters. However, the errors below one centimeter range from 400% - 1000%. The expression given in Equation (3.11) produces a magnetic moment of 0.67 Am^2 for this magnet. While this magnetic moment exactly matches the

empirical model just above the surface of the magnet, the two curves diverge such that the dipole model is about 10% of the strength of the empirical model (or a difference of 90%) for distances further out. This model is the one that is predominantly used throughout the paper because, despite it underestimating the magnet's strength, experimental data suggests that the stiffness seen on hardware implementations of the FPI is lower than is modeled even at this magnetic dipole strength. (This discrepancy may be the result of thermal problems or incomplete flux capture in the superconductor, but underestimating the magnet's strength appears to be a more conservative estimate that best matches data collected thus far). Another way to select the magnetic moment is to minimize the error at the field-cooled distance (in most cases in this paper, one centimeter). For this magnet, a magnetic moment of 1.9 Am^2 reduces the magnetic field strength error (when compared to the empirical model) at one centimeter to below 1%. The error just above the magnet's surface is 183% and in the far field the magnet predicts a strength with an error of about 75%.

Experimental Verification

Some effort has been made to characterize the actual magnetic fields of both the magnets and the flux-pinned systems used in the laboratory environment. Figure 3.14 shows a Gaussmeter attached to a three-axis translation stage that was used to conduct a series of experiments to characterize the magnetic field of various flux pinned systems, including the magnetic field with the magnet in equilibrium, the field-cooled superconductor without the magnet, and the back side of the field-cooled superconductor. The relevant collected data and a brief explanation of these experiments can be found in Appendix D.

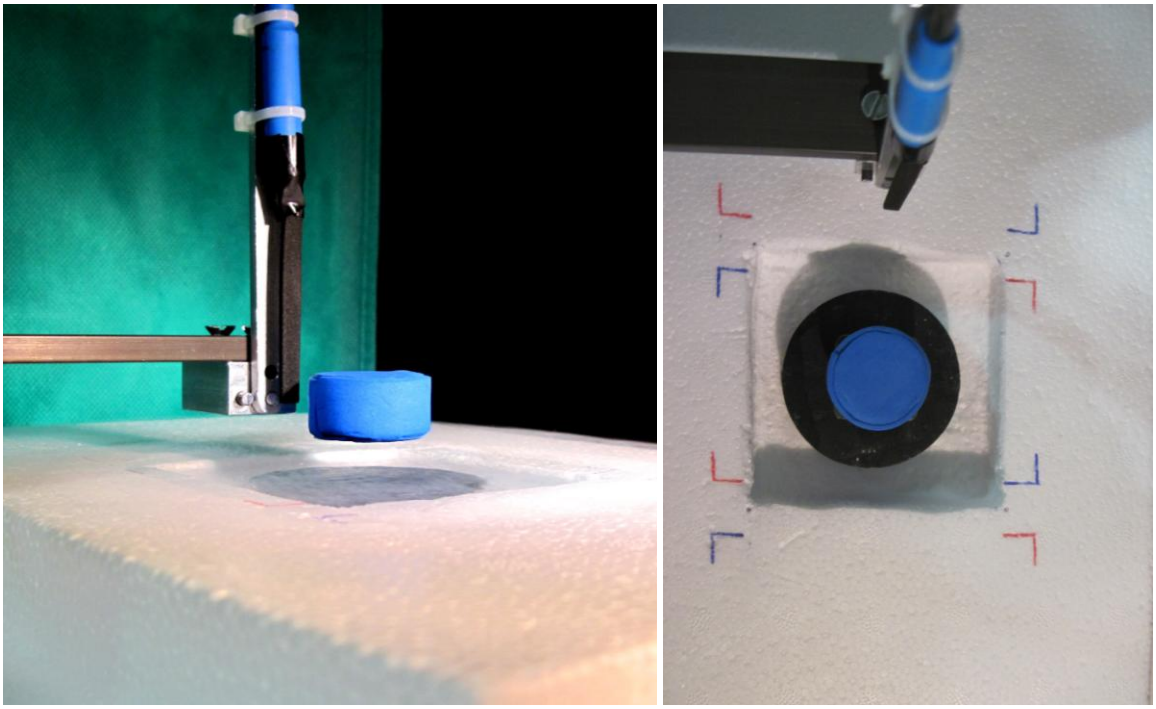

Figure 3.14. The Precision Lab Translator (PLT) used in the laboratory to characterize the magnetic field of a flux pinned system.

CHAPTER 4

DESIGN PRINCIPLES AND ELECTROMAGNETIC ACTUATION STRATEGIES FOR FLUX-PINNED INTERFACES

4.1 Flux-Pinned Spacecraft Design Considerations

There are several factors to consider when designing a flux-pinned interface for spacecraft, and each of these factors have implications for the modeling and actuation strategy that can be employed for that particular design. This section discusses the major elements in an FPI design, and provides the terminology and general applications for different designs that illuminates the results presented in this work.

4.1.1 Magnet and Superconductor Pairings

Single-Magnet Single-Superconductor

The simplest form of a flux-pinned interface is a single superconductor pinned to a single magnetic field source, which are then mounted onto separate spacecraft modules. This single-magnet single-superconductor (SMSS) FPI can be used as a stand-alone non-contacting spring and damper between two modules or form the basis for more complicated FPI designs. Because of its simplicity, the SMSS FPI is straightforward to control and actuate. It also allows the superconductor size to be appropriately matched to the strongest concentrations of flux from its sole magnetic source, enabling a high stiffness for a low mass penalty. Even large interface surfaces can be spanned with minimal mass using an array of strategically-placed SMSS FPIs with smaller, discrete superconductors. Despite these advantages, if only one SMSS

FPI is used, it can only provide limited maneuverability independently. However, when several are used together (but kept at distances sufficient to ensure that the magnets in one FPI do not significantly interact with the superconductors in another), they can provide a relatively straightforward way of manipulating multiple relative degrees of freedom between two spacecraft modules.

Multiple-Magnet Single-Superconductor

An FPI incorporating multiple magnets interacting with the same superconductor, or a multiple-magnet single-superconductor (MMSS) arrangement, increases the complexity of the FPI but also provides a set of design options not attainable with an SMSS. In particular, the MMSS (an example of which is shown in Figure 4.1) can be designed to provide varying stiffness or control effort in many different (and possibly time-varying) degrees of freedom. This FPI design type can also accommodate a mixture of permanent and electromagnets that can be arranged in different geometric configurations to be optimized with respect to various performance metrics or costs. The MMSS only requires one superconductor, which

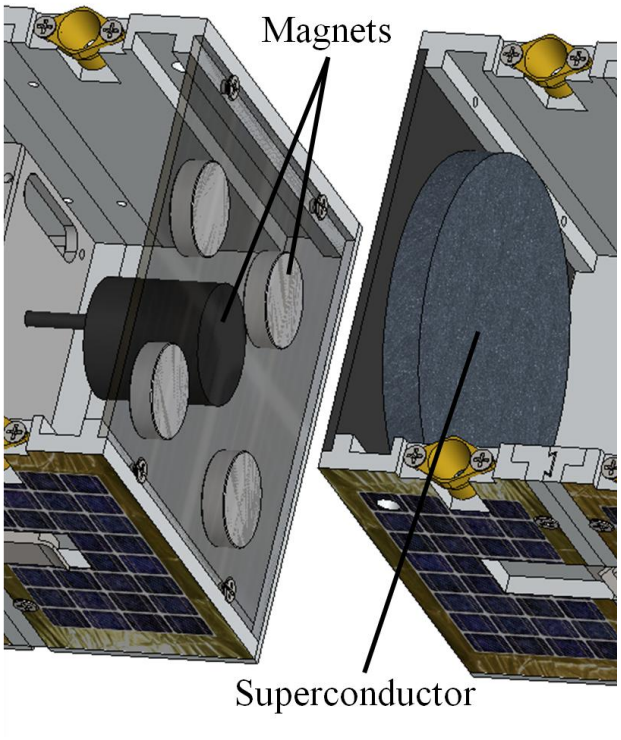

Figure 4.1. An example of a multiple-magnet single-superconductor design.

significantly reduces the complexities of the thermal system in place to keep the superconductor cold. However, this design is limited by the size of the superconductor and may use the superconductor mass inefficiently in order to capture flux of widely-spaced magnets. It is also more complex to model, because each magnet's influence on the superconductor also influences the other magnets in the interface.

Single-Magnet Multiple-Superconductor

In specific applications, it may make sense to employ a single-magnet multiple-superconductor (SMMS) design, examples of which are shown in Figure 4.2. This design offers a reduced superconductor mass for an increased interface area or a unique interface configuration options. The disadvantages are an increased complexity in the cooling system due to the larger number of superconductors and reduced or

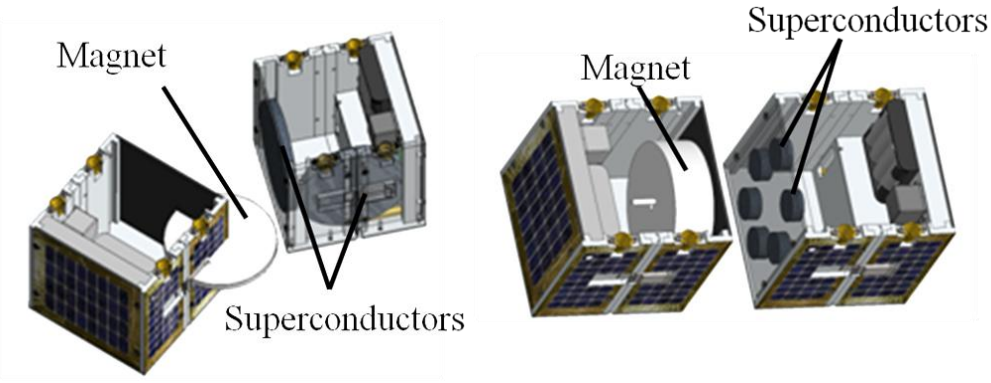

(a) (b)

Figure 4.2. Examples of single-magnet multiple-superconductor designs. (a) An FPI hinging mechanism (b) a single electromagnet reacting against many superconductors to reduce superconductor mass but react over a large surface area.

highly constrained maneuverability options. The SMMS technique might be considered for large spacecraft where maneuverability in one relative degree of freedom or a purely passive system is desirable, such as the augmented autonomous

docking of vehicles to the ISS. In this case, the magnet generally needs to be large enough and powerful enough to distribute flux to the different (spatially disparate) superconductors. This design may also necessitate a larger magnet (likely an electromagnet) spanning the distances between the different superconductors. Also, in order to avoid the difficult-to-model edge effects of the superconductors, maneuverability may need to be restricted to the lateral degree of freedom. In this degree of freedom, the smaller discrete superconductors in a plane may be roughly modeled as a continuous superconductor.

Another application for the SMMS would be a system where having an FPI interface over a right angle is desired, such as in a flux-pinned hinge mechanism. In this case, the same magnet is pinned over two superconductors to enable the hinging effect to take place. Provided the system is limited to motion in the constrained degrees of freedom provided by the FPI, the effect of the superconductor edges is limited.

Multiple-Magnet Multiple-Superconductor

Finally, a design involving multiple magnets and multiple superconductors (MMMS), where more than one magnet is imprinted into a superconductor while simultaneously being imprinted into separate superconductors, is possible, but introduces a number of complexities that would make it difficult to implement. The primary difficulty would lie in appropriately modeling the edge effects of the superconductor. Unlike the SMMS design, this modeling would be necessary in order to properly determine the dynamics of multiple magnets interacting over the superconductor boundaries in motion that is not restricted to a single degree of

freedom. Additional complexity would arise from the fact that multiple superconductors influence each magnet's motion, which increases the number of (highly nonlinear) potential wells to consider in the system design. In spite of its complexity, an MMMS FPI would likely be the hallmark of reconfigurable space systems with complicated kinematic evolutions based on flux pinning because it is the only kind of design that can capture the subtleties required to make that system architecture work.

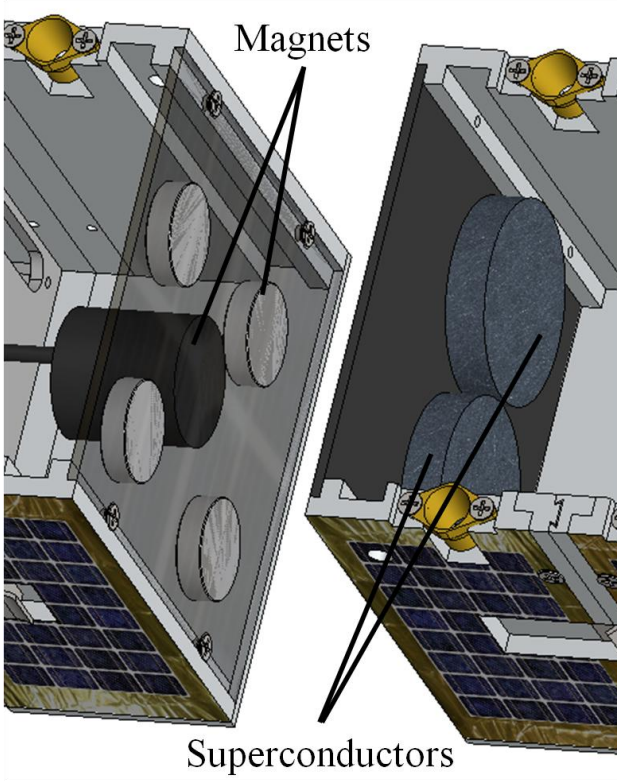

Figure 4.3. An example of a multiple-magnet multiple-superconductor design.

4.1.2 Magnetic Field Sources

Permanent Magnet Source

Using a permanent magnet (PM) as the sole magnetic field source in an FPI is advantageous because it is robust to failures in the power system on the magnet module, and it provides the passive dynamics of a flux-pinned system without requiring power or dissipating heat from the magnet itself. However, if permanent magnets are the sole source of magnetic flux in the FPI, maneuverability options may

be more limited and the mass penalty for larger-scale systems may be significantly higher. Thus, this FPI design is the best option for power-constrained or thermally sensitive systems where the capability of active tuning of the properties of the interface is not required or robustness to power failures is a highly desirable trait. They also offer long-duration performance with little cost to the spacecraft carrying the magnet array. These applications include orbital assembly and autonomous rendezvous that do not proceed to a docking phase.

It is possible to change the magnetic flux and thus the relative equilibrium in a PM-only FPI, but this requires the mechanical positioning or tilting of the magnet in place via a stepper motor or a linear actuator. Although this actuation technique may merit further study, it is not addressed in this paper. Another way to alter the FPI given a permanent-magnet interface is to turn off the FPI using temperature control (for example, turning off the cryocooler, or opening a sun shade). This maneuver releases the FPI by erasing the imprinted magnetic image in the superconductor. Although it is possible to re-cool the superconductor to imprint a new equilibrium, performing this maneuver on orbit may prove to be complicated.

Electromagnet Source

The electromagnet offers an adjustable alternative to a permanent magnetic field source. Electromagnets (EMs) can generally be scaled to higher strengths for less mass than permanent magnets of comparable strength, making them a better choice for larger systems. Electromagnets offer variable-strength magnetic fields and straightforward control strategies, but because they are dependent on an electrical current to interact within the FPI, they constantly use power and dissipate heat. These

characteristics making EM-based FPIs better suited to short-duration maneuvers where fine-tuned active control is required, such as the last phase of a docking/berthing maneuver. However, rapidly changing currents in the electromagnets (for example, due to pulse width modulation) may adversely affect the amount of flux in the superconductor (see Chapter 8 for more detail). Thus, careful trade studies should be conducted to determine in EM-only FPI designs are suitable for a given mission.

Mixed Source

In order to obtain the best characteristics of both magnetic field sources, a mixed-source FPI can also be used. In a mixed-source FPI, permanent magnets can provide the basis of a passively stable, robust equilibrium that is maintained regardless of power failures, while other, EM field sources, can be turned on and off to adjust the equilibrium as necessary. This arrangement can produce systems that energize-to-release, where the electromagnet is turned on only to cancel out the permanent magnetic field and enable the FPI to disengage. This design would be well-suited to temporary rendezvous and docking applications and modular repair and refueling maneuvers. Mixed-source FPIs are also well-suited to applications where a payload is mounted in a non-contacting, vibration-isolated platform that needs specific pointing capabilities, such as a telescope or camera. In this case, the permanent magnets would provide the baseline stable platform, and the electromagnets would turn on and off as necessary to tilt the platform in the appropriate direction, in a similar manner to the actuators in the James Webb Telescope design.

4.1.3 Magnetic Field Symmetry

As described in Chapter 1, FPIs can be tuned to provide different stiffness in specific designer-selected degrees of freedom. Magnetic field sources that are axisymmetric experience no stiffness in the degree of freedom associated with that symmetry because motion in that degree of freedom experiences no change in magnetic flux. An asymmetric magnet, on the other hand, has stiffness all degrees of

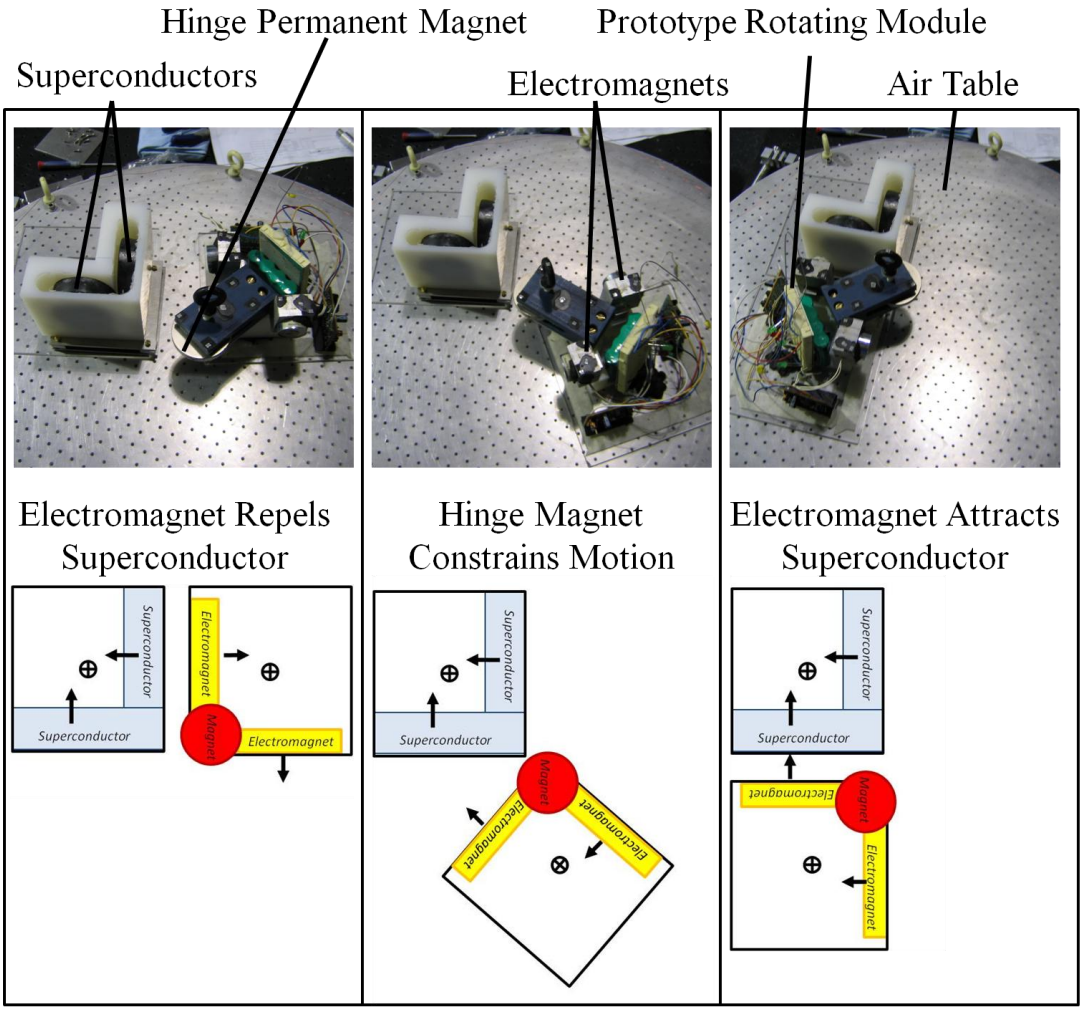

Figure 4.4. A three-stage rotational maneuver with an FPI acting as a hinge joint. The arrows in the schematic represent the dipole direction of the electromagnets and frozen-image in the superconductor as appropriate.

freedom. Thus, in applications where 6 degree-of-freedom stiffness is preferred, the magnetic field of the equilibrium position can be designed to be asymmetric. Alternatively, a properly designed FPI that exploits the magnetic field symmetry can be used to create a flux-pinned hinge, or other kinematic mechanisms.[26] This principle is illustrated in Figure 4.4, a configuration which has been successfully implemented in hardware.[94]

4.1.4 FPI Baseline Design

Given the diversity of FPI design techniques, it is a challenging endeavor to simulate the performance of all of the possible configurations. In order to provide a standard basis of comparison among different actuation techniques, a baseline design was selected that serves as the basis for the results shown in this paper. This design, shown in Figure 4.5, is a MMSS design with mixed magnetic field sources. It has an asymmetric array of permanent magnets at the center of the interface that provides stiffness in all degrees of freedom and guarantees stability even in a power failure case. Ringed around the outside of the interface is an array of four electromagnets for actuating the equilibrium in multiple degrees of freedom. This positioning is designed to improve the moment arm of the electromagnet-induced torques. This type of FPI was chosen because it has been successfully demonstrated on a three-DOF air bearing testbed (discussed in Chapter 6) and has a variety of spacecraft

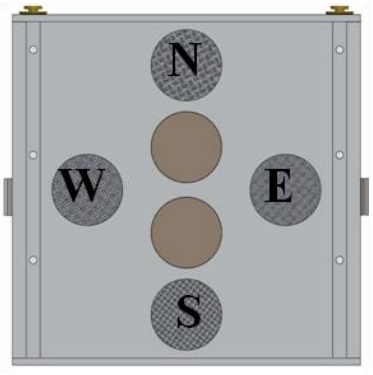

Figure 4.5. The magnetic field array of the FPI baseline design, with two permanent magnets in the center ringed by four electromagnets labeled North, East, South, and West.

applications, as described above.

Although the results of the following simulations primarily represent the performance of this specific FPI design, conclusions that can be drawn from these results can be cautiously applied as general principles to other designs. However, it should still be noted that this design is not optimized and sensitivity studies need to be examined to establish stronger general conclusions for different configurations.

4.2 Simulating the Actuation of an FPI

In order to fully understand the factors influencing the full nonlinear steady-state response of a MMSS FPI, a simulation based on the frozen-image (described in Chapter 3) – with the complete six-degree-of-freedom model – was performed over a variety of actuator input conditions. The simulation parameters used in the baseline FPI configuration (described in Section 4.1.4) are based loosely on the hardware used in the 2010 microgravity flight (described in greater detail in Chapter 7).[97]

The values for the system parameters that were used in the following simulations

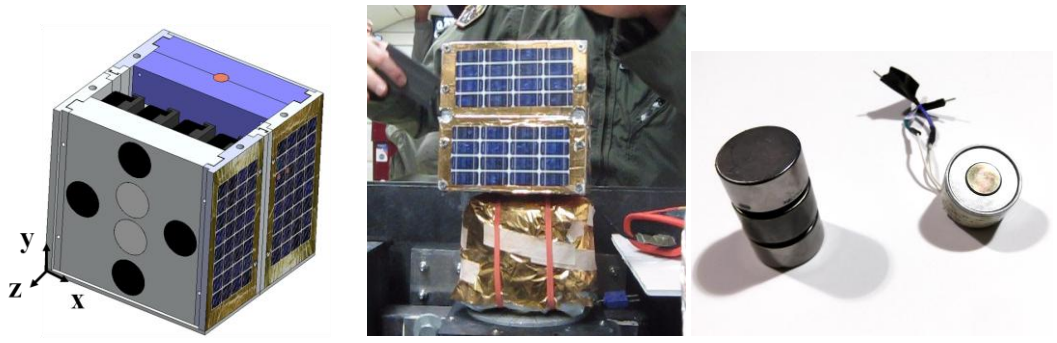

(a) **(b)** **(c)**

Figure 4.6. (a) A CAD rendering of the spacecraft module that provided the basis for the simulation parameters, including axes labels (b) A photograph of the same module during microgravity testing (c) three of the permanent magnets (left) and one electromagnet (right) that were used in the hardware implementation of the baseline design.

are published in Table 4.2. While the CubeSat mockup hardware has slightly different dimensions, such as a higher inertia, the module was approximated to be 10 cm on a side and 2 kg, with the inertia of a homogenous cube. The damping coefficient is a higher approximation than most experimental data to facilitate the system analysis. Values for the input vectors for the model described in Chapter 3 are also shown in Figure 4.6.

The geometry of the magnetic side of the baseline FPI design is shown in Figure 4.5. In the hardware version of this interface, the center magnets are two N52 Neodymium permanent magnets with one-inch diameter (pictured in Figure 4.6(c)). They have the same dipole direction and magnitude, which was calculated using the equations in Chapter 3 and the parameters listed in Table 4.3. The magnetic field strength at the surface and the dimensions are taken from the specifications sheet.

Table 4.2 Summary of System Simulation Parameters.

Parameter	Symbol	Value
Damping	c	0.2 N s/m
System Mass	m	2 kg
Equilibrium Field-Cooled Distance from Inertial Origin to Center of Mass of Spacecraft	$\mathbf{r}_{cube,FC}$	$\begin{bmatrix}0 & 0 & 0.06\end{bmatrix}^T$ m
Center of Mass of Spacecraft to Center of Plate of Magnets (Body Axes)	$\mathbf{C}$	$\begin{bmatrix}0 & 0 & -0.5\end{bmatrix}^T$ m
Inertia of Homogenous-Cube Module	$\mathbf{I}_{cube}$	$\begin{bmatrix}0.003 & 0 & 0 \\ 0 & 0.003 & 0 \\ 0 & 0 & 0.003\end{bmatrix}$ kg·m²

Table 4.3 Summary of Magnet Simulation Parameters.

Parameter	Symbol	Value
Permanent Magnet		
Surface Field Strength	*B*	0.533 Tesla
Magnet Surface to Center of Mass	*d*	0.00635 m
Dipole Locations from Center of Spacecraft Face (Body Axes)	$\boldsymbol{L}_{PMX}$	$\mathbf{L}_{PM1} = \begin{bmatrix} 0 & 0.01524 & 0 \end{bmatrix}^{\mathrm{T}}$ m $\mathbf{L}_{PM2} = \begin{bmatrix} 0 & -0.01524 & 0 \end{bmatrix}^{\mathrm{T}}$ m
Electromagnets		
Resistance	*R*	38 Ω
Number of Turns	*T*	5000
Encircled Area	*A*	5.1e-4 m^2
Dipole Locations from Center of Spacecraft Face (Body Axes)	$\boldsymbol{L}_{EMX}$	$\mathbf{L}_{EM1} = \begin{bmatrix} 0 & 0.04445 & 0 \end{bmatrix}^{\mathrm{T}}$ m North $\mathbf{L}_{EM2} = \begin{bmatrix} 0.03556 & 0 & 0 \end{bmatrix}^{\mathrm{T}}$ m East $\mathbf{L}_{EM3} = \begin{bmatrix} 0 & -0.04445 & 0 \end{bmatrix}^{\mathrm{T}}$ m South $\mathbf{L}_{EM4} = \begin{bmatrix} -0.03556 & 0 & 0 \end{bmatrix}^{\mathrm{T}}$ m West

The electromagnets in the FPI use simulation parameters based on the four identical electromagnets from the hardware implementation of the flight. These electromagnets are steel-core tubular electromagnets from Magnetic Sensor Systems, pictured in Figure 4.6(c). However, in order to provide more illustrative results, their properties were altered to the parameters listed in Table 4.3, which produce a magnetic dipole moment nearly equivalent to that of the permanent magnets when at 10 V. The electromagnets were mounted (and simulated) such that positive voltages produce the same direction of magnetic dipole as the permanent magnets. The vectors to each of these magnets from the center of the plane containing the magnets is also listed in Table 4.3, where the electromagnets are denoted by cardinal directions to indicate

where they are on the interface in Figure 4.5 (i.e. “North” and “South” are in line with the permanent magnets).

In hardware, the electromagnets can be powered in a range of ±15 V, so this range limit is used in the simulation. Unless otherwise specified, when the electromagnets are field-cooled into the system, they are simulated with a voltage of 10 V at equilibrium. Fielding cooling is simulated as taking place at a one-centimeter separation distance between the superconductor surface and the plane of the magnets but zero relative rotation between them. (Given the 10 cm cube, this equilibrium reads as 6 cm in the *z* direction because the position vector is defined by the line from the origin on the superconductor surface to the center of mass of the spacecraft on the plots).

The following simulations illustrate the system’s differing responses in the time and frequency domain for the spacecraft’s position and orientation dynamics. They examine the system dynamics resulting from the actuation of the “North” electromagnet in the baseline FPI (Section 4.1.4). In all simulations both permanent magnets are field-cooled into the superconductor. The “North” electromagnet (which lies along the spacecraft’s *y* axis) is given a static step command voltage at the first time step in order to produce a dynamic response in the interface.

In runs specified as “zero-field-cooled” (or ZFC), the North electromagnet was turned off during the cooling process and does not have a frozen-image in the superconductor model. In runs where the actuator is specified as “field-cooled,” (or FC10), it was turned on at positive ten volts during the superconductor cooling process and so has a corresponding frozen-image in the model. In runs where the other three

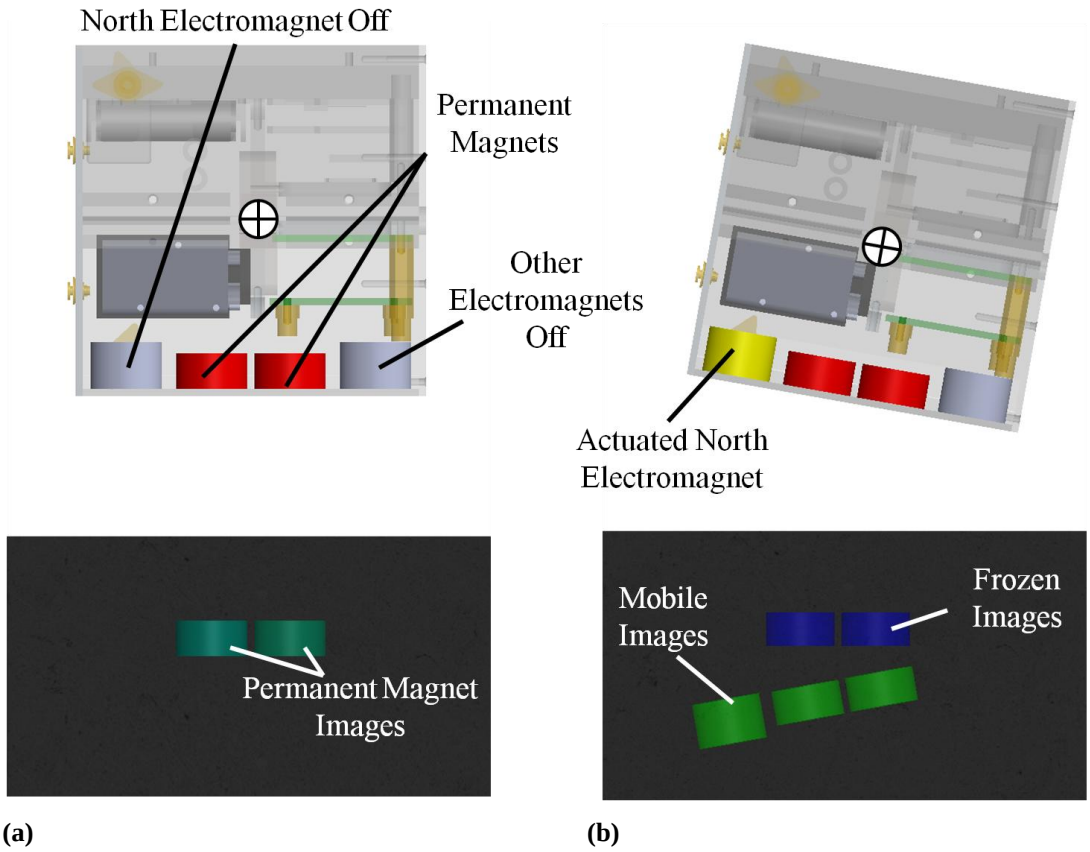

Figure 4.7. (a) A side view of a field-cooled equilibrium where the North electromagnet is zero-field-cooled and the other magnets are off (b) when the electromagnet is turned on it produces a mobile image and the system settles to a new equilibrium.

electromagnet actuators (East, South, and West) are specified as "all others on," each of the electromagnets were field-cooled at ten volts and held at ten volts for the duration of the run. In cases where they are specified as "all others off", each of the remaining three electromagnets was turned off during field-cooling and remained off for the duration of the run. For example, Figure 4.7 shows the field-cooled and actuated positions of a zero-field-cooled actuator with all other magnets off and Figure 4.8 shows the field-cooled and actuated positions of a field-cooled electromagnet with all others off.

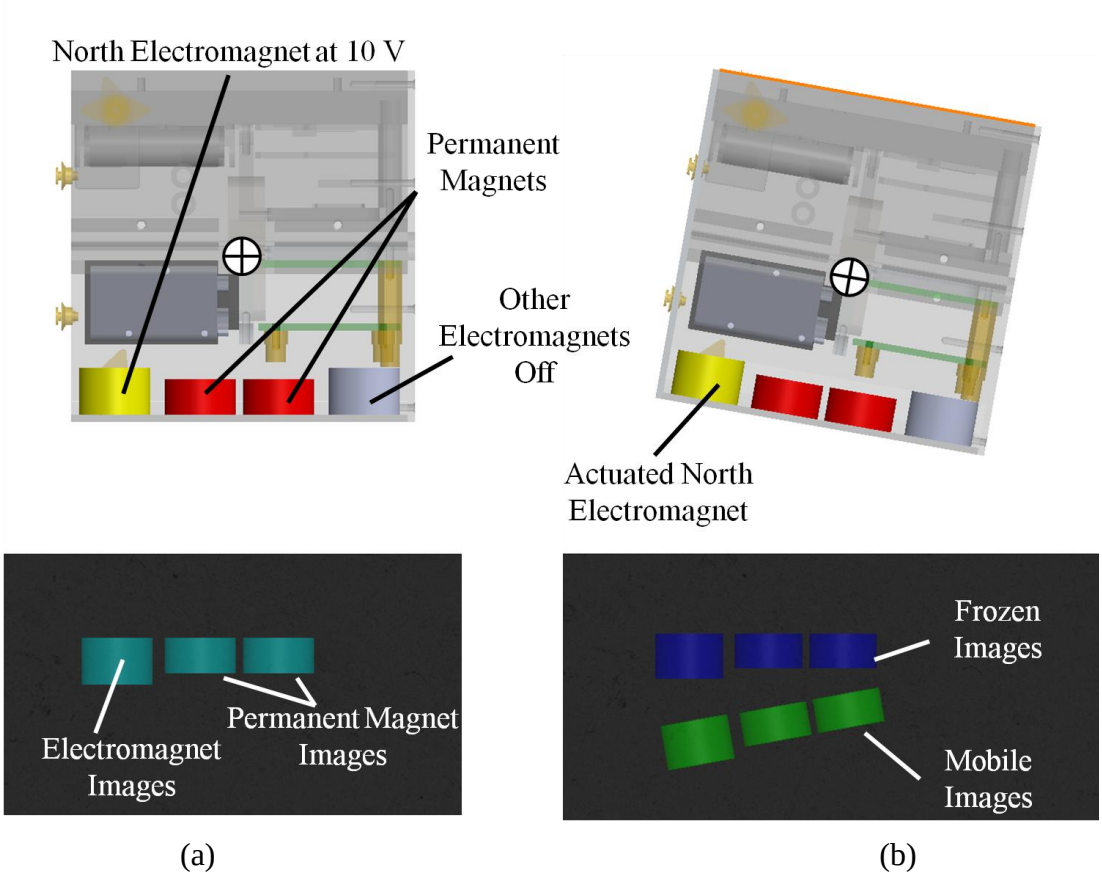

Figure 4.8. (a) A side view of a field-cooled equilibrium where the North electromagnet is field-cooled at 10 V and the other magnets are off (b) when the electromagnet is given a non-equilibrium voltage the system settles to a new equilibrium.

4.3 Actuation Performance

4.3.1 Factors Influencing Actuation Performance

The most straightforward way to influence the equilibrium position of an FPI is to manipulate the magnetic field of the magnets in the interface directly. The baseline FPI design alters its equilibrium by manipulating the voltages applied to the electromagnets. These simulations in particular examine the effects of changing the voltage of a single electromagnet (the "North" electromagnet) given different FPI conditions. Three factors influence the resulting new equilibrium of the system: the

strength of the actuation, the field-cooled status of the actuator, and the state of the other actuators in the FPI.

As the electromagnet is tuned to different voltages (and therefore different currents and different dipole strengths), the superconductor reacts to maintain the field-cooled flux distribution. Thus, as the magnetic flux becomes weaker than the field-cooled value, the superconductor will act to bring the equilibrium in closer to the superconductor so that it captures more flux and better matches its imprinted flux distribution. Figure 4.9 illustrates this effect. Not only does the resulting relative position and orientation between the spacecraft modules change with a change in actuation voltage, the stiffness of the FPI connection also changes, as evidenced by the changing natural frequencies of the system.

Because of the unique physics of flux pinning, the setup of the interface during the cooling process has a significant influence on the behavior of the system once the FPI is in place. As seen in the frozen-image model, each magnet in the vicinity of the superconductor when it crosses below its critical temperature produces a frozen-image of the same strength reflected over the surface of the superconductor. These frozen-images provide the basin of attraction for the interface. Any magnet that is not powered or not in the vicinity of the superconductor when it is cooled still produces a mobile image, and thus be repelled from the superconductor and can therefore actuate the system as shown in Figure 4.7 and Figure 4.8. Thus, the second factor influencing the behavior of the FPI is the actuator's field-cooling status, i.e., if the electromagnet was turned on or off during the imprinting of the superconductor. A zero-field-cooled magnet (one that was off during the superconductor's cooling process) behaves

differently over a range of input voltages than one that was field-cooled at a given voltage.

Finally, the effect of a single actuator is influenced by the status of the other actuators in the FPI. Because each electromagnet in its field-cooled position and strength acts as a damped spring in the system, the state of the other electromagnets matters in the final dynamic response of the system. Thus, the development of actuation commands for a single actuator must be developed in conjunction with an understanding of how the other actuators in the system influence the final equilibrium.

In order to understand the influence of the strength of the actuation command, the field-cooling setup and the status of the other actuators, simulations were performed over the full range of available voltages (-15 V to 15 V) for four different FPI conditions. These conditions are: 1) the North electromagnet turned off during field-cooling (zero-field-cooled) with all of the other electromagnets off, 2) the North electromagnet turned on during field-cooling at 10 V with all of the other electromagnets off, 3) the North electromagnet zero-field-cooled with all of the other electromagnets turned on, and 4) the North electromagnet field-cooled at 10 V with all of the other electromagnets on. The following subsections explore the relative position and orientation time responses and the frequency responses of the baseline FPI design under a variety of different conditions.

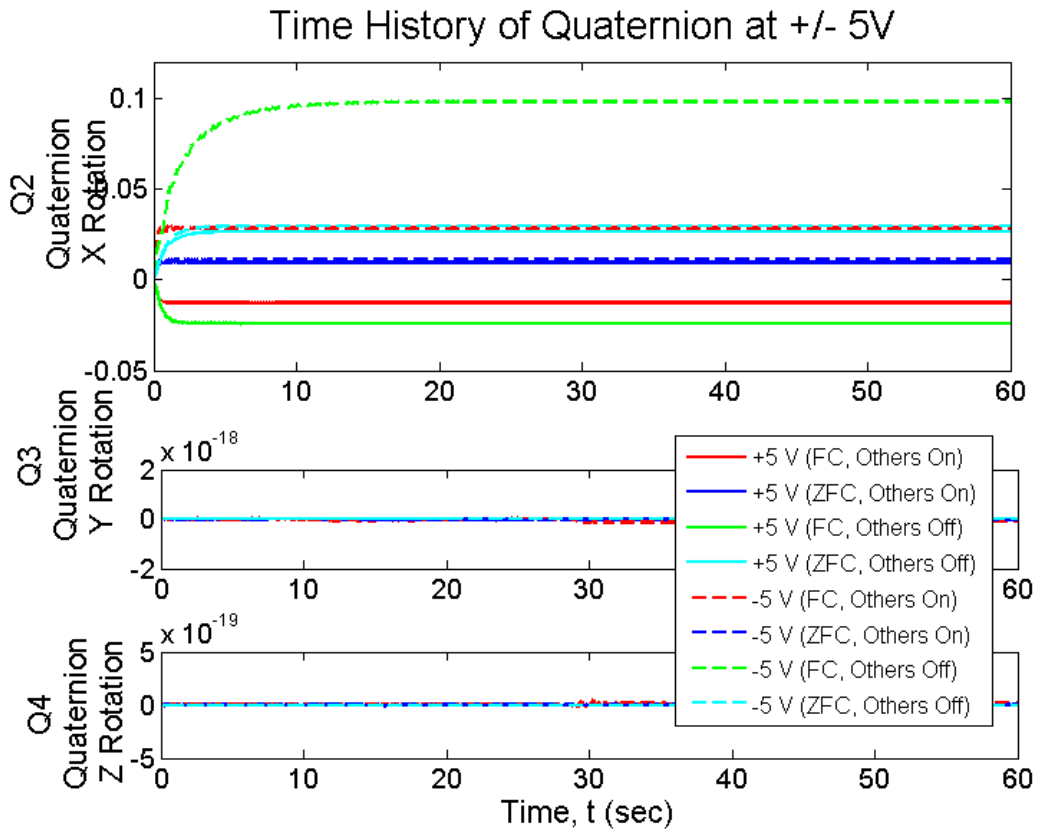

Figure 4.10. Quaternion time responses of all of the four FPI conditions at +/- 5 V. Since the actuated (North) electromagnet is in line with the permanent magnets, no disturbance is induced in the *y* or *z* rotations.

4.3.2 Representative Relative Position and Orientation Responses

Observations from the Response over the Simulation Run Time

The time history of the relative position of the spacecraft with respect to the superconductor, shown in Figure 4.11, indicates a number of important traits about the behavior of an actuated FPI. One of the first observations is that the *x* position is not perturbed in any way due to the actuation of the system (although small numerical errors on the order of 10^{-19} are visible). Given the fact that the inertia is modeled as homogenous and the actuation occurs in the North electromagnet, which lies along the *y* axis with the permanent magnets, this result is not surprising. It does, however,

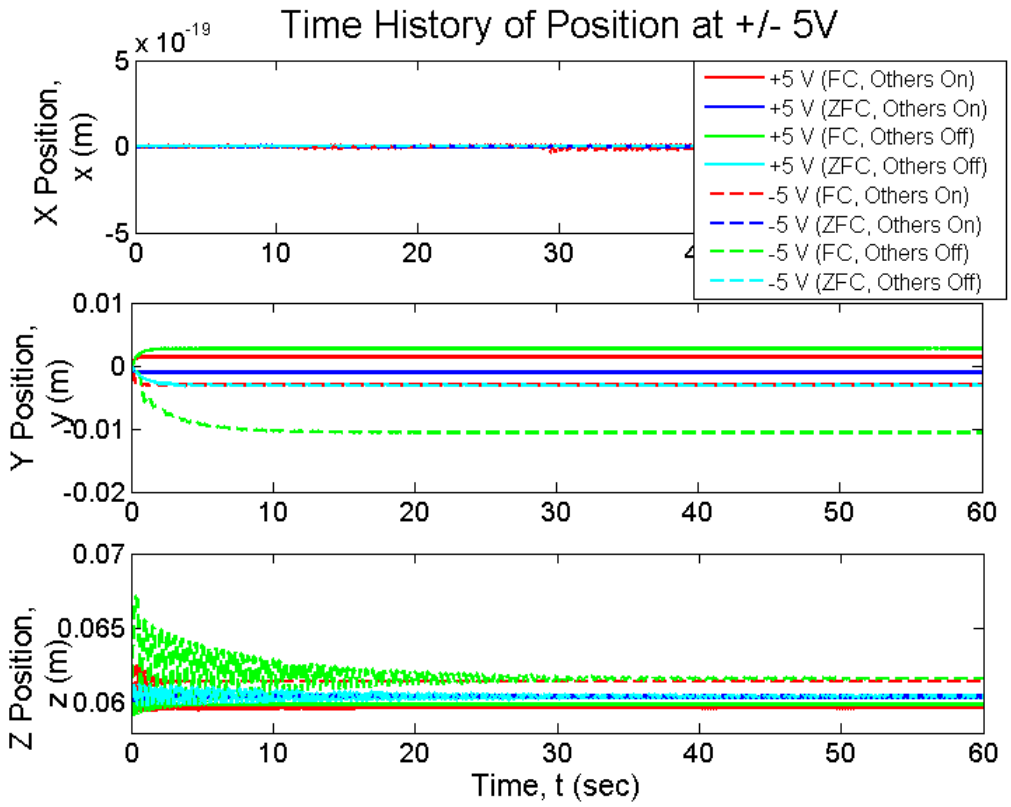

Figure 4.11. Position time responses of all of the four FPI conditions at +/- 5 V. Since the actuated (North) electromagnet is in line with the permanent magnets, no disturbance is induced in the *x* position.

confirm that nonlinear model does not predict a cross-coupling of the motion between the *x* translation and the other degrees of freedom studied here, and lends credence to the veracity of the simulation results. Variations in inertia can induce motion in this direction, but since that is not the focus of this study, the *x* direction motion is not discussed further.

Another observation that can be made about Figure 4.11 is that these representative responses settle to a steady state well before the end of the 60-second simulation. This result is relevant because subsequent analyses report the average state of the system at the end of the 60-second simulation. These time histories suggest that

60 seconds is sufficiently long to enable the system to reach its steady state. To confirm this suspicion, a set of data was collected for runs at 120 seconds and compared to the results for the 60 second runs. The differences were negligible. The text notes the rare cases where this generalization is not true.

The orientation time responses for the full 60-second simulation time for voltages of +/- 5 V (corresponding to the position plots in Figure 4.11) are shown in Figure 4.10. The same broad conclusions can be drawn from this plot: the *y* and *z* rotations only show small numerical errors and are not perturbed by this step input, and the quaternions generally achieve a steady state well before the end of the simulation time, meaning that the average value at 60 seconds is approximately the steady state of the response.

Observations from the Response over a Truncated Time

Figure 4.12 and Figure 4.13 look at a more detailed view of system's position response by only presenting the first five seconds of data for the system's free response to an open-loop step change in the North electromagnet voltage at +/- 5V. The data is spread over two plots for clarity - Figure 4.12 shows the plots where all of the other electromagnets are off and Figure 4.13 shows the data when all other electromagnets are on. The corresponding quaternion plot is shown in Figure 4.14.

As can be expected from the passive behavior of the system, nonlinearities are apparent in the data, particularly in the *z* position direction. The *z* position data is also the most oscillatory and takes the longest to damp out.

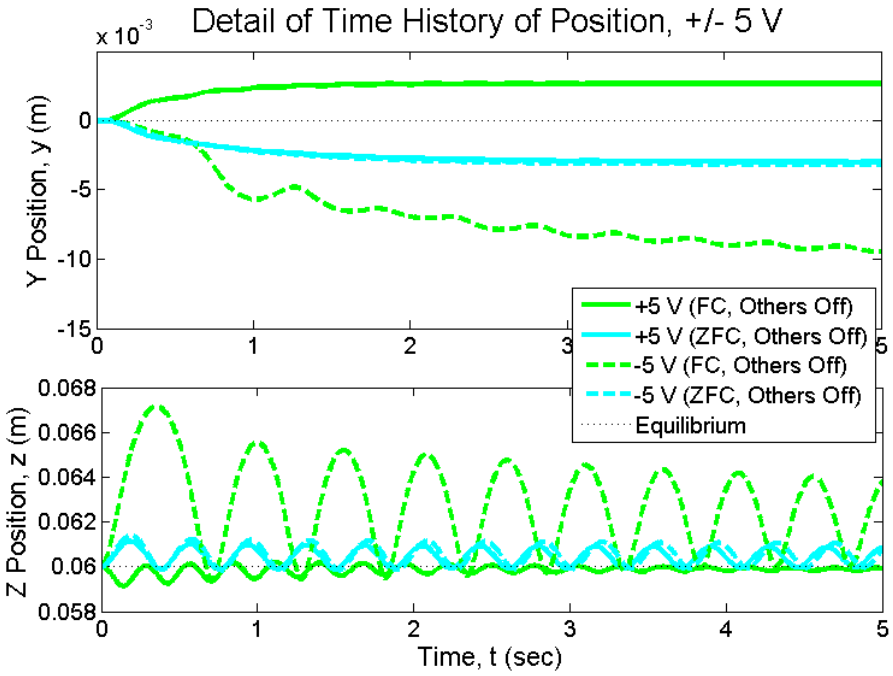

Figure 4.12. Detailed view (0 – 5 seconds) of the time response of the system in both the zero-field-cooled state and field-cooled state (10 V) when all of the other magnets are off.

Positive and Negative Response Symmetry

One of the more interesting things to note in Figure 4.12, Figure 4.13, and Figure 4.14 is the fact that for all zero-field-cooled states (the blue and light blue plots), the positive and negative voltages of the same magnitude produce nearly the exact same responses, while the opposite-signed field-cooled voltages result in motion in completely different directions. This observation results from the fact that the zero-field-cooled actuator can only produce a mobile (repulsive) image in the superconductor. At modest strengths, the model implies that a voltage difference in either direction produces the same deflection equivalent to the electromagnet pushing away from the superconductor. However, the fact that the electromagnet is also

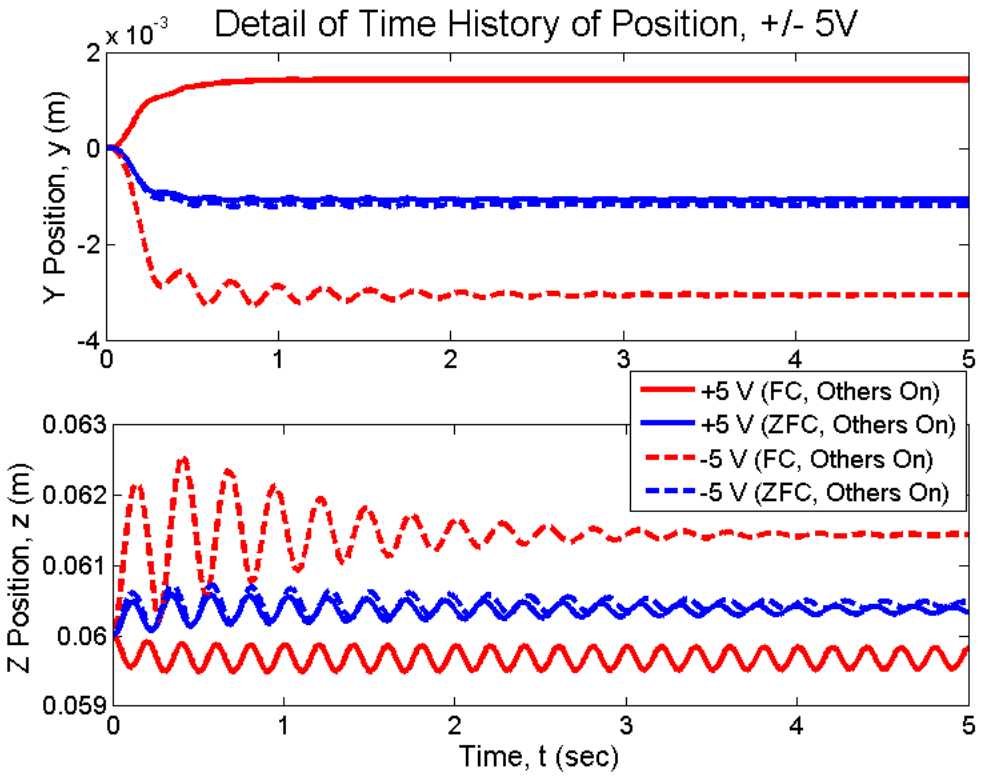

Figure 4.13. Detailed view (0 – 5 seconds) of the time response of the system in both the zero-field-cooled state and field-cooled state (10 V) when all of the other magnets are on.

influenced by the existing frozen and mobile images from the permanent magnets causes the negative polarities to produce slightly higher equilibria.

The behavior of these zero-field-cooled actuators has significant implications for the development of control architectures for FPIs because changing the sign of the control voltage does not produce motion in the opposite direction. An FPI designer might exploit this observation to selectively employ zero-field-cooled actuators on systems where motion in only one direction is desired (for example, in a docking interface where motion in a particular direction represents a collision).

The field-cooled actuator, on the other hand, can produce bi-directional motion of approximately equal magnitude in both directions for moderate control voltages. This

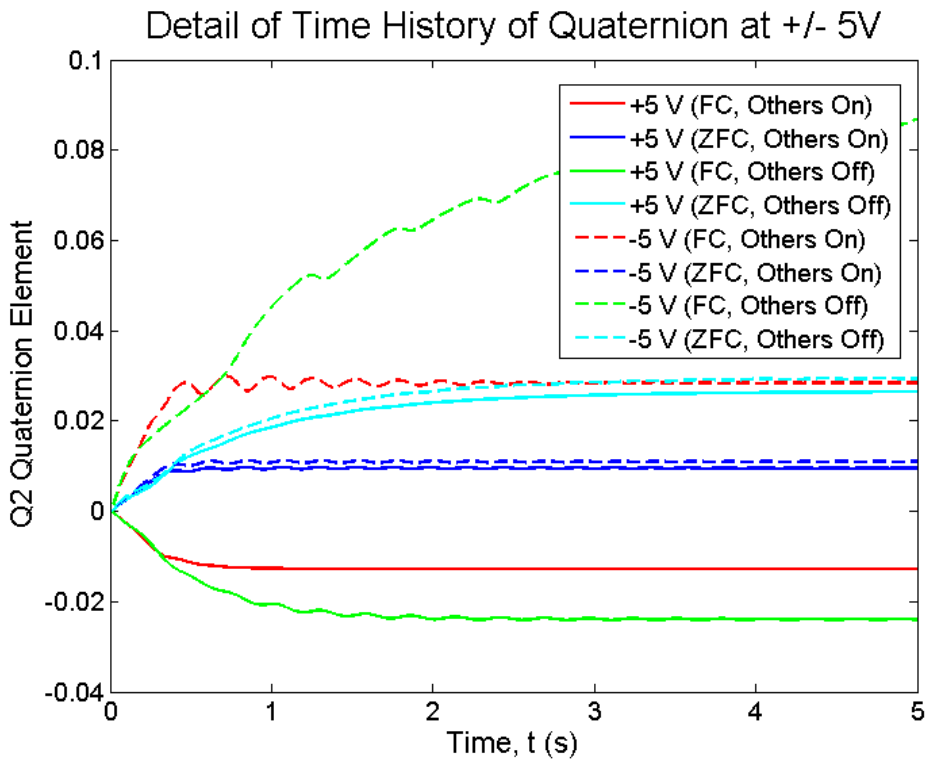

Figure 4.14. Detailed view (0 – 5 seconds) of the time response of the quaternions of the system under different conditions.

type of actuator design is best suited to a vibration-isolated non-contacting pointing platform, such as one that might be used in the pointing of mirror segments in a large aperture telescope, where this flexibility and symmetry may be most useful.

Transient Responses

The transient response of an actuation is an important design consideration for FPIs because most applications for the technology involve operating the FPI when the spacecraft are very close together. If operated as a passive system with no feedback control over the electromagnets, these transients (which can be large relative to the final settling value) may cause a collision or a disengagement of the FPI itself.

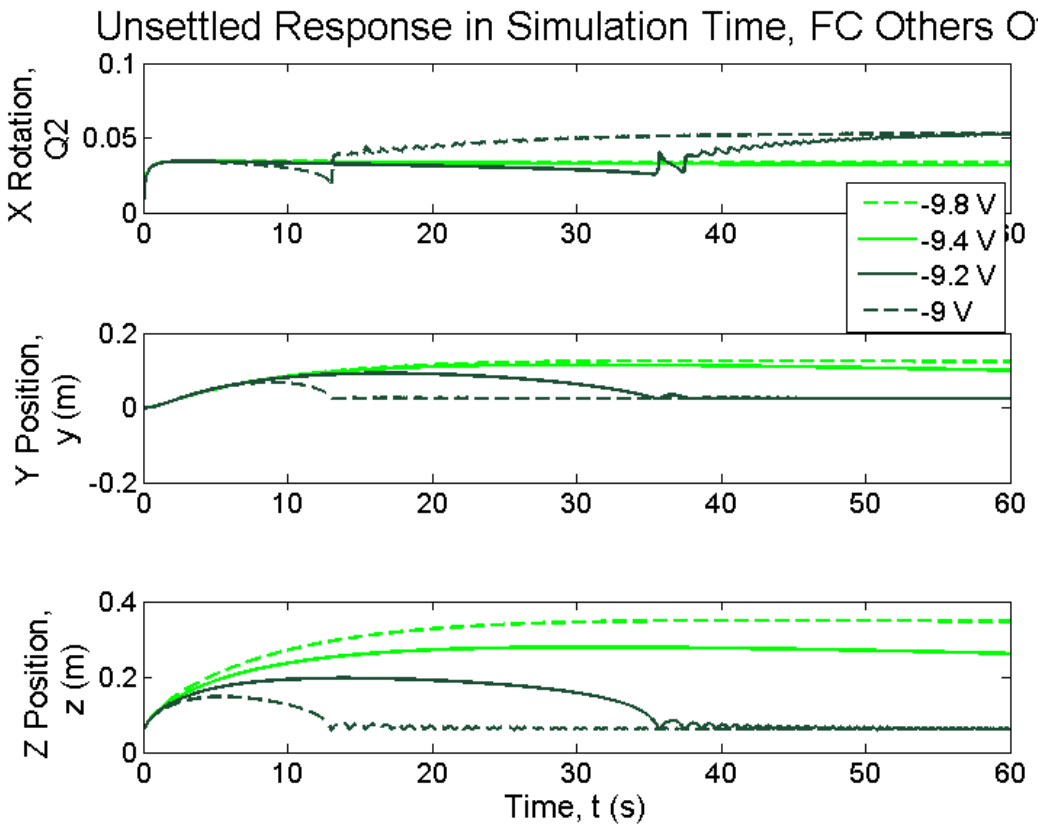

Figure 4.15. The position responses induced by low negative voltages for a field-cooled system with all other magnets off. Note that the first plot is for *x* rotation, not position.

For the representative time responses in Figure 4.12, Figure 4.13, and Figure 4.14, the transient response is fairly muted and appears to manifest primarily as a small oscillation in the first few seconds of the response. However, as the actuation voltage gets stronger, the transient response can become more dramatic, particularly in the position states. Figure 4.15 shows the system's response to a field-cooled actuator with all of the other magnets off where the transients dominate the system behavior for the length of the simulations. The dark green data (-9.2 V and -9.0 V) show the system settling within the simulation time. The lighter green plots (-9.4 V and -9.6 V) shows the same behavior as the previous two, but do not settle during the simulation time.

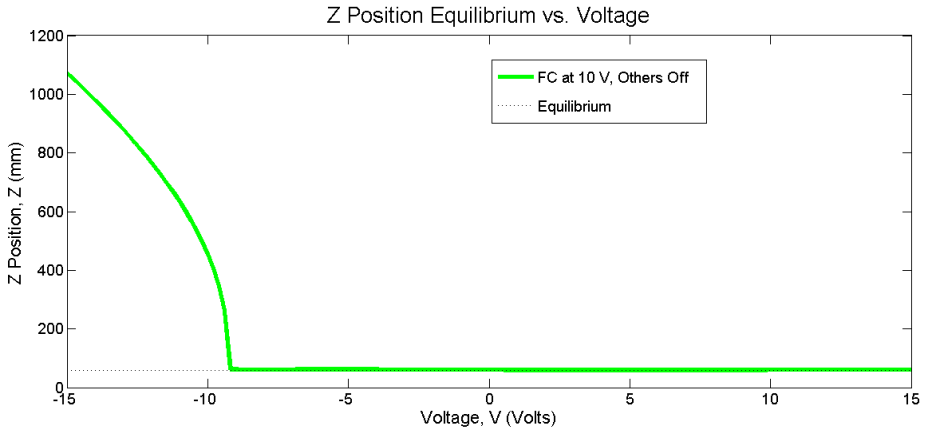

Figure 4.16. Over the range of voltages, the field-cooled magnet with others off does not settle a low voltage ranges in the period of time given for the simulation. Thus, the average final position at the end of 60 seconds dramatically increases.

Thus, in a plot of the system's average position after 60 s of simulation time versus applied voltage (Figure 4.16), the *z* position shows a sudden jump because the system is still in its transient phase. Similar sudden changes occur in the *x* rotation and *y* position as well. Values below this threshold of -9.4 V are subsequently ignored for this data set.

It is worth noting that because this simulation does not model the effective range of flux pinning, it is possible for the simulations to produce unrealistic performance data as shown in Figure 4.15. For the hardware on which the simulation is based, this threshold is around 10 cm. In this example, the transient response exceeded the 10 cm threshold of effective flux pinning range, so in reality the system would undock from the superconductor. However, in the simulation the system's apparent transient response is instead stretched over a long time period as the system gradually comes back to an equilibrium near the superconductor.

4.3.3 Notable Discrepancies in the Relative Position and Orientation Response

The results discussed in Section 4.3.2 are typical of the -15 V to + 15 V range studied in these simulations. However, the two major deviations from these trends can be found in the aggregate simulation results are worth further discussion. The first occurs in the FPI condition with a field-cooled actuator and all of the other magnets turned off. For the majority of the voltage range simulated, the magnet settles near an equilibrium that is mostly negative in *y* position and positive in *x* rotation states. However, between -6.90 V and -6.91 V, a transition occurs, as shown in Figure 4.17.

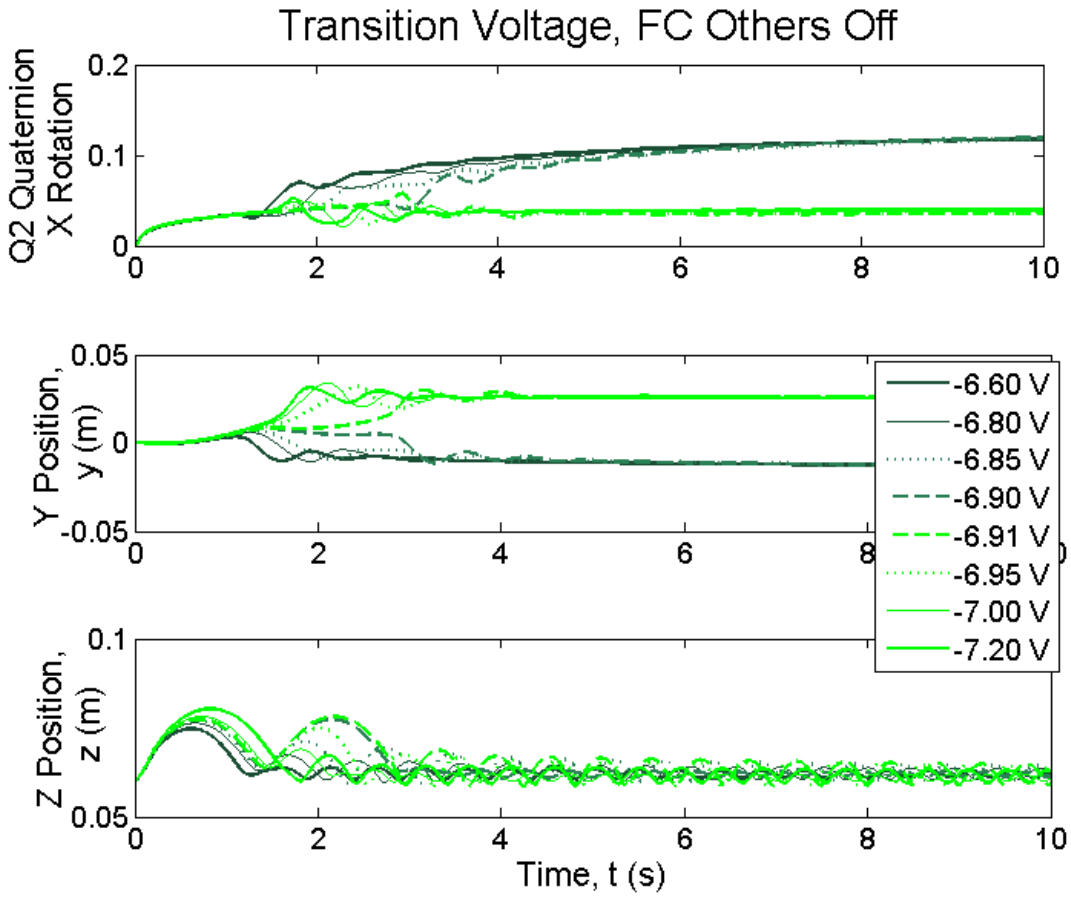

Figure 4.17. The divergence of the position and orientation responses of the field-cooled magnet with all others off. Prior to -6.91 V, the system settles near equilibriums in one region and after that voltage it settles near equilibriums in a different region. Note that the first plot is for *x* rotation, not position.

For voltages below -6.91 V, the system settles to a positive *y* position and a much lower *x* rotation value than previously. The *z* position transitions as well, although the scale of the plots makes it difficult to observe.

The second discrepancy from earlier trends exhibits a similar transition, but in the zero-field-cooled system with all of the magnets off, as shown in Figure 4.18. At values above +13.2 V the system transition to a new region of equilibriums, where the bulk of the -15 V to +15 V range follows equilibriums with positive *x* rotation values and small *y* and *z* displacements. At +13.4 V, however, the system shifts to negative *x*

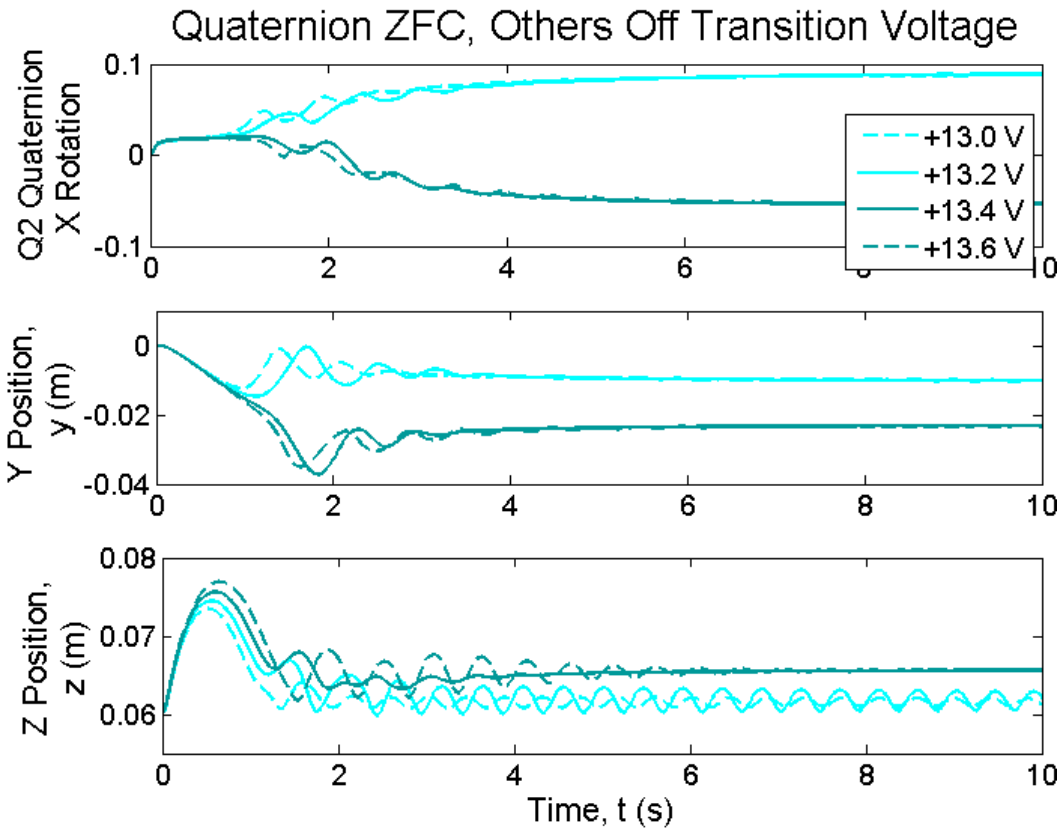

Figure 4.18. The divergence of the position and orientation responses of the zero-field-cooled magnet with all others off. Prior to +13.2 V, the system settles near equilibriums in one region and after that voltage it settles near equilibriums in a different region. Note that the first plot is for *x* rotation, not position.

rotation values and larger-magnitude *y* and *z* displacements. Essentially, under specific circumstances, the simulation appears to show a bifurcation of the system response, where the system settles to two different areas of equilibria.

Figure 4.19 shows the average *x* rotation and *y* position at 60 seconds versus voltage. As a result of these sudden bifurcations, the equilibrium values shift dramatically from their earlier trend, at -6.91 V for the field-cooled case and +13.4 V for the zero-field-cooled case. (Values above -9.4 V in the field-cooled condition are

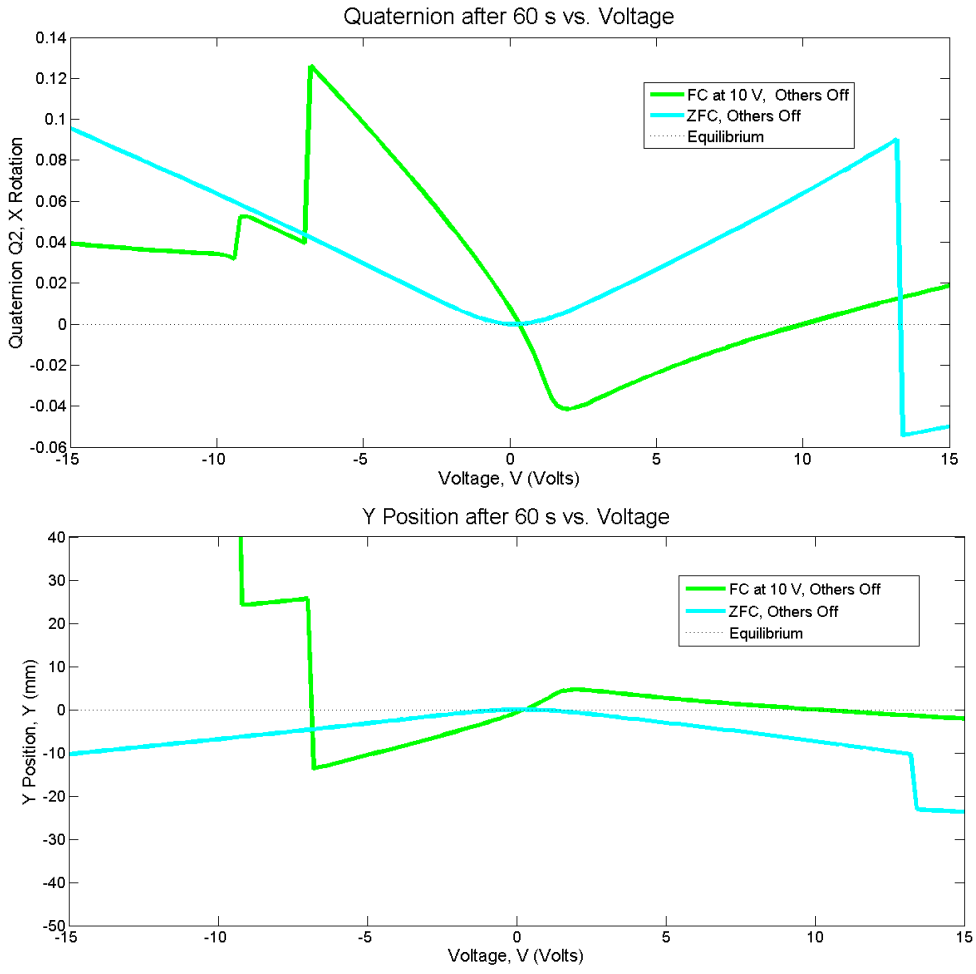

Figure 4.19. The average position of the *x* rotation and *y* displacement versus voltage. The plot shows the sudden bifurcation at -6.91 V for the field-cooled case and +13.4 V for the zero-field-cooled case. Values below -9.2 V in the field-cooled case are not settled and do not represent an equilibrium behavior.

the result of the unsettled system as discussed earlier).

The fact that both of these discrepancies occur when the other magnets in the system are off, regardless of the field-cooling state of the magnet, is helpful in understanding the cause of this sudden bifurcation. No such discrepancies are observed in the higher-stiffness systems where the other magnets are all on. At 10 V, the simulated electromagnets become nearly as powerful as the permanent magnets in the array. Thus, one possible explanation for the sudden bifurcations in Figure 4.17 and Figure 4.18 is that at a high enough magnitude of voltage, the permanent magnets are drawn out of their own field-cooled potential well and settle to a potential well dominated by the actuator's magnetic field.

In the case of the field-cooled system, the actuator was initially cooled with a +10 V. As the voltage values of the electromagnet are driven to increasingly negative values – which repel against both their mobile and frozen image – the permanent magnets in the array become increasingly attracted to the potential well caused by the +10 V frozen-image. At -6.91 V, the system finally rotates sharply enough to induce the entire system to shift up the *y* axis and settle to a smaller angle about the *x* axis. When the other magnets are on, the larger stiffness in the system delays this shift such that it is not observed in the -15 V to + 15 V range.

In the case of the zero-field-cooled magnet, the high positive voltages in the electromagnet also induce a strong repulsion from its own mobile image. However, being stronger and of the same polarity as the permanent magnets, the electromagnet becomes strongly attracted to the potential well of its neighboring permanent magnet. At +13.4 V, the electromagnet is drawn into that potential well, causing the system to

shift down the *y* axis and settle to a slightly negative *x* rotation and slightly higher *z* displacement.

The presence of these sudden bifurcations highlights another design principle for complex FPIs. Because the magnets are all in close proximity and all react to the superconductor's magnetic field, it is possible for the (complex, multi-magnet) system to have more than one equilibrium. Although this model is not a perfect representation of the dynamics of the system, this behavior has been noted in laboratory work with hardware. (The magnet array has been observed to settle to an equilibrium where the magnets are in their neighbor's potential wells.) Thus, while the system's behavior is bounded, it may hop to a new region if the system is designed to allow it. If this effect is undesirable, the magnets should be spatially distant from one another to avoid one magnet falling into the potential well formed by a different magnet. That being said, if relative large displacements are called for in the FPI design, this type of hopping may represent one of the best ways to actuate the system. One of the designs for the FPI orbital flight demonstration, discussed in Chapter 8, uses this principle.

4.3.4 Comparison of FPI Conditions over Applied Actuator Voltage Range

Average Position and Orientation after 60 Seconds

Now that the system's time response behavior is fully explored, it is possible to directly compare the average final states of the system after the 60-second simulation time for different FPI conditions, and to develop expressions that, for this system, map the input voltage to the nominal output equilibrium. Figure 4.20, Figure 4.21, and Figure 4.22 all show the system's equilibrium as a function of actuator voltage. Discrepancies in the system's behavior, as noted before, are not shown. Several important observations can be seen in these plots.

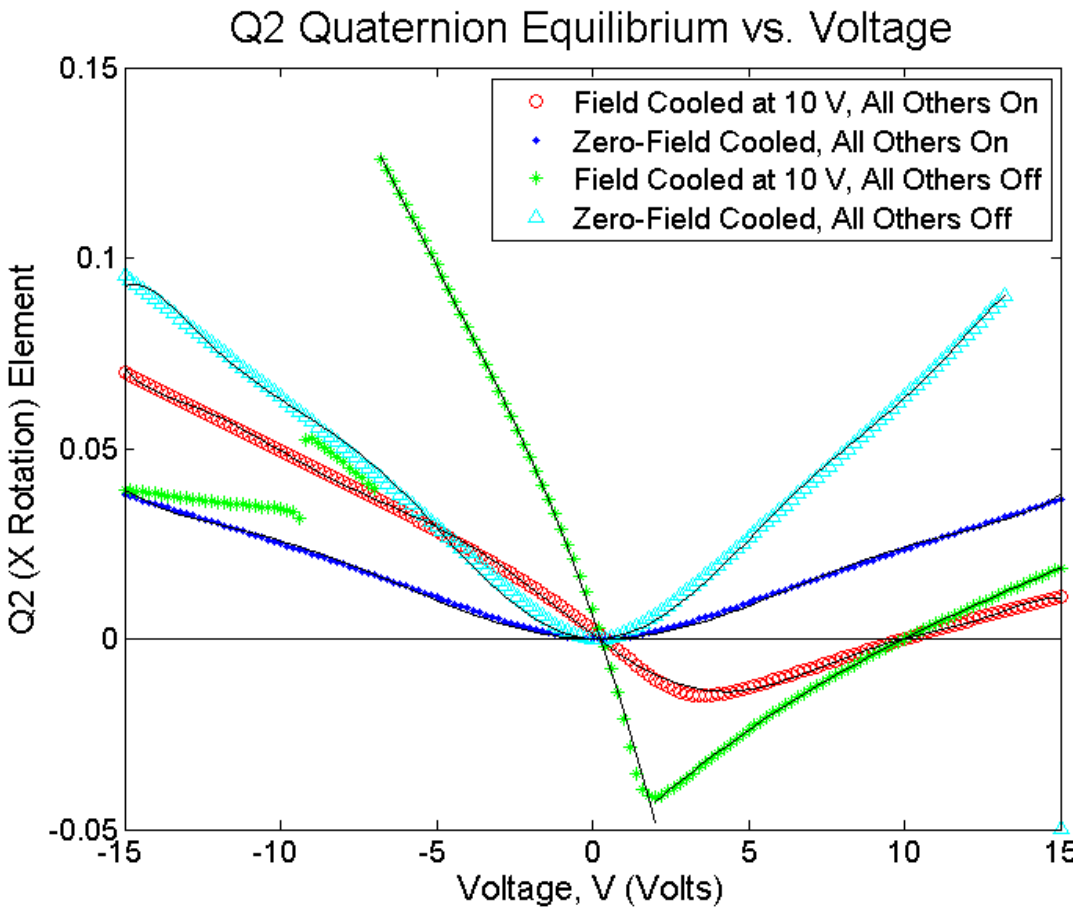

Figure 4.20. The *x* rotation state as a function of voltage and FPI condition.

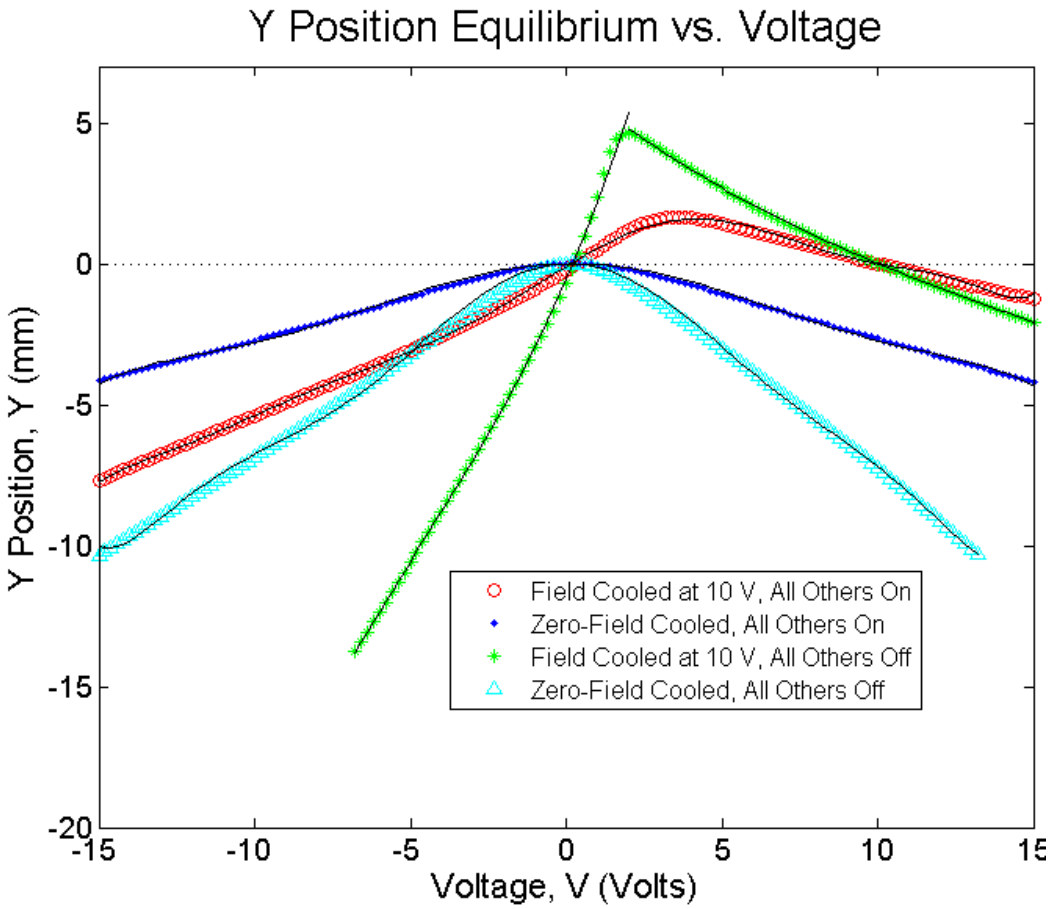

Figure 4.21. The *y* position state as a function of voltage and FPI condition.

Although shown for a single time history in previous sections, these plots clearly show the basic symmetry of the zero-field-cooled states (shown as dark blue points and light blue triangles) about the zero voltage point. (As noted before, however, these states are not exactly symmetric due to the influence of the positive permanent magnets). These plots also generally stay on the same side of the axis, producing uni-directional motion regardless of the voltage polarity. The equilibrium position at field-cooling is found at the zero voltage mark, where the *x* rotation and *y* position plots intersect the *x* axis, and the *z* position plot intersects the line corresponding to 60 mm, its equilibrium. It is also interesting to note that the zero-field-cooled equilibrium in

the *z* position seems to follow almost the exact same values whether the other magnets are turned off or on for mid-range voltages.

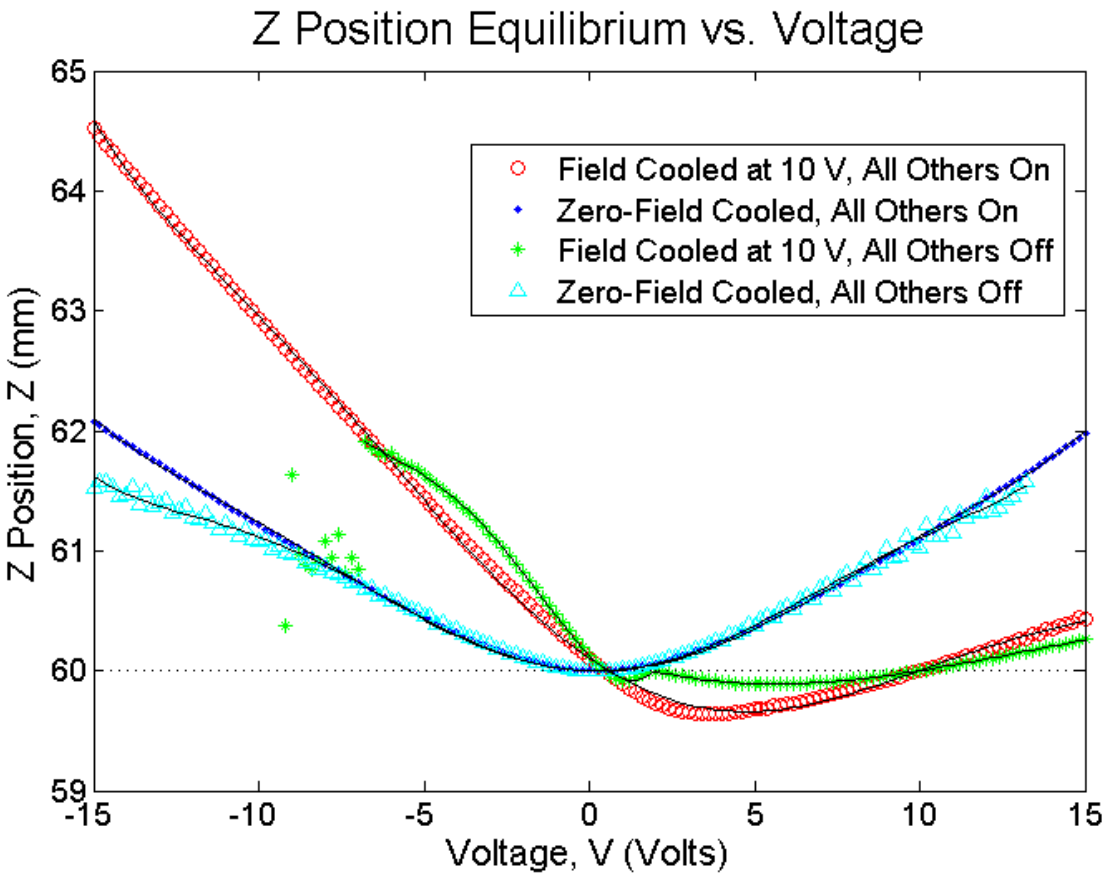

Figure 4.22. The *z* position state as a function of voltage and FPI condition.

The field-cooled values, on the other hand, intersect their respective equilibrium axes at +10 V, the field-cooling strength of the magnet. They also have another intercept near zero (although not necessarily at zero because the magnet's frozen-image slightly alters the equilibrium even with the magnet turned off). In between these two intercepts the values have one sign, and above +10 V and below their lower threshold, the plots have the opposite sign. This observation corresponds to the fact that weakening the magnet from its field-cooled strength starts to bring the system in

closer to the superconductor, while strengthening the magnet or changing its polarity pushes the system further away.

The effect of the other magnets in the system, while only examined in the on or off state in this study, clearly has an impact on the system's equilibrium. In particular, the observed sudden bifurcations do not occur in the studied voltage range when all of the electromagnets are on. Also, when the actuator is given strong negative voltages, having the other magnets on appears to moderate the *x* rotation and *y* final equilibriums, keeping them lower than the cases where the magnets are turned off. However, while having all of the magnets on appears to induce smaller *z* displacements for positive actuator voltages, at negative actuator voltages these plots produce the largest displacements.

Dominant Z Frequency Content

As seen in the time responses of the system, the *z* position exhibits the strongest oscillatory behavior of the excited states. In order to compare the stiffness of the simulated FPIs, an FFT was produced for the *z* position of at each actuator voltage. The largest peak on the magnitude plot was then identified as the dominant frequency. Figure 4.23 shows the resulting dominant frequencies as a function of applied voltage.

The dominant frequency in the zero-field-cooled states mirrors the symmetry over the *y* axis shown by the position and orientation plots (except where the region shift occurs in the FPI with the other magnets off). At an actuator voltage of zero the system is in equilibrium and the system does not have a dominant frequency because the perturbations recorded by the simulation are only induced by the actuator itself.

Since the actuator does not induce a perturbation at zero volts the system does not react.

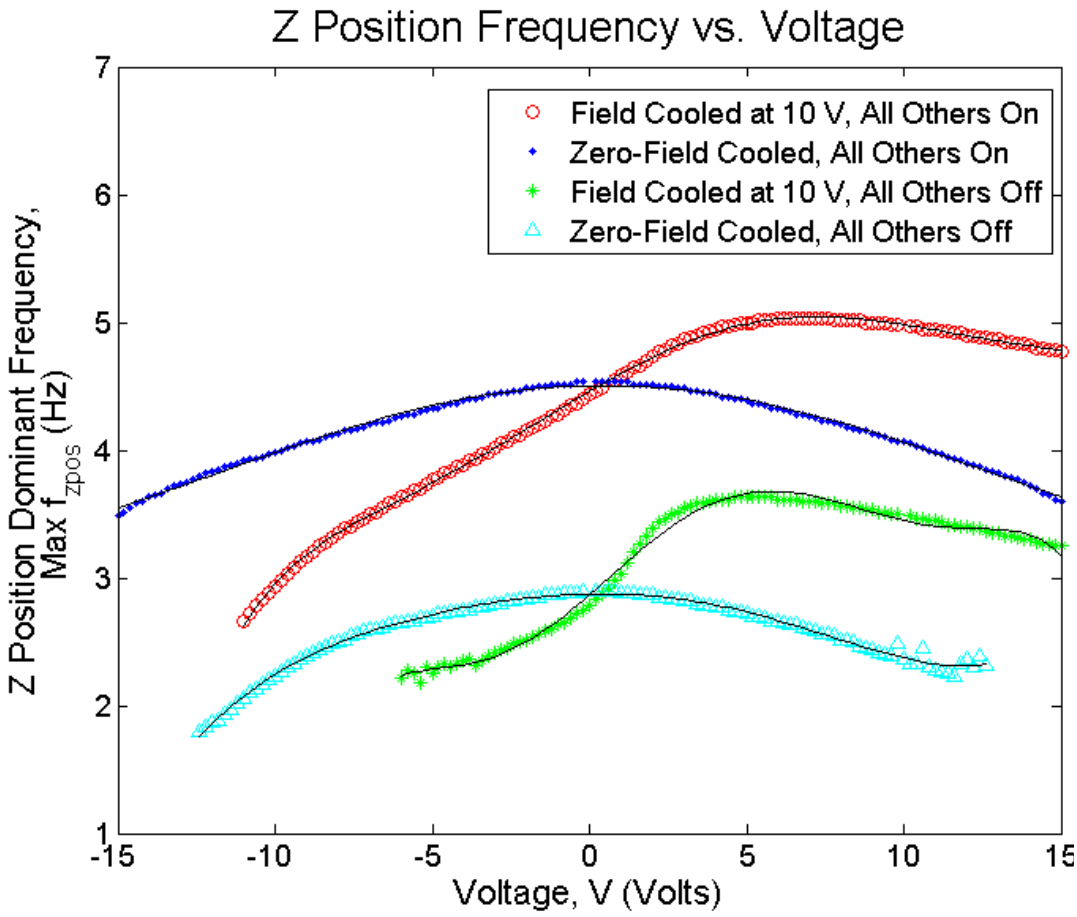

Figure 4.23. The dominant *z* position frequency as a function of voltage and FPI condition.

The field-cooled FPIs have a more complex relationship with frequency. For voltages lower than +10 V, the dominant frequency shifts to higher values. This effect is the result of the weaker magnets shifting to a closer equilibrium in an attempt to re-establish the flux distribution when the magnets were stronger. However, after about +5 V the system starts to lose stiffness because the weakness of the electromagnet is not compensated by the reduction in the equilibrium positions. These plots are in equilibrium at +10 V so the system is not excited and a dominant frequency does not

exist (although the system would clearly exhibit stiffness from the permanent magnets if an external perturbation were applied). A small gap in the plot shows this fact.

The systems with all of the magnets turned on exhibit higher dominant frequencies (and a correspondingly higher stiffness) than those without the other magnets on. In fact, the highest dominant frequencies (around 5 Hz) are found in the field-cooled FPI with all of the magnets on. Clearly, if a high-stiffness FPI is desirable, more magnets should be field-cooled into the system.

An FPI controller designer can use these observations to build a system that meets the mission objectives. If vibration isolation is of primary concern, it is possible to raise and lower the actuator's voltage to tune the natural frequency of the FPI. If a high stiffness is required, including an FPI design with large numbers of passive magnets would be best. If the system needs to avoid exciting frequencies above a certain range when performing an actuation, the zero-field-cooled system is optimal because actuation only decreases its natural frequency (neglecting bifurcation).

4.3.5 Summary of FPI Conditions and Mapping Inputs to Ouputs

The observations above facilitate an analysis of the uses of these various FPI conditions. A polynomial fit to the resulting equilibrium as a function of voltage also provides a way to determine, given the FPI conditions, what output a given input actuator voltage produces.

Field-Cooled at 10 V, Others Off

This FPI condition appears to produce the largest displacements for negative voltage commands, although it experiences a bifurcation in equilibrium and large transient displacements at these values. This FPI condition may be well-suited to applications where a large resulting displacement over a small range of voltage is desired. The large transients in the system can also be used to disengage an FPI, for example in an undocking maneuver. However, its relationship between voltage and final equilibrium position is highly nonlinear and exhibits suddenly large equilibrium changes for relatively small voltage changes, especially around 2 V. This sharp transition necessitates fitting two different polynomials to the curve, whose coefficients and R^2 values are shown in Table 4.4 and Table 4.5. The system has a moderate dominant frequency that varies from 2 – 3.5 Hz over the range of values seen in the simulation. The polynomial coefficients for the frequency are also contained in Table 4.4, but are valid for the region $-6 \leq V \leq 9.8, 10.2 \leq V$.

Table 4.4. Polynomial Coefficients for FC, Off -6.8≤V≤2. Frequency (f) coefficients are valid from -6≤V≤9.8, 10.2≤V. Polynomials map from volts to quaternion values (Q2), mm (Y, Z), and Hz (f).

Quantity	$Q2$	Y	Z	f
V^6	0	0	0	$-1.65e^{-6}$
V^5	0	0	0	$4.14e^{-5}$
V^4	0	0	$1.27e^{-6}$	$-6.35e^{-5}$
V^3	$-1.04e^{-4}$	$1.20e^{-5}$	$1.86e^{-5}$	-0.0041
V^2	-0.0016	$1.71e^{-4}$	$6.57e^{-5}$	0.0068
V^1	-0.024	0.0026	$-2.78e^{-4}$	0.21
V^0	0.0062	$-5.44e^{-4}$	0.060	2.87
R^2	.9989	.9990	.9994	.9914

Table 4.5. Polynomial Coefficient Vales for FC, Off 2≤V<15. Polynomials map from volts to quaternion values (Q2) and mm (Y, Z).

Quantity	$Q2$	Y	Z
V^3	$5.72e^{-6}$	$-6.63e^{-7}$	$-3.05e^{-7}$
V^2	$-2.79e^{-4}$	$3.16e^{-5}$	$1.21e^{-5}$
V^1	0.0080	$-8.94e^{-4}$	$-1.07e^{-4}$
V^0	−0.058	0.0064	$1.61e^{-4}$
R^2	.9998	.9998	.9996

Zero-Field-Cooled, Others Off

The zero-field-cooled FPI condition produces generally symmetric displacements and stiffness for both positive and negative values. It exhibits predictable motion for most of the studied voltage range, although it does exhibit a bifurcation at larger positive voltages. In the regime of positive voltages, this FPI condition produces larger *z* displacements than field-cooled systems and moderate displacements in the *y* position and *x* rotation. It exhibits lower stiffnesses than most of the other conditions studied here. The coefficients and R^2 values coefficients for the fitted polynomial matching the input voltage to the output are shown in Table 4.6. This FPI condition may be suited to a low-stiffness station-keeping maneuver where the ability to reject moderate disturbances and a predictable equilibrium profile are more important factors than stiffness or the ability to produce large equilibrium changes.

Table 4.6. Polynomial Coefficients for ZFC, Off V≤13.2. Frequency (f) coefficients are valid from $-12.4 \leq V \leq -0.2, 0.2 \leq V \leq 12.6$. Polynomials map from volts to quaternion values (Q2), mm (Y, Z), and Hz (f).

Quantity	$Q2$	Y	Z	f
V^8	$-1.71e^{-10}$	$1.87e^{-11}$	0	0
V^7	$-3.29e^{-10}$	$3.51e^{-11}$	0	0
V^6	$8.24e^{-8}$	$-9.02e^{-9}$	$2.13e^{-10}$	$-3.69e^{-9}$
V^5	$8.30e^{-8}$	$-8.61e^{-9}$	$8.05e^{-11}$	$1.25e^{-8}$
V^4	$-1.44e^{-5}$	$1.58e^{-6}$	$-9.47e^{-8}$	$2.81e^{-6}$
V^3	$-1.58e^{-6}$	$6.86e^{-8}$	$6.30e^{-8}$	$1.66e^{-6}$
V^2	0.0014	$-1.56e^{-4}$	$1.84e^{-5}$	$-2.39e^{-4}$
V^1	$-3.22e^{-4}$	$2.26e^{-5}$	$-7.69e^{-6}$	-0.0060
V^0	0	0	0	0.0061
R^2	.9980	.9981	.9942	.9921

Field-Cooled, Others On

This FPI condition produces the highest frequencies seen in the simulations, as well as the largest *z* displacements. At high actuator voltages it produces low *x* rotations and *y* displacements with moderate *z* displacements. It does not exhibit any bifurcations in the studied voltage range and exhibits predictable (although asymmetric) trends in all of its states. The polynomial fit coefficients and corresponding R^2 values are shown in Table 4.7. The high stiffness of this FPI and its ability to produce large *z* displacements may make this FPI condition well-suited to on-orbit assembly or grappling maneuvers.

Table 4.7. Polynomial Coefficients for FC, On -15≤V≤15. Frequency (f) coefficients are valid from $-11 \leq V \leq 0.4, 0.8 \leq V \leq 9.8, 10.2 \leq V$. Polynomials map from volts to quaternion values (Q2), mm (Y, Z), and Hz (f).

Quantity	$Q2$	Y	Z	f
V^{10}	0	4.70e^{-14}	0	0
V^{9}	$-8.45e^{-12}$	9.31e^{-13}	0	0
V^{8}	$1.16e^{-11}$	$-2.65e^{-11}$	0	0
V^{7}	$4.89e^{-9}$	$-5.38e^{-10}$	0	0
V^{6}	$-3.72e^{-9}$	$5.11e^{-9}$	$1.28e^{-10}$	$-1.77e^{-7}$
V^{5}	$-1.04e^{-6}$	$1.14e^{-7}$	$-1.58e^{-9}$	$5.09e^{-6}$
V^{4}	$-2.26e^{-7}$	$-3.31e^{-7}$	$-6.62e^{-8}$	$6.74e^{-6}$
V^{3}	$1.00e^{-4}$	$-1.10e^{-5}$	$5.80e^{-7}$	$-9.43e^{-4}$
V^{2}	$2.84e^{-4}$	$-2.20e^{-5}$	$1.91e^{-5}$	-0.0038
V^{1}	-0.0062	$6.74e^{-4}$	$-1.90e^{-4}$	0.14
V^{0}	0.0010	$-1.14e^{-4}$	$1.04e^{-4}$	4.46
R^2	.9991	.9993	.9995	.9995

Zero-Field-Cooled, Others On

The final FPI condition considered in this study involves the actuator being turned off during the field-cooling process, but all of the other electromagnets on at +10 V. This condition produces displacements and dominant frequencies that are roughly symmetric over the *y* axis and do not exhibit any bifurcations in the voltage range. These FPIs produce larger *z* displacements than the other conditions while producing moderate *y* positions and *x* rotations at positive voltages. For negative voltages, this FPI condition produces the smallest *y* displacements and *x* rotations. Like the field-cooled condition with all of the magnets on, this condition produces relatively high stiffness values; however, these values are symmetric around the equilibrium point. Table 4.8 details the coefficients of a best-fit polynomial for the different states or

frequencies as a function of voltage. These characteristics make this FPI condition suitable for precise vibration-isolated payload pointing platforms, where a high stiffness and tunable dominant frequency are advantageous.

Table 4.8. Polynomial Coefficients for ZFC, On-6.8≤V≤2. Frequency (f) coefficients are valid from -0.2≥V, 0.2≤V. Polynomials map from volts to quaternion values (Q2), mm (Y, Z), and Hz (f).

Quantity	$Q2$	Y	Z	f
V^6	$5.21e^{-9}$	$-5.72e^{-10}$	$1.38e^{-10}$	0
V^5	$-2.79e^{-9}$	$3.36e^{-10}$	$-5.40e^{-11}$	0
V^4	$-2.31e^{-6}$	$2.54e^{-7}$	$-6.55e^{-8}$	$6.27e^{-6}$
V^3	$1.17e^{-6}$	$-1.49e^{-7}$	$3.50e^{-8}$	$-1.00e^{-5}$
V^2	$4.28e^{-4}$	$-4.73e^{-5}$	$1.69e^{-5}$	-0.0055
V^1	$-1.70e^{-4}$	$1.48e^{-5}$	$-8.74e^{-6}$	0.0050
V^0	0	0	0	4.50
R^2	.9968	.9969	.9994	.9960

CHAPTER 5

STABILITY AND CONTROL OF A FLUX-PINNED INTERFACE

5.1. The Single-Magnet Single-Superconductor FPI

5.1.1. Spacecraft Applicability

In order to fully analyze FPI stability and develop control methodologies for an FPI system, it is necessary to focus on a simple design that is mathematically tractable while still being technologically useful and applicable. Focusing on the properties of a single-magnet single-superconductor (SMSS) FPI design reaches a balance between these goals.

Although the SMSS design is mathematically straightforward, it must also be useful in an FPI to be worth investigation. Independently, an FPI of this design may not seem particularly useful since it can only actively change its equilibrium in a single degree of freedom. However, when multiple SMSS FPIs are used to control a spacecraft, it is possible to manipulate the relative motion between the two spacecraft in all six degrees of freedom. (This capability requires a sufficient number of actuators that are positioned to correctly reach the desired motion). Examples of relative motion in four degrees of freedom using four SMSS FPIs are shown in Figure 5.1. Thus, given the benefits of fully characterizing the stability and control of an FPI that has a number of applications on orbit, this work examines the behavior of a single SMSS.

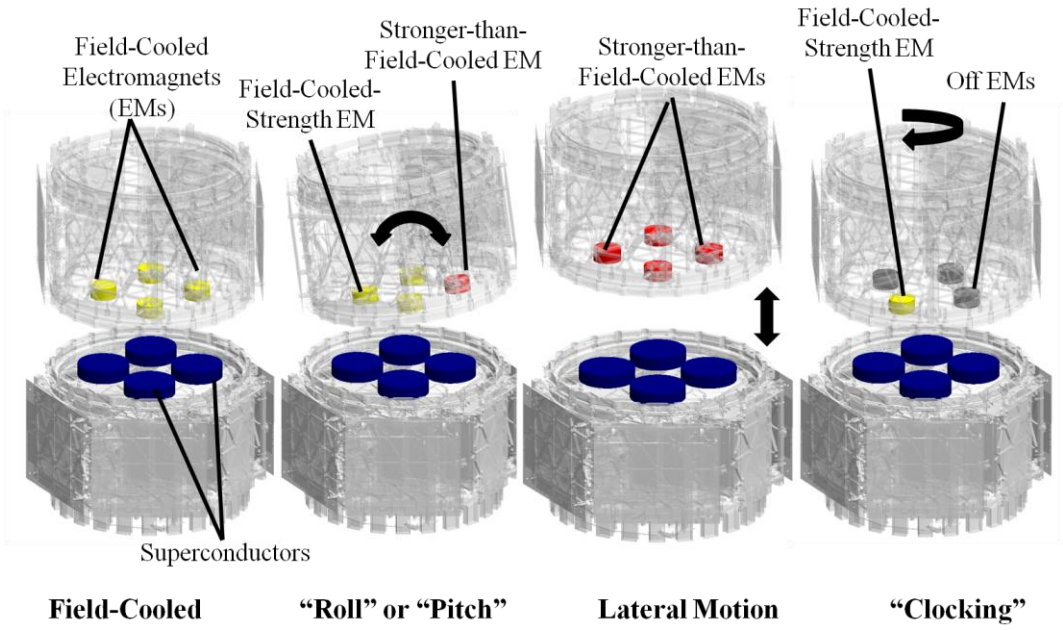

Figure 5.1. Examples of relative spacecraft maneuvers that are achievable with four SMSS FPIs.

5.1.2. System Parameters and Notation

In this work, the SMSS FPI is a single electromagnet pinned over a hard superconductor at a field-cooling distance of $\mathbf{r}_{FC}$ and a field-cooling magnetic dipole moment of $\boldsymbol{\mu}_{FC}$. The magnetic moment of the electromagnet at a given point in time is denoted by $\boldsymbol{\mu}_1$. An inertial frame (N) is fixed in the superconductor and a moving body frame (B) is attached to the magnet. Figure 5.2 shows how these parameters are related to the SMSS FPI. The standard frozen-image

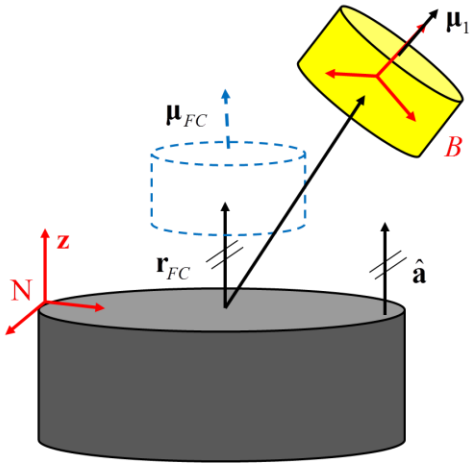

Figure 5.2. The basic parameters for the analysis in this chapter.

model can be applied here because there is no need for complex multi-magnet notation. Thus, the system has a mobile and a frozen image (not pictured) reflected in the superconductor corresponding to the one source electromagnet. These images are the basis of the forces and torques acting on the system.

In this chapter, the frame in which the derivative is being applied needs to be specified explicitly. Thus, the following notation is used to distinguish between body-frame and inertial-frame derivatives where appropriate in the text:

$$\frac{{}^{N}d}{dt}=\dot{\mathbf{x}}={}^{N}\mathbf{x},\frac{{}^{N}d}{dt^{2}}=\ddot{\mathbf{x}}={}^{NN}\mathbf{x} \tag{5.1}$$

$$\frac{{}^{B}d}{dt}={}^{B}\mathbf{x},\frac{{}^{B}d}{dt^{2}}={}^{BB}\mathbf{x} \tag{5.2}$$

where B denotes body frame and N denotes inertial frame. Noting this, for an uncontrolled system, the magnetic moment of the magnet does not change with respect to the body frame over time.

$${}^{B}\boldsymbol{\mu}_{1,passive}=0 \tag{5.3}$$

However, for the actively controlled system, the change in the magnetic moment is the way the system's behavior is altered, so:

$${}^{B}\boldsymbol{\mu}_{1,active}={}^{B}\boldsymbol{\mu}_{1}(t) \tag{5.4}$$

The remainder of this chapter uses this model to analyze the stability and basic control of an SMSS FPI.

5.2. Background Development

5.2.1. Energy Analysis

In order to develop an energy-based Lyapunov argument for the stability of the FPI interface, it is necessary to develop the energy equations for the potential and kinetic energy for the SMSS FPI using the frozen-image model. In general, the potential energy of a magnetic dipole under the influence of the magnetic field is described by: [114]

$$U = -\boldsymbol{\mu}_1 \cdot \mathbf{B}_{tot} \tag{5.5}$$

where $\mathbf{B}_{\text{tot}}$ is the magnetic field acting on the system. The potential energy acting on the system from the frozen image is thus as follows:

$$U_f = -\boldsymbol{\mu}_1 \cdot \left[\frac{\mu_0}{4\pi} \left(\frac{3\left(\boldsymbol{\mu}_f \cdot \hat{\boldsymbol{\rho}}_f\right)\hat{\boldsymbol{\rho}}_f}{{\rho_f}^5} - \frac{\boldsymbol{\mu}_f}{{\rho_f}^3} \right) \right] = -\boldsymbol{\mu}_1 \cdot \mathbf{B}_f \tag{5.6}$$

However, when describing the energy of the system, the frozen-image model has a peculiarity: for a magnet under the influence of its own mobile (or mirror) image, the potential energy is different by a factor of two, as detailed in Giaro et. al.[115] and used in work by Cansiz, Hull, and Gundogdu.[116] The expression for the potential energy of the mobile image is thus:

$$U_m = -\boldsymbol{\mu}_1 \cdot \left[\frac{\mu_0}{8\pi} \left(\frac{3\left(\boldsymbol{\mu}_m \cdot \hat{\boldsymbol{\rho}}_m\right)\hat{\boldsymbol{\rho}}_m}{{\rho_m}^5} - \frac{\boldsymbol{\mu}_m}{{\rho_m}^3} \right) \right] = -\boldsymbol{\mu}_1 \cdot \frac{1}{2}\mathbf{B}_m \tag{5.7}$$

This factor of two is not present when describing the system purely in the form of forces and torques between dipoles. Thus, given these expressions, for the frozen-image model Equation (5.5) can be re-written as:[117]

$$
\begin{aligned}
U &= -\boldsymbol{\mu}_1 \cdot \left(\left(\frac{\mu_0}{4\pi} \right) \left(\frac{3\left(\boldsymbol{\mu}_f \cdot \hat{\boldsymbol{\rho}}_f\right)\hat{\boldsymbol{\rho}}_f}{{\rho_f}^5} - \frac{\boldsymbol{\mu}_f}{{\rho_f}^3} \right) + \left(\frac{\mu_0}{8\pi} \right) \left(\frac{3\left(\boldsymbol{\mu}_m \cdot \hat{\boldsymbol{\rho}}_m\right)\hat{\boldsymbol{\rho}}_m}{{\rho_m}^5} - \frac{\boldsymbol{\mu}_m}{{\rho_m}^3} \right) \right) \\
&= -\boldsymbol{\mu}_1 \cdot \left(\mathbf{B}_f + \frac{1}{2}\mathbf{B}_m \right)
\end{aligned}
\tag{5.8}
$$

The kinetic energy of the flux-pinned system is based only on the properties of the source magnet, since the images do not have mass or inertia. Thus, the kinetic energy is:

$$
T = \frac{1}{2} m \left(\overset{N}{\mathbf{r}}_1 \cdot \overset{N}{\mathbf{r}}_1 \right) + \frac{1}{2} \boldsymbol{\omega}_{B/N} \cdot \mathbf{I}_1 \cdot \boldsymbol{\omega}_{B/N} \tag{5.9}
$$

where $\overset{N}{\mathbf{r}}_1$ is the inertial derivative of the position of the magnet $\mathbf{r}_1$, m is the mass of the magnet, $\mathbf{I_1}$ is the inertia dyadic of the magnet, and $\boldsymbol{\omega}_{B/N}$ is the relative angular rate of the magnet-fixed body frame and the superconductor-fixed inertial frame.

The force acting on the source magnet can be written two ways. Using the potential energy, the expression is:[117]

$$
\mathbf{F}_{mag} = \nabla \left(\boldsymbol{\mu}_1 \cdot \left(\mathbf{B}_f + \frac{1}{2}\mathbf{B}_m \right) \right) \tag{5.10}
$$

However, using the expression for the forces between two dipoles, no factor of one half is needed. The expression for the forces acting on the source magnet are (from Equation (3.14) expanded to include frozen and mobile images):

$$
\begin{aligned}
\mathbf{F}_{mag} = & \frac{3\mu_0\mu_m\mu_1}{4\pi\rho_f{}^4}\left[\hat{\boldsymbol{\rho}}_m\left(\hat{\boldsymbol{\mu}}_m\cdot\hat{\boldsymbol{\mu}}_1\right)\right] \\
& + \frac{3\mu_0\mu_m\mu_1}{4\pi\rho_f{}^4}\left[\hat{\boldsymbol{\mu}}_m\left(\hat{\boldsymbol{\rho}}_m\cdot\hat{\boldsymbol{\mu}}_1\right)\right] \\
& + \frac{3\mu_0\mu_m\mu_1}{4\pi\rho_f{}^4}\left[\hat{\boldsymbol{\mu}}_1\left(\hat{\boldsymbol{\rho}}_m\cdot\hat{\boldsymbol{\mu}}_m\right)\right] \\
& - \frac{3\mu_0\mu_f\mu_1}{4\pi\rho_f{}^4}\left[5\hat{\boldsymbol{\rho}}_m\left(\hat{\boldsymbol{\rho}}_m\cdot\hat{\boldsymbol{\mu}}_m\right)\left(\hat{\boldsymbol{\rho}}_m\cdot\hat{\boldsymbol{\mu}}_1\right)\right] \\
& + \frac{3\mu_0\mu_f\mu_1}{4\pi\rho_f{}^4}\left[\hat{\boldsymbol{\rho}}_f\left(\hat{\boldsymbol{\mu}}_f\cdot\hat{\boldsymbol{\mu}}_1\right)\right] \\
& + \frac{3\mu_0\mu_f\mu_1}{4\pi\rho_f{}^4}\left[\hat{\boldsymbol{\mu}}_f\left(\hat{\boldsymbol{\rho}}_f\cdot\hat{\boldsymbol{\mu}}_1\right)\right] \\
& + \frac{3\mu_0\mu_f\mu_1}{4\pi\rho_f{}^4}\left[\hat{\boldsymbol{\mu}}_1\left(\hat{\boldsymbol{\rho}}_f\cdot\hat{\boldsymbol{\mu}}_f\right)\right] \\
& - \frac{3\mu_0\mu_f\mu_1}{4\pi\rho_f{}^4}\left[5\hat{\boldsymbol{\rho}}_f\left(\hat{\boldsymbol{\rho}}_f\cdot\hat{\boldsymbol{\mu}}_f\right)\left(\hat{\boldsymbol{\rho}}_f\cdot\hat{\boldsymbol{\mu}}_1\right)\right]
\end{aligned}
\tag{5.11}
$$

Similarly, the torque acting on the magnet due to the images' magnetic field is given by the equation:[117]

$$\boldsymbol{\tau}_{mag} = \boldsymbol{\mu}_1 \times \left(\mathbf{B}_f + \mathbf{B}_m\right) \tag{5.12}$$

5.2.2. Lyapunov Stability Criteria

Lyapunov's Direct Method[118] is an important tool in characterizing the stability of dynamical systems (particularly those with nonlinearities, such as flux-pinning). The goal of a Lyapunov analysis is to show that the motion of a system remains arbitrarily close to its equilibrium, provided that the system starts close to that equilibrium. Consider a general continuous-time system with an equilibrium state x_e:

$$\frac{d}{dt}x(t) = f(x(t)) \tag{5.13}$$

$$f(x_e(t)) = 0 \tag{5.14}$$

An equilibrium state is Lyapunov stable if for any $\varepsilon > 0$ there exists a function $\delta(\varepsilon) > 0$, such that:[119]

$$\|x(t_0) - x_e(t_0)\| < \delta \Rightarrow \|x(t) - x_e(t)\| < \varepsilon \qquad \text{for } \forall t \geq t_0 \tag{5.15}$$

Without a loss of generality, the equilibrium state may be translated to the origin using a change of variables, simplifying Equation (5.15) such that:

$$\|x(0)\| < \delta \Rightarrow \|x(t)\| < \varepsilon \qquad \text{for } \forall t \geq 0 \tag{5.16}$$

Now, consider a continuous scalar function $V(x(t))$. This function is called a Lyapunov function for the system described in Equation (5.13) if the following three conditions are met (as listed by Schaub and Junkins):[119]

1. $V(x(t))$ is positive definite about the equilibrium point
2. $V(x(t))$ has continuous partial derivatives
3. The derivative of $V(x(t))$ is negative semi-definite

If such a Lyapunov function can be found for a system, that system is stable in the sense of Lyapunov relative to that equilibrium. However, if a function fails to meet these criteria the system is not necessarily unstable; another function or stability theory must be used instead. This definition also does not guarantee convergence to the equilibrium; it merely states that a system that starts sufficiently close to its equilibrium will have bounded motion within that region. In order to obtain a guarantee of asymptotic stability, the Lyapunov function must meet the above criteria and be explicitly negative definite.

5.2.3. Passive Systems

A passivity-based analysis is fundamentally based on the idea that a system is stable if finite energy inputs produce finite energy outputs. Thus, a passivity-based approach to analyzing a system is focused on finding an input-output mapping that shows the system is passive. Passive systems are ones in which the elements are generally well-behaved, such as resistors or capacitors. If a system can be shown to be passive, analyzing the system becomes much easier because the well-developed analysis and control synthesis tools for passive systems become available. This approach is also advantageous because it does not depend on a highly accurate model to show stability and can handle variations in mass, stiffness, and other system parameters.[120]

Mathematical Development

In order to describe passivity, it is first necessary to describe some of the mathematical concepts involved. One of the most important mathematical concepts in passivity is the inner product. A real vector space χ is defined as the real inner product space if for every pair of vectors $\mathbf{x}, \mathbf{y} \in \chi$ there exists a real number $\langle \mathbf{x}, \mathbf{y} \rangle$ that satisfies the following properties:[121]

1. $\langle \mathbf{x}, \mathbf{y} \rangle = \langle \mathbf{y}, \mathbf{x} \rangle$
2. $\langle \mathbf{x} + \mathbf{y}, \mathbf{z} \rangle = \langle \mathbf{x}, \mathbf{z} \rangle + \langle \mathbf{y}, \mathbf{z} \rangle \qquad \forall \mathbf{x}, \mathbf{y}, \mathbf{z} \in \chi$
3. $\langle \alpha \mathbf{x}, \mathbf{y} \rangle = \alpha \langle \mathbf{x}, \mathbf{y} \rangle \qquad \forall \mathbf{x}, \mathbf{y} \in \chi, \forall \alpha \in \mathbb{R}$
4. $\langle \mathbf{x}, \mathbf{x} \rangle \geq 0$

5. $\langle \mathbf{x}, \mathbf{x} \rangle = 0$ if and only if $\mathbf{x} = 0$

The function $\langle \cdot, \cdot \rangle$ then is called the inner product of the space χ. The dot product defines the inner product in $\mathbb{R}^n$. The inner product space has the property that:

$$|\langle \mathbf{x}, \mathbf{y} \rangle| \leq \|\mathbf{x}\|_{\chi} \|\mathbf{y}\|_{\chi} \tag{5.17}$$

This inequality, known as the Schwartz inequality, plays a role in showing a system is passive. The inner product of a truncated system can also be defined. A truncated system is defined as:

$$\boldsymbol{u}_T(t) = \begin{cases} \boldsymbol{u}(t), & 0 \leq t \leq T \\ 0, & t > T \end{cases} \quad T \in \mathbb{R}^+ \tag{5.18}$$

Then, the inner product of a truncation can be defined as:

$$\langle \mathbf{x}_T, \mathbf{y} \rangle = \langle \mathbf{x}, \mathbf{y}_T \rangle = \langle \mathbf{x}_T, \mathbf{y}_T \rangle \stackrel{def}{=} \langle \mathbf{x}, \mathbf{y} \rangle_T \tag{5.19}$$

The space of finite energy functions (commonly noted as L_2) is another important mathematical element in the passivity framework. When the functions x,y: $\mathbb{R} \rightarrow \mathbb{R}$

$$\langle x, y \rangle = \int_0^{\infty} x(t) y(t) dt \tag{5.20}$$

From this definition, the space L_2e, or the extended L_2 space, is defined as the space of all functions whose truncation belongs to L_2. Functions that are not in L_2 may have a truncation that is in L_2e (for example, e^t).

Definition of Passivity

With these mathematical tools, passivity can now be defined. A system is very strictly passive if there exists $\delta > 0$, $\varepsilon > 0$, and β such that:[121]

$$\left\langle \mathbf{u}, H\mathbf{u} \right\rangle_T = \left\langle \mathbf{u}, \mathbf{y} \right\rangle_T \geq \delta \left\| \mathbf{u}_T \right\|_{L_2}^2 + \varepsilon \left\| \mathbf{y}_T \right\|_{L_2}^2 + \beta \qquad \forall \mathbf{u} \in L_{2e,} \forall t \in \mathbb{R}^+ \tag{5.21}$$

Or, in other words:

$$\int_0^T \mathbf{u} \cdot H\mathbf{u} dt = \int_0^T \mathbf{y} \cdot \mathbf{u} dt \geq \delta \int_0^T \mathbf{u} \cdot \mathbf{u} dt + \varepsilon \int_0^T \mathbf{y} \cdot \mathbf{y} dt + \beta \tag{5.22}$$

The constant β term takes into account energy that is stored at t = 0. If the conditions are met, the input-output mapping $\mathbf{u} \to H\mathbf{u}$ is said to be very strictly passive. If ε = 0, the mapping is said to be strictly passive, and if δ = 0, as well, the mapping is simply passive.

5.3. Uncontrolled FPI Stability and Performance

5.3.1. Passivity of a Linear Model of FPIs

If the linear model of flux pinning is used to model the SMSS FPI, where the magnet acts as if it connected to the superconductor with a mass-spring-damper system, it is possible to show that the system is passive. Consider a system with the following equations of motion:

$$\begin{aligned} &\mathbf{y} = \dot{\mathbf{r}} && \dot{\mathbf{r}}(0), \mathbf{r}(0) = 0 \\ &\mathbf{M}\ddot{\mathbf{r}} + \mathbf{K}\mathbf{r} = \mathbf{u}(t) \end{aligned} \tag{5.23}$$

Writing the Hamiltonian of the system:

$$H(t) = \frac{1}{2}\dot{\mathbf{r}} \cdot \mathbf{M} \cdot \dot{\mathbf{r}} + \frac{1}{2}\mathbf{r} \cdot \mathbf{K} \cdot \mathbf{r} \geq 0 \tag{5.24}$$

and taking the derivative:

$$\dot{H}(t) = \dot{\mathbf{r}}\left[\mathbf{M} \cdot \ddot{\mathbf{r}} + \mathbf{K} \cdot \mathbf{r}\right] \tag{5.25}$$

Substituting in the equation of motion:

$$\dot{H}(t) = \mathbf{y} \cdot [\mathbf{u}] \tag{5.26}$$

Integrating both sides from 0 to T:

$$\int_0^T \mathbf{y} \cdot \mathbf{u} dt = \int_0^T \dot{H} dt = H(T) - H(0) \tag{5.27}$$

If *H(0)* is redefined, the result is:

$$\int_0^T \mathbf{y} \cdot \mathbf{u} dt = H(T) - \left(-H(0)\right) = H(T) - \left(\beta\right) \tag{5.28}$$

Since the Hamiltonian was defined as positive, the result is:

$$\begin{aligned} &H(T) \geq 0 \\ &\langle \mathbf{y} \cdot \mathbf{u} \rangle + \left(\beta\right) \geq 0 \\ &\langle \mathbf{y} \cdot \mathbf{u} \rangle \geq \beta \end{aligned} \tag{5.29}$$

Thus, according to Equation (5.21), the mapping from the input **u** to output **y** (or the mapping between force and velocity) is passive.

5.3.2. Lyapunov Function for Uncontrolled FPIs

Although the linear result works for small displacements, it is important to develop the characteristics of the full nonlinear model as well. Lyapunov's Direct Method is used in this analysis in order to illustrate the stability of the uncontrolled flux pinning interaction in a mathematical context. The first step in this process is to develop Lyapunov function describing an SMSS FPI. Then, one must show that the developed equation meets the criteria for Lyapunov stability. Although not guaranteed to generate a Lyapunov function, the expression for the total energy of the system is a common starting point for many such analyses. It also has the added advantage of being a physically meaningful property.[119] Thus, the total energy of the SMSS FPI

system (using the expressions in Equation (5.5) and Equation (5.9)), and the basis of the SMSS FPI Lyapunov function is:

$$V(\mathbf{r}_1) = \frac{1}{2} m \left({}^{N}\mathbf{r}_1 \cdot {}^{N}\mathbf{r}_1 \right) + \frac{1}{2} \boldsymbol{\omega}_{B/N} \cdot \mathbf{I}_1 \cdot \boldsymbol{\omega}_{B/N} + U \tag{5.30}$$

where U is the potential energy due to flux pinning.

5.3.3. Stability of a Passive SMSS FPI

Given Equation (5.30) as a potential Lyapunov function, it must be shown to meet the three criteria of a Lyapunov function before proving the stability of the passive system. First, $V(x(t))$ must be positive definite about its equilibrium point. The equilibrium point for the SMSS FPI is:

$$\mathbf{r}_1 = \mathbf{r}_{FC}, \boldsymbol{\mu}_1 = \boldsymbol{\mu}_{FC} \tag{5.31}$$

where the equilibrium magnetic dipole is defined as being positive. For simplicity and without a loss of applicability to FPIs, the field-cooled position is assumed to be parallel to the surface of the superconductor $\hat{\mathbf{a}}$. Since a system in equilibrium has no velocity, it is possible to rewrite Equation (5.30) :

$$V(\mathbf{r}_{FC}) = \frac{1}{2} m(0) + \frac{1}{2}(0) - \boldsymbol{\mu}_{FC} \cdot \left(\mathbf{B}_{tot}(\mathbf{r}_{FC}, \boldsymbol{\mu}_{FC}) \right) \tag{5.32}$$

The relative position vectors between the magnets and their images and the dipole orientations at the equilibrium are:

$$\boldsymbol{\rho}_m(\mathbf{r}_{FC}) = 2(\hat{\mathbf{a}} \cdot \mathbf{r}_{FC})\hat{\mathbf{a}} \tag{5.33}$$

$$\boldsymbol{\rho}_f(\mathbf{r}_{FC}) = \mathbf{r}_{FC} - \mathbf{r}_{FC} + 2(\hat{\mathbf{a}} \cdot \mathbf{r}_{FC})\hat{\mathbf{a}} = 2(\hat{\mathbf{a}} \cdot \mathbf{r}_{FC})\hat{\mathbf{a}} = \boldsymbol{\rho}_m(\mathbf{r}_{FC}) \tag{5.34}$$

Equation (5.34) shows that in equilibrium, the two position vectors for the mobile and frozen images are equivalent (the two images are co-located). The relationship between the frozen and mobile dipole moments is then:

$$\boldsymbol{\mu}_m\left(\boldsymbol{\mu}_{FC}\right)=\left(\boldsymbol{\mu}_{FC}-2(\hat{\mathbf{a}}\cdot\boldsymbol{\mu}_{FC})\hat{\mathbf{a}}\right) \tag{5.35}$$

$$\boldsymbol{\mu}_f\left(\boldsymbol{\mu}_{FC}\right)=\left(2\left(\hat{\mathbf{a}}\cdot\boldsymbol{\mu}_{FC}\right)\hat{\mathbf{a}}-\boldsymbol{\mu}_{FC}\right)=-\boldsymbol{\mu}_m\left(\boldsymbol{\mu}_{FC}\right) \tag{5.36}$$

These equations show that at equilibrium the two images have the same magnitude, but are in opposite directions. At equilibrium, the force and torques clearly go to zero:

$$\begin{aligned}\mathbf{F}_{tot}=&\frac{3\mu_0\mu_m\mu_1}{4\pi\rho_m{}^4}\left[\hat{\boldsymbol{\rho}}_m\left(\hat{\boldsymbol{\mu}}_m\cdot\hat{\boldsymbol{\mu}}_1\right)+\hat{\boldsymbol{\mu}}_m\left(\hat{\boldsymbol{\rho}}_m\cdot\hat{\boldsymbol{\mu}}_1\right)+\hat{\boldsymbol{\mu}}_1\left(\hat{\boldsymbol{\rho}}_m\cdot\hat{\boldsymbol{\mu}}_m\right)\right]\\&-\frac{3\mu_0\mu_m\mu_1}{4\pi\rho_m{}^4}5\hat{\boldsymbol{\rho}}_m\left(\hat{\boldsymbol{\rho}}_m\cdot\hat{\boldsymbol{\mu}}_m\right)\left(\hat{\boldsymbol{\rho}}_m\cdot\hat{\boldsymbol{\mu}}_1\right)\\&+\frac{3\mu_0\mu_m\mu_1}{4\pi\rho_m{}^4}\left[\hat{\boldsymbol{\rho}}_m\left(\left(-\hat{\boldsymbol{\mu}}_m\right)\cdot\hat{\boldsymbol{\mu}}_1\right)+\left(-\hat{\boldsymbol{\mu}}_m\right)\left(\hat{\boldsymbol{\rho}}_m\cdot\hat{\boldsymbol{\mu}}_1\right)+\hat{\boldsymbol{\mu}}_1\left(\hat{\boldsymbol{\rho}}_m\cdot\left(-\hat{\boldsymbol{\mu}}_m\right)\right)\right]\\&-\frac{3\mu_0\mu_m\mu_1}{4\pi\rho_m{}^4}5\hat{\boldsymbol{\rho}}_m\left(\hat{\boldsymbol{\rho}}_m\cdot\left(-\hat{\boldsymbol{\mu}}_m\right)\right)\left(\hat{\boldsymbol{\rho}}_m\cdot\hat{\boldsymbol{\mu}}_1\right)\\\mathbf{F}_{tot}=&\,0\end{aligned} \tag{5.37}$$

$$\begin{aligned}\boldsymbol{\tau}_{tot}=&\frac{\mu_0\hat{\boldsymbol{\mu}}_{mj}\hat{\boldsymbol{\mu}}_i}{4\pi\rho_m{}^3}\left[3\left(\hat{\boldsymbol{\mu}}_m\cdot\hat{\boldsymbol{\rho}}_m\right)\left(\hat{\boldsymbol{\mu}}_1\times\hat{\boldsymbol{\rho}}_m\right)+\left(\hat{\boldsymbol{\mu}}_m\times\hat{\boldsymbol{\mu}}_1\right)\right]\\&+\frac{\mu_0\hat{\boldsymbol{\mu}}_{mj}\hat{\boldsymbol{\mu}}_i}{4\pi\rho_m{}^3}\left[3\left(\left(-\hat{\boldsymbol{\mu}}_m\right)\cdot\hat{\boldsymbol{\rho}}_m\right)\left(\hat{\boldsymbol{\mu}}_1\times\hat{\boldsymbol{\rho}}_m\right)+\left(\left(-\hat{\boldsymbol{\mu}}_m\right)\times\hat{\boldsymbol{\mu}}_1\right)\right]\\\boldsymbol{\tau}_{tot}=&\,0\end{aligned} \tag{5.38}$$

When substituting the appropriate potential terms into Equation (5.32) the result is:

$$\begin{aligned}V(\mathbf{r}_{FC})=&\frac{\mu_0}{4\pi}\boldsymbol{\mu}_{FC}\cdot\left(\frac{1}{\rho_m{}^3}\left(3\left[\boldsymbol{\mu}_m\left(\boldsymbol{\mu}_{FC}\right)\cdot\hat{\boldsymbol{\rho}}_m\right]\hat{\boldsymbol{\rho}}_m-\boldsymbol{\mu}_m\left(\boldsymbol{\mu}_{FC}\right)\right)\right)\\&-\frac{1}{2}\frac{\mu_0}{4\pi}\boldsymbol{\mu}_{FC}\cdot\left(\frac{1}{\rho_m{}^3}\left(3\left[\boldsymbol{\mu}_m\left(\boldsymbol{\mu}_{FC}\right)\cdot\hat{\boldsymbol{\rho}}_m\right]\hat{\boldsymbol{\rho}}_m-\boldsymbol{\mu}_m\left(\boldsymbol{\mu}_{FC}\right)\right)\right)\end{aligned} \tag{5.39}$$

Clearly, the terms from the mobile and frozen image are different by a factor of one half – preventing them from canceling to zero. In fact, the energy state at equilibrium then becomes:

$$V(\mathbf{r}_{FC}) = \frac{1}{2}\frac{\mu_0}{4\pi}\left(\frac{1}{(2r_{FC})^3}\left(-12r_{FC}^2\left(\hat{\mathbf{a}}\cdot\boldsymbol{\mu}_{FC}\right)^2 + 2\left(\hat{\mathbf{a}}\cdot\boldsymbol{\mu}_{FC}\right)^2 - \mu_{FC}^2\right)\right) \tag{5.40}$$

Again, for the translational case only, the field-cooled dipole direction is parallel to the superconductor's norm. Thus, Equation (5.40) simplifies further to:

$$V(\mathbf{r}_{FC}) = \frac{1}{2}\frac{\mu_0}{4\pi}\left(\frac{1}{(2r_{FC})^3}\left(-12r_{FC}^2\mu_{FC}^2 + \mu_{FC}^2\right)\right) \tag{5.41}$$

Thus, using Giaro's corrected potential energy function for the mobile image (Equation (5.7)), the system's energy is not zero at equilibrium. This value can be set to be the datum for the system's potential energy. Since energy increases for motion in any direction from its equilibrium, the energy of the system is positive definite. Provided there are no step changes in the magnetic moment (which cannot occur for an uncontrolled system), energy is a continuous and differentiable scalar function. Therefore the second Lyapunov criterion is also satisfied.

The last criterion required of a Lyapunov function is that its derivative must be negative semi-definite. Equation (5.30) is the energy of the system, and there are no active elements for the uncontrolled system. Thus, it is clear that the derivative of the Lyapunov function should be zero from the conservation of energy (neglecting dissipative elements). However, proving this is a process that requires equating terms that are derived from the forces and torques between dipoles (which do not have the one-half term) and potential energy (which does include the one-half term). Thus,

special care must be taken to ensure that the appropriate terms are included in the Lyapunov equation derivative.

Given this precaution, the potential energy from Equation (5.5) can be substituted in to Equation (5.30) to produce the following derivative:

$$\dot{V}(\mathbf{r}_1) = \overset{N}{\mathbf{r}}_1 \cdot \left(m \overset{NN}{\mathbf{r}}_1 \right) + \boldsymbol{\omega}_{B/N} \cdot \left(\mathbf{I}_1 \cdot \overset{N}{\boldsymbol{\omega}}_{B/N} \right) - \frac{^N d}{dt} \left(\boldsymbol{\mu}_1 \cdot \left(\mathbf{B}_f + \frac{1}{2} \mathbf{B}_m \right) \right) \tag{5.42}$$

Using the chain rule to distribute the inertial derivative of the potential energy:

$$\dot{V}(\mathbf{r}_1) = \overset{N}{\mathbf{r}}_1 \cdot \left(m \overset{NN}{\mathbf{r}}_1 \right) + \boldsymbol{\omega}_{B/N} \cdot \left(\mathbf{I}_1 \cdot \overset{N}{\boldsymbol{\omega}}_{B/N} \right) - \overset{N}{\boldsymbol{\mu}}_1 \cdot \left(\mathbf{B}_f + \frac{1}{2} \mathbf{B}_m \right) - \boldsymbol{\mu}_1 \cdot \frac{^N d}{dt} \left(\mathbf{B}_f + \frac{1}{2} \mathbf{B}_m \right) \tag{5.43}$$

The transport theorem can be used to take the inertial derivative of the source magnet's magnetic moment:

$$\begin{aligned} \dot{V}(\mathbf{r}_1) = {} & \overset{N}{\mathbf{r}}_1 \cdot \left(m \overset{NN}{\mathbf{r}}_1 \right) + \boldsymbol{\omega}_{B/N} \cdot \left(\mathbf{I}_1 \cdot \overset{N}{\boldsymbol{\omega}}_{B/N} \right) - \left(\overset{B}{\boldsymbol{\mu}}_1 + \boldsymbol{\omega}_{B/N} \times \boldsymbol{\mu}_1 \right) \cdot \left(\mathbf{B}_f + \frac{1}{2} \mathbf{B}_m \right) \\ & - \boldsymbol{\mu}_1 \cdot \frac{^N d}{dt} \left(\mathbf{B}_f + \frac{1}{2} \mathbf{B}_m \right) \end{aligned} \tag{5.44}$$

where $\overset{B}{\boldsymbol{\mu}}_1$ is the derivative of the magnetic moment of the magnet with respect to the body frame. For the uncontrolled case, the magnetic moment $\boldsymbol{\mu}_1$ is not changing with respect to its body frame. Thus:

$$\overset{B}{\boldsymbol{\mu}}_1 \cdot \left(\mathbf{B}_f + \frac{1}{2} \mathbf{B}_m \right) \to 0 \tag{5.45}$$

However, it is important to keep this term accessible because it will not go to zero in the controlled case. From here Equation (5.44) can be simplified using the properties of cross and dot products:

$$\dot{V}(\mathbf{r}_1) = {}^{N}\mathbf{r}_1 \cdot \left(m\, {}^{NN}\mathbf{r}_1 \right) + \boldsymbol{\omega}_{B/N} \cdot \left(\mathbf{I}_1 \cdot {}^{N}\boldsymbol{\omega}_{B/N} \right) - \boldsymbol{\omega}_{B/N} \cdot \left(\boldsymbol{\mu}_1 \times \left(\mathbf{B}_f + \frac{1}{2}\mathbf{B}_m \right) \right) - \boldsymbol{\mu}_1 \cdot {}^{N}\frac{d}{dt}\left(\mathbf{B}_f + \frac{1}{2}\mathbf{B}_m \right) \tag{5.46}$$

If the system is only influenced by the forces and torques due to flux pinning (i.e., the system is not influenced by gravity), the equations of motion for this system are:

$$m\, {}^{NN}\mathbf{r}_1 = \mathbf{F}_{mag} - \mathbf{F}_{damp} \tag{5.47}$$

$$\mathbf{I}_1 \cdot {}^{N}\boldsymbol{\omega}_{B/N} = -\boldsymbol{\omega}_{B/N} \times \mathbf{I}_1 \cdot \boldsymbol{\omega}_{B/N} + \boldsymbol{\tau}_{mag} - \boldsymbol{\tau}_{damp} \tag{5.48}$$

Then, the equations of motion can be substituted into Equation (5.46):

$$\dot{V}(\mathbf{r}_1) = {}^{N}\mathbf{r}_1 \cdot \mathbf{F}_{mag} - {}^{N}\mathbf{r}_1 \cdot \mathbf{F}_{damp} + \boldsymbol{\omega}_{B/N} \cdot \left(-\boldsymbol{\omega}_{B/N} \times \mathbf{I}_1 \cdot \boldsymbol{\omega}_{B/N} \right) + \boldsymbol{\omega}_{B/N} \cdot \boldsymbol{\tau}_{mag} - \boldsymbol{\omega}_{B/N} \cdot \boldsymbol{\tau}_{damp} - \boldsymbol{\omega}_{B/N} \cdot \left(\boldsymbol{\mu}_1 \times \left(\mathbf{B}_f + \frac{1}{2}\mathbf{B}_m \right) \right) - \boldsymbol{\mu}_1 \cdot {}^{N}\frac{d}{dt}\left(\mathbf{B}_f + \frac{1}{2}\mathbf{B}_m \right) \tag{5.49}$$

Simplifying:

$$\dot{V}(\mathbf{r}_1) = {}^{N}\mathbf{r}_1 \cdot \mathbf{F}_{mag} - {}^{N}\mathbf{r}_1 \cdot \mathbf{F}_{damp} + \boldsymbol{\omega}_{B/N} \cdot \boldsymbol{\tau}_{mag} - \boldsymbol{\omega}_{B/N} \cdot \boldsymbol{\tau}_{damp} - \boldsymbol{\omega}_{B/N} \cdot \left(\boldsymbol{\mu}_1 \times \left(\mathbf{B}_f + \frac{1}{2}\mathbf{B}_m \right) \right) - \boldsymbol{\mu}_1 \cdot {}^{N}\frac{d}{dt}\left(\mathbf{B}_f + \frac{1}{2}\mathbf{B}_m \right) \tag{5.50}$$

The third term in this equation can be substituted with Equation (5.12), which defines the term $\boldsymbol{\tau}_{mag}$:

$$\dot{V}(\mathbf{r}_1) = {}^{N}\mathbf{r}_1 \cdot \mathbf{F}_{mag} - {}^{N}\mathbf{r}_1 \cdot \mathbf{F}_{damp} + \boldsymbol{\omega}_{B/N} \cdot \boldsymbol{\mu}_1 \times \left(\mathbf{B}_f + \mathbf{B}_m \right) - \boldsymbol{\omega}_{B/N} \cdot \boldsymbol{\tau}_{damp} - \boldsymbol{\omega}_{B/N} \cdot \left(\boldsymbol{\mu}_1 \times \left(\mathbf{B}_f + \frac{1}{2}\mathbf{B}_m \right) \right) - \boldsymbol{\mu}_1 \cdot {}^{N}\frac{d}{dt}\left(\mathbf{B}_f + \frac{1}{2}\mathbf{B}_m \right) \tag{5.51}$$

Subtracting terms as appropriate and rearranging:

$$\dot{V}(\mathbf{r}_1) = {}^{N}\dot{\mathbf{r}}_1 \cdot \mathbf{F}_{mag} + \frac{1}{2}\boldsymbol{\omega}_{B/N} \cdot \left(\boldsymbol{\mu}_1 \times \mathbf{B}_m\right) - \boldsymbol{\mu}_1 \cdot \frac{{}^{N}d}{dt}\left(\mathbf{B}_f + \frac{1}{2}\mathbf{B}_m\right) - {}^{N}\dot{\mathbf{r}}_1 \cdot \mathbf{F}_{damp} - \boldsymbol{\omega}_{B/N} \cdot \boldsymbol{\tau}_{damp} \tag{5.52}$$

Now, it is necessary to find the derivative of the magnetic field $\left(\mathbf{B}_f + \frac{1}{2}\mathbf{B}_m\right)$. First, define the following coefficient:

$$c_0 = \frac{\mu_0}{4\pi} \tag{5.53}$$

The inertial derivative of the relevant magnetic field is then (starting with Equation (3.3) and (3.4) and distributing the derivative and one-half term as appropriate):

$$
\begin{aligned}
\frac{{}^{N}d}{dt}\left(\mathbf{B}_f+\frac{1}{2}\mathbf{B}_m\right)=&\frac{1}{2}\frac{{}^{N}d}{dt}\left[\frac{3c_0\mu_m}{\left(\boldsymbol{\rho}_m\cdot\boldsymbol{\rho}_m\right)^{5/2}}\right]\left(\hat{\boldsymbol{\mu}}_m\cdot\hat{\boldsymbol{\rho}}_m\right)\hat{\boldsymbol{\rho}}_m\\
&+\frac{1}{2}\frac{3c_0\mu_m}{\left(\boldsymbol{\rho}_m\cdot\boldsymbol{\rho}_m\right)^{5/2}}\frac{{}^{N}d}{dt}\left[\left(\hat{\boldsymbol{\mu}}_m\cdot\hat{\boldsymbol{\rho}}_m\right)\right]\hat{\boldsymbol{\rho}}_m\\
&+\frac{1}{2}\frac{3c_0\mu_m}{\left(\boldsymbol{\rho}_m\cdot\boldsymbol{\rho}_m\right)^{5/2}}\left(\hat{\boldsymbol{\mu}}_m\cdot\hat{\boldsymbol{\rho}}_m\right)\frac{{}^{N}d}{dt}\left[\hat{\boldsymbol{\rho}}_m\right]\\
&-\frac{1}{2}\frac{{}^{N}d}{dt}\left[\frac{c_0\mu_m}{\left(\boldsymbol{\rho}_m\cdot\boldsymbol{\rho}_m\right)^{3/2}}\right]\hat{\boldsymbol{\mu}}_m\\
&-\frac{1}{2}\frac{c_0\mu_m}{\left(\boldsymbol{\rho}_m\cdot\boldsymbol{\rho}_m\right)^{3/2}}\frac{{}^{N}d}{dt}\left[\hat{\boldsymbol{\mu}}_m\right]\\
&+\frac{{}^{N}d}{dt}\left[\frac{3c_0\mu_f}{\left(\boldsymbol{\rho}_f\cdot\boldsymbol{\rho}_f\right)^{5/2}}\right]\left(\hat{\boldsymbol{\mu}}_f\cdot\hat{\boldsymbol{\rho}}_f\right)\hat{\boldsymbol{\rho}}_f\\
&+\frac{3c_0\mu_f}{\left(\boldsymbol{\rho}_f\cdot\boldsymbol{\rho}_f\right)^{5/2}}\frac{{}^{N}d}{dt}\left[\left(\hat{\boldsymbol{\mu}}_f\cdot\hat{\boldsymbol{\rho}}_f\right)\right]\hat{\boldsymbol{\rho}}_f\\
&+\frac{3c_0\mu_f}{\left(\boldsymbol{\rho}_f\cdot\boldsymbol{\rho}_f\right)^{5/2}}\left(\hat{\boldsymbol{\mu}}_f\cdot\hat{\boldsymbol{\rho}}_f\right)\frac{{}^{N}d}{dt}\left[\hat{\boldsymbol{\rho}}_f\right]\\
&-\frac{{}^{N}d}{dt}\left[\frac{c_0\mu_f}{\left(\boldsymbol{\rho}_f\cdot\boldsymbol{\rho}_f\right)^{3/2}}\right]\hat{\boldsymbol{\mu}}_f\\
&-\frac{c_0\mu_f}{\left(\boldsymbol{\rho}_f\cdot\boldsymbol{\rho}_f\right)^{3/2}}\frac{{}^{N}d}{dt}\left[\hat{\boldsymbol{\mu}}_f\right]
\end{aligned}
\tag{5.54}
$$

Taking the derivatives and simplifying leads to:

$$
\begin{aligned}
\frac{{}^{N}d}{dt}\left(\mathbf{B}_f+\frac{1}{2}\mathbf{B}_m\right)=&\frac{1}{2}\left[-5\frac{3c_0}{\left(\boldsymbol{\rho}_m\cdot\boldsymbol{\rho}_m\right)^{7/2}}\right]\left({}^{N}\boldsymbol{\rho}_m\cdot\boldsymbol{\rho}_m\right)\left(\boldsymbol{\mu}_m\cdot\boldsymbol{\rho}_m\right)\boldsymbol{\rho}_m\\
&+\frac{1}{2}\frac{3c_0}{\left(\boldsymbol{\rho}_m\cdot\boldsymbol{\rho}_m\right)^{5/2}}\left[\left({}^{N}\boldsymbol{\mu}_m\cdot\boldsymbol{\rho}_m\right)+\left(\boldsymbol{\mu}_m\cdot{}^{N}\boldsymbol{\rho}_m\right)\right]\boldsymbol{\rho}_m\\
&+\frac{1}{2}\frac{3c_0}{\left(\boldsymbol{\rho}_m\cdot\boldsymbol{\rho}_m\right)^{5/2}}\left(\boldsymbol{\mu}_m\cdot\boldsymbol{\rho}_m\right)\left[{}^{N}\boldsymbol{\rho}_m\right]\\
&+\frac{1}{2}\left[3\frac{c_0}{\left(\boldsymbol{\rho}_m\cdot\boldsymbol{\rho}_m\right)^{5/2}}\right]\left({}^{N}\boldsymbol{\rho}_m\cdot\boldsymbol{\rho}_m\right)\boldsymbol{\mu}_m\\
&-\frac{1}{2}\frac{c_0}{\left(\boldsymbol{\rho}_m\cdot\boldsymbol{\rho}_m\right)^{3/2}}\left[{}^{N}\boldsymbol{\mu}_m\right]\\
&+\left[-5\frac{3c_0}{\left(\boldsymbol{\rho}_f\cdot\boldsymbol{\rho}_f\right)^{7/2}}\right]\left({}^{N}\boldsymbol{\rho}_f\cdot\boldsymbol{\rho}_f\right)\left(\boldsymbol{\mu}_f\cdot\boldsymbol{\rho}_f\right)\boldsymbol{\rho}_f\\
&+\frac{3c_0}{\left(\boldsymbol{\rho}_f\cdot\boldsymbol{\rho}_f\right)^{5/2}}\left[\left({}^{N}\boldsymbol{\mu}_f\cdot\boldsymbol{\rho}_f\right)+\left(\boldsymbol{\mu}_f\cdot{}^{N}\boldsymbol{\rho}_f\right)\right]\boldsymbol{\rho}_f\\
&+\frac{3c_0}{\left(\boldsymbol{\rho}_f\cdot\boldsymbol{\rho}_f\right)^{5/2}}\left(\boldsymbol{\mu}_f\cdot\boldsymbol{\rho}_f\right)\left[{}^{N}\boldsymbol{\rho}_f\right]\\
&+\left[3\frac{c_0}{\left(\boldsymbol{\rho}_f\cdot\boldsymbol{\rho}_f\right)^{5/2}}\right]\left({}^{N}\boldsymbol{\rho}_f\cdot\boldsymbol{\rho}_f\right)\boldsymbol{\mu}_f\\
&-\frac{c_0}{\left(\boldsymbol{\rho}_f\cdot\boldsymbol{\rho}_f\right)^{3/2}}{}^{N}\boldsymbol{\mu}_f
\end{aligned}
\tag{5.55}
$$

In Equation (5.49) the term with the magnetic field derivative is a dot product with the source magnetic moment. Thus, the dot product of the source magnetic moment can be distributed to the terms in Equation (5.55). The result (after simplification) is:

$$
\begin{aligned}
\boldsymbol{\mu}_1 \cdot \overset{N}{\frac{d}{dt}}\left(\mathbf{B}_f + \frac{1}{2}\mathbf{B}_m\right) = \frac{1}{2}\frac{3c_0}{\left(\boldsymbol{\rho}_m \cdot \boldsymbol{\rho}_m\right)^{4/2}}\Big[&\left(\boldsymbol{\mu}_m \cdot \boldsymbol{\mu}_1\right)\left(\hat{\boldsymbol{\rho}}_m \cdot \overset{N}{\boldsymbol{\rho}}_m\right) \\
&+\left(\hat{\boldsymbol{\rho}}_m \cdot \boldsymbol{\mu}_1\right)\left(\boldsymbol{\mu}_m \cdot \overset{N}{\boldsymbol{\rho}}_m\right) \\
&+\left(\hat{\boldsymbol{\rho}}_m \cdot \boldsymbol{\mu}_m\right)\left(\boldsymbol{\mu}_1 \cdot \overset{N}{\boldsymbol{\rho}}_m\right) \\
&-5\left(\boldsymbol{\mu}_m \cdot \hat{\boldsymbol{\rho}}_m\right)\left(\boldsymbol{\mu}_1 \cdot \hat{\boldsymbol{\rho}}_m\right)\left(\hat{\boldsymbol{\rho}}_m \cdot \overset{N}{\boldsymbol{\rho}}_m\right)\Big] \\
+\frac{3c_0}{\left(\boldsymbol{\rho}_f \cdot \boldsymbol{\rho}_f\right)^{4/2}}\Big[&\left(\boldsymbol{\mu}_f \cdot \boldsymbol{\mu}_1\right)\left(\hat{\boldsymbol{\rho}}_f \cdot \overset{N}{\boldsymbol{\rho}}_f\right) \\
&+\left(\hat{\boldsymbol{\rho}}_f \cdot \boldsymbol{\mu}_1\right)\left(\boldsymbol{\mu}_f \cdot \overset{N}{\boldsymbol{\rho}}_f\right) \\
&+\left(\hat{\boldsymbol{\rho}}_f \cdot \boldsymbol{\mu}_f\right)\left(\boldsymbol{\mu}_1 \cdot \overset{N}{\boldsymbol{\rho}}_f\right) \\
&-5\left(\boldsymbol{\mu}_f \cdot \hat{\boldsymbol{\rho}}_f\right)\left(\boldsymbol{\mu}_1 \cdot \hat{\boldsymbol{\rho}}_f\right)\left(\hat{\boldsymbol{\rho}}_f \cdot \overset{N}{\boldsymbol{\rho}}_f\right)\Big] \\
+\left[\frac{1}{2}\frac{3c_0}{\left(\boldsymbol{\rho}_m \cdot \boldsymbol{\rho}_m\right)^{5/2}}\left(\boldsymbol{\mu}_1 \cdot \boldsymbol{\rho}_m\right)\boldsymbol{\rho}_m - \frac{1}{2}\frac{c_0}{\left(\boldsymbol{\rho}_m \cdot \boldsymbol{\rho}_m\right)^{3/2}}\boldsymbol{\mu}_1\right] &\cdot \overset{N}{\boldsymbol{\mu}}_m \\
+\left[\frac{3c_0}{\left(\boldsymbol{\rho}_f \cdot \boldsymbol{\rho}_f\right)^{5/2}}\left(\boldsymbol{\mu}_1 \cdot \boldsymbol{\rho}_f\right)\boldsymbol{\rho}_f - \frac{c_0}{\left(\boldsymbol{\rho}_f \cdot \boldsymbol{\rho}_f\right)^{3/2}}\boldsymbol{\mu}_1\right] &\cdot \overset{N}{\boldsymbol{\mu}}_f
\end{aligned}
\tag{5.56}
$$

The inertial derivative of the frozen image's magnetic moment is zero for both the controlled and uncontrolled case, since this quantity is set into the superconductor at field-cooling and does not change. The inertial derivative of the mobile magnetic moment is:

$$
\overset{N}{\boldsymbol{\mu}}_m = \left(\overset{B^*}{\boldsymbol{\mu}}_m + \boldsymbol{\omega}_{B^*/N} \times \boldsymbol{\mu}_m\right) \tag{5.57}
$$

where B* indicates the body frame of the mobile image. Clearly, the body derivative of the mobile magnetic moment goes to zero in the uncontrolled case such that:

$$\left[\frac{1}{2}\frac{3c_0}{\left(\boldsymbol{\rho}_m\cdot\boldsymbol{\rho}_m\right)^{5/2}}\left(\boldsymbol{\mu}_1\cdot\boldsymbol{\rho}_m\right)\boldsymbol{\rho}_m-\frac{1}{2}\frac{c_0}{\left(\boldsymbol{\rho}_m\cdot\boldsymbol{\rho}_m\right)^{3/2}}\boldsymbol{\mu}_1\right]\cdot{}^{B^*}\boldsymbol{\mu}_m\to 0 \tag{5.58}$$

However, the $\boldsymbol{\omega}_{B^*/N}\times\boldsymbol{\mu}_m$ term remains, even in the uncontrolled case. Thus, Equation (5.56) becomes:

$$\begin{aligned}\boldsymbol{\mu}_1\cdot\frac{{}^{N}d}{dt}\left(\mathbf{B}_f+\frac{1}{2}\mathbf{B}_m\right)=\frac{1}{2}\frac{3c_0}{\left(\boldsymbol{\rho}_m\cdot\boldsymbol{\rho}_m\right)^{4/2}}&\left[\begin{array}{l}\left(\boldsymbol{\mu}_m\cdot\boldsymbol{\mu}_1\right)\hat{\boldsymbol{\rho}}_m\\ \quad+\left(\hat{\boldsymbol{\rho}}_m\cdot\boldsymbol{\mu}_1\right)\boldsymbol{\mu}_m\\ \quad+\left(\hat{\boldsymbol{\rho}}_m\cdot\boldsymbol{\mu}_m\right)\boldsymbol{\mu}_1\\ \quad-5\left(\boldsymbol{\mu}_m\cdot\hat{\boldsymbol{\rho}}_m\right)\left(\boldsymbol{\mu}_1\cdot\hat{\boldsymbol{\rho}}_m\right)\hat{\boldsymbol{\rho}}_m\end{array}\right]\cdot{}^{N}\hat{\boldsymbol{\rho}}_m\\ +\frac{3c_0}{\left(\boldsymbol{\rho}_f\cdot\boldsymbol{\rho}_f\right)^{4/2}}&\left[\begin{array}{l}\left(\boldsymbol{\mu}_f\cdot\boldsymbol{\mu}_1\right)\hat{\boldsymbol{\rho}}_f\\ \quad+\left(\hat{\boldsymbol{\rho}}_f\cdot\boldsymbol{\mu}_1\right)\boldsymbol{\mu}_f\\ \quad+\left(\hat{\boldsymbol{\rho}}_f\cdot\boldsymbol{\mu}_f\right)\boldsymbol{\mu}_1\\ \quad-5\left(\boldsymbol{\mu}_f\cdot\hat{\boldsymbol{\rho}}_f\right)\left(\boldsymbol{\mu}_1\cdot\hat{\boldsymbol{\rho}}_f\right)\hat{\boldsymbol{\rho}}_f\end{array}\right]\cdot{}^{N}\hat{\boldsymbol{\rho}}_f\\ +\left[\frac{1}{2}\frac{3c_0}{\left(\boldsymbol{\rho}_m\cdot\boldsymbol{\rho}_m\right)^{5/2}}\left(\boldsymbol{\mu}_1\cdot\boldsymbol{\rho}_m\right)\boldsymbol{\rho}_m-\frac{1}{2}\frac{c_0}{\left(\boldsymbol{\rho}_m\cdot\boldsymbol{\rho}_m\right)^{3/2}}\boldsymbol{\mu}_1\right]&\cdot\left(\boldsymbol{\omega}_{B^*/N}\times\boldsymbol{\mu}_m\right)\end{aligned} \tag{5.59}$$

The derivative of the mobile and frozen relative distances can be found by:

$${}^{N}\boldsymbol{\rho}_m=2\left(\hat{\mathbf{a}}\cdot{}^{N}\mathbf{r}_1\right)\hat{\mathbf{a}} \tag{5.60}$$

$${}^{N}\boldsymbol{\rho}_f={}^{N}\mathbf{r}_1 \tag{5.61}$$

Then Equation (5.59) becomes:

$$\boldsymbol{\mu}_1 \cdot \frac{{}^N d}{dt}\left(\mathbf{B}_f + \frac{1}{2}\mathbf{B}_m\right) = \frac{3c_0}{\left(\boldsymbol{\rho}_m \cdot \boldsymbol{\rho}_m\right)^{4/2}}\begin{bmatrix}\left(\boldsymbol{\mu}_m \cdot \boldsymbol{\mu}_1\right)\hat{\boldsymbol{\rho}}_m \\ +\left(\hat{\boldsymbol{\rho}}_m \cdot \boldsymbol{\mu}_1\right)\boldsymbol{\mu}_m \\ +\left(\hat{\boldsymbol{\rho}}_m \cdot \boldsymbol{\mu}_m\right)\boldsymbol{\mu}_1 \\ -5\left(\boldsymbol{\mu}_m \cdot \hat{\boldsymbol{\rho}}_m\right)\left(\boldsymbol{\mu}_1 \cdot \hat{\boldsymbol{\rho}}_m\right)\hat{\boldsymbol{\rho}}_m\end{bmatrix} \cdot \left(\hat{\mathbf{a}} \cdot {}^N\mathbf{r}_1\right)\hat{\mathbf{a}}$$
$$+ \frac{3c_0}{\left(\boldsymbol{\rho}_f \cdot \boldsymbol{\rho}_f\right)^{4/2}}\begin{bmatrix}\left(\boldsymbol{\mu}_f \cdot \boldsymbol{\mu}_1\right)\hat{\boldsymbol{\rho}}_f \\ +\left(\hat{\boldsymbol{\rho}}_f \cdot \boldsymbol{\mu}_1\right)\boldsymbol{\mu}_f \\ +\left(\hat{\boldsymbol{\rho}}_f \cdot \boldsymbol{\mu}_f\right)\boldsymbol{\mu}_1 \\ -5\left(\boldsymbol{\mu}_f \cdot \hat{\boldsymbol{\rho}}_f\right)\left(\boldsymbol{\mu}_1 \cdot \hat{\boldsymbol{\rho}}_f\right)\hat{\boldsymbol{\rho}}_f\end{bmatrix} \cdot {}^N\mathbf{r}_1 \tag{5.62}$$
$$+\left[\frac{1}{2}\frac{3c_0}{\left(\boldsymbol{\rho}_m \cdot \boldsymbol{\rho}_m\right)^{5/2}}\left(\boldsymbol{\mu}_1 \cdot \boldsymbol{\rho}_m\right)\boldsymbol{\rho}_m - \frac{1}{2}\frac{c_0}{\left(\boldsymbol{\rho}_m \cdot \boldsymbol{\rho}_m\right)^{3/2}}\boldsymbol{\mu}_1\right] \cdot \left(\boldsymbol{\omega}_{B^*/N} \times \boldsymbol{\mu}_m\right)$$

The $\left(\hat{\mathbf{a}} \cdot {}^N\mathbf{r}_1\right)\hat{\mathbf{a}}$ term in the first term in this expression explicitly requires that the mobile image only act in the direction of the superconductor's surface normal $\hat{\mathbf{a}}$. However, the mobile image is always constrained to act along the superconductor's norm. By definition, $\hat{\boldsymbol{\rho}}_m \| \hat{\mathbf{a}}$. The $\boldsymbol{\mu}_m$ and $\boldsymbol{\mu}_1$ terms in the mobile expression are also in the $\hat{\mathbf{a}}$ direction, as can be seen when Equation (3.5) and (3.9) are substituted in:

$$\left(\hat{\boldsymbol{\rho}}_m \cdot \boldsymbol{\mu}_1\right)\boldsymbol{\mu}_m + \left(\hat{\boldsymbol{\rho}}_m \cdot \boldsymbol{\mu}_m\right)\boldsymbol{\mu}_1 = -4\left(\hat{\mathbf{a}} \cdot \mathbf{r}_1\right)\left(\hat{\mathbf{a}} \cdot \boldsymbol{\mu}_1\right)\left(\hat{\mathbf{a}} \cdot \boldsymbol{\mu}_1\right)\hat{\mathbf{a}} \tag{5.63}$$

Thus, the other $\hat{\mathbf{a}}$ terms multiplied by the mobile image's terms in Equation (5.62) are redundant. So Equation (5.62) becomes:

$$\begin{aligned}\boldsymbol{\mu}_1 \cdot {}^N\frac{d}{dt}\left(\mathbf{B}_f + \frac{1}{2}\mathbf{B}_m\right) = {} & \frac{3c_0}{\left(\boldsymbol{\rho}_m \cdot \boldsymbol{\rho}_m\right)^{4/2}}\left[\begin{array}{l}\left(\boldsymbol{\mu}_m \cdot \boldsymbol{\mu}_1\right)\hat{\boldsymbol{\rho}}_m \\ \quad +\left(\hat{\boldsymbol{\rho}}_m \cdot \boldsymbol{\mu}_1\right)\boldsymbol{\mu}_m \\ \quad +\left(\hat{\boldsymbol{\rho}}_m \cdot \boldsymbol{\mu}_m\right)\boldsymbol{\mu}_1 \\ \quad -5\left(\boldsymbol{\mu}_m \cdot \hat{\boldsymbol{\rho}}_m\right)\left(\boldsymbol{\mu}_1 \cdot \hat{\boldsymbol{\rho}}_m\right)\hat{\boldsymbol{\rho}}_m\end{array}\right] \cdot {}^N\mathbf{r}_1 \\ & + \frac{3c_0}{\left(\boldsymbol{\rho}_f \cdot \boldsymbol{\rho}_f\right)^{4/2}}\left[\begin{array}{l}\left(\boldsymbol{\mu}_f \cdot \boldsymbol{\mu}_1\right)\hat{\boldsymbol{\rho}}_f \\ \quad +\left(\hat{\boldsymbol{\rho}}_f \cdot \boldsymbol{\mu}_1\right)\boldsymbol{\mu}_f \\ \quad +\left(\hat{\boldsymbol{\rho}}_f \cdot \boldsymbol{\mu}_f\right)\boldsymbol{\mu}_1 \\ \quad -5\left(\boldsymbol{\mu}_f \cdot \hat{\boldsymbol{\rho}}_f\right)\left(\boldsymbol{\mu}_1 \cdot \hat{\boldsymbol{\rho}}_f\right)\hat{\boldsymbol{\rho}}_f\end{array}\right] \cdot {}^N\mathbf{r}_1 \\ & + \left[\frac{1}{2}\frac{3c_0}{\left(\boldsymbol{\rho}_m \cdot \boldsymbol{\rho}_m\right)^{5/2}}\left(\boldsymbol{\mu}_1 \cdot \boldsymbol{\rho}_m\right)\boldsymbol{\rho}_m - \frac{1}{2}\frac{c_0}{\left(\boldsymbol{\rho}_m \cdot \boldsymbol{\rho}_m\right)^{3/2}}\boldsymbol{\mu}_1\right] \cdot \left(\boldsymbol{\omega}_{B^*/N} \times \boldsymbol{\mu}_m\right)\end{aligned} \tag{5.64}$$

Returning to the derivative of the Lyapunov equation (Equation (5.52)):

$$\begin{aligned}\dot{V}(\mathbf{r}_1) = {} & {}^N\mathbf{r}_1 \cdot \mathbf{F}_{mag} + \frac{1}{2}\boldsymbol{\omega}_{B/N} \cdot \left(\boldsymbol{\mu}_1 \times \mathbf{B}_m\right) - \boldsymbol{\mu}_1 \cdot {}^N\frac{d}{dt}\left(\mathbf{B}_f + \frac{1}{2}\mathbf{B}_m\right) \\ & - {}^N\mathbf{r}_1 \cdot \mathbf{F}_{damp} - \boldsymbol{\omega}_{B/N} \cdot \boldsymbol{\tau}_{damp}\end{aligned} \tag{5.65}$$

The first term in this expression can also be rewritten using Equation (3.14) expanded to include both the mobile and frozen image:

$$\begin{aligned}{}^N\mathbf{r}_1 \cdot \mathbf{F}_m = {} & {}^N\mathbf{r}_1 \cdot \left(\mathbf{F}_f + \mathbf{F}_m\right) = \frac{3c_0\mu_m\mu_1}{\rho_m{}^4}\left[\begin{array}{l}\left(\hat{\boldsymbol{\mu}}_m \cdot \hat{\boldsymbol{\mu}}_1\right)\hat{\boldsymbol{\rho}}_m \\ \quad +\left(\hat{\boldsymbol{\rho}}_m \cdot \hat{\boldsymbol{\mu}}_1\right)\hat{\boldsymbol{\mu}}_m \\ \quad +\left(\hat{\boldsymbol{\rho}}_m \cdot \hat{\boldsymbol{\mu}}_m\right)\hat{\boldsymbol{\mu}}_1 \\ \quad -\left[5\left(\hat{\boldsymbol{\rho}}_m \cdot \hat{\boldsymbol{\mu}}_m\right)\left(\hat{\boldsymbol{\rho}}_m \cdot \hat{\boldsymbol{\mu}}_1\right)\right]\hat{\boldsymbol{\rho}}_m\end{array}\right] \cdot {}^N\mathbf{r}_1 \\ & + \frac{3c_0\mu_f\mu_1}{\rho_f{}^4}\left[\begin{array}{l}\left(\hat{\boldsymbol{\mu}}_f \cdot \hat{\boldsymbol{\mu}}_1\right)\hat{\boldsymbol{\rho}}_f \\ \quad +\left(\hat{\boldsymbol{\rho}}_f \cdot \hat{\boldsymbol{\mu}}_1\right)\hat{\boldsymbol{\mu}}_f \\ \quad +\left(\hat{\boldsymbol{\rho}}_f \cdot \hat{\boldsymbol{\mu}}_f\right)\hat{\boldsymbol{\mu}}_1 \\ \quad -\left[5\left(\hat{\boldsymbol{\rho}}_f \cdot \hat{\boldsymbol{\mu}}_f\right)\left(\hat{\boldsymbol{\rho}}_f \cdot \hat{\boldsymbol{\mu}}_1\right)\right]\hat{\boldsymbol{\rho}}_f\end{array}\right] \cdot {}^N\mathbf{r}_1\end{aligned} \tag{5.66}$$

Clearly, the first two terms in Equation (5.64) are equivalent to those in Equation (5.66) . Thus, Equation (5.64) can be rewritten:

$$\begin{aligned}\boldsymbol{\mu}_1 \cdot \frac{{}^N d}{dt}\left(\mathbf{B}_f + \frac{1}{2}\mathbf{B}_m\right) &= \mathbf{F}_m \cdot {}^N\mathbf{r}_1 + \mathbf{F}_f \cdot {}^N\mathbf{r}_1 \\ &+ \left[\frac{1}{2}\frac{3c_0}{\left(\boldsymbol{\rho}_m \cdot \boldsymbol{\rho}_m\right)^{5/2}}\left(\boldsymbol{\mu}_1 \cdot \boldsymbol{\rho}_m\right)\boldsymbol{\rho}_m - \frac{1}{2}\frac{c_0}{\left(\boldsymbol{\rho}_m \cdot \boldsymbol{\rho}_m\right)^{3/2}}\boldsymbol{\mu}_1\right] \cdot \left(\boldsymbol{\omega}_{B^*/N} \times \boldsymbol{\mu}_m\right)\end{aligned} \tag{5.67}$$

The Lyapunov derivative in Equation (5.65) can now be augmented with Equation (5.67):

$$\begin{aligned}\dot{V}(\mathbf{r}_1) = {}&{}^N\mathbf{r}_1 \cdot \left(\mathbf{F}_f + \mathbf{F}_m\right) + \frac{1}{2}\boldsymbol{\omega}_{B/N} \cdot \left(\boldsymbol{\mu}_1 \times \mathbf{B}_m\right) - {}^N\mathbf{r}_1 \cdot \left(\mathbf{F}_f + \mathbf{F}_m\right) \\ &+ \left[\frac{1}{2}\frac{3c_0}{\left(\boldsymbol{\rho}_m \cdot \boldsymbol{\rho}_m\right)^{5/2}}\left(\boldsymbol{\mu}_1 \cdot \boldsymbol{\rho}_m\right)\boldsymbol{\rho}_m - \frac{1}{2}\frac{c_0}{\left(\boldsymbol{\rho}_m \cdot \boldsymbol{\rho}_m\right)^{3/2}}\boldsymbol{\mu}_1\right] \cdot \left(\boldsymbol{\omega}_{B^*/N} \times \boldsymbol{\mu}_m\right) \\ &- {}^N\mathbf{r}_1 \cdot \mathbf{F}_{damp} - \boldsymbol{\omega}_{B/N} \cdot \boldsymbol{\tau}_{damp}\end{aligned} \tag{5.68}$$

Ultimately, the forces due to the images cancel. Thus, the resulting equation is:

$$\begin{aligned}\dot{V}(\mathbf{r}_1) = {}&\frac{1}{2}\boldsymbol{\omega}_{B/N} \cdot \left(\boldsymbol{\mu}_1 \times \mathbf{B}_m\right) \\ &+ \frac{1}{2}\frac{c_0}{\left(\boldsymbol{\rho}_m \cdot \boldsymbol{\rho}_m\right)^{3/2}}\left[\frac{3}{\left(\boldsymbol{\rho}_m \cdot \boldsymbol{\rho}_m\right)^{2/2}}\left(\boldsymbol{\mu}_1 \cdot \boldsymbol{\rho}_m\right)\boldsymbol{\rho}_m - \boldsymbol{\mu}_1\right] \cdot \left(\boldsymbol{\omega}_{B^*/N} \times \boldsymbol{\mu}_m\right) \\ &- {}^N\mathbf{r}_1 \cdot \mathbf{F}_{damp} - \boldsymbol{\omega}_{B/N} \cdot \boldsymbol{\tau}_{damp}\end{aligned} \tag{5.69}$$

The magnitudes of the relative position vectors can be removed to make unit vectors:

$$\begin{aligned}\dot{V}(\mathbf{r}_1) = {}&\frac{1}{2}\boldsymbol{\omega}_{B/N} \cdot \left(\boldsymbol{\mu}_1 \times \mathbf{B}_m\right) \\ &+ \frac{1}{2}\frac{c_0}{\left(\boldsymbol{\rho}_m \cdot \boldsymbol{\rho}_m\right)^{3/2}}\left[3\left(\boldsymbol{\mu}_1 \cdot \hat{\boldsymbol{\rho}}_m\right)\hat{\boldsymbol{\rho}}_m - \boldsymbol{\mu}_1\right] \cdot \left(\boldsymbol{\omega}_{B^*/N} \times \boldsymbol{\mu}_m\right) \\ &- {}^N\mathbf{r}_1 \cdot \mathbf{F}_{damp} - \boldsymbol{\omega}_{B/N} \cdot \boldsymbol{\tau}_{damp}\end{aligned} \tag{5.70}$$

Now, the mobile image's magnetic field can be rewritten using Equation (3.3) and substituting in Equation (3.9).

$$\mathbf{B}_m = \frac{\mu_0}{4\pi\rho_m{}^3}\left(3\left[\left(\boldsymbol{\mu}_1 \cdot \hat{\boldsymbol{\rho}}_m\right)\right]\hat{\boldsymbol{\rho}}_m - \boldsymbol{\mu}_1\right) \tag{5.71}$$

Equation (5.69) contains this term. When it is substituted into the second term, Equation (5.69) becomes:

$$\begin{aligned}\dot{V}(\mathbf{r}_1) = &\frac{1}{2}\boldsymbol{\omega}_{B/N} \cdot \left(\boldsymbol{\mu}_1 \times \mathbf{B}_m\right) \\ &+ \frac{1}{2}\mathbf{B}_m \cdot \left(\boldsymbol{\omega}_{B^*/N} \times \boldsymbol{\mu}_m\right) \\ &- \overset{N}{\mathbf{r}}_1 \cdot \mathbf{F}_{damp} - \boldsymbol{\omega}_{B/N} \cdot \boldsymbol{\tau}_{damp}\end{aligned} \tag{5.72}$$

Equation (3.9) once again can be applied to the second term such that:

$$\begin{aligned}\dot{V}(\mathbf{r}_1) = &\frac{1}{2}\boldsymbol{\omega}_{B/N} \cdot \left(\boldsymbol{\mu}_1 \times \mathbf{B}_m\right) \\ &+ \frac{1}{2}\mathbf{B}_m \cdot \left(\boldsymbol{\omega}_{B^*/N} \times \left(\boldsymbol{\mu}_1 - 2(\hat{\mathbf{a}} \cdot \boldsymbol{\mu}_1)\hat{\mathbf{a}}\right)\right) \\ &- \overset{N}{\mathbf{r}}_1 \cdot \mathbf{F}_{damp} - \boldsymbol{\omega}_{B/N} \cdot \boldsymbol{\tau}_{damp}\end{aligned} \tag{5.73}$$

The term $\boldsymbol{\omega}_{B^*/N}$, or the rotation of the mobile image's body frame with respect to the inertial frame, is related to the $\boldsymbol{\omega}_{B/N}$ directly because the mobile image's motion is simply a reflection of the source magnet's motion over the plane of the superconductor. Thus, the two expressions are related in the following way:

$$\boldsymbol{\omega}_{B^*/N} = \boldsymbol{\omega}_{B/N} - 2(\boldsymbol{\omega}_{B/N} \cdot \hat{\mathbf{a}})\hat{\mathbf{a}} \tag{5.74}$$

Using this definition in Equation (5.73) and simplifying, the expression becomes:

$$\dot{V}(\mathbf{r}_1) = (\boldsymbol{\omega}_{B/N} \cdot \hat{\mathbf{a}})\left(\mathbf{B}_m \times \hat{\mathbf{a}}\right) \cdot \boldsymbol{\mu}_1 - (\hat{\mathbf{a}} \cdot \boldsymbol{\mu}_1)\mathbf{B}_m \cdot \left(\hat{\mathbf{a}} \times \boldsymbol{\omega}_{B/N}\right) - \overset{N}{\mathbf{r}}_1 \cdot \mathbf{F}_{damp} - \boldsymbol{\omega}_{B/N} \cdot \boldsymbol{\tau}_{damp} \tag{5.75}$$

The second term in this expression can be rearranged, using the properties of crossproducts, such that:

$$\dot{V}(\mathbf{r}_1) = (\boldsymbol{\omega}_{B/N} \cdot \hat{\mathbf{a}})\left(\mathbf{B}_m \times \hat{\mathbf{a}}\right) \cdot \boldsymbol{\mu}_1 - (\hat{\mathbf{a}} \cdot \boldsymbol{\mu}_1)\mathbf{B}_m \cdot \left(\boldsymbol{\omega}_{N/B} \times \hat{\mathbf{a}}\right) - \overset{N}{\mathbf{r}}_1 \cdot \mathbf{F}_{damp} - \boldsymbol{\omega}_{B/N} \cdot \boldsymbol{\tau}_{damp} \tag{5.76}$$

From vector calculus the following is true:

$$\left(\boldsymbol{\omega}_{N/B} \times \hat{\mathbf{a}}\right) = \left(\boldsymbol{\omega}_{N/B} \times \hat{\mathbf{n}}_3\right) = \overset{N}{\hat{\mathbf{n}}}_3 = \overset{N}{\hat{\mathbf{a}}} = 0 \tag{5.77}$$

Thus, Equation (5.76) becomes:

$$\dot{V}(\mathbf{r}_1) = (\boldsymbol{\omega}_{B/N} \cdot \hat{\mathbf{a}})\left(\mathbf{B}_m \times \hat{\mathbf{a}}\right) \cdot \boldsymbol{\mu}_1 - \overset{N}{\mathbf{r}}_1 \cdot \mathbf{F}_{damp} - \boldsymbol{\omega}_{B/N} \cdot \boldsymbol{\tau}_{damp} \tag{5.78}$$

Equation (5.71) can be rewritten further with a substitution from Equation (3.9):

$$\mathbf{B}_m = \frac{\mu_0}{4\pi\left(2r_1\right)^3}\left(-3(\hat{\mathbf{a}} \cdot \boldsymbol{\mu}_1)\left(\hat{\mathbf{a}} \cdot \hat{\mathbf{r}}_1\right)^2 \hat{\mathbf{a}} + 2(\hat{\mathbf{a}} \cdot \boldsymbol{\mu}_1)\hat{\mathbf{a}} - \boldsymbol{\mu}_1\right) \tag{5.79}$$

Substituting this expression back into Equation (5.78), and recognizing that the cross product of a vector with itself is zero:

$$\dot{V}(\mathbf{r}_1) = (\boldsymbol{\omega}_{B/N} \cdot \hat{\mathbf{a}})\left(\frac{\mu_0}{4\pi\left(2r_1\right)^3}\left(-\boldsymbol{\mu}_1\right) \times \hat{\mathbf{a}}\right) \cdot \boldsymbol{\mu}_1 - \overset{N}{\mathbf{r}}_1 \cdot \mathbf{F}_{damp} - \boldsymbol{\omega}_{B/N} \cdot \boldsymbol{\tau}_{damp} \tag{5.80}$$

Clearly, the first term will go to zero since the cross product will produce a vector that is perpendicular to $\boldsymbol{\mu}_1$, making the dot product go to zero. Finally, the derivative of the six-degree-of-freedom Lyapunov function for an SMSS FPI is:

$$\dot{V}(\mathbf{r}_1) = -\overset{N}{\mathbf{r}_1} \cdot \mathbf{F}_{damp} - \boldsymbol{\omega}_{B/N} \cdot \boldsymbol{\tau}_{damp} \tag{5.81}$$

Thus, $\dot{V}(r)$ is negative definite (and the system is thus asymptotically stable) if damping forces[122] are present. However, even without damping the Lyapunov equation is zero, so the uncontrolled system's response meets the criteria to be considered bounded and stable in the sense of Lyapunov.

5.3.4. Dynamics of a Uncontrolled SMSS FPI

To illustrate the dynamics of the uncontrolled system for comparison to the controlled case, the plant model in Figure 5.3 (with a constant input voltage) was used to create Figure 5.4. The plant model shows how the frozen image model is incorporated into the spacecraft equations of motion (in the 6DOF block) to produce the resulting relative motion of the bodies.

Figure 5.4 shows the results of a simulation of an electromagnet flux pinned over a

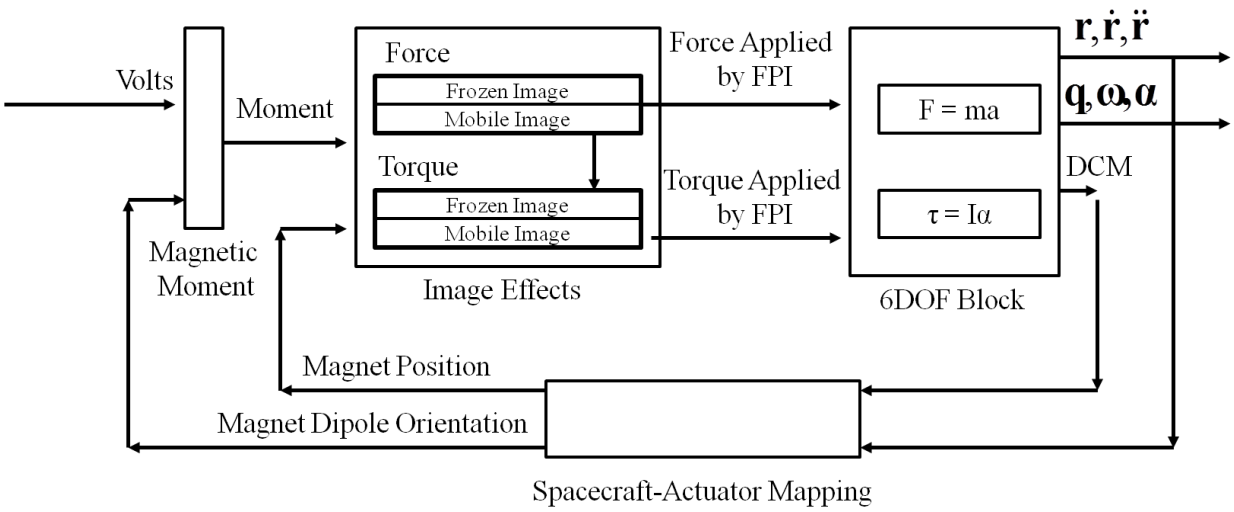

Figure 5.3. Spacecraft Control Loop with SMSS FPIs.

superconductor. The simulation assumed no damping, with a field-cooled position one centimeter in the *z* direction and a field-cooled voltage of 10 V. (This is the same electromagnet modeled in Chapter 4). The system is given an initial static offset from its equilibrium in all three translational degrees of freedom.

Like the more complicated FPI systems studied in this work, the SMSS FPI uncontrolled behavior exhibits strong high-frequency oscillations in its uncontrolled state. Clearly the system response remains bounded, as suggested by the Lyapunov equation, but the performance is undesirable for a spacecraft system where these vibrations may impact a payload. The nonlinearities are especially apparent in the *z* position state, where the magnet experiences higher stiffness closer to the superconductor, and lower stiffness further from it. This observation highlights the importance of using a nonlinear model to model the system response. The response also shows that the translational degrees of freedom induce perturbations in the rotational degrees of freedom, even though no initial offset in the rotational states was modeled for this simulation. The cross coupling in the various degrees of freedom shows the importance of a six-degree of freedom model that can capture these relevant dynamics.

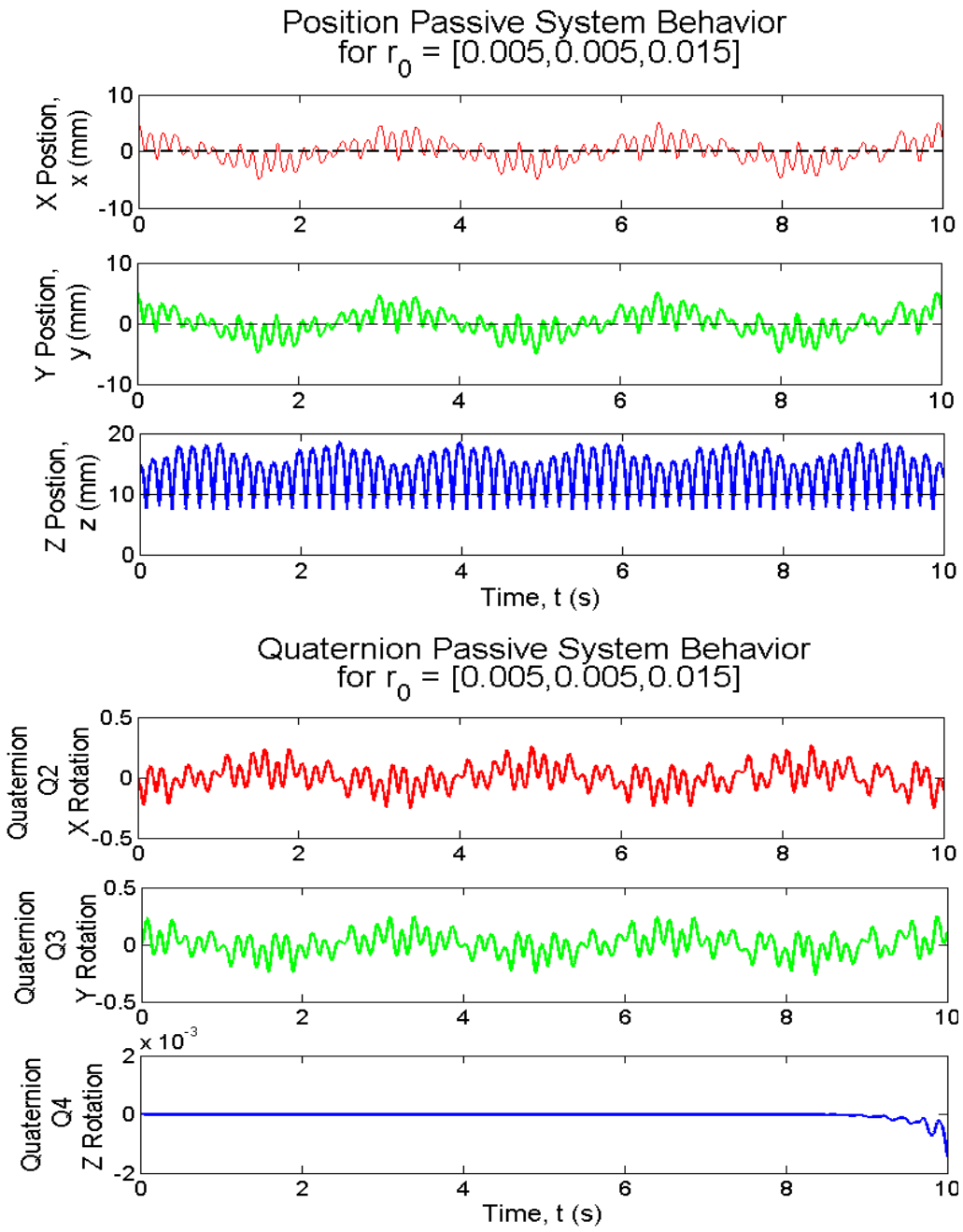

Figure 5.4. The uncontrolled system response to initial offsets in the *x*, *y*, and *z* positions.

5.4. Actively Controlled FPI Stability and Performance

5.4.1. Control Scheme

Although uncontrolled FPIs are clearly stable, the simulated response of the uncontrolled system can certainly be improved with a controller. Additionally, most FPI applications require the ability to control the system's behavior. Figure 5.5 shows

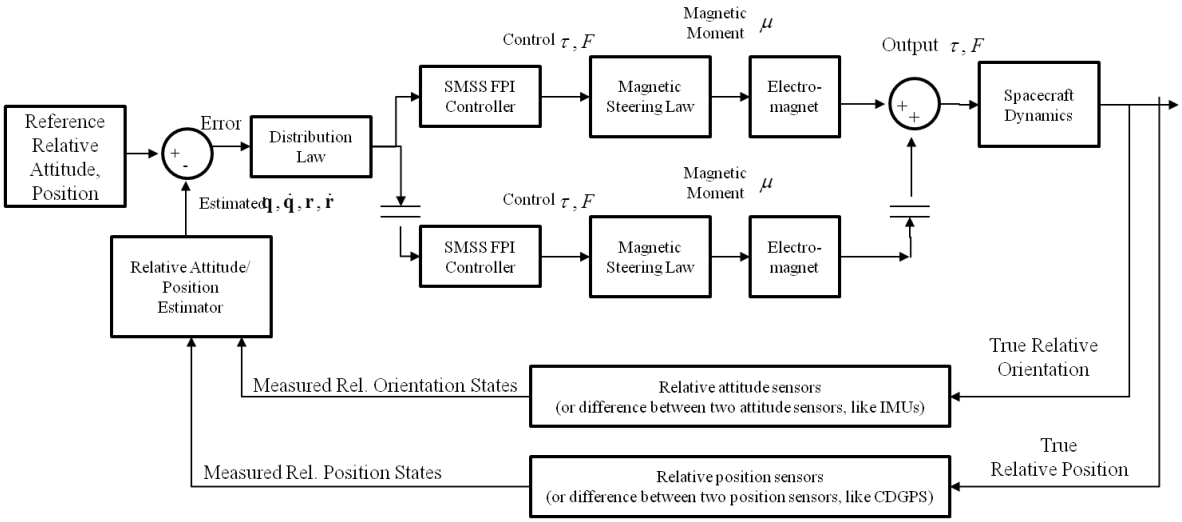

Figure 5.5. Spacecraft Control Loop with SMSS FPIs.

a concept of the relative-position control loop with a number of SMSS actuators. As seen in the image, a full six-degree-of-freedom attitude control requires the development of a distribution law to command the different SMSS FPI controllers to achieve the desired relative attitude and position at the spacecraft level. This particular effort is left for future work and is not discussed here.

At the level of individual SMSS FPIs, two elements are needed to successfully actuate the system. First, a controller is needed to determine the commanded force or

torque for that actuator. Then, these values need to be mapped to a magnetic moment value that can then be applied by the actuators.

Determining the commanded forces and torques can be accomplished with any standard control law, but this work uses a PID to generate a force command to the system:

$$\mathbf{F}_{cont} = k_p \cdot \mathbf{e} + k_d \cdot \frac{d}{dt}\mathbf{e} + k_i \cdot \int_0^t \mathbf{e} \tag{5.82}$$

where ***e*** is the difference between the desired state vector and the actual state vector. Since many effective and optimal PID or nonlinear controllers already exist, this work will not focus on the first step in the active control process, but rather rely on hand-tuned gains that keep the system within known hardware limitations based on laboratory experiments. However, more sophisticated controllers can be developed to work with the FPI dynamics; for example, a simple gain-scheduled control method for *z* axis control could entail only using control effort at *z* values above the equilibrium and letting the FPI dynamics operate passively below its equilibrium where the stiffness is naturally higher.

The second step in developing the control of an SMSS FPI is determining how to map the controller commands to the magnetic moment of the actuator. The next section discusses the derivation of this component of the control system.

5.4.2. Derivation of a Magnetic Steering Law

In an SMSS FPI, the only controller input is the magnetic moment of the pinned electromagnet. Thus, given a force or torque command, the magnetic steering law

determines the output magnetic moment (which, when implemented on hardware would be the current or voltage) to drive the electromagnet.

A derivation of the magnetic steering law starts with a model for the force applied to a magnet with a dipole moment of $\boldsymbol{\mu}_1(t)$ and a position $\mathbf{r}_1(t)$ with a field-cooled magnetic moment and position $\boldsymbol{\mu}_{FC}$ and $\mathbf{r}_{FC}$ respectively, as shown in Figure 5.2. Starting with a model of the force that a dipole of a particular magnetic moment will experience due to the images in the magnetic field:

$$\begin{aligned}\mathbf{F}_{cont} = & \\ & \frac{3\mu_0\mu_m\mu_1}{4\pi\rho_m^{\,4}}\left[\hat{\boldsymbol{\rho}}_m\left(\hat{\boldsymbol{\mu}}_m\cdot\hat{\boldsymbol{\mu}}_1\right)+\hat{\boldsymbol{\mu}}_m\left(\hat{\boldsymbol{\rho}}_m\cdot\hat{\boldsymbol{\mu}}_1\right)+\hat{\boldsymbol{\mu}}_1\left(\hat{\boldsymbol{\rho}}_m\cdot\hat{\boldsymbol{\mu}}_m\right)-5\hat{\boldsymbol{\rho}}_m\left(\hat{\boldsymbol{\rho}}_m\cdot\hat{\boldsymbol{\mu}}_m\right)\left(\hat{\boldsymbol{\rho}}_m\cdot\hat{\boldsymbol{\mu}}_1\right)\right] \\ & +\frac{3\mu_0\mu_f\mu_1}{4\pi\rho_f^{\,4}}\left[\hat{\boldsymbol{\rho}}_f\left(\hat{\boldsymbol{\mu}}_f\cdot\hat{\boldsymbol{\mu}}_1\right)+\hat{\boldsymbol{\mu}}_f\left(\hat{\boldsymbol{\rho}}_f\cdot\hat{\boldsymbol{\mu}}_1\right)+\hat{\boldsymbol{\mu}}_1\left(\hat{\boldsymbol{\rho}}_f\cdot\hat{\boldsymbol{\mu}}_f\right)-5\hat{\boldsymbol{\rho}}_f\left(\hat{\boldsymbol{\rho}}_f\cdot\hat{\boldsymbol{\mu}}_f\right)\left(\hat{\boldsymbol{\rho}}_f\cdot\hat{\boldsymbol{\mu}}_1\right)\right]\end{aligned} \tag{5.83}$$

Since the origin of the system can be selected at any inertial point, it is convenient to assume that the field-cooled position $\mathbf{r}_{FC}$ is in the direction of the superconductor's normal plane $\hat{\mathbf{a}}$, as indicated in Figure 5.2. Given this constraint, the parameters in Equation (5.83) are:

$$\begin{aligned}\boldsymbol{\rho}_m &= 2\left(\hat{\mathbf{a}}\cdot\mathbf{r}_1\right)\hat{\mathbf{a}} \\ &= \rho_m\left(\hat{\mathbf{a}}\cdot\hat{\mathbf{r}}_1\right)\hat{\mathbf{a}} \\ &= 2r_1\left(\hat{\mathbf{a}}\cdot\hat{\mathbf{r}}_1\right)\hat{\mathbf{a}}\end{aligned} \tag{5.84}$$

$$\begin{aligned}\boldsymbol{\rho}_f &= \mathbf{r}_1-\mathbf{r}_{FC}+2\left(\hat{\mathbf{a}}\cdot\mathbf{r}_{FC}\right)\hat{\mathbf{a}} \\ &= \left(r_1\hat{\mathbf{r}}_1+r_{FC}\hat{\mathbf{a}}\right)\end{aligned} \tag{5.85}$$

$$\begin{aligned}\boldsymbol{\mu}_m &= \left(\boldsymbol{\mu}_1 - 2(\hat{\mathbf{a}}\cdot\boldsymbol{\mu}_1)\hat{\mathbf{a}}\right)\\ &= \left(\mu_1\hat{\boldsymbol{\mu}}_1 - 2\mu_1(\hat{\mathbf{a}}\cdot\hat{\boldsymbol{\mu}}_1)\hat{\mathbf{a}}\right)\\ &= \mu_1\left(\hat{\boldsymbol{\mu}}_1 - 2(\hat{\mathbf{a}}\cdot\hat{\boldsymbol{\mu}}_1)\hat{\mathbf{a}}\right)\end{aligned} \tag{5.86}$$

$$\begin{aligned}\boldsymbol{\mu}_f &= \left(2\left(\hat{\mathbf{a}}\cdot\boldsymbol{\mu}_{FC}\right)\hat{\mathbf{a}} - \boldsymbol{\mu}_{FC}\right)\\ &= \left(2\mu_{FC}\hat{\mathbf{a}} - \mu_{FC}\hat{\boldsymbol{\mu}}_{FC}\right)\\ &= \left(\mu_{FC}\hat{\mathbf{a}}\right)\end{aligned} \tag{5.87}$$

where the subscript *f* indicates the frozen image, *m* indicates the mobile image, *FC* indicates the field-cooled state, and *1* indicates the source magnet. The images are both from source magnet *1* so those subscripts are dropped for clarity. Using these equations, Equation (5.83) can be rewritten as:

$$\begin{aligned}\mathbf{F}_{cont} = \frac{3\mu_0}{4\pi}\Bigg[&\frac{\mu_1\mu_m}{\rho_m{}^4}\left(\left[\left(\left(\hat{\mathbf{a}}\cdot\hat{\mathbf{r}}_1\right) - 4\left(\hat{\mathbf{a}}\cdot\hat{\mathbf{r}}_1\right)\left(\hat{\mathbf{a}}\cdot\hat{\boldsymbol{\mu}}_1\right)^2 + 5\left(\hat{\mathbf{a}}\cdot\hat{\mathbf{r}}_1\right)^3\left(\hat{\mathbf{a}}\cdot\hat{\boldsymbol{\mu}}_1\right)^2\right)\right]\hat{\mathbf{a}}\right)\\ &+\frac{\mu_1\mu_f}{\rho_f{}^5}\left(\left[\left(2r_{FC}\left(\hat{\mathbf{a}}\cdot\hat{\boldsymbol{\mu}}_1\right) + r_1\left(\hat{\mathbf{r}}_1\cdot\hat{\boldsymbol{\mu}}_1\right)\right)\right]\hat{\mathbf{a}}\right)\\ &+\frac{\mu_1\mu_f}{\rho_f{}^7}\left(-5\left[r_1^2 r_{FC}\left(\hat{\mathbf{r}}_1\cdot\hat{\boldsymbol{\mu}}_1\right)\left(\hat{\mathbf{r}}_1\cdot\hat{\mathbf{a}}\right) + r_{FC}^3\left(\hat{\mathbf{a}}\cdot\hat{\boldsymbol{\mu}}_1\right)\right]\hat{\mathbf{a}}\right)\\ &+\frac{\mu_1\mu_f}{\rho_f{}^7}\left(-5\left[r_1 r_{FC}^2\left(\hat{\mathbf{r}}_1\cdot\hat{\boldsymbol{\mu}}_1\right) + r_1 r_{FC}^2\left(\hat{\mathbf{a}}\cdot\hat{\boldsymbol{\mu}}_1\right)\left(\hat{\mathbf{r}}_1\cdot\hat{\mathbf{a}}\right)\right]\hat{\mathbf{a}}\right)\\ &+\frac{\mu_1\mu_f}{\rho_f{}^5}\left(\left[\left(r_1\left(\hat{\mathbf{r}}_1\cdot\hat{\mathbf{a}}\right) + r_{FC}\right)\right]\hat{\boldsymbol{\mu}}_1\right)\\ &+\frac{\mu_1\mu_f}{\rho_f{}^5}\left(\left[\left(r_1\left(\hat{\mathbf{a}}\cdot\hat{\boldsymbol{\mu}}_1\right)\right)\right]\hat{\mathbf{r}}_1\right)\\ &+\frac{\mu_1\mu_f}{\rho_f{}^7}\left(-5\left[r_1^3\left(\hat{\mathbf{r}}_1\cdot\hat{\boldsymbol{\mu}}_1\right)\left(\hat{\mathbf{r}}_1\cdot\hat{\mathbf{a}}\right) + r_{FC}^2 r_1\left(\hat{\mathbf{a}}\cdot\hat{\boldsymbol{\mu}}_1\right)\right]\hat{\mathbf{r}}_1\right)\\ &+\frac{\mu_1\mu_f}{\rho_f{}^7}\left(-5\left[r_1^2 r_{FC}\left(\hat{\mathbf{r}}_1\cdot\hat{\boldsymbol{\mu}}_1\right) + r_1^2 r_{FC}\left(\hat{\mathbf{a}}\cdot\hat{\boldsymbol{\mu}}_1\right)\left(\hat{\mathbf{r}}_1\cdot\hat{\mathbf{a}}\right)\right]\hat{\mathbf{r}}_1\right)\Bigg]\end{aligned} \tag{5.88}$$

Although it is possible to solve this equation numerically given the other states of the system, an analytical solution requires simplification. If, for example, if the FPI is primarily concerned with controlling the states perpendicular to the superconductor's plane (the *z* direction), Equation (5.88) can be simplified by substituting in $\mathbf{r}_1 = z\hat{\mathbf{a}}$, and using the fact that:

$$\left(\boldsymbol{\rho}_f \cdot \boldsymbol{\rho}_f\right)^{1/2} = \left(z^2 + 2z_{FC}z + z_{FC}^2\right) = \left(z + z_{FC}\right) \tag{5.89}$$

and

$$\left(\boldsymbol{\mu}_m \cdot \boldsymbol{\mu}_m\right)^{1/2} = \left(\boldsymbol{\mu}_1 - 2(\hat{\mathbf{a}} \cdot \boldsymbol{\mu}_1)\hat{\mathbf{a}}\right) \cdot \left(\boldsymbol{\mu}_1 - 2(\hat{\mathbf{a}} \cdot \boldsymbol{\mu}_1)\hat{\mathbf{a}}\right) = \mu_1 \tag{5.90}$$

The resulting simplification of Equation (5.88) produces a vector with components along the direction perpendicular to the plane of the superconductor and the direction of the magnetic moment of the electromagnet:

$$\begin{aligned}\mathbf{F}_{cont} = {} & \frac{3\mu_0}{4\pi}\left[\frac{\mu_1\mu_1}{(2z)^4} - 3\frac{\mu_1\mu_{FC}}{\left(z + z_{FC}\right)^4}\left(\hat{\mathbf{a}} \cdot \hat{\boldsymbol{\mu}}_1\right) + \frac{\mu_1\mu_1}{(2z)^4}\left(\hat{\mathbf{a}} \cdot \hat{\boldsymbol{\mu}}_1\right)^2\right]\hat{\mathbf{a}} \\ & + \frac{3\mu_0}{4\pi}\left[\frac{\mu_1\mu_{FC}}{\left(z + z_{FC}\right)^4}\right]\hat{\boldsymbol{\mu}}_1\end{aligned} \tag{5.91}$$

If the system is simplified further such that the magnetic moment vector is parallel to the normal of the superconductor's plane, the result simplifies further to:

$$\mathbf{F}_{cont} = \left(\frac{3}{32}\frac{\mu_0}{\pi}\frac{\left(\mu_1\right)^2}{\left(z\right)^4} - \frac{3}{2}\frac{\mu_0}{\pi}\frac{\mu_1\mu_{FC}}{\left(z + z_{FC}\right)^4}\right)\hat{\mathbf{a}} \tag{5.92}$$

Equation (5.92) is quadratic with respect to μ_1 . Thus, solving the quadratic formula to produce the final magnetic steering law (for motion and actuation in the *z* direction) yields:

$$\mu_{1,z} = \frac{-\frac{3}{2}\frac{\mu_0}{\pi}\frac{\mu_f}{\left(z+z_{FC}\right)^4} \pm \left[\left(-\frac{3}{2}\frac{\mu_0}{\pi}\frac{\mu_f}{\left(z+z_{FC}\right)^4}\right)^2 - 4\frac{3}{32}\frac{\mu_0}{\pi}\left(\frac{1}{z^2}\right)^2 u_z\right]^{0.5}}{\frac{6}{32}\frac{\mu_0}{\pi}\left(\frac{1}{z^2}\right)^2} \tag{5.93}$$

5.4.3. Magnetic Moment Selection

As can be seen in Equation (5.93), there are two possible magnetic moment values that produce the same force on the system. The FPI control designer can choose which value to implement in the steering law because they produce the exact same

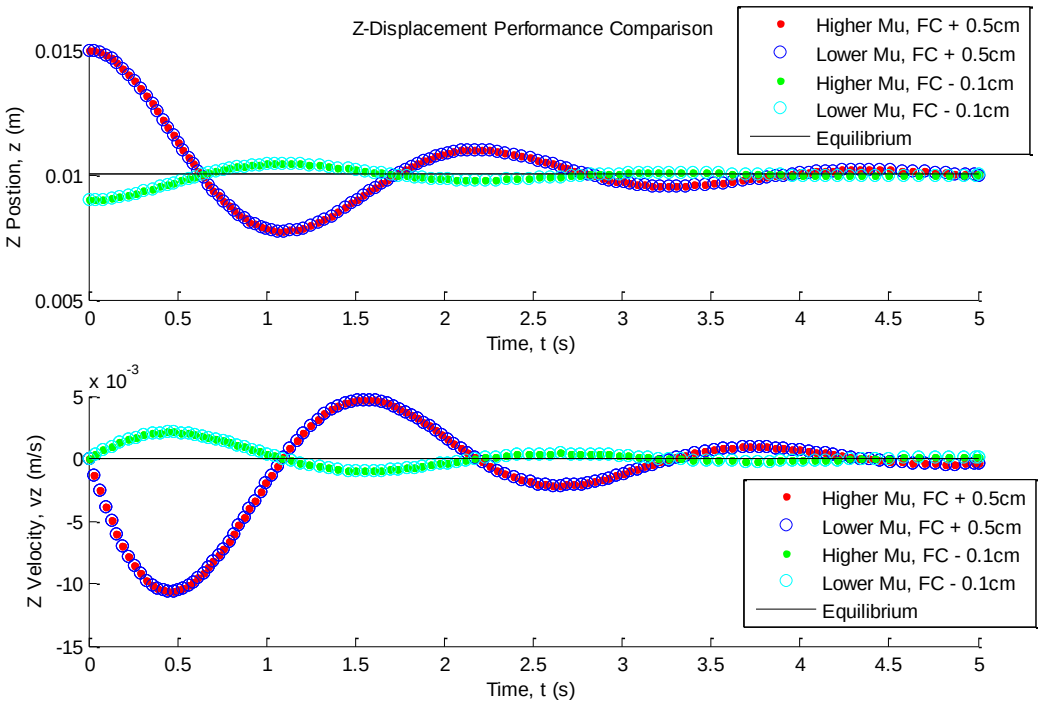

Figure 5.6. The *z* position and velocity performance of a magnet from two different initial displacements for both the higher and lower magnetic moment values.

performance characteristics from the perspective of the system response (as seen in Figure 5.6). However, the value associated with adding the numerator's terms (or μ_h for "higher") has very different system implications when compared to the value where the terms are subtracted (or μ_u for "lower"). In particular, the control effort between the two solutions varies considerably. As seen in Figure 5.7, the higher magnetic moment values require much higher voltages to achieve the same performance; however, they also converge to a steady state voltage of 10 V, which is

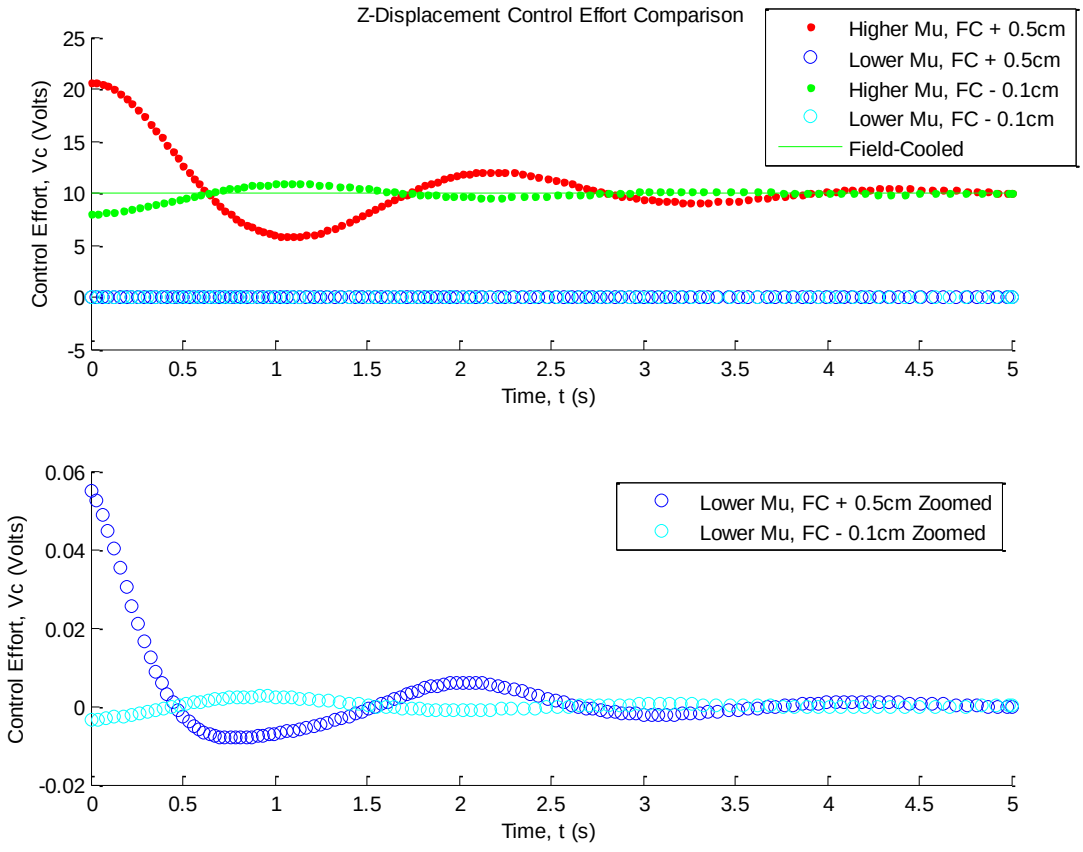

Figure 5.7. The *z* control effort of the system for the two different initial displacements for both higher and lower magnetic moment values. The lower plot is a re-scaled version of the upper.

the field-cooled value. Thus, when the system is in steady state, the disturbance rejection properties of an uncontrolled FPI still apply, which may be useful for disturbance rejection in unobserved or uncontrolled states.

The lower magnetic moment values, on the other hand, use significantly less control effort than the higher ones, but the steady state voltage becomes zero – the electromagnet turns itself off. This behavior may be advantageous if power is a particular concern because the electromagnet does not require a constant voltage at equilibrium. However, this solution to the magnetic steering law does have a few significant drawbacks. First, it will not provide any of the passive stability properties offered by a magnet in an FPI in equilibrium. Although for the *z* direction this may not be a problem since the system will be able to observe the change in the state and react accordingly, this behavior poses a problem for disturbances in states that are not observable or controllable by the control system. A magnet in an FPI will reject these disturbances based on the physics alone (regardless of the capabilities of the control system), but an unpowered electromagnet will not. Also, the lower magnetic moment solution to the steering law uses negative values to influence the system. Using a magnetic moment that is opposite of the field-cooled image is inherently unstable and may be risky for a use in actual systems.

5.4.4. FPI Active Control Performance

Proportional-Derivative Control

For an electromagnet pinned in an SMSS FPI using the magnetic steering law in Equation (5.92), a PD controller is capable of driving the FPI system to the desired

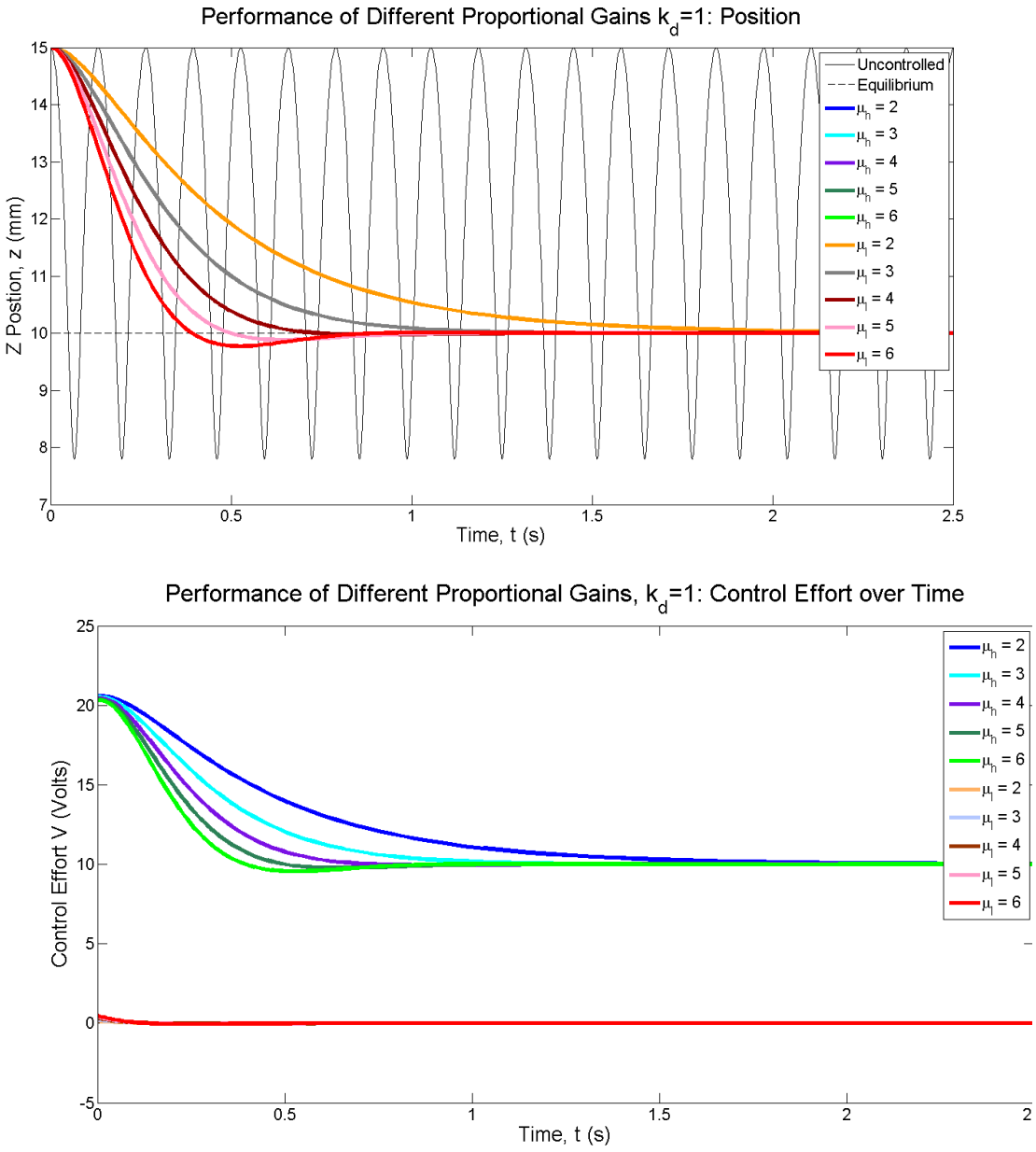

Figure 5.8. The position and control effort for an SMSS FPI compared to an uncontrolled (and undamped) response over different proportional gain values.

state from a position disturbance. As seen in Figure 5.8, the system's overdamped controlled response varies significantly from the (undamped) uncontrolled system (for a k_d of 1 and a k_p as shown). While the gains can be optimized over various system parameters, the active control strategy for FPIs fundamentally works.

Derivative Control

The lower values of the magnetic moment enable the control of a variation on the SMSS FPI in which an electromagnet is wrapped around a permanent magnet. In this

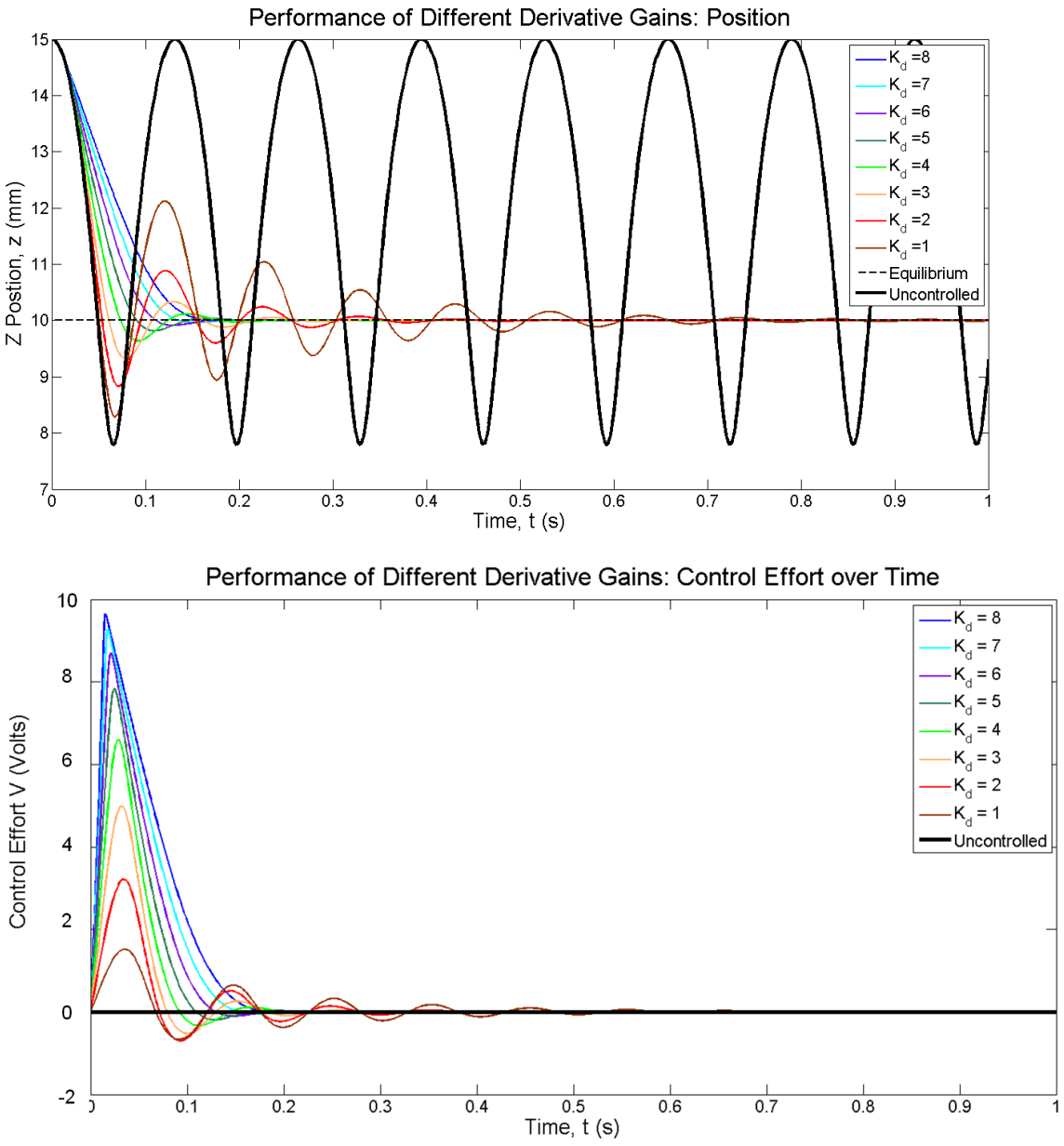

Figure 5.9. The position and control effort for a modified SMSS FPI as compared to an uncontrolled (and undamped) response over different gain values.

arrangement, the permanent magnet provides its passive stability properties to the FPI without requiring control effort at equilibrium. It also serves to provide basic proportional control to the system without any control effort. However, the system behavior can still be modified using a derivative-only controller with the lower magnetic moment solution to the steering law. For example, Figure 5.9 shows that a system implementing this modified SMSS FPI can be driven to its steady state quickly and effectively. This technique also preserves the stability properties of a passive FPI for no control effort cost. For this reason, this modified SMSS FPI is the basis of one of the orbital flight FPI designs, discussed in Chapter 8.

5.4.5. Stability of an Active SMSS FPI

If SMSS FPIs are to be successfully controlled, it is important to determine the bounds on the control forces and torques that are required to maintain stability. Thus, it is necessary to revisit the Lyapunov function expressed in Equation (5.30) and derive the conditions on these forces and torques that would guarantee Lyapunov stability. (It should be noted, however, that failing to meet these conditions does not necessarily imply that the system is unstable). Although the general form of the analysis in Section 5.3.2 can be followed for the controlled case, a few notable differences must be observed. First, the magnetic moment must not include step functions or other discontinuities so that the Lyapunov function maintains continuous partial derivatives and continuity. Given that this constraint is met, the derivative of the Lyapunov function is Equation (5.42):

$$\dot{V}(\mathbf{r}_1) = {}^{N}\mathbf{r}_1 \cdot \left(m\, {}^{NN}\mathbf{r}_1 \right) + \boldsymbol{\omega}_{B/N} \cdot \left(\mathbf{I}_1 \cdot {}^{N}\boldsymbol{\omega}_{B/N} \right) - {}^{N}\frac{d}{dt}\left(\boldsymbol{\mu}_1 \cdot \left(\mathbf{B}_f + \frac{1}{2}\mathbf{B}_m \right) \right) \tag{5.94}$$

Secondly, the equations of motion of the system now include control forces and torques:

$$m\, {}^{NN}\mathbf{r}_1 = \mathbf{F}_{mag} - \mathbf{F}_{damp} + \mathbf{F}_{cont} \tag{5.95}$$

$$\mathbf{I}_1 \cdot {}^{N}\boldsymbol{\omega}_{B/N} = -\boldsymbol{\omega}_{B/N} \times \mathbf{I}_1 \cdot \boldsymbol{\omega}_{B/N} + \boldsymbol{\tau}_{mag} - \boldsymbol{\tau}_{damp} + \boldsymbol{\tau}_{cont} \tag{5.96}$$

Thus, these control terms appear in the Lyapunov derivative as follows:

$$\begin{aligned} \dot{V}(\mathbf{r}_1) = {}^{N}\mathbf{r}_1 \cdot \left(\mathbf{F}_{mag} - \mathbf{F}_{damp} + \mathbf{F}_{cont} \right) + \boldsymbol{\omega}_{B/N} \cdot \left(\boldsymbol{\tau}_{mag} - \boldsymbol{\tau}_{damp} + \boldsymbol{\tau}_{cont} \right) \\ - {}^{N}\frac{d}{dt}\left(\boldsymbol{\mu}_1 \cdot \left(\mathbf{B}_f + \frac{1}{2}\mathbf{B}_m \right) \right) \end{aligned} \tag{5.97}$$

Rearranging:

$$\begin{aligned} \dot{V}(\mathbf{r}_1) = \left({}^{N}\mathbf{r}_1 \cdot \mathbf{F}_{mag} \right) + \left(\boldsymbol{\omega}_{B/N} \cdot \boldsymbol{\tau}_{mag} \right) - \left({}^{N}\boldsymbol{\mu}_1 \cdot \left(\mathbf{B}_f + \frac{1}{2}\mathbf{B}_m \right) \right) - \left(\boldsymbol{\mu}_1 \cdot {}^{N}\frac{d}{dt}\left(\mathbf{B}_f + \frac{1}{2}\mathbf{B}_m \right) \right) \\ - {}^{N}\mathbf{r}_1 \cdot \mathbf{F}_{damp} + {}^{N}\mathbf{r}_1 \cdot \mathbf{F}_{cont} - \boldsymbol{\omega}_{B/N} \cdot \boldsymbol{\tau}_{damp} + \boldsymbol{\omega}_{B/N} \cdot \boldsymbol{\tau}_{cont} \end{aligned} \tag{5.98}$$

The first four terms are known to cancel in the uncontrolled system, with the exception of the terms described in Equations (5.45) and (5.58). Both of these terms involve the body derivative of the magnetic moments, and in the uncontrolled case they were set to zero. However, in the controlled case, these terms do not go to zero and so they must be included in the derivative of the Lyapunov equation. Thus, canceling out the terms that are known to go to zero from the passive case, and including the terms that are now non-zero:

$$\dot{V}(\mathbf{r}_1) = -\overset{B}{\boldsymbol{\mu}}_1 \cdot \left(\mathbf{B}_f + \frac{1}{2}\mathbf{B}_m \right) - \frac{1}{2}\frac{c_0}{\left(\boldsymbol{\rho}_m \cdot \boldsymbol{\rho}_m\right)^{3/2}}\left[3\left(\boldsymbol{\mu}_1 \cdot \hat{\boldsymbol{\rho}}_m\right)\hat{\boldsymbol{\rho}}_m - \boldsymbol{\mu}_1\right] \cdot \overset{B^*}{\boldsymbol{\mu}}_m$$
$$-\overset{N}{\mathbf{r}}_1 \cdot \mathbf{F}_{damp} + \overset{N}{\mathbf{r}}_1 \cdot \mathbf{F}_{cont} - \boldsymbol{\omega}_{B/N} \cdot \boldsymbol{\tau}_{damp} + \boldsymbol{\omega}_{B/N} \cdot \boldsymbol{\tau}_{cont} \tag{5.99}$$

Using the rewritten expression for the mobile magnetic field in Equation (5.71), Equation (5.99) becomes:

$$\dot{V}(\mathbf{r}_1) = -\overset{B}{\boldsymbol{\mu}}_1 \cdot \mathbf{B}_f - \frac{1}{2}\overset{B}{\boldsymbol{\mu}}_1 \cdot \mathbf{B}_m - \frac{1}{2}\mathbf{B}_m \cdot \overset{B^*}{\boldsymbol{\mu}}_m$$
$$-\overset{N}{\mathbf{r}}_1 \cdot \mathbf{F}_{damp} + \overset{N}{\mathbf{r}}_1 \cdot \mathbf{F}_{cont} - \boldsymbol{\omega}_{B/N} \cdot \boldsymbol{\tau}_{damp} + \boldsymbol{\omega}_{B/N} \cdot \boldsymbol{\tau}_{cont} \tag{5.100}$$

The third term represents includes the change of the mobile image with respect to its own body image, which is equivalent to the change in the source magnet's change with respect to the *B* frame. Thus, the expression can be rewritten:

$$\dot{V}(\mathbf{r}_1) = -\overset{B}{\boldsymbol{\mu}}_1 \cdot \mathbf{B}_f - \overset{B}{\boldsymbol{\mu}}_1 \cdot \mathbf{B}_m - \overset{N}{\mathbf{r}}_1 \cdot \mathbf{F}_{damp} + \overset{N}{\mathbf{r}}_1 \cdot \mathbf{F}_{cont} - \boldsymbol{\omega}_{B/N} \cdot \boldsymbol{\tau}_{damp} + \boldsymbol{\omega}_{B/N} \cdot \boldsymbol{\tau}_{cont} \tag{5.101}$$

So, the forces and torques must meet the following criteria to remain guaranteed stable in the sense of Lyapunov:

$$0 \geq -\overset{B}{\boldsymbol{\mu}}_1 \cdot \mathbf{B}_f - \overset{B}{\boldsymbol{\mu}}_1 \cdot \mathbf{B}_m - \overset{N}{\mathbf{r}}_1 \cdot \mathbf{F}_{damp} + \overset{N}{\mathbf{r}}_1 \cdot \mathbf{F}_{cont} - \boldsymbol{\omega}_{B/N} \cdot \boldsymbol{\tau}_{damp} + \boldsymbol{\omega}_{B/N} \cdot \boldsymbol{\tau}_{cont} \tag{5.102}$$

Alternatively:

$$\overset{N}{\mathbf{r}}_1 \cdot \mathbf{F}_{cont} + \boldsymbol{\omega}_{B/N} \cdot \boldsymbol{\tau}_{cont} \leq \overset{B}{\boldsymbol{\mu}}_1 \cdot \left(\mathbf{B}_f + \mathbf{B}_m \right) + \overset{N}{\mathbf{r}}_1 \cdot \mathbf{F}_{damp} + \boldsymbol{\omega}_{B/N} \cdot \boldsymbol{\tau}_{damp} \tag{5.103}$$

Essentially, the change in work done by control forces and torques must not exceed the work done by the damping forces and torques combined with the dot product of the change in the source magnet's magnetic moment and the total magnetic field in an SMSS FPI. Note that this term is not quite associated with the system's

potential energy because it does not include the one-half coefficient in front of the mobile magnetic field.

CHAPTER 6

FPI DEMONSTRATIONS IN A LABORATORY TESTBED ENVIRONMENT

6.1. The Role of Laboratory Experimental Work in FPI Development

Developing relevant experimental hardware in the laboratory is a key aspect of the FPI maturation process that naturally follows the formulation of the technology's theoretical and analytical framework. The process of implementing FPIs in hardware allows researchers to begin to address feasibility and design issues that determine the utility of the technology in practice. Unlike microgravity experiments (discussed in Chapter 7), laboratory development work allows researchers to implement and assess design changes soon after they are conceived, which then informs the technology's next design iteration. This feedback loop enables the experimenters to converge on solid design principles while still retaining the laboratory environment's flexibility and relatively low development costs. Laboratory development and the attainment of TRL 3 or 4 ultimately provides the practical foundation necessary for FPIs to become a viable spacecraft technology.

The cornerstone of most laboratory-based work in spacecraft dynamics and controls is a reduced-friction testbed that simulates a space environment in selected degrees of freedom. Although many designs exist, the most common type utilizes air bearings to produce near-frictionless motion using pressurized gas as a lubricant. However, most of the FPI hardware was designed on a CubeSat scale because the small standardized form-factor is well suited to low-cost technology development projects. Few existing air-bearing testbed designs are appropriate for evaluating the

performance of multi-body close-proximity CubeSat-scale technologies such as flux-pinned interfaces for spacecraft. Thus, to add a robust laboratory element to the FPI research endeavor, it became necessary to design and fabricate a completely new planar air-bearing testbed. The FloatCube testbed, as it came to be called, was a joint effort involving input from William Wilson and Joseph Shoer, the system's entire design cycle was a part of this research: concept development, construction, testing, and its final implementation as an experimental platform for FPIs. The pertinent elements of the design, operation, and performance of the resulting testbed are described in Section 6.2, which draws content from a joint paper with William Wilson.[96]

Several projects have exploited this effective reduced-friction dynamics testbed to advance FPI technology in the laboratory. The testbed has played an instrumental role in developing and validating component-level subsystems and basic concepts early in the FPI laboratory development stage, as described in section 6.4.1. Building on the successes of these prototype systems, a subsequent project advanced to a system-level demonstration that highlighted the efficacy of an FPI-connected formation of spacecraft under PID-controlled slews. This work was conducted jointly with Matt Sorgenfrei and Sanjay Joshi at the University of California at Davis, and some of the content from section 6.4.2 is derived from the joint publication detailing this experiment and its results. These achievements in laboratory-based demonstrations and experiments set FPIs apart from many other novel spacecraft technologies and set the stage for increasingly sophisticated and flight-like development efforts.

6.2. A Multi-Body Planar Air Bearing Testbed for CubeSat-Scale Spacecraft

6.2.1. Selection of a Planar Air-Bearing-Based Testbed Design

Most dynamics and control testbeds for spacecraft come in three varieties: neutral buoyancy testbeds that attempt to reduce the effect of gravity by achieving neutral buoyancy in a fluid,[123,124] robotically controlled testbeds that use robotic arms and gantries to simulate the motion of a satellite,[125,126] and air-bearing reduced-friction environments that lubricate relevant degrees of freedom with pressurized gas.[127] Sophisticated testbeds often include combinations of these approaches to achieve a space-like dynamic environment in up to six different degrees of freedom. Of these three techniques, however, neutral buoyancy and robotically-controlled testbeds often require large, expensive, or complicated infrastructure that make such designs cost-prohibitive for CubeSat-scale development projects. Air-bearing testbeds offer a more scalable concept, making this type of testbed most suited to the development of a testing environment for kilogram-scale spacecraft.

Over the last 45 years, air-bearing systems have been a popular tool in the development of a variety of spacecraft technologies.[128] They function by forcing pressurized gas through small holes in the bearing face, which establishes a thin film of gas that supports the test platform above a smooth surface. This gas also serves as a lubricant that enables low-friction motion of the bearing over the surface, simulating a free-floating satellite in a space environment. When a testbed is designed to study attitude dynamics and control, it typically employs spherical air bearings that produce reduced-friction attitude motion, such as the Naval Postgraduate School's Three Axis Attitude Dynamics and Control Simulator[129] and Virginia Tech's Distributed

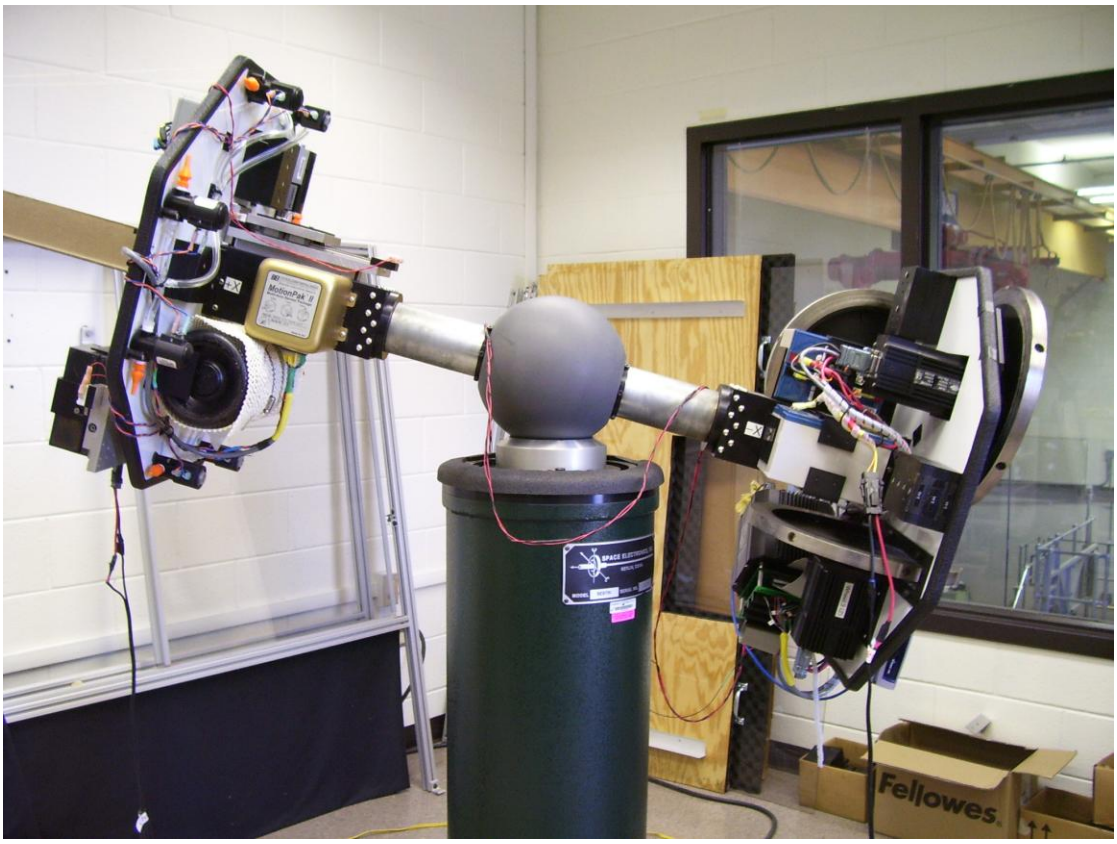

Figure 6.1. The spherical air bearing testbed in the Space Systems Simulation Lab at Virginia Tech, which is intended to enable attitude dynamics and control research.

Spacecraft Attitude Control System Simulator (shown in Figure 6.1).[130] On the other hand, if the testbed is intended to play a role in understanding multi-body dynamics or translational motion, the system typically uses planar bearings that operate over a smooth surface. This type of air bearing provides one rotational and two translational degrees of freedom and has been used in Stanford's ARL testbed.[131] Since FPIs represent a method of connecting multiple spacecraft together, the testbed developed for FPI research had to be capable of supporting multi-body dynamics. Thus, the resulting design used a planar air-bearing system.

No existing planar testbed for multi-body, close-proximity technologies has been explicitly developed to accommodate multi-body CubeSat dynamics. The Formation

Control Testbed, which was developed at the Jet Propulsion Laboratory in support of the Terrestrial Planet Finder (TPF) mission, is an example of a sophisticated planar air-bearing based testbed developed for traditionally-sized spacecraft. This testbed consists of three air bearing vehicles approximately 1.64 meters high and 358 kilograms in mass, which translate and rotate on a smooth surface for three degree-of-freedom motion for testing, and include a spherical air bearing and a vertical stage to provide full six degree-of-freedom control.[125] The TPF satellites were designed to be many orders of magnitude larger than CubeSats and the cost of the system is likely inaccessible to the standard small-scale CubeSat program. On the other end of the scale, the testbed platforms developed for the Synchronized Position Hold Engage Re-orient Experimental Satellites (SPHERES) project at MIT are on the order of 0.1 meters high and 0.1 meters on a side.[132] This testbed, consisting of air-bearing platforms that moved in purely planar motion over a flat surface, was intended to provide a low-cost, easily-accessible testing precursor to the later, more sophisticated vehicle deployment on the International Space Station. These platforms are much more suited to CubeSat applications, making them a rare exception to other testbeds of this nature; however, they were explicitly designed for the SPHERES platform and were not optimized for hosting CubeSats or their components. The FloatCube testbed, on the other hand, was designed explicitly to accommodate the CubeSat-scale multi-body dynamics experiments necessary to advance the technology development of FPIs, while remaining adaptable enough to accommodate many different experimental goals.

6.2.2. FloatCube Testbed Overview

Key Testbed Elements

As a planar air-bearing-based spacecraft simulator, the FloatCube testbed consists of several elements that work in concert to provide a low-friction testing environment. The four major components in the system are: 1) the operating surface, 2) the sensing system, 3) one or more FloatCube platforms, and 4) the payload segment(s) being tested. A smooth glass plate is used to provide a surface suitable for air bearing operation. Cameras mounted above the testing surface form a vision system that tracks vehicle positions during tests. FloatCube air bearing platforms can be mounted with CubeSat-scale payloads at a component- or system- level of sophistication. A total of four platforms have been constructed in the current implementation of the testbed, all of which can be used simultaneously to support multiple payload interactions (for example, in a close-proximity formation flying experiment). These major elements of the testbed can be seen in Figure 6.2.

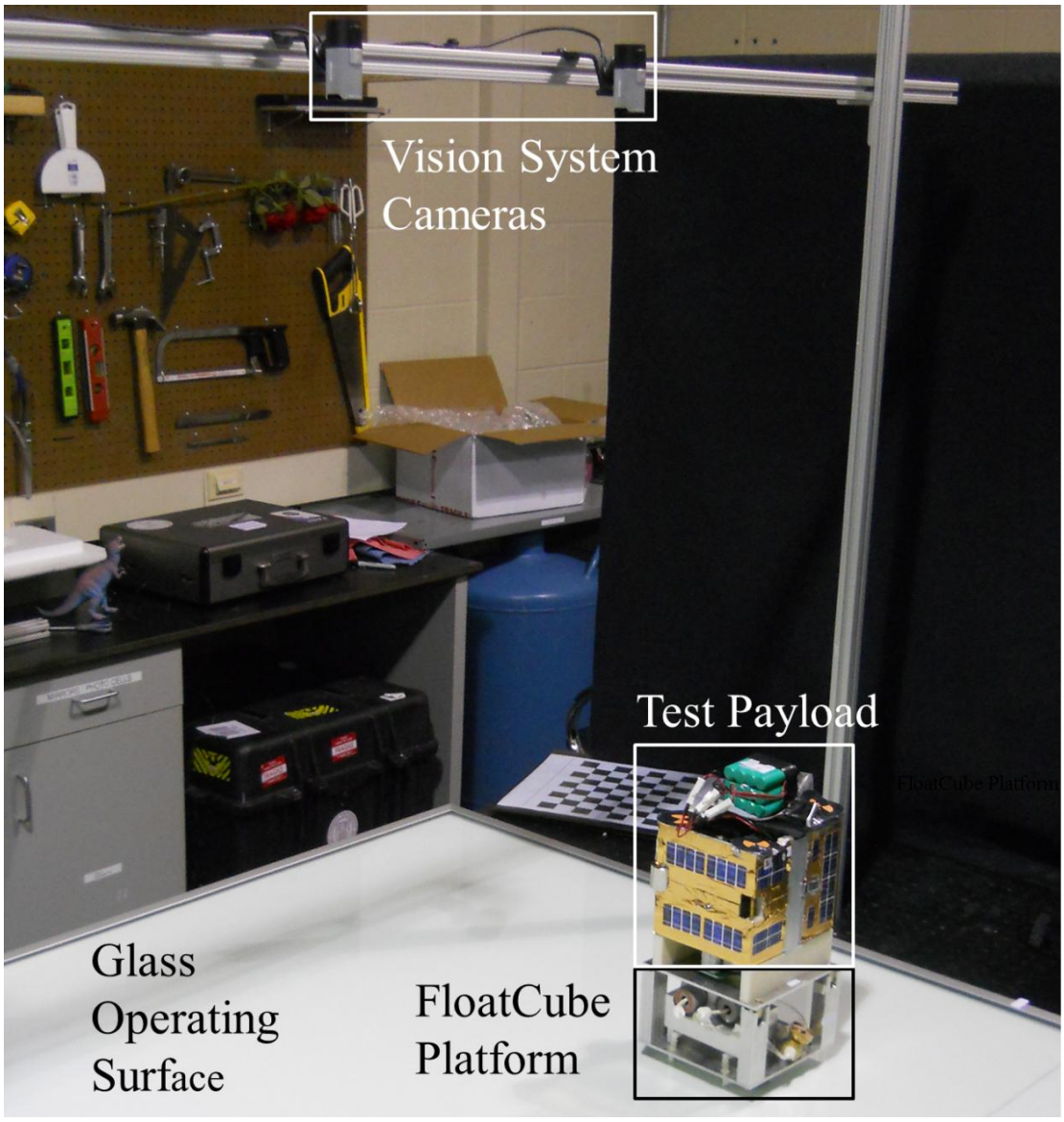

Figure 6.2. The FloatCube testbed showing all of the major system elements.

Operating Surface

For the air bearing-supported platforms to function, they must operate on a smooth, flat surface that is oriented with gravity normal to the surface plane. This surface is typically made of highly polished granite, poured plastic, or plate glass. The most significant differences among these options for operating surfaces are smoothness, portability, and cost. For the FloatCube testbed, the testing surface is a

$16ft^2 \times 0.25in$ ($1.49m^2 \times 6.35mm$) plate glass square with aluminum edging placed on top of an optical table. The plate glass minimizes the cost and supporting structure at the expense of a more variable surface topography.

It is important to ensure the testing surface is level to prevent variations in the operational environment from affecting experimental results. Thus, several steps were taken to make the glass plate level on the supporting surface. First and foremost, the glass was placed on top of a layer of foam board resting on the optical table in order to enable the glass to roughly self-level. Then the operating surface was divided into an evenly-space grid and at each intersection the angle relative to gravity was measured using a commercially-available level. After creating a map of the angles in the grid, general trends were noted (for example, if all of the *x* angles were positive, the entire glass was clearly sloping in a positive *x* direction). These coarse trends were taken out by manually adjusting the height of the legs of the optical table supporting the glass surface. This process was repeated until the surface no longer had a consistent trend in one direction. In order to compensate for the local variations in the glass, small shims were placed between the optical table and the foam board. These shims caused a slight bowing of the glass, changing its local topography and enabling a measure of control over the variations in the glass surface.

Finally, to ensure the leveling process produced reasonable results, after iterating on the leveling procedure to within the measuring capability of the level (within one degree), the system was tested with a FloatCube platform. The floating platform was placed on different parts of the table and released to determine if variations in the glass caused unintentional motion, and in which directions that motion occurred. Areas that

were still not flat even after further refinement were noted as poor operations areas and care was taken that testing on the surface did not initiate or stray into the testing surface area with known undesirable topography.

Sensing System

Knowing the motion of the payload during maneuvering and testing is an essential part of a functional dynamical testbed system. Thus, the FloatCube testbed was developed to include a global sensing system capable of tracking even inert or passive modules. While many testbeds of this type include complex sensing packages such as the VICON camera systems,[124,126] the FloatCube sensing system includes additional constraints that prevent these sophisticated systems from being viable solutions. In addition to requiring that the sensor would not appreciably influence the dynamics of the system, the sensing system needs to have millimeter-level resolution over a large percentage of the 16 ft^2 (1.49m^2) glass testing surface and fit into a budget appropriate for a low-cost CubeSat development testbed. Given these requirements, a vision system with custom motion tracking software was selected to perform this role in the testbed.

Figure 6.3. The vision system sensors mounted over the operating surface on a T-slot structure.

The camera system was developed for basic functionality with minimal cost, and so it was constructed using off-the-shelf consumer webcams that mount to a simple aluminum T-slot structure over the glass. These Microsoft LifeCam Studio USB

cameras are capable of collecting data at up to 30 frames per second at 480x640 pixel resolution. Two cameras are used to produce a composite data-collection range for a larger field-of-view without sacrificing resolution.[133] The vision system is operated by a piece of software developed in-house based on the open-CV computer vision library.[134] This code tracks high-contrast target points FloatCube platforms as they move during test maneuvers. The system works best in even lighting conditions with a white testing surface for increased contrast (thus the foam board underneath the plate glass is white).

At the startup of a test run, the user identifies the tracking points by clicking on the target points using a mouse on the video feed. Once the points have been locked in, the system continues to track the points until one of the points leave the field of view, or the modules move quickly enough relative to the frame rate of the camera that the system cannot identify the same tracking point from frame to frame. In both cases, the system stops collecting data until the points are again reset into the system by the user.

The output of the vision system is a text file containing the pixel positions of the tracked points as well as the centroid position and rotation angle of the identified vehicles (provided that the same points were selected in the same order by the user in between interruptions in the data collection). The data it collects is not currently set up for a real-time in-the-loop control system, but it does provide a global truth of the motion of the vehicles on the testbed. In FloatCube experiments, the camera data has been able to provide position and velocity data that has been shown to closely match that obtained by the internal measurement units used on some test payloads. For example, Figure 6.4 shows the angular rate and angle data collected by the camera

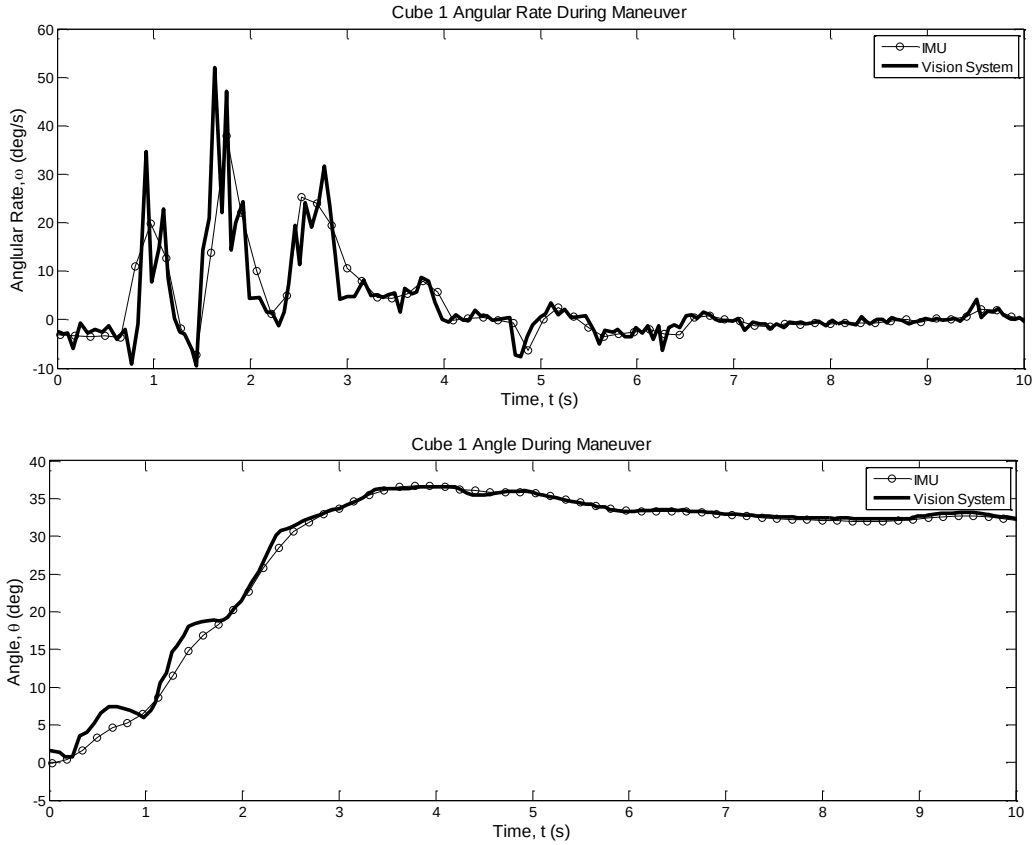

Figure 6.4. Overlay of IMU and vision system data for angle and rate of a payload slew maneuver

system and the on-board payload IMU sensor during a controlled slew maneuver. The camera collected the position data directly, and the IMU collected the rate data directly. Both signals were integrated or differentiated appropriately to overlay on both plots.

FloatCube Platforms

The most important piece of hardware in the testbed is the air bearing-levitated platform itself, referred to individually as a FloatCube platform. The FloatCube platform is composed of several major components: the air bearings, the pressure system, and the underlying support structure. The FloatCubes do not require power, so

payloads must include their own power source. However, in order to operate the FloatCube bases it is necessary to have two CO_2 gas cartridges loaded into the system. These cartridges must be replaced once the system drops below the operational pressure for the bearings.

Having multiple free-floating bases enables multi-body testing, and so the SSDS FloatCube testbed has four FloatCube platforms, representing two generations of the design. Each generation has slight variations in materials and mounting strategies. The base design for this platform was developed specifically to support the CubeSat satellite standard, and is discussed in further detail in subsequent sections along with insights into the merits of different design choices.

Payload Segment

The FloatCube testbed was designed to be versatile to accommodate a variety of dynamics and controls testing and development at the CubeSat scale. Instead of developing an integrated system with permanently-mounted CubeSats affixed to the floating platform vehicle, the system was designed to allow the floating platform to separate entirely from the independent payload segment. The interface between the floating apparatus and the experimental hardware was designed to be as simple as possible. The testbed can accept a variety of mounting options to accept CubeSat vehicles, engineering models, and component assemblies for testing. In Figure 6.2, an engineering-model-level assembly is shown during a FloatCube test. Provided that the payload can be held securely to the floating platform, no other integration is needed for testing to commence.

System Costs

The industry's interest in CubeSats is due in part to their low development cost. Therefore, the FloatCube system uses total cost as a key metric for evaluating the overall system design. The cost for components and fabrication of the testbed is derived from the commercial vendors used in supplying the components for the SSDS FloatCube testbed. These costs are delineated in Table 6.1 which does not include line items for any payload components because these vary significantly based on the desired tests and sophistication of the items being tested. Labor costs are estimated as they can vary widely. The operating surface and vision system represent a one-time cost that can support multiple platforms. The only recurring cost is a commercially available rubbing alcohol cleaning fluid (~$3 per bottle) for the air bearings and testbed, and approximately $1 per 16g CO_2 cartridge. With a cost of about $4500 (or less if aluminum FloatCubes are used exclusively and the vision system is not implemented) and only a small recurring cost, the FloatCube testbed should be affordable to most CubeSat projects, given that a standard launch cost of a CubeSat is cited at $30,000.[61]

Table 6.1. Estimated Fixed Costs of Testbed Components.

Item	Description	Cost
Aluminum FloatCube Platform	Total cost for 1 Aluminum FloatCube	$700
Platform Pressure System	*Air bearings, CO_2, regulators, joints, bearings etc.*	*$550*
Platform Structure	*Materials*	*$150*
Plastic FloatCube Platform	Total cost for 1 Plastic FloatCube	$1325
Platform Pressure System	*Air bearings, CO_2, regulators, joints, bearings etc.*	*$550*
Platform Structure	*Rapid Prototype Printing*	*$725*
Shipping	*Cost to receive the commercially-built structure*	*$50*
Operating Surface	Plate glass with aluminum edging	$250
Vision System	2 Cameras, cables, software	$200
Total Testbed	**Total fixed cost for testbed as built (2 Aluminum platforms, 2 plastic platforms and vision system)**	**$4500**

6.2.3. FloatCube Platform Design

The FloatCube platforms house the air bearings and pressure system, and provide mounting for test payloads. Since it is such a critical piece of hardware, this section describes the main subsystems and design decisions for the implemented system, shown in Figure 6.5. Key aspects of the design include a self-contained pressure system, a custom structure design, and a payload mounting interface. Each of these elements emphasizes low cost, ease of purchase or manufacture of components, and compatibility with a wide range of test articles on the order of kilograms.

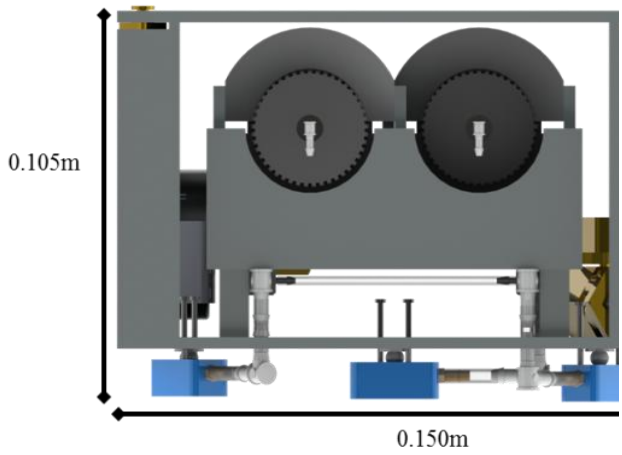

Figure 6.5. The FloatCube platform design.

Pressure System

The air bearings, along with a supply of compressed gas, provide the mechanism for supporting the FloatCube platforms above the testbed surface and establishing the low-friction environment necessary for spacecraft

testing. The FloatCube design uses three rectangular New Way S121201 planar bearings per platform, which were selected for their small size, relatively high (36N) load capacity, and low cost. These bearings are arranged in a symmetrical pattern around the platform's center, which provides platform stability with a small number of bearings to reduce cost and friction, and to improve the experiment duration.

Even small misalignments between the surface and bearing film surface significantly reduce the lifting capacity of the bearings and increase the friction the platform experience. Therefore, in order to maintain even loading and avoid these misalignments, the bearings rest on a spherical joint attached to the structure. This joint consists of a 5 mm diameter Delrin ball and washer epoxied to the bottom of the platform's structure such that it aligns with the hemispherical cavity in the bearing's top surface. The spherical joints can clearly be seen on the platform in Figure 6.6. This arrangement allows the bearings to remain parallel to the operating surface by self-aligning to accommodate small changes in the topography of the testing surface.

One key design feature of the FloatCube is that it allows these spherical bearings

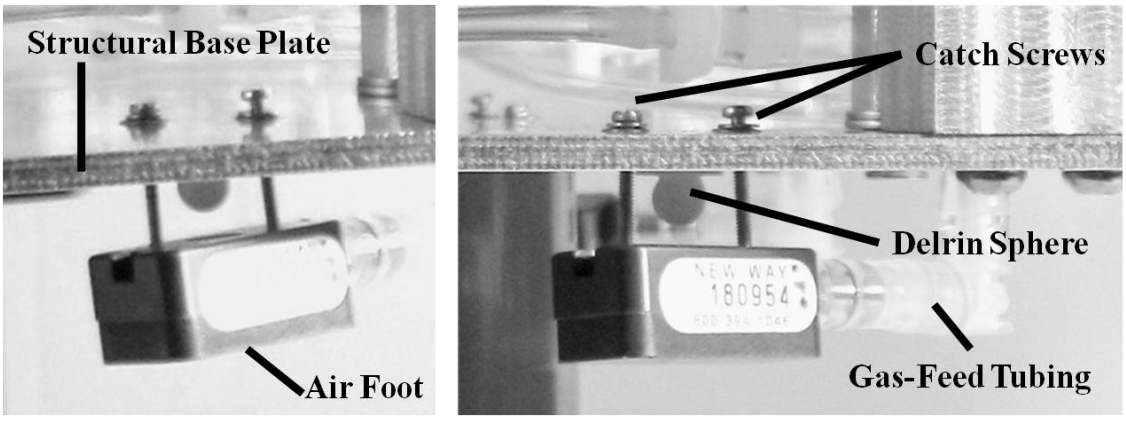

Figure 6.6. The FloatCube platform's spherical joint.

to rotate freely during experimentation, but can still enable the feet to remain attached to the structure when not on the operating surface. The air feet are connected to the structure with long screws that pass through the base plate via a clearance hole. Washers prevent the head of the screw from passing through the hole when the platform is lifted off the testing surface. Due to the fact that the holes are large enough to leave the spherical joint unconstrained in an operational configuration, these screws do not interfere with operation of the bearings.

During the FloatCube development, empirical studies indicated that any physical connection between the levitating platform and other hardware (for example, a hose for connecting the system to the compressed-air supply from the wall) imposes enough force on the platform to significantly influence the platform's movement and dynamics. Thus, all platform hardware and expendables are designed to be self-contained onboard the platform during operation. This self-contained design necessitates that the platforms host their own gas supply and pressure system.

The system developed for the FloatCubes centers on the manually adjustable Genuine Innovations regulators, which can be tuned to ensure that the gas reaches the bearings at a pressure between 60 and 80 psi (0.414 to 0.552 mPa). These specific regulators were chosen because they can directly connect to standard threadless CO_2 cartridges, which is one of the most common sources of small quantities of compressed gas available off-the-shelf. Air bearings can function with this gas with no effect on their performance. Use of the cartridges allows an economical solution to supplying gas to the bearings without the need for a large air supply, hoses extending out of the platform, or external pumps to refill pressure vessels. Two cartridges are

Table 6.2. Pressure System Parameters.

Variable Name	Variable Symbol	Value
Typical Operating Pressure	$\boldsymbol{P}$	75 psi (0.517 mPa)
Pressure Ranges	$\boldsymbol{P_{min}}$ - $\boldsymbol{P_{max}}$	60 - 80 psi (0.414 to 0.552 mPa)
Air Foot Flow Rate	$\boldsymbol{F_{air\ bearing}}$	0.0001 m3/min
Number of Air Feet per Platform	$\boldsymbol{n_{ab}}$	3
Total Mass of Available CO2	$\boldsymbol{m_{CO2}}$	32g
Molar Mass of CO2	$\boldsymbol{n_{CO2}}$	44.01 g / mol
Calculated Float Time @ Typical Pressure	$\boldsymbol{t_{float}}$	11 min 30 s

used in the system to maximize the available experiment time. Equation (6.1) uses the ideal gas law to determine a theoretical testing time provided by one set of two cartridges per FloatCube platform:

$$t_{float} = \frac{\boldsymbol{m_{CO2}} \cdot R \cdot T}{n_{ab} \cdot \boldsymbol{n_{CO2}} \cdot F_{ab} \cdot P} \tag{6.1}$$

where t_{float} is the floating time or the total time of air bearing use in minutes, m_{CO2} is the total mass of CO_2 available in the pressure system, F_{ab} is the air bearing flow rate,[135] n_{ab} is number of air feet in the system, n_{CO2} is the molar mass of CO_2, and R, T, and P are the constant, temperature, and pressure from the ideal gas law. Values for these variables as implemented on the SSDS FloatCube system are shown in Table 6.2.

Although the calculated floating time is about 11 minutes per cartridge set, several timed tests were completed to determine the float time empirically. These tests, each started with a full cartridge of 32 total grams of CO_2, revealed a moderately higher floating time than estimated, with a mean of 12 min 7 sec. This discrepancy between the empirical time and the calculated time can be attributed to fluctuating pressure in the system, non-standard temperature in the testing environment, and imperfect flow from the air bearings. Any leaks in the pressure system also affect the real floating time observed.

After many different tubing strategies were tested, it was discovered that the stiffness of the tubing could impart forces onto the air feet, causing reducing floating performance since the feet would not lay flat on the operating surface. The air bearings are designed to fit standard 1/8” tubing and the regulators have 1/16” tubing adapters. Thus, the final design generally utilizes the smaller tubing to provide more flexibility in the system and to reduce the forces acting on the air feet. The 1/8” tubing segments are attached in a “C” shape from the air foot adapter, through a hole in the base plate, and then again parallel to the base plate. From there, an in-line adapter was used to convert to the 1/16” tube standard which the rest of the pressure system uses. Figure 6.7 shows the routing path of the pressure system.

Two types of tubing interfaces are used in the FloatCube pressure system: barbed tube fitting and luer locks, both of which are rated to 125 psi (0.862 mPa). The regulators are connected to the rest of the system by luer locks so they can easily be replaced in the event of a component failure. All other connections in the system are made with barbed tube fittings. Although initially

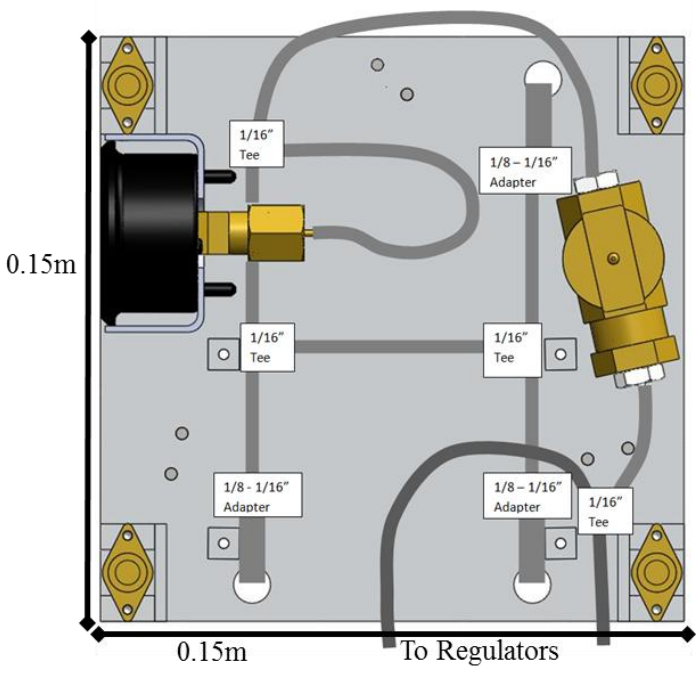

Figure 6.7. The FloatCube platform’s pressure system.

these fittings were reinforced with small zip ties, it was discovered that the zip ties tended to deform the tubes around the 1/16” barbs, exacerbating leaks; therefore, they were not included in the final design.

A manual value is located between the regulators and the rest of the pressure system in order to allow operators to turn off the gas flow and conserve CO_2 when the platform is not in use. The final design of the system calls for a large metal valve rated to 1000 psi (6.89 mPa) with two female 1/8” NPT connections. Two male adapters connect the 1/16” barbed fitting to the 1/8” NPT interface on the valve. A small amount of Teflon tape is wrapped around the threads of the NPT connectors to ensure an air-tight system.

Another critical part of the pressure system is the 100 psi (0.689 mPa)-rated pressure gauge. This instrument enables the tuning of the regulators to ensure they supply the correct pressures to the air feet before an experiment. They also allow the experimenter to monitor the CO_2 supply during experimentation. The components comprising the pressure system, along with important specifics, are listed in Table 6.3.

Once the completed pressure system was built, each attachment point was checked for a good seal. This testing was accomplished by submerging the floating platform in water while gas was flowing to the air feet (which does not damage the feet as long as the pressure is maintained). Any leaks were highlighted by the bubbles in the water and were addressed before using the platform for experimentation. The system was also tested with pressurized air available from a wall supply. Mating luer locks attached to the point where the regulators and CO_2 cartridges are typically placed were then connected to the wall interface. Although not suitable for dynamics

Table 6.3. Pressure System Components.

Component Name	Component Description	Quantity per Platform	Estimated Total Cost
Air bearing	New Way S121201 rectangular air bearing	3	$390
Gas regulator	Genuine Innovations CO2/gas composite regulator	2	$80
CO2 cartridge	Standard commercially available threadless 16g or 12g CO2 cartridge	2	$2 / run / platform
Spherical joint	Ball, washer, 2x screws	3	$10
Manual valve	High-pressure T-handle brass ball valve	1	$12
Pressure gauge	Multipurpose dial gauge	1	$14
Quick release tube locks	Luer Locks, male and female barbs	2	$8
Tubing	0.125in (3.175mm) and 0.0625in (1.588mm) OD tubing	1 ft 0.125in (0.308 m) 3ft 0.0635in (0.916 m)	$10
Connectors	Tees, elbows, and 1/8" to 1/16" adaptors	4 1/16" tees	$20
Total	**FloatCube Pressure System**	**1**	**$546**

experimentation, this testing enabled refinement of the bearing placement, the tubing lengths, and other factors that affect performance, without using CO_2 cartridges.

Platform Structure

The unique requirements of the FloatCube structure necessitated a custom-built design rather than a commercial solution. In addition to supporting the air bearings, pressure system, and the payload, the FloatCube platform is required to provide operational access to the valve and gauge and enable the rapid replacement of expended CO_2 cartridges. The final design of the system incorporates a base plate and pillar design that accommodates a compact tubing layout with fully removable CO_2 cartridge casings. Two generations of this design have been built at Cornell. The first generation platforms are made out of machined aluminum components, while the

second generation was made out of DuraForm GF in a commercial rapid-prototype printer.

The first key aspect of the FloatCube platform structure is its sizing. Single CubeSats are designed to be 1 kg in a 10 cm cube, but many laboratory component prototypes are necessarily larger or more massive than standard flight hardware. Thus, the FloatCube platforms were designed with a payload support plate of a 15 cm square area. Thus, components with a higher fidelity to flight are fully supported, while laboratory development parts can still use standard-sized electronic and mechanical components. The FloatCube platform was also designed to host much more than a 1 kg payload, anticipating that prototype hardware would not be optimized for mass. Thus, the system contains three air bearings each capable of supporting over 3 kg. These feet are arranged in a widely-spaced circular pattern around the geometric center of the platform footprint to maintain stability even if the center of mass of the payload is offset from the center of the platform.

The next critical aspect of the FloatCube structure was developed to support the pressure system. In particular, the Genuine Innovations regulators present a number of challenges in mounting and integration. Since the regulators do not have standard screw holes or mounting brackets, each are fitted with a collar that slides between the

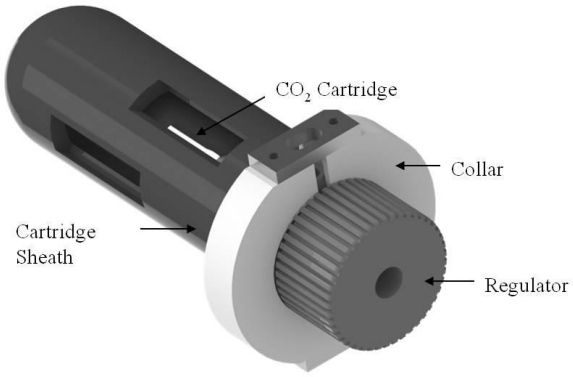

Figure 6.8. The regulator, CO_2 cartridge, and collar assembly separate from the rest of the FloatCube system.

adjustable output nozzle and the cartridge sheath, as shown in Figure 6.8. These collars – which are not removed in normal FloatCube operation or maintenance – serve as the structural interface to the rest of the FloatCube system. Slots in the main FloatCube structure hold the two regulators and sheaths securely during testing operations, while still enabling the user to replace the cartridges by detaching the entire regulator/collar/sheath assembly from the structure. The collars also provide a grip on the regulator when puncturing the CO_2 cartridges before each experiment. The system pressure is adjusted by turning the cylindrical cap at one end of the regulator. This motion is easily confused with the procedure for puncturing the CO2 cartridges, and so in the process of initiating the gas flow it is easy to mistakenly change the output pressure into the system. These collars help users avoid this mistake.

Material choice and construction method affect several aspects of the FloatCube platform design. The first-generation FloatCubes were constructed using machined aluminum parts, while the second-generation platforms were printed commercially with rapid-prototyped plastic. While both generations serve the same primary function, small differences in these generations provide insight into the advantages and disadvantages of differing materials and fabrication techniques. Figure 6.9 shows two completed FloatCube platform base structures, one made of individual aluminum parts and the other one piece created by rapid prototyping.

Table 6.4. FloatCube Mass Specifications.

	Aluminum (Gen 1)	Rapid-Prototype (Gen 2)
Platform Air Feet Load Capacity (3 Feet)	11.0 kg	11.0 kg
FloatCube Platform Mass	1.6 kg	1.3 kg
Theoretical Payload Capacity	9.4 kg	9.7 kg
Effective Payload Capacity (with margin)	**6.4 kg**	**6.7 kg**

One of most significant differences between the two generations of the completed platforms is the weight of the final platform structure. As seen in Table 6.4, the plastic FloatCubes are 0.3 kg lighter than the aluminum generation. Reducing the platform weight increases the available payload weight envelope, since the load capacity of the air feet is the limiting mass factor for both generations. Although the technical limitations for the air feet are listed in the table, it is standard practice to provide at least 3 kg of margin (to ensure better floating), so the payload systems designed for FloatCube use are kept below 6kg. The reduced mass of the rapid prototype FloatCubes also minimizes the effect that the platform inertia and mass has on the system dynamics.

The different fabrication methods have different costs and assembly times. The machining fabrication for the aluminum structures was completed for free in the student machine shop at Cornell, making them apparently less expensive to produce. However, the fabrication and assembly was subject to the variable machine shop schedules and availability, so it took three weeks to complete the parts for both platforms. Machining individual components also required the screws and time to integrate the system once the machining was complete. The cost of materials for the machined aluminum FloatCube structure was approximately $150.

The rapid prototype FloatCubes were made at QuickParts and shipped in under two weeks, and did not require any time in a machine shop. Besides the installation of the pressure system, these FloatCubes did not require any structural assembly. However, the rapid prototyped FloatCubes were much more expensive than the aluminum generation (due in part to the need for rapid construction and shipping), costing $725 each for the structural fabrication alone with an additional $50 for shipping.

Functional differences in the two generations can be observed, but they only minimally affect the system performance. For example, the rapid prototyped platforms are less rigid than the aluminum ones and are therefore subject to more bowing, which may lead to poor contact with the operating surface and the air bearings. Also, the specific plastic in the rapid prototyped modules does not have high shear strengths, so the structure cannot support its own weight when lifted by the pillars, which can shear off if handled in this way. The aluminum generation does not have this problem. Another consideration is that the rapid prototyped systems cannot be easily modified – once the components are mounted to the material and the dimensions are set, it is difficult to adjust. Thus, the component-level machining approach may be better if the specifications for the system may change or need many modifications in the future. Ultimately these trade-offs among weight, cost, integration time, and other factors should be evaluated to meet the needs of the specific program.

Payload Mounting

To enable rapid integration of the payload with the FloatCube platforms, the interface between the payload and the structure is designed to be rigid for testing but easy to disengage, so the design does not rely on standard screws or brackets. The two generations of FloatCubes accomplish this in slightly different ways. In the first generation (aluminum) FloatCubes, the payload base plate attaches to the FloatCube structure with quick release locks. The payload plate has holes on each corner to line up with the female quick-release receptacles embedded in the pillars of the FloatCube structure. Small spring-loaded connectors can be installed through the holes on the payload plate and locked in place to completely secure the two structures. The second generation (rapid prototype) FloatCubes, on the other hand, were designed with upraised pegs on the top of each pillar, and so the payload plate can be set onto the pillars without any additional components. This design allows for more rapid separation of the two segments, but does not secure the payload during transport to and from the operating surface. Figure 6.9 shows these two attachment methods

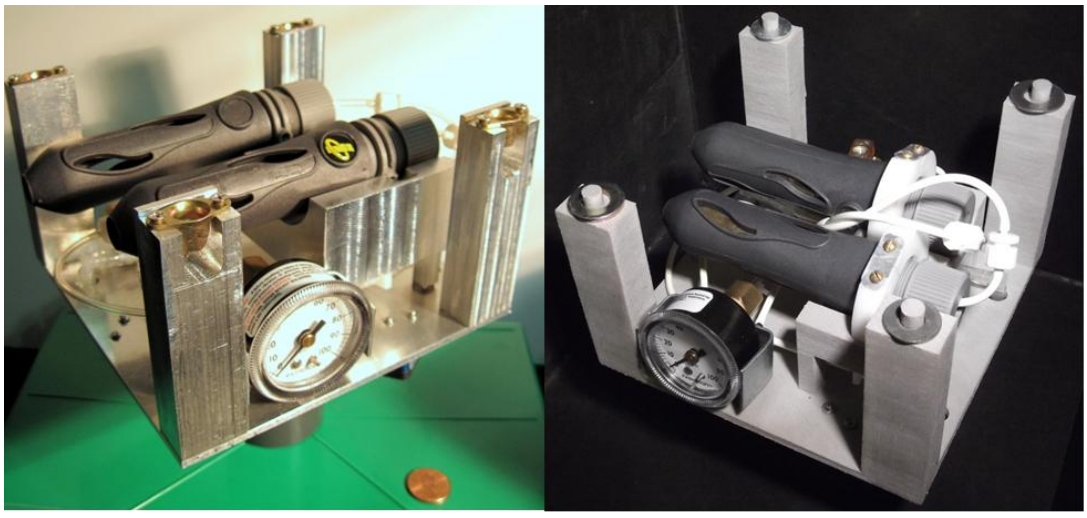

Figure 6.9. The Aluminum (left) and Rapid-Prototyped Plastic (right) FloatCube platforms.

realized on existing platforms, with the quick release connection on the left platform and the pegs on the right platform.

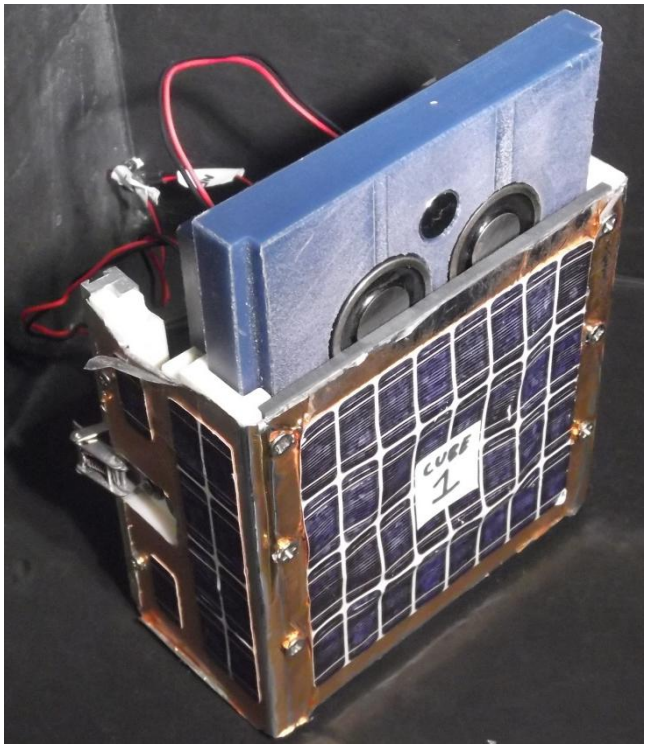

Figure 6.10. The shell and card structure used for component testing.

The FloatCubes are designed to use several mounting techniques for the payload segment to test everything from component-level equipment up to fully-realized hardware. For at-scale integrated CubeSats, the system payload plate can be mounted with a set of aluminum constraints around the footprint of the satellite.

The FloatCube platform is designed to facilitate testing by accepting completed hardware and providing a premade structure to adapt to less advanced designs. The card/shell design (discussed in detail in Section 6.3.1 and shown in Figure 6.10) provides a structural interface that can be rapidly integrated with electronics.

6.2.4. Testbed Operation and Performance

Testbed Operating Procedures

Inevitable variations in the testing environment lead to slightly different results for the same tests. In an effort to minimize the effect of these variations, a standard set of

operating procedures is used when operating the FloatCubes. Three setup routines are performed before initiating a FloatCube experiment. The first routine is the initialization of the vision system. The cameras must be checked for proper operation using a testing script written for that purpose. Then, the data collection software is opened and the calibration sequence is started. This procedure uses a calibration checkerboard of known dimensions that is placed in the field of view of each camera at different points. The system identifies the checkerboard pattern and uses the data it gathers from both cameras to correct misalignments and to determine the overlap between the frames of the cameras. Once the calibration procedure is complete and the FloatCubes are ready for testing, tracking targets are affixed to the top corners of the testing platforms. The experimenter then identifies the targets on the video feed and the system begins to track and record their position.

The second start-up routine prepares the FloatCube platforms for testing. The first step is to ensure that the testing surface interface is clear of any debris that could interfere with the air bearings by cleaning the entire surface with scientific cleaning wipes and rubbing alcohol. The FloatCubes are then loaded with CO_2 cartridges. After ensuring the valve is closed, the two cartridges are punctured simultaneously. The valve is then opened and the system pressure is checked using the onboard gauge. Small variations in pressure are to be expected as the cartridges discharge, so the regulators should be set to approximately 70 psi (0.482 mPa) to keep the supply pressure within the air bearings' optimal operating range despite fluctuations. With the gas flowing, the bottom surfaces of the air feet are cleaned with rubbing alcohol. Care should be taken to avoid scratching or otherwise disfiguring the delicate gas-porous

membrane on the bottom surface of the air bearing. The valve is then turned off and the platform returned to its stand for payload integration.

The last phase of the setup is the payload integration phase. Once the CO_2 cartridges are punctured, the payload plate and its associated hardware can be mounted to the top of the FloatCube structure. Then, with the gas flowing, the integrated vehicle can be placed on the operating surface. It is important that the FloatCubes be allowed to freely self-align to the testing surface during this process. Sufficient space must be left for the air tubing to move freely as the air bearings align themselves to the testing surface. Floating performance is best when each of the three air feet are evenly loaded and aligned with the testing surface. The valve should then be turned off to ensure the vehicle is stationary when the vision system tracking points are being trained into the system. In order to avoid scratching the glass and the air feet, the platforms should not be moved when the gas is not flowing. Once the vision system points are set, the valves can be turned on and the experiment can commence.

During the test, the experimenter must keep in mind many factors: the vehicles' proximity to the edge of the testing surface, the pressure of the FloatCube platform, the status of the vision system's tracking points, and the known topography of the glass. Once the experiment is complete, the payload is removed from the FloatCube platforms and stowed safely, the platforms themselves are placed back on their tabletop stands (which prevent the air feet from coming into contact with any surface besides the glass), and the vision system software is turned off after the data is saved.

Friction and Torque Performance

In order to evaluate the FloatCube effectiveness at providing a low-friction environment, the results from two different FloatCube platform tests were analyzed to determine typical friction coefficient and torque values that are experienced by the platforms during operation. In order to give an estimate of static friction on the table, a FloatCube platform was placed at rest on the testing surface with the gas flowing. A string was attached to the platform and threaded through a pulley system at the edge of the operating surface. Then, increasing amounts of mass were added to the hanging end of the string until the platform began to move. The mass on the end of the string was then recorded. After averaging seven of these tests, the coefficient of static friction f_s was found to be 1.0 X 10^{-3}, with a standard deviation of 2.4 X 10^{-4}.

The kinetic friction and friction torque estimates were determined from open-loop FloatCube platform tests that carried a CubeSat model payload with an onboard Inertial Measurement Unit (IMU) and momentum wheel. In the test, the vehicle's payload was commanded to spin the wheel to a given constant speed. The change in momentum induces a torque in the system, causing the vehicle to rotate on the glass. However, since friction is acting on the system, once the commanded speed is achieved, the vehicle loses momentum via the constantly applied friction torque. Once the system came to rest, the wheel was commanded to turn off, which induces another torque on the system in the opposite direction.

Data from both the FloatCube vision system and the IMU captured the motion of the system, and the angular rate data collected during the spin-down (friction torque only) portion of the maneuvers were used to determine the friction torque and

coefficient of kinetic friction. The friction torque $\boldsymbol{\tau_{fric}}$ was determined by fitting a linear model to the slope of the angular rate (also known as the angular acceleration $\boldsymbol{\dot{\omega}}$**)** during the spin-down portion of the maneuver. Using the CAD-derived platform inertia $\boldsymbol{I}$, Equation (6.2) provided the value for the friction torque.

$$\tau_{fric} = I_{assembly} \cdot \dot{\omega} \tag{6.2}$$

An example of the angular rate data from a FloatCube spin-down maneuver as described is shown in Figure 6.11. The fitted linear models for the friction torque for both the wheel-on spin-down and wheel-off spin-down portions of the maneuver is shown overlaid on the same figure. Using data from eight similar maneuvers, each

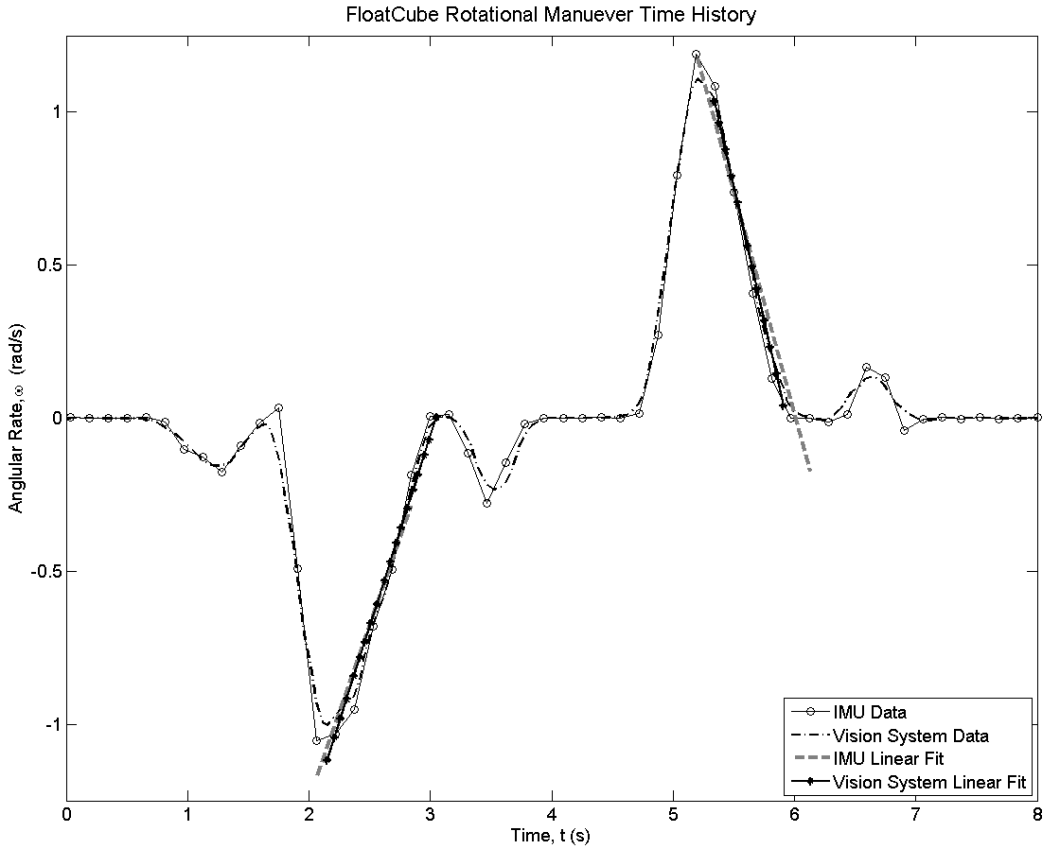

Figure 6.11. A linear model of friction fitted to the IMU and vision system data on an open-loop torque maneuver.

with two regions where friction was the only torque acting on the system, the fitted friction torque was found to be 0.0188 N·m. The mean R^2 value for these polynomials was 0.917 with a standard deviation of 0.103 over all of the fitted data.

With this friction torque value, it is possible to estimate the coefficient of kinetic friction f_k given the vehicle's mass, $m_{assembly}$, gravitational acceleration g, and horizontal distance from the projection of the platform's center of mass on the plane of the air bearings to the air bearing, d, as shown in Equation (6.3).

$$f_k = \frac{\tau_{fric}}{m_{assembly} \cdot g \cdot d} \tag{6.3}$$

Estimates for the friction torque and kinetic friction are shown in Table 6.5.

Table 6.5. Estimated Fixed Costs of Testbed Components.

Assembly Parameter	Symbol	Value
Inertia (about its center of mass)	$\boldsymbol{I_{assembly}}$	0.0156 kg•m2
Mass	$\boldsymbol{m_{assembly}}$	4.70748 kg
Distance (between air foot and center of mass projected on to plane of air feet)	$\boldsymbol{d}$	63.784 mm
Friction torque	$\boldsymbol{\tau_{fric}}$	Mean: 0.0188 N•m Standard Deviation: 0.0127 N•m
Coefficient of static friction	$\boldsymbol{f_s}$	Mean: 0.0010 Standard Deviation: 0.00024
Coefficient of kinetic friction	$\boldsymbol{f_k}$	Mean: 0.0041 Standard Deviation: 0.0028

6.2.5. Conclusions about the FloatCube Testbed

The FloatCube planar air-bearing testbed provides a useful low-cost multi-body reduced-friction testing environment for CubeSat-scale technology development. The testbed offers a number of advantages to technology developers across the spectrum of technology maturity levels. Given the architecture of the overall system, the details of the floating platform design, and the operational considerations of the testbed, it is

possible for the interested developer to use this design as the basis for similarly affordable multi-body testing platforms for CubeSats. The modular card/shell payload architecture makes the FloatCubes flexible enough to accommodate experiments using hardware at both the breadboard and systems level, while the vision system enables data collection for passive vehicles or validation for vehicles with internal sensing. The structural design of physically independent vehicles enables the testing of multi-module formations and multi-step interaction routines, in keeping with the increasingly complex maneuvers being developed for spacecraft at this scale. Ultimately testbeds such as the FloatCubes will play an increasingly important role in the validation and testing of kilogram-scale spacecraft, just as CubeSats are taking on increasingly ambition missions.

6.3. CubeSat-Scale Satellite Prototypes

6.3.1. The Card-Shell Architecture

To fully exploit the capabilities of the FloatCube testbed, it is necessary to develop a corresponding testbed payload architecture capable of accommodating a variety of different laboratory-based experiments. The card-shell design architecture was developed to fill this need by enabling the rapid integration of electronics or other components into a CubeSat-based structural sheath. By standardizing the interfaces between subsystems and promoting a modular, self-contained subsystem design style, the card-shell architecture has quickly become the basis for the payloads in the majority of the FPI laboratory testing – and in the 2010 microgravity flight hardware.

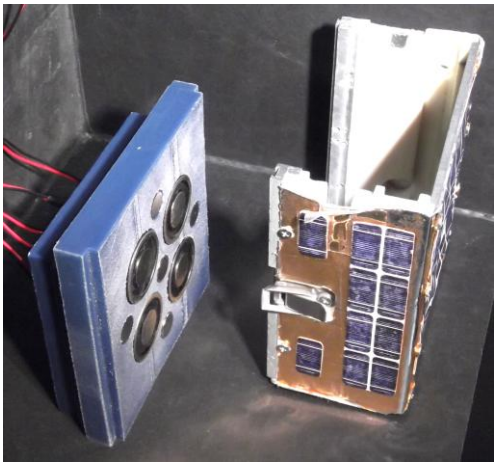

Figure 6.13. An example of a card (a), left, and empty shell (b), right.

In this architecture, cards are blocks of material that contain an integrated subsystem and are generally completely independent of the outer structure of the payload (as seen in Figure 6.13(a)). Shells (shown in Figure 6.13(b)) are structural containers that interface with the FloatCube testbed and have walls designed to hold a card in place. The cards have extruded tabs of a standard size and shape on either side that fit vertically into the slots in the shell's walls, as shown in Figure 6.12. Because a shell can accommodate any card, a relatively small number of shells were fabricated and then reused for different experiments. New cards, however, are generally fabricated for each project in order to accommodate their different experimental goals of components.

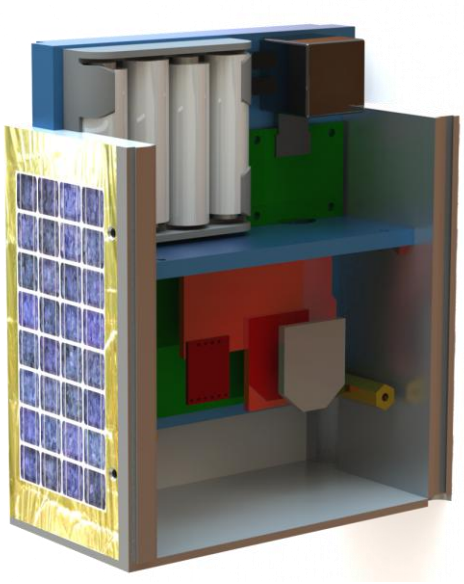

Figure 6.12. A card (blue) with an integrated sensing and communications subsystem sliding into an aluminum shell.

Standard shells and cards are constructed out of a combination of aluminum and plastic. For shells, the base plates and side walls are constructed out of aluminum and the front face is made out of plastic to reduce mass. Most cards are made out of ultra-high molecular weight polyethylene and may be mounted with aluminum or plastic structural elements to support additional

components. An integrated card-shell assembly such as the one shown in Figure 6.15 is known as a half-cube. Half-cubes can be used individually to test component-level equipment such as an IMU sensing system. However, two half-cubes can also be combined via an aluminum dovetail at the edges of all shells to form a complete "cube," or FluxCraft, as shown in Figure 6.14(a). These FluxCraft – or two integrated half-cubes linked together via a dovetail and a latch – form the basis of the CubeSat mockups and spacecraft prototypes built in the

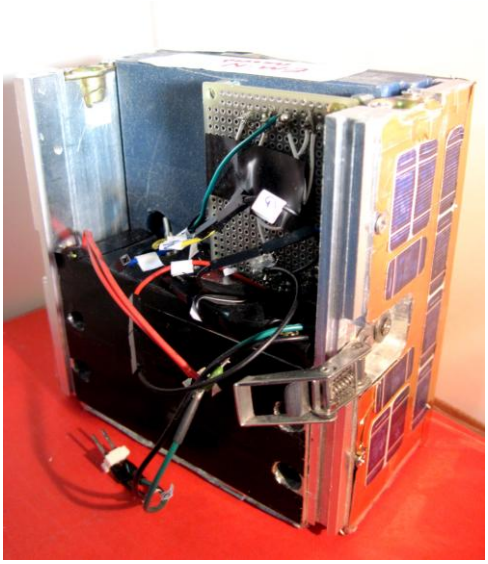

Figure 6.15. A half-cube assembly where the plastic blue card containing the system's electronics is integrated with the outer structural shell.

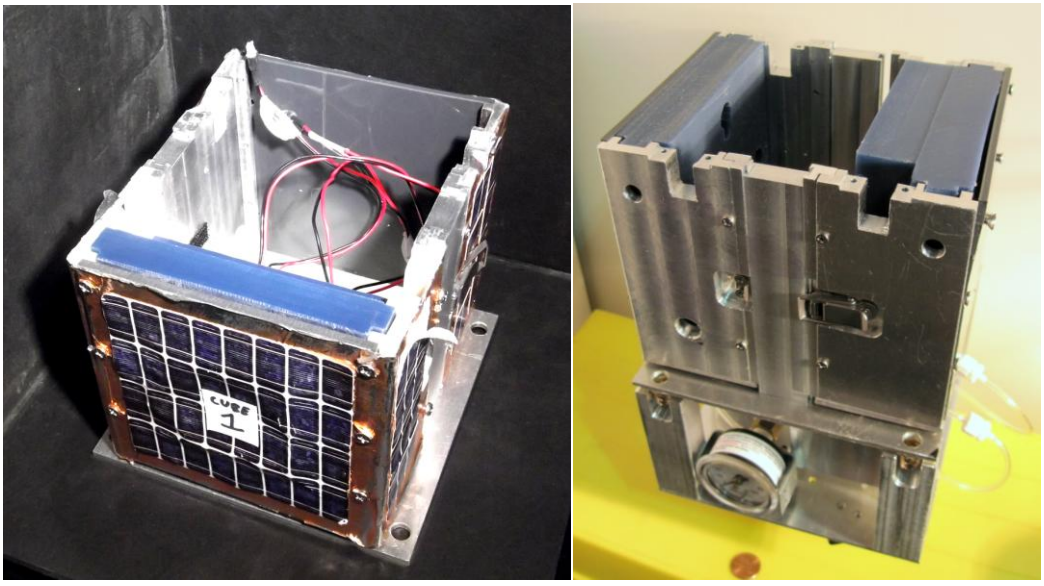

(a) (b)

Figure 6.14. (a) A cube assembly made up of two half-cubes and (b) a cube assembly mounted on top of a FloatCube platform.

lab. A cube built for a specific project or mission may incorporate any permutation of shell and card designs to accomplish the goals of the experiment. The integrated cube can also be mounted as the payload atop a FloatCube platform (such as shown in Figure 6.14(b)) to enable dynamics and controls testing of the hardware. Alternatively, a lid can be locked over the completed cube to enable testing in a microgravity environment, as shown in Figure 6.16. An assembled FluxCraft is 12.5 cm on a side and have masses ranging from 1 – 5 kg, depending on its internal components. When mounted on a FloatCube, the two half-cubes are attached using a dovetail piece that expands one dimension of the structure to 15 cm.

6.3.2. Shell Designs for FPI Testing

Although most shells developed in the lab follow the same design – where the card

Figure 6.16. Two CubeSat mockups based on the card-shell architecture in a microgravity test.

and its components are completely enclosed by the shell's structure – a number of FPI experiments required the inclusion of a rotational FPI design where cylindrical magnets are mounted on the corners of the satellite prototype structure to serve as a non-contacting hinge when interacting with a superconductor. Thus, a new shell was designed to enable permanent magnets to protrude through the corner walls of the structure. Figure 6.17(a) shows this shell with one magnet in place (in the center of the photograph) as part of an integrated cube. Essentially, the shell has a top and a bottom component that slide together around the magnets to hold them in place, as shown in Figure 6.17(b). However, this design prevents the shell from accommodating standard cards, so in the first iteration of the design a smaller modified card slot was included to enable the same modularity and reusability inherent in the standard card-shell architecture.

The first version of this shell design was created out of plastic with a rapid-

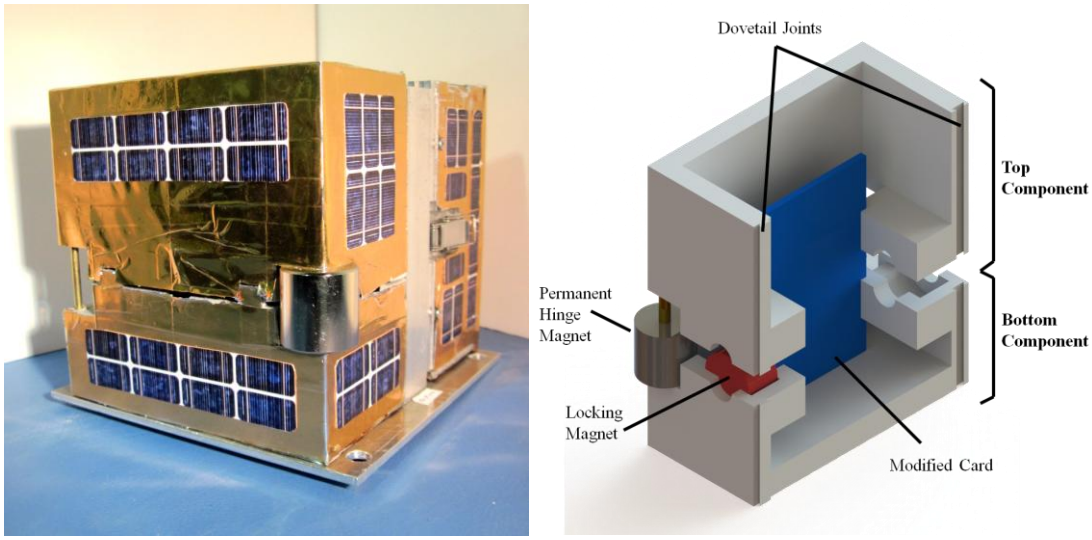

(a) (b)

Figure 6.17. (a) A photograph of the shell uniquely designed to position a magnet at each corner for rotational FPIs. (b) A labeled CAD rendering of the shell.

prototype printer. Although this technique avoided a lengthy assembly and integration period, as with the FloatCube platforms, the resulting shell lacks the flexibility of a system that can be disassembled and modified. Thus, a second iteration on this shell design was created out of aluminum and plastic components. Both generations have been used in various FPI experiments.

6.3.3. Card Designs for FPI Testing

Three general classes of cards were developed to facilitate the testing of FPIs in the card-shell architecture: superconductor cards, magnet cards, and sensing cards. Variations may exist from project to project, but these broad design concepts were applied to almost every card developed for the FPI experimental work.

Superconductor/YBCO Cards

The superconductor cards have two functions: to hold one or more YBCO disks securely in place so that the forces and torque from the FPI are translated to the rest of the structure, and to facilitate the cooling and insulation of the disk to cryogenic temperatures. All of these cards, shown in Figure 6.18, are made out of plastic material to improve insulation, reduce the chance of accidental cryogenic burns, and to reduce the thermal contraction of the material around the superconductor disk.

In the laboratory environment, the cooling of the YBCO component of the FPI is almost always accomplished using a bath of liquid nitrogen. Thus, the most commonly used YBCO card (shown in Figure 6.18(a)) is a small plastic basin equipped with tabs for sliding into the shell walls. A separate removable component with tabs at the top holds the YBCO disk such than it can be slid into the shell and end up vertically

centered in the plastic basin, pressed against the outer wall to minimize its distance from other interacting FPI components. The half-cube containing the YBCO card can then be positioned near a magnetic field source for field cooling. A small hole in the top of the removable YBCO structure provides an opening in which liquid nitrogen can be added to the basin.

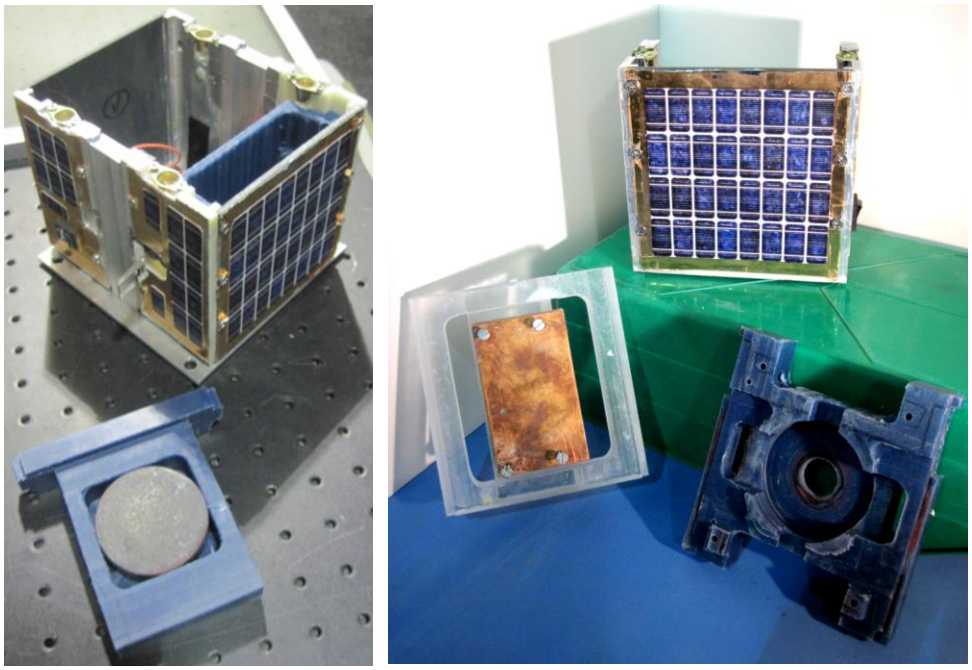

(a) (b)

Figure 6.18. (a) The YBCO card most commonly used for laboratory testing. (b) Superconductor card designs for facilitating an interface between the YBCO disk and a cryocooler.

One phase of the FPI design work has focused entirely on designing a thermal system capable of cooling the superconductor below its critical temperature using a cryocooler. To this end, two different YBCO cards (shown in Figure 6.18(b)) were designed to interface with the cold head of the cryocooler while minimizing the heat paths to the system. One design is a plastic card that holds the YBCO disk in the center and has unnecessary material removed. The gaps in the card are then filled with

an aerogel blanket for insulation. The cryocooler interacts with the YBCO via a hole cut in the shell's wall. Another design clamps the YBCO disk in a copper sheath coated with thermal-contact grease. The cryocooler's coldhead interacts with this copper sheath through a hold in the shell's wall. The YBCO-copper assembly is then mounted to the card's back strut using plastic screws. Aerogel insulation fills any remaining gaps in the card.

Magnet Cards

Magnet cards are the FPI's complement to the superconductor cards. The purpose of these cards is to securely hold an array of permanent and electromagnets in a desired configuration, and to provide the means by which any electromagnets in the

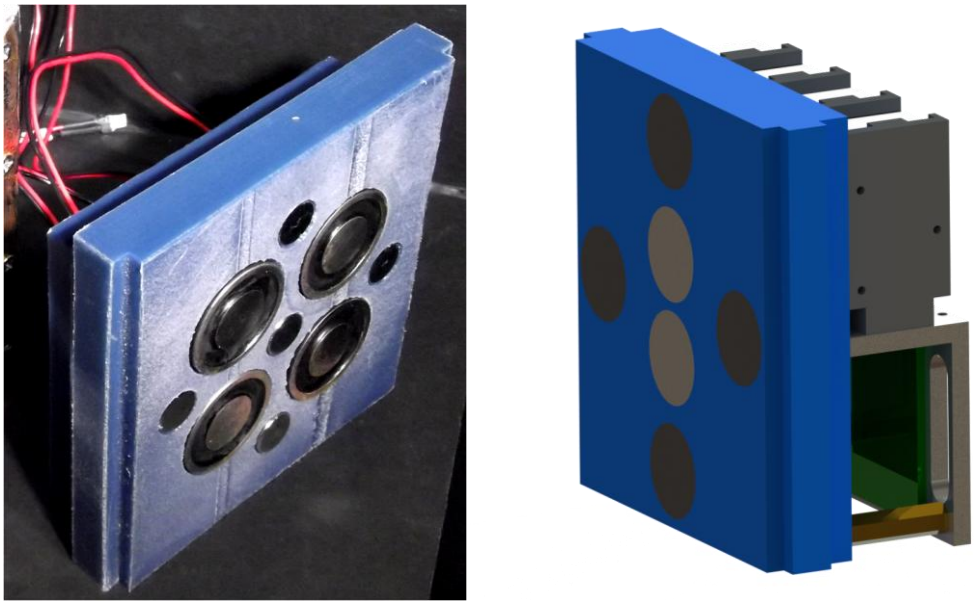

(a) (b)

Figure 6.19. (a) A magnet card design with large electromagnets and small permanent magnets and (b) a different magnet card design with two permanent magnets in the center ringed by electromagnets.

array are powered and controlled. The magnets are generally held in diameter-appropriate cavities with a small through-hole leading to the back of the card to allow electromagnet wires to reach the microcontroller or to facilitate the magnet's removal. Many of the magnet card designs have also incorporated mountings for battery packs and microcontrollers, but in more complicated cube arrangements, these components are shared between the half-cubes.

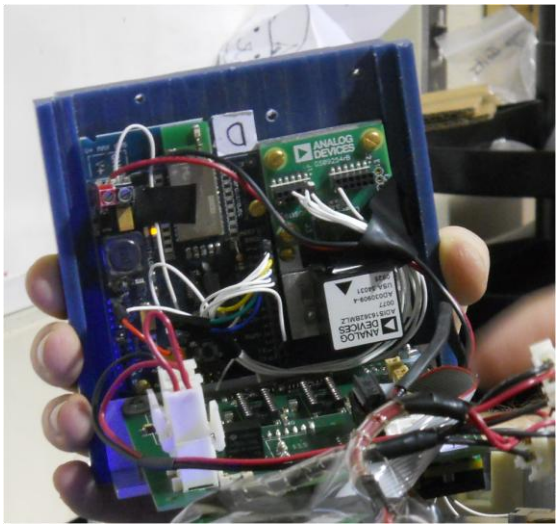

Figure 6.20. A sensing card with an integrated microcontroller, IMU, power management board, and reaction wheel control electronics.

Sensing Cards

Sensing cards such as the one in Figure 6.20 host the on-board communications, sensing, power management, and (where applicable) actuation subsystems. Each sensing card has a BlueTooth-enabled Arduino microcontroller to receive commands from a controlling PC, but otherwise their design varies significantly by project.

The communication subsystem is typically accomplished via the BlueTooth antenna, but an Xbee architecture was also implemented (via Arduino shield) in one project for inter-cube data sharing. Most of these cards have an on-board Analog Devices IMU, but some instantiations also have two SICK UM18 ultra-sonic range sensors. For simpler designs, the microcontroller directly handles the sensing data, but custom-made PCBs have been developed to manage the more sophisticated systems.

In some cards the sensing data is saved to a flash drive onboard the card, and in others it is transmitted to the controlling PC (or another cube) to be recorded or passed to a controller. The sensing cards also typically house the voltage regulators in the system to manage the power from the 9-V or AA battery packs. One version of the sensing card also includes LEDs to indicate a powered-on status. Although it is not common, one of the implemented FPI projects utilized an on-board reaction wheel system, which was also integrated and managed by the sensing card.

6.3.4. Cube Designs for FPI Testing

Occasionally it is more efficient to significantly modify the standard card-shell architecture. For example, it is difficult for the card-shell architecture to accommodate the use of multiple superconductors, particularly if they must be mounted on perpendicular faces. Thus, projects with these requirements instead use a block of foam cut to have the same outer dimensions as a completed FluxCraft and have an

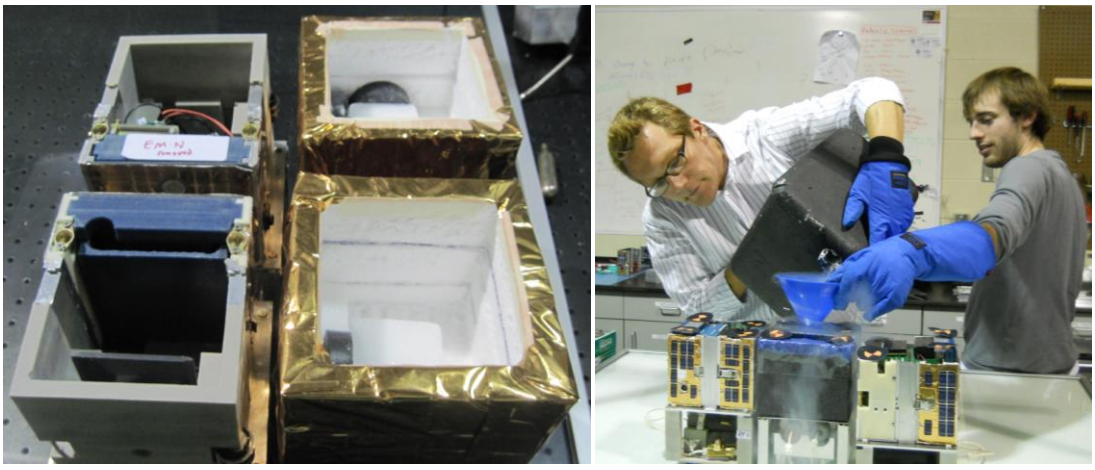

Figure 6.21. (a) Two standard FluxCraft (left) next to foam cubes (right) built to house multiple YBCO disks. (b) Two experimenters fill a foam cube (center) with liquid nitrogen for testing.

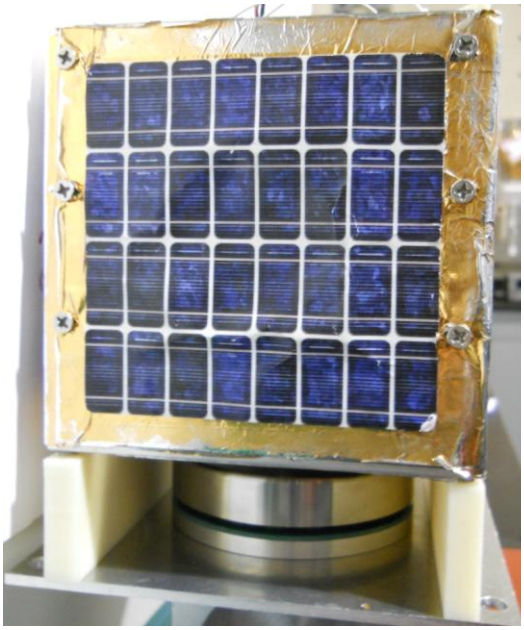

Figure 6.22. A structural extension with a reaction wheel mounted underneath a FluxCraft.

inner structure to hold the YBCO disks in place, as shown in Figure 6.21. The entire insulated cube can then be filled with liquid nitrogen. However, as foam is easily damaged and is often permeable to LN2, these cubes need to be lined with liquid-proof material such as silicone or tarp.

Although the size of the FluxCraft already exceeds that of a 1-U CubeSat, occasionally some of the hardware intended for testing on the FloatCubes does not fit into a shell structure. In these instances, a structural extension can be added between the FluxCraft base plate and the plate supporting the FloatCube payloads, as shown in Figure 6.22.

6.4. FPI Demonstrations and Experiments on the FloatCube Testbed

The FloatCube testbed has been in operation at various stages of development since the summer of 2010. It has hosted a number of different FPI development projects, primarily using FluxCraft-based hardware designs. These experiments have spurred the development of a series of increasingly sophisticated FPI hardware which has enabled testing on a broad set of maneuvers and designs. This work has brought numerous FPI concepts to TRL 3 and 4. Initial laboratory experiments were simple component-level validation tests of basic FPI concepts. The results obtained from these experiments informed the hardware design of the 2010 microgravity project and

thus helped lay the groundwork for some of the most advanced FPI tests to date. These fundamental experiments quickly grew into a comprehensive system-level demonstration of FPI-based multi-body reconfiguration and experiment analyzing FPI performance in a slewing formation of spacecraft. They have also laid the groundwork for studies of inter-cube FPI control analyses. The details of these experiments are detailed in the following subsections.

6.4.1. Component-Level Testing of Basic FPI Concepts

Immediately after the FloatCube testbed became operational, a series of laboratory proof-of-concept validation experiments were performed to illustrate the FPI's efficacy in a variety of two-spacecraft interaction scenarios. These tests also served to

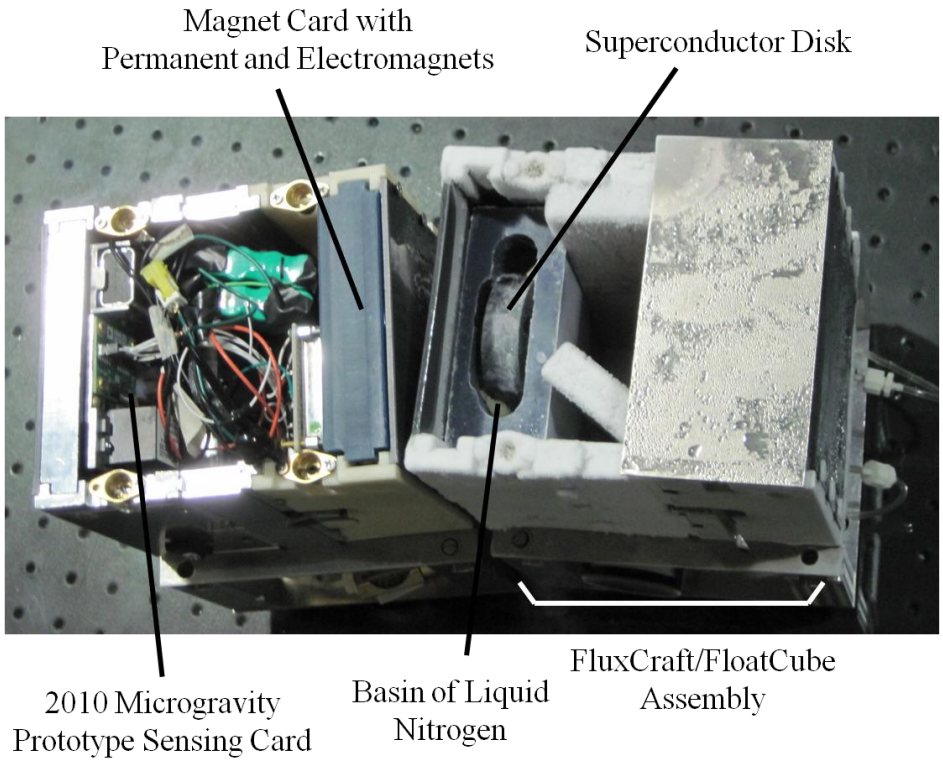

Figure 6.23. The FluxCraft/FloatCube assembly setup for initial component and concept validation efforts.

refine the hardware designs for equipment destined for the 2010 microgravity flights (discussed in Chapter 7). These runs typically used a setup shown in Figure 6.23, with a small liquid-nitrogen-based YBCO card and a magnet card interacting with a separation distance on the order of one centimeter.

The first tests on the FloatCube platform occurred before the camera vision system was implemented and before integrated sensing cubes were fully functioning and collecting on-board data. Thus, many of the first data sets validating basic FPI concepts on the FloatCube testbed are in the form of hand-held camera video. However, these videos show the two interacting modules exhibiting the passive stability seen in simpler flux-pinned systems. They also reveal that the FPI system has strong multi-degree-of-freedom stiffness values. The system was stiff enough to allow an experimenter to manually manipulate one module and have the second remain in a non-contacting formation with the first. This behavior was observed even when moving the magnets directly away from the superconductor's face, which is generally the translational motion that exhibits the weakest stiffness in an FPI. These qualitative behaviors provided the basis for other maneuvers that are fundamental to the utility of flux-pinned interfaces to close-proximity spacecraft.

Rendezvous and Impact Attenuation

As discussed in Chapter 1, FPIs can be used to augment spacecraft rendezvous and docking maneuvers. Initial FloatCube tests using the module setup in Figure 6.23 were able to demonstrate a passive docking maneuver simulating a control system failure in which only permanent magnets are able to interact with the superconductor. As seen in the sequence of screenshots in Figure 6.24, the modules were initially set

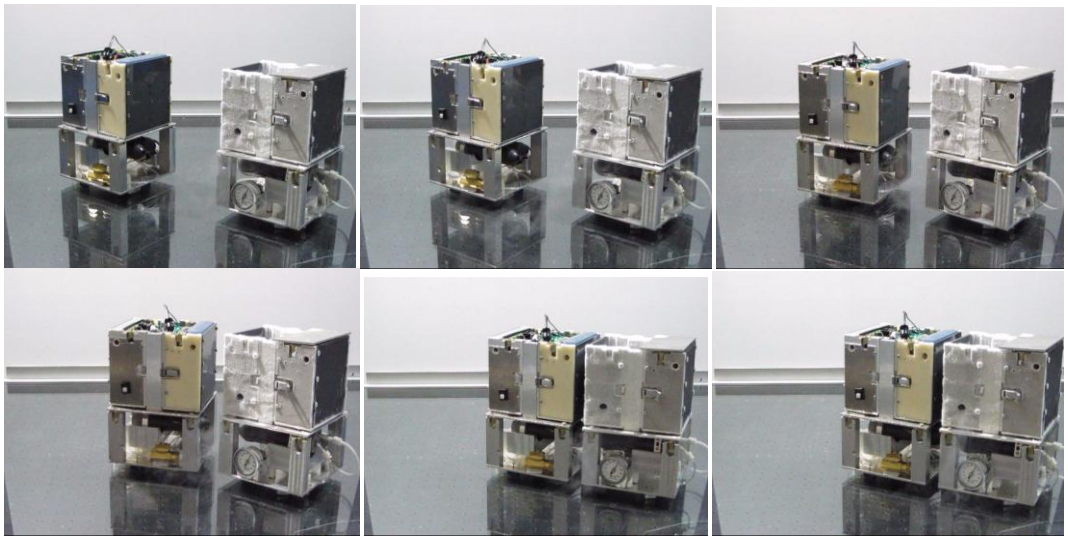

Figure 6.24. Sequential screenshots from a video showing an FPI passively aligning and docking the two FluxCraft from a distance of approximately 10 cm, and the two modules moving as a unit once they are docked.

approximately a body diameter apart and the module bearing the magnets (on the left) was given a small initial velocity in the direction of the superconductor module. Under the influence of the passive FPI dynamics, the magnet module accelerates towards the superconductor module, eventually reaching equilibrium at the one centimeter field-cooled separation distance. The system exhibited impact-attenuation behaviors during this close-proximity portion of the maneuver. Once the relative equilibrium was achieved, the two modules moved as a unit due to residual momentum from the maneuver.

Electromagnetic Actuation

The primary method of actuating an FPI is by changing the magnetic flux interacting with the superconductor. The first demonstration of this concept in a multiple-magnet single-superconductor (MMSS) arrangement was performed on the FloatCube table. In this demonstration, a permanent magnet was field-cooled into the superconductor, but the electromagnets were not. As discussed in Chapter 4, a zero-

field-cooled actuator repels the superconductor. However, with the stiffness of the permanent magnet, the system rotates away from the electromagnet, as shown in Figure 6.25. This behavior was observed in the open-loop response of the FluxCraft, as shown in the two screenshots in Figure 6.26

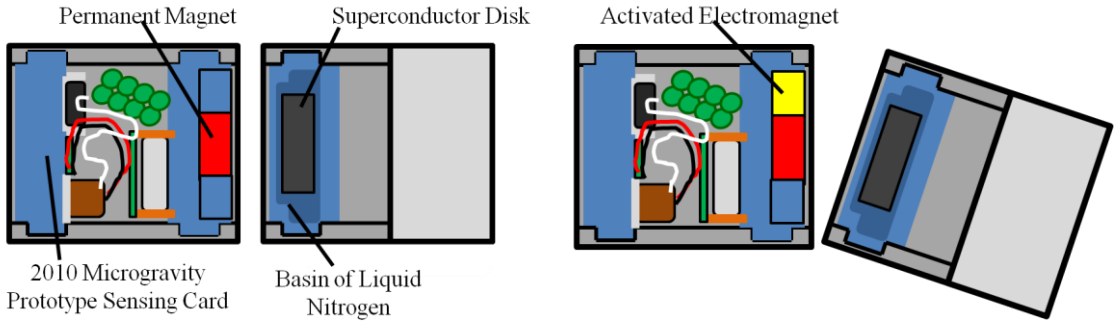

Figure 6.25. When the zero-field-cooled electromagnet is activated, the system rotates away from the electromagnet.

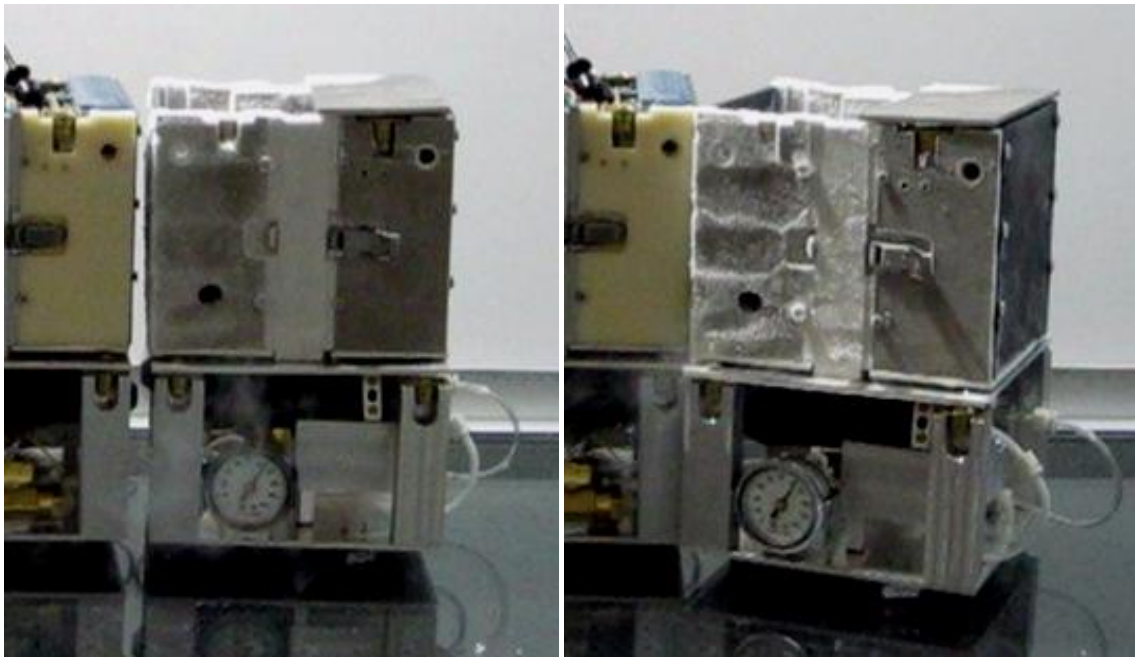

Figure 6.26. Electromagnetic actuation with the magnet module (left module in each picture) held fixed as the superconductor module rotates due to the activation of a zero-field-cooled electromagnet.

Non-Contacting Multi-Body Interactions

In order to be used in close-proximity formation flying, flux-pinned interfaces must be able to stiffly connect multiple spacecraft while maintaining passive stability and other desirable dynamical properties. Three FluxCraft were connected via FPIs, as shown in Figure 6.27, to observe this behavior. The outer two modules contain magnets on the walls facing inward in the formation. The central module is a passive foam cube with superconductors on both walls facing the magnet modules. At the time this test was completed, the camera vision system had been added to the testbed, so centroid position and module orientation information (relative to the testbed) is available from a maneuver, as shown in Figure 6.28. In the selected data, the three modules are performing a rotational maneuver about the center of the formation.

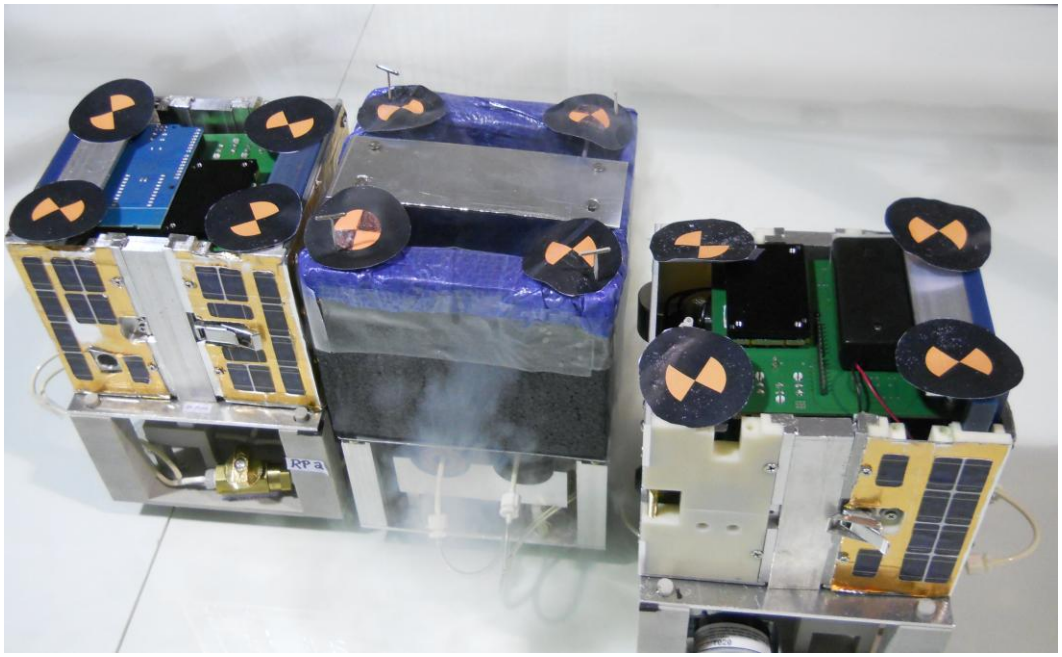

Figure 6.27. A three-module flux-pinned formation of FluxCraft that exhibits non-contacting passively stable stiffness and damping at each interface. From left to right are Cube 3, Cube 2, and Cube 1.

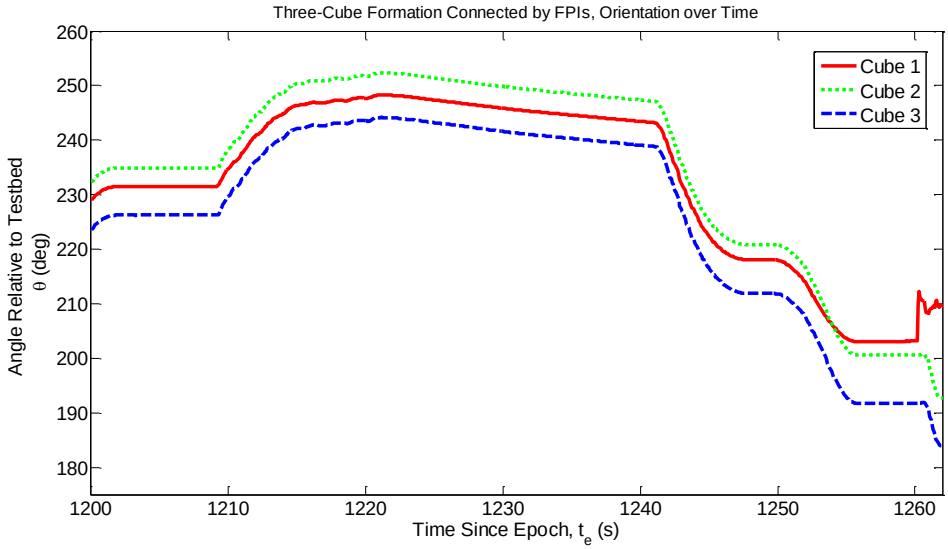

Figure 6.28. Data collected from the camera vision system of a three-module formation of FluxCraft connected by FPIs perform a rotational maneuver around the center of the formation.

Clearly the modules retain a consistent relative angle throughout the maneuver, suggesting that the stiffness from the FPIs at each link is sufficient to maintain a constant relative orientation in the formation.

Multi-Body Reconfiguration Using FPIs

Flux-pinned interfaces are also enabling technologies for novel spacecraft reconfiguration techniques, and so multi-body reconfiguration concepts were demonstrated on the FloatCube testbed. This particular demonstration was unique because it was featured on National Geographic's television series "The Known Universe." The maneuver performed on the FloatCube table consisted of four modules moving from a roughly linear configuration to a roughly box-like configuration, as shown in Figure 6.29. Three FPIs were engaged, with one standard linear FPI between the two inner modules, and two FPIs that served as hinge joints about which the outer modules rotated. This demonstration is classified as a component-level result because

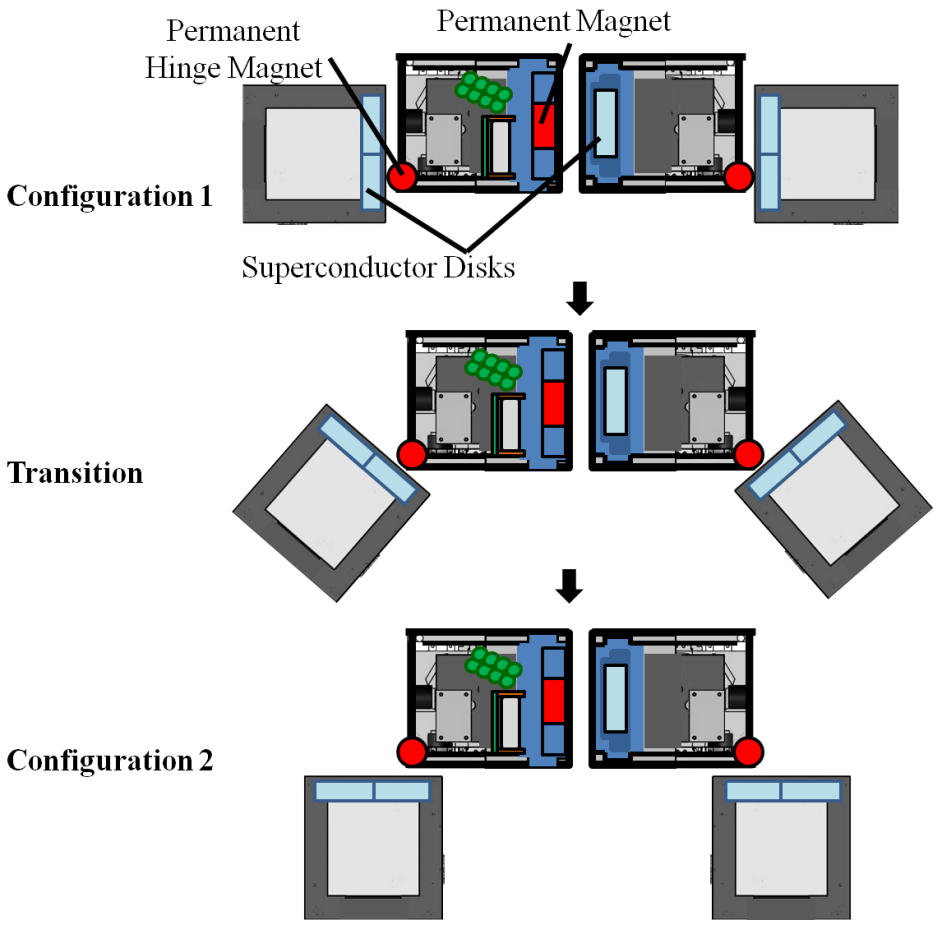

Figure 6.29. The multi-body reconfiguration maneuver performed on the FloatCube table for National Geographic.

it did not contain the necessary systems onboard the modules to trigger the reconfiguration maneuver independently. It was, however the first four-body formation using FPIs ever to be tested, and represented an increase in the equipment sophistication from previous reconfiguration experiments.[94]

6.4.2. FPI Performance in a Slewing Spacecraft Formation

The FloatCube component-level tests are instrumental in advancing FPI concepts to TRL 3, where they have been demonstrated in a laboratory prototype. Once technologies have reached this level, the system designs and their hardware

implementations are refined to the point where they contain multiple integrated subsystems and can provide access to more sophisticated experiments. The Controlled Operations for Reconfigurable Technology eXperiments (CORTX) project represents FPI technology's leap to higher-fidelity, system-level demonstrations.[136]

CORTX Project Objectives and Experiment Design

The goal of the CORTX project is to examine the performance of a reconfigurable two-cube formation of spacecraft connected by an FPI while performing a rest-to-rest 30-degree slew. Although the project does not investigate the dynamics or control of the reconfiguration maneuver itself, the concept is shown in Figure 6.30.

The FPI design for this experiment is based on previously successful FPI reconfiguration experiments,[94] and so it uses a strong cylindrical permanent magnet with its axis of symmetry perpendicular to the operating surface to provide the stiffness during the reconfiguration maneuver, and two other locking magnets (also cylinders, but with their axis of symmetries parallel to the operating surface) to keep the system in the desired final state. For the duration of the experiments, the system is

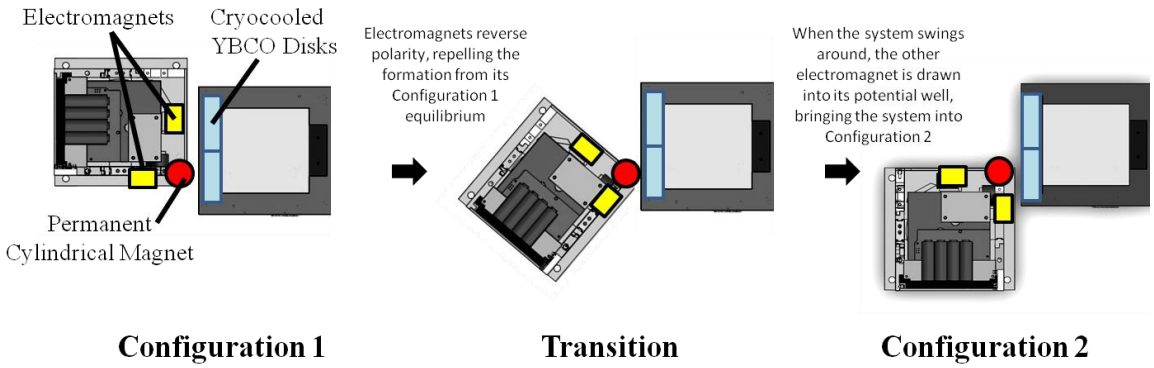

Figure 6.30. An overhead view of a reconfiguration maneuver using the FPI design used in the CORTX experiment.

locked into either Configuration #1 or Configuration #2. Configuration #1 is a roughly linear arrangement designed to simulate a launch configuration. Configuration #2 is an "L-like" shape that a CubeSat formation may use for sensing or maneuver optimization purposes.

For both configurations a spring-like stiffness is provided by the permanent hinge magnet and by the locking magnet closest to the superconductor. In the experiments detailed in this paper, the locking electromagnets were replaced with permanent magnets to produce a higher stiffness without variations in the battery-supplied current. Because the reconfiguration maneuver was not a focus of the experiment, the use of permanent magnets does not affect the system's behavior. The hinge magnet for this experiment is an N52 Neodymium cylinder that is one inch high and one inch in diameter. Three inch-diameter and quarter-inch-thick N52 Neodymium toroid magnets were stacked together to form the locking magnets. These magnets interact with two YBCO disks 5.8 cm in diameter and 1.8 cm thick that are cooled in a bath of liquid nitrogen (LN2).

For each experimental run, the spacecraft formation (consisting of the two

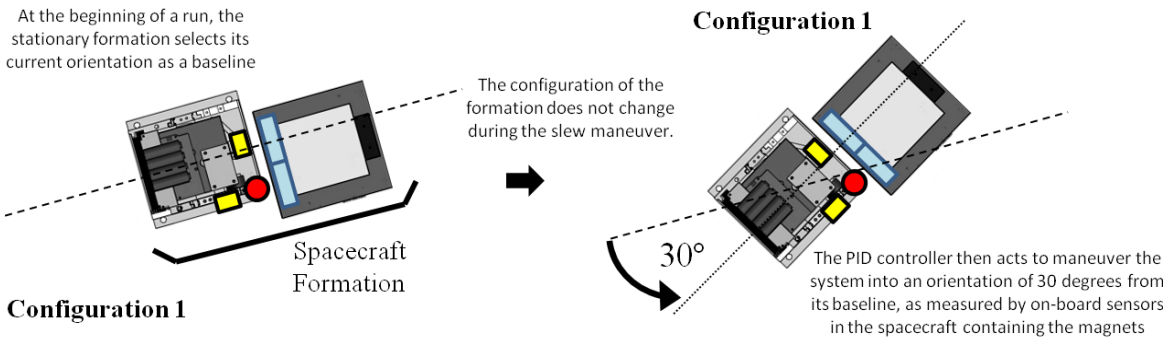

Figure 6.31. An overhead view of the slewing maneuver performed by the spacecraft formation for each experimental run.

CubeSat mockups connected by their FPI in a fixed configuration) sets its initial orientation as a baseline, and then uses a PID controller to perform a 30-degree slew, as seen in Figure 6.31. The formation retains its initial configuration because of the stiffness in the FPI connecting the spacecraft. Thus, the FPI in this experiment is a passive non-contacting interface between the modules in the formation and serves a role as a functioning subsystem in a system-level demonstration.

The FluxCraft module designs for this project are shown in Figure 6.32. The formation consists of an active module, which contains a number of onboard sensors and actuators as well as the magnet card for the system, and a passive module, which is a foam cube containing superconductors in a liquid nitrogen bath. The pool of liquid nitrogen in the design introduces variations in the inertial properties as the nitrogen boils off throughout the duration of the experiment. The free-surface motion also has the potential to induce additional dynamics into the system. The full assembly of the

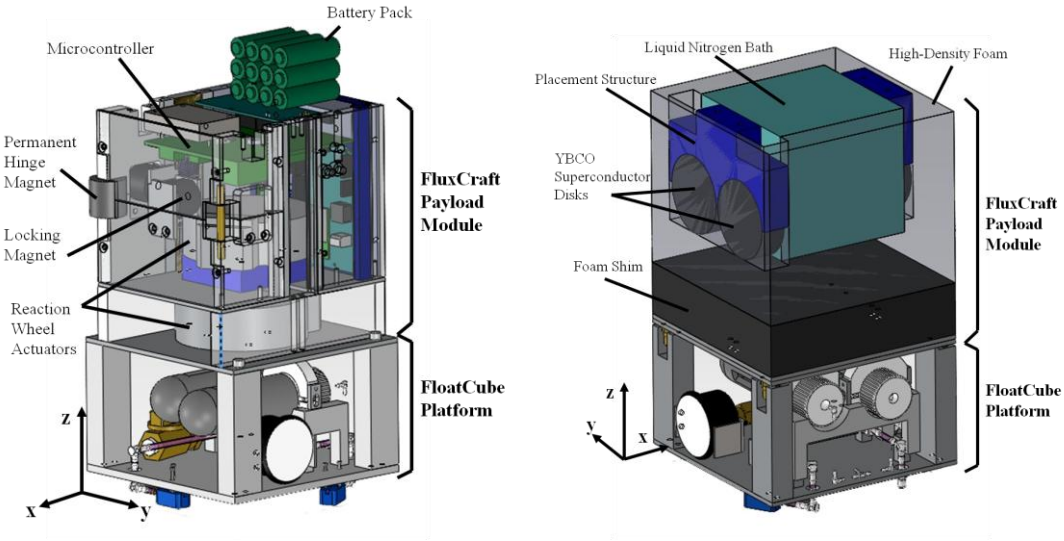

(a) (b)

Figure 6.32. The complete FloatCube-FluxCraft assemblies that are used in the experiment. (a) the active FluxCraft atop a FloatCube platform and (b) the passive FluxCraft atop a FloatCube platform.

active FluxCraft and its FloatCube has a mass of 4.856 kg and the passive assembly has a total mass of 3.035 kg.

Attitude Sensing and Control Subsystem

In order to collect information on the position and orientation of the modules on the FloatCube testbed, the overhead camera-based sensing system recorded position and orientation data in up to 30 frames per second. For the configuration used in this experiment, the static resolution of position accuracy is 3.06 mm and angular accuracy is 1.2 degrees, although rapid motions (large displacements on the order of the frame rate of the camera) can cause reduced accuracy or a loss of data. The slewing maneuver in this experiment (shown in Figure 6.31) was designed to avoid these limitations. The data from the camera system are not integrated into the feedback control loop for the experiments described in this work; they are used only to assess the performance of the system in post-processing data analysis

The active FloatCube, however, is equipped with an Analog Devices ADIS16362 Inertial Measurement Unit (IMU) that can collect information in six degrees of freedom, with a typical angular random walk of 2 °/√hr and 0.5 °/s of angular rate precision. Data is collected at approximately 820 Hz, but this data is down-sampled to 6.4 Hz when transmitted to the controller on the PC in order to minimize the time delays associated with packaging and transmitting the data across the wireless connection. Nevertheless, the measured one-way time delay in the system is 380 ms, almost all of which is attributable to BlueTooth protocols in handling incoming and outgoing data. In an effort to minimize the effect of these lengthy protocols, the FluxCraft microcontroller bundles together five IMU data samples into a single

packet, which is then transmitted to the PC. The PC hosts the PID controller to facilitate the experimentation with different gain selection strategies, and at this point the packet is opened and processed.

The first processing step that the PC takes is to subtract out the IMU bias values, which are found in a calibration step completed prior to each experiment. Then, this signal is passed to the controller. This discrete-time implementation of a PID calculates the command torque by multiplying the proportional gain by the error in the angular position of the array, the integral gain by the integral of the angular position error, and the derivative gain by the error in the angular velocity (i.e., the derivative of the error in angular position). Since the IMU directly reads angular rate, the weighted average of the five values in the packet is taken as the "current" value. It is worth noting that this approach effectively applies a low-pass filter on the incoming IMU data.

The controller software then calculates the estimated change in the angle corresponding to the angular rates recorded in the packet. At each of the five sample time steps, Boole's rule is used to integrate the five previous angular rate values (using values from previous packs as necessary or zeros if it is the first packet). The output of this process is a set of four values representing the change in the angle that occurred between each data sample. The summation of these values over time produces an angle estimate for the module. This angle can be directly compared to the desired angle (30 degrees) to produce the proportional error term. The integral error term is found in much the same way – however, in this case Boole's rule is applied to the five previous angular *positions* (as opposed to rates) and summed.

Given these values, the controller then calculates the commanded torque value. However, the reaction wheels in the FluxCraft are rate-governed and cannot be controlled with a commanded torque directly. Thus, a number of characterization tests were performed in order to estimate the mapping between a commanded speed and the output torque, and the resulting transformation is completed on the torque command prior to it being sent to the FluxCraft actuators.

The actuators, as shown in Figure 6.33(a), consist of two Maxon90 brushless motors acting as reaction wheels, both of which are aligned so that they provide torque in the axis perpendicular to the operating surface. One motor is mounted inside of the FluxCraft and the other is attached to an external panel between the FloatCube platform and the FluxCraft wall. Each motor has a maximum spin speed of 300 rad/s (2900 rpm) and a rotor inertia of 0.000306 kg·m2. Commands sent to the actuators are parsed such that the total commanded torque is shared equally between the motors on a given FluxCraft.

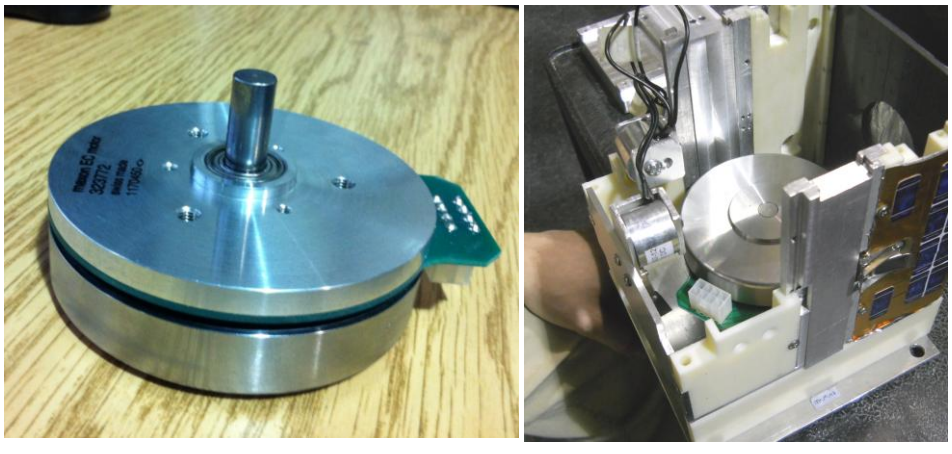

(a) (b)

Figure 6.33. (a) A Maxon motor used as a reaction wheel in the active FluxCraft in the CORTX experiment. (b) The same motor being integrated into the bottom of a FluxCraft.

Experimental Procedure

Each experiment typically lasts an hour and includes 15 – 20 different runs. It is preceded by the standard FloatCube setup procedure described in Section 6.2.4. The only relevant additions include the field-cooling process. After the FluxCraft payloads are fitted to their FloatCube platforms, the two modules are arranged in their test configuration for field-cooling. The magnets are secured in place on the testing module, and the desired equilibrium distance is set (for consistency, the cylindrical magnet was touching the face of the passive cube at a tangent point, near the center of the superconductor). Liquid nitrogen is then added to the passive FluxCraft until the module reaches a thermal equilibrium. This cooling procedure takes 5-7 minutes in order to ensure the superconductors are below their critical temperature. Once the flux-pinning effect is verified, the PC software connects to the active FluxCraft in order to begin collecting IMU data. At the same time, the camera vision system is calibrated and set to track the points on the top of the FluxCraft. Once both data sources are confirmed to be functional, the data collection phase of the experiment begins.

Once the FluxCraft-FloatCube assemblies are mounted on the operating table and the data collection sources are confirmed operational, the experiment begins. The test operator at the PC calibrates the IMU for sixty seconds while the system is stationary. Then, the controller is activated to a desired formation angle of 30 degrees. The behavior of a typical system is recorded in the IMU and vision system data in Figure 6.34. Each experimental run is allowed to continue until it achieves a performance to within a threshold of the desired value, or the test operator determines that an

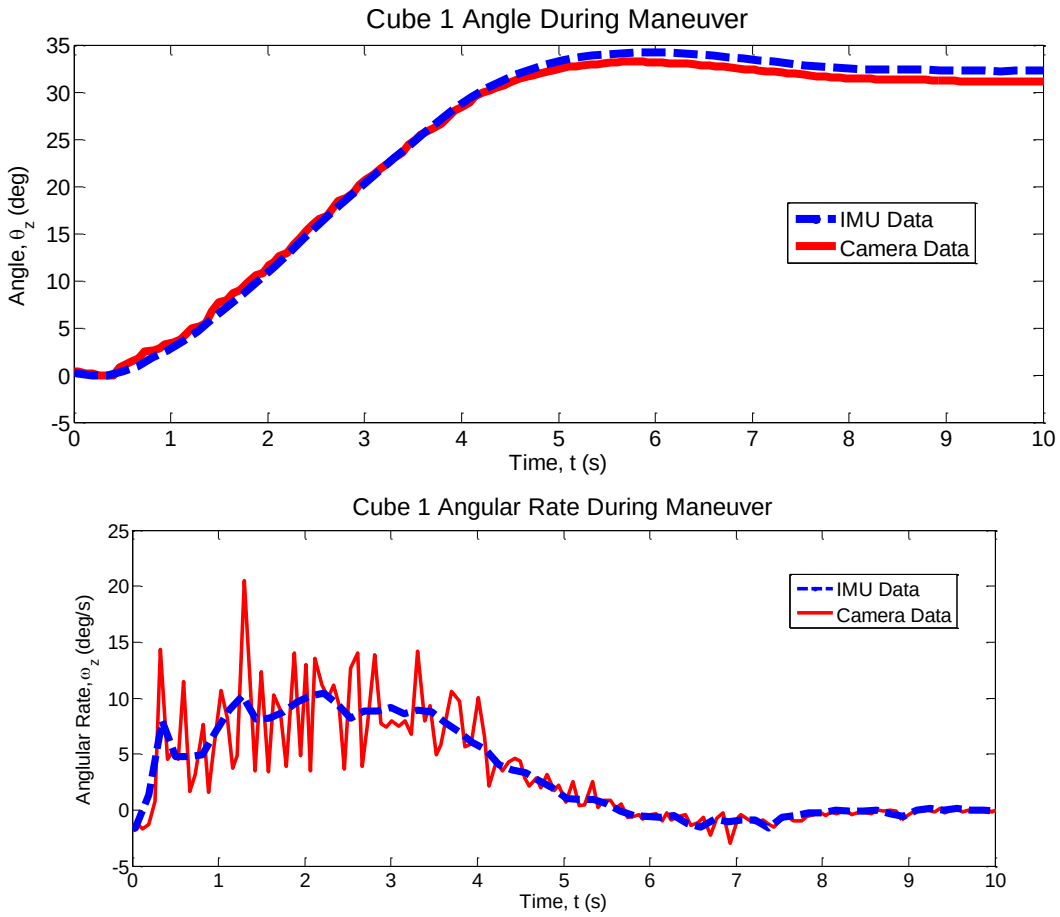

Figure 6.34. Representative example of a closed-loop response of the CORTX hardware testbed, in which both sensing systems are used and the signals are integrated or differentiated to generate time-history of both angular position and angular velocity for both sensors.

experimental variation is causing errors in the run. Examples of experimental variations include: a) batteries falling below their minimum allowable charge, b) pressure in the CO2 system not providing sufficient lifting force to provide frictionless motion, c) LN2 levels in the passive cube falling below the acceptable threshold, or d) glass surface conditions requiring alteration (such as a re-cleaning of the operating surface if frozen condensation interferes with the experiment). These conditions are consistently monitored by test personnel and preventative measures taken to ensure any potential problems are addressed before an experimental run is conducted. Once

the system appears to reach equilibrium, the controller is turned off and the equipment is reset for the next run.

FPI Behavior in a Slewing Formation

This work represents the first experimental validation of a flux-pinned interface in a system-level experiment for reconfigurable spacecraft. The FPI is capable of providing a stiff flexible connection analogous to that of a mass-spring system. In order to better characterize the FPI's behavior during the system's 30-degree slews, the frequency data from thirteen runs in Configuration #1 (with a mix of gain values) were averaged together to produce a set of data for this type of analysis. The averaged frequency response of the angular rate of the active FloatCube/FluxCraft assembly (containing the magnets, IMU, and the reaction wheels) is pictured in Figure 6.35. The camera data was collected at 16 Hz and the IMU data was collected at 6 Hz, and neither of these modes are in the range of the axes shown. The rigid-body response manifests itself at a frequency around 0.3 Hz, although there is relatively little content

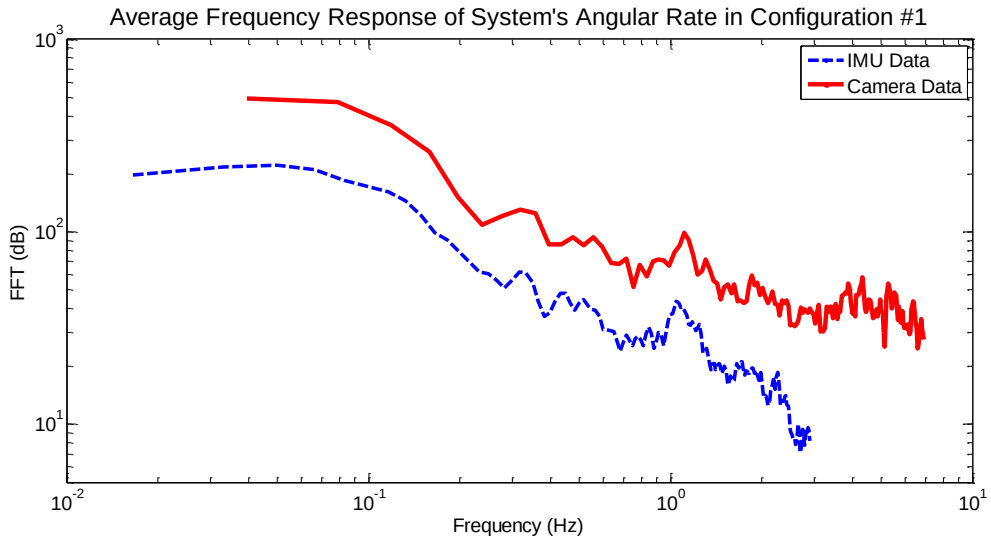

Figure 6.35. Average frequency response of the angular rate of the active module in Configuration #1.

at this frequency because the second-order response of the collective motion of the slewing system does not exhibit a strong oscillatory response. The additional higher-frequency content in the camera data can be attributed to the fact that this signal was numerically differentiated to obtain a time history of the angular rate.

Given this context for interpreting the frequency data, it is clear that peaks that are present in both the IMU and the camera data are of particular interest, since both sensors have different noise characteristics and sampling frequencies. The strongest peak in the angular rate data occurs at 1.11 Hz in the camera data and 1.05 Hz in the IMU data, for an average of 1.08 Hz. This peak likely represents the dominant flexible mode in the system due to the flux-pinned interface. Using a simplistic model of the system, where two masses are connected by an FPI modeled as a linear spring, it is possible to calculate the equivalent linear spring constant. Given the masses of the two assemblies (4.856 kg and 3.035 kg) and assuming 1.08 Hz is the natural frequency of the system, the linear approximation of the system's spring constant is 86 N/m, neglecting the influence of damping.

As useful as linear approximations can be, the frequency plots reveal a more complicated dynamical system than can be captured by a linear spring. Although the peaks are

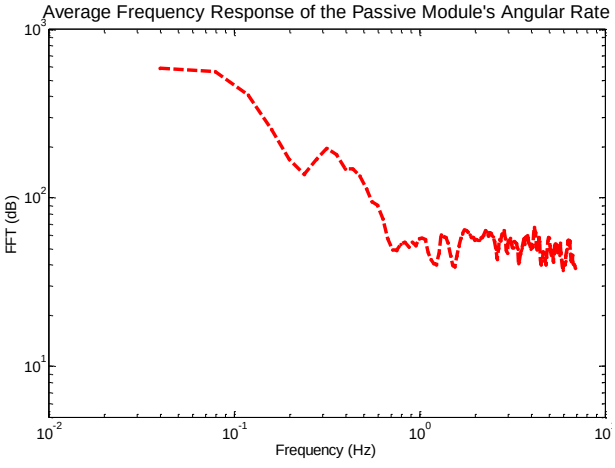

Figure 6.36. Average frequency response of the angular rate of the passive module in Configuration #1.

relatively weak and may be attributable to other system characteristics, the IMU and camera data both appear to have a double-peaked protrusion around 0.45Hz and 0.55 Hz, as well as a weaker higher-frequency peak at 1.3 Hz. It is possible that this frequency content is the result of the nonlinear behavior of the system, although it is difficult to definitely claim it is due to the FPI itself. Examining the frequency response of the camera data captured for the passive module in the system, shown in Figure 6.36, provides another dimension by which to analyze this data. The plot, which only contains camera data since the passive FluxCraft did not contain an IMU, shows a weak peak at 1.31 Hz in addition to the large low-frequency rigid body mode. The presence of this mode in the dynamics of the passive module (while showing nothing in the 0.45 – 0.55 Hz range) lends credence to the idea that the 1.31 Hz mode may be related to the nonlinearities in FPI.

In addition to providing the first system-level demonstration of an FPI in use in a reconfigurable spacecraft formation, the data obtained from the experiment has provided a set of interesting observations about the characteristics of the FPI. These results can be used to develop a more detailed model of the FloatCube/FluxCraft system in future research. Nevertheless, the results presented in the preceding sections demonstrate that flux-pinned interfaces are a viable mechanism for spacecraft reconfiguration, even in the presence of flexible modes resulting from this non-contacting interface.

6.4.3. Inter-Cube Electromagnet Control Algorithms

While the CORTX project sought to analyze the behavior of an FPI that served as a passive subsystem in a larger spacecraft formation slewing maneuver, the EINAR (Electromagnet Interface for Noncontacting Actuation and Reconfiguration) project was developed explicitly to test active control strategies for inter-cube electromagnets in an FPI. In particular, the EINAR system provides a platform for experimentally assessing the control and steering techniques detailed in Chapter 5. The main FluxCraft developed for this experiment, shown in Figure 6.37, hosts a magnet card with four large electromagnets and an array of smaller permanent magnets that supply the system with a passively stable equilibrium that can still be overwhelmed by the powerful actuators (to provide a platform for testing ways in which the system might intentionally be driven unstable, for example, to simulate a undocking maneuver).

The IMU sensors used in the CORTX project do not provide the signal stability or accuracy necessary to provide relative motion data suitable for use in a controller in a system where the anticipated relative deflections are on the order of millimeters. Although both FluxCraft in the EINAR system contain these IMUs, the FluxCraft with the magnet card is also equipped with a pair of ultrasonic sensors mounted on the top of the shells. When this data is fused with the relative data from the two IMUs using

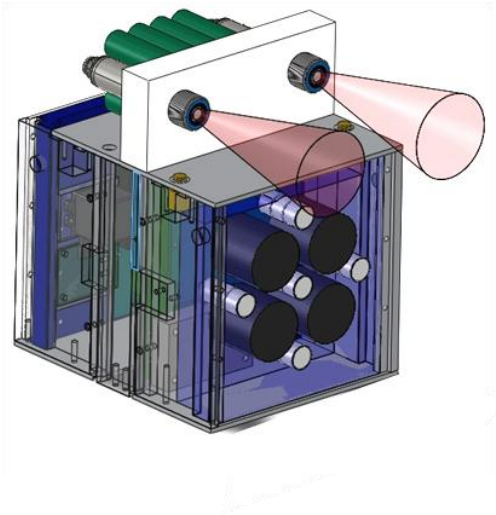

Figure 6.37. The FluxCraft containing magnet and sensing cards for autonomous control capabilities.

an unscented Kalman filter, the system can more accurately determine its states and thus control them to the precision necessary. The EINAR experiment would then look as shown in Figure 6.37, where the ultrasonic sensors reflect off an upraised panel mounted over the FluxCraft containing the superconductor card. While the EINAR FluxCraft are fully integrated and tested, data has not yet been collected for experimental validation or performance analysis. However, the development of this hardware has already provided insight into the practical implementations of an increasingly flight-like FPI system in a laboratory environment, thus helping to pave the way on the path to designing an orbital FPI flight system.

CHAPTER 7

MICROGRAVITY FLIGHT TECHNOLOGY VALIDATION MISSIONS

7.1 Microgravity Testing and the Technology Advancement of FPIs

Demonstrating a system in an appropriate relevant environment is a critical stage in the technology maturation process since it precedes the development of a flight-ready design that can be flown in space. Successful attainment of this level of advancement (a TRL 5 or 6) proves that the technology is prepared for an orbital mission. For spacecraft in general, this phase entails testing components or systems in a space-like dynamic, thermal, or vacuum environment, depending on the key influences on the system behavior. For flux-pinned interfaces, two environmental influences are of particular importance: gravity and the thermal environment. The FPI's highly-coupled degrees of freedom make it difficult to fully capture the dynamics of a flight-like system in standard Earth-surface gravitational conditions. Thus, a relevant FPI flight experiment must approximate the microgravity environment of an orbital system. Also, because the superconductor must be kept below its critical temperature, a relevant demonstration must address a method of cryogenically cooling the superconductors.

Two microgravity demonstration missions were carried out – one in 2009 and one in 2010 – to advance components of the FPI system to this stage of development. Both missions were performed via the NASA Facilitated Access to the Space environment for Technology (FAST) program, which provides experimental-grade microgravity test flights to space-technology researchers. These flights typically last less than two

hours total and provide about 30 parabolas, or 15 minutes, of microgravity time. The microgravity portion of each parabolic flight path lasts for 30 seconds, followed by 30 seconds of a 2-*g* environment. Each mission spanned two flight days, so various FPI equipment has logged over an hour in microgravity in total.

The 2009 microgravity mission was initiated in May of that year when a proposal was accepted by the NASA FAST program. The two awarded flight days took place in August of that year. The goal of this project was to demonstrate the first example of a flux-pinned interface in a microgravity environment; and in particular to capture the performance of a flux-pinned non-contacting revolute joint between a CubeSat mockup and a set of cooled superconductors in a free-floating module. This component-level demonstration cooled the superconductors using a dewar filled with liquid nitrogen that was equipped to safely manage the cryogen in a microgravity environment. The free-floating dewar was then connected to a CubeSat module via an FPI, and a high-speed motion capture camera was used to track the dynamics of the system.

The 2010 mission built on the success of the first flights and increased in sophistication and ambition. It was the culmination of a year-long undergraduate and graduate effort to build up the FPI technology testing capabilities of the lab. The NASA grant was awarded in May of 2010 and the flight dates were September 30 and October 1 of that year. This project was intended to flight-validate a cryocooler-based thermal system for the superconductors in an FPI, to capture high enough quality dynamics data to validated models of the system, and to fly more sophisticated CubeSat-scale mockups with increased sensing capability. This experiment utilized a

meter-long cryocooler mounted to the microgravity plane's surface with a superconductor mounted to the end of its coldfinger. Modules containing magnets were then manually manipulated while free-floating above the superconductor, and data was captured via the motion-capture camera and on-board IMU sensors.

This chapter describes the details of the objectives, designs, hardware, and experimental results for both the 2009 and 2010 FPI microgravity demonstration missions on the Zero-G Boeing 727. Both of these missions involved experiment development, design analysis, and fabrication of the test FPI hardware leading up to the demonstration. This work also encompasses being an experimenter on each of the flight days, and work to analyze and publish the results after both missions. Section 7.2 describes the initial 2009 mission, including project management and engineering of all systems. The content in this section is derived in part from team project reports and write-ups that were completed in conjunction with the other members of the Flux Pinning Research Team: William Wilson (the principal investigator on the project), Joe Shoer, and Max Knobel. The 2010 FPI microgravity mission, which was a principal investigation for this work, is described in section 7.3. The content in this section is derived from a conference publication which was written in conjunction with other members of the flight team: William Wilson, Jillian Gorsuch, and Joe Shoer.

7.2 FPI Revolute Joint 2009 Microgravity Demonstration

7.2.1 Goals and Background for the Demonstration

The 2009 microgravity flight project was developed for two purposes: first, to demonstrate an FPI in microgravity as the next logical step in the technology development process, particularly for non-contacting revolute joint applications, and second, to obtain relevant six-degree-of-freedom dynamics data that would be difficult to obtain in a laboratory environment. Both of these goals informed the design and implementation of the experiment and its associated hardware.

The 2009 mission was modeled around a laboratory hardware development effort that served as the baseline experiment design for the microgravity grant proposal. In the spring of 2009, a component-level FPI hinge design was successfully built and tested in the Space Systems Design Studio laboratory by M. Eng. student William Wilson.[94] The hardware for this demonstration consisted of simple electronics, superconductors in a small liquid nitrogen bath, and a combination of permanent and electromagnets supported on pieces of glass, as seen in Figure 7.1(a). These modules were operated on an air table (as seen in Figure

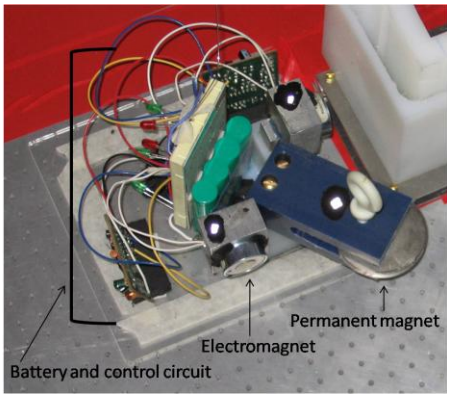

(a)

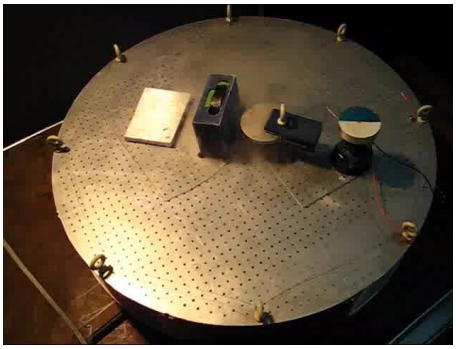

(b)

Figure 7.1. (a) The component-level hardware that served as a predecessor to the 2009 microgravity demonstration. (b) The experimental setup for a laboratory-based demonstration of a non-contacting FPI revolute joint.

7.1 (b)) which provided a reduced-friction environment for testing the design. The effectiveness of this demonstration in a laboratory environment led to the development of an experiment that would perform the same maneuver with similar technology in a microgravity environment.

A microgravity plane flight was selected as the next phase of the project's development for several reasons. An advancement of the maturity of the technology called for a more sophisticated system to be tested in a relevant environment. For FPIs, a relevant dynamic environment must enable the full expression of the system's nonlinear couplings among multiple degrees of freedom. While approximations of this environment can be accomplished using pendulum-style systems in a laboratory, the only way to provide unconstrained motion in the full six degrees of freedom is to allow the system to freely float in microgravity.

Unconstrained experimentation in microgravity can be achieved or approximated in several ways, including neutral buoyancy in a fluid, drop towers, and microgravity flights. Techniques involving neutral buoyancy, such as water tanks[137] or helium-based zeppelins,[138] are often plagued by other influences on the system behavior, such as variations in the fluid motion or temperature, and are not widely available to external researchers. Drop towers often only provide three seconds of microgravity testing at a time,[139] making it difficult to obtain dynamics data in the frequency range exhibited by FPIs on a CubeSat scale. Microgravity plane flights, on the other hand, are well-established as research and development tools that provide up to 30 seconds of microgravity at a time without the variations caused by fluid motion or temperature changes. These flights enable experimenters to interact with their equipment during

the testing process and observe the results as they are obtained. Thus, a microgravity flight was clearly the optimal solution for an FPI demonstration.

7.2.2 Experiment Design

The experiment design for the microgravity mission involved a mock CubeSat equipped with an array of permanent magnets and electromagnets forming an FPI with a free-floating vehicle containing YBCO superconductors and liquid nitrogen (LN2), as seen in Figure 7.2. Two magnet-bearing CubeSat modules were designed to interact with the free-floating dewar. One was created to form a passively stable FPI in a low-stiffness station-keeping demonstration. The second CubeSat mockup was designed to mimic the laboratory experiments and form a non-contacting revolute joint with the second module containing two YBCO disks. Because the results of the station-keeping experiment were primarily observational, that portion of the experiment design is not addressed further.

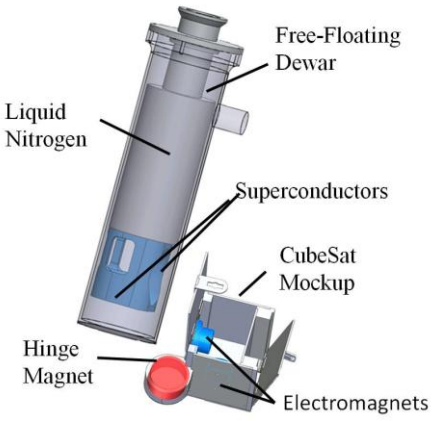

Figure 7.2. The free-floating dewar with cryocooled superconductors and CubeSat mockup containing magnets that formed the FPI in the 2009 microgravity demonstration.

The magnet module for the revolute joint consisted of a large cylindrical permanent hinge magnet extruding from the corner of the CubeSat module and two "locking" electromagnets on the adjacent faces. In the experiment, the magnetic flux from each of these magnets were imprinted into the superconductor disks prior to the flight using a custom-built apparatus to hold the dewar while it was being filled with LN2. During the

flight, the two modules would be positioned near one another to engage the FPI and manipulated to show the hinging motion of the non-contacting joint. The hinging motion involved the CubeSat mockup moving about the center of the large cylindrical hinging magnet, not the center of mass of the system, to reconfigure between two equilibrium states, both shown in Figure 7.3. During that hinging maneuver, the flight team collected high-speed video recording of high-contrast points on the equipment to gather data on the behavior of the system.

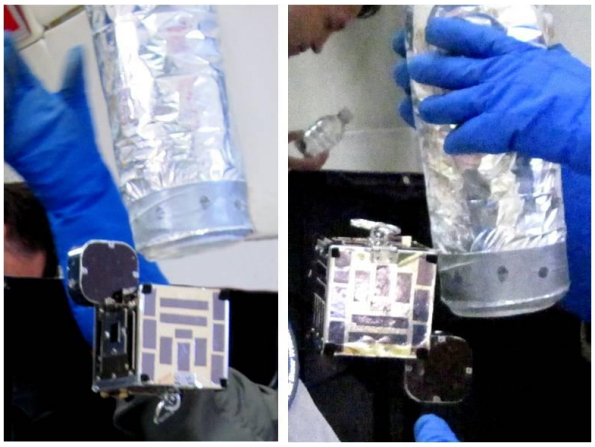

Figure 7.3. The magnet module in its two equilibrium configurations during the flight.

The manipulation of the system's equilibrium was designed to be triggered by altering the state of the electromagnets. In theory, the electromagnet closest to a superconductor is turned on such that it provides a stable FPI in order to keep the system in one configuration. When the system is actuated, the polarity of the electromagnet is then reversed, repelling the superconductor and moving the system towards its new equilibrium. The second electromagnet then engages to produce a passively stable FPI that maintains the new configuration. In practice, however, the system was very weakly pinned, and so forces from actuating the electromagnets were not sufficient to produce the reconfiguration maneuver. Thus, the system was actuated manually by the experimenters handling the equipment during the microgravity segments of the flight.

7.2.3 Experimental Hardware

At the end of the spring of 2009, existing laboratory equipment was not suitable for a microgravity flight environment. Thus, in the three months between the proposal acceptance and the flight, completely new hardware had to be developed to meet the requirements imposed by the experiment and NASA. The key free-floating components included the CubeSat mockups (also known as the magnet modules) and the free-floating LN2 dewar. Various supporting equipment included a motion capture camera and computer, vacuum system, and containers for attaching equipment to the plane's structure. Most of the equipment was fabricated by the microgravity team in-house in the months before the flight, while some specialized parts, most notably the free-floating dewar, was partially designed by the team and then contracted to commercial vendors.

Free-Floating Magnet Modules/CubeSat Mockups

The free-floating magnet modules were designed to approximate the CubeSat satellite standard, as CubeSats are a likely choice for a future orbital demonstration of flux pinning. These modules contain simplified subsystems similar to those found in orbital CubeSats, including an array of fixed permanent and electromagnets, an aluminum structure, various electronics and batteries to support the electromagnets, and a wireless Bluetooth-enabled Arduino microcontroller. The magnet modules do not contain any on-boarding sensing because the goals of the relatively simple component-level experiment could be accomplished without the increased complexity of an on-board sensing system. Also, unlike CubeSats which typically use solar cells

for power, these modules use replaceable AA batteries for convenience and reduced cost.

The primary purpose of the CubeSat mockups is to house and control the magnet array in a free-floating module. The revolute joint magnet module's array consists of three magnets: one permanent hinge magnet and two locking electromagnets. The hinge magnet consists of an N52-grade Neodymium permanent magnet that extrudes from one corner of the CubeSat mockup. Its purpose is to provide a symmetric field of magnetic flux that can be pinned into the superconductors in the free-floating dewar. Since the superconductors do not resist motion about the axis of symmetry of the magnet, the CubeSat mockup is free to hinge about the magnet's center. Motion in other directions, however, corresponds to a change in magnetic flux through the superconductors and thus induce the superconductors to apply the forces and torques necessary to restore the equilibrium. The other two magnets in the module's array are cylindrical electromagnets, which are mounted on the side walls that share an edge with the corner where the hinge magnet is attached. These magnets are oriented such that their axis of symmetry is perpendicular to the wall to which they are attached. Thus, from the perspective of the superconductor, the activated electromagnets produce asymmetries in the magnetic field, and can thus lock out the non-stiff degree of freedom about the hinge magnet's axis of symmetry.

The main structure of the magnet module follows the 10cm cube envelope for a 1-U CubeSat standard, but the specifics of the design deviate from that of orbital CubeSats so that it could be optimized for a microgravity flight environment and an FPI revolute joint experiment. The primary structure of the system consists of a stiff square aluminum base plate that hosts four aluminum posts on each corner. Thinner solid aluminum plates are attached between the posts to protect and provide attachment points for the module's electronics. A standard CubeSat structure would be skeletonized to reduce weight, but using this design can complicate the fabrication and mounting techniques for the system. So instead to reduce weight, some of the non-load-bearing walls in the CubeSat mockups are made out of plastic. Also, most CubeSats are integrated once and don't need to provide users easy interior access, for example to change batteries. However, these modules were constrained by such requirements, so the rear plate and top plate are attached to the cube via hinges that enable users easy access to the cube's interior, as shown in the CAD drawings in Figure 7.4. The hinging walls can then be locked shut during the experiments.

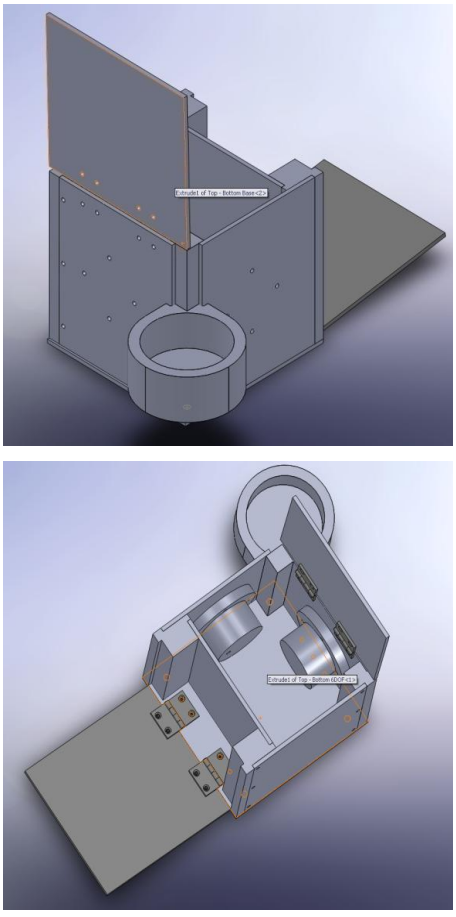

Figure 7.4. The design of the CubeSat mockup with its hinging walls deployed

The primary experiment-driven design element that deviates from the 1-U CubeSat standard is the extrusion supporting a large cylindrical hinge magnet. In order to better track the reconfiguration of the two free-floating modules, the hinging magnet is mounted outside of the main body of the CubeSat mockup, and thus outside of the standard 1-U CubeSat envelope. In order to compensate for the added stresses on the structure in that corner of the module, the supporting post was thickened and cut to interlock with the magnet container. The CubeSat mockup is shown under construction and as-flow in Figure 7.5.

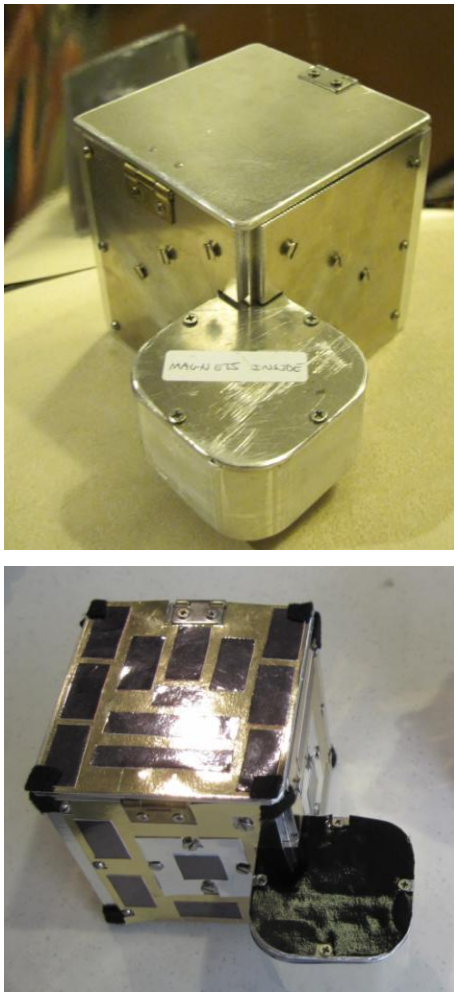

Figure 7.5. The magnet module used in the 2009 microgravity mission in flight

The electronics on-board the CubeSat mockups were designed to support open-loop wireless commands from the main laptop computer. The Arudino BT microcontroller on the magnet module serves as both a microprocessor and communications device for this purpose. The laptop user connects to the magnet module's Arduino via its integrated BlueTooth antenna, which then enables the operator to manipulate the pins on the microcontroller. A circuit of H-bridges then allows those pin commands to control the polarity of the electromagnet array. The power for all of the circuitry in the module comes from a battery pack of six AA batteries.

LN2 Free-Floating Dewar

In order to implement the second half of the prototype FPI, the second free-floating module was designed to hold two superconductor disks perpendicular to each other and to provide a method of cooling them below their critical temperature. This free-floating dewar was designed in conjunction with and fabricated by Precision Cryo, a small company with expertise in manufacturing custom LN2 systems. The key aspects of the design of this system include the superconductors and their arrangement, the LN2 tank and valve design, and the thermal insulation system.

The superconductor disks chosen for this demonstration were two 58 mm diameter and 18 mm thick Yttrium Barium Copper Oxide (YBCO) single-grain disks. These were chosen to maintain consistency with previous laboratory hardware and experimental results. The disks were set up in a configuration that mimics the original air table demonstration, at a right angle to each other with the circular part of the cylinder facing the walls of the dewar, as shown in Figure 7.6. The superconductors are held in place via a small custom insert, fabricated at Cornell, which can be bolted to the bottom of the nitrogen tank. This YBCO holding structure is designed to hold the superconductor disks in thermal contact with the LN2 during the microgravity experiment, causing the superconductors to cool below their critical temperature. This fixture was also designed to place the YBCO disks as close as

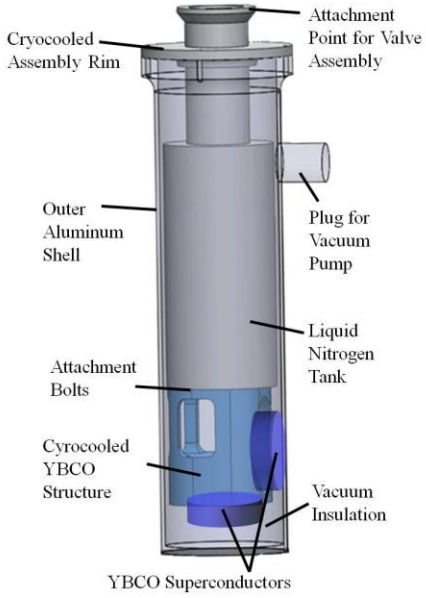

Figure 7.6. Details of the elements in the free-floating dewar module.

possible to the edges of the dewar without physically contacting the walls to allow flux pinning to be as strong as possible during the experiment.

Options for cooling equipment to cryogenic temperatures in a microgravity environment are limited. Dewars of cryogenic cooling fluids and cryocoolers are the two feasible options that have a history of use in orbit and can still function on a microgravity flight. This experiment uses a dewar of liquid nitrogen instead of a cryocooler for several reasons. First, cryocoolers tend to be more expensive than dewars or LN2, and so a dewar was more feasible for this demonstration. Also, all previous lab experimentation up to that point had exclusively used LN2 baths to cool the superconductor disks. Without previous experience in using cryocoolers and only a short time to create a working flight system, the dewar solution presented less risk from an experiment-success perspective.

However, the decision to use a dewar of LN2 posed a number of challenges in a microgravity environment. The most difficult requirement to meet was ensuring that the LN2 remains within the dewar even under microgravity conditions while, simultaneously, allowing the gaseous nitrogen to vent in order to prevent a potentially dangerous pressure buildup. In normal laboratory conditions, LN2 containers do not need to be completely sealed, so pressure build-up is not typically an issue. The free-floating dewar module solves this issue by incorporating pressure-release valves coupled with an in-line phase-separating device to enable the gas to freely pass through but prevent any cryogenic liquid from escaping. The valve assembly, pictured in Figure 7.7, incorporates a ball valve, two pressure-release valves, and two in-line phase separators. As shown in the labeled diagram in Figure 7.8, the ball valve at the

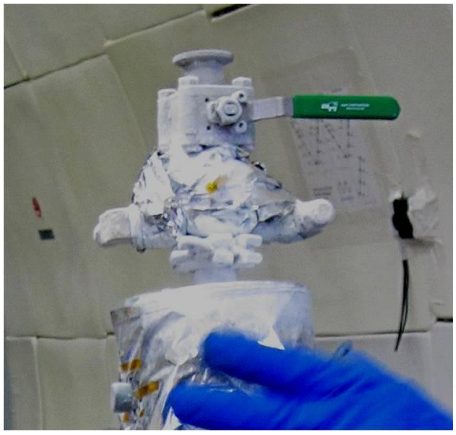

Figure 7.7. The valve assembly mounted on the free-floating dewar module, which prevents liquid nitrogen from escaping and pressure from building up.

top of the assembly can be opened manually with an extruding handle and is used to fill the dewar with LN2 prior to the flight. This valve is locked shut with a set screw prior to the experiment to prevent LN2 from leaking. The two pressure valves are connected in line with the phase separators, ensuring that only gaseous nitrogen leaves the system. One valve is set to release pressure at 4 psi and the other is set to release at 10 psi. These valves are oriented in opposite directions so that sudden high-pressure bursts of gas do not impart a large total net force to the assembly in microgravity.

Another complication associated with using liquid nitrogen is the need for a custom-built pressure vessel. NASA has exacting specifications on the documentation and testing required for pressure vessels on microgravity flights, all documented in JPR 1710.13C. These requirements are somewhat relaxed if the system can be considered a Class E pressure vessel – in particular, if it was developed by a commercial company and the volume of the system is below two cubic feet (56 L). That requirement, coupled with the CubeSat-scale design of the experiment,

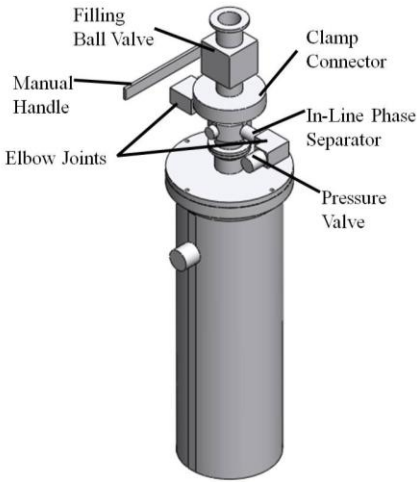

Figure 7.8. The valve assembly mounted on the free-floating dewar module.

led to a commercially-fabricated dewar design with a tank that can hold 0.8 L of liquid nitrogen.

In addition to having a method of cryogenically cooling the superconductors, the dewar has a system designed to isolate the cryogenic portion of the dewar from the heat loads of the ambient environment. This improves the duration of the experiment and ensures that the outer walls of the dewar are not at cryogenic temperatures, making it safer to handle. The overall thermal insulation system in the dewar is designed to limit the heat conduction paths to the superconductors and LN2 tank, and to minimize convection and radiation acting on the system overall. The conduction paths and convection effects are managed by the design of the system, which contains two nested sections separated by an insulating vacuum. The internal section is kept at cryogenic temperatures by direct thermal contact with the LN2 tank. Therefore, the top portion of the internal section connects directly to the valve assembly. The outer section is an aluminum shell that fits over the cryocooled section without touching, except where they connect at the top flange with an O-ring and bolts.

In order to produce an effective thermal barrier between the cryocooled and outer sections, a dry-scroll vacuum pump can attach to a port on the outer shell of the dewar and draw the inside of the chamber down to a pressure of 10 milliTorr – an effective insulating vacuum. Once the vacuum is at the desired pressure during pre-flight preparations, a plug is inserted to maintain this pressure for the experiment portion of the flight. This plug is equipped with an emergency release valve set to 5-9 psi that unseals in the event that a positive pressure builds inside the vacuum chamber.

To reduce the effect of radiative heat transfer on the system and to ensure the outer surface of the dewar did not reach cryogenic temperatures, the outer surface of the module is covered with reflective thermal insulation blankets. A removable sleeve of reflective insulation was also used to cover the valve assembly. Combined with the other aspects of the thermal isolation system, this design kept the superconductors cold for about half of each flight, at which point the LN2 had completely evaporated.

Data Acquisition and Control System

Because neither the CubeSat mockups nor the free-floating dewar module contain on-board sensors or control systems, an external system was developed to enable experimenters to manipulate and record the experiment. This system includes a Dell Latitude E4300 laptop computer (shown in Figure 7.9(a)) with a built-in Bluetooth module that connected to the Bluetooth-enabled microcontrollers in the magnet

(a) (b)

Figure 7.9. The equipment used in the data capture and control system. (a) The controlling laptop computer and (b) the high-speed motion-capture camera used to record the system dynamics.

module. A custom Graphical User Interface (GUI) allows users to enter keyboard strokes corresponding to different pre-programmed electromagnet configurations. These open-loop commands are then time stamped, recorded, and sent to the magnet module's microcontroller.

In order to collect data on the experiment, the laptop is connected to a high-speed motion-capture Basler A600 camera (shown in Figure 7.9(b)) capable of data rates up to 100 frames per second at a resolution of 656×491 pixels. Although the laptop does not contain the processing power necessary to extract the dynamics of the system from the video stream as it is recorded, it saves and timestamps the video files in 30-second bursts for later processing. The camera is powered by a custom-made AA battery pack strapped to the laptop computer. During the flight, the camera is mounted such that it has an unobstructed view of the experiment workspace. The two researchers monitoring the free-floating

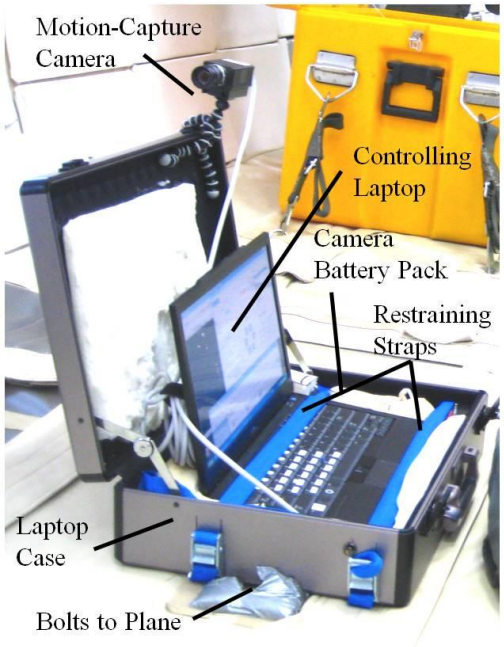

(a)

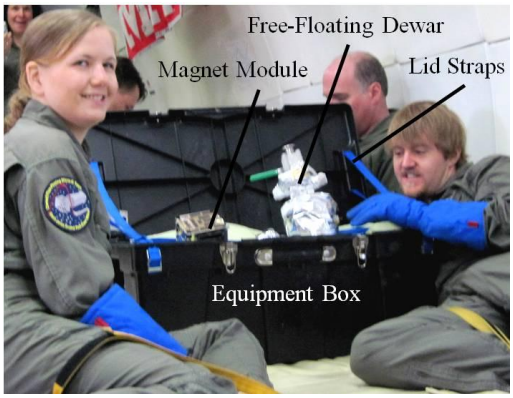

(b)

Figure 7.10. The microgravity experiment structures for (a) The controlling laptop computer and (b) the free-floating modules.

equipment work to keep the system in the camera's field of view so that the relevant dynamics data is captured by the camera.

Plane Attachment Structures

The final pieces of equipment necessary for the microgravity flight are the structures that hold the equipment to the plane. For the 2009 mission, two attachment structures were created – a briefcase that holds the laptop, camera, and battery pack, and a converted toolbox that houses the free-floating dewar and magnet module. The laptop briefcase, pictured in Figure 7.10(a), is attached to the plane's bolt pattern with a 3/8" bolt on each side. This commercial computer case is fitted with foam and restraining straps to keep the equipment in place in microgravity. The toolbox for the experimental modules is also modified to include foam with dedicated cutouts for the equipment it stores. The bottom of the box is reinforced with steel bars that use four bolts to attach to the plane. Straps are used to hold the lid of the box open in microgravity. An image of the equipment box during the flight is shown in Figure 7.10(b). Both of these structures underwent a thorough structural analysis to evaluate its behavior under standard operations and crash loads.

7.2.4 Operations and Procedures

In order to understand the strengths and limitations of the results of the 2009 FPI demonstration, it is important to know the procedures that were followed for the experiment. Since the FAST award granted two microgravity flights, the days were divided into two different experiments. The first day was dedicated to a six-degree-of-freedom FPI experiment that produced weak subjective results, so it is not described

further. The second flight day was dedicated to the successful microgravity demonstration of a non-contacting revolute FPI joint.

On this flight, three experimenters operated the experiment on the plane, and one remained on the ground to perform various setup and clean up duties. Of those on the plane, one was positioned by the laptop and camera assembly, enabling him to operate the magnet module and monitor the motion-capture feed during the experiment. The other experimenters controlled the free-floating modules, ensuring they did not leave the experiment area during microgravity and securing them during the 2-g portions of the flight. The experimenter on the ground prepared the modules for flight while the members of the flight team were in their medical briefing.

The relevant procedures for the experiment can be divided into four phases: pre-flight, pre-experiment, data collection, and stowage.

Pre-Flight Phase

In order to be prepared for the flight, it was critical that the superconductors were properly field-cooled and the free-floating dewar was filled with liquid nitrogen and sealed prior to boarding the plane. This process took nearly 40 minutes and required continuous monitoring during the period in which the flight team was undergoing the medical and pre-flight briefing. Thus, the lone ground experimenter was responsible for this operation. These tasks were started about an hour before flight to ensure they were completed on time.

First, the superconductors were placed in their mounting structure after it was bolted to the empty LN2 tank. The outer shell of the free-floating dewar was then placed over that assembly, and the two segments were bolted together around the O-

ring at the top rim. This assembly was then placed in an aluminum structure fitted with magnets in the appropriate locations for field-cooling, as seen in Figure 7.11(a). At this point the system was secured in a cooler and doused with a container of LN2 to begin to lower the system's temperature.

(a)

(b)

Figure 7.11. Pre-flight procedures including (a) Placing the dewar into a field-cooling fixture and (b) Filling the dewar with LN2

Then, the pump was attached to the port on the dewar module's outer surface and activated. Once the pump pulled a sufficient vacuum on the chamber, the port was sealed. The vacuum-insulated dewar was then fitted with the valve assembly with the ball filling valve open. The ground experimenter then began filling the dewar from a reservoir near the experiment's ground work station. A significant amount of LN2 boiled off in the process of cooling the dewar to cryogenic temperatures, making this a violent process. Thus, the experimenter wore protective equipment throughout the duration of the filling process, as shown in Figure 7.11(b). Once the system reached a thermal equilibrium and liquid nitrogen filled the LN2 tank, LN2 level was maintained by occasionally adding LN2 from the reservoir until the flight team was ready to board the plane. Then, the experimenter closed the ball valve, placed the set screw to lock the valve shut, and capped the valve with a removable reflective cover.

During the maintenance phase of the LN2 cooling process, the experimenter replaced or charged the batteries for the computer, camera, and magnet module. He

also performed quick functionality checks to ensure the systems were in working order; for example, by taking a test video clip with the high-speed motion-capture camera or holding a test magnet close to the magnet module's electromagnets to ensure their polarity changed on command. Once the flight team was ready to board the plane, the free-floating modules, laptop, and camera were turned off, collected from the ground workstation, and brought to the plane to be secured in their plane attachment structures prior to take-off.

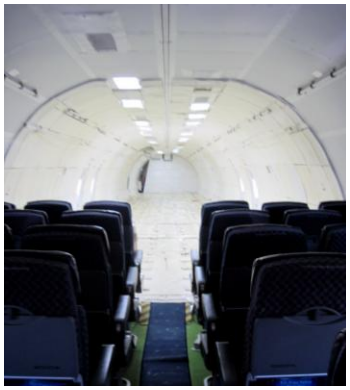

Figure 7.12. The view from the seating area of the plane looking toward an empty experimental section.

Pre-Experiment Phase

The pre-experiment phase of operations occurred in the normal-gravity setup period after takeoff and the first few parabolas, before the microgravity experiments began. The equipment began this phase stored in the plane attachment structures, which were put in place in the days leading up to the experimental flights. After takeoff, the flight team moved from the seating section of the plane to the padded experimental section (both shown in Figure 7.12) where the structures and equipment were bolted to the plane in the arrangement shown in Figure 7.13. In the few minutes before the microgravity parabolae were started, the three experimenters took their places and strapped themselves to the plane with the provided Velcro and nylon restraints. Once secured, each experimenter inspected the equipment under his or her control, turning it on and checking battery life where appropriate.

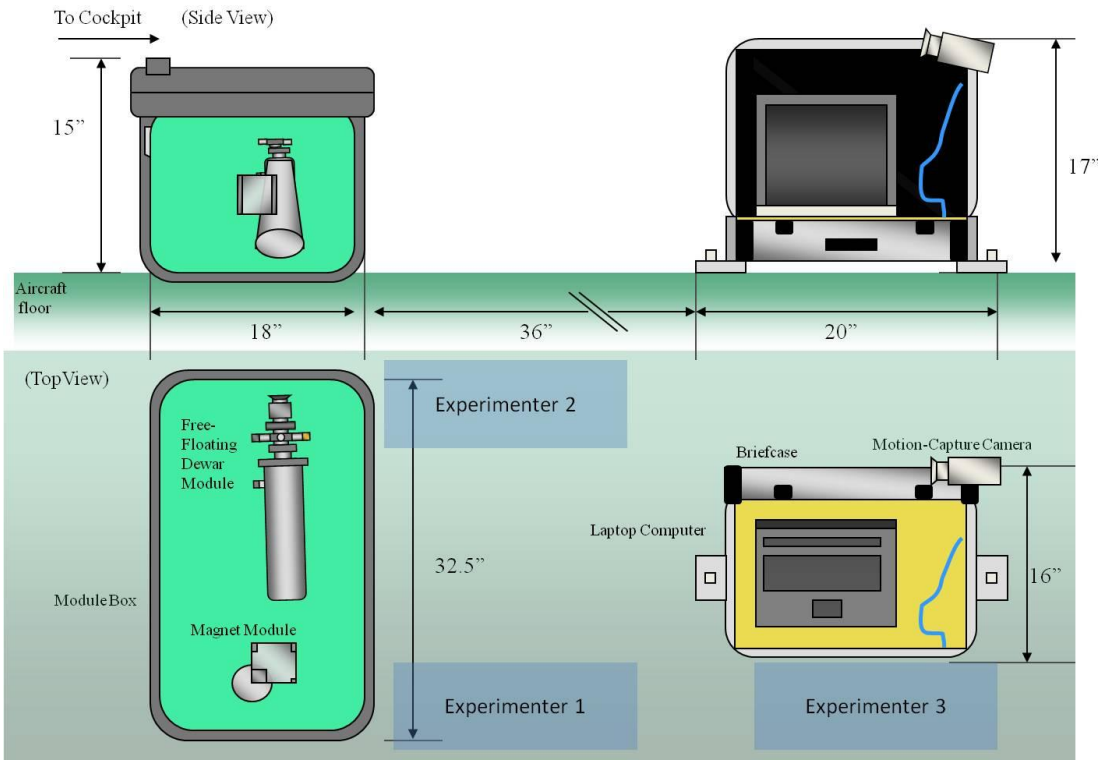

Figure 7.13. The experimental layout from a side view and top view.

Both researchers near the free-floating dewar donned cryogloves and opened the lid of the container holding the modules. They secured the lid with straps and then loosened the free floating modules in the foam for easy access during the flight. One experimenter switched on the magnet module and confirmed the module received power. The researcher at the computer then connected the laptop to the magnet module and performed a command check and a camera check. Once these actions were complete, the system was ready for the microgravity portion of the flight.

In order to ensure that the flight team was prepared for working in microgravity, the first three parabolas were dedicated to the team’s environmental acclimation. During the first parabola, the experimenters did not move at all, so that they had the chance to experience microgravity without any disorientation caused by attempting to work with the equipment. In the second parabola, the team simulated an experimental

run by moving around and pantomiming the experiment without actually manipulating the equipment. The last acclimation parabola involved the team pulling out the equipment and capturing video, but not attempting to command the system. Once these three test parabolas were complete, the team was prepared to collect experimental data.

Data Collection Phase

During each microgravity parabola the experiment followed the same general pattern: once the microgravity portion of the parabola began, the flight team members managing the free-floating modules would extract them from their container and position them in an FPI equilibrium position in front of the camera. The flight team member operating the computer would establish the testing type for that parabola and trigger the motion-capture camera recording burst. The two module handlers would then ensure the modules did not leave the experimental area (defined by the field of view of the camera and the space used by neighboring experiments) as shown in Figure 7.14. These experimenters also ensured that the equipment was secured in the foam for the 2-g portions of the flight and took photos and video with hand-held cameras when test activity permitted.

Figure 7.14. The two experimenters manipulating the free-floating modules during an experiment.

Three pre-established testing types were used to examine the flux-pinning interaction between the two modules. The test type was determined by the flight team member operating the computer at the beginning of each parabola, based on the

quality of the microgravity, the status of the equipment, and the apparent effectiveness of different testing types. The first type of test was to actuate the module interface using the electromagnets via computer input and the Bluetooth connection. During this test type, the experimenter operating the computer would manipulate the controls to the system while the experimenters with the free-floating modules attempted to disturb the equipment as little as possible. The second type of test was for the module handlers to physically disturb the system and record the reaction. The third test activity was for the module handlers to position the modules for optimal viewing of the recording cameras to produce images the clearly illustrated the concept of flux pinning and test activities, even if it interfered with the natural dynamics of the system. These testing types were repeated until the experimentation phase of the flight was complete.

Stowage Phase

After the microgravity portions of the flight were complete, the equipment was powered down and stowed back in the plane attachment containers and secured for landing. On both flight days the LN2 tank emptied before the final parabola of the day, so no methods were necessary for its disposal. The data recorded on the laptop was retrieved and analyzed in conjunction with the hand-held video after the plane landed, so the status of the experiment was not clear until days after the flight. These findings are discussed in the next section.

7.2.5 Experimental Results

The first microgravity demonstration of a non-contacting revolute joint between spacecraft connected by flux pinning was successful in capturing data showing the hinge in operation in a microgravity environment. By taking the original laboratory demonstration at a technology readiness level of 3 or 4 to a relevant dynamic environment in a simple component-level experiment, the technology readiness level of this type of FPI was increased to a 5. The data leading to these results have been published by the flight team[161] but are summarized here for completeness.

Of the approximately 30 parabolas available to experimenters on the flight day, the first three were dedicated to team acclimation and therefore did not produce any data. The LN2 tank was emptied by parabola 25, and without a thermocouple installed, it was not possible to tell if the system maintained temperatures below the critical temperature of the YBCO disks. Several of the parabolas suffered from low-quality microgravity conditions from turbulence or inexact flight patterns, and many of the flights had significant enough variations in the environment to necessitate that the free-floating modules be re-positioned by the flight team before they moved out of the camera's field of view. Additionally, although the parabolic arc provides 30-second bursts of lower-than-standard gravity, only 15-20 seconds of that time is held in a consistent gravity environment suitable for testing. Thus, a relatively small subset of parabolas contained reliable data of pure free-floating dynamics of the FPI. However, even given these constraints, data on the revolute joint was observable from the motion-capture camera.

The large hinge magnet in the system produced a larger stiffness than had been observed in the previous FPI microgravity attempts on the first flight day, enabling the hinging motion to be captured on camera. However, even though more powerful electromagnets were used in the microgravity demonstration than were used in the laboratory analog, the electromagnets appeared to be too weak to actuate the system during the experiment. This result is likely due to a degradation of the superconductor's captured flux in the more variable thermal environment of the microgravity system. Fortunately, it was possible to manually excite the system and observe the desired dynamical behavior.

The system demonstrated a near-zero stiffness between the cooled superconductors and the hinge magnet when rotated about its dipole axis, and a non-zero stiffness constraining the system to move only about that degree of freedom. Figure 7.15 shows several frames from the high-speed motion-capture camera, which have been rotated to ensure the free-floating dewar remains fixed. Motion capture points on the dewar and CubeSat mockup, superimposed as lines on the image, provide an estimate of the axis of rotation for the maneuver as the point at which the lines intersect. Two different clips of the same maneuver are compared side-by-side - a video totaling 1.1 seconds showing the system with an active FPI, and a 0.66-second video of the same system but without an active FPI.

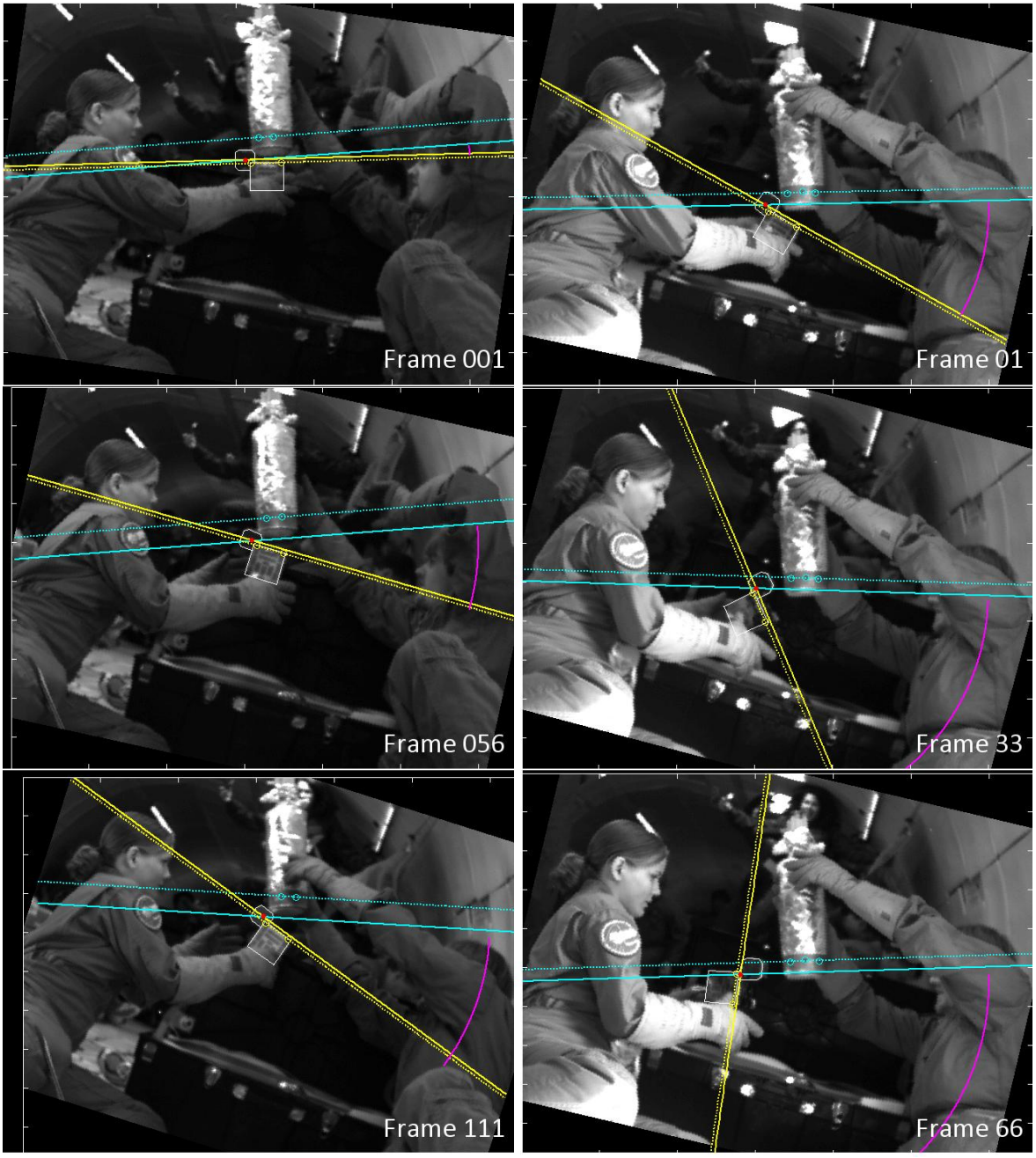

(a) (b)

Figure 7.15. Demonstration of a flux-pinned hinge on a CubeSat mockup at 100 frames per second.[161] (a) On the left, flux pinning stiffens the motion of the outlined CubeSat, which rotates about the hinge axis of the magnet (intersection of the solid lines). (b) On the right, the FPI is not engaged, causing the axis of rotation to drift from the center of the hinge magnetic.

Figure 7.15(a) shows the system constrained by an active FPI, which constrains the axis of rotation to remain relatively close to the center of the protruding hinge

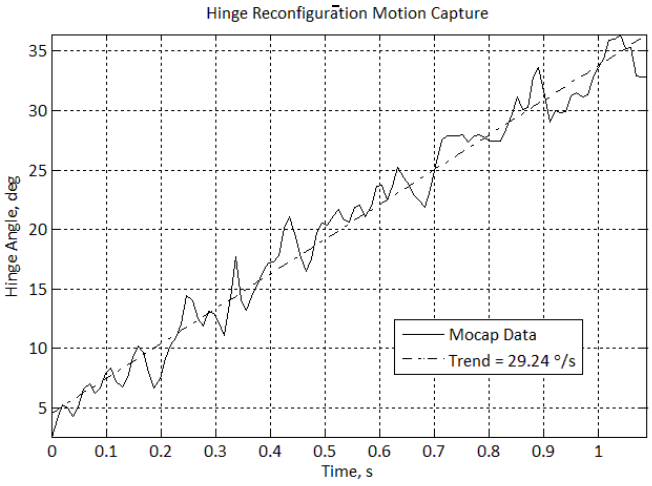

Figure 7.16. Rotation angle of the flux-pinned CubeSat mockup and free-floating dewar about the hinge axis as a function of time.

magnet even as the magnet module swings around from one equilibrium to the other. The rotation angle of the flux-pinned system as a function of time is plotted in Figure 7.16. Although the data contains noise from the pixilated nature of the sensor system, the overall rotation of the system with the active FPI is smooth and consistent at approximately 30 degrees per second.

Figure 7.15 (b), on the other hand, shows the system's behavior when the superconductor is no longer cold enough to flux pin. After the magnet module's release, it immediately begins to drift away from the dewar, and does not maintain the close relative distance that FPI-connected spacecraft experience. The axis of rotation of the system is not clearly constrained to the dipole axis of the hinge magnet; in fact, it leaves the body of the module entirely by the end of the clip. These behaviors are typical of a close-proximity system without active control or an FPI in place to alter the dynamics of the system.

This analysis of the high-speed video suggests that the active FPI was able to constrain the free-floating modules to rotate about a specific joint axis defined by the dipole axis of the powerful hinge magnet. Without flux pinning, the CubeSat mockup fails to maintain a close separation distance with the dewar and tumbles about an axis that drifts to its center of mass.

7.2.6 Conclusions from the 2009 Demonstration

The 2009 microgravity mission to demonstrate an FPI in a relevant dynamic environment successfully produced data that advanced the technology readiness of FPI-based non-contacting revolute joints for spacecraft. The implemented FPI was able to maintain a close separation distance between the two free-floating modules and provide for a selectively-constrained system in which the system was able to move about the desired degree of freedom but was constrained in other directions.

The transition from a laboratory environment to a microgravity environment also led to a number of other insights about implementing FPIs in increasingly flight-traceable experiments, particularly in thermal and sensing design of the system. First, the thermal subsystem design is of critical importance, but is also likely to be the source of uncertainty or complications. While LN2 dewars work well in a laboratory environment, designing the system to accommodate a cryogenic fluid in microgravity limited the experiment duration and design, and appeared to produce a somewhat degraded performance in the superconductors. The use of LN2 also required a lengthy pre-flight procedure that consumed the attention of a team member for the entire filling and cooling process.

Another important conclusion from the flight came from the difficulty in obtaining data from the motion-capture camera given the uneven lighting and low-contrast environment. Also, since the camera was fixed to the plane and the modules were not, it was difficult to obtain a set of data long enough to see the relevant dynamics in the system. Placing sensors on board the free-floating modules would have improved this concern significantly.

These insights have informed subsequent FPI research and development efforts, including the additional microgravity mission discussed further in this chapter.

7.3 Project RAGNAR 2010 Microgravity Demonstration

7.3.1 Motivation and Background for the 2010 Demo

For FPIs to advance to a level of technological maturity to be suited for an orbital demonstration, they must be proven effective in a relevant environment. In 2009, the first iteration of a component-level FPI successfully demonstrated a revolute joint in microgravity, but the strength of the results was hampered by the unreliable LN2 cooling solution and low-stiffness pinning, among other factors.[161] In order to build on this work, a second-generation FPI microgravity experiment was developed with a more traceable-to-flight cooling solution and a higher-stiffness FPI mounted on a higher-fidelity CubeSat mockup. This mission, known as RAGNAR (Robust, Autonomous Grappler for Non-contacting Actuation and Reconfiguration) was flown on NASA's Facilitated Access to the Space environment for Technology (FAST) program in Sept. and Oct. of 2010.

Building the RAGNAR modules to a small-satellite scale allows for easy portability to a satellite mission because the relatively low cost and complexity of small satellites make them the most likely candidate for an orbital mission demonstrating FPI technology. Working at this scale also enabled the team to exploit the newly developed FloatCube laboratory testbed that was designed to allow unconstrained three degree-of-freedom motion of CubeSat-scale modules.

The primary mission of the RAGNAR project is to rapidly advance the development of FPIs for spacecraft by demonstrating key components of a working FPI in a relevant environment. The experiment involved recording the behavior of an FPI in microgravity to better characterize the dynamics of the interface and provide a comparison for the frozen-image model used in simulations. These results allow the dynamical model of FPIs to be refined for use in the design of future missions. This more accurate model allows for a better understanding of the capabilities of any simulated FPI. In addition to studying the passive behavior of FPIs, the RAGNAR system is also equipped to study the dynamics of an electromagnetically actuated FPI. While the data were inconclusive on the actively controlled portions of the experiment, this component of the project serves as the basis of the advanced design for a fully autonomous, actively controlled FPI. Together, these technological achievements aim to bring more elements of the FPI design to a technology readiness level of 5 or 6.

The 2010 microgravity mission is also designed to address the shortcomings of the 2009 demonstration. In particular, the thermal system was designed to provide a greater traceability-to-flight for an orbital demonstration by utilizing a cryocooler as its primary cooling method rather than a liquid nitrogen dewar. These CubeSat mockups used in this demonstration also contain sensor, communications, and control subsystems that more closely resemble a flight CubeSat system than the 2009 hardware.

The final goal of the RAGNAR experiment is to develop a system capable of accommodating future FPI demonstrations and experiments. In particular, the

experiment's thermal, communication, and structural subsystems provide a more mature set of designs that can easily be adapted to subsequent FPI experiments. The CubeSat mockups are designed to easily accommodate a variety of internal components and configurations to maximize the reusability of these modules as test articles. The cryocooler is also designed to be used on future experiments and be traceable to a future orbital demonstration.

As is shown in subsequent sections of this paper, the RAGNAR project successfully accomplished these goals and considerably advanced the development of FPIs.

7.3.2 Experiment Design

The RAGNAR experiment is based around a plane-mounted Q-drive cryocooler with a YBCO superconductor disk attached to its coldfinger. This platform for cooling the superconductor remained stationary relative to the plane, while various free-floating magnetic field sources formed an FPI with this station as shown in Figure 7.17. Two different magnetic modules were used to track the behavior of the system: a tracking magnet consisting of a foam-covered permanent testing magnet, and a CubeSat-based magnet module equipped with more sophisticated on-board systems to better approximate the systems on an actual satellite. The tracking magnet was intended to be used for gathering passive dynamics data to match to the system model, while the CubeSat

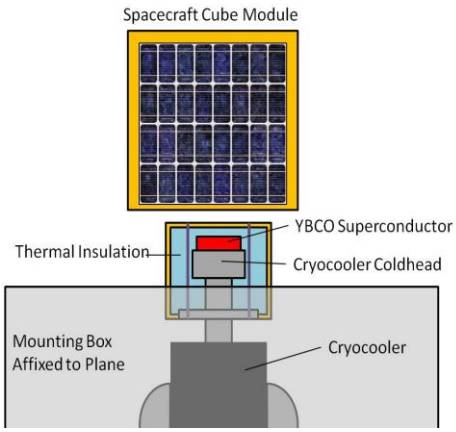

Figure 7.17. A schematic of the FPI used in the experiment.

magnet module was intended to show active control of the system by commanding its electromagnets and actuating the system.

7.3.3 Experimental Hardware

The hardware used in Project RAGNAR comprised several distinct components working in concert to simulate a close proximity spacecraft operation. The three primary subcomponents of the RAGNAR system are: the magnetic modules, which produced the magnetic-field portion of the FPI, the thermal system, which contained the cooled superconductor in the FPI, and the sensor/control subsystem which recorded the data and controlled the experiment. During the experiment, the three subcomponents were physically separate, interacting only wirelessly or through a flux pinning interaction. As with the 2009 mission, the experiment also included structures to attach the equipment to the plane for the experiment. The laptop briefcase containing the sensing and control system from the 2009 experiment was simply re-used, and a new Pelican case was obtained to house the cyrocooler assembly. These elements are not discussed in depth because they do not vary significantly from the equipment described in the 2009 experiment summary.

Magnetic Modules: Tracking Magnet and CubeSat Mockup

The two free-floating modules that provide the magnetic fields in the FPI for the experiment consist of a Neodymium magnet covered in foam (shown in Figure 7.18a) and a module approximating a CubeSat (shown in Figure 7.18b and c). The magnet, with its smaller mass (60.5 g) and closer approximation of a dipole magnetic field, was used as a tracking target for motion capture data illustrating the dymanics of a FPI

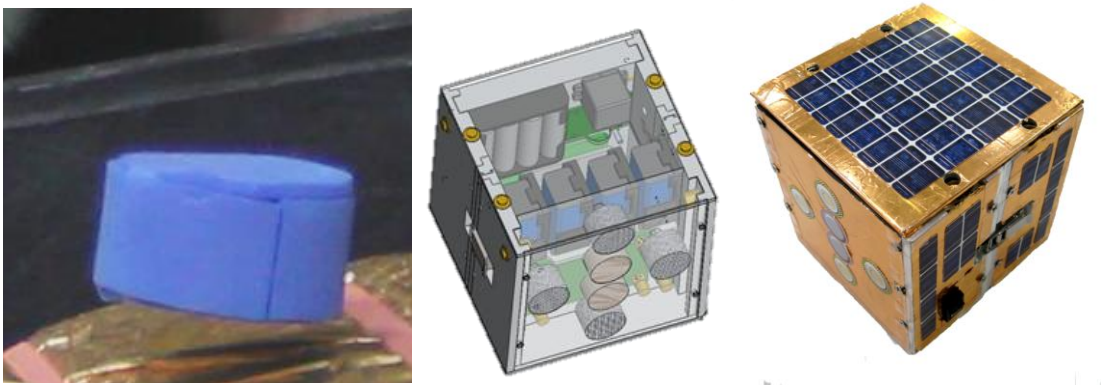

(a) (b) (c)

Figure 7.18. (a) The foam-covered neodymium tracking magnet (b) The CubeSat module design rendering (c) Fully assembled CubeSat module.

in microgravity. The magnet, which is calculated to have a field strength of 0.5233 T, is 2.54 cm in diameter and 1.27 m high, with an inertia of:

$$\begin{bmatrix} 0.3252\text{e-}5 & 0 & 0 \\ 0 & 0.3252\text{e-}5 & 0 \\ 0 & 0 & 0.4879\text{e-}5 \end{bmatrix} m^2 \cdot kg$$

The CubeSat mockup module, on the other hand, is designed to approximate a CubeSat satellite. For the mockup, each side is approximately 12.5 cm, and the total mass is 2.9 kg. Although this mass is nearly three times that of a standard CubeSat, the extra mass is necessary to provide robustness in the design that is needed to withstand an experimental microgravity flight environment. The inertia is:

$$\begin{bmatrix} 0.00883 & -0.00016 & 0.00003 \\ -0.00016 & 0.0101 & -0.00001 \\ 0.00003 & -0.00001 & 0.00936 \end{bmatrix} m^2 \cdot kg$$

The CubeSat mockup supports a variety of experimental components for both RAGNAR and future experiments. The modules are composed of two half cube structures, each with a slot that allows a card to be inserted and removed without

disassembling the entire structure. Changing the experiment is a matter of removing the card and inserting a new one into the module. The cards are secured in half-cubes and the two half-cubes are secured together to form the module. The hardware is secured together using spring-loaded quick release pins, making the assembly and reconfiguration of the modules possible in a matter of seconds. The fully assembled hardware can be seen in Figure 7.18(c). Several different types of cards have been built to give the spacecraft modules the functionality necessary for flux pinning experiments.

The magnets that form the magnetic component of the FPI in the CubeSat mockup are mounted on one type of card used in the experiments. This card includes two permanent magnets of the same size and strength as the tracking magnet, both mounted in the center of the cube in the same dipole direction to provide stiffness in all degrees of freedom. Four electromagnets ring the permanent magnets, each 2.54 cm in diameter and capable of being powered to 12 V. These actuators can be remotely activated in either magnetic dipole direction when desired, but were not powered during the field cooling process. A second type of card provides communications with the computer used in the experiment, commands the use of the electromagnets, and provides motion history data for the movements of the module in which it was contained. This sensing card uses wireless Bluetooth to receive commands from the computer which are then given to the electromagnets in the magnet card. The sensing card also contains an inertial measurement unit (IMU) with a gyroscope and several accelerometers. The IMU provides a record of the module's

motion during the experiments and records the data to an onboard flash memory card mounted on the sensing card.

Superconductor and Cryocooler Assembly

The YBCO superconductor disk, which provides the second part of the FPI, is mounted directly to a cryocooler assembly which keeps the superconductor below its critical temperature. The thermal subsystem components are detailed in Figure 7.19. The cryocooler, a Q-Drive 2S102K pulse-tube model, was powered by the plane's onboard suppy and cooled by venting heat to the surrounding air. In addition to the internal cryocooler fans, two more fans were used in conjunction with ventilation ducts to ensure steady airflow through the cryocooler housing and achieve better cooling performance. The YBCO temperature can be monitored during the experiment via a thermocouple bonded to its surface. The thermocouple reader is positioned next to the cryocooler in clear view of the experimenter managing the magnetic module. All of these components are housed in a flight-rated Pelican case which protects the

(a) **(b)** **(c)**

Figure 7.19. (a) YBCO superconductors (b) The Q-drive cryocooler used in the experiment (c) The structural housing and ventilation system for the experiment

equipment and allows it to be mounted to the aircraft. A top-down view of this assembly is shown in Figure 7.20.

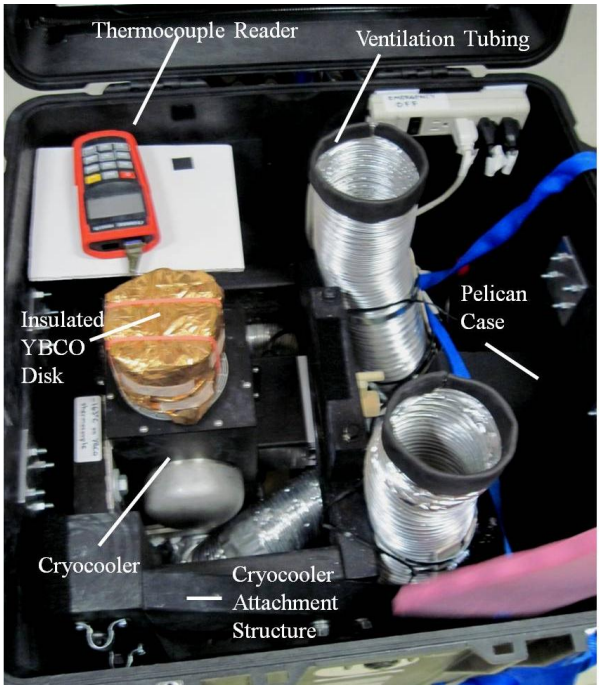

Figure 7.20. The arrangement of the equipment in the cryocooler attachment case.

Sensing and Command System

The primary sensor in this system is the same high-speed 100 fps 640x480 motion capture camera used in the 2009 microgravity experiment. This camera provides high-framerate video of the experiments, which can be used in subsequent motion-capture analysis to track the dynamical behavior of the FPI system. In the RAGNAR setup, the camera is mounted next to the experiment's laptop computer, as seen in Figure 7.21, approximately four feet away from the experimental FPI testing area. In addition to recording this video data, the laptop records the commands it sends to the CubeSat mockup and an associated timestamp. The experimenters can then sync the dynamics data with the electromagnetic inputs to the system. These data sources, coupled with the recorded on-board IMU data in the CubeSat module, enables experimenters

Figure 7.21. The laptop sensing and commanding station across from the cryocooler assembly.

to understand the complete picture of the state of the system during the experiments.

7.3.4 Operations and Procedures

Understanding the procedures that were followed during the operational phase of the mission is critical to interpreting the results of the experiment. The team was granted two flight days and made the decision to perform both the tracking magnet and CubeSat mockup experiments on both flight days. However, the first flight day produced the highest-quality results from experiments that used the free-floating tracking magnet to explore flux pinning dynamics in microgravity. The second flight day was primarily dedicated to using the cube module to demonstrate a simulated close proximity spacecraft operation.

Because the RAGNAR system uses a cryocooler rather than a dewar of LN2, the procedures for each phase of the flight (pre-flight, pre-experiment, data collection, and stowage) are significantly different from those used during the 2009 mission. One of the most important differences is that the ground preparation requirements were significantly reduced and therefore did not require continual monitoring by a member of the team.

(a) (b)

Figure 7.22.(a) An experimenter seated behind the laptop/camera assembly structure, which sends commands to the spacecraft module and collects the data from the high-speed motion capture camera (b) Two additional experimenters were responsible for the free-float objects and up-close data collection.

Three members of the research team were present on the aircraft as experimenters

during each flight. One experimenter controlled the laptop, overseeing the data collection and sending commands to the cube module through a custom GUI when required, as shown in Figure 7.22(a). The other two experimenters were both adjacent to the cryocooler system assembly and operated the remaining equipment, as shown in Figure 7.22(b). Their tasks included operating the cryocooler and thermocouple, taking video data from a second perspective to capture any data difficult to detect from the laptop station angle, and controlling the free-floating modules in microgravity when they were engaging the FPI.

Pre-Flight Procedures

The RAGNAR pre-flight experiment procedures primarily revolve around checking the flight equipment and establishing a field-cooled image in the cooled superconductor. In order to check that the equipment is functional, the experimenters check the battery life of the equipment, take a test motion-capture video, and ensure that the data storage cards are in place on the CubeSat mockups. Once these checks are performed, the equipment is shut down to conserve battery life.

The cyrocooler assembly was mounted in the plane in the days prior to the experimental flights, so the field-cooling process took place on board the plane itself. As seen in Figure 7.17, the RAGNAR setup has the YBCO disk wrapped in thermal insulation and mounted to the top of the cyrocooler's cold finger. Thus, prior to the cooling of the YBCO disk, a magnetic module was placed on a spacer over thermal insulation covering the cryocooler, providing a separation distance for both of the magnetic modules during the experiment of approximately 1.6 cm (from the top surface of the superconductor to the bottom surface of the magnet). The cryocooler

requires under 1.5 hours to cool the YBCO disk to below its critical temperature, so the cryocooler was activated at least an hour before the flight and left to run. Unlike the 2009 experiment, this process did not need to be monitored by a team member, and so once the setup was complete, the team was free to perform other activities before take-off. The cryocooler container was left open to facilitate ventilation up until take-off.

Pre-Experiment Procedures

Immediately prior to take-off, the cryocooler container was closed in order to comply with NASA safety procedures. Closing the case reduced the ventilation of the system and caused a heat build-up in the system, reducing the cooling power of the cryocooler. Once experimenters were allowed to move into the experimental section of the plane, the container was immediately opened to begin the ventilation process. The lid was also strapped open to ensure it did not interfere with the experiment. The magnetic module that was field-cooled into the system was placed into position to ensure that the magnetic flux was still captured in the YBCO disk. One of the experimenters turned the CubeSat mockup on. The laptop computer was turned on and connected to the CubeSat mockup and camera. After a quick check of the camera and command GUI, the team was ready for the microgravity portion of the flight.

As with the 2009 experiment, the first three parabolas were reserved for the flight team's acclimation to the environment. Fortunately, two of the three flight members had participated in the 2009 experiment and were able to work in the environment almost immediately. Unfortunately, on the first flight day the lack of ventilation in the box during take-off caused the YBCO disk to warm above its critical temperature, and

the first 10 parabolas were devoted to re-cooling the system with the magnetic module in place. Removing insulation from the cryocooler container on the second flight day prevented this problem from repeating.

Data Collection Phase

The same cryocooler and YBCO configuration was used for both flights; the only difference in the flight setup between the first and second day was the main magnetic module used for the experiment. On both flight days, the FPI was originally field-cooled with the spacecraft module mock-up configuration, and later in the experiment the system was re-cooled with the image of the tracking magnet. When the tracking magnet was the primary magnetic field source, it was directly controlled and physically manipulated by one of the experimenters. Its dynamics were captured primarily via the high-speed motion capture camera and other hand-help video footage. When the spacecraft module was the primary magnetic field source, it was manipulated both manually and via laptop commands. The dynamics of the spacecraft module were recorded via the motion capture camera and handheld video devices in addition to IMU sensors both on-board the module and mounted inside the plane fixture.

Stowage Phase

The final phase of the experiment involved turning off the cryocooler, laptop, and CubeSat mockup and storing them in their containers for landing. The data from the IMUs on the CubeSat mockups were subsequently retrieved from their mini-SD card storage and saved to the computer for later analysis.

7.3.5 Experimental Results

Flight Data Processing

The relevant flight data comes from several minutes of video-recorded flux pinning interactions with both the tracking magnet and the CubeSat mockup. The raw camera footage was processed through the tracking software MaxTRAQ, which identifies high-contrast points in each frame of the video and outputs a file with a timestamp and an x and y pixel location of each identified point in the image. The highest attainable sampling frequency was limited by the camera's limit of 100 frames per second, however, most of the data were collected out of the software at a lower frequency (near 26 fps). Camera drift was removed by tracking points known to be stationary relative to the plane by the camera and then subtracting out that point's motion from the other tracked points in each frame.

The angles and distances relevant to the system were then calculated in units of pixels and degrees. Data points were converted into millimeters where appropriate by using the known size of the tracking target, calculating its size in pixels, and multiplying all other points in that data set by that conversion factor. This approach assumes that in-frame motion causes minimal changes in the pixel size of the object. Finally, the equilibrium positions were calculated using frames where the tracking target is resting in place, and these values were subtracted out of the data set to allow the values to center near zero. The data sets were de-trended for the frequency analysis.

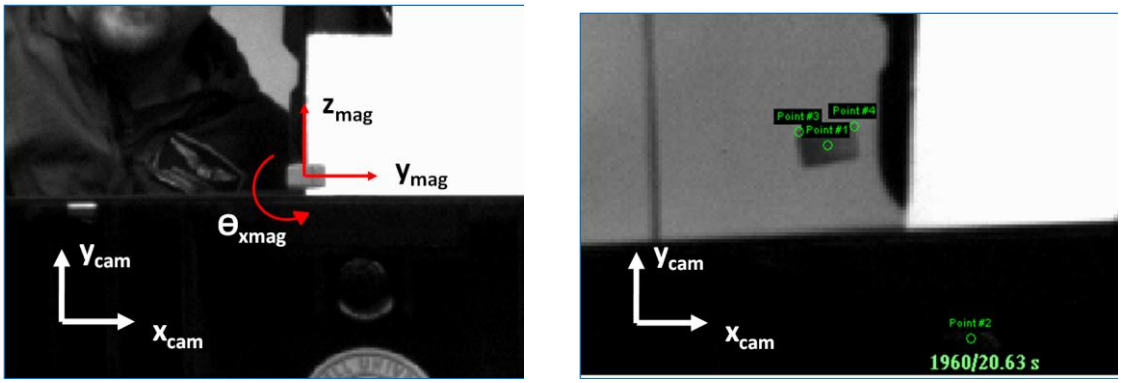

(a) (b)

Figure 7.23. (a) The coordinate systems used in the magnet data. (b) The points collected for the magnet data.

The tracking magnet data was selected from four of the best parabolas (those with the least variation from perfect microgravity conditions) in which the magnet was flux pinned to the superconductor. This data set included at least 8 excitation events in which the magnet was given a manual impulse of a known displacement and unknown velocity. Three degrees of freedom were calculated for each excitation event: the y_{mag} and z_{mag} position of the magnet, and the rotation about the x_{mag} axis, as defined in Figure 7.23(a). Since the magnet is axisymmetric about its *z* axis, any rotation about that axis has no stiffness due to flux pinning, so that degree of freedom was ignored in the data and any rotations in that direction were not considered in this analysis except to ensure that the magnet did not have a large spin rate so as not to influence the motion of other degrees of freedom due to spin stabilization.

The motion of the tracking magnet was calculated by tracking the corners of the top of the magnet and estimating the magnet's center as shown in Figure 7.23(b). The points were assumed to be in the magnet's *y*-*z* plane. The angle about the magnet's *x* axis was calculated directly from the angle of the magnet's top two corners. The *y* position of the center of the magnet was assumed to be halfway between the two corners, and the *z* position was estimated directly. The direct estimate has more uncertainty due to the inexact nature of the point, whereas the calculations have uncertainty due to the combining of error from other points, but the points themselves were known more precisely. The error for a *y* position data set, which was calculated from more precise raw points, and the corresponding *z* position data set, which was directly estimated manually with coarser data points, are shown in Figure 7.24.

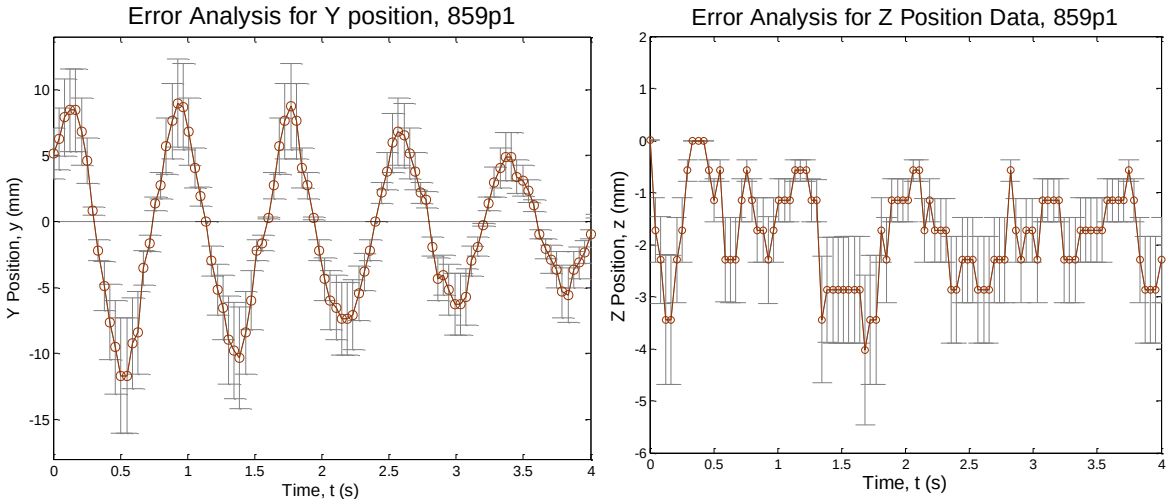

(a) **(b)**

Figure 7.24. (a) Calculated magnet position data (y direction) with error bars. (b) Directly estimated magnet position data (z direction) data with error bars.

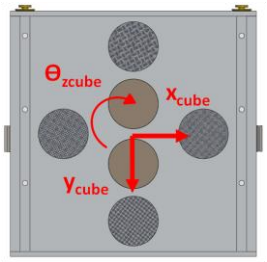

Figure 7.26. The orientation for the magnetic module of the spacecraft cube is oriented in the –*z* direction in the camera frame.

The CubeSat mockup data was collected over 5 of the higher quality parabolas, with 20 free-float events occurring during the time in which the FPI was engaged. As is discussed further in the results section, weaker pinning and a higher vulnerability to unsteadiness in the microgravity environment made the CubeSat dynamics much more difficult to capture, so the response of the system due to manual and electromagnet actuations were not easily discernible, and each free-float event lasted for less time. Thus, the data were zeroed against the initial system states for that parabola instead of an equilibrium point. The cube was oriented on the camera frame as shown in Figure 7.26. Five degrees of freedom were calculated for each free float event: the *y* and *z* position of the cube, and the rotation about all three axes, as defined in Figure 7.25(a). Unlike the axisymmetric magnet, the cube's distinct features make it possible to determine the body-frame coordinates as it rotates in the frame of the camera.

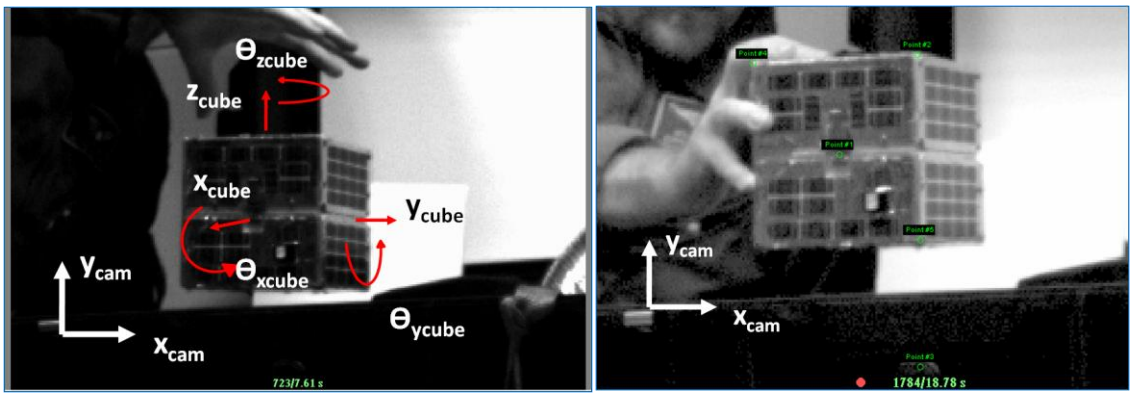

(a) (b)

Figure 7.25. (a) The coordinate systems used in the cube data. (b) The points collected for the cube data overlaid on a screen shot from the captured video.

The cube motion was calculated by tracking the corners of the top and right side of the *y*-*z* cube face. The center of the cube's *y*-*z* face was also tracked as shown in Figure 7.25(b). The direct estimate of the center of the *y*-z cube face contains less uncertainty than the magnet's center due to the fact that the cube face center has distinguishing features that were easier to track. The rotation about the *x* axis was calculated the same way as the magnet's *x* rotation angle was calculated: using the angle between the top line of the face and the camera's frame. The rotation angles about the *y* and *z* axis, however, were calculated using the length of the cube edge in the *y* and *z* directions compared to the known length of the edge at zero rotation. The cosine relationship of the foreshortening of the edges makes it possible to extract the values of the rotation.

IMU data was also captured for the CubeSat mockup experiments. The Analog Devices IMU, which is the same one used in the laboratory testbed work, captures data at over 800 Hz. This high sample rate makes it difficult to record the information quickly enough to record in real time, so data was periodically dropped to allow the system the time necessary to record the rates and accelerations captured by the sensor. A sample of the IMU data collected during an experimental run is shown in Figure 7.27, where the lines represent a smoothed interpolation of the data and the points are the raw data recorded by the system. Unfortunately, this dropped-data approach and the difficulty of matching timestamps on the laptop to those on the CubeSat mockup led to inconclusive results when analyzing the electromagnetic actuation of the system. For example, the vertical dashed line in the data represents the time at which the laptop computer sent a command to the electromagnets in the CubeSat mockup

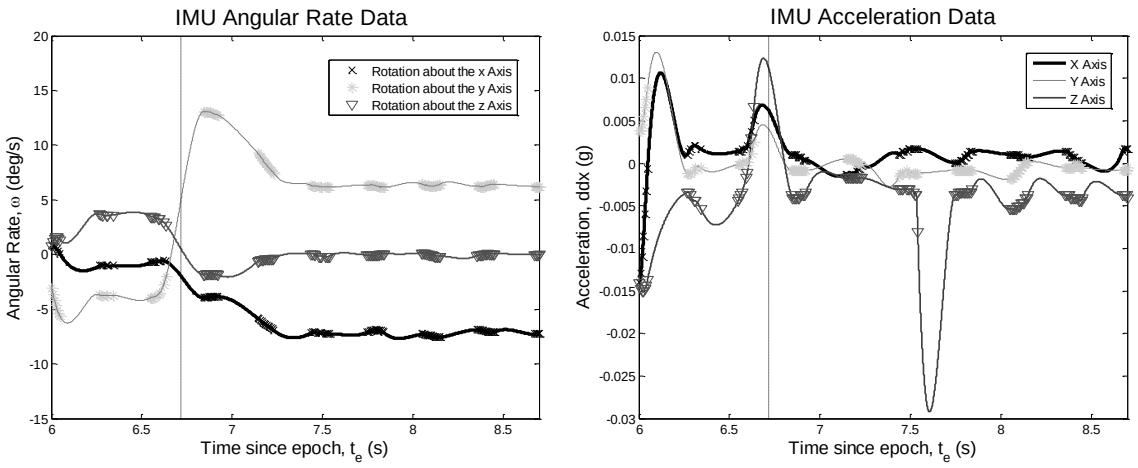

(a) (b)

Figure 7.27. (a) IMU angular rate data captured during a CubeSat run (b) IMU acceleration data captured during a CubeSat run.

that would have induced a rotation about the *y* axis. However, data is not continuous in the region of interest and the uncertainty in the timestamps makes it difficult to determine if the electromagnet was triggered at the beginning of the apparent rotation of the CubeSat mockup, or if the module had already started rotating due to another disturbance in the environment.

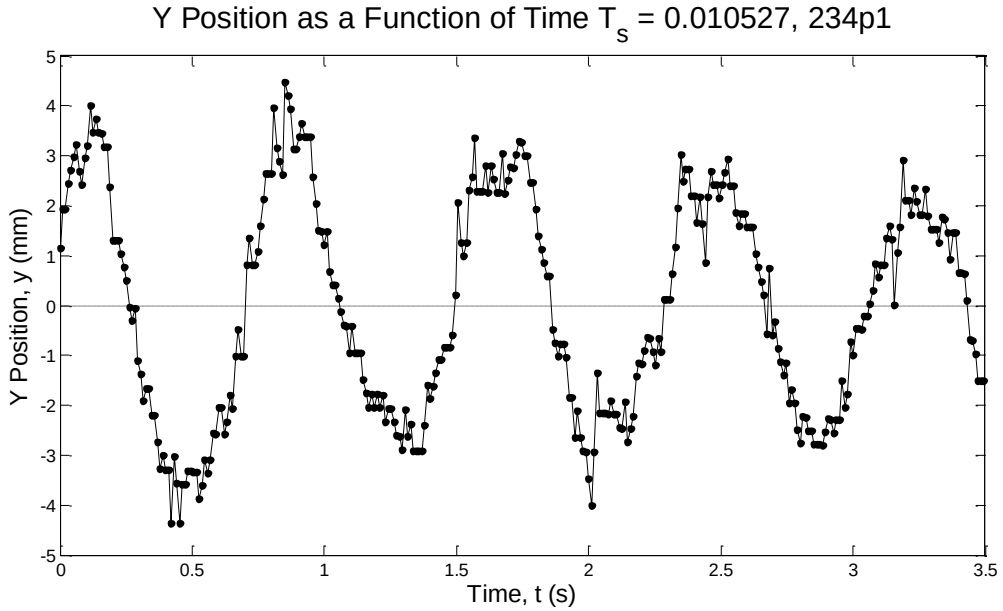

Figure 7.28. Time history of y position data collected at the maximum sampling rate, 95fps.

Tracking Magnet Dynamics

The recorded tracking magnet dynamics showed clear signs of nonlinear oscillations in a moderately stiff FPI. The system rejected perturbations experienced in the microgravity environment (caused by turbulence as the plane flew the parabolic flight pattern) and was able to stay stiffly connected to the superconductor for as long as the plane's arc approximated a microgravity environment (up to 17 seconds of free-response time). The equilibrium position in the microgravity environment is offset from the field-cooled position by about 8 mm, and all of the data is shown relative to the equilibrium position.

The motion-capture analysis software was not capable of automatically tracking the relevant points on the magnet, so the tracking had to be completed manually. Performing this analysis can be a time-consuming process, particularly at a near-100 Hz sampling frequency.

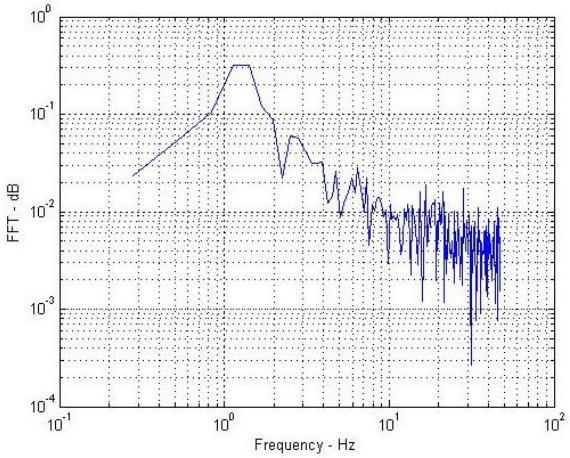

Figure 7.29. Example of the frequency analysis of the 95 Hz data set in Figure 7.27.

Figure 7.28 shows a selection of *y* position data for the magnet recorded from the motion-capture camera at the full 95 frames per second. The frequency analysis of this data (the *y* data is shown in Figure 7.29) suggests that the dominant frequencies are all on the order of 10^0 Hz. Thus, the 95Hz data was downsampled to 20 frames per second or higher without creating a sparse data set that does not fully capture the predominant dynamics of the system.

An analysis of the frequency content of the passive tracking magnet response can be seen in Figure 7.30. For this plot, the frequency responses of three excitation events with different initial conditions from the same parabola were averaged together. Each response time was truncated to be approximately 4.8 seconds long, and the sampling frequency for all of the data was sampled at 24 fps. Although the system is not linear, it can be useful to apply linear tools to the system, so the linear damping coefficient is estimated for each frequency. The dominant frequency in the *y* position direction is 1.25 Hz and the linear damping coefficient *c*, estimated from the full width of the primary peak at half of the maximum altitude, is 0.148 kg/s. For the *z* position frequency response, the frequency value was estimated to be slightly lower, at 1.04 Hz and the damping coefficient was estimated to be higher, at 0.248. The rotation about the *x* axis was measured to have a dominant frequency near 1.25 Hz as well, and a damping coefficient of 0.157.

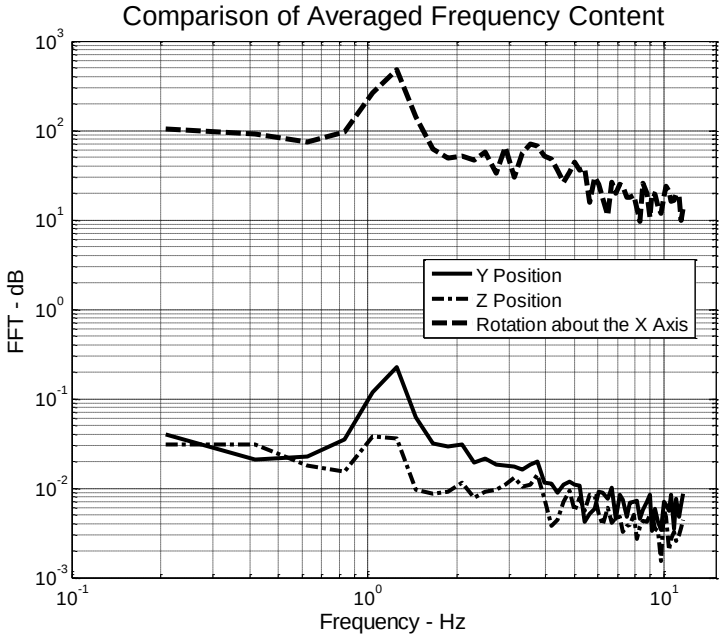

Figure 7.30. Averaged frequency response data for the *y* position, *z* position, and rotation about the *x* axis.

At small displacement values, flux pinning can be approximated as a damped harmonic oscillator. For the tracking magnet, this is especially true of the *y* position

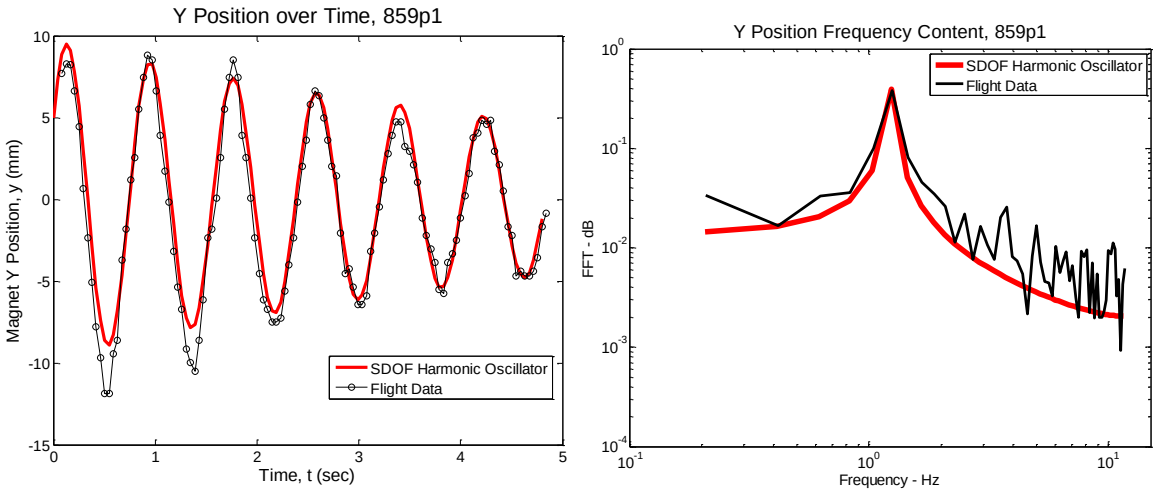

(a)

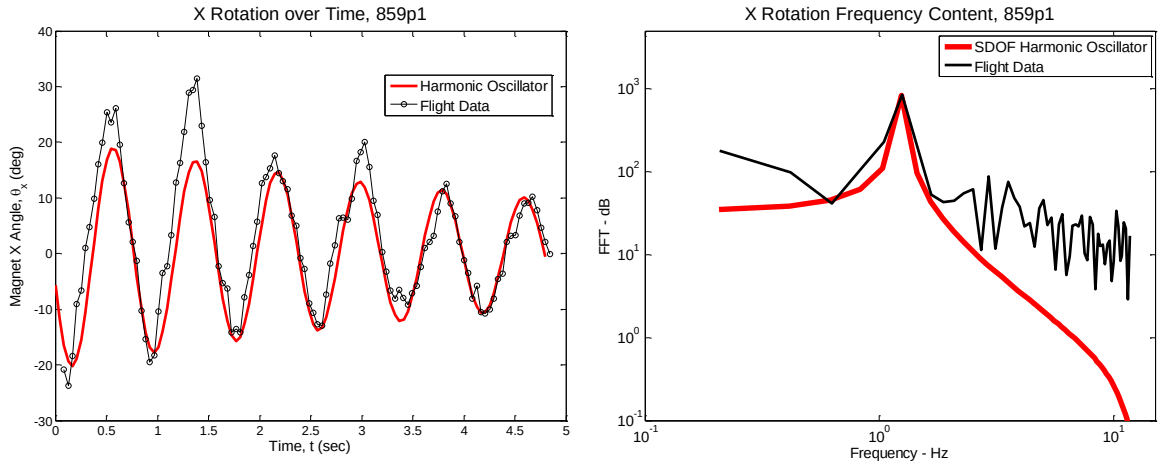

(b)

Figure 7.31. Time history and frequency flight data compared to a simple damped harmonic oscillator for the (a) *y* position and (b) *x* rotation of the magnet.

and rotation about the *x* axis. A representative flight data set is plotted against the results of this model in Figure 7.31. The *y* position values and the *x* rotation values show a convincing correlation to the linear harmonic oscillator expressions, suggesting that the transverse motions of the tracking magnet FPI can be approximated with a linear response, even with amplitudes as high as a centimeter from the equilibrium.

In order to estimate the linear equivalent of the damped natural frequency and damping coefficient, each tracking magnet data set was compared to the response of a

harmonic oscillator in which the damped natural frequency, damping ratio and initial velocity were tuned to provide a minimum residual sum of the squares value between the simulated response and the flight data. This procedure was completed for each data set and then averaged together. Using this method, the equivalent linear damping ratio is 0.0184 for the *y* position and 0.071 for the *x* rotation angle. The damped natural frequency is 1.22Hz for the *y* position and 1.23 Hz for the *x* rotation angle. Although the *z* position does not fit a linear pattern even at small displacements, the average best-fit linear damping ratio is 0.055 and the damped natural frequency is 1.25 Hz.

A linear approximation of the system can therefore capture some of the tracking magnet FPI system characteristics, particularly for the data sets that did not appear to excite strong nonlinear modes. However, it is clear that this approximation does not capture all of the relevant dynamics in the system, particularly in the *z* position data (an example of which can be seen in Figure 7.32). Also, certain excitation events (such as perturbing the magnet by pushing it closer to the superconductor than its original

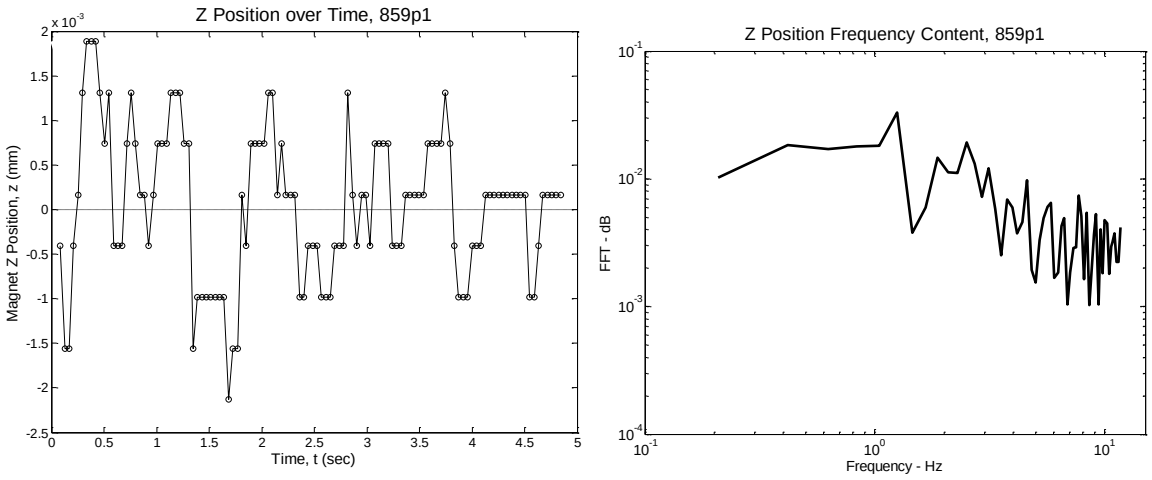

Figure 7.32. Time history and frequency flight data for a representative *z* position.

equilibrium) appeared to excite nonlinear modes in the other degrees of freedom as well. In order to attempt to capture these critical nonlinearities, it is necessary to move to a more sophisticated model of the dynamics.

The frozen-image model, discussed in Chapter 3, is a nonlinear analytical model of flux pinning that can be used to calculate the forces and torques acting on a spacecraft under the influence of an FPI. This model assumes an infinite superconductor and dipole magnets, so while it can produce analytical expressions to describe the system's behavior, it is subject to limitations in its applicability to real FPI systems. In order to use the frozen-image model to produce a nonlinear approximation of the flight dynamics, it is necessary to approximate the tracking magnet's strength as a dipole. Given the dimensions of the magnet and the measured strength at the magnet's surface (0.5233 T), a magnetic dipole moment of the system is approximated by:

$$\boldsymbol{\mu}_i = \left(\frac{2\pi B_i d_i^{\,3}}{\mu_0} \right) \hat{\boldsymbol{\mu}}_i \tag{7.1}$$

where B_i is the surface strength of the magnetic field of the dipole measured along its axis and d_i is the distance from the center of the magnet to its surface.

In addition to the magnet's strength, the field-cooling and initial conditions are inputs to the model. The field-cooled position can be estimated as the equilibrium position, which is found by measuring the position of the system relative to the known location of the superconductor in the frame of the camera prior to any excitation. For the flight data of interest, this value is 1.5 cm above the superconductor. The initial conditions are known from the video data, which shows the tracking magnet being physically displaced in the frame of the camera. For example, in the data run being

compared to the simulation, the magnet is displaced -3.48 mm in the *y* position and -4.31 mm (closer to the superconductor) than the equilibrium distance in the *z* direction. There is also an initial angle of 6.432 degrees. The initial velocity and acceleration of the magnet is assumed to be zero. It is also possible to produce damping coefficients based on the linear damping ratios (ζ), damped natural frequencies (ω_d) found previously, and the mass of the magnet (m) using the equation:

$$c = 2\zeta m\left(\frac{\omega_d}{\sqrt{1-\xi^2}}\right) \tag{7.2}$$

The calculated damping coefficients are then 0.00853 kg/s for the *y* position, 0.0333 kg/s for the *x* rotational state and (although not a very accurate estimate) 0.0262 kg/s for the *z* position.

In order to best evaluate the nonlinear model's efficacy in capturing the nonlinear dynamics in the system, the run that was selected for a more detailed analysis has over 10 seconds of data in which nonlinear modes appear to be excited in all of the observable degrees of freedom, as seen in the multi-modal frequency response of the data shown in Figure 7.33. The simulation and flight data are overlaid in Figure 7.34.

The nonlinear model is clearly a more complex representation of the results than the linear model offers, but the overall conclusion can be drawn that the initial simulation does not match the flight system's behavior closely. However, similarities between the simulated and experimental results can be observed. In the *z* position data, the simulated results show nonlinear response at positions below the equilibrium line, where the FPI exhibits a much stiffer reaction to the magnet, preventing it from completing a traditional linear sinusoidal response. The *z* position flight data bears out

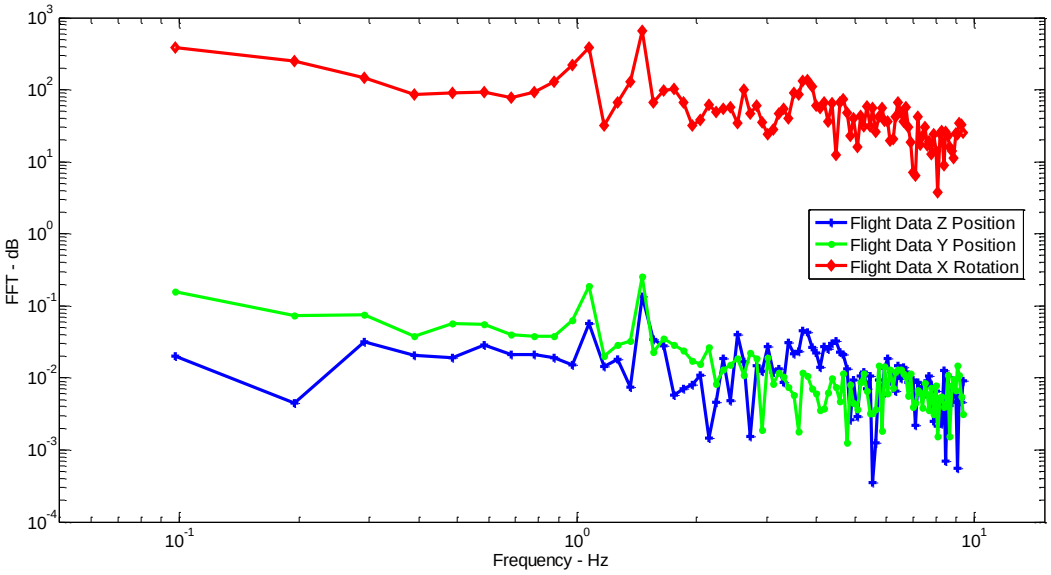

Figure 7.33. The nonlinear frequency response of the different degrees of freedom in the selected flight data.

this relationship to the equilibrium as well, as the flight data shows the magnet spending less time below its equilibrium and exhibiting shallow non-sinusoidal behavior when it in that region. In the *y* position, the first peak is approximated well, but the flight data falls out of sync with the simulated data after that point. The flight data and simulated data both exhibit a distinctive beat pattern that, while not of the same frequency or amplitude, appears to roughly follow the same form.

Although the similarities in the data are worth noting, the differences between the simulation and flight data are much more apparent. It is clear that in general the damping coefficient in the simulation is much higher than the damping exhibited by the system during the experiment, particularly in the *x* rotation degree of freedom.

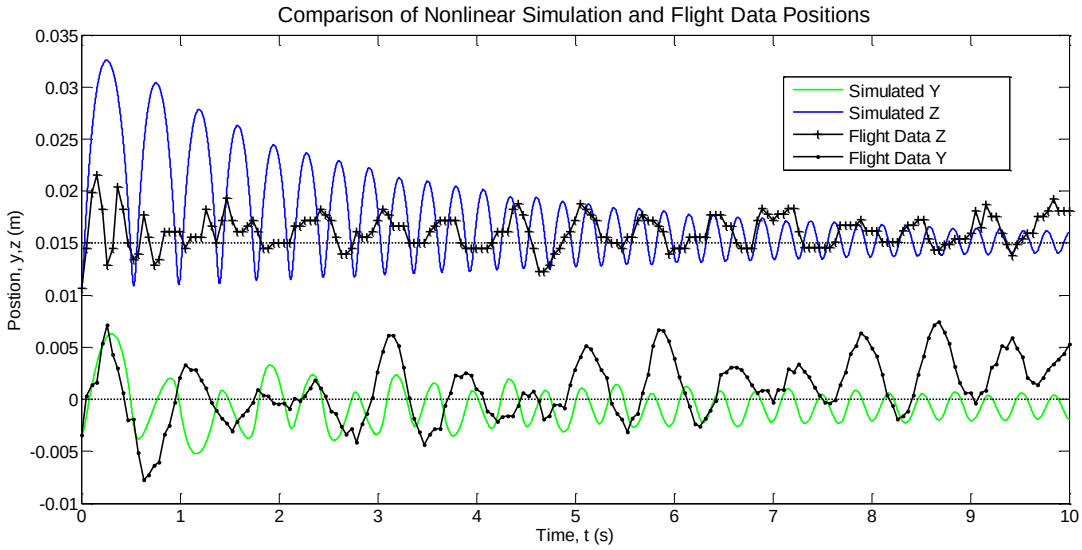

(a)

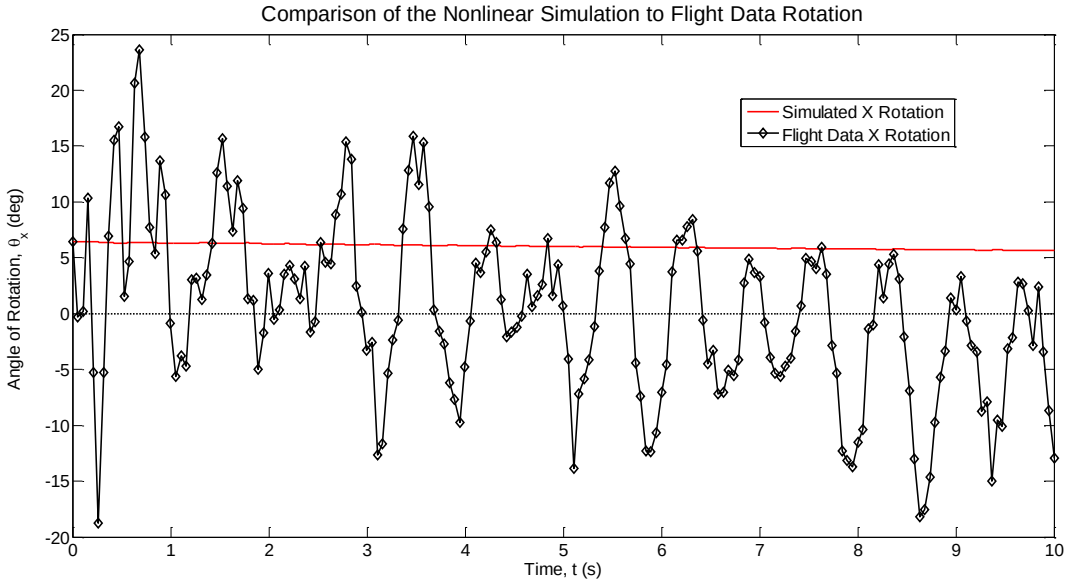

(b)

Figure 7.34. Nonlinear model and flight data comparison in the (a) *y* and *z* positions and (b) *x* rotation.

The flight data in the *z* position has an initial apparent higher-frequency transient response that is not captured by the simulation data. Once the flight data settles into a more consistent pattern, it appears to have a frequency of roughly half that anticipated

by the simulation. The initial amplitude of the simulation's response is also just under twice the actual flight data. These facts point to the conclusion that, in the *z* position at least, the pinning was not as stiff as it was initially expected to be.

In the *y* position, the simulation is also repeating the beat sequence at a slightly higher frequency than the flight data appears to be, which also points to a lower-than-expected stiffness in the flight data. The damping in this degree of freedom is clearly very low compared to the simulation and even prior, more linear excitations. There is also a trend away from the equilibrium at the end of the data set, which is not captured by the simulation. This trend may be the result of the strong trending in the rotational degree of freedom that is also not captured in simulation.

The rotation about the *x* axis exhibits strong differences between the flight data and the simulation. In particular, the flight data shows a much stronger oscillatory behavior with high amplitudes of 20-30 degrees. The simulated motion predicted small oscillations, but on the order of one degree in amplitude. This behavior is one of the most marked differences between the simulation and the flight data, indicating that one of the assumptions in the system may not be correct. For example, the presence of these strong oscillations in the flight data may indicate that the system was imparted with a non-zero initial angular velocity that cannot be measured in the video. It is also possible that the damping coefficient is much higher in simulation, effectively stopping the high oscillations seen in the flight data.

Taken as a whole, these results suggest several conclusions. First, the damping in the system is clearly less than predicted by the linear estimates. It is also clear that the angular rotation of the system departs significantly from the expected behavior, but it

is unclear whether that departure is due to uncertainties in the experimental setup, or in fundamental differences between the simulation and reality. Also, the position data in both degrees of freedom suggest that the RAGNAR FPI produced a lower stiffness than expected. This observation can be the result of a few different factors. The estimated dipole strength may have overestimated the actual strength of the magnet. It is possible that the field-cooling distance estimated from the system setup is actually farther away than calculated. Another possibility is that fluctuations in the YBCO disk's temperature caused it to lose flux, and thus causing it to produce a reduced-stiffness response.

In order to illustrate how simulation values can be selected to take these conclusions into account, Figure 7.35 shows the results of a simulation with different parameters compared to the same flight data. This model uses a weaker surface strength (0.4233 T) to produce a smaller magnetic moment for the dipole. It also imparts a non-zero initial angular velocity (-0.5 deg/s) and decreases the damping ratio of the z position and the x rotation states by one order of magnitude. The other parameters were taken from the initial simulation.

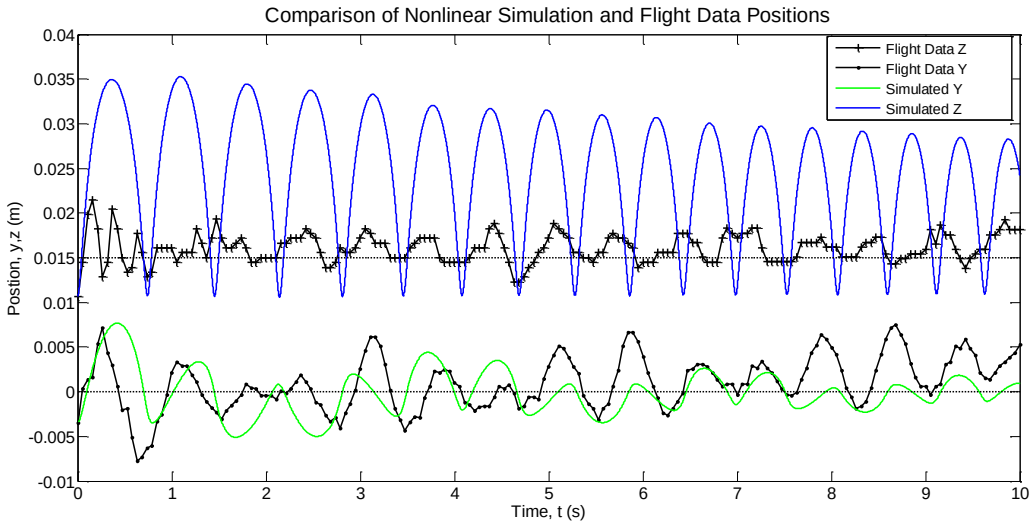

(a)

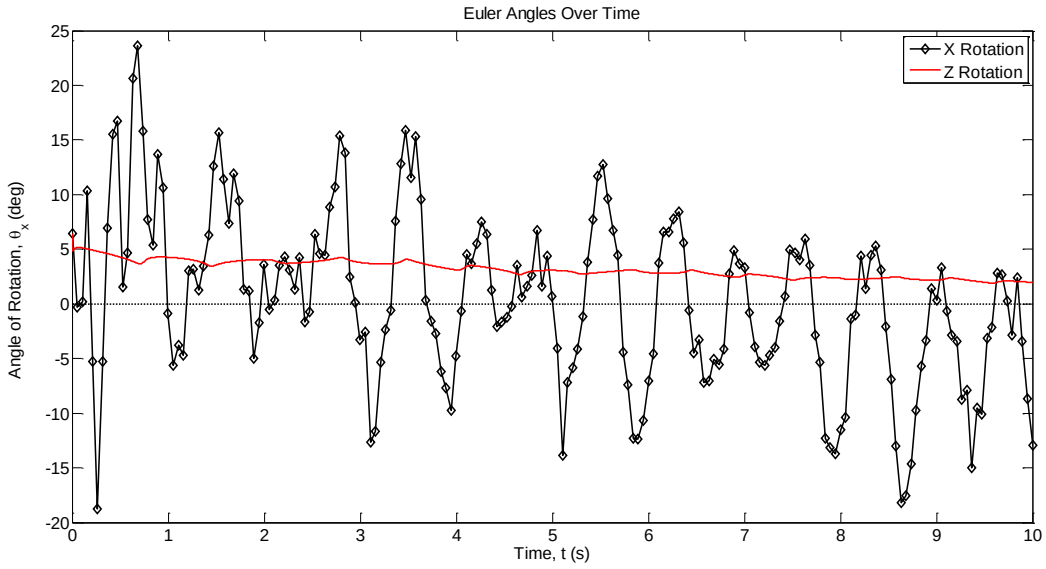

(b)

Figure 7.35. Nonlinear model and flight data comparison in a model with updated values for (a) *y* and *z* positions and (b) *x* rotation.

The results of this updated simulation appear to match better in the *y* and *z* position data, particularly in the frequency domain, which is likely due to the 0.1 Tesla change in the magnet's input surface strength. The reduced damping in the *z* direction appears to bring the simulation more in line with the system's behavior, but the amplitude is

still two-to-three times that of the flight data. This discrepancy may be caused by inexact modeling of the initial conditions of the system, particularly the inability to determine initial imparted velocities or accelerations. The *y* position appears to be of comparable amplitude, damping, and frequency between the simulation and flight data, but there are clearly notable differences between the data sets. These differences may in fact be the result of cross-coupling with the poorly-modeled *x* rotation degree of freedom. While decreasing the damping ratio of the *x* rotation appears to allow the system to trend toward its equilibrium faster, and thus follow the general trend of the flight data, the oscillations in the data are still very low-amplitude compared to the flight data. Once again, the oscillations may be an error in modeling the initial conditions of the system, but the significant discrepancies suggest that the frozen-image model may not model the rotational degree of freedom particularly well. More accurate flight data is needed for comparison to determine a more general conclusion on this front.

CubeSat Mockup Dynamics

While the flight team clearly observed flux pinning effects with the CubeSat mockup, the dynamical response of the system exhibited low-stiffness behavior and the FPI had difficulty rejecting perturbations due to changes in the microgravity environment. A representative sample of the cube's performance is shown in Figure 7.36. This data shows the cube hovering in a position for only 0.4 seconds before beginning to drift away from the test area. After only a second the effect of this drifting was large enough to necessitating the termination the free-float segment (the experimenter monitoring the CubeSat module's motion was required to move it back

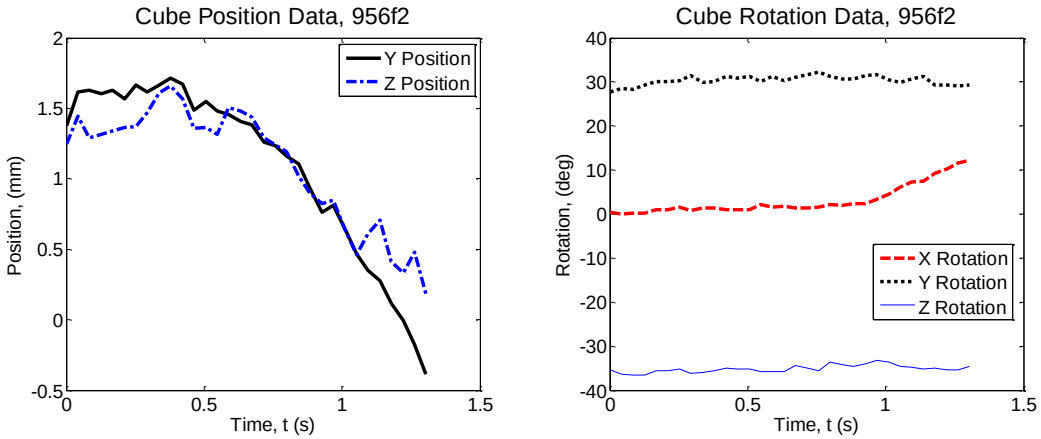

(a) **(b)**

Figure 7.36. (a) Sample CubeSat mockup position data and (b) rotation data.

into position over the experiment area). This performance was typical of the other

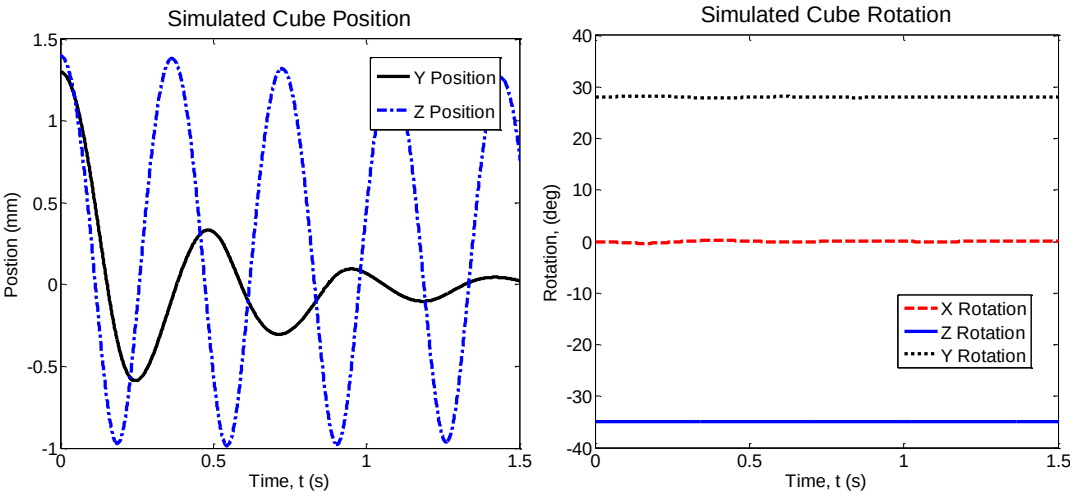

(a) (b)

Figure 7.37. An example of the simulated performance of the passive CubeSat mockup dynamics given an offset from the equilibrium in the *x*, *y*, and *z* position for the (a) position and (b) rotational dynamics.

CubeSat mockup experiments, and the continual interruption of the free-floating dynamics made it difficult to obtain a segment of data long enough to compare to simulated results. However, it is clear that the simulations would not have matched the flight data because simulations of the CubeSat mockup dynamics (discussed in more detail in Chapter 5) had shown that the permanent magnets in the FPI were sufficient

to maintain the CubeSat mockup's equilibrium in the presence of disturbances, as shown in the clip of simulated data in Figure 7.37.

There are several possible reasons for this significant departure from the CubeSat mockup's flight dynamics and expected dynamics. First of all, it is possible that the uncertainties in the experimental setup were significant enough to make the simulated results not applicable to the implemented system. In particular, the cryocooler experienced fluctuations in temperature (as read by the thermocouple attached to the superconductor disk) that may have caused a loss or shift in flux. It is possible that the system experienced hysteresis in the microgravity environment as the CubeSat mockup was being handled around the superconductor, causing unmodeled behavior to result. It is also possible that the model's assumptions broke down on the flight, making a comparison invalid. For example, unmodeled edge effects of the superconductor or the non-dipole field of the magnets may have played a larger role in the dynamics of the system than was predicted. The size of the module also caused the frequency of the system when perturbed to be large enough that very few cycles could be recorded during each of the 20 second intervals of microgravity. The effects of the FPI were observed by experimenters during the experimental runs, but the frequency content and stiffness of the system were not reliable from the data. Although the CubeSat mockup did not produce experimental data suitable for comparison to simulation, these discrepancies do provide insight into possible pitfalls of the current model and suggest that further research is needed to fully understand and implement a system as complex as the full CubeSat mockup FPI in microgravity.

7.3.6 Conclusions from the 2010 Demonstration

The RAGNAR project, as the second microgravity flight in which a flux-pinned interface for spacecraft was flown, successfully demonstrated a working FPI in microgravity with a more mature thermal and spacecraft system than in the previous flight. The hardware developed for these experiments provides the basis for future work done on testing FPIs. The unambiguous footage of a magnet operating in the FPI provided a rich set of data that can be correlated against linear and nonlinear models of flux pinning.

The magnet system in microgravity had a different equilibrium than its field cooled position in the *z* direction by about 8 mm, which was not modeled. The magnet system's dominant frequencies can be adequately sampled by a 24 fps data sample, and in the linear spring-mass-damper model is a reasonable approximation for small motions of the magnet, particularly in the *x* rotation and *y* position. Natural frequencies of the system were found to be on the order of 1.25 Hz and damping ratios were on the order of 0.01 – 0.07. However, the *z* direction motion is not accurately approximated by a linear system and should not be modeled as such.

The nonlinear model, which assumes an infinite superconductor and perfect dipoles, shows a complex relationship to the flight data, but overall trends are preserved, including a beat pattern in the *y* position data and the nonlinear inverted peaks in the *z* position. The simulated prediction of the response shows a stiffer system than the flight data, indicating a weaker pinning effect actually occurred during the experiment. This weaker pinning may occur when the field-cooling process is interrupted or if the magnetic field strength is weaker than the calculated dipole

approximation. When the flight data is compared to a simulation with less damping and a lower magnet strength, it appears to be able to match the frequency content and general form of the flight data in the position data, but the rotational state retains significant differences between the simulation and experiment. More data with precisely known initial conditions is necessary to make this determination.

Because the spacecraft module was designed around a flux-pinned interface with relatively low strength interactions, the interface was vulnerable to interference forces from the plane environment. Future flux pinning experiments will have to investigate options for significantly increasing this relative strength of the magnets to allow a more clear demonstration of the predicted interactions and prevent significant interference from the flight environment. The design decision to not collect all of the data from the IMU led to inconclusive results from that data source, and the low stiffness of the FPI made it impossible to obtain video data comparable to the simulation. Despite these drawbacks, the FPI was observed influencing the dynamics of the CubeSat mockup in microgravity and the flight experiment led to a number of design insights in the implementation and testing of FPIs.

Ultimately, the results of this microgravity experiment have proven to be a starting point for a number of new initiatives and improvements that have helped fast-track flux-pinned interfaces for spacecraft up the Technology Readiness Level scale.

CHAPTER 8

PRACTICAL CONSIDERATIONS FOR AN ORBITAL DEMONSTRATION OF FLIGHT FLUX-PINNED INTERFACES

8.1 Towards an Orbital FPI Demonstration

The ultimate goal of FPI technology development efforts in both the laboratory and microgravity environments has been to advance flux-pinned interfaces to a level of sophistication capable of an on-orbit implementation. A successful orbital demonstration (and the corresponding attainment of a technology readiness level of 7) would mark the entry of FPIs into the portfolio of viable spacecraft technology options for close-proximity maneuvers. It would also designate the formal transition of the FPI development effort from a university-led, research-oriented endeavor to an industry-based, customer-driven enterprise. Thus, flying an FPI on orbit is the critical final step before space systems can realize the many benefits of FPI-augmented proximity operations envisioned in Chapter 1.

Because an orbital demonstration is the main aspiration of ongoing FPI research, examining the particular challenges associated with orbital FPI system designs has been one thrust of the work described in this dissertation. The conclusions of these efforts have been used to create proposals to a number of technology development programs, which have in turn provided a focus for the refinement of a baseline orbital FPI design.

There are many avenues that lead to an orbital FPI demonstration, but with the retirement of the Space Shuttle and corresponding lack of domestic transport to the

International Space Station, the most straightforward path to an FPI demonstration is a self-contained satellite launch. Given a satellite-based demonstration, the goals of the first FPI demonstration must be simple enough to ensure that critical FPI subsystems – such as the thermal design – are the primary focus of the mission, yet should be ambitious enough to pave the way forward for applications such as formation flying, grappling, and autonomous docking. A demonstration of station-keeping and relative positioning using flux pinning achieves this balance, thus most existing orbital FPI concepts center on this objective.

With station-keeping and relative positioning as the baseline goal of the first FPI demonstration, two different system architectures have been developed. The first uses two 3-U CubeSats to directly leverage the CubeSat-scaled FPI research leading up to an orbital mission. The second architecture moves to a slightly larger nanosatellite (in this case approximately 50 kg) to leverage a legacy Cornell-developed bus that is particularly well-suited to an FPI demonstration. In order to illustrate what an orbital FPI mission might entail, the CubeSat and nanosatellite concept are briefly described in Section 8.2. Joseph Shoer was involved in some of the design work for the CubeSat mission, and some of the nanosatellite FPI thermal design work was developed by undergraduate student Sammy Nowierski.[140]

In developing these orbital mission concepts, several issues arise that are unique to the implementation of an FPI on orbit. Specifically, the system needs to be field-cooled properly to be effective during mission operations. Thus, outlines of four field-cooling techniques are addressed in Section 8.3.1 Also, the superconductors and magnets in the system are affected by the magnetic field of the Earth, the spacecraft,

and the actuation of the electromagnets. The impact of these factors on the orbital system and FPI design is in Section 8.3.

8.2 Orbital FPI Concepts

8.2.1 FPI CubeSat Mission

As suggested in Chapter 6 and Chapter 7, a CubeSat-scale mission design has provided the baseline size and mass scaling for the majority of the experimentation and demonstration efforts both in the lab and in the microgravity environment. Thus, when moving to concepts for an orbital FPI, using a CubeSat standard becomes an obvious choice. In addition to having previous FPI design experience at this scale, CubeSats are typically much easier to launch than traditional spacecraft and are less expensive to develop. However, their small mass and form-factor may limit the usefulness of the demonstration and inhibit broader application of the technology to traditional spacecraft. The orbital FPI mission described below represents a viable technology demonstrator mission that could be accomplished in a two-year-to-flight-readiness timescale with current technology and an appropriate level of funding and personnel.

Mission Goals and Design

The CubeSat FPI demonstration concept aims to show a series of non-contacting station-keeping, relative pointing, and re-orientation maneuvers that use electromagnets and permanent magnets in one satellite and a cryocooled YBCO disk in the other satellite to establish a flux-pinned interface between the two.

An FPI mission would require more volume than a single CubeSat, in large part due to the presence of a small cryocooler onboard. Thus, the bus is designed around two 3-U stacks, which are connected via staged tethers and act as a single unit during launch and ejection from the vehicle. Once on orbit, the still-connected spacecraft perform a health check-out for several orbits while the batteries charge. Then, the two spacecraft perform the first stage of the separation sequence by burning through the first of the staged tethers using NiChrome wire. Small nonferrous springs between the two satellites then push the second stage of the tethers to their maximum extension at approximately five centimeters. In this position, the cryocooler is turned on to field-cool the equilibrium into the system. This process is anticipated to not take more than a few orbits to complete, depending on the power available and the orbit of the system.

Once temperature sensors embedded in the superconductor verify that the YBCO has achieved its critical temperature, a series of checkout maneuvers are performed to ensure the system has established an operational FPI. For example, with the tethers and springs still in place, the electromagnets attempt to reduce the relative distance between the spacecraft. The dynamics results from these tests will enable mission operators to determine if the FPI is functioning as expected.

At this point the system collects as much data as possible while the spacecraft are still physically connected. Once this phase of the mission is complete, the final tethers are cut again using NiChrome wire to sever the last physical connection between the two modules. With the tethers gone but the FPI engaged, the system enters a station-keeping phase of the experiment, where the two satellites remain at their relative equilibrium without the need for active control. A sensor suite records the relative

positions and attitudes of the spacecraft, allowing researchers to establish the stiffness, damping, and other performance metrics of the system during this time.

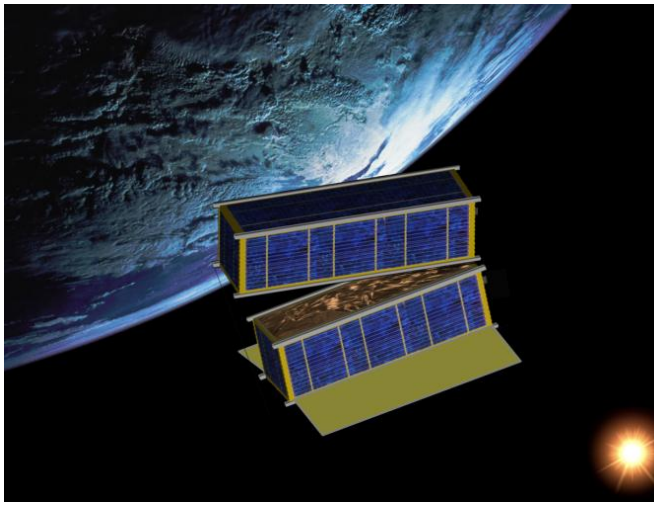

Figure 8.1. A conceptual image of a CubeSat-based relative-pointing orbital FPI demonstration

The final phase of the mission involves actuating the system with onboard electromagnets to alter the relative equilibrium between the spacecraft, as illustrated in Figure 8.1. Various commands and the system's response are then tested over the course of the rest of the mission's life.

Table 8.1. Estimated Performance Metrics for a CubeSat FPI.

Performance Metric	Relative Position /Attitude Data	Actuation Data	Estimate
Flux-Pinned Interfaces Stiffness	x		>10 N/m
Displacement Range of Electromagnetic Actuation	x	x	± 2 cm ± 15°
Tolerance of Final States after Relation Motion Maneuvers	x	x	<1 mm, <1°
Amplitude of Disturbances During Station-Keeping	x		<1 mm, <1°
Bandwidth of Relative Position and Attitude control	x	x	0.01 – 10 Hz
Closest Satellite Proximity in the Event of a Control Failure	x		> 2cm

FPI Design

The FPI in this orbital CubeSat architecture is a multiple-magnet single-superconductor (MMSS) design, where the magnets are on one satellite and the superconductor is on the other. Sample expected performance metrics for a system of this design and the necessary data to evaluate those metrics are shown in Table 8.1.

FPI Superconductor/Thermal System

The reduced size of the system and the restrictive power and thermal demands of the cryocooler necessitate limiting the superconductor-side of the FPI to a single YBCO disk in one of the satellites. As shown in Figure 8.2, the YBCO disk is directly mounted on the coldfinger of a miniature cryocooler to ensure it can be cooled below its critical temperature. Analyses have shown that with a basic multi-layer insulation thermal protection, in the worst-case scenario (where the heat from direct sunlight and Earth albedo is completely absorbed into the superconductor), the cryocooler is required to provide 0.5 – 0.75 W of cooling power. The coldhead and YBCO disk are thermally insulated from the rest of the spacecraft to ensure a large cryocooler power margin.

Commercial cryocoolers with this performance already exist in mass and size scales that meet CubeSat standards. For example, the Ricor K508 or K548 miniature cryocoolers have masses of 450 g and 600 g respectively and either one fits into a 2-U CubeSat. The power required to operate the larger K548 cryocooler can be provided by commercially-available deployable solar panels and the power stored in two EPS battery banks is sufficient to enable operation throughout eclipse. However, if the thermal analysis of the orbit suggests that the smaller K508 cryocooler is sufficient, it

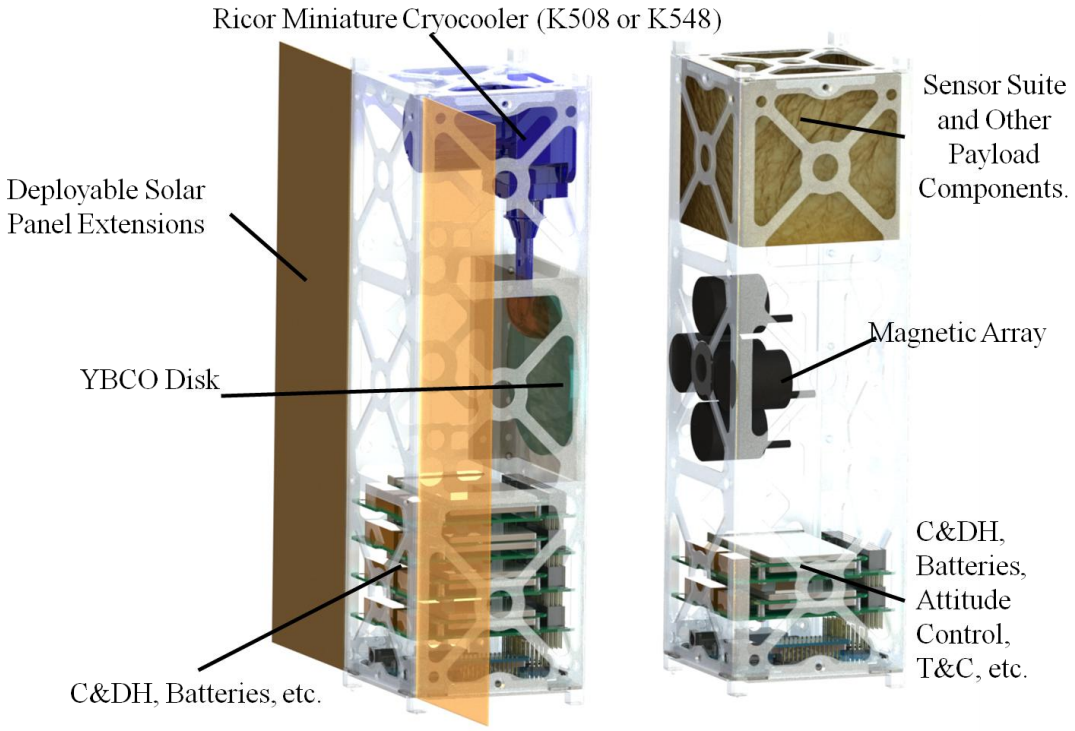

Figure 8.2. The relevant components of the CubeSat FPI demonstration

may not be necessary to include any deployable solar panels. The flight-qualified K508 cryocooler can remove 0.5 W of input power in approximately 5 minutes and is a heritage component from the MSL rover.[141] In either case, the CubeSat thermal design can be resolved with existing off-the-shelf components and flight-tested hardware.[142]

FPI Magnet Array

The second 3-U CubeSat contains the magnet array and the driver electronics for the relative-motion phase of the flight. The magnet array contains a set of permanent magnets centered over the superconductor to maintain passive station-keeping and system stability. The electromagnets ring the permanent magnets to provide a larger

moment arm for inducing relative orientation changes. Since most CubeSat achieve a low earth orbit, the magnet array is likely to interact with the Earth's magnetic field, which along with gravity-gradient, causes the system to settle to a stable orientation relative to Earth. (The effect is discussed in more detail in Section 8.3.2).

Actuation in this FPI design happens in a manner similar to the techniques investigated in Chapter 4. Ringed electromagnets disturb the magnetic field around the FPI, causing a shift in the equilibrium due to the new field. Although a simple way of implementing an FPI capable of relative pointing maneuvers, this technique may be vulnerable to flux degradation effects discussed in Section 8.3.2.

FPI Sensors

In order to realize the mission architecture described above, the system needs at least three types of sensors to ensure the system is working properly: 1) thermal sensors embedded in the superconductor to ensure the YBCO disk is below its critical temperature before and during the maneuver, 2) relative position and attitude sensors between the spacecraft to evaluate FPI performance metrics, and 3) current sensors in the actuators to verify the time history of the electromagnet states.

The thermal sensors can be simple thermocouples that collect low-frequency temperature samples to verify that the superconductor remains below its critical temperature. During the cool-down process, sample rates on the order of 0.1 Hz are likely acceptable, but with slightly higher rates prior to the final separation phase. Occasional verification samples before, during, and after FPI maneuvers should also provide the needed thermal data.

In order to evaluate the relative dynamics of the system under the influence of the FPI, some combination of IMUs, camera systems, range-sensors, or carrier differential GPS (CDGPS) boards needs to be implemented on the system. It is likely that the limited power and space in the CubeSat architecture will necessitate low-end data sampling and quality. Given the frequency data observed for similar microgravity and laboratory tests, the dominant FPI frequency will be around 1 Hz. Thus, a sample frequency of 10 Hz would be optimal during the experimental portions of the experiments, but a sampling frequency of 0.5 Hz is the minimum allowable sampling to unambiguously see the FPI dynamics.

The current sensors are only necessary during the active-control portion of the mission and are used to verify that the electromagnet's commands were appropriately transmitted to the actuator. This data allows researchers to correlate the inputs and outputs of the system during these maneuvers.

8.2.2 FPI Nanosatellite Mission

The acknowledged limitations in the CubeSat architecture led to the development of a similar mission profile at a nanosatellite-scale. This mission concept, known as the Flux-pinned Proximity Rendezvous Operations eXperiment (F-PROX), is the most mature orbital FPI design currently available. The system architecture and mission design were initially developed at Cornell, but have since been refined via a multi-level collaboration with representatives of broad sectors of the space community, including academia, commercial industry, the department of defense, and NASA. These partners have helped refine the F-PROX mission (shown in Figure 8.3) into a

Figure 8.3. A nanosatellite-based relative-pointing orbital FPI demonstration

fully realizable project, capable of achieving a flight-ready status in three years with appropriately higher levels of funding and resources.

Mission Goals and Design

The goals and sequence of events in the F-PROX mission mirror those of the CubeSat FPI demonstration. F-PROX is designed to demonstrate the stability, controllability, and robustness of a non-contacting flux-pinned interface between two nanosatellite-scale spacecraft modules. This mission goal was selected because it provides all of the necessary data and technological development necessary to enable more sophisticated applications (including docking, formation flying, and grappling) to quickly build on the successes of this flight.

As discussed below, the F-PROX mission uses a legacy bus design from CUSat, which launches as a unit and then separates into two fully functional satellites. In a similar manner, the F-PROX mission launches and ejects as two satellites rigidly connected together. Once on orbit, the system performs various status checks and charges its batteries to prepare for the field-cooling phase of the mission. In order to hold the system in place during the field-cooling process, the system will have a custom-made mechanical standoff (such as a reduced strength phased-deployment lightband structure) in between the satellites. Once the system's FPI has been engaged and confirmed, the structure is jettisoned and the system gathers passive and active

performance data in up to six degrees of freedom. An overview of this mission

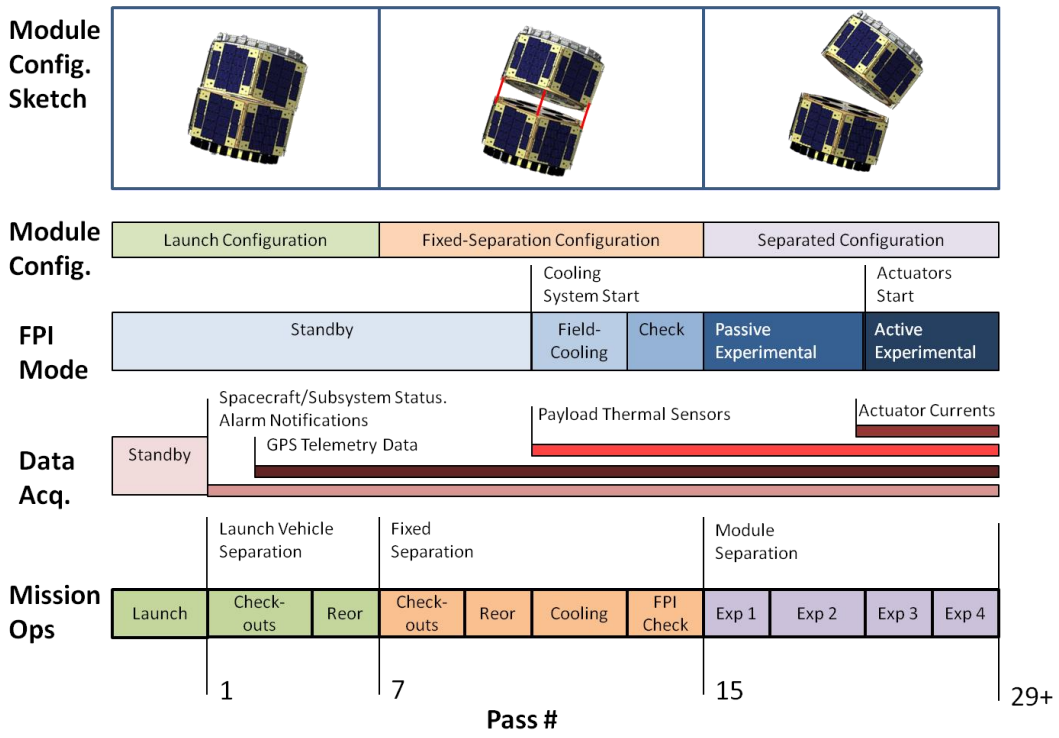

Figure 8.4. The F-PROX mission timeline, showing the different configurations at various points during the mission.

timeline can be seen in Figure 8.4.

Bus Design and CUSat Legacy Hardware

Due to the inherent high-risk nature of technology development missions, the F-PROX system was designed to be flown in a nanosatellite bus to reduce costs and system complexity. To further that goal, the design builds on the CUSat mission– Cornell's winning entry in the University Nanosatellite Program– by leveraging its refined small-satellite bus design (shown in Figure 8.6). CUSat is a two-satellite stack that launches together and, using an ESPA ring, springs apart once on orbit. The two satellites can then perform station-keeping and on-orbit inspection maneuvers.

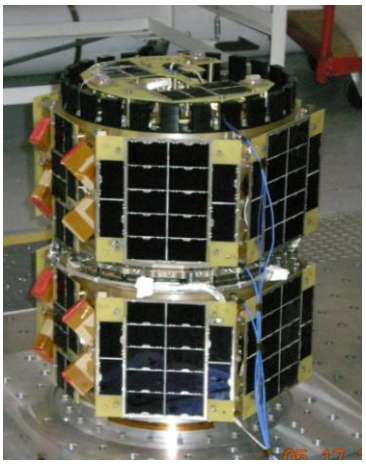

Figure 8.6. An image of the integrated CUSat bus during environmental testing.

Most existing subsystems on the CUSat bus have already been through over five years of development and refinement, making the integrated bus an advanced and technologically mature baseline for an FPI payload design. Although an FPI demonstration does not require propulsion and will require a redesign of the thermal subsystem, the majority of CUSat's systems are capable of supporting an FPI mission with little modification. An overview of the transferable subsystems are shown in Figure 8.5.

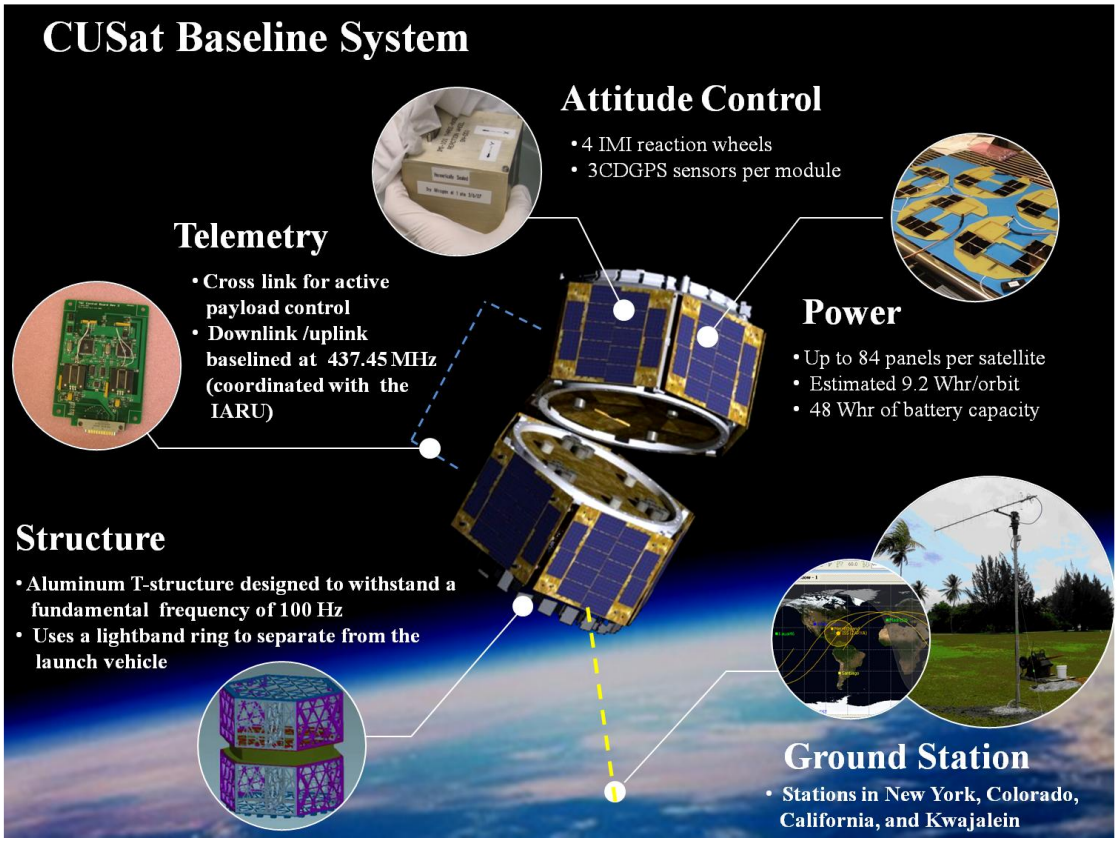

Figure 8.5. The CUSat Baseline systems that can be re-purposed for an orbital FPI mission

CUSat is manifested on a launch slated for December of 2012. After this point, the spacecraft bus is flight-qualified, adding considerable maturity to future missions seeking to re-use elements of the design. The legacy hardware and software from CUSat strengthens the F-PROX mission design by improving the technology readiness level of many of the subsystems and thus reducing the level of risk for mission.

FPI Design

The larger spacecraft envelope and mass budget enables the F-PROX mission to include a much more sophisticated FPI system than the CubeSat design. This FPI uses a multiple-magnet multiple-superconductor (MMMS) design to demonstrate passive inter-module stability and electromagnetically-driven relative pointing and control in up to six degrees of freedom. In the specific design discussed below, three superconductors each interact with up to ten magnets apiece. In addition to the sensors integrated with the bus, the FPI consists of three primary elements: the superconductor assembly, the magnetic assembly, and the safety-lock electromagnets. An overview of these systems is shown in Figure 8.7.

FPI Thermal/Superconductor System

The thermal design for the F-PROX mission occupies a critical place in the overall system design because it is vital to the success of the mission and represents the most complex addition to the CUSat legacy bus. Preliminary analyses show that a worst-case scenario requires a single superconductor assembly (shown in Figure 8.8) to reject 0.8 W of power to maintain the superconductor at a temperature of 77 K. While previous missions have successfully achieved these temperatures using passive

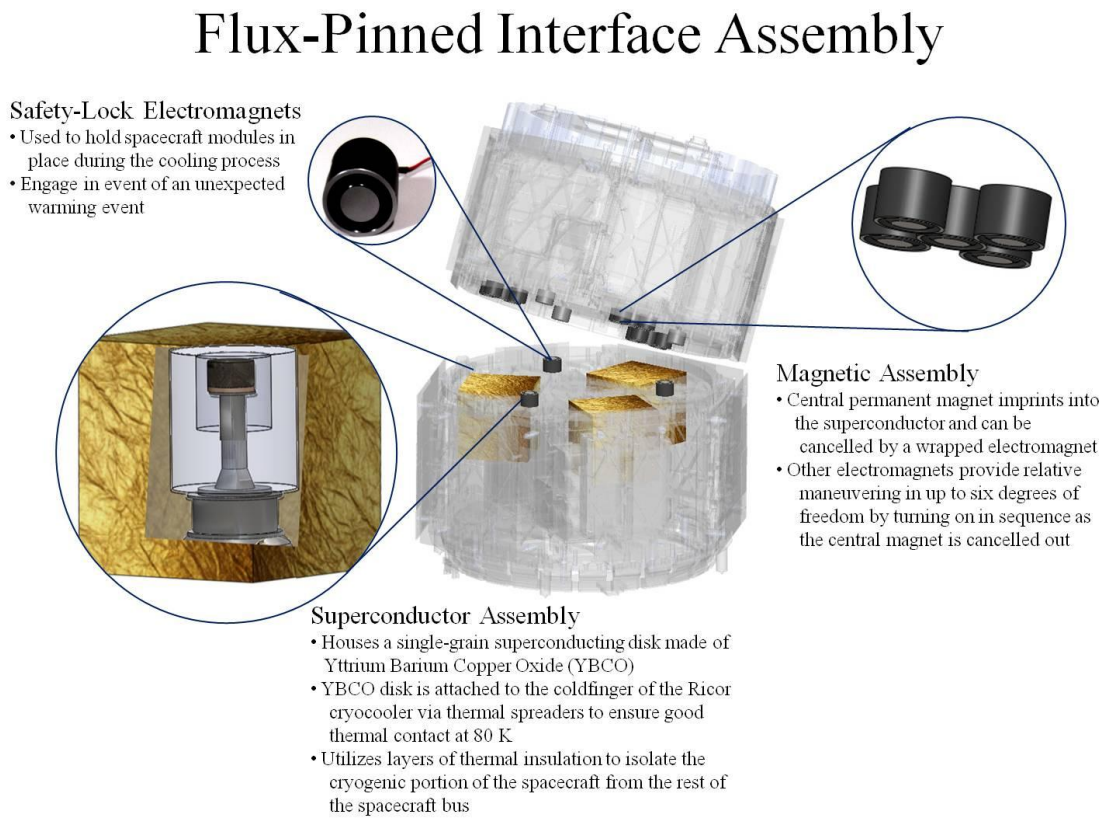

Figure 8.7. An overview of the F-PROX FPI subsystem elements.

thermal control techniques,[143] this design utilizes a series of cryocoolers to ensure the temperature requirements are met. Thus, each superconductor assembly is baselined with a Ricor K543 cryocooler design, which has a cooling capacity of 1 W at 77 K and a mass of 715 grams. Although three of these cryocoolers are shown in the model in Figure 8.7, further thermal analysis may show that two coolers are sufficient for nominal cases. The excess heat from these coolers is absorbed into the spacecraft bus to be re-radiated to space. If it becomes necessary, radiators can be added to the system to further reject the system's waste heat.

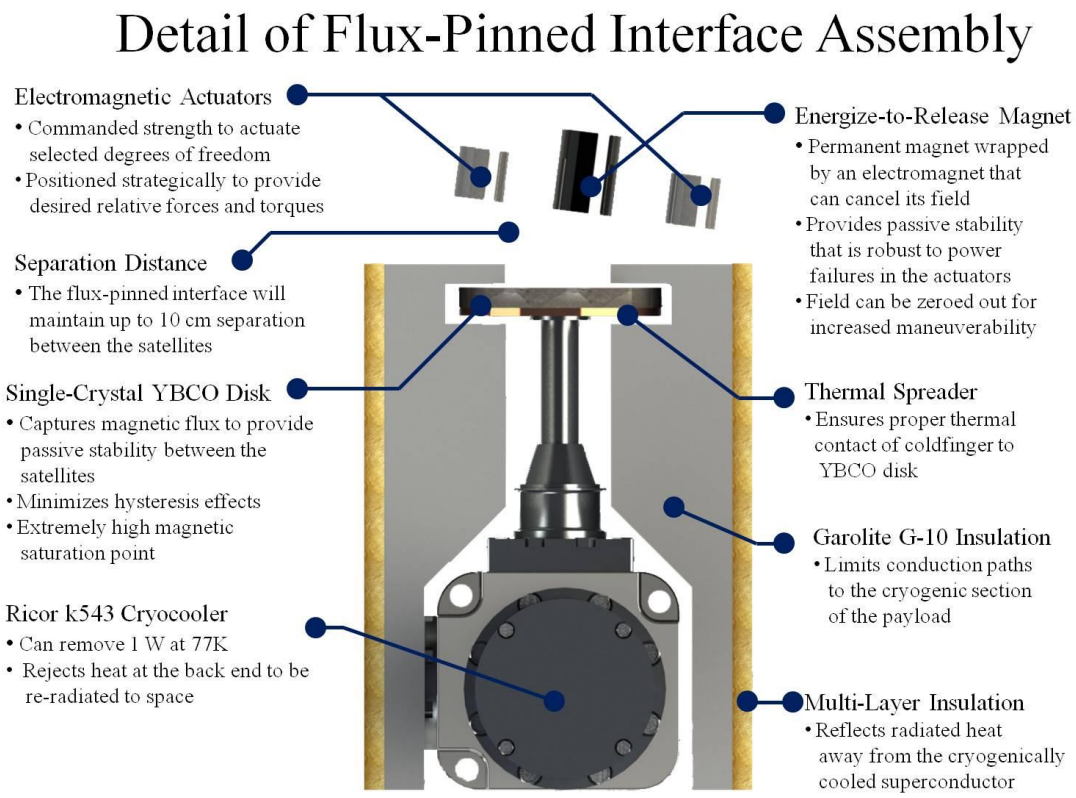

Figure 8.8. A detail of the F-PROX FPI design.

FPI Magnetic Array and Safety-Lock Electromagnets

The magnetic array in the nanosatellite system is built around a large energize-to-release magnet that provides a passive stability during station-keeping maneuvers. During active control maneuvers, however, its field can be canceled out by a concentric electromagnet wrapped around its outer edge. This ability enables the two satellites to maneuver to much larger displacements than would be allowed with a permanently pinned magnet.

The concept behind the active maneuvering in this FPI is different than that of the CubeSat mission. In this FPI, only the image of the energize-to-release permanent magnet is imprinted into the superconductor. In order to manipulate the lateral relative

motion of the satellite, this magnet is strengthened or weakened with its wrapped electromagnet (causing an out-and-in motion relative to the plane of the superconductors). Differentially manipulating these strengths can cause a relative roll and pitch motion as well. However, the transverse and "clocking" or yaw degree of freedom is accomplished by manipulating the neighboring electromagnets in the array, which are powered to match the strength of the permanent magnet. For these maneuvers, the target neighboring electromagnets are slowly turned on while the energize-to-release electromagnet slowly cancels its magnetic field. At the end of the maneuver (depicted in Figure 8.9), the magnet array has centered the neighboring electromagnet over the imprinted frozen-image from the energize-to-release magnet.

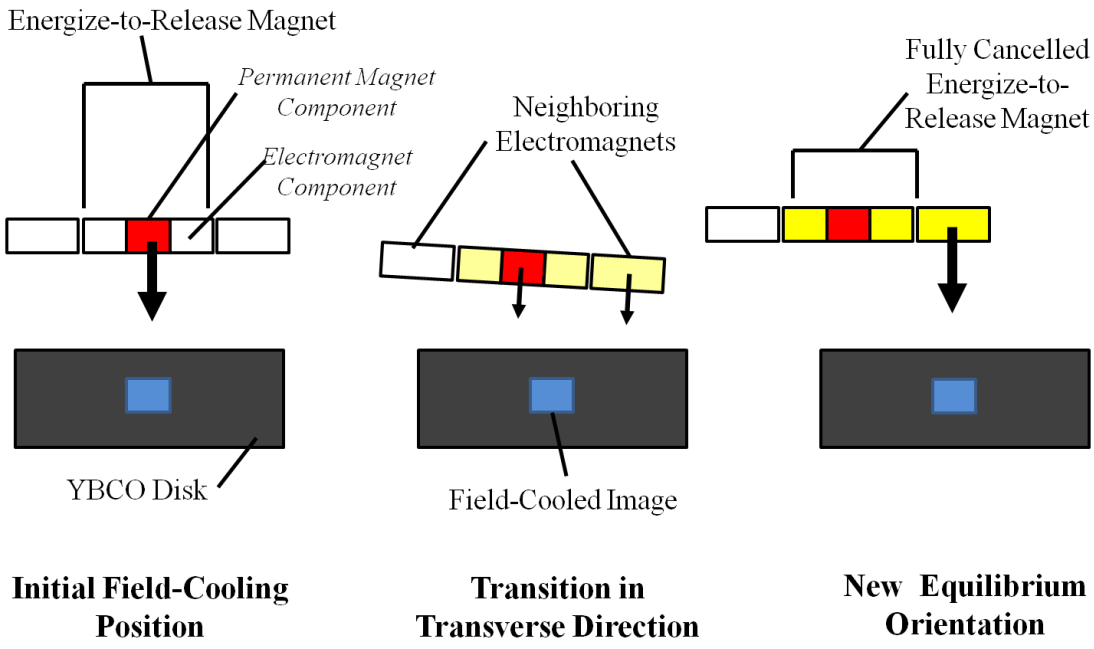

Figure 8.9. The transverse maneuvering technique employed by the F-PROX mission design.

FPI Sensors

The F-PROX mission require similar sensing capabilities to the CubeSat mission design, including thermocouples, current sensors in the electromagnets, and relative position and attitude sensors for characterizing FPI dynamics. The CUSat bus contains CDGPS boards and cameras that will be flight-proven pending a successful launch in December. Both of these can be used in conjunction with high-TRL IMU sensors to provide the data needed to establish the FPI performance.

8.2.3 FPI-Induced Mission Risks

It is also worth examining the major FPI-induced technological risks in a mission dedicated to flight-validating an FPI mission. Some of the highest-impact FPI risk events and their mitigation approaches are described in Table 8.2.

Table 8.2. Risk Elements for an FPI Orbital Mission.

Risk Event	Risk Statement Cause/Effect	Mitigation Approach Controls and Verification
Superconductor Fails to Achieve Critical Temp.	Thermal system failure, unanticipated heat loads / FPI fails to engage, all mission goals not met	Redundant high-TRL thermal systems, using a high temperature superconductor/Preflight testing, extensive thermal modeling
Staged Separation of Spacecraft Modules Fails	Damage during launch, separation band failure / FPI unable to actuate, some mission goals not met	High-TRL deployment system / Deployment testing, possible Moog gravity offloading system testing
Undesired Equilibrium in Field-Cooled Image	Inexact, inaccurate, or non-existant positioning during superconductor temperature transition / Range of actuatable motion is limited or non-existant	Possible FPI reset ability / Magnetic modeling, simulations, and magnetic moment measurement to calibrate results
FPI Controller Software Malfunctions/Fails	Unanticipated results or delays in processing / Mission delayed due to software patch uploads	High-TRL, flight proven software with limited new code, check point, restart functionality / Pre-flight HIL testing and modeling

8.3 Considerations for an Orbital System

8.3.1 Superconductor Field-cooling

Once FPI prototypes move beyond the laboratory, the problem of properly cooling and imprinting the magnetic images in the superconductors becomes one of the most challenging issues in the FPI system design. Accurately field-cooling the superconductor is a critical step in the implementation of the FPI, thus it merits additional scrutiny.

Spacecraft designers have two distinct strategies to choose from when developing the field-cooling system architecture for an FPI-augmented mission. The first option is to cool the superconductor with the appropriate magnetic flux distribution before launch and keep the system cold throughout the system's mission. The second option is to cool the superconductor on-orbit with a physical magnetic array. Both of these options are readily accessible as methods of field-cooling the superconductors in an FPI. The following subsections detail the possibilities for each method.

Other, more speculative methods may exist for field-cooling. For example, it may be possible to induce the desired supercurrent vortices into the superconductor directly with wires embedded in the superconductor disk. No work has been done to show this type of field-cooling is feasible, but it may be an area for future research. These potential approaches to field-cooling are not discussed in more detail in this work.

Ground Field-Cooling Option

The most straightforward way to imprint the superconductor with the desired flux distribution is to field-cool the system on the ground and design the thermal system to

maintain the cryogenic temperatures throughout launch and orbit insertion. In order to implement this approach, an active cooling technique (a cryocooler or dewar of cryogenic liquid) would likely be required. Although such a system may be difficult to implement in a launch environment, many space telescopes have successfully launched cold systems, primarily using dewars of liquid helium. The Infrared Astronomical Satellite (IRAS) for example, was launched with many of its components immersed in a dewar of liquid helium (which boils at temperatures on the order of 5 K).[144] The Spitzer Space Telescope[145] was also designed to have its cold science assemblies in contact with liquid helium throughout the launch and mission initialization phases. The Suzaku mission also utilized a dewar of cryogens to enable a cold launch.[146] Missions may also have their cryocooler powered on for a "cold launch" environment; [147] however, this approach requires battery power capable of running the cryocooler throughout the launch. In the context of the thermal requirements for these missions, achieving the critical temperature of high-temperature superconductors (at 80 K or above) should be well within the range of existing technology.

This strategy has the advantage of enabling the field-cooling to be verified prior to launch, as well avoiding the need for complex or time-consuming on-orbit operations required to cool the superconductor on-orbit. However, because this strategy does not call for an orbital strategy for field-cooling the superconductor, it bears some operational risk if the temperature were to rise significantly during the launch, causing the superconductor to lose its trapped flux. This approach may also add complexity to

the launch phase of the mission by requiring the monitoring of mission-critical hardware during this phase.

Orbital Field-Cooling Option

There are a number of ways to accomplish the field-cooling of a superconductor on orbit, but the optimal design decision depends on the mission requirements and the FPI application. The field-cooling design exploiting an external magnetic field-cooling source varies significantly based on the mission architecture. In general, the on-orbit field-cooling procedure can be accomplished one of four ways: using an internal magnetic source and mechanically flipping the superconductor to face the desired FPI interaction direction, maintaining the position between the intended FPI modules using another method for the duration of the cooling process, using an expendable magnetic "cap" to set the equilibrium, or, in the case of an FPI grappler, using magnetic cartridges on the host spacecraft to imprint the flux. Each of these possibilities is discussed in more detail below.

Internal Magnetic Source

If the mission design requires a self-contained method of field-cooling its superconductor and the thermal design does not require a rigidly-fixed superconductor disk, an internal solution to the field-cooling process may be optimal. In this

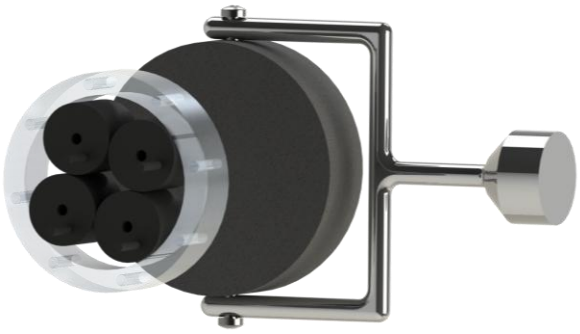

Figure 8.10. A field-cooling design where the superconductor (back) is mechanically flipped after imprinting with an internal magnetic array (front).

system, the spacecraft carries an internal copy of the magnetic array intended for imprinting flux into the superconductor. This array is positioned at the same distance as the desired equilibrium, but reflected to a location inside the spacecraft. The superconductor is field-cooled facing this array, as shown in Figure 8.10. Once the process is over, the magnets in the array are turned off, and the superconductor is mechanically flipped such that the surface that was facing the field-cooling array is then facing the direction of the FPI interface.

This design enables the superconductor disk to be re-imprinted with a magnetic array in the event of a loss of flux or (if the array is made up of electromagnets) if a new equilibrium is desired. It also adds another layer of control available to the spacecraft operators, since the magnets behind the superconductor can potentially be activated to interact with the magnet-side of the FPI on the incoming module. The superconductor's orientation can also be controlled using the motors that flip it from its field-cooling state to its FPI interaction state. However, it adds significant complexity to the thermal design if the system is operating at temperatures that require significant thermal isolation and active cooling. It also requires a moving part to work, which adds risk of failure or degraded lifetime performance.

Relative Position Locking

Some missions will connect modules using an FPI for relative pointing and vibration-isolation purposes. In this scenario, it is possible to perform the field-cooling in a specially-designed mission phase where the two modules are held in place at the desired equilibrium while the system is brought to cryogenic temperatures. If the modules are not connected at launch, they can rendezvous on orbit and use active

control to maintain the field-cooling position until the process is complete. If, like in the F-PROX mission, the two modules are connected at launch, a phased deployment to the field-cooling equilibrium allows the system's relative position to be held in place during the cooling process. Once complete, the locking mechanism (whether a low-energy ESPA-like band, a mechanical bolt with pyros, or a NiChrome wire fitted with a spring for inter-module stiffness) can then be released, leaving the system engaged in an FPI.

The advantage of this setup is that the exact magnetic field source engaged in the FPI is used for field-cooling (so small variations in the magnet's construction or strength do not affect the system). The two modules are also already close to their FPI equilibrium position when it is engaged, which minimizes the transient dynamics induced by bringing the superconductor and magnet together from a large distance. In the case of the phased-deployment method, the temperature of the superconductors (and the presence of flux pinning) can be confirmed prior to the full separation of the modules.

However, this design does require that the equilibrium position be maintained without flux pinning for the duration of the cooling process. For a system maintaining position using active control, variations in the relative position may cause an inexact capture of the equilibrium flux distribution into the superconductor, causing increased uncertainties in the final FPI equilibrium. For phased-deployment systems, additional mechanisms are required to lock in the equilibrium, adding technical risk and complexity to the system.

Magnetic Cap

Another mission concept may call for a spacecraft with the superconductor-side of the FPI to then interface with other magnet-side FPIs on orbit, such as in a rendezvous or docking scenario. One way to field-cool these superconductors using an external magnetic source is to launch the system with a disposable magnetic "cap" over the superconductor assembly designed to mimic the mating magnet-side of the FPI at the desired equilibrium distance. This magnetic cap can be hard-mounted to the satellite during the launch and cool-down phases of the mission, and then jettisoned using explosive bolts or other standard mechanisms before engaging the FPI.

The magnetic cap approach is a low-risk field-cooling solution that requires little integration and no moving parts. Thus, this system may be useful for small-satellite or low-cost missions where the desired relative distance is small and simplicity is key. It has the disadvantage of using a different magnet array than the one that is engaging the FPI, making it vulnerable to differences in the magnetic field of the field-cooled images and the actual magnets in the FPI. Low-stiffness FPIs with larger relative distances may also be impractical to field-cool in this way, since it would require a larger extrusion to set the magnets at the proper equilibrium distance. It is also a one-time-use solution that produces orbital debris when the cap is jettisoned.

Grappler Magnetic Cartridge

If a grappler-style FPI is being implemented (where the superconductors are on the end-effector of the arm), the superconductors can be field-cooled with a sequence of different magnetic configurations to enable it to interact with different magnet-side arrays. As shown in Figure 8.11, the grappler's host spacecraft may contain magnetic

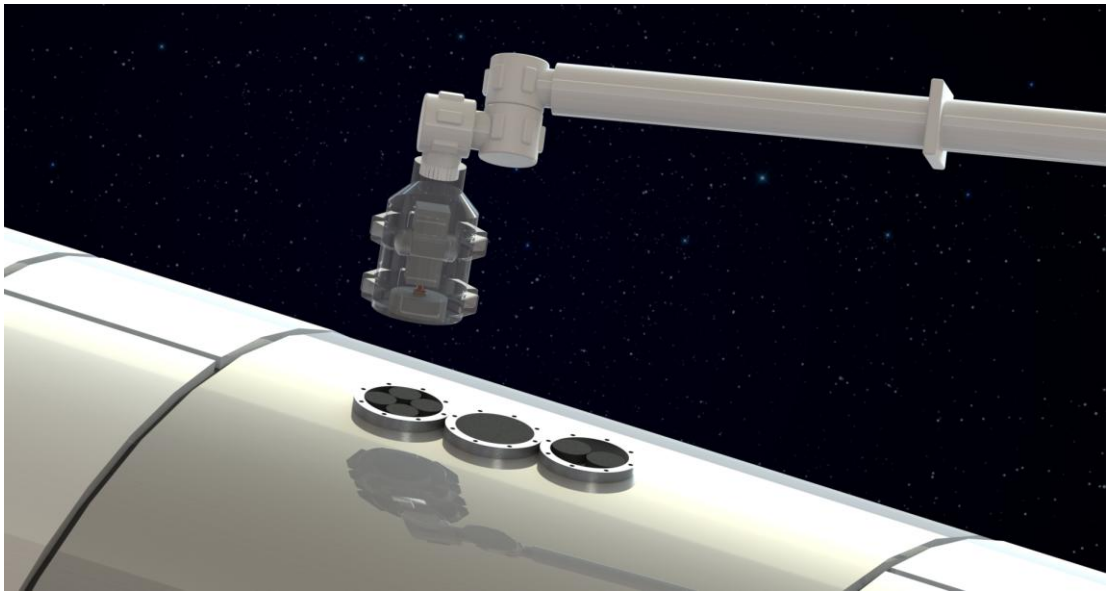

Figure 8.11. An FPI grappler is imprinted with a magnetic field configuration by maintaining the desired equilibrium over a reusable magnetic cartridge on the body of the grappler's host spacecraft.

"cartridges" affixed to its outer surface in an area within the workspace of the grappler. To field-cool the system, the end-effector is brought down to temperature while being held over the appropriate magnetic cartridge at the desired equilibrium distance. The grappler is then free to interface with any spacecraft equipped with a corresponding magnetic field configuration. In order to change the magnetic imprinting in the superconductor, the system can be allowed to warm above its critical temperature (perhaps by pointing the grappler at the sun or other heat sources, as shown in Figure 8.12), then positioned

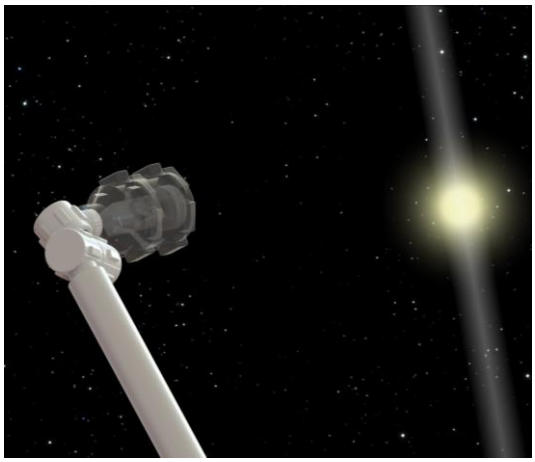

Figure 8.12. The superconductors in the grappler end-effector can be pointed toward the sun to reset the equilibrium by warming the system above its critical temperature.

over the next desired magnetic cartridge for re-cooling.

This field-cooling technique exploits the thermal actuation abilities of the FPI to provide a reusable and flexible architecture for grappling a variety of satellites with different magnetic arrays. This approach may be useful for on-orbit refueling and repair missions in particular. The disadvantage of using a different magnetic array to field-cool than the one in the actual FPI is still a problem for this design. The presence of a large set of magnetic cartridges on the side of the host spacecraft may cause problems when the cartridges are too close to the magnet-side of the other spacecraft. These magnets may also undesirably influence the dynamics of the host spacecraft in Earth's magnetic field (an issue discussed below). This approach only works well for designs where a manipulator arm can be positioned accurately and held in position- and many FPI applications do not involve this apparatus.

8.3.2 Ambient or Changing Magnetic Fields and Their Effect on FPIs

FPIs inherently rely on strong magnetic fields to produce stiff connections at useful relative distances. Thus, one of the issues that will need to be fully resolved before FPIs can be practically implemented on space systems is how the magnetic fields of the FPI interact with the ambient magnetic fields from both the Earth and the spacecraft's electronics.

The Influence of the Earth's Magnetic Field

One of the most obvious effects of having a strong magnetic field on the spacecraft is the tendency for the spacecraft to align with Earth's magnetic field. This effect can be irrelevant for systems that are not concerned with controlling attitude (in which

case, the system passively achieves an alignment with the Earth's magnetic field and stabilize, although it is influenced by changes in the local magnetic field strength). Since the Earth's magnetic field is stronger near its surface, this effect is most pronounced in low-earth orbit and less relevant to systems in higher orbits. For some systems, this torque may be undesirable and steps must be taken to cancel its effects, either in the mission design or with an active control system onboard. In other systems, this torque can be exploited to provide additional benefits to the mission. For example, magnetic torque rods, also known as coils or magnetorquers, apply current to an electromagnet to perform detumbling maneuvers,[47] to desaturate reaction wheels,[148] or to add damping to a spacecraft whose attitude is stabilized using other methods such as gravity gradient techniques.[149] Depending on the goals of the mission and the FPI design, FPI apparatus may be able to provide similar benefits. Thus, FPI mission designs to address this effect strongly depend on the objectives of the mission and the strength of the effect.

The torque acting on the spacecraft is found with the following equation:

$$\boldsymbol{\tau} = \boldsymbol{\mu} \times \mathbf{B} \tag{8.1}$$

where $\boldsymbol{\tau}$ is the torque acting on the spacecraft, $\boldsymbol{\mu}$ is the net magnetic dipole moment of the spacecraft (either from a torque rod or FPI apparatus), and $\mathbf{B}$ is the ambient magnetic field of the earth that point in space. The Earth's magnetic field can be roughly modeled as a tilted magnetic dipole, producing a magnetic field strength of:[150]

$$B = \left(\frac{\mu_E}{r^3} \right) \left[3\cos^2 \theta_m + 1 \right]^{1/2} \tag{8.2}$$

where μ_E is the dipole magnetic moment strength of the Earth (to within 25% of the final field values, a dipole moment of 7.9×10^{15} Tm^3 can be used),150 r is distance of the point from the center of the earth, and θ_m is the angle of the point from the dipole axis. Using this model, in a 400 km orbit the Earth's magnetic field strength can vary from 0.5×10^{-4}T (near the poles, θ_m of zero) to 0.25×10^{-4}T (near the equator, θ_m of 90 degrees).

The net magnetic moment of the FPI interacting with this magnetic field is dependent on the design and status of the FPI. However, at equilibrium the engaged FPI can be assumed to have a magnetic dipole moment equivalent to that of its magnetic array. To provide approximate numbers, the permanent magnet used in the 2010 microgravity flight designed for CubeSat-scale interactions can be modeled as a dipole with surface strengths between 0.4 and 0.5 T. The approximated magnetic dipole moment is then between 0.51 and 0.64 Am^2. The Magnetic Sensor Systems electromagnets mounted on the RAGNAR system (with an area of $5.1\times10^{-4}m^2$, resistance of 29 Ω, and 1015 turns) can be modeled as having a magnetic moment of 0.27 Am^2 when powered at 15 V (although this model likely over estimates their strength because it fails to take into account changes in diameter as a result of winding and the thickness of the magnets). Most FPIs – even at the CubeSat scale – utilize multiple magnets of this strength or stronger. The RAGNAR CubeSat mockup magnet array has two permanent magnets and four electromagnets, so adding the moments as if they were coincident gives it a rough weakest-case magnet moment of 1.28 Am^2 and a strongest-case magnetic moment of 2.36 Am^2. For comparison, a CubeSat-scale SSBV magnetorquer can achieve a magnetic moment of 0.2 Am^2 and a larger

magnetorquer for standard spacecraft can achieve magnetic moments on the order of 1 – 100 Am^2.[151,152]

To illustrate a simple bounding case, it is possible to calculate the disturbance torque from the system carrying a magnet array for an FPI. Assuming the dipole moment of the spacecraft is perpendicular to the magnetic field direction, the largest torque experienced by the magnetic array of the RAGNAR CubeSat mockup (all electromagnets on while the spacecraft is at Earth's pole) is 1.18×10^{-4} N·m, while the weakest torque (with just the permanent magnets on at the equator) is 3.2×10^{-5} N·m. This analysis assumes all of the magnets in the magnet array are oriented the same direction and that the superconductor does not contribute significantly to the magnetic dipole of the FPI in equilibrium (as is suggested by the frozen-image model), which may not be the case. However, the torque estimates are within standard ranges for environmental disturbance forces in space[153], and can be handled by a standard attitude control subsystem.

If these Earth-induced torques acting on the FPI need to be cancelled or mitigated, several options exist. The most obvious method to avoid unnecessary torqueing due to interactions with Earth's magnetic field is to include electromagnets in the magnet array. This design allows the magnets to be turned off (or allows the permanent magnets to be cancelled out by their electromagnet counterparts) when the FPI is not in use, and offers some measure of control over the amount of torque induced on the spacecraft from the Earth (even at the expense of FPI performance). It may also be easiest to use another attitude control device, such as a reaction wheel array, to control these induced torque. However, the magnet array in the FPI can also be designed to

enhance near-field strength while reducing far-field strength to help offset the influence of the ambient magnetic field.

While interactions with the Earth's magnetic field are clearly an effect that needs to be considered in the orbital system design, the system technologies to address this concern are within the realm of existing technology. In some cases, the magnetic torqueing may be essentially irrelevant or too weak to be a consideration. In other cases, the FPI and attitude control design for the mission may need to be designed to minimize its effects. For yet other situations, it may even be a beneficial attitude stabilization tool for FPI-equipped satellites in low earth orbit.

Electromagnetic Interference from Spacecraft Electronics

Another consideration when examining the influence of external magnetic fields on FPI performance is the magnetic field induced by the currents onboard the host spacecraft. Magnetization losses – and associated degraded flux pinning performance – is a documented effect in high-temperature superconductors (HTSCs) placed in an external AC field.[154,155] While most spacecraft operate on DC power supplies, high-frequency equipment such as antennas may degrade the performance of an FPI under certain circumstances.

To date, this effect in bulk YBCO superconductors (rather than superconducting wire or thin-films) has only been examined for frequency contents at 100s of Hz or lower[74,156], which is well outside of the MHz-scale or higher frequencies used by most satellite antennas. However, current research is underway to examine the effects at much higher frequencies. For example, Hamilton Carter, a physicist at New Mexico State University, is currently conducting high-frequency measurements of AC losses

in bulk YBCO on the order of 50 – 100 kHz. Although not quite in the range of most antennas, this work represents an expanding knowledge of high-frequency influences on superconductor performance.

Flux Degradation Due to Actuation

One major consideration for the long-term duration of FPIs on orbit is the fact that using electromagnets as actuators necessitates the use of a changing magnetic field on the superconductor. However, as discussed above, alternating currents have been found to degrade the amount of flux trapped in the body of the superconductor. Understanding the conditions and extent of this effect is critical to properly implementing an FPI on orbit.

As Ueda, et. al. has shown,[74] a YBCO disk of similar size to those used in the experimental work detailed in Chapters 6 and 7 can have significant flux reduction at relatively small frequency oscillations. Ueda immerses a 48 mm diameter, 15 mm thick YBCO disk (compared to the 56 mm diameter 18 mm thick disk used in this work) in a bath of liquid nitrogen in the presence of a 0.2 T magnetic field. Once the disk is cooled, an AC field at 0.2 T in amplitude and various frequencies is applied to the disk. The trapped magnetic field is measured over time using Hall probes.

Ueda finds that the fraction of the trapped flux at the surface of the YBCO disk decreases as much as 22% over just 20 cycles at 0.1 Hz. Although not explicitly characterized or encountered in the FPI laboratory work, this apparent degradation due to the presence of intentional magnetic flux changes needs to be examined in further detail to assess its impact on a long-term FPI orbital system. For example, Ueda finds that the loss effects are reduced to less than 5% when the amplitude of the AC

magnetic field is kept to below 20% of the field-cooled value. Other researchers have found that no flux reduction occurs below a given frequency-dependent amplitude threshold, although these thresholds are generally small.[157] It is also possible that a surface-field reduction does not significantly affect the behavior of thick superconductors in FPIs, and that this information can lead to further insights about engineering design minimums for superconductor thickness.

Another group of researchers, Smolyak, et. al.,[156] suggests that the equilibrium between samples of YBCO and an electromagnet are most stable when interacting at lower frequencies, and shows that larger separation distances lend themselves to lower "break-off" frequencies where the sample loses sufficient flux to end the levitation or suspension in the presence of the superconductor. They calculate resonant frequencies for their setup (which uses thin-disk YBCO) on the order of 225 Hz and suggest that at frequencies below this value the superconductor attempts to "track" the changes in magnetic flux, resulting in larger internal changes in flux, and thus more risk of a loss of sufficient pinning flux. The effect is also amplitude dependent, suggesting that limits on the amplitude change in an FPI may lead to a longer operational lifetime.

Although little work has been done explicitly applying this limitation to FPI designs, it is possible to develop FPI control strategies that take into account limitations on control magnetic field amplitude and frequency and still maintain the useful properties of the interface. It may also spur research into systems that can re-imprint flux into the superconductor periodically to counter this effect and extend the lifetime of the system.

8.4 Conclusions about FPIs on Orbit

The F-PROX mission provides a clear illustration of what an orbital FPI demonstration might look like when implemented on a nanosatellite scale. By proposing a simple, self-contained, non-contacting relative-pointing maneuver, the mission design lays the groundwork for more advanced implementations of future FPI technologies including docking, grappling, and formation flying. The system can leverage existing nanosatellite bus designs to implement a viable linear FPI. Although specifics of the FPI design, particularly the critical thermal system, should be given due attention for an actual orbital mission, preliminary analyses show that such a system is achievable, given the proper resources, in the next three years.

FPIs do introduce a few specific considerations into an orbital system that need to be addressed. One of the most important of these considerations is the method for imprinting the superconductors with the necessary flux to interact with the magnets in the FPI. At least five possible methods of accomplishing field-cooling are possible from a technological standpoint, but optimal technique to use is heavily dependent on the mission objectives and design. Another area of particular interest is the influence of magnetic fields on the FPI system. The FPI's interactions with the Earth's magnetic field may need to be counteracted if precise attitude control is required for a mission in low earth orbit, but this requirement is not prohibitively difficult to accomplish with existing technology.

The degradation of flux in the superconductor due to variations in the magnetic fields raises concerns about lifetime and limitations on the FPI electromagnetic actuation and its placement relative to other spacecraft components such as the

antenna. This effect needs to be examined more thoroughly in the context of orbital FPI implications to determine how much of a design barrier this effect may be. However, current studies have shown that that limiting the amplitude of the actuation relative to the embedded flux and avoiding low-frequency repetitive actuation may limit these effects if they prove to be problematic for FPIs on orbit.

CHAPTER 9

CONCLUSIONS AND PROSPECTS FOR FLUX-PINNED SPACECRAFT

9.1 FPI Progress and Prospects

In the past five years, flux-pinned interfaces for spacecraft have undergone a dramatic rise in maturity in both the technological and theoretical domains. The basic concept work for this technology grew from an understanding of the needs of space systems and knowledge of superconducting physics. From there, researchers have found numerous examples of the technology's applicability to close-proximity spacecraft operations. A study of existing techniques for these close-proximity operations show that FPIs offer unique and advantageous properties not currently available to spacecraft designers and thus merit additional development.

From a theory perspective, FPIs have advanced to the point where physics-based models of flux pinning have been successfully applied to spacecraft and provide a basis for simulating dynamical behavior, estimating performance, and synthesizing controllers. The limitations of the model are well-understood and characterized. Mathematical proofs of the system's stability lend support to claims of the system's reliability and utility. The development work in this area has provided the underpinnings of the technology's successful implementation in the hardware domain.

The progress in a theory-based understanding is rivaled only by progress in FPI's technological development (shown in Figure 9.1). FPI hardware demonstrations have moved from simple laboratory prototypes to full-scale sophisticated systems. Elements of the technology have been proven in a microgravity environment, giving parts of the

system a coveted TRL 5. Concept feasibility and preliminary analysis work has been performed in anticipation of an orbital-based demonstration that could propel FPI technology to a TRL 7 and into the hands of spacecraft developers.

Given the acknowledged benefits offered by FPIs to a variety of close-proximity operations, the increasing maturity of the FPI system in recent years, and the widespread interest in the technology among all sectors of the space community (academia, industry, defense, and NASA), the outlook for FPI technology is strong. The FPI research team at Cornell has already built partnerships with representatives of the space industry and relevant government institutions to ensure that this technology has a path forward for further development and implementation. Perhaps then FPIs can play a role in improving the mission architectures (formation flying, autonomous rendezvous and docking, on-orbit re-servicing, etc.) envisioned and developed by generations of spacecraft designers since Gemini.

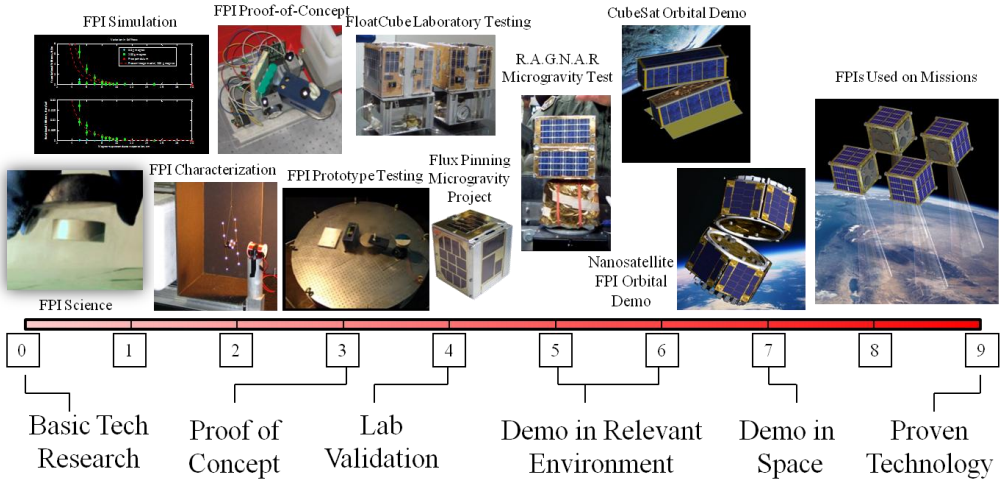

Figure 9.1. FPI progress through the various technology readiness levels.

9.2 Applications of Flux-Pinned Interfaces for Spacecraft

The results of this dissertation have demonstrated the theoretical and technological foundations necessary to enable a variety of FPI applications. To conclude this work, a summary of how FPIs can transform close-proximity spacecraft operations by both augmenting existing capabilities and creating new opportunities on orbit. These applications include: non-contacting pointing platforms, flux-pinned formation flying,[158] autonomous assembly of a virtual structure for large-aperture telescopes,[159] docking interface augmentation,[160] flux-pinned cooperative grapplers, magnetic kinematic mechanisms for spacecraft reconfiguration,[161] and solar sail enablers.[162]

9.2.1 Non-Contacting Pointing Platforms

One of the most broadly applicable features of FPI technology is its ability to provide stiff, alterable connection between satellites on orbit. Using the same principles, one can connect a payload segment of a spacecraft to its bus via an FPI, providing a unique non-contacting method of vibration isolation and six-degree-of-freedom pointing. Like a standard Stewart platform, FPIs can provide up to six degrees of freedom to achieve an arbitrary pose, as shown in Figure 9.2, and so can be applied to earth-observation cameras or space telescopes that may need pointing relative to the spacecraft bus. However, the FPI offers the ability to tune stiffness of the connection to change the natural frequency of the system and attenuate specific frequencies between the bus and the payload transmitting to the payload, which represents a capability not typically available among existing Stewart platforms. Because this capability demonstrated many of the benefits of FPIs as a technology,

Figure 9.2. A CAD rendering a spacecraft equipped with a flux-pinned interface, with cryocooled superconductors on the bottom module and controlled electromagnets on the top module.

this application has been selected as a baseline for the first FPI orbital demonstration, described in Chapter 8.

9.2.2 Modular Spacecraft and Formation Flying

FPIs can also be used to provide stiff non-contacting connections between different modules in modular spacecraft and formation flying scenarios. The well-known advantages of a modular spacecraft system include the ability to quickly and autonomously repair broken subsystems, upgrade payloads, and refuel on-orbit. If these subsystem modules are connected to one another via an FPI, the collection of modules can maintain close, passively stable relative distances that simplify the power transmission and communications challenges of modular spacecraft. The process of detaching the old module and reconnecting and realigning the replacement module requires only basic control of the magnetic fields in the FPI. FPIs offer a unique way of performing the station-keeping of modular spacecraft on-orbit, while still exhibiting the advantages that such designs are intended to exploit.

This ability also extends to novel formation flying techniques where the modules are instead complete spacecraft working in tandem to accomplish some specific goal. For example, formation flying earth-observing satellites can provide three-dimensional images of the earth. However, FPIs offer formation flying capabilities at relative distances on the order of centimeters to a meter, which is a very challenging regime

for standard active control techniques and not offered by most current formation flying technologies. Figure 9.3 shows a concept in which satellites use superconductors and magnets to create stiff connections between the elements in the formation.

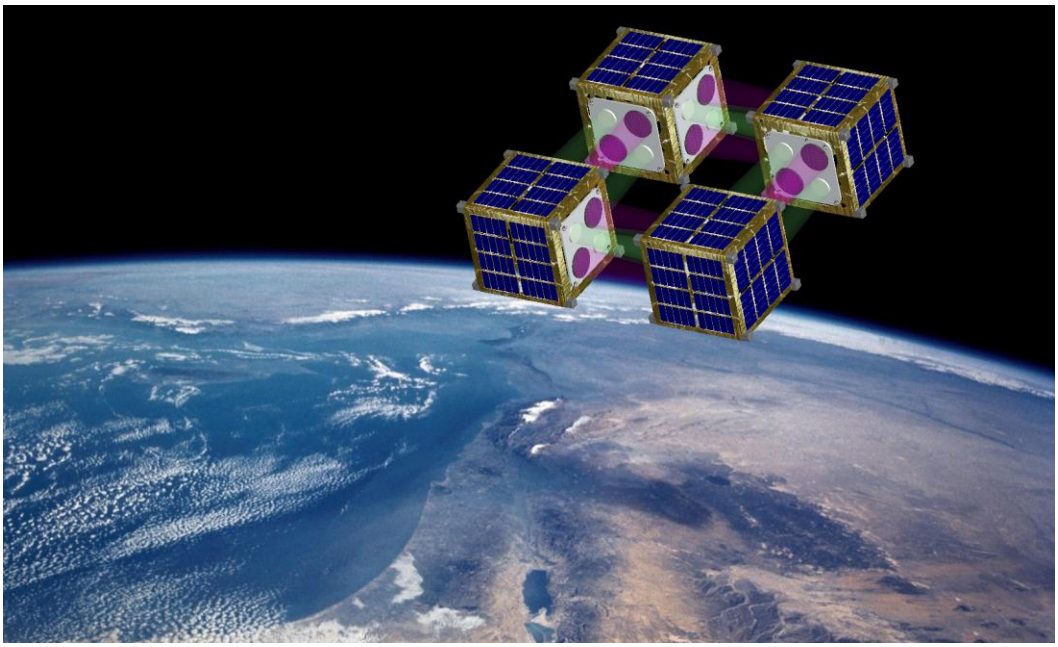

Figure 9.3. Concept of a satellite formation flying mission where groups of satellites can be held stiffly in place at relative distances on the order of tens of centimeters or less.

9.2.3 Autonomous Assembly and Virtual Structures

In more forward-looking applications, the properties of FPI connections may also assist in the autonomous assembly of large-scale space structures. Due to limitations in launch fairings, many advanced space systems currently must utilize a highly-folded origami-style design that then performs advanced deployment sequences in space, such as the James Webb Space telescope. Others, such as the International Space Station, require multiple launches and direct human manipulation to assemble. FPIs can be designed to set up a passively stable potential well that draws the desired

component into place with passive techniques, and then stiffly locks the component in place. If perfected, this technique could be used to form virtual self-assembling structures that can then be used to assemble complex space systems such as mirror segments in a large space telescope, as shown in Figure 9.4.

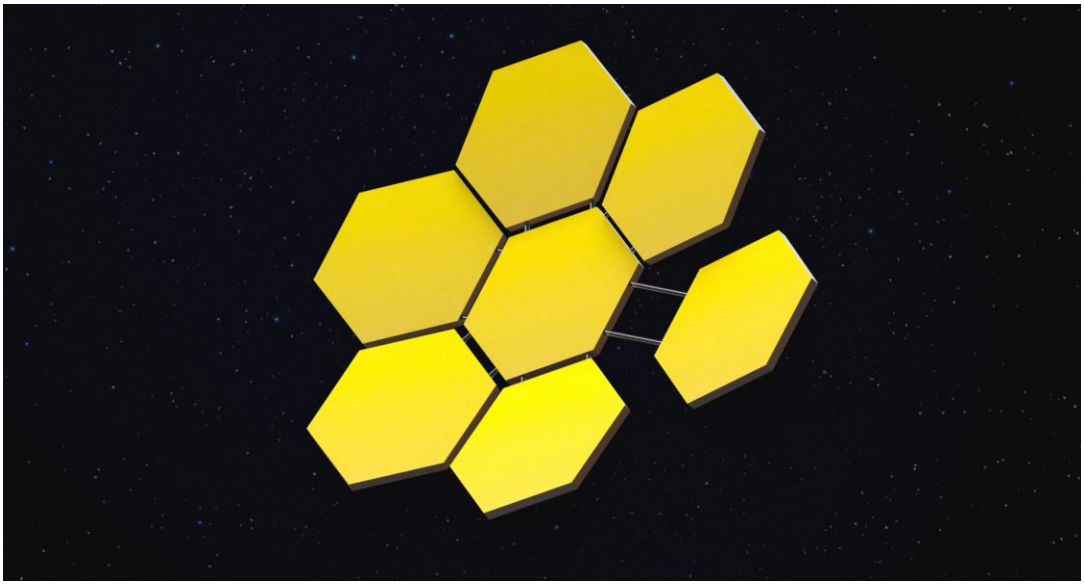

Figure 9.4. Flux-pinned interfaces can be used to build virtual structures for multi-launch payloads that must assemble on-orbit such as large-aperture space telescopes.

9.2.4 Rendezvous and Docking Augmentation

Rendezvous and docking, as shown in Figure 9.6, is a natural application for FPI technology. Since flux pinning does not work outside of a range of approximately a meter, active control is necessary to manipulate the spacecraft to the close-range phase of the maneuver. Once in this phase, however, the FPI augmentation provides benefits at each point in the sequence of events, as shown in Figure 9.5. The nonlinear potential well formed by the flux-pinned system corrects misalignments without requiring any feedback control, and therefore allows the system to be robust to errors in the guidance system when in close proximity. An equilibrium can be established at

Figure 9.6. An FPI-augmented docking sequence can be used to assist autonomous rendezvous routines in the final phases of the maneuver.

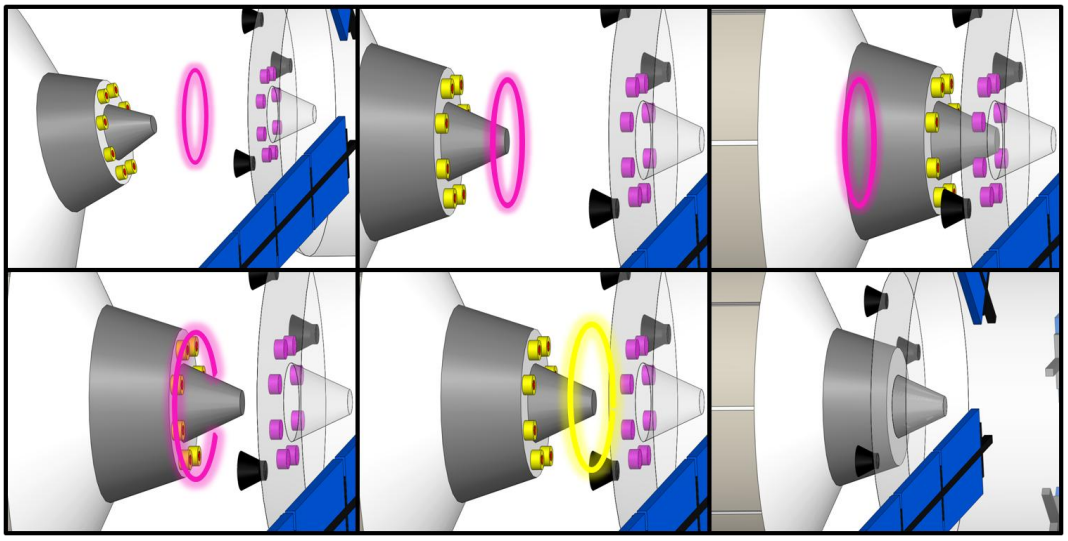

Figure 9.5. A conceptual spacecraft with flux-pinned docking augmentation in the six stages of docking, with permanent magnets in red, electromagnets in yellow, and HTSCs in purple. Flux pinning corrects alignment and slows relative velocity of approaching spacecraft (top, left). Magnets draw approaching spacecraft to preset equilibrium within reception range (top, center). Magnets resist collision and damp rebound (top, right). FPI has captured spacecraft at stable equilibrium (bottom, left). Electromagnets activate to draw spacecraft to new, closer equilibrium (bottom, center). Spacecraft deploy their physical interface to achieve structural connection (bottom, right).

a pre-selected safe distance between the modules, and the FPI provides impact attenuation forces if the modules move closer than that equilibrium. This effect reduces the chances of a collision and helps to mitigate the impact if one does occur.

Once at an equilibrium point, electromagnets can alter the magnetic field in the FPI in order to successfully soft-dock in a controlled and passively-stable manner.

9.2.5 Cooperative Grapplers

The same characteristics that make an FPI useful in a rendezvous sequence also make it ideal for grappling cooperative spacecraft as well. Provided that the object being manipulated is outfitted with a magnetic field connector, the superconductors on the grappling hand can manipulate a target without needing to contact it. This approach to grappling can help preserve delicate structures on the spacecraft (or other object) being handled because it does not subject the target to contact loading or other disturbances. In its simplest iteration, the only accommodation the target spacecraft must make for this type of grappler is to include a ring of permanent magnets on its surface at a hard point. The permanent magnets require no electronics integration and basic mechanical integration. In fact, spacecraft currently in production can start adding these interfaces to their existing product with little effort or risk in anticipation

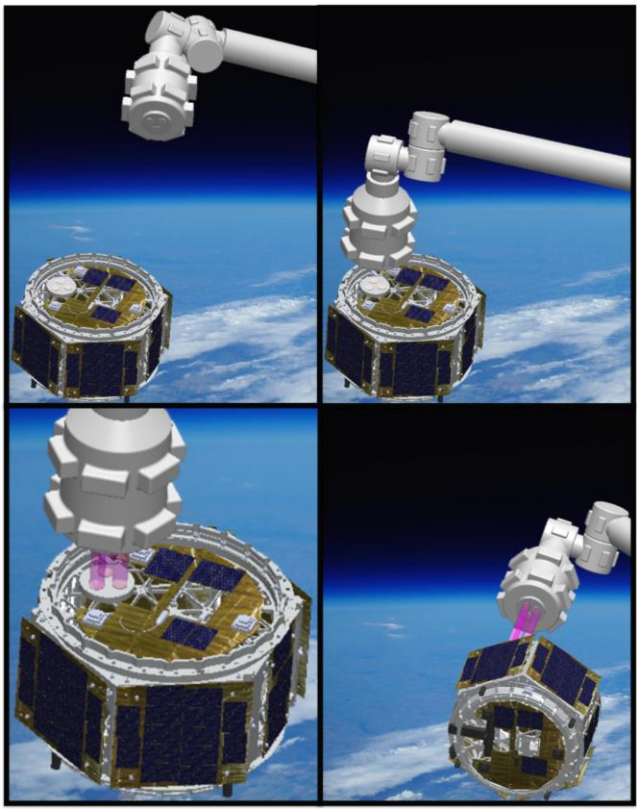

Figure 9.7. A sequence showing the utility of an FPI-based cooperative grappler. A satellite equipped with an appropriate magnetic patch can be manipulated by the grappler without contact between the two.

of a superconductor-based servicing mission in future years. Figure 9.7 shows a sequence where the grappling arm manipulates a satellite without contacting it.

9.2.6 On-Orbit Reconfiguration

On-orbit reconfiguration allows a satellite to take on a different geometry to accommodate changing mission requirements. FPIs provide the unique capability of enabling non-contacting close-proximity satellites to reconfigure relative to one another by controlling the stiffness in each degree of freedom. As discussed before, asymmetries in the magnetic field in an FPI provide stiff degrees of freedom that can be used to construct flux-pinned kinematic constraints whereas intentional symmetries in the magnetic field produce non-stiff degrees of freedom that allow for movement in those directions. These effects can be used to design non-contacting joints made of flux-pinned components. For example, a flux-pinned cylindrical magnet can effectively serve as a non-contacting hinge with an unrestricted degree of freedom about its axis of symmetry. With a mechanism to change the magnetic field, this hinge

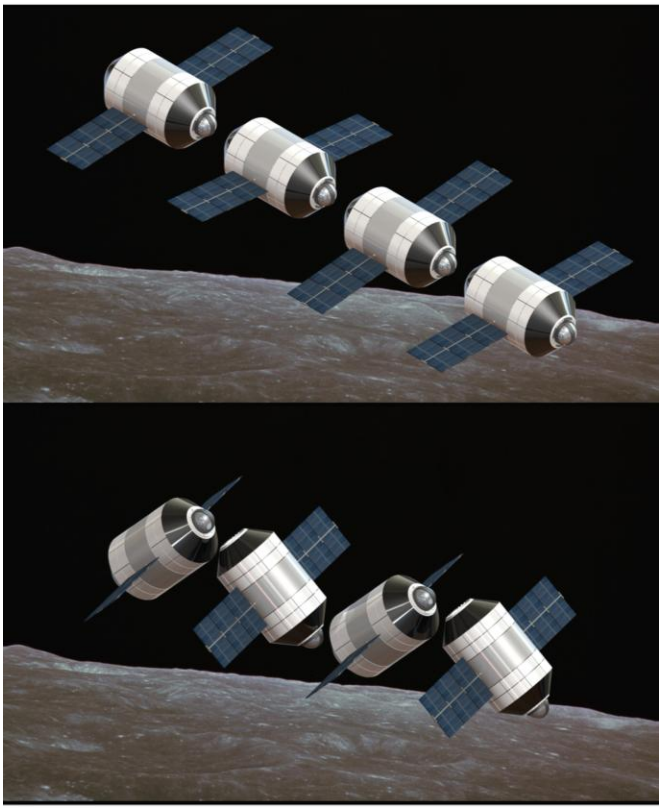

Figure 9.8. A non-contacting reconfiguration maneuver enabled by interchangeable FPIs .

can easily be converted into a fixed connection or a different type of joint. Structures can be set up to evolve into desirable configurations based on these constraints and the potential energy wells in the system, as shown in Figure 9.8 leading to a novel approach to spacecraft reconfiguration.

9.2.7 Flux-Pinned Solar Sail Concepts

In more futuristic concepts, FPIs at a small scale may enable new designs for solar sail propulsion. Traditional solar sail architectures involve large ultra-thin reflective membranes stretched across lightweight structural elements, which are primarily designed to support a large surface area with minimal mass dedicated to infrastructure. A number of fundamental engineering challenges are inherent in such designs, including packing and deploying the sail, controlling the spacecraft once the sail has been deployed, and protecting the solar sail from the space environment.[162] FPIs provide an alternative fractionated solar sail design in which the sail itself is composed of small discrete particles held in place by superconductive flux-pinning forces. Two designs of these particulate solar sails can exploit flux pinning. The first, a so-called particle-cloud sail, involves reflectively-coated superconducting particles passively cooled in space held in place with large loops of superconducting wire inducing a magnetic field.

The second architecture, the integrated solar sail shown in Figure 9.9, uses flux pinning to connect small satellites known as ChipSats.[163] An individual ChipSat is on the scale of a square centimeter, making its individual functionality limited, but since they are easy to mass-produce and essentially expendable, they can be used as distributed sensors over large areas in high-risk environments. If they can be flux-

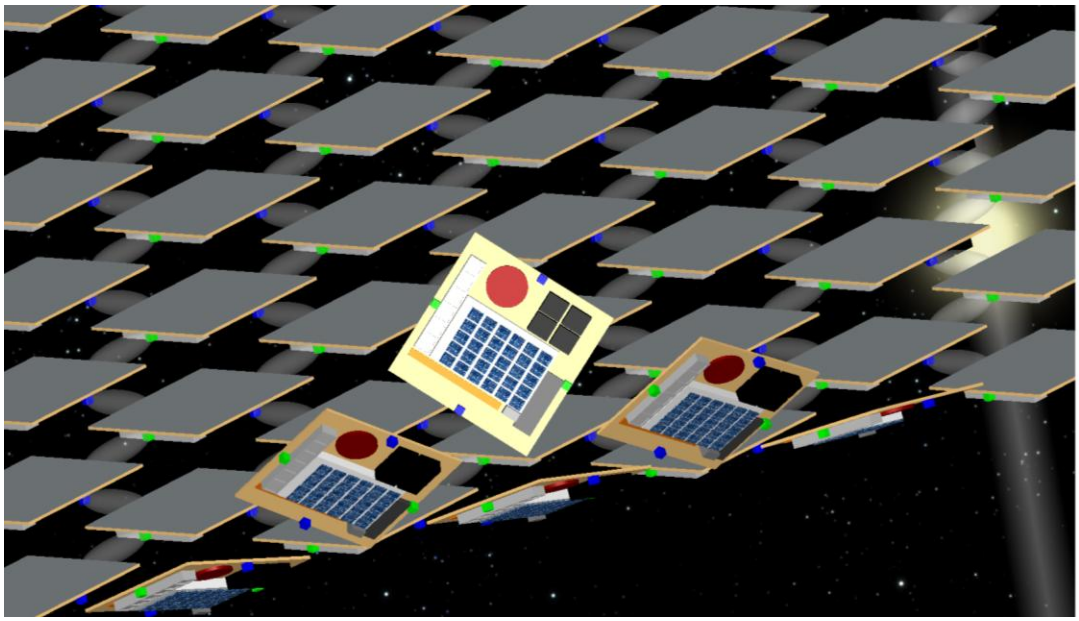

Figure 9.9. An integrated solar sail concept that combines flux pinning with ChipSat technology to produce a swarm of satellites capable of sailing to a destination then breaking into components to provide distributed sensing capabilities.

pinned together into a large sheet, ChipSats fitted with a reflective face can then collectively act as a solar sail. This design has unique actuation and deployment techniques, which represent significant engineering challenges, but as a low-TRL design this concept may provide direction for future research endeavors.

9.3 Summary of Contributions of the Work

This dissertation summarizes a significant cross-section of the development work related to both the theory and technology of flux-pinned interface for space systems performed from 2007 – 2012 in Cornell University's Space Systems Design Studio. When work was started on this project, the basic concepts of the FPI were established and basic characterization work of a superconductor-magnet system had been completed. Now, after five years, the following achievements have been contributed to this growing and rapidly maturing field:

- Development of design principles for close-proximity spacecraft interactions influenced by flux pinning
- Extension of the frozen image model of flux pinning to include the full nonlinear multi-magnet six-degree-of-freedom equations of motion
- Proof of the stability of a general class of FPIs
- Establishment of FPI actuation principles and control techniques inspired by passivity principles
- Formulation of a magnetic steering law for FPI control
- Experimental validation of FPI architectures in both a laboratory and microgravity environment
- Formulation of mission architectures and flight-operations strategies

These contributions, coupled with numerous collaborative endeavors involving dozens of undergraduate researchers, half a dozen other graduate researchers, faculty from Cornell and other institutions, and industry/civil servant researchers, have helped establish FPIs as a viable and promising technology.

9.4 FPI Future Work

However, even as comprehensive as FPI research has been to date, the wide-ranging applications and variety in implementations available to FPI designers leave a number of unstudied directions and issues that are still completely open questions. Subsequent FPI research should attempt to address these unanswered questions in order for the space community to reap benefits from the full breadth of FPI capabilities. Although not exhaustive, some of the most important of these remaining challenges are:

- Implementation of advanced models of flux pinning to achieve better agreement between simulation and hardware

- Optimal control strategies that take into account physical and model limitations

- More extensive laboratory testing for superconductors, particularly with regard to high-frequency electromagnetic interference and low-frequency electromagnetic actuation effects

- Technology development of application-specific low-TRL designs, such as the FPI grappler or solar sail concept

- Additional optimality studies to establish the best superconductor material, optimal magnetic array design, etc.

- Refinement a thermal design that meets the FPI requirements both for microgravity and orbital testing

- Development and demonstration (in space) of advanced orbital FPI designs

Ultimately, the goal of FPI development should be to bring the technology to a sufficient maturity that it can be useful to spacecraft designers, researchers, and users alike.

APPENDIX A:

FLUX-PINNING-AUGMENTED DOCKING SEQUENCE

This section provides additional details regarding an FPI-augmented docking sequence originally published at the Space 2010 conference.[160]

A1 The Rendezvous and Docking Procedure with FPIs

A typical spacecraft mission involving docking can be divided into five major phases.[12]

1. Launch
2. Phasing
3. Far range rendezvous
4. Close range rendezvous
5. Mating

As flux pinning can generally be used on the scale of the augmented spacecraft's length, it can best be applied to this sequence during the close range rendezvous segment. Flux pinning can in some cases also provide an ideal mating solution as well, as in the case of a frequently reconfiguring modular spacecraft that does not require physical connections between modules.

Flux pinning can be used during the close approach phase of docking to improve currently used procedures. A typical docking process, as described in Fehse 2003,[12] involves several stages of maneuvering at close range to complete the docking sequence, some of which are listed below:

1. Reduction of approach velocity and misalignments

2. Reception
3. Impact attenuation
4. Capture
5. Retraction and structural alignment
6. Structural connection

Once the spacecraft are in close proximity, they must first reduce relative velocity and misalignment of their docking interface. As the craft close to the range of a few meters, they must achieve alignment to place the docking interface within reception range. In the reception phase, the docking interfaces of the two spacecraft enter each other's reception range, the range in which physical contact of the spacecraft is possible. Before physical contact can be made, the relative velocity between the craft must be reduced. This reduces the impact shock between the vehicles when contact is made, decreases rebound velocity, and increases time available for the capture process. Once reception and impact attenuation have been accomplished, the capture structures of the docking interface can engage, preventing the two vehicles from escaping from each other. After capture, the spacecraft must be aligned so that a structural connection can be made. This connection must provide stiffness to keep the vehicles together under any loading conditions the system can experience.

Current docking routines, such as those employed on the European Space Agency's Autonomous Transfer Vehicle, or ATV, employ primarily visual sensors at close range. The ATV uses multiple onboard visual sensors in conjunction with visual data from the International Space Station.[8] Despite the computing effort and active control guiding visual-based docking, it is an inherently difficult and dangerous process because strategies are vulnerable to loss of communications, power failures, and unpredicted errors that affect the control system. One example of such a failure was the 2005 Demonstration of Autonomous Rendezvous Technology (DART) project, which attempted to autonomously rendezvous with a satellite, but due in part to erroneous navigational code instead collided with its target.[18] This failure during a technology demonstration of actively controlled docking demonstrates the need for a

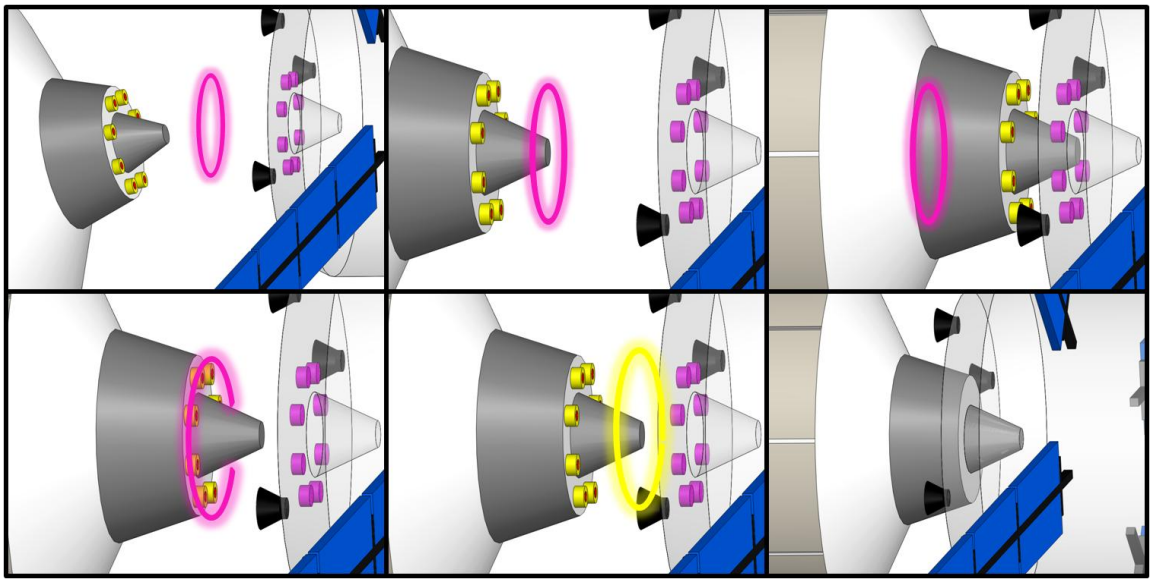

Figure A.1. A conceptual spacecraft with flux-pinned docking augmentation in the six stages of docking, with permanent magnets in red, electromagnets in yellow, and HTSCs in purple. Flux pinning corrects alignment and slows relative velocity of approaching spacecraft (top, left). Magnets draw approaching spacecraft to preset equilibrium within reception range (top, center). Magnets resist collision and damp rebound (top, right). FPI has captured spacecraft at stable equilibrium (bottom, left). Electromagnets activate to draw spacecraft to new, closer equilibrium (bottom, center). Spacecraft deploy physical interface to achieve structural connection (bottom, right).

more robust method of accomplishing spacecraft docking.

Flux pinning can be used to accomplish some or all of these docking stages, as is illustrated in Figure A.1. In a simple example, the target spacecraft would mount a superconductor with a pinned image as part of its docking interface, while the approaching vehicle would have a permanent magnet that matches the pinned image. As the spacecraft enter the range where magnetic fields can significantly affect their interactions, flux pinning can bring the two craft to a known, safe relative equilibrium. The magnet on the approach vehicle will seek the distance and alignment of the pinned image in the superconductor, performing a reduction of the system's relative velocity and misalignment. Provided that the preset equilibrium position is within reception range, the vehicles will also be passively drawn into reception. The damping present in flux pinning interactions can provide significant impact attenuation between the spacecraft. With correctly chosen magnets and superconductors, the flux-pinned interface will bring the relative velocity and misalignment between vehicles to zero and leave them in a known and passively stable equilibrium position. So long as the pinning is maintained, this equilibrium can serve as the capture of the spacecraft.

The addition of an electromagnet to the approaching spacecraft can extend the use of flux pinning to the retraction and structural alignment phase of the docking sequence. The electromagnet can provide fine actuation of the established flux-pinned equilibrium position. It can be used to bring the craft closer together or to reorient the craft to a more convenient alignment, providing any needed retraction and structural alignment. For spacecraft needing to physically connect, they can now deploy physical docking apparatus. Modular spacecraft, with segments that do not require physical

contact, can rely on the established flux pinning to maintain connectivity between modules.

Though based on the interaction between a magnetic field source and a superconductor, the specific flux-pinned interface used for spacecraft docking can be designed to fit a wide variety of missions. Current demonstrations of flux pinning assisted docking has focused on applications for nanosatellites, specifically CubeSat modules of various sizes. With a cross-sectional area of 10 cm^2 and a height of 10, 20, or 30 cm, premade standard electronics inserts, and a flexible launching system, the CubeSat platform is ideal for university projects and technology demonstrations. Observations of a 100g Neodymium magnet has been used to characterize the flux pinning interaction with a 56cm diameter single domain superconductor,[19] component sizes that fit well into CubeSat designs. As is show in Shoer 2008, the dipole moment of a magnet correlates to the magnet's mass. Therefore magnet mass can be used as a significant performance predictor. Magnets in the range shown have noticeable flux pinning effects up to ranges of about 10 cm, with very high stiffnesses as the magnets approach the surface of the superconductor. Though current work has focused on applications in this range of component sizes, the scaling effects observed suggest that larger spacecraft can be augmented with similar performance flux-pinned interfaces by increasing the size of magnet and superconductor components. With FPIs of sufficient strength, flux pinning augmentation could be used to increase the ease and safety of docking on larger spacecraft such as the ATV.

A2 Design Parameter Considerations

Implementation of flux-pinned augmentation for docking interfaces will require optimization of the components making up the onboard FPIs. General requirements for spacecraft that will play an important role in flux pinning docking augmentation systems include component mass, power requirements, and volume requirements. Magnet mass has a positive correlation to field strength, so as the forces necessary to make flux pinning useful on a spacecraft of a certain size increase, the magnet mass required to achieve this will likewise increase. Permanent magnets are typically more massive than electromagnets of comparable strength, but the reduced mass of electromagnets come at a cost of increased power requirements. The electromagnets are also more flexible in terms of mission design as their strength and direction can be changed via voltage inputs. Permanent magnets provide a more robust failure mode, however, as loss of power will not disengage flux pinning. A combination of permanent magnets surrounded by electromagnetic coils offers the most robust mission performance, as it provides both flexibility (by effectively cancelling the permanent magnet with the electromagnet if so desired) and a safe failure mode, but incurs both a mass and power cost. Magnet volume constraints will typically scale with mass.

APPENDIX B:

PROSPECTS AND CHALLENGES OF

PARTICULATE SOLAR SAIL PROPULSION

This section provides additional details regarding the FPI-based solar sailing concepts originally published in 2008.[162]

B1 Introduction to Solar Sailing

Solar sailing is a form of propellantless propulsion that uses solar photon emissions to affect the motion of a spacecraft via momentum exchange. Because this solar-pressure effect is weak, solar sails are designed with a large surface area in order to maximize the collection of photons with the least structural mass. This design paradigm has traditionally led to sails made of ultra-thin reflective films supported by gossamer structures, which are tightly stowed for launch and undergo a high-risk deployment once in orbit. Although recent advancements in lightweight boom and film technologies have made progress toward addressing many of the challenges inherent in this approach, a number of fundamental engineering difficulties remain.

These challenges, inherent to a large, delicate structure, include stowing and deploying the sail, controlling the spacecraft once the sail has been deployed, maintaining sail performance within the space environment[164], and testing a full-scale model in a relevant environment on Earth[165]. These issues could be greatly simplified if the sail were instead comprised of smaller, more manageable components that acted together as a large structure. Some recent sail designs have applied this concept on a large scale: for example, NASA's 20m quadrant sail prototype (shown in Figure B.1(a)) uses an axisymmetric arrangement of several smaller sails. However, these

designs still call for large, thin-membrane segments to provide most of the overall surface area and are thus still subject to the same difficulties confronting single-membrane solar sails. This investigation assesses the value of fractionating a solar sail one step further: creating a sail from homogenous constituent components on the scale of centimeters or smaller, as shown in Figure B.1(b).

Not only does a particulate solar sail provide a unique solution to the current

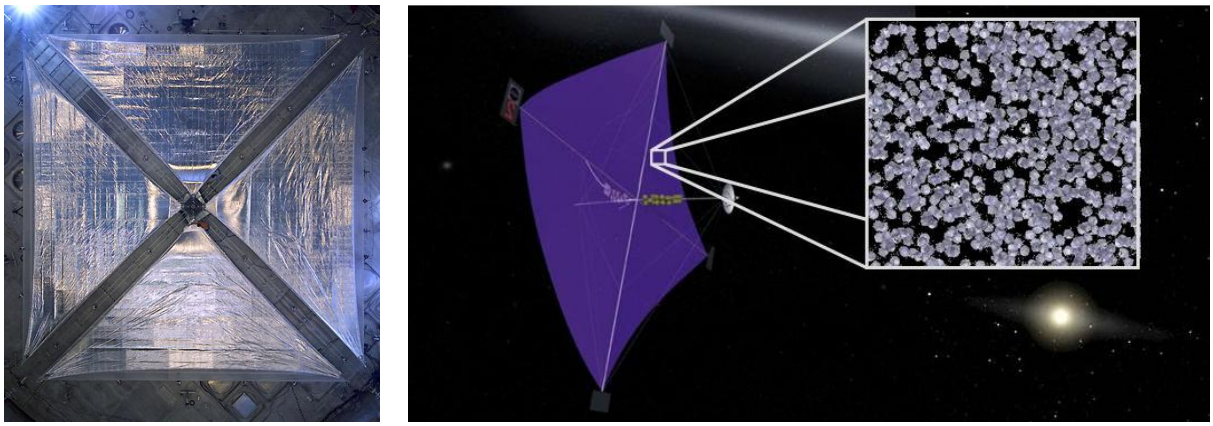

(a) (b)

Figure B.1. Fractionation of Solar Sails. (a) A NASA 20-m four-quadrant solar sail fully deployed in testing. This solar sail is comprised of four smaller sails, making the handling, deployment, and control of the finished product much more manageable than a single, large sail of the same size. Image courtesy of NASA. (b) A conceptual depiction of a particulate solar sail, where the sail material is divided into much smaller components, further reducing the difficulties in manufacturing and launching of the sail while offering increased robustness and novel opportunities. Background image courtesy of NASA.

engineering complexities of solar sailing, it also provides the flexibility and robustness inherent in a discrete fractionated space system. This system could be assembled in multiple launches to take advantage of incremental mission funding and the availability of smaller launch vehicles. Such a system may also lend itself better to in-situ repair missions. Further, a sail made of small independent particles would be highly robust to both launch-vehicle failures and micrometeoroids. The discrete nature of the particulate solar sail's surface allows small portions to be damaged without

affecting the overall performance of the sail, making this sail design especially suitable for proposed missions to asteroids and comets or other small-body rendezvous where the risk of such collisions is high.[166,167] These potential advantages motivate the present research into particulate solar sailing architectures.

Holding on to large numbers of small particles for use as a solar sail requires a means of maintaining a passively stable yet reconfigurable formation of these particles. One potential method of creating a particulate solar sail lies in the well-established phenomenon in superconducting physics known as magnetic flux pinning. When a type II high-temperature superconductor is exposed to a magnetic field of sufficient strength, it "pins" the magnetic flux such that the superconductor remains in a damped, passively stable equilibrium in up to six degrees of freedom relative to the magnetic flux source. This action-at-a-distance force can easily be manipulated by changing the magnetic flux, which in turn alters the equilibrium position of the superconductor.

Flux-pinned connections are well-suited to operations in space. Previous research has proposed using these flux-pinned interfaces as a method of stabilizing formations of satellites and constructing large space structures.[19,158] Distributed space systems such as a very-large-aperture telescope might also be controlled and stabilized with flux-pinned interfaces.[159] By extension, the particulate solar sail can exploit the flux-pinning effect using superconductive sail particles and magnetic or thermal actuators.

This section examines two example particulate solar sail architectures in more detail, including design considerations for the particles, implications on deployment techniques, sail control concepts, and theoretical performance parameters. The two

architectures studied are the 1) particle cloud sail and 2) the integrated payload sail. From this analysis, preliminary conclusions are drawn regarding the range of expected performance and the types of solar sailing missions to which the particulate solar-sail architectures may be best suited.

B1.1 Solar Sail Concepts

The basic ideas behind solar sailing have been known for over a century, although the necessary refinement of the concept has taken place only in the last few decades.[167] The technology has matured significantly in the past few years, raising the Technology Readiness Level of solar sailing to 7.

The fundamental principle of solar sailing is illustrated in Figure B.2. If the solar sail is a perfect reflector, the combined impulse of the incident and reflected photons produce a resulting force on the solar sail that is nearly normal to the plane of the sail. By orienting the sail such that the resulting force opposes the motion of the

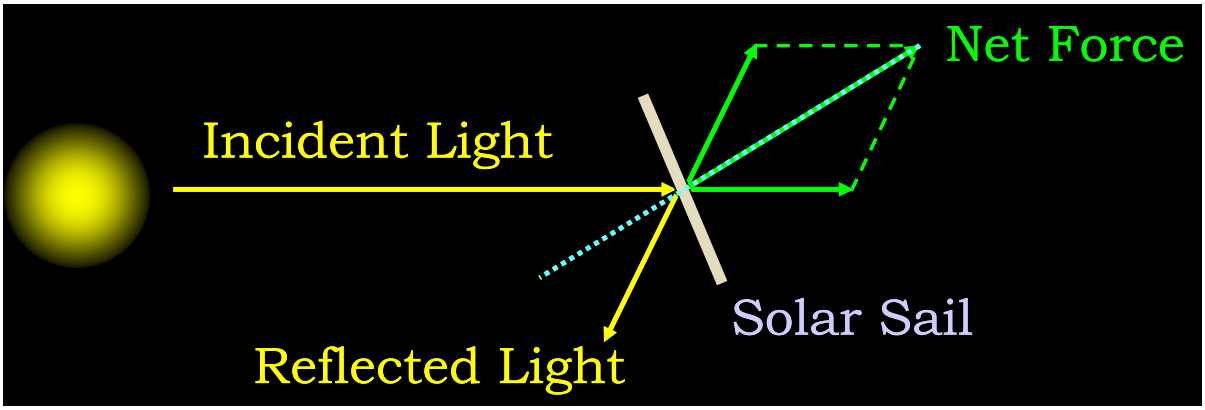

Figure B.2. The Basic Principle Behind Solar Sailing. If the sail in the diagram were moving in an orbit around the sun in the plane of the paper with an instantaneous velocity upwards on the page, this sail would be increasing its orbital angular momentum since the net force is reinforcing the motion of the orbit.

spacecraft's orbit, the sail causes the spacecraft to lose orbital angular momentum and spiral inwards towards the attracting body. On the other hand, if the resulting force vector is aligned such that the net force is increasing the orbital angular momentum, the orbit's energy grows, and the spacecraft spirals out from the sun. Changing the angle of the sail's surface normal relative to the sun can thus actuate the solar sail's orbit in a desired manner. [167]

Certain metrics characterize the efficiency of the sail design and its expected thrust and payload capabilities. The two most critical are the characteristic acceleration a_0 and the sail loading σ, which are given respectively in the following equations assuming a perfectly reflective surface (represented by the factor of 2):

$$a_0 = \frac{2\eta P}{\sigma} \tag{B.1}$$

$$\sigma = \frac{m_T}{A} \tag{B.2}$$

where η is the sail efficiency factor that takes into account losses from billowing and creases, P is the solar light pressure acting on the sail, m_T is the total mass of the spacecraft (payload and sail combined), and A is the surface area of the solar sail.[1] The characteristic equation describes the acceleration that one square kilometer of sail could expect to experience at a distance of 1 AU, where the solar pressure is 4.56×10^{-6} N m^{-2}.[11]

One distinguishes between payload mass m_P and sail mass m_S, where the summation of these two masses is equivalent to the total mass m_T. This distinction leads to another parameter, known as the payload mass fraction R[1]:

$$R = \frac{m_P}{m_P + m_S} \tag{B.3}$$

The higher the mass fraction, the more nearly ideal the spacecraft propulsion system design, as the goal is to maximize the amount of payload while minimizing the propulsion infrastructure mass. A mass fraction of 1/3 is used in McInnes for purposes of demonstrating the relative scales of the various parameters. Substitution yields:

$$a_0 = \frac{2\eta P}{\sigma_S + \left(m_P \middle/ A \right)} \tag{B.4}$$

$$\sigma_S = \frac{m_S}{A} \tag{B.5}$$

where the parameter σ_S is known as the sail assembly loading. This parameter represents the efficiency of the sail's design: lower values indicate greater efficiency. It is difficult to determine a realistic range for these values since a solar sail has yet to be implemented in a flight demonstration. As of 2007, proposed designs have claimed the following values: sail efficiency factors (η) between 0.75 and 0.92 and sail assembly loading values (called "areal density" in the reference) between 20 g m^{-2} and 112 g m^{-2}, with more optimistic predictions of 12 g m^{-2} to 14 g m^{-2} with a larger, scaled-up design.[168] These value ranges are likely best-case scenarios, but they can be used to obtain an approximate basis for comparing current solar sail designs and the performance of particulate solar sails.

B2 Example Particulate Solar Sail Architectures

For this study, two very different particulate architectures were chosen to demonstrate the range of possibilities. Both of the following sections include a discussion on particle properties, structural mechanisms, deployment techniques, and control concepts relevant to the specific architecture under consideration. The performance of the architecture is then assessed as a function of the performance parameters and any specific advantages/enabling technologies or disadvantages/unique problems associated with the particulate solar sail.

B2.1 Particle Cloud Sail

The particle cloud design consists of a conducting wire mesh that uses the magnetic field induced by current flowing through loops in the mesh to flux pin trillions of reflectively coated superconducting particles on the order of 10^{-4} m in size into a dense arrangement between the wires. Figure B.3 shows a schematic of this design. The reflective superconducting particles act as the main collector of photons. As the momentum exchange occurs, the dust particles accelerate, and via their flux pinned connection to the rest of the spacecraft, cause the payload to accelerate as well. However, due to the faint pressure of the sunlight, this acceleration induces only very small motions in the particles. So, the small-displacement assumptions on which many mathematical models of flux pinning are based hold for this architecture.

The particles within this architecture require some design effort in order to ensure that the conditions necessary for the particulate solar sail concept to work will be present. Flakes and grains of a type II HTSC such as YBCO can be coated with the same vapor-deposited reflective aluminum coating intended for traditional solar sail

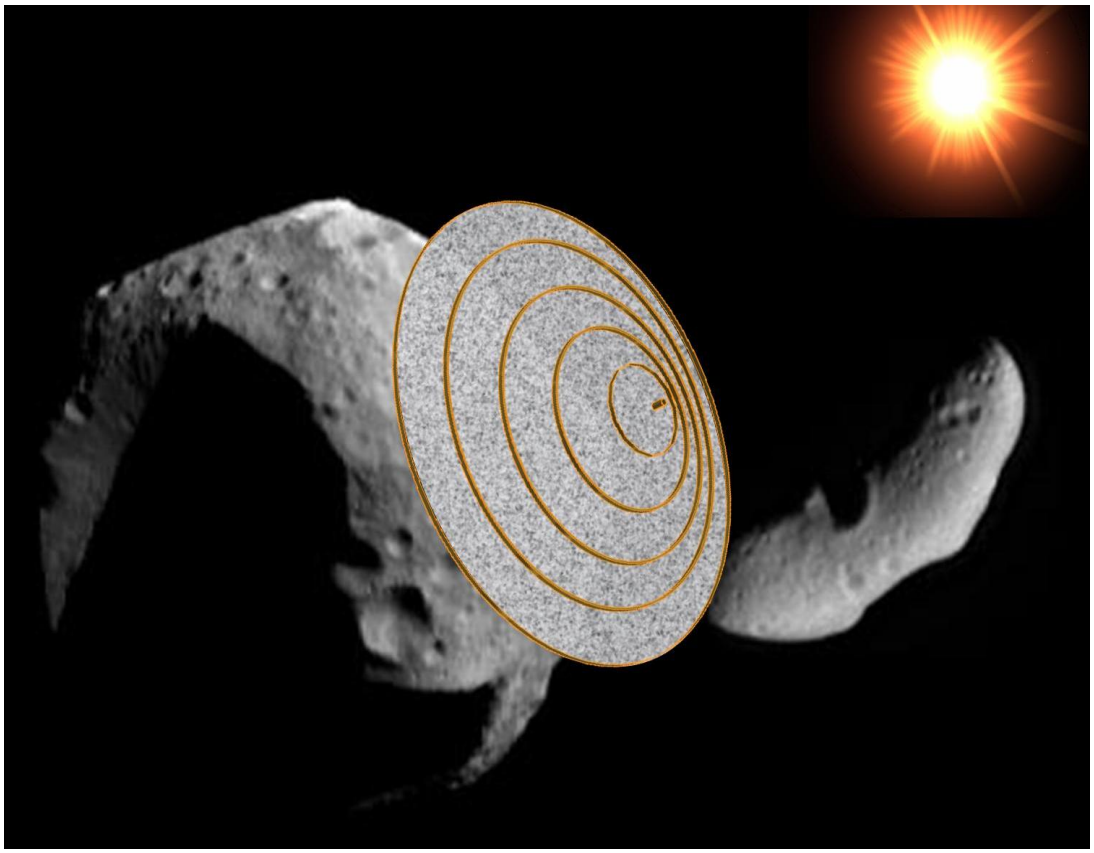

Figure B.3. The particle cloud solar sail concept, where rings of wire trap small particles of reflective superconducting dust.

films (see Figure B.4). This coating is on the order of 0.1 μm thick[11] and would not affect the superconducting properties of the HTSC. The primary driver for the shape and material of the particles for the particle cloud architecture is the temperature of the particles. The particles must remain below their transition temperature in order to remain flux pinned to the sail structure. Since the particles are also being exposed to significant amounts of sunlight, one must design the reflective properties and geometry appropriately. It might be that thicker particles (longer in the sun-normal direction) are best for rejecting heat. Further, the size of the individual superconducting particles must be large enough to contain the defects in grain structure that are required for flux pinning.

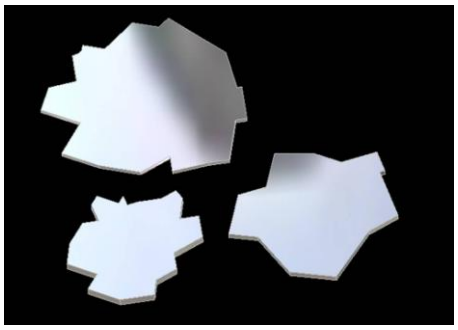

Figure B.4. Particle cloud architecture particle concept. The particles in this architecture are "flakes" and "grains" on the order of 10^{-4} m. The particle is simple to manufacture, as they are simply small pieces of superconductor coated with a reflective material.

The structural design of this architecture is a wire mesh of concentric circles, where current is pumped through the wires in such a way that no two adjacent wires have current flowing in the same direction (as shown in Figure B.5). Thus, the fields of the wires make them repel one another, forcing the structure to fully expand without the use of inflation or mechanical-deployment systems. If necessary, additional rigidization can be added via a space-curing resin proposed for the structural elements of a traditional solar sail[11] to ensure that the wires remain stiff hoops. Further, the interacting fields of the wires produce a magnetic flux distribution that has circular lines of equal flux (a zero-stiffness degree of freedom for the flux-pinned superconductive particles) in a plane parallel to the structural elements. Thus, while the superconducting particles are free to move in the plane of the sail structure, they will be constrained to the surface that is collecting the photons to produce thrust.

In order to arrive at this point, the particle cloud sail is launched as a container (or several containers on separate launches) with a densely packed arrangement of the superconductive particles, requiring no folding or other special packing requirements. Once in a desired orbit, the particles of the particulate solar sail are released from a container on the spacecraft and captured magnetically by the unfolded sail structure. The deployment of the particulate sail is not driven by any of the concerns typical of a delicate membrane, reducing the risk of failure during this phase of the mission.

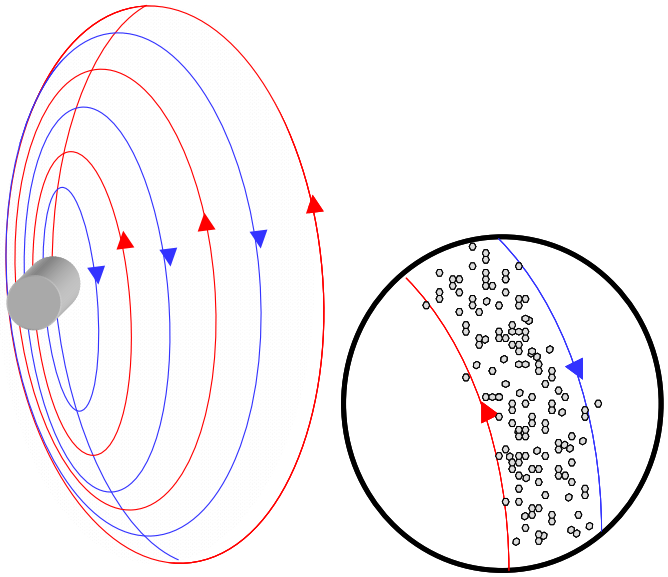

Figure B.5. Particle Cloud Structural Design. The structural design for this architecture consists of wires spaced on the order of 10^{-2} m, with each wire alternating the direction of the current flow so that the adjacent wires repel one another and cause the structure to deploy. The current is provided by the main spacecraft bus, shown as a grey cylinder above.

One of the primary challenges in this architecture is the timing and proximity of the particle release to the spacecraft structure, and the staged process of deploying and activating the structure in order to ultimately produce a relatively homogenous distribution of particles in each ring. Doing so may involve field cooling the particles before they are deployed so that they are trapped by the coils after release.[4]

Once the system is deployed, the particle cloud sail need only maintain the current flow in the wires to maintain the structural integrity of the sail. Changing the current in the wires (thereby changing the amount of magnetic flux applied to the particles) changes the properties of the flux-pinning connections, including equilibrium location and stiffness. Thus, this design provides a way to actively control the stiffness of each ring of particles independently, akin to using ropes to control the tension in marine sails or smart material booms to warp a traditional solar sail. Clearly this control is limited by the current available and the magnetic flux capacity of the particles in order

to retain their flux pinning behavior. Certain sections of the sail can be released entirely in order to rapidly change the properties of the sail itself (including the center of mass and the center of solar pressure), leading to the possibility of an agile solar sail.

The performance of this sail will depend on the efficiency of the particle design and the density of the particles. Due to the fact that the particle variation will be high and the orientation of these particles will not be controlled, it is likely that a particulate solar sail will not reflect photons as efficiently as a standard thin-film solar sail. As a 0.7 efficiency factor is considered low for a traditional solar sail in current designs, it is reasonable to estimate an efficiency factor of 0.6 for a particle cloud solar sail. Further, the density of the superconductive particles (both the mass density of individual particles and the packing density of the particles into the magnetic rings) must be determined. The mass density of the type II superconductor YBCO is a good first order approximation, leading to an estimation of 5 g cm^{-3} for the mass density of the particles.[169] Further, assuming that the layer of particles is on the order to 10^{-5} m thick, the sail assembly load factor for a particle cloud sail is 50 g m^{-2}. Although this number is still in a higher range of currently estimated sail assembly loading factors for traditional solar sails, it does indicate that a particle cloud solar sail may be able to perform comparably to its thin-film counterparts. To determine the characteristic acceleration, the packing density of the particles is assumed to achieve a 95% coverage of the surface area it encompasses, leading to a value of 0.1 mm s^{-2}. This characteristic acceleration is an order of magnitude below those anticipated for traditional solar sail designs, but this value is not low enough to dismiss the concept of

the particle cloud sail altogether. The performance may be improved by optimization of the particle design and better estimation techniques for the loss due to non-perfect reflection. The unique strengths of this design may merit an engineering trade-off between performance and unique capability.

B2.2 Integrated Payload Sail

The integrated payload sail is a completely different approach to a discrete segment-based solar sail. This architecture draws on an emerging technology known as a satellite-on-a-chip,[170,163] where all of the functionality of a standard spacecraft resides on a centimeter-scale chip, as shown in Figure B.6. Although a spacecraft the size of a small coin clearly does not function as a full-sized spacecraft in all ways, ChipSats can be produced cheaply in large amounts. This capability, as well as new behaviors available by virtue of small-scale physics, opens the way for large-scale distributed sensing and other behaviors that large spacecraft cannot achieve. The integrated-payload sail architecture attaches flux-pinned interfaces to these very small satellites and enables them to join together into a large sheet of discrete, non-contacting, linked units. When large numbers of the chips form a larger sheet, the solar pressure acts on the sheet as a whole, allowing this linked formation of ChipSats to move as a solar sail. One unique aspect of this architecture is that the sail itself is now composed of distributed sensors (as shown in

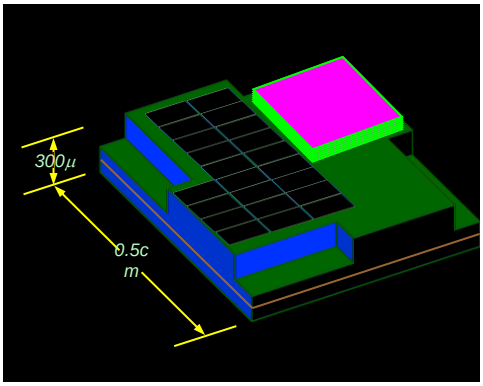

Figure B.6. A Chip-Sized Satellite.

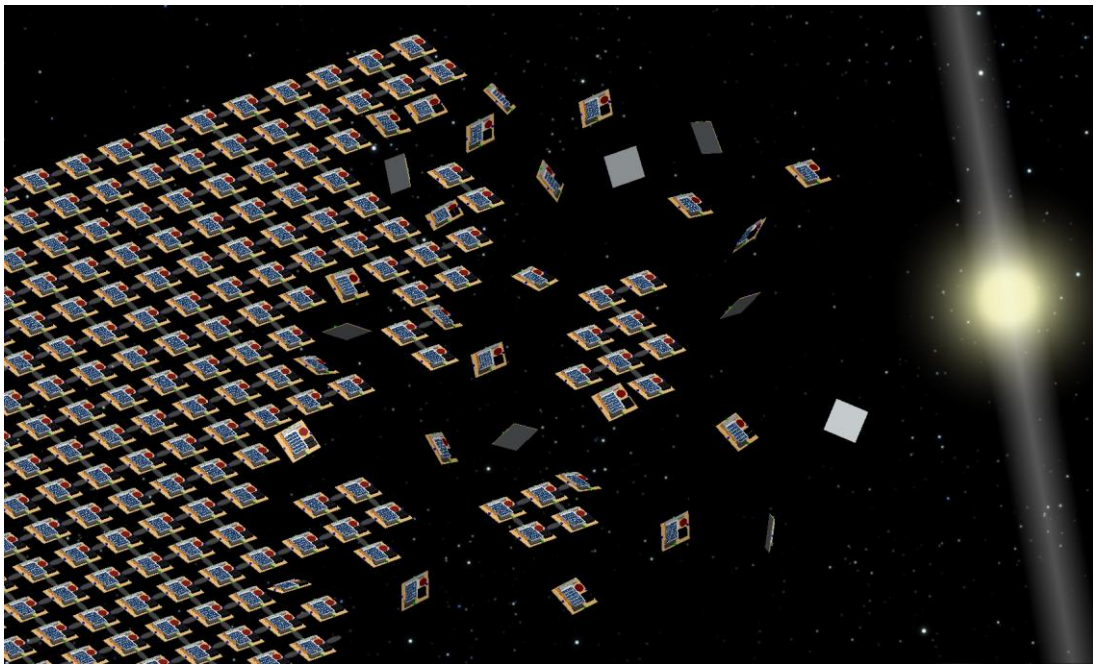

Figure B.7. The Integrated Payload Solar Sail. SpaceChips form together to make one macroscopic structure that acts as a solar sail.

Figure B.7). Because these particles are flux-pinned together and are essentially independent spacecraft (despite their unusual size), this architecture can be modeled with the small-motions flux-pinned formation equations of motion described in reference 91.

The particle scale design for this architecture is simply that of an individual chip, since the satellite-on-a-chip concept is already in development by several research groups. Thus, the particles will have a surface area of approximately one square centimeter and a thickness of less than 20 micrometers.[15] The only modifications necessary would be those that ensure the ChipSat's compatibility with the thermal requirements for the flux pinning interfaces and the reflectivity required for an effective solar sail. Specifically, one side of the chip is coated with the same vaporized aluminum described above in order to produce a close-to-ideal reflection of the sun's photons,

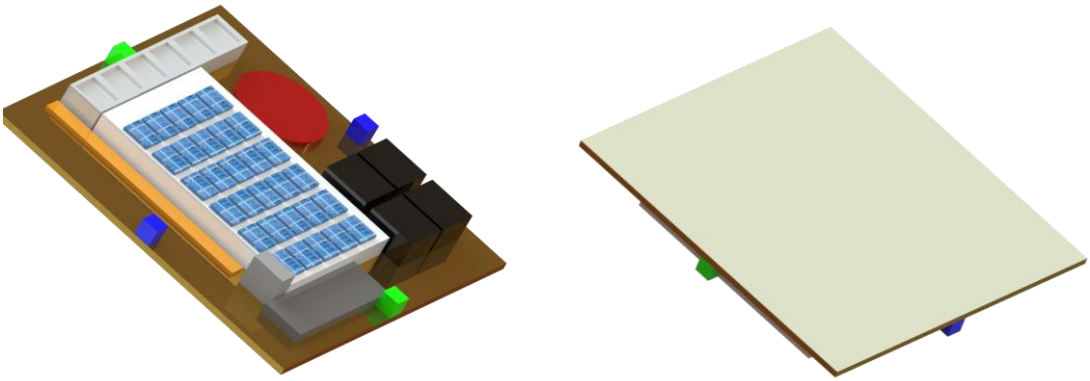

Figure B.8. Integrated Payload Sail Particle Design. The particle for the integrated payload sail design consists of a ChipSat module coated with reflective aluminum on the sun-facing side (shown on the right) and the ChipSat subsystems on the opposite side (shown on the left). The flux-pinning interfaces are represented by the green cubes (magnets) and the blue cubes (superconductors).

leaving some regions for photovoltaics. The other side (facing away from the sun) houses the attachments for small grains of superconducting material and permanent magnets where they will be shielded from the sun's rays (see Figure B.8). It may be necessary to devise additional cooling techniques to maintain the desired temperature, depending on the thermal properties of the original ChipSats. As with the particle-cloud sail, the least amount of superconductor and magnet necessary to hold the integrated payload sail together depends on the specific design of the interface.

The interface must be carefully designed to encourage a sheet-like emergent behavior with the reflective side pointing toward the sun. A design that requires minimal active sensing and coordination is ideal. Producing this behavior comes from two segments of the mission timeline: the transient state, from the deployment out of the launch fairing until the solar sail is constructed, and the steady state, where the collection of ChipSat particles must hold a shape without an external structure. The transient portion of the mission can be approached one of two ways: random

deployment and swarming module behavior to construct the larger structure or orchestrated deployments that produce the desired result without independent action by the modules. Research is being conducted on swarming laws for larger modules connected via flux-pinned interfaces in order to produce large aperture telescopes,[6] but it may not be possible to implement these laws on the less sophisticated ChipSat modules. If that proves to be the case, the simplest solution is an orderly deployment mechanism that allows strings of ChipSat particles to flux pin together in the correct orientation before leaving the vicinity of the deployment module. The dynamics of a flux-pinned structure under the influence of solar pressure has not been studied. However, some work has been done on the stability of the response of a larger-scale flux-pinned structure to external disturbances with promising results that indicate the flux-pinned system remains stable and maintains its formation in the presence of disturbances.[5] More study is needed to expand this simulation to better model this chip-scale architecture.

The integrated payload sail does not have a global, centrally-controlled current loop with which the magnetic field in the sail can be easily manipulated. Although it is possible to work electromagnets into a control scheme for such a sail, the most obvious control mechanism is thermal actuation. If the superconductor's temperature is raised above its transition temperature, the connection can effectively be turned off. This heating may be accomplished via a small resistor in the superconductor or by exposing the superconductor to intense light (possibly by changing its aspect relative to the sun). If this ability is combined with a pivoting flux pinning kinematic joint,[4] the ChipSat in question would be able to hinge back like a door opening (as in Figure

B.9). Although the details on how to move the particles once the joint has been turned off need to be resolved, having that capability would offer unprecedented versatility in a solar sailing system. The center of solar pressure could be moved virtually anywhere simply by causing the particles on certain portions of the sail to point away from the sun, all without dramatically changing the center of mass. Rapid orientation maneuvers could be conducted by tilting each of the particles relative to one another, possibly by changing the flux pinned equilibrium position via altering the magnetic

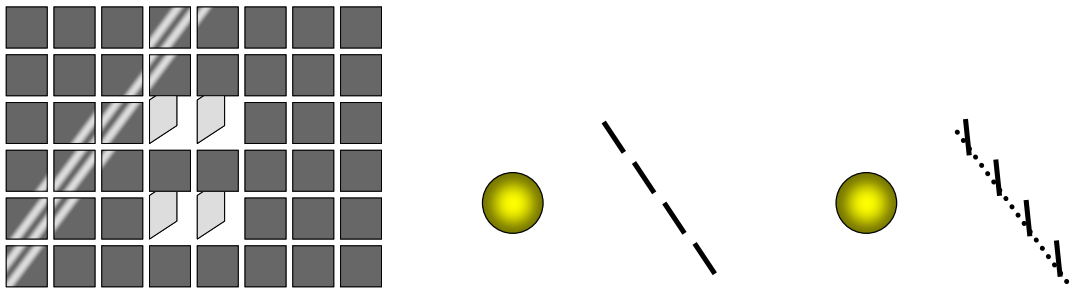

(a) (b)

Figure B.9. Particle-Level Actuation. (a) When combined with pivoting flux pinned joints, thermally turning off specific joints could allow the mission designer to change the thrust vector of the sail very rapidly compared to the delicate procedure of moving a large traditional solar sail. (b) Coordinated maneuvers of the particles relative to one another could avoid cumbersome pivoting of large structures while still producing effectively the same end result.

flux. The integrated payload sail could produce an effective incidence angle, without having to pivot a large bulky structure (Figure B.9(b)).

In order to assess the performance of such a solar sail, it is useful to describe the system in terms of the performance parameters developed to evaluate traditional solar sails. Because this sail design integrates the payload and the sail, the payload mass fraction has a theoretical limit of 1. Although this value may decrease slightly if additional mass were required, for example, to amplify and relay the ChipSats' radio signals, the mass payload fraction is much higher than the values anticipated for

traditional solar sails. On the other hand, ChipSats are expected to perform many more functions than a typical film on a traditional solar sail, resulting in a higher mass per area. The values for one variant on a prototype design of a ChipSat include a surface area of one square centimeter and a mass of approximately 9 mg including a small flux-pinning interface.[15] Assuming that the area of the solar sail is the effective reflecting area and not the total physical area (since the chips represent the reflecting area, but are separated by a small gap due to the flux pinning), the sail loading factor σ is 90 g m^{-2}. As seen from the values presented in section B1.1, this value is somewhat high, but still within the range proposed by current sail designs. It is also possible to optimize the design of a ChipSat to maximize the surface area and reduce this number to be competitive with traditional solar sail performance. The characteristic acceleration a_0 can be calculated assuming an efficiency factor similar to traditional solar sails. Although the integrated payload sail will not have "billowing" due to the non-stiff membrane, small errors in the angle between each ChipSat will produce similar inefficiencies. Also, since the same vapor-deposited reflective aluminum can be deposited on to the ChipSat, the integrated payload sail can be expected to have the same reflective properties of the traditional sail. If a perfectly reflective surface and an efficiency of 0.85 are assumed, the characteristic acceleration for an integrated payload sail is approximately 0.09 mm s^{-2}. This value is an order of magnitude below that of designs for a traditional solar sail, indicating that this particular design is not currently to the point of competing with traditional solar sail designs for efficiencies and thrust. While it is possible to refine the ChipSat design for this application in

mind, in order to improve its performance, this design is more plausible for use in niche missions where the sacrifice in performance is worth its unique applications.

B3 Conclusions about Particulate Solar Sails

The particulate solar sail is a unique approach to solar-sail design that may never fill the role of a conventional thin-film solar sail but nevertheless promises unique advantages and applications that make it an interesting alternative. By using small discrete particles held in place by superconductive flux pinning forces, this type of solar sail is capable of circumventing some of the issues that plague thin-film solar sails. The particulate solar sail could improve the ease of manufacturing and handling of the sail prior to launch, eliminate the need for elaborate folding techniques in order to launch, avoid the problems associated with deploying a large delicate membrane in space, and resist catastrophic damage from micrometeoroid impacts. Also, having a discrete surface, the particulate solar sail has many of the advantages of fractionated space systems, including increased fault tolerance and robustness.

The particle-cloud sail is an implementation where flux-pinned superconducting particles are held in place by the magnetic field produced by current-carrying wire loops. This concept faces four major design challenges: 1) choosing an appropriate material, coating, and shape for the particles making up the sail to ensure thermal and reflective conditions are met, 2) maintaining the stiffness of the large flexible wires to ensure that the rings remain in the same plane, 3) deploying the particles in such a way that each ring has an approximately homogenous particle distribution; and 4) determining a power source that can provide the necessary currents for a reasonably sized particle cloud sail without dominating the payload mass.

Provided these design issues can be addressed, the particle cloud sail would be well suited to operations in locations close enough to the sun to use the solar sail, but far enough away to decrease some of the thermal concerns for the superconductive particles. The fact that dust, micrometeoroids, and other small collision hazards present little danger to the performance of this design and the potential agility in maneuvering implies that this design may be able to fill a niche where thin film solar sails are risky, such as multiple small body rendezvous in the asteroid belt, comet rendezvous, or a long-term mission through a planet's rings. Unlike conventional chemically propelled spacecraft, a particle-cloud solar sail could maneuver through these dangerous areas for significant stretches of time, visiting dozens of separate bodies and increasing our knowledge of the solar system.

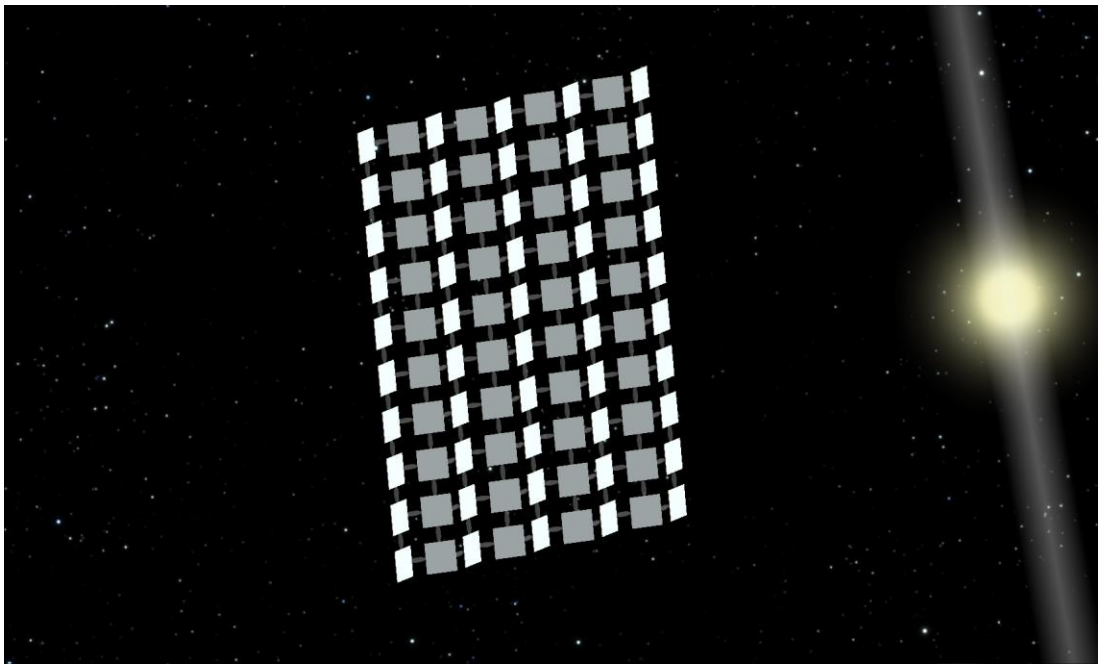

Figure B.10. An integrated solar sail can bend at coordinated joints to reduce the amount of light hitting its surface and therefore control its acceleration.

In contrast, the integrated payload sail uses satellite-on-a-chip modules equipped with flux-pinning interfaces so that the modules can link without contacting to produce a collective solar sail. The four major challenges for this design are: 1) creating a large, correctly oriented, non-contacting flux-pinned structure in space with unsophisticated modules that lack fine position and attitude actuation, 2) making sail-level decisions (such as when to pivot certain particles and when to reorient the sail) when the modules are non-contacting and have limited communication bandwidth, 3) manipulating the orientation of individual chips once one of the joints has been turned off, and 4) predicting the long-term steady state response of the non-rigid structure to the effects of solar pressure and other disturbances.

The integrated-payload sail has strengths that differ from those of the particle-cloud architecture, but it has equally exciting applications if the aforementioned challenges can be resolved. The key feature of this design is the fact that the sail is composed of miniature spacecraft capable of sensing a very small amount of data individually, but capturing an impressive spread of data collectively. Since thermal issues can be resolved by adding insulation to the chips themselves (instead of attempting to design the small particles to balance emission and absorption), this design is less sensitive to its proximity to the sun. Thus, it could be used as a large-scale long-duration distributed sensor to monitor sun ejections in order to provide an early warning for massive sun storms that can cause significant damage and disruption back on Earth. The fact that these distributed spacecraft function as a solar sail instead of small disposable sensors allows the integrated payload sail to perform station-keeping operations[171], keeping the sensors operational for longer periods of time. It also

allows the sail to be moved to orbits and inclinations that might be of greater interest once the craft has already been deployed. A further application for this type of sail includes long-distance distributed sensor readings. Solar sails are known to have "significant performance gains over comparable propulsion systems"[13] for solar system escape missions. An integrated payload sail could travel beyond the solar system, occasionally releasing "breadcrumb" SpaceChip modules as communication relays or scattering modules in the heliopause to help better understand how the solar system evolved. If a long-range mission calls for a rendezvous with a celestial body, the integrated payload sail could shut off the flux pinning interfaces holding it together on arrival and once again become a collection of sensing modules. These chips can then scatter, covering a much wider sensing area than monolithic missions, with a much greater efficiency than a chemically propelled spacecraft carrying a payload of small SpaceChips.

Thin-film and particulate solar sails have a different set of technological challenges. Just as the traditional membrane solar sail has matured as a technology because of the promise of new missions that it enables and the lure of propellantless propulsion, it may be that some of the fascinating prospects for the particulate solar sail designs will also spur future work into confronting the challenges that stand in the way of the transition from concept to practical technology.

APPENDIX C:

COOLING A YBCO DISK WITH A Q-DRIVE CRYOCOOLER

From 2010 – 2012, undergraduate student Sammy Nowieski conducted experimental and simulation work examining the cooling of a YBCO disk (58 mm in diameter and 18 mm high).[172] The following plots are the relevant collected data from the experiments she conducted (more information on her simulations can be found in her paper). These plots are included in this dissertation for two reasons: 1) they provide insight into the FPI thermal cooling design, which has proven to be one of the most difficult subsystems to implement in hardware and 2) they were a critical part in the analysis used to understand the cryocooler implementation of the FPI on the microgravity testbed. These experiments were performed in the RAGNAR configuration, with the test article (aluminum or YBCO) mounted to the upward-facing coldfinger. Temperature data was collected with a thermocouple.

C1 The Effect of Cyrocooler Setting on Cooling Performance

The Q-drive cryocooler used in the lab does not have specific gradations to indicate different performance levels, and no data was available to gauge how much of a performance decrease would result if the cryocooler's knob was accidentally placed at a setting below its maximum operating position (marked by a red arrow). The data is shown in Figure C.1. The results show that a 9° difference results in a temperature difference of almost 20 K after 30 minutes. A 5° difference results in similar (or even better) performance in cooling up until about 15 minutes, and then the "maximum operating position" clearly appears to cool more quickly.

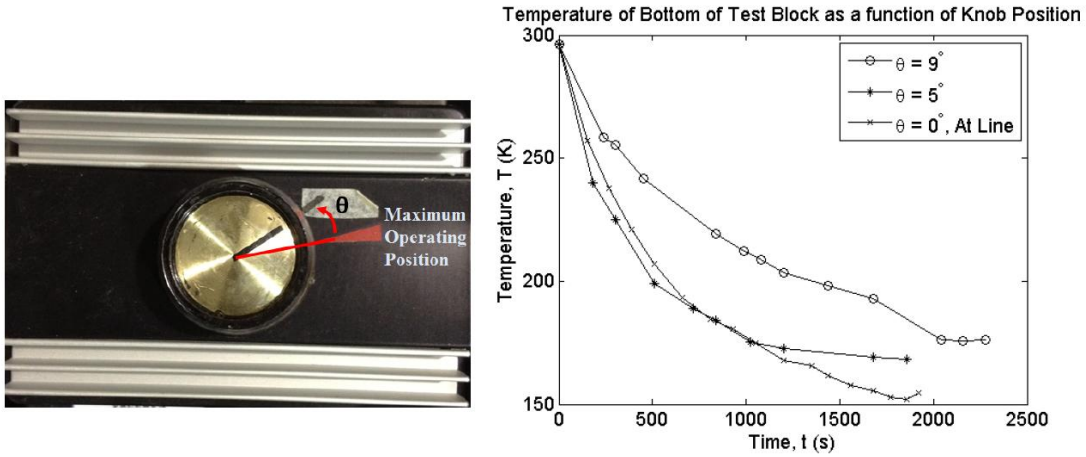

a) Cryocooler knob position

b) Temperature of the bottom of an aluminum block with various knob settings

Figure C.1. (a) The cryocooler knob and the angle setting definition. (b) The temperature of the aluminum test block over time for different knob settings.

C2 The Effect of Aerogel Layers on Cooling Performance

Another effect that was investigated with the cryocooler was the number and location of aerogel insulation blanket around the test article. One test for some of the microgravity hardware was to see if it was possible to not insulate the top face of the YBCO in order to keep the relative distance between a magnet and the YBCO disk small. The results are shown in Figure C.2. Essentially, the tests show that the more insulation that is used, the better the performance of the system. None of the tests achieved YBCO's critical temperature on the top surface of the disk (the face interacting with the FPI) during the test. However, the best performing system involved two layers of aerogel blanket wrapped around the circumference of the YBCO and cold finger, with two layers of aerogel covering the top face (the one interacting with the FPI). Subsequent tests later showed that three aerogel layers around the circumference started to interfere with the ventilation of the cryocooler and actually reduced the performance of the system.

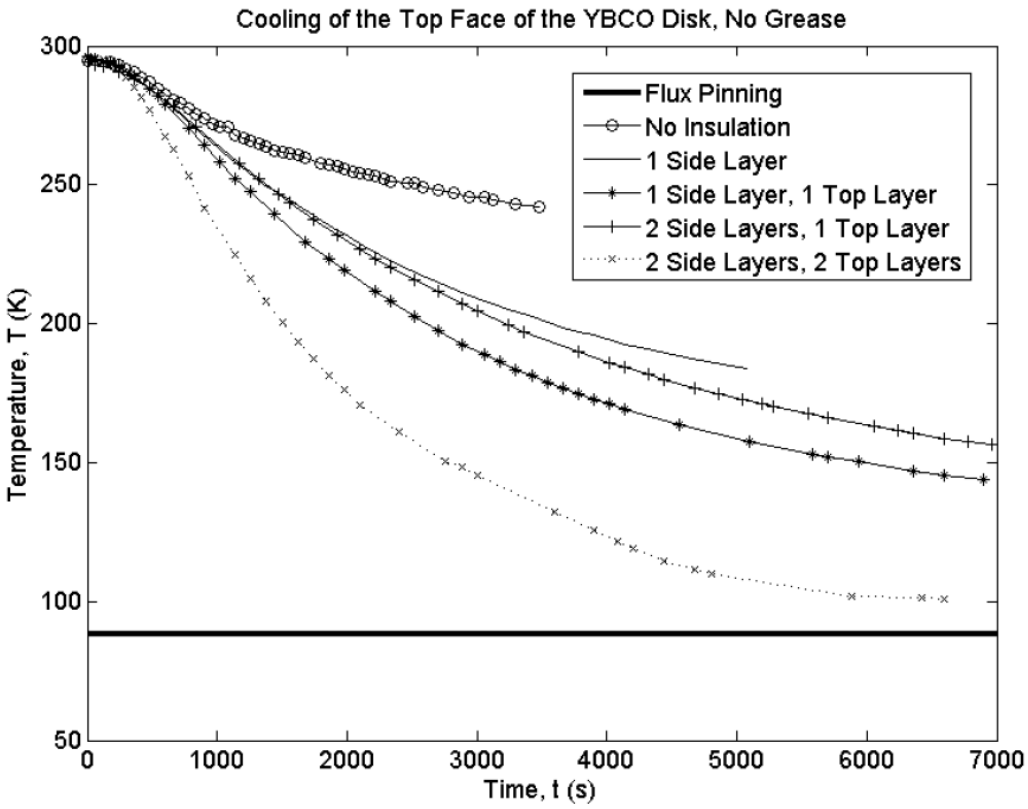

Figure C.2. (a) The cryocooler knob and the angle setting definition. (b) The temperature of the aluminum test block over time for different knob settings.

C3 The Effect of Thermal Grease on Cooling Performance

One of the main concerns with implementing a thermal system using a cryocooler was achieving good thermal contact between the metallic cold finger and the YBCO disk throughout the temperature ranges of the tests. Thus, two different types of thermal grease were tested (N grease, intended for cryo temperatures, and H grease, intended for high temperatures). The results are shown in Figure C.3. These plots suggest that having thermal grease improves the rate at which the superconductor cools down, but the final temperature it can achieve is the same. It also shows that the H grease, which was developed for high-temperature applications, is actually better than the N grease (although the coating surface area and application techniques may have affected these results). A disadvantage of using the grease is that it appears to get

slightly absorbed into the YBCO disk, which can be messy and has a unknown impact on YBCO properties.

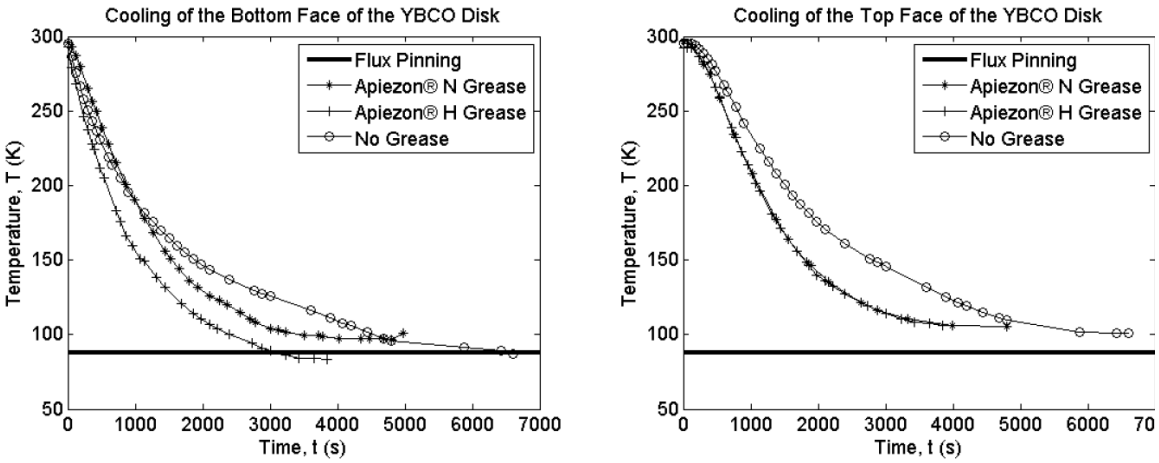

a) Temperature of the bottom face of the YBCO

b) Temperature of the top face of the YBCO

Figure C.3. Temperature versus time for a YBCO disk using different thermal greases (a) the temperature at the bottom face of the disk, near the thermal grease, and (b) the temperature at the top of the disk where the magnet interacts with the superconductor.

APPENDIX D:

MEASURED MAGNETIC FIELDS OF

VARIOUS SUPERCONDUCTOR CONFIGURATIONS

In the spring of 2011 Chris Jewison, an undergraduate researcher who collaborated on this project, designed and built the Precision Lab Translator (PLT) apparatus to measure the three-axis magnetic field with a commercial gaussmeter. Then, in the fall of 2011 he led a small team consisting of Kevin Lo, Frances Zhu, and Ellen Chuang to collect data around a YBCO superconductor disk in various flux pinning configurations to document the effects of flux pinning on the surrounding magnetic field.

D1 Experimental Runs

All experiments were conducted with a 58 mm diameter 18 mm thick single-grain YBCO superconductor. The "blue" magnet is an N52 Neodymium magnet one inch in diameter and half an inch thick. The surface field is quoted at 0.5233 T. It was positioned at grid point (40,40,11.65) mm for field cooling. The surface of the superconductor defines the $z = 0$ plane. All experiments cooled the superconductor with a small bath of LN2.

The different experiments conducted with the PLT setup that are relevant to flux pinning are:

Experiment 2

A flux-pinned system with the YBCO field-cooled with the blue magnet, but data collected with the blue magnet removed from the test setup.

Experiment 3

The superconductor as in Experiment 2, but flipped over such that the data was collected on the back side of a field-cooled superconductor.

Experiment 4

A collection of data from the same grid points, with the superconductor in place but no field-cooling. This data set provides the control for the magnetic fields in the rest of the data.

Experiment 5

A flux-pinned system with the YBCO field-cooled with the blue magnet centered over it and data collected with the blue magnet still in place.

Experiment 8

A flux-pinned system with a smaller N52 magnet field-cooled in place over the superconductor, and data collected with the magnet in place.

Experiment 9

The magnetic field of the blue magnet alone.

Experiment 11

The magnetic field of the small magnet alone.

D2 Data Archive

Experiment 2

Relative positions in mm			Magnetic field in Gauss		
x position	y position	z position	Bx	By	Bz
0	0	7.51	9.1	15.4	10.7
0	20	7.51	25.5	20.2	16.1
0	40	7.51	36.6	-0.3	7.5
0	60	7.51	21.7	-8.8	10.4
0	80	7.51	8.7	-6.5	9.5
20	80	7.51	10.3	-20.6	12.3
20	60	7.51	40.9	-46.8	-23.4
20	40	7.51	84.6	6.7	-97.4
20	20	7.51	57.2	58	-33.4
20	0	7.51	12.6	30.7	10.6
40	0	7.51	-1.3	45.5	-1.4
40	20	7.51	-16.4	102.2	-122
40	40	7.51	2.1	-51.2	-205
40	60	7.51	29	-132.9	-45.3
40	80	7.51	6.7	-26.1	12.6
60	80	7.51	-7.7	-17.6	10.4
60	60	7.51	-64.9	-65.7	-1.5
60	40	7.51	-130.3	-27.9	-89.5
60	20	7.51	-65.7	30.7	-50.8
60	0	7.51	-15.1	18.1	4.2
80	0	7.51	-7.3	6.5	2.6
80	20	7.51	-24.2	0	-3.4
80	40	7.51	-37	-9.7	0.8
80	60	7.51	-19	-10.9	6.1
80	80	7.51	-5	3.5	5.5
80	80	17.51	-6.5	-5.8	2.2
80	60	17.51	-20.1	-11.1	-1.9
80	40	17.51	-28.7	-8.8	-7.7
80	20	17.51	-19.8	3.4	-5.3
80	0	17.51	-6.8	5.5	0.5
60	0	17.51	-9.3	22.1	13.1
60	20	17.51	-36.3	35.4	-24.2
60	40	17.51	-60.6	-28	-50.3
60	60	17.51	-31.6	-35.5	-13.6
60	80	17.51	-7.2	-15.6	4.8
40	80	17.51	-5.8	-25.2	3
40	60	17.51	-7	-58.9	-47.7

Relative positions in mm			Magnetic field in Gauss		
x position	y position	x position	Bx	By	Bz
40	40	17.51	-1.1	-1.1	-150.1
40	20	17.51	4.5	45.9	-69.6
40	0	17.51	-2.3	29.2	-7.2
20	0	17.51	8.7	26.5	-2.9
20	20	17.51	38.6	40.9	-31.7
20	40	17.51	49.1	-10.3	-61.2
20	60	17.51	23.2	-38.2	-22.6
20	80	17.51	6.4	-15.2	2.6
0	80	17.51	7.2	-7.7	4.1
0	60	17.51	16.3	-9.5	1.3
0	40	17.51	26.1	-1	-3.7
0	20	17.51	20.9	11.5	0
0	0	17.51	12	10.8	2.8
0	0	27.51	9.6	6.5	-1.3
0	20	27.51	13.9	5.6	-7
0	40	27.51	17.4	-3.3	-9.6
0	60	27.51	13.2	-8.9	-5.7
0	80	27.51	7.2	-6.4	0.2
20	80	27.51	6.1	-12.3	-2.9
20	60	27.51	15.1	-18.2	-19.9
20	40	27.51	23.7	-4.9	-37.9
20	20	27.51	17.4	15.8	-23
20	0	27.51	8.9	14.2	-6.2
40	0	27.51	3.6	17.7	-8.9
40	20	27.51	-1.3	22.6	-35.4
40	40	27.51	2.1	-3.4	-49.1
40	60	27.51	-4.3	-24	-28.7
40	80	27.51	-2.9	-16.8	-4.1
60	80	27.51	-4.9	-12.1	-2.3
60	60	27.51	-14.7	-13.6	-13.5
60	40	27.51	-21.1	2	-26.9
60	20	27.51	-12	15.5	-19
60	0	27.51	-6.1	14.2	-3.8
80	0	27.51	-6.4	7.9	-0.2
80	20	27.51	-12.9	7.6	-3.1
80	40	27.51	-17.6	3.8	-1.4
80	60	27.51	-14.4	-2.7	0.9
80	80	27.51	-7.2	-4.9	1.6
80	80	37.51	-3.3	-3.9	-0.2
80	60	37.51	-8.1	-4.5	-3.3
80	40	37.51	-11.9	0.5	-6.2
80	20	37.51	-9.3	6.9	-2.5
80	0	37.51	-5.6	7.2	-0.2
60	0	37.51	-5.2	11.6	-3.9
60	20	37.51	-8.5	11.9	-11.3

Relative positions in mm			Magnetic field in Gauss		
x position	y position	x position	Bx	By	Bz
60	40	37.51	-12.3	-1.7	-19.9
60	60	37.51	-7.7	-10.3	-11.6
60	80	37.51	-3.4	-7.3	-2.7
40	80	37.51	-0.6	-10.4	-6
40	60	37.51	-0.5	-12.4	-20.2
40	40	37.51	2.9	-0.3	-30.9
40	20	37.51	2	12.2	-24.6
40	0	37.51	0.1	12.6	-8.5
20	0	37.51	5.2	9.8	-6.8
20	20	37.51	12.8	7.9	-17.1
20	40	37.51	13.4	0.8	-17.9
20	60	37.51	9.4	-9.2	-10.9
20	80	37.51	4.2	-9.6	-3.8
0	80	37.51	5.5	-5.3	-1
0	60	37.51	9.8	-4.3	-3.7
0	40	37.51	13.2	-0.2	-6.6
0	20	37.51	11.6	5.3	-6.1
0	0	37.51	7.2	6	-2.5
0	0	77.51	3.2	2	-1.9
0	20	77.51	3.6	1.2	-3.1
0	40	77.51	3.7	0.2	-3.1
0	60	77.51	3.2	-1.1	-2.7
0	80	77.51	2.5	-0.9	-1.3
20	80	77.51	2	-1.5	-2.1
20	60	77.51	2.4	-1	-3.5
20	40	77.51	3	0.6	-4.2
20	20	77.51	2.9	2	-3.9
20	0	77.51	2.4	2.9	-2.5
40	0	77.51	1.3	3	-3.1
40	20	77.51	1.3	2.1	-4.9
40	40	77.51	1.3	-0.4	-4.2
40	60	77.51	1	-1.5	-3.3
40	80	77.51	1.3	-1.8	-2.5
60	80	77.51	0.1	-1.6	-1.8
60	60	77.51	-0.2	-1.3	-3.3
60	40	77.51	-0.3	0.2	-3.9
60	20	77.51	-0.3	1.6	-3.3
60	0	77.51	0.2	2.8	-2.2
80	0	77.51	-0.6	2.2	-1.7
80	20	77.51	-1.3	1.4	-2.9
80	40	77.51	-1.3	0.2	-2.3
80	60	77.51	-1.3	-0.9	-1.7
80	80	77.51	-0.7	-1.1	-1.1

Experiment 3

Relative positions in mm			Magnetic field in Gauss		
x position	y position	z position	Bx	By	Bz
0	0	7.51	-3.2	-3.9	-1.1
0	20	7.51	-7.2	-1.6	0.1
0	40	7.51	-9.7	-0.4	-3.3
0	60	7.51	-6.4	4.1	-3.1
0	80	7.51	-0.7	4.2	-1.7
20	80	7.51	-2.3	9.5	-2.2
20	60	7.51	-14.6	17.8	2.2
20	40	7.51	-29.5	-1.8	27.4
20	20	7.51	-24.3	-14.9	14.5
20	0	7.51	-5.8	-8.9	-1.2
40	0	7.51	-1.2	-15.5	-1.1
40	20	7.51	-7.3	-34.9	45.3
40	40	7.51	-6.7	12.5	82
40	60	7.51	-0.7	37	24
40	80	7.51	1.5	13	-2.6
60	80	7.51	5.2	9.1	-2.8
60	60	7.51	20.8	24.1	7.4
60	40	7.51	40.2	5.3	41.3
60	20	7.51	22.2	-25.7	11.3
60	0	7.51	4.8	-10.9	-0.7
80	0	7.51	4.9	-3.7	-2.6
80	20	7.51	14.2	-5.5	-4.1
80	40	7.51	20	2.7	-0.7
80	60	7.51	12.5	6.4	-2.6
80	80	7.51	5.1	4.7	-3.1
80	80	17.51	4.2	3.8	-1
80	60	17.51	9.5	4.7	-0.3
80	40	17.51	14.5	1	1.3
80	20	17.51	11.9	-2.4	2
80	0	17.51	5.2	-3.9	-0.6
60	0	17.51	7.4	-9.3	2.6
60	20	17.51	16.4	-10.8	11.7
60	40	17.51	17.3	1.2	21
60	60	17.51	11.1	13.2	10
60	80	17.51	4	7.3	0.6
40	80	17.51	0.6	9.4	2.4
40	60	17.51	-1.9	17.9	20.1
40	40	17.51	-2.2	10.6	35.1
40	20	17.51	-1.1	-10.1	19.4
40	0	17.51	0.4	-10.5	3.6
20	0	17.51	-5.6	-6.2	3.2

Relative positions in mm			Magnetic field in Gauss		
x position	y position	x position	Bx	By	Bz
20	20	17.51	-12.9	-6.1	13.2
20	40	17.51	-14.4	8.1	22.2
20	60	17.51	-8.4	10.8	8.1
20	80	17.51	-1.7	7.1	0.6
0	80	17.51	-1.4	3.4	-0.3
0	60	17.51	-4.2	4	0.6
0	40	17.51	-7.3	4	5.1
0	20	17.51	-6.6	-0.9	3.4
0	0	17.51	-3.4	-3.5	0.6
0	0	27.51	-1.9	-2.1	1.7
0	20	27.51	-4.2	-1.8	2.6
0	40	27.51	-4.6	1.2	3.3
0	60	27.51	-2.9	4.1	2.9
0	80	27.51	-0.9	3.4	1.2
20	80	27.51	-1.1	5.5	1.8
20	60	27.51	-4.6	8.2	7.2
20	40	27.51	-7.6	0.7	13.2
20	20	27.51	-7.7	-4.4	10.2
20	0	27.51	-3.4	-5.2	4
40	0	27.51	-1	-7	5.7
40	20	27.51	1.1	-6.9	14.5
40	40	27.51	-1	4.9	24.7
40	60	27.51	-1	11.6	10.4
40	80	27.51	0.2	7.9	2.6
60	80	27.51	3.3	5.6	1.9
60	60	27.51	7.1	7.6	7.1
60	40	27.51	9.7	4	12.8
60	20	27.51	7.8	-5.3	10.2
60	0	27.51	5.5	-4.3	2.7
80	0	27.51	5.4	-1.8	1.8
80	20	27.51	8	-1.4	3.6
80	40	27.51	9.2	3.8	6
80	60	27.51	7	6.2	3.6
80	80	27.51	4.1	3.5	0
80	80	37.51	3.3	2.8	0.6
80	60	37.51	5.1	3.3	2.2
80	40	37.51	6.4	1	3.3
80	20	37.51	5.6	-1.3	3
80	0	37.51	4	-2.2	1.3
60	0	37.51	3.6	-3.4	4.2
60	20	37.51	7.2	-2.5	6
60	40	37.51	8	3	6.8
60	60	37.51	4.5	6.8	5.5
60	80	37.51	1.6	4.8	3.1
40	80	37.51	0.8	5.5	2.5

Relative positions in mm			Magnetic field in Gauss		
x position	y position	x position	Bx	By	Bz
40	60	37.51	1	7.1	7.1
40	40	37.51	0.5	3.3	11.8
40	20	37.51	-0.7	-3.5	10.5
40	0	37.51	-0.5	-4.9	4.8
20	0	37.51	-0.7	-3.5	3.8
20	20	37.51	-3.4	-2.5	8.3
20	40	37.51	-4.5	3.3	8.8
20	60	37.51	-3.1	6.3	5.5
20	80	37.51	-1	4.4	1.6
0	80	37.51	-1.1	2.9	0.8
0	60	37.51	-3	3.6	2
0	40	37.51	-4.1	1.8	3.8
0	20	37.51	-3.1	-1	3.4
0	0	37.51	-1.6	-1.8	2.1
0	0	76.51	0.4	-0.2	1.6
0	20	76.51	0.2	0.2	2
0	40	76.51	0	0.9	2.1
0	60	76.51	0.2	1.3	1.8
0	80	76.51	0.5	1.6	1.3
20	80	76.51	0.9	1.8	1.6
20	60	76.51	0.6	1.6	2.1
20	40	76.51	0.5	0.9	2.5
20	20	76.51	0.5	0.1	2.5
20	0	76.51	0.5	-0.3	2.1
40	0	76.51	1.1	-0.5	2.2
40	20	76.51	1.2	0	2.8
40	40	76.51	1.3	1	2.8
40	60	76.51	1.3	1.6	2.5
40	80	76.51	1.2	1.8	1.7
60	80	76.51	1.6	1.7	1.6
60	60	76.51	1.7	1.7	2.1
60	40	76.51	1.8	1	2.4
60	20	76.51	1.8	0.1	2.1
60	0	76.51	-1.7	-0.3	1.8
80	0	76.51	1.8	-0.2	1.2
80	20	76.51	2.1	0.1	1.4
80	40	76.51	2.3	0.8	1.6
80	60	76.51	2	1.2	1.5
80	80	76.51	1.8	1.4	1

Experiment 4

Relative positions in mm (DO NOT EDIT, for reference only)			**Magnetic field in Gauss (ENTER DATA HERE)**		
x position	y position	z position	Bx	By	Bz
0	0	13.7	1.2	0.6	0.5
0	20	13.7	1.3	0.8	0.6
0	40	13.7	1.3	0.9	0.5
0	60	13.7	1.4	0.8	0.8
0	80	13.7	1.3	0.8	0.9
20	80	13.7	1.4	0.9	0.9
20	60	13.7	1.4	0.9	0.8
20	40	13.7	1.3	0.9	0.8
20	20	13.7	1.3	0.8	0.7
20	0	13.7	1.4	0.8	0.6
40	0	13.7	1.3	0.9	0.6
40	20	13.7	1.4	0.9	0.6
40	40	13.7	1.3	0.9	0.8
40	60	13.7	1.4	0.9	0.8
40	80	13.7	1.3	0.9	0.8
60	80	13.7	1.4	0.9	0.7
60	60	13.7	1.3	0.9	0.8
60	40	13.7	1.4	0.9	0.8
60	20	13.7	1.4	0.9	0.9
60	0	13.7	1.5	1.2	0.9
80	0	13.7	1.5	1.1	0.9
80	20	13.7	1.6	1.2	0.9
80	40	13.7	1.5	1.1	0.8
80	60	13.7	1.5	1.2	0.9
80	80	13.7	1.6	1.1	0.9
80	80	23.7	1.6	1.2	0.9
80	60	23.7	1.6	1.1	1
80	40	23.7	1.6	1.2	0.9
80	20	23.7	1.6	1.2	1
80	0	23.7	1.7	1.2	1
60	0	23.7	1.7	1.2	0.9
60	20	23.7	1.6	1.2	0.9
60	40	23.7	1.6	1	0.9
60	60	23.7	1.7	1.1	0.9
60	80	23.7	1.7	1.1	1
40	80	23.7	1.7	1.2	0.9
40	60	23.7	1.7	1.2	1.1
40	40	23.7	1.7	1.2	0.9
40	20	23.7	1.8	1.2	1.1
40	0	23.7	1.7	1.3	1

Relative positions in mm			Magnetic field in Gauss		
x position	y position	x position	Bx	By	Bz
20	0	23.7	1.7	1.3	1.2
20	20	23.7	1.7	1.3	1.3
20	40	23.7	1.7	1.3	1.2
20	60	23.7	1.6	1.2	1.1
20	80	23.7	1.7	1.2	1.1
0	80	23.7	1.7	1.1	1.2
0	60	23.7	1.7	1.2	1.1
0	40	23.7	1.7	1.3	1.2
0	20	23.7	1.7	1.3	1.2
0	0	23.7	1.8	1.3	1.2
0	0	33.7	1.8	1.4	1.3
0	20	33.7	1.7	1.3	1.3
0	40	33.7	1.8	1.3	1.2
0	60	33.7	1.8	1.2	1.1
0	80	33.7	1.9	1.3	1.2
20	80	33.7	1.8	1.3	1
20	60	33.7	1.7	1.3	1.2
20	40	33.7	1.8	1.3	1.2
20	20	33.7	1.8	1.3	1.2
20	0	33.7	1.8	1.3	1.3
40	0	33.7	1.8	1.2	1.2
40	20	33.7	1.8	1.3	1.1
40	40	33.7	1.8	1.3	1.2
40	60	33.7	1.8	1.2	1.1
40	80	33.7	1.8	1.2	1.2
60	80	33.7	1.7	1.4	1.2
60	60	33.7	1.8	1.4	1.3
60	40	33.7	1.8	1.4	1.2
60	20	33.7	1.8	1.4	1.3
60	0	33.7	1.8	1.3	1.3
80	0	33.7	1.7	1.4	1.2
80	20	33.7	1.7	1.4	1.2
80	40	33.7	1.7	1.3	1.2
80	60	33.7	1.7	1.3	1.1
80	80	33.7	1.7	1.4	1.2
80	80	43.7	1.8	1.3	1.2
80	60	43.7	1.7	1.3	1.2
80	40	43.7	1.8	1.3	1.2
80	20	43.7	1.8	1.3	1.2
80	0	43.7	1.8	1.4	1.3
60	0	43.7	1.8	1.4	1.3
60	20	43.7	1.8	1.4	1.3
60	40	43.7	1.9	1.4	1.2
60	60	43.7	1.9	1.4	1.3
60	80	43.7	1.9	1.5	1.3

Relative positions in mm			Magnetic field in Gauss		
x position	y position	x position	Bx	By	Bz
40	80	43.7	1.8	1.4	1.3
40	60	43.7	1.9	1.4	1.2
40	40	43.7	2	1.5	1.3
40	20	43.7	1.8	1.4	1.3
40	0	43.7	2	1.4	1.4
20	0	43.7	1.9	1.5	1.5
20	20	43.7	2	1.6	1.4
20	40	43.7	1.9	1.5	1.4
20	60	43.7	2	1.6	1.4
20	80	43.7	2	1.4	1.3
0	80	43.7	1.9	1.4	1.4
0	60	43.7	2	1.3	1.2
0	40	43.7	2.1	1.6	1.3
0	20	43.7	2	1.6	1.5
0	0	43.7	2	1.5	1.4
0	0	81.7	2	1.4	1.6
0	20	81.7	2.1	1.6	1.4
0	40	81.7	2.1	1.5	1.4
0	60	81.7	2	1.6	1.3
0	80	81.7	2.1	1.4	1.4
20	80	81.7	1.9	1.4	1.3
20	60	81.7	2	1.4	1.4
20	40	81.7	2	1.3	1.3
20	20	81.7	1.9	1.4	1.3
20	0	81.7	1.9	1.5	1.3
40	0	81.7	1.9	1.5	1.4
40	20	81.7	1.9	1.5	1.5
40	40	81.7	2.1	1.5	1.4
40	60	81.7	2	1.5	1.4
40	80	81.7	2.1	1.5	1.3
60	80	81.7	2	1.6	1.4
60	60	81.7	2.1	1.6	1.5
60	40	81.7	2	1.5	1.3
60	20	81.7	2	1.5	1.4
60	0	81.7	2.1	1.6	1.4
80	0	81.7	2	1.6	1.4
80	20	81.7	2	1.6	1.4
80	40	81.7	2.1	1.7	1.6
80	60	81.7	2	1.6	1.4
80	80	81.7	1.9	1.4	1.4

Experiment 5

Relative positions in mm			Magnetic field in Gauss		
x position	y position	z position	Bx	By	Bz
0	0	12.5	2.8	3.7	41.9
0	20	12.5	15.1	12.2	104.7
0	40	12.5	52.3	29.6	217
18.4	40	12.5	718	740	2090
18.4	20	12.5	21.7	36.2	255
18.4	0	12.5	-1.1	3.5	61.3
40	0	12.5	2	-10.8	75.2
40	20	12.5	17.5	-66.5	406
40	20	22.5	35.9	221	200
40	0	22.5	-2.7	35.9	60.5
20	0	22.5	11.8	31.1	53.1
20	20	22.5	143.1	231	136.8
20	40	22.5	1224	1583	-994
0	40	22.5	159.8	66.6	90.6
0	20	22.5	60.1	46.6	73.8
0	0	22.5	12.8	15.4	38.1
0	0	32.5	23.2	25.9	17.3
0	20	32.5	78.8	57.3	5.3
0	40	32.5	149.8	26.7	-46.7
20	40	32.5	350	304	-608
20	20	32.5	143.4	184	-4.9
20	0	32.5	31.1	52.7	25.7
40	0	32.5	16.9	50.9	28.6
40	20	32.5	-40.2	214	-4.2
60	0	32.5	-11.1	21.7	30.3
60	20	32.5	-29.5	90.1	56.4
60	40	32.5	-186.5	54.7	56.8
80	40	32.5	-61.4	41.6	51.7
80	20	32.5	-16.7	25.6	33.5
80	0	32.5	-7.7	18.3	18.9
80	0	22.5	-4.2	9.2	21.3
80	20	22.5	-21.8	21.9	41.6
80	40	22.5	-53.1	29.1	60.5
60	40	22.5	-387	253	214
60	20	22.5	-70.6	73.5	11.8
60	0	22.5	-9.6	26.1	39.2
60	0	12.5	2.6	5.3	43.3
60	20	12.5	-22.5	28.3	141.5
60	40	12.5	-284	128.6	386
80	40	12.5	-3.8	16.7	69.9
80	20	12.5	3.8	9.6	44.7

Relative positions in mm			Magnetic field in Gauss		
x position	y position	x position	Bx	By	Bz
80	0	12.5	-0.5	5.7	23.6
0	80	12.5	-18.6	13	60.1
0	60	12.5	-48.3	28.6	146.9
20	60	12.5	-351	292	761
20	80	12.5	-21.7	76.6	122.4
40	80	12.5	11.6	86.7	157.5
40	70	12.5	366	415	71.1
40	60	22.5	40.8	178	79.2
40	80	22.5	-22.9	84.4	52.9
20	80	22.5	-574	455	241
20	60	22.5	-125.8	25.1	78.8
0	60	22.5	-37.7	29.5	54.7
0	80	22.5	1.3	40	22.8
0	80	32.5	-110.6	72.6	76.4
0	60	32.5	-79.6	57.7	22.6
20	60	32.5	-97.4	164.9	-93.4
20	80	32.5	-25.8	93.8	17.1
40	80	32.5	44.5	149.4	-30.3
40	60	32.5	224	408	-417
60	80	32.5	52.2	89.3	30.8
60	60	32.5	220	163.8	-100.2
80	60	32.5	71.1	29.5	15.9
80	80	32.5	32.6	30	17.3
80	80	22.5	26.8	23.6	41.2
80	60	22.5	60.9	28.4	68.8
60	60	22.5	310	271	21.7
60	80	22.5	40.5	85.5	59.2
60	80	12.5	15.1	38.4	90.6
60	60	12.5	116.5	151	386
80	60	12.5	19.7	13.1	90.3
80	80	12.5	11	11.4	48.4
0	0	42.5	26	43.9	7.7
0	20	42.5	76.6	88.1	-23.3
0	40	42.5	150.4	61.1	-63.7
0	60	42.5	105	-39.4	-22.5
0	80	42.5	35.8	-57	8.4
20	80	42.5	22.3	-100.8	-6.8
20	60	42.5	83.8	-182.7	-229
20	40	42.5	118.5	16.1	-378
20	20	42.5	76.8	160	-131
20	0	42.5	21.2	74.1	-2.3
40	0	42.5	-10.9	59.6	-2.6
40	20	42.5	-72.2	116.9	-100.4
40	40	42.5	-169.4	-16	-245
40	60	42.5	-112.9	-148	-112.2

Relative positions in mm			Magnetic field in Gauss		
x position	y position	x position	Bx	By	Bz
40	80	42.5	-32.4	-72.6	-10.8
60	80	42.5	-27.3	-30.9	2.6
60	60	42.5	-76.1	-35.9	17.3
60	40	42.5	-112.3	14.2	17.5
60	20	42.5	-70.6	33.4	21.6
60	0	42.5	-28.5	28.6	27.1
80	0	42.5	-16.8	11.8	5.3
80	20	42.5	-31.5	9.9	3.6
80	40	42.5	-41.3	3.7	9.2
80	60	42.5	-32.3	-7.4	9.8
80	80	42.5	-16.4	-8.9	9.6
0	80	77.5	11	-13.9	-10.7
0	60	77.5	17.5	-19.5	-26.2
0	40	77.5	24	-8.6	-34.6
0	20	77.5	20.4	13.4	-22.3
0	0	77.5	14.5	18.5	-11.7
20	0	77.5	7.7	21.8	-18.4
20	20	77.5	9.6	18.6	-38.5
20	40	77.5	9.6	1.6	-50.5
20	60	77.5	8.9	-21	-40.2
20	80	77.5	6.3	-20.3	-17.2
40	80	77.5	-4.5	-19.1	-16
40	60	77.5	-8.5	-16.8	-33.6
40	40	77.5	-10.4	2.9	-41.4
40	20	77.5	7.8	16.7	-24.2
40	0	77.5	-1.2	18.9	-11.2
60	0	77.5	-6.2	12.8	-9.5
60	20	77.5	-15.9	8.8	-17.5
60	40	77.5	-18.4	4.5	-17.9
60	60	77.5	-17.4	-8.1	-14.7
60	80	77.5	-11.5	-11.5	-8.6
80	80	77.5	-8.6	-6.4	-3.4
80	60	77.5	-13.3	-1.3	-3.1
80	40	77.5	-15	0.8	-3.9
80	20	77.5	-12.7	4.2	-7.4
80	0	77.5	-8.5	6.7	-3.7

Experiment 8

Relative positions in mm			Magnetic field in Gauss		
x position	y position	z position	Bx	By	Bz
0	0	11.5	-2.3	-3.7	-12.1
0	20	11.5	-5.2	-6.8	-26.5
0	40	11.5	-8.9	-2.3	-40.3
20	40	11.5	-87.9	-12.4	-386
20	20	11.5	-11.6	-18.2	-152.4
20	0	11.5	-1.3	-2.1	-33.2
40	0	11.5	-1	-2.5	-46.5
40	20	11.5	-11.9	-56.1	-636
40	20	21.5	16.6	-201	10.6
40	0	21.5	1.3	-30.7	-27.2
20	0	21.5	-6.6	-17.8	-21.9
20	20	21.5	-64.2	-83.1	-56.7
20	40	21.5	-203	-34.2	-23.3
0	40	21.5	-26.2	0.5	-27.9
0	20	21.5	-16.2	-10.3	-21.8
0	0	21.5	-5.4	-6.5	-13.2
0	0	31.5	-7.6	-9.2	-10.1
0	20	31.5	-18.9	-12.9	-8.1
0	40	31.5	-27.3	-2.2	-8.8
20	40	31.5	-102.1	4.8	35.5
20	20	31.5	-52.2	-66	13.5
20	0	31.5	-8.5	-22.6	-12.8
40	0	31.5	0.5	-26.6	-8.1
40	20	31.5	4.5	-107.8	107
60	0	31.5	4.8	-20.7	-5.8
60	20	31.5	57.4	-41.8	16.3
60	40	31.5	123.1	18.8	42.4
80	40	31.5	33	-0.1	-7.8
80	20	31.5	23.6	-6.6	-1.9
80	0	31.5	7.1	-5.6	-5.2
80	0	21.5	5.2	-5.4	-10.5
80	20	21.5	18.6	-6.8	-17.1
80	40	21.5	32.3	-0.3	-19.8
60	40	21.5	304	20	-20.1
60	20	21.5	82.1	-60.2	-31.9
60	0	21.5	7.1	-18.3	-18.4
60	0	11.5	-0.3	-4.6	-33.2
60	20	11.5	14.3	-15.8	-143.9
60	40	11.5	105.8	-17.2	-237
80	40	11.5	1.8	-1.8	-32.1

Relative positions in mm			Magnetic field in Gauss		
x position	y position	z position	Bx	By	Bz
80	20	11.5	1.2	-2.7	-27.4
80	0	11.5	0.6	-1.9	-14.6
0	80	11.5	1.4	-2.3	-10.7
0	60	11.5	4.1	-2.1	-19.3
20	60	11.5	22.2	-14.2	-74.1
20	80	11.5	1.8	-5.4	-22.1
40	80	11.5	-1.1	-8.9	-37.8
40	60	11.5	-3.5	-88.1	-381
40	60	21.5	4.7	-234	47.1
40	80	21.5	2.5	-29.2	-17.8
20	80	21.5	11.1	-17	-13.5
20	60	21.5	72.5	-48.5	-21.4
0	60	21.5	17	-6.1	-14.3
0	80	21.5	5.6	-5	-8.8
0	80	31.5	7.2	-6.5	-4.1
0	60	31.5	17	-6.9	-4.1
20	60	31.5	39.6	-32	8.7
20	80	31.5	10.2	-15.9	-4.6
40	80	31.5	-0.9	-25.6	-4.2
40	60	31.5	16.9	-82.9	62.1
60	80	31.5	-8.8	-19.7	-5.6
60	60	31.5	-39.7	-47.5	29.4
80	60	31.5	-20.9	-14.4	-6.8
80	80	31.5	-8.1	-9.9	-6
80	80	21.5	-5.6	-6.6	-13.2
80	60	21.5	-16.2	-13.5	-30.8
60	60	21.5	-67.2	-101.3	-98.6
60	80	21.5	-8.2	-15.6	-23.4
60	80	11.5	-5.2	-8.8	-26.8
60	60	11.5	-42	-40.6	-142.3
80	60	11.5	-7.8	-5.6	-31.7
80	80	11.5	-3.2	-2.9	-13.6
80	80	41.5	-7	-9.7	-2.6
80	60	41.5	-16.7	-13.1	0.4
80	40	41.5	-24	-2.5	3.7
80	20	41.5	-14.8	8.5	-0.9
80	0	41.5	-5.6	8.1	-2.7
60	0	41.5	-3.5	17.5	-0.3
60	20	41.5	-17.1	32.2	22.9
60	40	41.5	-41.6	-1.4	67.1
60	60	41.5	-28.8	-29.2	35.1
60	80	41.5	-10.5	-17.6	3.2
40	80	41.5	-2.3	-18.4	3.8
40	60	41.5	7.7	-34.3	45
40	40	41.5	16.2	-7.3	117.7

Relative positions in mm			Magnetic field in Gauss		
x position	y position	z position	Bx	By	Bz
40	20	41.5	9.5	40.2	45.1
40	0	41.5	2.9	20.8	1.6
20	0	41.5	8.3	13	-0.9
20	20	41.5	21.6	19.4	12.7
20	40	41.5	38.1	2.6	30.3
20	60	41.5	20.6	-13.6	13.5
20	80	41.5	6.1	-11.6	0.6
0	80	41.5	6.4	-5.2	-1.8
0	60	41.5	13.1	-6.5	-2.5
0	40	41.5	19.2	-1.8	-2.5
0	20	41.5	13.4	5.6	-0.6
0	0	41.5	6.9	5.3	-2.5
80	0	78.5	-2.1	3.4	3
80	20	78.5	-3.8	2.9	5.7
80	40	78.5	-4.6	-0.2	7.1
80	60	78.5	-4.1	-2.6	6.1
80	80	78.5	-2.7	-3.5	3.2
60	80	78.5	-1.7	-4.6	5.2
60	60	78.5	-2.6	-3.7	9.4
60	40	78.5	-2.7	0.6	12.2
60	20	78.5	-1.9	3.8	8.8
60	0	78.5	-1.1	4.8	4.2
40	0	78.5	1.3	4.9	4.8
40	20	78.5	1.7	4.4	9.8
40	40	78.5	2.1	0.4	13.5
40	60	78.5	1.4	-3.1	10.7
40	80	78.5	0.9	-4	5.6
20	80	78.5	4.1	-2.7	4.7
20	60	78.5	5.3	-2.1	7.6
20	40	78.5	5.9	1	9.1
20	20	78.5	4.8	3.2	6.4
20	0	78.5	3.4	4	3.3
0	0	78.5	3.7	2.5	1.6
0	20	78.5	4.9	2.3	2.8
0	40	78.5	5.7	0.8	4.1
0	60	78.5	5.3	-0.6	3.7
0	80	78.5	4	-1.4	2.9

Experiment 9

Relative positions in mm			Magnetic field in Gauss		
x position	y position	z position	Bx	By	Bz
0	0	6.85	17.1	19.1	23.1
0	20	6.85	48.9	32.9	39.7
0	40	6.85	81.2	20.4	56.9
0	60	6.85	58.6	-20.7	54.7
0	80	6.85	23.5	-21.8	34.6
20	80	6.85	39.7	-87.2	54.9
20	60	6.85	231	-202	94.8
20	40	6.85	460	181.8	-12.7
20	20	6.85	133.3	172.4	51.8
20	0	6.85	23.3	55.3	30.3
40	0	6.85	7.3	68.3	38.6
40	20	6.85	45.5	436	-41
40	40	6.85	382	353	-1871
40	60	6.85	153.2	-937	-441
40	80	6.85	33.1	-144.8	58.1
60	80	6.85	-30	-82.1	49.1
60	60	6.85	-328	-321	2.5
60	40	6.85	-672	185.8	-114.1
60	20	6.85	-163.1	194.2	77.6
60	0	6.85	-24.1	50.6	32.6
80	0	6.85	-14.8	22.2	23.9
80	20	6.85	-51	19.6	28.7
80	40	6.85	-136	-14.2	30.3
80	60	6.85	-82.1	-30.1	53.1
80	80	6.85	-21.9	-22.2	34.3
80	80	16.85	-24.4	-28.7	13.5
80	60	16.85	-68	-29.7	10.4
80	40	16.85	-93.3	0.9	2.1
80	20	16.85	-58.2	24.5	10
80	0	16.85	-22.3	24.8	12.3
60	0	16.85	-23.7	48.4	10.7
60	20	16.85	-88.6	99.6	-25.3
60	40	16.85	-252	30.6	-151.3
60	60	16.85	-136.2	-139.6	-98.6
60	80	16.85	-29.6	-71.8	8.1
40	80	16.85	10.7	-107	7.5
40	60	16.85	11.1	-273	-319
40	40	16.85	17.4	71	-573
40	20	16.85	-8.2	210	-113.1
40	0	16.85	-3.8	71.9	4.2
20	0	16.85	27.3	57.8	14.7

Relative positions in mm			Magnetic field in Gauss		
x position	y position	z position	Bx	By	Bz
20	20	16.85	100.5	122.2	-43.4
20	40	16.85	224	10.2	-210
20	60	16.85	131.8	-142	-84.7
20	80	16.85	34.3	-67.5	14.6
0	80	16.85	26.4	-26.8	14.6
0	60	16.85	64.3	-33.1	8.1
0	40	16.85	83.1	26.7	21.8
0	20	16.85	55	45.5	19.8
0	0	16.85	25.3	28.8	14.2
0	0	26.85	20.6	27.1	6.9
0	20	26.85	43.1	33.1	-3.4
0	40	26.85	61.7	12.3	-11.6
0	60	26.85	50	-10.4	2.6
0	80	26.85	27.9	-17.5	9.4
20	80	26.85	34.7	-53.2	-6.5
20	60	26.85	79.1	-74.3	-81.2
20	40	26.85	107.8	26.8	-118
20	20	26.85	64.7	77.6	-49.5
20	0	26.85	25.6	48.2	-4.3
40	0	26.85	5.7	57.7	-16.7
40	20	26.85	9.2	105.8	-106.8
40	40	26.85	8.3	21.2	-272
40	60	26.85	14.7	-115.1	-155.6
40	80	26.85	0.4	-73.1	-23.6
60	80	26.85	-29.9	-52.7	-6.1
60	60	26.85	-80.9	-62.2	-67.1
60	40	26.85	-107.8	18.5	-130.1
60	20	26.85	-63.3	59.3	-51.1
60	0	26.85	-20.2	44.7	-8.5
80	0	26.85	-22.1	21.8	2.5
80	20	26.85	-49.5	25.5	-3.1
80	40	26.85	-70.3	5.6	-9.7
80	60	26.85	-52.6	-21.8	-7.8
80	80	26.85	-23.3	-23.6	4.5
80	80	36.85	-18.7	-17.2	-0.7
80	60	36.85	-39.1	-14.6	-11.1
80	40	36.85	-46.1	7.3	-13.7
80	20	36.85	-31.1	20.4	-7.2
80	0	36.85	-14.4	17.5	-5.2
60	0	36.85	-21.5	30.6	-16
60	20	36.85	-44.2	35.5	-49.3
60	40	36.85	-55.9	0.2	-80.8
60	60	36.85	-46.5	-34.4	-48.3
60	80	36.85	-21.9	-33.4	-11.1
40	80	36.85	-5.4	-47.5	-25.6

Relative positions in mm			Magnetic field in Gauss		
x position	y position	z position	Bx	By	Bz
40	60	36.85	-2.2	-56.1	-104.9
40	40	36.85	-0.6	12	-153.4
40	20	36.85	-6.1	45.2	-70.4
40	0	36.85	-3.8	39.8	-19.4
20	0	36.85	12.2	33.7	-14
20	20	36.85	30.2	41.9	-45.6
20	40	36.85	51.5	3.4	-83.9
20	60	36.85	44.5	-33.8	-64.9
20	80	36.85	24.8	-37	-16.2
0	80	36.85	23.5	-20.9	-4.3
0	60	36.85	37.8	-18.9	-20.2
0	40	36.85	45.2	4.4	-25.6
0	20	36.85	34.9	20.9	-14.6
0	0	36.85	20.2	21	-1.4
0	0	76.85	7.2	7.5	-5.8
0	20	76.85	8.7	5.6	-9.2
0	40	76.85	10	0.9	-11.7
0	60	76.85	9.4	-3.4	-10.1
0	80	76.85	7.5	-5.6	-6.8
20	80	76.85	5.6	-7.6	-10.3
20	60	76.85	7.1	-4.8	-17.5
20	40	76.85	7.6	1.7	-20.1
20	20	76.85	6.5	7.7	-14.2
20	0	76.85	5.2	9.1	-8.9
40	0	76.85	1.2	9.9	-10.8
40	20	76.85	1	6.4	-17.4
40	40	76.85	1.3	1.7	-22.7
40	60	76.85	1.8	-5.2	-19.3
40	80	76.85	2.1	-7.7	-12.4
60	80	76.85	-3.5	-7.2	-10.1
60	60	76.85	-5.2	-3.7	-15.6
60	40	76.85	-5.3	1.2	-18.2
60	20	76.85	-3.7	5.7	-14.7
60	0	76.85	-2.1	8.1	-9.2
80	0	76.85	-4.2	6.7	-6.1
80	20	76.85	-7	4.8	-9.3
80	40	76.85	-8	1.3	-10.8
80	60	76.85	-7.2	-3.1	-9.2
80	80	76.85	-4.6	-4.8	-5.4

Experiment 11

Relative positions in mm			Magnetic field in Gauss		
x position	y position	z position	Bx	By	Bz
0	0	4.15	-1.3	-2.7	12.8
0	20	4.15	-6.4	-4.5	29
20	40	4.15	-13.6	-2.9	35.4
20	40	4.15	-193.9	-48.9	325
20	20	4.15	-27.9	-50.1	154.4
40	0	4.15	-1.9	-5.8	30.2
40	0	4.15	0.5	-7.2	37.8
40	20	4.15	-2.9	-154.1	394
40	20	14.15	24.4	214	127.3
20	0	14.15	1.2	15.1	31.1
20	0	14.15	5.9	12.3	23.2
20	20	14.15	52.3	66.2	80.5
0	40	14.15	197.2	-36.7	151.7
0	40	14.15	12.7	-1	32.9
0	20	14.15	9.4	6.8	26.1
0	0	14.15	3.8	3.4	12.3
0	0	24.15	6.9	6.7	6.3
0	20	24.15	17.9	8.5	8.7
20	40	24.15	26.8	0.1	16.6
20	40	24.15	165.8	7.3	-72.8
20	20	24.15	54.7	69.5	1.2
40	0	24.15	7.5	20.4	10.6
40	0	24.15	-4.2	31.9	9.6
100	20	24.15	17.5	163.9	-71.8
60	0	24.15	-3.9	15.7	12.6
60	20	24.15	-65.7	49.6	14.6
80	40	24.15	-205	2.4	-35.1
80	40	24.15	-35.1	-1.7	14.7
80	20	24.15	-20.7	5.9	9.4
80	0	24.15	-6.4	4.5	8.3
80	0	14.15	-3.5	3.4	10.7
80	20	14.15	-12.3	4.8	21.2
60	40	14.15	-21.1	0.1	28.3
60	40	14.15	-436	2.6	143.4
60	20	14.15	-58.5	22.9	63.3
60	0	14.15	-5.6	6.9	21.3
60	0	4.15	0.8	-2.6	25.3
60	20	4.15	16.5	-19.4	107.1
80	40	4.15	374	-9.9	222
80	40	4.15	10.8	-0.7	30.8

Relative positions in mm			Magnetic field in Gauss		
x position	y position	z position	Bx	By	Bz
80	20	4.15	2.8	-2.3	21.4
80	0	4.15	0.8	-1.1	10.2
0	80	4.15	3.6	-2.3	12.8
20	60	4.15	11.8	1.9	24.5
20	60	4.15	66.3	-37.3	126.7
40	80	4.15	7.7	-7.4	35.3
40	80	4.15	0.6	-17.2	48.2
40	60	4.15	-20.9	-260	510
40	60	14.15	-4.2	326	164.7
20	80	14.15	-1.4	14.3	41.3
20	80	14.15	-3.7	6.4	26.9
0	60	14.15	-58.3	33.8	94.1
0	60	14.15	-7.6	4.4	22.6
0	80	14.15	-1.3	2.1	12.2
0	80	24.15	-5.7	5.2	7.3
20	60	24.15	-19.8	6.3	9.6
20	60	24.15	-73.5	43.9	-2.9
40	80	24.15	-4.5	15.3	11.2
40	80	24.15	6.5	29.8	18.6
100	60	24.15	35.4	160.2	-95.7
60	80	24.15	6.5	19.3	16.7
80	60	24.15	46.8	85.1	26.8
80	60	24.15	15.8	14.1	18.1
80	80	24.15	6.9	9.1	11.9
80	80	14.15	2.8	3.6	14.6
60	60	14.15	8.7	9.5	30.4
60	60	14.15	45.2	57.2	150.2
60	80	14.15	3.4	7.3	33.3
60	80	4.15	-3.4	-8.1	23.9
80	60	4.15	-28.5	-44.9	108.2
80	60	4.15	-4.3	-2.2	27.3
80	80	4.15	-1.9	-1.9	13.4
0	0	34.15	7.6	9.2	6.9
0	20	34.15	19.2	16.7	8.4
0	40	34.15	30.3	-0.3	-2.5
0	60	34.15	19.7	-13.1	3.3
20	80	34.15	8.1	-9.2	5.3
20	80	34.15	9.1	18.4	5.1
20	60	34.15	39.8	-53.4	-18.2
20	40	34.15	83.9	6.8	-87.8
20	20	34.15	35.5	53.3	-31.9
40	0	34.15	7.1	21.7	-0.9
40	0	34.15	-3.7	20.5	2.1
40	20	34.15	-2.9	51.7	-66.5
40	40	34.15	-26.2	4.7	-188.5

Relative positions in mm			Magnetic field in Gauss		
x position	y position	z position	Bx	By	Bz
40	60	34.15	2.6	-82	-38.6
60	80	34.15	2.6	-26.4	4.1
60	80	34.15	-7.2	-15.2	4.2
60	60	34.15	-36.3	-28.5	-3.7
60	40	34.15	-75.7	-15.4	-27.4
60	20	34.15	-34.7	27.1	-14.3
80	0	34.15	-8.8	11.4	0.4
80	0	34.15	-6.1	5.5	2.9
80	20	34.15	-16.8	2.1	1.6
80	40	34.15	-23.3	-2.2	1.8
80	60	34.15	-13.5	-6.8	3.7
80	80	34.15	-4.2	-5.4	4.5
80	80	74.15	-2.1	-2.3	-1.8
80	60	74.15	-3.7	-1.7	-3.9
80	40	74.15	-4.9	-0.3	-4.8
80	20	74.15	-4.1	2.1	-3.9
60	0	74.15	-3.1	2.8	-2.1
60	0	74.15	-3.3	4.2	-4.2
60	20	74.15	-3.9	3.8	-7.3
60	40	74.15	-4.9	-0.2	-10.7
60	60	74.15	-3.9	-3.7	-8.1
40	80	74.15	-2.2	-4.1	-3.8
40	80	74.15	-0.3	-5.3	-5.4
40	60	74.15	-0.6	-3.8	-11.6
40	40	74.15	-0.5	0.9	-14.8
40	20	74.15	-0.5	5.3	-10.4
20	0	74.15	-0.2	5.5	-5.4
20	0	74.15	2.4	5.1	-4.8
20	20	74.15	3.8	4.5	-9.9
20	40	74.15	4.8	1.2	-12.1
20	60	74.15	4.2	-3.1	-9.3
0	80	74.15	2.9	-4.9	-4.5
0	80	74.15	3.7	-3.1	-2.6
0	60	74.15	5.5	-2.6	-5.3
0	40	74.15	6.1	0.5	-6.9
0	20	74.15	4.8	2.9	-5.6
0	0	74.15	2.9	3.7	-3.3

APPENDIX E:

A GENERALIZED FRAMEWORK FOR LINEARLY CONSTRAINED CONTROL MOMENT GYRO STEERING

This section includes the full text of a journal paper[173] that grew from a 2009 work on CMG steering laws and Rodrigo Zeledon's follow-on to that work. He co-authored this paper with content from conference papers. This project's contributions are focused on the overview of CMG steering laws and the mathematical architecture for a general class of laws, while Rodrigo's contributions focused on the triplet steering law and its performance.

Nomenclature

A = system matrix augmented with constraint law

α = scalar constant

β_1 = scaling value for the first row of the Jacobian in the constraint equation

β_2 = scaling value for the second row of the Jacobian in the constraint equation

β_c = non-zero scaling value for the cross-product component of the constraint equation

C = $m \times n$ matrix of general constraint equations relative to the gimbal rates

$\tilde{C}$ = $m \times n$ matrix of general constraint equations relative to the gimbal angles

D = $m \times 1$ matrix of the solution to the constraint equations relative to the gimbal rates

$\tilde{D}$ = $m \times 1$ matrix of the solution to the constraint equations relative to the gimbal angles

d = scalar term in the constraint equation

Δ = determinant of the *A* system matrix

h = magnitude of the angular momentum of an individual CMG

J = 3×*n* system Jacobian matrix

n = number of CMGs in an array

m = number of scalar constraint equations in a constraint-based steering law

Φ = *n*×1 matrix of gimbal angles (made up of ϕ_i)

$\dot{\Phi}$ = *n*×1 matrix of gimbal rate commands (made up of $\dot{\phi}_i$)

ϕ = individual CMG gimbal angles

τ_C = commanded 3×1 matrix of torque scalars for spacecraft-body reference axes

τ_j = single, scalar torque component of τ_C

τ_{x_i} = the value of scalar x-component torque distributed to the *i*th triplet

E1 Introduction

Control moment gyroscopes (CMGs) are momentum-exchange actuators used to control the attitude of a spacecraft. One or more gimbals tilt the CMG's rotor, and in doing so, the gimbal precesses the CMG's angular-momentum vector to produce a torque that is largely due to a kinematic constraint. Therefore CMGs require less power to produce the same torque than reaction wheels, which accelerate or decelerate the rotor instead. CMGs are particularly useful in applications requiring high slew rates or large torques. Although several types of CMGs exist, including variable-speed CMGs[174] and double-gimbal CMGs,[175] the single-gimbal CMG (SGCMG) offers a combination of cost effectiveness and mechanical simplicity that makes it attractive

for implementation in space systems[176]. This paper considers only single-gimbal CMGs and drops the "SG" from the acronym, in keeping with common practice. Since the rotor of a CMG gimbals about only one axis, it can provide only a single actuation degree of freedom. A minimum of three is necessary to achieve full attitude control instantaneously, although it is more common to use an array of four or more for singularity avoidance or redundancy purposes. A CMG array is controlled by a steering law, an algorithm that governs how the CMGs move within the array (usually via commanded gimbal rates) to provide the required three-axis torque. CMG steering laws determine the gimbal rates necessary for the CMG array in response to a torque commanded by the attitude-control system for feedback control of the spacecraft attitude dynamics.

A significant drawback of CMG arrays is the presence of kinematic singularities at certain gimbal configurations. These singularities are points at which the array is incapable of instantaneously producing torque in a particular direction, which results in a loss of controllability. A major research focus in the community has been designing steering laws for CMG arrays such that an attitude-control system is capable of handling these singularities despite the practical hardware- and operations-related limitations of contemporary space systems.[177,178,179]

A certain class of CMG steering laws uses linear constraints (in hardware or software) to avoid singularities while finding an instantaneous solution without inducing error in the torque imparted to the spacecraft. Despite that several variations of this steering law exist in the literature,[180,181] a generalized form of this particular CMG steering law has yet to be presented. Once in a generalized form, the problem is

freed from specific array geometries or constraint laws, which opens up the design space to the possibility of optimized configurations. This paper presents a generalized mathematical description of steering laws with linear constraints and uses the familiar array of three scissored pairs to explain the formulation. It then provides an example based on Cornell University's Violet nanosatellite, which uses six CMGs in triplet combinations, to demonstrate the validity of the formulation.

E2 Background and Context for CMG Steering Laws

While CMG steering laws have been studied at length for decades, they are still an area of active research primarily because no one category of solutions appears to satisfy all of the requirements for an ideal steering law. Most published approaches to this problem fall roughly into one of six categories,[182] although there is overlap: the Moore-Penrose pseudoinverse,[183] singularity-robust pseudoinverse and similar solutions,[184,185,186,187,188] offline-planning,[189] preferred gimbal-angle laws,[190] gradient or null-motion methods,[184,191,192,193] and constraint-based steering laws.[180,181] Each method has different advantages and characteristics, but a perfect solution has yet to be found.[182] Table E1 lists the characteristics of broad categories of steering laws and assesses them in terms of the attributes of ideal steering laws.

Even if a perfect steering law does not exist, describing the characteristics of such an ideal helps clarify the shortcomings of existing laws and direct future research. Although the performance criteria for steering laws can be broken down into more descriptive subcategories,[183] in general, an ideal steering law must

1) Accommodate singularities
2) Provide error-free torque to the precision of the hardware

3) Accommodate hardware limitations (such as gimbal-rate saturation and computational throughput)
4) Provide efficient performance (such as maximal usage of the available momentum space)
5) Require no knowledge of future torque commands
6) Be general enough to support the full range of maneuvers and CMG configurations (e.g. CMG failure cases)

Table E1 Summary of General Steering Law Characteristics.

Steering Law	Singularity Avoidance Method	Induced Torque Error	Gimbal Saturation Possible	Full Momentum Workspace Used	Instantaneous	Generalized for All Array Configurations
Ideal Steering Law	**Unknown**	**No**	**No**	**Yes**	**Yes**	**Yes**
Moore-Penrose Pseudoinverse	None	No	Yes	Yes	Yes	Yes
Singularity Robust Inverse w/ Torque Error	Inexact mapping of command to output torque	Large near singularity, small otherwise	Yes	Yes	Yes	Yes
Offline Planning	Path planning and/or optimization	No	No	Yes	No	Yes
Preferred Gimbal Angle	Initial gimbal angles keep array non-singular for specific torque commands	No	Yes	No	Yes, if properly initialized	No
Gradient/Null Motion	CMG null motion in non-singular direction	No	Yes	Yes, but has finite gimbal rates only if no impassable singularities present	Yes	No
Constrained	Operating in non-singular gimbal-angle subspace	None within workspace, but limited workspace	Dependent on array configuration	Dependent on array configuration	Yes	No

Any CMG based attitude-control system must be implemented with the array's singularities in mind. Steering laws that prevent the CMGs from encountering singularities at all are broadly referred to as singularity-avoidance laws, whereas those that are designed to enable the array to pass through singularities are called singularity-robust laws. Steering laws that do not address singularities, such as the

Moore-Penrose pseudoinverse, are generally inappropriate unless the attitude-control design restricts the array's workspace to a nonsingular region.[194] Instead of being used directly, such laws may be part of a more subtle scheme that does handle singularities.

Accuracy is an important performance metric for steering laws because CMGs are particularly well suited to highly agile spacecraft, such as commercial imaging satellites. Therefore the applications for which most CMG arrays are being considered have demanding requirements for precise attitude control. A large category of CMG steering laws--the Singularity Robust variety--intentionally adds error to the solution as a way to sidestep singularities, producing torque errors that are relatively small except when the array is nearly singular. While this method is easily implemented and can produce usable torque, that torque is precise enough and nonsingular only within a small sub-region of the available momentum. If the array approaches singularity, gimbal rates can exceed the hardware limits; accuracy is sacrificed, and the determinacy of the solution is not guaranteed. Accuracy requirements for agile spacecraft make exactness the driver instead of the mere simplicity of such laws.

CMG steering laws should also be designed to prevent infeasible commands to the hardware. In particular, an ideal steering law should never call for excessive gimbal rates or accelerations. Some categories of steering laws can produce gimbal rate saturation, resulting in reduced controllability. While these laws can provide some measure of singularity avoidance, an ideal solution necessitates that they do so without requiring gimbal saturation.

Any successful steering law must be shown to provide torque and momentum performance appropriate for the size, weight, and power of the array. The efficiency of

different classes of steering laws is a metric that is open to debate, but it is generally agreed that methods that severely constrain the operating envelope of the array by design, particularly in CMG failure cases, are not ideal. Some types of steering laws fall into this category by sacrificing momentum workspace to handle singularities (including some constrained laws such as scissored pairs of CMGs). However, an ideal law would maximize the use of the array's total momentum envelope while limiting the number of individual CMGs and the power used.

A steering law must also be capable of interpreting a torque command and implementing it in real time on the spacecraft with no explicit knowledge of the future. This requirement on array steering is distinct from any feedforward that the attitude-control might implement. Instantaneous responsiveness is ideal because laws that can manage it can directly map commands into CMG motion without the imprecision that comes with unavoidably imperfect future knowledge. Off-line approaches to developing singularity-free paths for the CMG array,[195] while often providing excellent simulated performance (if the algorithm is properly formulated and not overconstrained), generally require computationally intensive models that may be impractical on actual spacecraft hardware. Furthermore, these approaches cannot account for all of the subtleties, such as noise and unmodeled dynamics, which are inevitably present in any closed-loop system. Thus, it is desirable for an ideal steering law to be instantaneously responsive.

Finally, steering laws should be independent of the particular maneuvers commanded by the spacecraft and should not need to be replaced with an entirely different algorithm in the case of a CMG failure. The more general the steering law is

with respect to the maneuver and the array geometry, the more robust the system is to unexpected torque commands or failure cases. Unfortunately, a generalized steering law is much more complicated to design, and thus many steering laws specify applicable array geometries.[182,192,193] While these solutions are often very well-suited to their specific array geometry, an ideal steering law would be general enough to handle changes in the array configuration.

While Table E1 by no means offers as detailed or as nuanced a description as these different techniques deserve, it does provide a clearer picture of which steering laws are more promising. Some of the categories are intrinsically non-ideal by the proposed metrics. For example, offline planning approaches are by definition not instantaneous. So, it follows that the ideal solution to CMG steering is probably not to be found among these categories. However, working to understand some of the other laws in a more general way may provide the framework necessary for developing an ideal steering law. Algorithms that use constraints to steer the array on a non-singular path falls into one such category.

The remainder of this paper examines a generalized formulation for steering laws based on linear constraints. These laws constrain the motion of the CMGs, taking into account torque and angular momentum limitations a priori, in order to prevent the array from encountering internal singularities. By studying a more general form of this class of steering laws, it is possible to gain insight on better ways of designing them. While this paper focuses on linear constraints in particular, constraints need not always be linear with respect to the gimbal rates, as found by Kurokawa.[181,196] However, the linear formulation provides distinct advantages in implementation,

making them worthy of in-depth study. Section E3 describes a general form for these steering laws and describes special cases of this form. Section E4 presents simulation results for a new linearly-constrained steering law designed for Cornell's Violet nanosatellite, an in-orbit CMG testbed.

E3 Generalized Form for Linearly-Constrained Steering Laws

E3.1 Description

An expression for the commanded torques in terms of the gimbal rates is shown in Eq. (E.1):

$$\tau_C = J(\Phi)\dot{\Phi} \tag{E.1}$$

where J is the Jacobian for the CMG array (the partial derivative of its total momentum with respect to the gimbal angles), τc is the commanded torque vector in body coordinates, and $\dot{\Phi}$ is the n×1 array of gimbal rates meant to achieve that torque. This equation is solved using a pseudoinverse as shown in Eq. (E.2):

$$\dot{\Phi}(\tau) = J(\Phi)^{+}\tau_C \tag{E.2}$$

Many pseudoinverses exist[197] and can be used to solve for the CMG gimbal rates. The singularity-robust pseudoinverse[184] is an example. However, CMG steering laws, including those considered in this work, begin with an approach that uses the Moore-Penrose pseudoinverse, shown in Eq. (E.3):

$$\dot{\Phi}(\tau) = J(\Phi)^{T}\left(J(\Phi)J(\Phi)^{T}\right)^{-1}\tau_C \tag{E.3}$$

The $J(\Phi)J(\Phi)^T$ term can be rank deficient, and therefore non-invertible, which is the mathematical basis for array singularity. So, as the first step in ensuring that the inverse of the $J(\Phi)J(\Phi)^T$ term exists, constraint equations can be appended to the Jacobian. Equation (E.4) is a general description of a set of linear constraint equations:

$$D = C\dot{\Phi} \tag{E.4}$$

where D is an m×1 matrix, and C is an m×n matrix. Equation E1 can be augmented as follows:

$$\begin{bmatrix} \tau_C \\ D \end{bmatrix} = \begin{bmatrix} J(\Phi) \\ C \end{bmatrix} \dot{\Phi} = A\dot{\Phi} \tag{E.5}$$

which leads to an augmented system matrix A. A non-zero D and C provide a more general form of a steering law that is based on the Moore-Penrose pseudoinverse. Alternatively, one can argue that C and D are zero in Eq. (E.3) and that the resulting solution simply minimizes the norm of the gimbal rates. Equation (E.6) shows the more general form of a linearly constrained steering law:

$$\dot{\Phi}(\tau) = A(\Phi)^T \left(A(\Phi)A(\Phi)^T \right)^{-1} \tau_C \tag{E.6}$$

Using the constraint matrices not only minimizes the norm but can also provide the singularity avoidance properties required of an effectual steering law. Using an augmented form of A that includes the system kinematics and the constraints on the system, can ensure full rank for the inverse and thus avoid singularities. This description of linearly constrained steering laws provides a first step toward generalizing this class of steering laws. Since an appropriate set of D and C matrices

can produce a singularity-free motion, the selection of these values is not trivial. Subsequent sections offer some insight into this process.

E3.2 Principles of Constraint Design

The generalized form of the constrained steering laws in Eq. (E.6) can accommodate diverse arrays and numbers of constraints. While the constraints must be linear with respect to the gimbal rates, common types of constraints take this form. For example, a holonomic constraint that specifies the gimbal angles explicitly can be written in the following form:

$$\tilde{D} = \tilde{C} \cdot \Phi(\tau) \tag{E.7}$$

Differentiating this type of constraint, assuming that the constraint is a linear combination of the gimbal angles and thus the $\tilde{C}$ matrix is constant, puts it into the form of Eq. (E.4):

$$\dot{\tilde{D}} = \tilde{C} \cdot \dot{\Phi}(\tau) = C \dot{\Phi}(\tau) = D \tag{E.8}$$

This approach requires the specification of the initial conditions. The scissored-pair steering law is an example of this type of constraint and is discussed in more depth in subsequent sections. In general, freedom from singularities requires specific initial conditions (akin to preferred gimbal angles) and carefully chosen constraints. If they are chosen correctly, the resulting CMG gimbal motion is thereby constrained to a singularity-free subspace of all possible gimbal-angle combinations.

In general, such a formulation also allows for an arbitrary number of constraints, as an array of CMGs may be capable of producing singularity-free motion with either an underconstrained or an overconstrained Jacobian. However, for

simplicity, the examples in the remainder of this paper consider only fully constrained systems, where the number of constraints *m* must result in a square Jacobian. Thus, when considered against the number of CMGs available, *n*, for a three-dimensional space, the total number of constraints is:

$$m = n - 3 \tag{E.9}$$

The result is a deterministic, one-to-one mapping of momentum to gimbal angles. Naturally, a healthy spacecraft has $n \geq 3$ CMGs; any additional constraints exploit the null space represented by four or more CMGs. For example, controlling a three-dimensional momentum space with four CMGs requires only one constraint. A fully constrained system produces a square *A* matrix, which in turn means that the pseudoinverse in Eq. (E.6) can be replaced with a simple matrix inverse. It is also worth noting that in order for a constraint-based steering law to operate properly, the constraint must be fully enforced despite its numerical implementation. Therefore, some amount of low-bandwidth feedback may be required to avoid an accumulation of numerical error that increasingly violates the constraint.

Finally, Eq. (E.5) suggests that in order for the *A* matrix to be non-singular, the constraint matrix *C* must contain rows that are linearly independent of the Jacobian *J* at any time. Constraint equations must therefore comprise a complementary subspace to the rows of the Jacobian and simultaneously ensure that the *J* partition remains rank 3.

E3.3 Example: Scissored-Pair CMGs

The well-established, linearly constrained steering law known as a scissored-pair arrangement provides a convenient example demonstrating how known steering laws fit into the generalized framework.[180] In a scissored-pair configuration, two CMGs with parallel gimbal axes are constrained such that their gimbal angles are equal in magnitude and opposite in direction ($\phi_1 = -\phi_2$). Alternatively, the angles can be constrained to be the same ($\phi_1 = \phi_2$), but with gimbal axes exactly opposite each other. This simple constraint can be enforced either in hardware (which offers some additional benefits),[198] or in software. The scissoring motion caused by this constraint produces an output torque along a fixed direction determined by the gimbal axes, as shown in Figure E.1. Therefore, complete six degree-of-freedom control requires three scissored pairs, i.e. six individual CMGs. The arrangement shown in Figure E.4 is used for the purposes of this example.

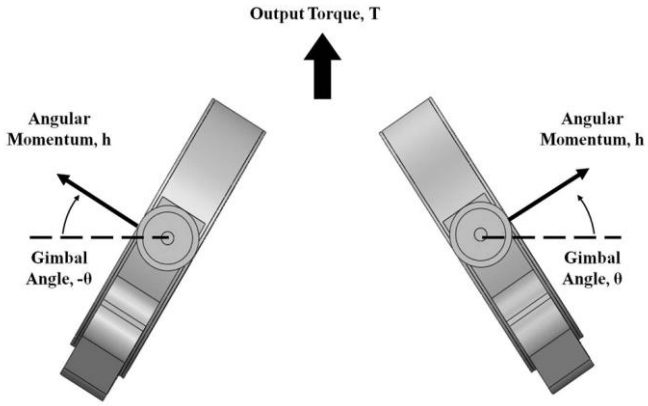

Figure E.1. Scissored Pair of CMGs.

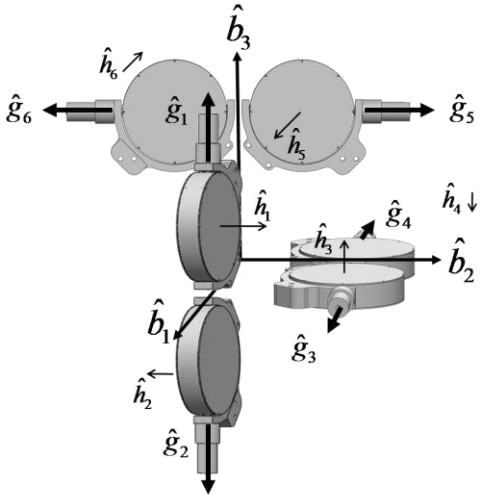

Figure E.4. Arrangement of Three Orthogonal Scissored Pairs.

Scissored-pair arrangements of CMGs are singularity free except at the saturation singularities, where the pair produces the maximum momentum of which it is capable. If unconstrained, each of the pairs of CMGs would offer a 2*h*-radius circular momentum envelope with a singularity at the origin. With the constraint, the pair operates within a reduced but nonsingular cube-shaped envelope 4*h* on a side. Because saturation limit of the constrained system is well inside the overall array momentum boundaries, this configuration of CMGs is generally not considered cost-effective despite its singularity-avoidance properties and its relative simplicity.

Figure E.4 shows six CMGs aligned along the three orthogonal axes in pairs with opposite gimbal axes. Whether or not a scissored-pair constraint is in force, its Jacobian is:

$$J = h\begin{bmatrix} -\cos\phi_1 & -\cos\phi_2 & 0 & 0 & -\sin\phi_5 & \sin\phi_6 \\ -\sin\phi_1 & \sin\phi_2 & -\cos\phi_3 & -\cos\phi_4 & 0 & 0 \\ 0 & 0 & -\sin\phi_3 & \sin\phi_4 & -\cos\phi_5 & -\cos\phi_6 \end{bmatrix} \tag{E.10}$$

For this arrangement to act as a collection of scissored pairs, the constraint equations can be expressed as the set of three equations:

$$\phi_1 - \phi_2 = 0;\ \phi_3 - \phi_4 = 0;\ \phi_5 - \phi_6 = 0 \tag{E.11}$$

Taking the derivative of these constraints as suggested in Eq. (E.8) produces a similar constraint on the gimbal rates. In a matrix form, the gimbal-rate constraints are

$$\begin{bmatrix} 0 \\ 0 \\ 0 \end{bmatrix} = \begin{bmatrix} 1 & -1 & 0 & 0 & 0 & 0 \\ 0 & 0 & 1 & -1 & 0 & 0 \\ 0 & 0 & 0 & 0 & 1 & -1 \end{bmatrix} \dot{\Phi} \tag{E.12}$$

From Eq. E5, the augmented linear equation is

$$\begin{bmatrix} \tau_1 \\ \tau_2 \\ \tau_3 \\ 0 \\ 0 \\ 0 \end{bmatrix} = \begin{bmatrix} -h\cos\phi_1 & -h\cos\phi_2 & 0 & 0 & -h\sin\phi_5 & h\sin\phi_6 \\ -h\sin\phi_1 & h\sin\phi_2 & -h\cos\phi_3 & -h\cos\phi_4 & 0 & 0 \\ 0 & 0 & -h\sin\phi_3 & h\sin\phi_4 & -h\cos\phi_5 & -h\cos\phi_6 \\ 1 & -1 & 0 & 0 & 0 & 0 \\ 0 & 0 & 1 & -1 & 0 & 0 \\ 0 & 0 & 0 & 0 & 1 & -1 \end{bmatrix} \dot{\Phi} = A_{SP}\,\dot{\Phi} \quad \text{(E.13)}$$

which defines A_{SP} as the scissored-pair A matrix. The required initial condition is that the gimbal angles for each pair begin with equal magnitude and opposite sign. The constraint enforces the requirement throughout subsequent motions. This fact allows one to simplify Eq. (E.13) and produce the determinant

$$\det\left(A_{SP}\right) = -8h^3\cos\left(\phi_1\right)\cos\left(\phi_3\right)\cos\left(\phi_5\right) \quad \text{(E.14)}$$

The singularity-avoidance properties of this particular steering law are evident in the determinant of the newly formed A_{SP} matrix from Eq. (E.13). The singular points, i.e., where Eq. (E.14) vanishes, are where ϕ_1, ϕ_3, and ϕ_5 become $-\pi/2$ or $\pi/2$ for each scissored pair. A_{SP} remains nonsingular at any point within this range. These angles represent the saturation of the gimbals, showing that the system has full rank for gimbal angles below saturation. While this result simply confirms what has already been known about scissored-pair steering laws, it serves as an example of the power of the generalized formulation.

E4 Triplet Steering Law

The generalized form of the linear constrained steering law can also be used to better inform the development of new steering laws of this variety. The "triplet" steering law was developed using the generalized framework and can be shown to yield effective singularity-free motion with the many advantages that constrained steering laws inherently possess.

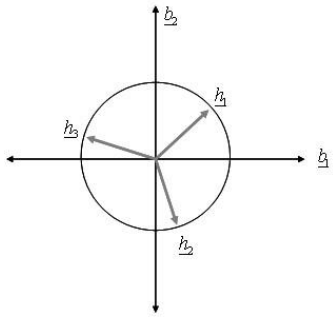

Figure E.2. Planar representation of CMG momentum in a zero-momentum state.

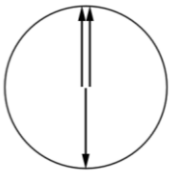

Figure E.3. Internal singularity for triplet arrangement.

E4.1 Theoretical Discussion

The case of a planar CMG momentum envelope, where the gimbal axes of the CMGs are all parallel, provides a convenient starting point for the development of a steering law for sets of parallel CMGs. In such an array, a single CMG leads to a one-dimensional momentum manifold because only a single gimbal angle changes. With two CMGs, the momentum vectors can add to produce torque in both directions that span the plane, as long as the gimbal rates are kept within saturation limits. The mapping from a two-dimensional torque to two gimbal rates is one-to-one, which means that there is no alternative, singularity-free path that avoids those cases when the Jacobian is singular.

However, if three CMGs' momentum vectors lie in this plane (a "triplet"), the additional CMG adds a degree of freedom (so that, for example, an infinite number of gimbal angles relative to the body axes can correspond to the zero momentum state, as shown in Figure E.2). The three-CMG configuration has an internal singularity in

which the three momentum vectors are collinear and two momentum vectors exactly cancel out. Such an arrangement is shown in Figure E.3. The momentum of this triplet array can be represented by the vector sum of the three component momentum vectors--that is, by arranging the three vectors head to tail. In this momentum-space representation, the internal singularity manifold is a ring 1*h* in radius around the center of the axes.

Solving for the gimbal rates in a CMG triplet requires one constraint equation for a two-dimensional workspace. This constraint must be designed to successfully avoid the internal singularity while also providing the require9d torque by exploiting the null space of the Jacobian. The triplet configuration has a 2×3 Jacobian, as shown in Eq. (E.15), where J_1 and J_2 are the top and bottom rows of the Jacobian, respectively.

$$J_{Planar} = \begin{bmatrix} -\sin\phi_1 & -\sin\phi_2 & -\sin\phi_3 \\ \cos\phi_1 & \cos\phi_2 & \cos\phi_3 \end{bmatrix} = \begin{bmatrix} J_1 \\ J_2 \end{bmatrix} \tag{E.15}$$

In order to ensure that the constraint equation maintains the rank of *J*, the constraint equation must be linearly independent of the two rows of the Jacobian at any instant and must keep those two rows independent of one another. If the cross-product of two vectors is non-zero, the two vectors are linearly independent. Therefore, a singularity-free constraint equation must include a scaled component in the direction of the cross-product of the two rows of the Jacobian. Equation (E.16) shows the constraints written in the form of Eq. (E.4):[199]

$$D = d = \left[\beta_1 J_1 + \beta_2 J_2 + \beta_c \left(J_1 \times J_2 \right) \right] \dot{\Phi} = C \dot{\Phi} \tag{E.16}$$

where *d* is a scalar solution to the constraint equation, β_1 and β_2 are scaling values for the component of the vector in the direction of the Jacobian rows, and β_c is a non-zero scaling value for the constraint equation. The solution presented as an example uses a value of zero for β_1 and β_2 and a value of one for β_c, such that the constraint equation is as shown in Eq. (E.17).

$$D = \left[J_1 \times J_2 \right] \dot{\Phi} = \left[\sin(\varphi_3 - \varphi_2) \quad \sin(\varphi_1 - \varphi_3) \quad \sin(\varphi_2 - \varphi_1) \right] \dot{\Phi} = C \dot{\Phi} \qquad \text{(E.17)}$$

D determines the null motion needed to steer the array away from the internal singularity at 1*h*. Because *C* is orthogonal to the two rows of *J*, the singularities of the augmented matrix *A* (Eq. (E.5)) are simply the singularities of *J*.

E4.2 Null-Space Constraint

Using the generalized constrained steering law formulation, the burden of designing the steering law shifts to designing a set of useful constraint equations. Within the context of a triplet CMG array, the theoretical guidelines for the constraint design make it possible to implement an efficient steering law that exploits the insights provided by the framework suggested by Eq. (E.5).

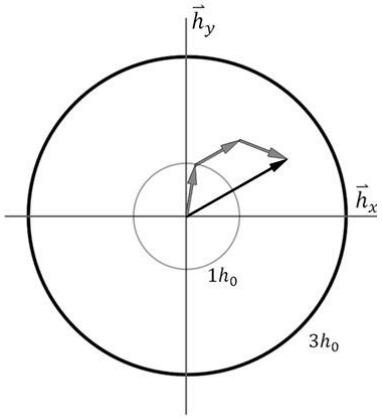

Figure E.4. Triplet CMGs in a trapezoid configuration.

One of the constraint designs that has proven to be exceptionally effective uses null-space commands to keep the CMGs in a "trapezoid" configuration in

momentum space.[200] As shown in Figure E.4, one of the CMG momentum vectors in the trapezoid configuration is kept parallel to the array momentum vector, while the other two CMG momentum vectors form the sides of a trapezoid. All three vectors are parallel only at the edge of the momentum envelope. At the internal singularity at 1*h* the two vectors forming the sides are orthogonal to the vector parallel to the total momentum vector—an ideal configuration for traversing the singularity.

For any total momentum vector within the array's momentum envelope, there are six sets of gimbal angles that cause the momentum vectors to form a trapezoid such that they sum to the same total momentum vector. Some may be redundant. The proposed steering law first determines which of the six trapezoid configurations is closest to the current (non-trapezoidal) gimbal angle configuration. The "closest" configuration is the one that requires the least amount of null motion to move between it and the current configuration and is therefore the desirable target for the gimbal angles.[200] In implementation, this step is accomplished by computing the six possible trapezoidal sets of gimbal angles, and then comparing those six possibilities to the current set of gimbal angles. The trapezoidal gimbal angle set that is the closest in the 2-norm sense is then selected as the target configuration.[200]

The angles for the target trapezoid configuration are used in Eq. (E.18) to solve for *D*:

$$D = \begin{bmatrix} \sin(\varphi_3 - \varphi_2) & \sin(\varphi_1 - \varphi_3) & \sin(\varphi_2 - \varphi_1) \end{bmatrix} K \left(\begin{bmatrix} \varphi_{1t} \\ \varphi_{2t} \\ \varphi_{3t} \end{bmatrix} - \begin{bmatrix} \varphi_1 \\ \varphi_2 \\ \varphi_3 \end{bmatrix} \right) \tag{E.18}$$

where φ_{nt} is the target gimbal angle for the *n*th CMG, and *K* is a 3×3 diagonal matrix of gains. The values of the entries of *K* determine how much effort is used to drive the CMGs to their closest trapezoid configuration and are chosen such that as much null-space effort as possible is used to keep the array close to a trapezoid without exceeding gimbal limits. The selection of entries in *K* can be done with brief numerical iteration or an optimization function. For the simulations presented in this paper, the *K* values were chosen using a numerical optimization routine that searches through a grid of possible *K* matrices.[200] All of these values are used to evaluate Eq. (E.18) to produce a set of possible *D* values. These *D* values are then used in Eq. (E.5) to solve for a set of $\dot{\varphi}$ values that correspond to every potential *K* matrix. Values that would cause the gimbal rate or acceleration limits to be exceeded are discarded. From the remaining pool of *K* values, which now all meet the hardware limitations of the system, the *K* matrix that moves the array closest towards the desired trapezoid configuration in the next time step is selected. The resulting optimal *K* matrix cannot cause the system to exceed hardware limitations because it was explicitly selected to meet these constraints. Once the optimal values of the *K* matrix found, the corresponding gimbal rates are then sent to the actuators.

When implemented, this algorithm is not used close to the zero-momentum state because at zero momentum, there are infinitely many possible trapezoids instead of the usual six configurations. While torque is still available in any direction, the algorithm must be given a way of deciding the appropriate configuration of the momentum vectors without rapidly switching back and forth between two different

target trapezoids. The constraint is therefore modified such that within a small radius of the zero momentum state, a Moore-Penrose pseudoinverse rule is used instead. Since the radius in which the pseudoinverse rule is used is much smaller than 1h, no problems with singularities are encountered by using the pseudoinverse, and the issue of very large gimbal rates near zero momentum is avoided. In the implementation on Cornell's Violet nanosatellite, the pseudoinverse rule is used only within 0.1h, which allows for enough null motion between 0.1h and 1h to properly condition the array. In the general case, the radius should be as small as possible but still large enough that the momentum can traverse the origin with bounded gimbal rates. In general, the choice of this radius depends on the application-specific requirement on simultaneously available torque and momentum.

E4.3 Expansion to Three-Dimensional Momentum Values

While one CMG triplet spans only two degrees of freedom, it is straightforward to expand this steering law to all three attitude degrees of freedom. Two sets of triplets (six CMGs) are positioned such that the two planes are not parallel—i.e., gimbal axes are offset relative to one another and can be used together to exert torque in three directions. The angle between the planes determines the array's capability in spacecraft axes; so, it would likely follow from agility requirements and the spacecraft's own inertia tensor. If the triplets are nonsingular, this configuration results in complete singularity-free control over two planes at an angle to one another and therefore spans the three-dimensional range of momentum values. In the example considered here, the triplets' gimbal axes are orthogonal to one another, as shown in

Figure E.5. A three-axis triplet steering law requires two constraint equations, as described in Eq. (E.19).

$$\begin{bmatrix} \tau_x \\ \tau_y \\ \tau_z \\ D_1 \\ D_2 \end{bmatrix} = \begin{bmatrix} 1 & 0 & 0 & 1 & 0 & 0 \\ 0 & 1 & 0 & 0 & 0 & 0 \\ 0 & 0 & 0 & 0 & 1 & 0 \\ 0 & 0 & 1 & 0 & 0 & 0 \\ 0 & 0 & 0 & 0 & 0 & 1 \end{bmatrix} \begin{bmatrix} \tau_{x_1} \\ \tau_y \\ D_1 \\ \tau_{x_2} \\ \tau_z \\ D_2 \end{bmatrix} = \begin{bmatrix} 1 & 0 & 0 & 1 & 0 & 0 \\ 0 & 1 & 0 & 0 & 0 & 0 \\ 0 & 0 & 0 & 0 & 1 & 0 \\ 0 & 0 & 1 & 0 & 0 & 0 \\ 0 & 0 & 0 & 0 & 0 & 1 \end{bmatrix} \begin{bmatrix} J_{1_{2\times3}} & 0_{2\times3} \\ C_{1_{1\times3}} & 0_{1\times3} \\ 0_{2\times3} & J_{2_{2\times3}} \\ 0_{1\times3} & C_{2_{1\times3}} \end{bmatrix} \begin{bmatrix} \dot{\varphi}_1 \\ \dot{\varphi}_2 \\ \dot{\varphi}_3 \\ \dot{\varphi}_4 \\ \dot{\varphi}_5 \\ \dot{\varphi}_6 \end{bmatrix} \quad \text{(E.19)}$$

where *J*1 represents the 2×3 Jacobian of the first CMG triplet and *J*2 the 2×3 Jacobian of the second triplet. *C*1 and *C*2 are the 1×3 constraint equations, as described in Eq. (E.17), and *D*1 and *D*2 are solved for as described in Eq. (E.18). The requested torque in the shared x-direction needs to be distributed to both CMG arrays, such that the sum of τ_{x_1} and τ_{x_2} in Eq. (E.19) equals the requested torque in the x-direction. The transformation matrix in Eq. (E.19) is determined by the orientation of the two triplets.

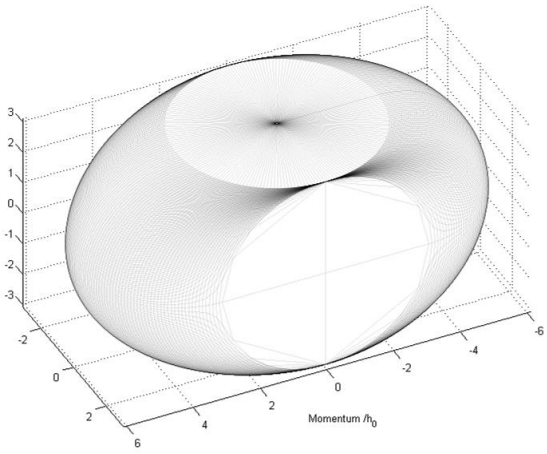

Figure E.6. Momentum envelope for two orthogonal triplets.

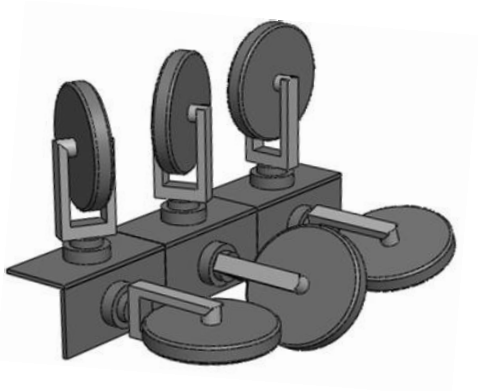

Figure E.5. Two Triplets of CMGs at Right Angles.

In this case, the gimbal axes are pointed in the *y* and *z* directions such that the momentum envelope is greater in the *x* direction. The momentum envelope for this configuration is shown in Figure E.6. The maximum extent is 6*h* in the direction orthogonal to both gimbal axes and 3*h* in the other two directions.

Table E2 Summary of Simulation Parameters.

Momentum per CMG
h = 0.31 Nms
Maximum CMG gimbal rate
$\dot{\varphi}_{\max}$ = 1.6 rad/s
Maximum CMG gimbal acceleration
$\ddot{\varphi}_{\max}$ = 9.6 rad/s^2
Inertia matrix (in satellite body axes)
$I_{body} = \begin{bmatrix} 2.001 & 0.116 & -0.010 \\ 0.116 & 2.017 & -0.009 \\ -0.010 & -0.009 & 2.161 \end{bmatrix}$
Gimbal axes for CMGs 1-6 (in satellite body axes)
$\hat{g}_1 = \begin{bmatrix} 0 \\ -\sqrt{2}/2 \\ -\sqrt{2}/2 \end{bmatrix}, \hat{g}_2 = \begin{bmatrix} 0 \\ \sqrt{2}/2 \\ \sqrt{2}/2 \end{bmatrix}, \hat{g}_3 = \begin{bmatrix} 0 \\ -\sqrt{2}/2 \\ -\sqrt{2}/2 \end{bmatrix}$ $\hat{g}_4 = \begin{bmatrix} 0 \\ \sqrt{2}/2 \\ -\sqrt{2}/2 \end{bmatrix}, \hat{g}_5 = \begin{bmatrix} 0 \\ -\sqrt{2}/2 \\ \sqrt{2}/2 \end{bmatrix}, \hat{g}_6 = \begin{bmatrix} 0 \\ -\sqrt{2}/2 \\ \sqrt{2}/2 \end{bmatrix}$

E4.4 Orthogonal Triplet Steering Simulation Results

The orthogonal-triplet steering law must be tested in both simulated and hardware environments in order to be considered a viable candidate for steering arrays for other spacecraft missions. This steering law is ultimately intended to be tested onboard Violet, Cornell University's entry into the University Nanosat-6 competition. Violet will be the first-ever high-agility nanosatellite, with up to 10 deg/s, 10 deg/s^2 and 60 deg/s^3 agility. In this role, it will serve as an experimental testbed for validating CMG steering laws in orbit. Violet carries eight CMGs of which six can be used simultaneously, offering many possible array geometries, such as a pair of orthogonal triplets. Because the orthogonal-triplet steering law will be tested on Violet's hardware, the simulation testing environment uses parameters from Violet's CMG array, listed in Table E2.[46] The inclusion of the gimbal acceleration limit is especially

important because this steering law will be implemented on actual flight hardware which cannot produce infinite gimbal accelerations.

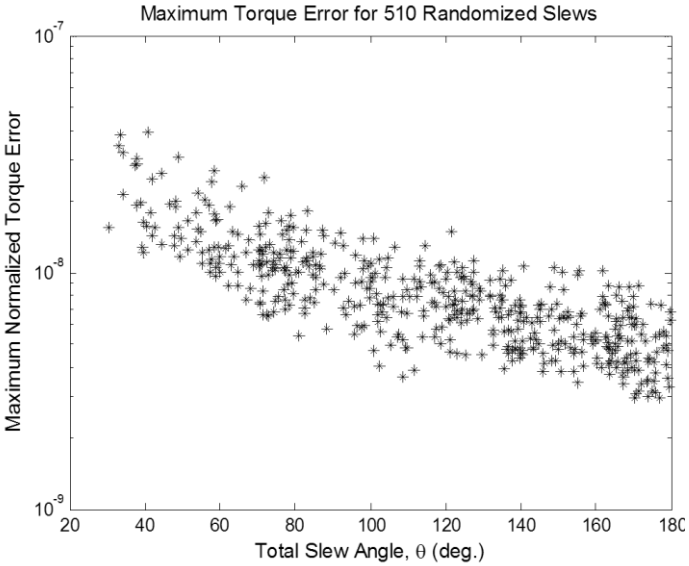

Figure E.8. Log maximum torque normalized error vs. total slew angle.

In order to demonstrate the proposed steering law and thus the efficacy of the generalized formulation for linearly-constrained laws, the results of 510 rest-to-rest slew simulations are shown in Figure E.8, Figure E.7, and Table E3. The slews are randomized rotations between 30 and 180 degrees (which covers the interesting cases where the slews either cross or come close to the singularity) and are about randomized eigenaxes. The slews are shaped through an algorithm that ensures continuous derivatives at both ends of the slew. The final attitude of the spacecraft in each slew is properly randomized in order to ensure a

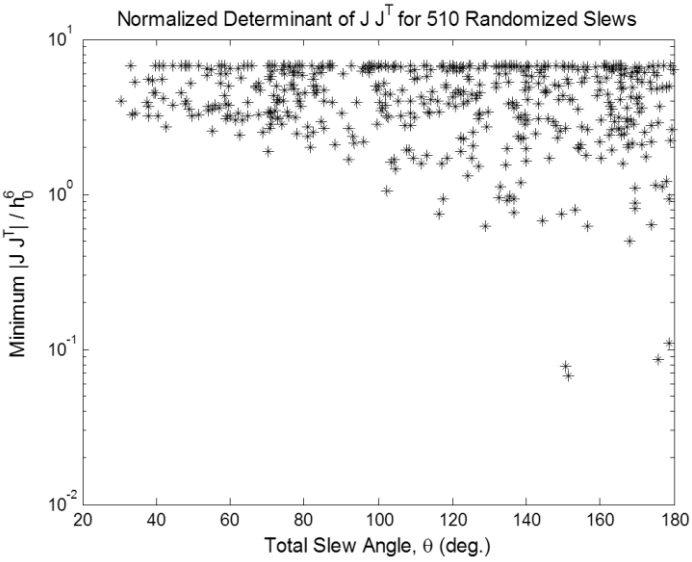

Figure E.7. Log minimum determinant of the normalized $J(\Phi)J(\Phi)^T$ vs. total slew angle.

uniform distribution.[201] Violet's kinematic limits are used to generate the slew, and Violet's hardware constraints taken into account in the steering law. Similar rest-to-rest slews exemplifying the capabilities of a six-CMG array will be completed in orbit.

Table E3 Summary of Monte Carlo Results.

Value Per Slew: \ Over All MC Runs:	**Min.**	**Max.**	**Mean**	**Standard Deviation**
Maximum Gimbal Rate (rad/s) $\dot{\varphi}_{\max}$	0.0551	0.4680	0.2388	0.0750
Maximum Gimbal Acceleration (rad/s^2) $\ddot{\varphi}_{\max}$	0.9254	9.3092	5.2164	1.8835
Maximum Torque Error (Nm) τ_{error}	0.087e-7	1.161e-7	0.265e-7	0.153e-7
Maximum Momentum of the Array (Nms) h	0.5572	1.2066	0.9085	0.1715

The minimum determinant of $J(\Phi)J(\Phi)^T$ is plotted as a function of the total slew angle in Fig. 8 on a semi-log plot in the y-axis. The determinant in the plot has been normalized by dividing out a factor of h^6 (which has a value of 8.875×10^{-4} in this simulation given Violet's h of 0.31 Nms) since $J(\Phi)$ is scaled by h. It is clear that the minimum determinant values do not reach the singularity value of zero over these 510 runs, providing confidence that the steering law is providing sufficient singularity avoidance. This result is supported by Fig. E9, which indicates a very low (10-8 Nm) normalized torque error over the randomized slews. Although this method produces exact solutions to the commanded torque, the system still has small errors associated with the array's inability to immediately match the magnitude of the demanded torque.

These errors are the direct result of the imposed constraints on the available gimbal accelerations. The values in this plot were normalized by dividing out the factor of six times the maximum CMG torque (2.976 Nm for Violet).

Additional statistics on the Monte Carlo results are published in Table E3. The different values for an individual slew are listed down the first column and the statistical value for each is given in the appropriate row. The maximum values for the gimbal rate and acceleration never exceed the hardware limitations described in Table E2. The very low torque error is also evident in these statistics.

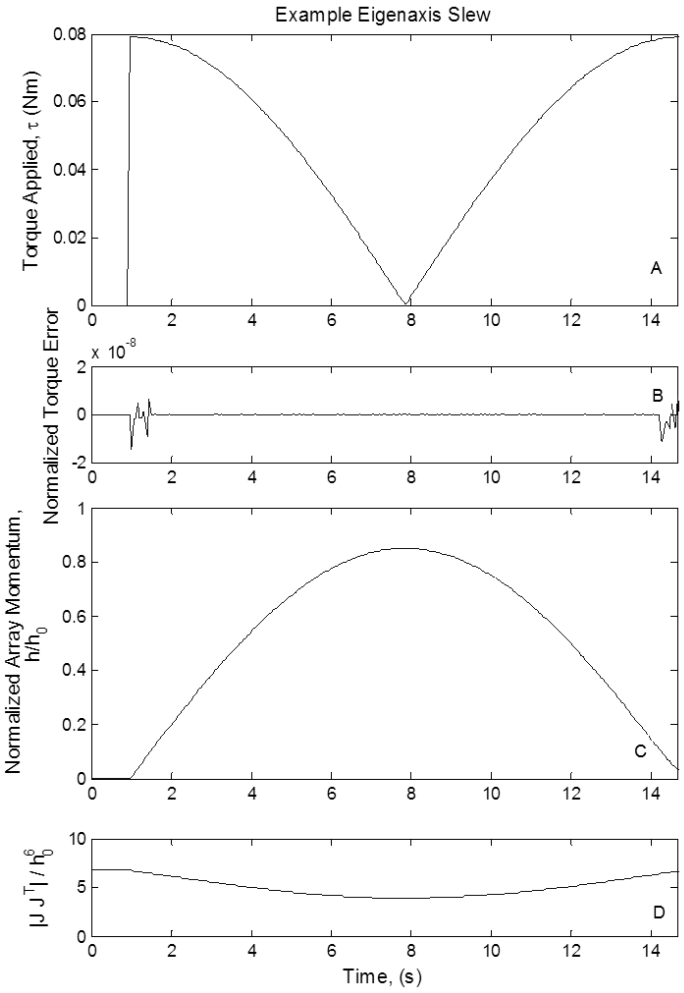

Figure E.9. Example slew torque applied (by CMG array on spacecraft), torque error normalized by 6x the max CMG torque, array momentum normalized by h, and determinant of $J(\Phi)J(\Phi)^T$ normalized by h^6

To provide more detailed descriptions of the steering law's effect on a slew, results for a randomly selected example slew are shown in Figure E.9 and Figure E.10. Figure E.9shows the rotation angle and angular velocity and their errors with respect to the target slew. As is evident in the plots, both errors remain small throughout the sample maneuver. Figure E.10shows the torque applied by the CMGs, the error with respect to the torque requested by the spacecraft, the magnitude of the angular momentum of the CMG array, and the determinant of $J(\Phi)J(\Phi)^T$. The array is able to provide the requested torque with very low error, even when the array is near the region where singularities are possible ($1\,h$). While a decrease in the determinant of $J(\Phi)J(\Phi)^T$ is noticeable, it is still far from zero, especially when the h^6 scaling is taken into account. The motion of the CMGs throughout the example maneuver can be seen in Figure E.11, with a detail of the gimbal rates included for clarity in Figure E.12. The gimbal

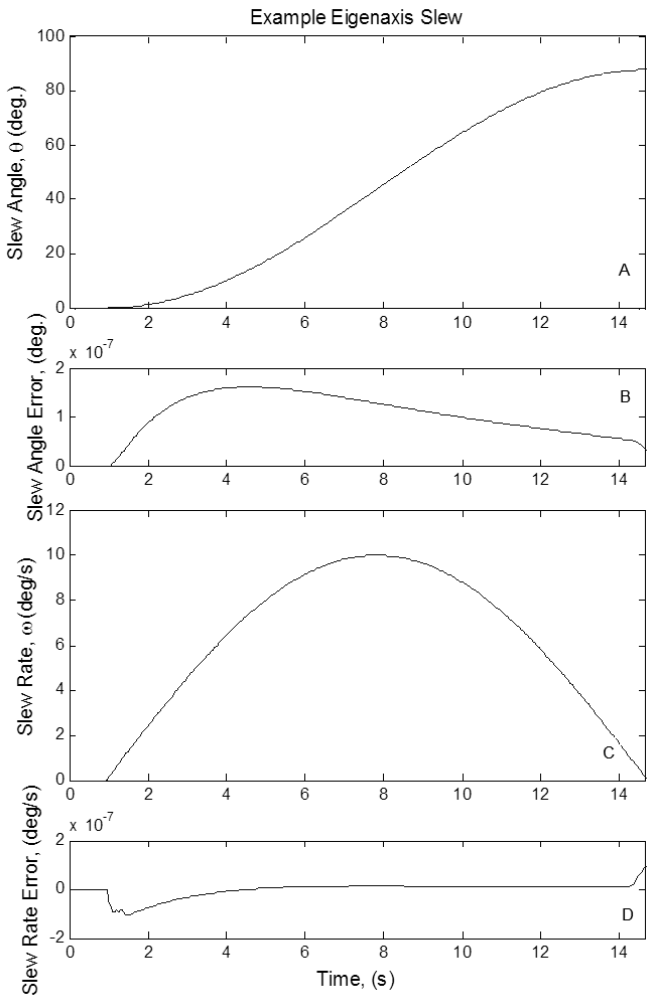

Figure E.10. Example slew rotation angle, angle tracking error, angular rate, and rate error.

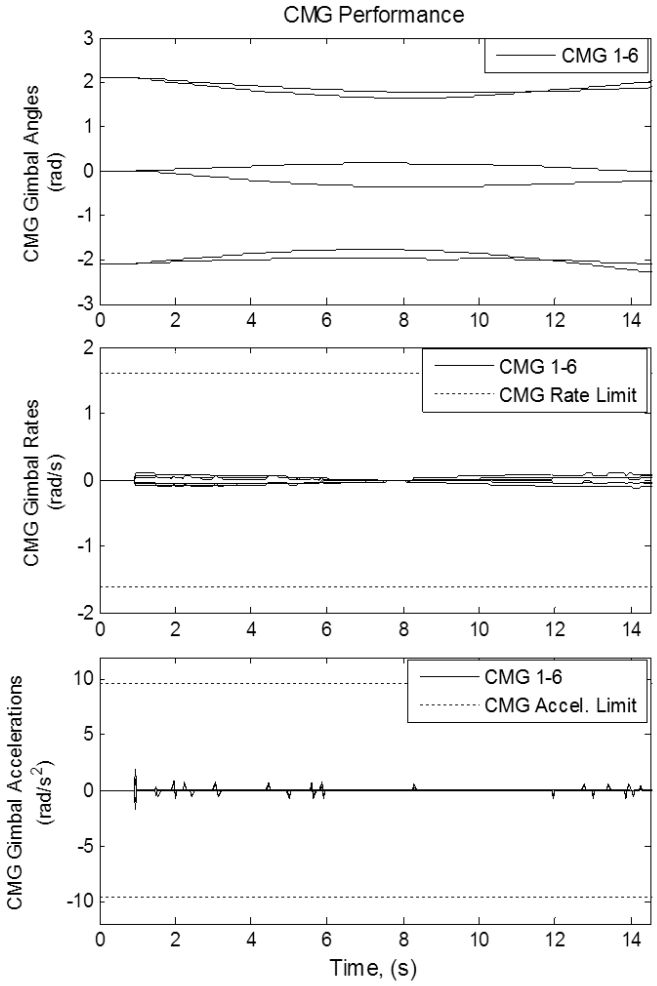

Figure E.11. Example slew CMG gimbal angles, rates and accelerations, as well as the limitations associated with the constraints of the hardware.

rates and accelerations remain within their hardware constraints for the entirety of the slew, which contributes to the low torque error since the commanded CMG motion is physically realizable.

E5 Conclusions

A constrained steering law provides an error-free, instantaneous algorithm for applying attitude-control torques with control moment gryo (CMG) arrays while avoiding singularities. The general framework proposed here for describing the steering laws with constraint equations that are linear with respect to the gimbal rates suggests that by choosing linear constraints that lie in a subspace orthogonal to the CMG Jacobian, an augmented system Jacobian *A* can be made singularity free. This fact is demonstrated with a simple scissored-pair array example. Taking this idea one step further, one can define two-dimensional singularity-free momentum envelopes with a triplet set of CMGs. These triplets use a constraint that is orthogonal to the rows of the system Jacobian. It is possible to obtain momentum in all three attitude degrees of freedom by

using two sets of CMG triplets arranged in non-parallel planes with a steering law responsible for distributing the torque between the two singularity-free triplets.

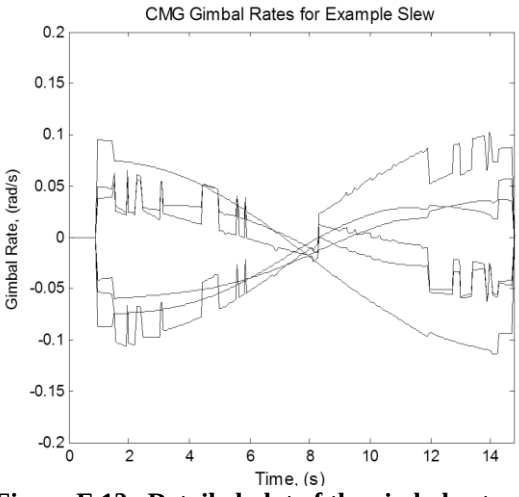

Figure E.12. Detailed plot of the gimbal rates.

An example of such a steering law is demonstrated through a simulation that shows its singularity avoidance properties. A Monte Carlo simulation using randomized slews shows that the example steering law performance is not slew-dependent. Although this steering law is triplet-specific and neither requires a minimal number of CMGs nor is general to a variety of CMG arrays, this example demonstrates the power of the generalized framework for developing singularity free steering laws. Further work should investigate the possibility of using non-holonomic constraints in the context of the generalized formulation, and extensions of this work should attempt to describe a generalized formulation for all constraint-based methods, even those that are nonlinear in the gimbal rates. Once such an algorithm is developed, a study of various CMG configurations can be performed to determine which geometries provide the best balance of cost-effectiveness and technological feasibility.

REFERENCES

[1]Fell, P. J., "Multiple satellite orbit determination for neighboring satellies," NASA STI/Recon Technical Report, 1975.

[2]Carney, T. M., "An Automatic Terminal Guidance System for Rendezvous With a Satellite," NASA Technical Note D-923, 1961.

[3]Skeer, M. H., "Space Tug Operational Requirements for Satellite Placement, Revisit and Retrieval – Case 105-6," NASA-CR-113350, 1970.

[4]Oberg, J., "Gemini-7: Lessons and Legends (A 30th Anniversary Revisit)," 1995. [http://www.jamesoberg.com/gemini7.html. Accessed 6/16/12.]

[5]Hu, Y., and Ng, A., "Robust Control of Spacecraft Formation Flying," *Journal of Aerospace Engineering*, Vol. 20, No. 4, Oct. 2007, pp.209-214.

[6]Breger, L. and How, J. "Safe Trajectories for Autonomous Rendezvous of Spacecraft," *Journal of Guidance, Control, and Dynamics*, Vol. 31, No. 5, September-October 2008, p. 1478-1495.

[7]Fitz-Coy, N. G.; Cochran, J. E., Jr., "Space Station/Shuttle Orbiter dynamics during docking," NASA. Marshall Space Flight Center Structural Dynamics and Control Interaction of Flexible Structures, 1987, p 133-174.

[8] "Rendezvous and Docking Technology", ATV Information Kit, www.esa.com. Accessed 8/7/2010.

[9]Ambrose, R., Wilcox, B., Reed, B., Matthies, L., Lavery, D., and Korsmeye, D., "DRAFT Robotics, Tele-Robotics, and Autonomous Systems Roadmap," National Aeronautics and Space Administration, Washington D.C., November 2010.

[10]Rush, J., Israel, D., Ramos, C., Deutsch, L., Dennehy, N., and Seibert, M., "DRAFT Communication and Navigation Systems Roadmap," National Aeronautics and Space Administration, Washington D.C., November 2010.

[11]Woffinden, D., and Geller, D., "Navigating the Road to Autonomous Orbital Rendezvous," *Journal of Spacecraft and Rockets*, Vol. 44, No. 4, July- Aug 2007, pp. 898–909.

[12]Fehse, Wigbert, *Solar Autonomous Rendezvous and Docking of Spacecraft*, University of Cambridge, Cambridge, UK, 2003.

[13]Polites, M. E., "Technology of Automated Rendezvous and Capture in Space," *AIAA Journal of Spacecraft and Rockets*, Vol. 36, no. 2, March-April 1999, p. 280-291.

[14]Sabol, C., Burns, R,, and McLaughlin, C., "Satellite Formation Flying Design and Evolution," *Journal of Spacecraft and Rockets*, Vol. 38, No. 2, March-April 2001, pp. 270-278

[15]Zimpter, D., Barrington, R., and Mulder, T., "Flight Dynamics and GN&C for Spacecraft Servicing Missions," *AIAA Guidance, Navigation, and Control Conference*, Toronto, Canada, Aug 2-5 2010.

[16]Izzo, D., Pettazzi, L., and Ayre, M., "Mission Concept for Autonomous on Orbit Assembly of a Large Reflector in Space," 56th International Astronautical Congress, 2005.

[17]Aikenhead, B. A., Daniell, R. G., and Davis, F. M., "Canadarm and the Space Shuttle," Journal of Vacuum Science & Technology A: Vacuum, Surfaces, and Films, Vol. 1, No. 2, pp. 126-132.

[18] NASA, "Overview of the DART Mishap Investigation Results," *NASA* Publication [online publication], May 2006, URL: www.nasa.gov/pdf/148072main_DART_mishap_overview.pdf [cited 15 Jan 2011].

[19]Shoer, J., "Flux-Pinned Interfaces for the Assembly, Manipulation, and Reconfiguration of Modular Space Systems," AIAA Guidance, Navigation, and Control Conference, Honolulu, HI, August 2008.

[20]Serway, R. A., Moses, C. J., Moyer, C. A., "Superconductivity," Modern Physics, 3rd ed., Brooks/Cole, 2005, Web Essays & Appendices [http://academic.cengage.com/resource_uploads/static_resources/0534493394/4891/SerwayCh12-Superconductivity.pdf. Accessed 6/15/12.]

[21]Schonhuber, P. and Moon, P. C., "Levitation forces, stiffness, and force-creep in YBCO high-Tc superconducting thin films," Applied Superconductivity, Vol. 2, No. 7, 1994, pp. 523-534.

[22]Davis, L. C., "Lateral restoring force on a magnet levitated above a superconductor," Journal of Applied Physics, Vol. 67, No. 5, 1990, pp. 2631-2636.

[23]Wu, M. K., Ashburn, J. R., Torng, C. J., Hor, P. H., Meng, R. L., Gao, L., Huang, Z. J., Wang, Y. Q., and Chu, C. W., "Superconductivity at 93 K in a New Mixed-Phase Y-Ba-Cu-O Compound System at Ambient Pressure," *Physical. Review Letters,* Vol. 58, No. 9, 1987, pp 908-910, 1987.

[24]Stavrev, S., "Modelling of High Temeprature Superconductors for AC Power Applications", Ph. D. dissertation, Department of Electrical Engineering, Technical University of Varna, Bulgaria, 2002.

[25]Jones, L., and Peck, M., "Control Strategies Utilizing the Physics of Flux-Pinned Interfaces for Spacecraft," *AIAA Guidance, Navigation, and Control Conference*, Portland, OR, 2011.

[26]Shoer, J., and Peck, M., "Reconfigurable Spacecraft as Kinematic Mechanisms Based on Flux-Pinning Interactions," *Journal of Spacecraft and Rockets*, Vol. 46, No. 2, pp. 466-469, 2009.

[27]Shoer, J., and Peck, M., "Simulation of Multibody Spacecraft Reconfiguration through Sequential Dynamic Equilibria," *AIAA Guidance, Navigation, and Control Conference*, Toronto, ON, Aug 2-5, 2010.

[28]Legostaev, V. P., "Russian space programs: Achievements and prospects of automatic control applications." Annual Reviews in Control, Vol. 29, 2005, pp. 1-11.

[29]Rumford, T. E., "Demonstration of Autonomous Rendezvous Technology (DART) Project Summary," *Proceedings of the SPIE,* Vol. 5088, 2003.

[30]Friend, R. B., "Orbital Express Program Summary And Mission Overview," Proc. of SPIE Vol. 6958, 2008.

[31]Strandmoe, S., DePasquale, E., Escane, I., Augelli, M., Personne, G., Cavrois, B., Fau, N., Yu, M., Zink, M., Clerc, X., Chaize, M., Clerc, H., Gogibus, E., Brun, P., Roussel, S., Requiston, H., Delage, R., Martel, F., Chavy, S., Veltz, Ch., Martinez Fadrique, F. M., Juarez, I., Casas-Cuadrado, C. M., Bonnet, M., and Caluwaerts, D., "Automated Transfer Vehicle (ATV) Flight Control Achievements," *7th International ESA Conference on Guidance, Navigation & Control Systems*, 2008, County Kerry, Ireland.

[32]"NSS Congratulates SpaceX on a Magnificent First Docking of Dragon Capsule and Successful Launch of NSS 'Special Payload'," Targeted News Service, 2012.

[33]Bergin, C., "SpaceX's Dragon already achieving key milestones following Falcon 9 ride," *NASASpaceflight*, 2012. [http://www.nasaspaceflight.com/2012/05/spacexs-dragon-achieving-milestones-falcon-9-ride/. Accessed 6/20/12.]

[34]Garcia, I., and How, J. P., "Trajectory Optimization for Satellite Reconfiguration Maneuvers with Position and Attitude Constraints," 2005 American Control Conference, Portland, OR, 2005.

[35]Kim, Y. and Mesbahi, M., "Dual-Spacecraft Formation Flying in Deep Space: Collision-Free Reconfigurations," Journal of Guidance, Control, and Dynamics, Vol. 26, No. 2, pp. 375-379, 2003.

[36]Kim, Y., Mesbahi, M., and Hadaegh, F. Y., "Multiple-Spacecraft Reconfiguration through Collision Avoidance, Bouncing, and Stalemate," Journal of Optimization Theory and Applications, Vol. 122, No. 2, pp. 323-343, 2004.

[37]Kapila, V., Sparks, A. G., Buffington, J. M., and Yan, Q., "Spacecraft Formation Flying: Dynamics and Control," Journal of Guidance, Control, and Dynamics, Vol. 23, No. 3, pp. 561-564, 2000.

[38]Balogh, A., Carr, C. M., Acuna, M. H., Dunlop, M. W., Beek. T. J., Brown, P., Fornacon, K.-H., Georgescu, E., Glassmeier, K.-H., Harris, J., Musmann, G., Oddy, T., and Schwingenschuh, K., "The Cluster Magnetic Field Investigation: overview of in-flight performance and initial results," Annales Geophysicae, Vol. 19, 2001, pp. 1207-1217.

[39]Krieger, G., Hajnsek, I., Papathanassiou, K. P., Younis, M., and Moreira, A., "Interferometric Synthetic Aperture Radar (SAR) Missions Employing Formation Flying," *Proceedings of the IEEE*, Vol. 98, No. 5, 2001, 816-843.

[40]Saks, N., Boonstra, A., Rajan, R. T., Bentum, M., Belien, F., and Klooster, K., "DARIS, a Fleet of Passive Formation Flying Small Satellites for Low Frequency Radio Astronomy," *Small Satellite Systems and Services - The 4S Symposium*, 2010, Funchal, Madeira, Portugal, pp. 1-15.

[41]Mamen, R., "Applying space technologies for human benefit; the Canadian experience and global trends," *International Conference on Recent Advances in Space Technologies*, 2003, Ottawa, Canada.

[42]Coleshill, E., Oshinowo, L., Rembala, R., Bina, B., Rey, D., and Sindelar, S., "Dextre: Improving maintenance operations on the International Space Station," *Acta Astronautica*, Vol. 64, Issue 9-10, 2009, pp. 869-874.

[43]Earnshaw, S., "On the nature of the molecular forces which regulate the constitution of the luminferous ether," Transactions of the Cambridge Philosophical Society, Vol. 7, 1842, pp. 97-112.

[44]Swinerd, G., "How Spacecraft Fly: Spaceflight Without Formulae," *Praxis Publishing, Ltd.*, 2008.

[45]French, D. B., "Hybrid Control Strategies for Rapid, Large Angle Satellite Slew Manuevers," Master's Thesis, Department of Aeronautical and Astronautical Engineering, Air Force Insititute of Technology, 2003.

[46]Gersh, J., and Peck, M., "Violet: A High-Agility Nanosatellite for Demonstrating Small Control-Moment Gyroscope Prototypes and Steering Laws," *AIAA Guidance, Navigation, and Control Conference*, Chicago, 2009.

[47]Wang, P. and Shtessel, T. B., "Satellite Attitude Control Using only Magnetorquers," Proceedings of the American Control Conference, pp.222-226, 1998.

[48]Aung, M., Ahmed, A., Wette, M., Tien, J., Scarf, D., Landin, B., Purcell, G., and Regehr, M., "An overview of formation flying technology development for the Terrestrial Planet Finder mission," *IEEE Aerospace Conference 2003*, Big Sky, MT, 2004.

[49]Kwon, D. E., "Electromagnetic Formation Flight of Satellite Arrays", Master's Thesis, Department of Aeronautical and Astronautical Engineering, Massachusetts Institute of Technology, 2005.

[50]Miller, D. W., Sedwick, R. J., Kong, E. M. C., and Schweighart, S., "Electromagnetic Formation Flight For Sparse Aperture Telescopes," 2002 IEEE Aerospace Conference Proceedings, Vol. 2, pp. 2-729 - 2-741, 2002.

[51]Sakaguchi, A., "Micro-Electromagnetic Formation Flight of Satellite Systems," Master's Thesis, Department of Aeronautics and Astronautics, Massachusetts Institute of Technology, 2007.

[52]Neave, M. D., "Dynamic and Thermal Control of an Electromagnetic Formation Flight Testbed," Master's Thesis, Department of Aeronautics and Astronautics, Massachusetts Institute of Technology, 2005.

[53]Schaub, H., Parker, G. G., and King, L. B., "Challenges and Prospects of Coulomb Spacecraft Formations," AAS John L. Junkins Astrodynamics Symposium, College Station, TX, May 23–24, 2003.

[54]Schaub, H., Parker, G. G., and King, L. B., "Challenges and Prospects of Coulomb Spacecraft Formation Control," Journal of the Astronautical Sciences Vol. 52, Nos. 1-2, Jan.–June., 2004, pp. 169–193.

[55]Zhang, Y., Yang, L., Zhu, Y., Ren, X., and Haung, H., "Self-docking capability and control strategy of electromagnetic docking technology," *Acta Astronautica*, Vol. 69, Issue 11-12, 2011, pp. 1073-1081.

[56]Zhang, Y., Yang, L., Zhu, Y., Huang, H., Cai, W., "Nonlinear 6DOF control of spacecraft docking with inter-satellite electromagnetic force", *Acta Astronautica*, Vol. 77, 2012, pp. 97-108.

[57]Waydo, S., Henry, D., and Campbell, M., "CubeSat Design for LEO-Based Earth Science Missions," *IEEE Aerospace Conference Proceedings*, Vol. 1, 2002, pp. 435-445.

[58]Funase, R., Takei, E., Nakamura, Y., Nagai, M., Enokuchi, A., Yuliang, C., Nakada, K., Nojiri, Y., Sasaki, F., Funane, T., Eishima, T., and Nakasuka, S., "Technology demonstration on University of Tokyo's pico-satellite "XI-V" and its effective operation result using ground station network," *Acta Astronautica*, Vol. 61, Issues 7-8, 2007, pp. 707-711.

[59]"Boeing Successfully Completes CubeSat Mission to Advance Nano-Satellite Technology," Boeing, [www.boeing.com. Accessed 6/20/12.]

[60]Heidt, H., Puig-Suari, J., Moore, A. S., Nakasuka, S., and Twiggs, R. J., "CubeSat: A new Generation of Picosatellite for Education and Industry Low-Cost Space Experimentation," *14th Annual AIAA/USU Conference on Small Satellites*, 2000.

[61]Lan, W., Brown, J., Toorian, A., Coelho, R., Brooks, L., Suari, J. P., and Twiggs, R., "CubeSat Development in Education and into Industry." AIAA Space 2006, AIAA, San Jose, California, 2006.

[62]Nugent, R., Munakata, R., Chin, A., Coelho, R., Puig-Suari, J., "The CubeSat: The Picosatellite Standard for Research and Education." AIAA Space 2008 Conference and Exposition, San Diego, California, 2008.

[63]Johnson, L., Whorton, M., Heaton, A., Pinson, R., Laue, G., and Adams, C., "NanoSail-D: A solar sail demonstration mission," Acta Astronautica, Vol. 68, Issues 5-6, 2011, pp. 571-575.

[64]Gill, E., Sundaramoorthy, P., Bouwmeester, J., and Sanders, B., "Formation Flying to Enhance the QB50 Network," *Small Satellite Systems and Services Symposium*, Funchal, Portugal, 2010.

[65]Matsumoto, K., Kikuchi, H., Uno, N., and Tanaka, Y., "Magnetic flux pinning properties of oxide superconductors produced by melt processes," *Cryogenics*, Vol. 20, Issue 1, 1990, pp. 5-10.

[66]Elschner, S., Breuer, F., Noe, M., Rettelbach, T., Walter, H., and Bock, J., "Manufacturing and testing of MCP 2212 bifilar coils for a 10 MVA fault current limiter," *IEEE Transactions of Superconductivity*, Vol. 12, 2003.

[67]Fujimoto, H., "Superconducting and mechanical properties of RE-Ba-Cu-O/Ag bulk superconductors," *IEEE Transactions on Applied Superconductivity*, Vol. 15, Issue 2, 2005, pp. 3098-3101.

[68]Takao, T., Kameyama, S., Doi, T., Tanoue, N., and Kamijo, H., "Increase of Levitation Properties on Magnetic Levitation System Using Magnetic Shielding Effect of GdBCO Bulk Superconductor," *IEEE Transactions on Applied Superconductivity*, Vol. 21, Issue 3, 2011, pp. 1543-1546.

[69]Silhanek, A. V., Gillijns, W., Moshchalkov, V. V., Metlushko, V., and Ilic, B., "Tunable pinning in superconducting films with magnetic micro-loops," *Applied Physics Letters*, Vol. 89, Issue 18, 2006.

[70]Rentschler, T., Kemmler-Sack, S., Hartmann, M., Hubener, R. P., Kessler, P., and Lichte, H., "Influence of Nd substitution on the superconducting properties of ceramics in the 2212 system Bi2−wPbwSr2−xCa1−yNdx+yCu2O8+z," *Physica C: Superconductivity*, Vol. 200, Issues 3-4, 1992, pp. 287-295.

[71]Hogg, Michael J., Kahlmann, Frank, Barber, Zoe H., and Evetts, Jan E., "Angular hysteresis in the critical current of $YBa_2Cu_3O_7$ low-angle grain boundaries," *Superconductor Science and Technology*, Vol. 14, 2001, pp. 647-650.

[72]Navau, C., and Sanchez, A., "Stability and hysteretic losses in superconductor-permanent magnet levitation systems," *Physica C*, 2002, pp. 372-376.

[73]Nikolo, M., "Superconductivity: A guide to alternating current susceptibility measurements and alternating current susceptometer design," *American Journal of Physics*, Vol. 63, No. 1, 1995, pp. 57 – 65.

[74]Ueda, H., Itoh, M., Ishiyama, A., "Trapped Field Characteristics of HTS Bulk in AC External Magnetic Field," IEEE Transactions on Applied Superconductivity, Vol. 13, No. 2, 2003, pp. 2283-2286.

[75]Ford, P. J., and Saunders, G. A., "High-temperature superconductivity – ten years on," *Contemporary Physics*, Vol. 38, No. 1, 1997, pp. 63-81.

[76]Rossing, T. D., and Hull, J. R., "Magnetic Levitation," *The Physics Teacher*, 199, pp. 552 – 562.

[77]Kramer, E. J., "Scaling laws for flux pinning in hard superconductors," Journal of Applied Physics, Vol. 44, No. 3, 1973, pp. 1360-1370.

[78]Fujimoto, H., Kamijo, H., Higuchi, T., Nakamura, Y., Nagashima, K., "Prelimiary Study of a Superconducting Bulk Magnet for the Maglev Train," *IEEE Transactions on Applied Superconductivity*, Vol. 9, No. 2, 1999, pp. 301-304.

[79]Davis, L. C., Logothetis E. M., and Soltis, R. E., "Stability of Magnets Above Superconductors," Journal of Applied Physics, Vol. 64, No. 8, 1988, pp. 4212-4218.

[80]Brandt, E. H., "Rigid levitation and suspension of high-temperature superconductors by magnets," American Journal of Physics, Vol. 58, No. 1, 1990, pp. 43-49.

[81]Yang, Y., "Vertical and Lateral Forces When a Permanent Magnet Above a Superconductor Traverses in Arbitrary Directions," *Superconductor Science and Technology*, Vol. 21, 2008.

[82]Sjostrom, M., "Hysteresis Modelling of High Temperature Superconductors", Ph. D. dissertation, Communication Systems Department, Swiss Federal Institute of Technology, Lausanne, Switzerland, 2001.

[83]Ma, K. B., Postrekhin, Y. V., and Chu, W. K., "Superconductor and magnet levitation devices," *Review of Scientific Instruments*, Vol. 74, No. 12, Dec. 2003, pp. 4989-5017.

[84]Hull, J., "Superconducting Bearings," *Superconducting Science and Technology*, Vol. 13, 2000, R1-R15.

[85]Brown, O., and Eremenko, P., "Fractionated Space Architectures: A Vision For Responsive Space," 4th Responsive Space Conference, AIAA, 2006.

[86]Shoer, J. and Peck, M., "A Flux Pinned Magnet-Superconductor Pair for Close-Proximity Station Keeping and Self-Assembly of Spacecraft," AIAA Guidance, Navigation, and Control Conference and Exhibit. 2007.

[87]Norman, M., "Modeling and Properties of a Flux-Pinned Network of Satellites," AAS/AIAA Astrodynamics Specialist Conference, Mackinac Island, MI, Aug 19-23, 2007.

[88]Shoer, J. and Peck, M. "Stiffness of Flux-pinned for Virtual Structures for Modular Spacecraft," Journal of the British Interplanetary Society, vol. 62, no. 2, pp. 57-65, 2009.

[89]Gersh-Range, J. A., Arnold, W. R., Peck, M. A., and Stahl, H. P., "A parametric finite-element model for evaluating segmented mirrors with discrete edgewise connectivity," Proceedings of the SPIE, Vol. 8125, 2011.

[90]Gersh-Range, J. A., Arnold, W. R., Peck, M. A., and Stahl, H. P., "A flux-pinning mechanism for segment assembly and alignment," Proceedings of the SPIE, Vol. 8150, 2011.

[91]Norman, M., "Station-Keeping and Reconfiguration of a Flux-Pinned Satellite Network" Proceedings of the AIAA Guidance, Navigation, and Control Conference, Honolulu, HI, August 18-21, 2008.

[92]Norman and Peck, "Stationkeeping of a Flux-Pinned Satellite Network," Journal of Guidance, Control, and Dynamics, Vol. 33, No. 5, pp. 1683-1686, 2010.

[93]Shoer and Peck, "Sequences of Passively Stable Dynamic Equilibria for Hybrid Control of Reconfigurable Spacecraft," AIAA Guidance, Navigation, and Control Conference, Chicago, IL, Aug 10-13, 2009.

[94]Wilson, W., Shoer, J., and Peck, M., "Demonstration of a Magnetic Locking Flux-Pinned Revolute Joint for Use on CubeSat-Standard Spacecraft." AIAA Guidance, Navigation and Control Conference and Exhibit. AIAA, Chicago, 2009.

[95]Wilson, W. and Peck, M. "An Air-Levitated Testbed for Flux Pinning Interactions at the Nanosatellite Scale," AIAA Modeling and Simulation Technologies Conference. AIAA, Toronto, 2010.

[96]Wilson, W. R., Jones, L. L., and Peck, M. A., "A Low-Cost Planar Air Bearing Testbed for CubeSat-Scale Spacecraft," Journal of Dynamic Systems, Measurement and Control (submitted).

[97]Jones, L., Wilson, W., Gorsuch, J., Shoer, J., and Peck, M., "Flight Validation of a Multi-Degree-of-Freedom Flux-Pinned Spacecraft Model," AIAA Guidance, Navigation, and Control Conference, Portland, Oregon, 2011.

[98]Jones, L. and Peck, M., "Stability and Control of a Flux-Pinned Docking Interface for Spacecraft ," AIAA Guidance, Navigation, and Control Conference, Toronto, ON, Aug 2-5, 2010

[99]Kamerlingh-Onnes, H., "Further experiments with liquid helium. On the change of the electrical resistance of pure metal at very low temperature", Leiden Comm. 122b, pp. 3- 5, pp. 13-15, pp. 21-25, 1911.

[100]Brandt, E. H., "Levitation in Physics," *Science*, Vol. 243, No. 4889, 1989, pp. 349-355.

[101]Abrikosov, J. A. A., "Magnetic Properties of Superconductors of the Second Group," Experimental Theoretical Physics (USSR) 32, p.1442, 1957 (translation: Soviet Phys. – JETP 5, p. 1174, 1957)

[102]Silcox, J., and Rollins, R. W., "Hysteresis in Hard Superconductors," Applied Physics Letters, Vol. 2, 1962, pp. 231-233.

[103]Sheahan, T. P., "Introduction to High-Temperature Superconductivity", New York:Plenum Press, 1994.

[104]Larkin, A. I., and Ovchinnikov, Y. N., "Pinning in Type II Superconductors," Journal of Low Temperature Physics, Vol. 34, Nos. 3 - 4, 1979, pp. 409-428.

[105]Gurevich, A., and Kupfer, H., "Time scales of the flux creep in superconductors," Physical Review B, Vol. 48 No. 9, 1993, pp. 6477 – 6487.

[106]Hakola, Antti, "High-Temperature Superconductivity," Helsinki University of Technology, 2008. [http://tfy.tkk.fi/aes/AES/projects/prlaser/supercond.htm. Accessed 6/15/12.]

[107]Halbritter, J., "Granular Superconductors and Their Intrinsic and Extrinsic Surface Impedance," Journal of Superconductivity, Vol. 8, No. 6, 1995, pp. 691-703.

[108]Liang, R., Dosanjh, P., Bonn, D. A., Hardy, W. N., and Berlinsky, A. J., "Lower critical fields in an ellipsoid-shaped YBa2Cu3O6.95 single crystal," Physical Review B, Vol. 50, No. 6, 1994, pp. 4212-4216.

[109]Kordyuk, A., "Magnetic levitation for hard superconductors," *Journal of Applied Physics*, Vol. 83, No. 1, 1998, pp. 610-612.

[110]Hammond, P., "Electric and magnetic images," Proceedings of the IEE – Part C: Monographs, Vol. 107, Issue 12, 1960, pp. 306-313.

[111]Griffiths, D., *Introduction to Electrodynamics.* Pearson Education Inc., Upper Saddle River, New Jersey, 1999, pp. 246-282.

[112]Yung, K. W., Landecker, P. B., and Villani, D.D., "An Analytic Solution for the Force Between Two Magnetic Dipoles," *Magnetic and Electrical Separation*, Vol. 9, 1998, pp. 39-52.

[113]"Surface Fields 101," K&J Magnetics, Inc. [http://www.kjmagnetics.com/blog.asp?p=surface-fields-101. Accessed 6/22/12.]

[114] Simon, M. D., Heflinger, L. O., and Geim, A. K.., "Diamagnetically Stabilized Magnet Levitation," *American Journal of Physics*, Vol. 69, No. 6, June 2001, pp. 702-713

[115] Giaro, K., Gorzkowski, W., and Motylewski, T., "A Correct Description of the Interaction Between a Magnetic Moment and Its Image," *Physica C.* Vol. 168, April 1990, pp. 479-481.

[116] Cansiz, A., Hull, J. R., Gundogdu, O., "Translational and rotational dynamic analysis of a superconducting levitation system," Superconductor Science and Technology, Vol. 18, Issue 7, 2005.

[117] Griffiths, D., *Introduction to Electrodynamics.* Pearson Education Inc., Upper Saddle River, New Jersey, 1999, pp. 246-282

[118] Lyapunov, A. M., Ed. By Fuller,A. T., The General Problem of the Stability of Motion, Taylor & Francis: Bristol, PA. 1992 (originally published in 1892).

[119] Schaub, H., and Junkins, J. Analytical Mechanics of Space Systems. AIAA, Reston, VA, 2003.

[120] Forbes, J. R., "Extensions of Input-Output Stability Theory and the Control of Aerospace Systems," Ph. D. Thesis, Department of Aerospace Science and Engineering, University of Toronto, 2011.

[121] Marquez, H. J., "Nonlinear Control Systems: Analysis and Design," Wiley-Interscience, 2003.

[122] Davis, L. C., Logothetis, E. M., and Soltis, R.E. "Stability of Magnets Levitated Above Superconductors," *Journal of Applied Physics*, Vol. 64, No. 8, October 15, 1988, pp. 4212-4218.

[123]Thuot, P. J., and Harbaugh, G. J., 1995, "Extravehicular Activity Training and Hardware Design Consideration", Acta Astronautica, **36**(1), pp. 13-26.

[124] Sharf, I., B. Laumonier, M. Persson, J. Robert, 2008, "Control of a Fully-actuated Airship for Satellite Emulation," *Video Proceedings of IEEE International Conference on Robotics and Automation*, ICRA2008, Pasadena, CA.

[125] Schnurr, R., O'Brien, M., and Cofer, S., 1989, "The Goddard Space Flight Center (GSFC) Robotics Technology Testbed", *Proceedings of the NASA Conference on Space Telerobotics*, Pasadena, CA.

[126] Doebbler, J., Davis, J. J., Valasek J., and Junkins, J. L., 2008, "Mobile Robotic System for Ground Testing of Multi-Spacecraft Proximity Operations", AIAA 2008-6548, *AIAA Modeling and Simulation Technologies Conference and Exhibit*, Honolulu, HI.

[127] Regehr, M. W., Acikmese, A. B., Ahmed, A., Bailey, R., Bushnell, C., Clark, K. C., Hicke, A., Lytle, B., MacNeal, P., Rasmussen, R. E., Singh, G., and Shields, J., 2004, "The Formation Control Testbed," IEEEAC paper #1396, *Aerospace Conference*, Pasadena, CA.

[128] Schwartz, J. L., Peck, M. A., and Hall, C. D., 2003, "Historical Review of Air-Bearing Spacecraft Simulators," AIAA Journal of Guidance, Control and Dynamics, **26**(4), pp. 513-522.

[129] Agrawal, B., and Rasmussen, R., "Air Bearing Based Satellite Attitude Dynamics Simulator for Control Software Research and Development," Hardware-in-the-Loop Testing, Vol. 6, Proceedings of the SPIE Conference on Technologies for Synthetic Environments, Society of Photo-Optical Instrumentation Engineers, Bellingham, WA, 2001, pp. 204–214.

[130] Schwartz, J. L., and Hall, C. D., 2003, "The Distributed Spacecraft Attitude Control System Simulator: Development, Progress, Plans," NASA Space Flight Mechanics Symposium, Greenbelt, MD.

[131] Schubert, H., and How, J., 1997, "Space Construction: An Experimental Testbed to Develop Enabling Technologies," *Proceedings of the Conference on Telemanipulator and Telepresence Technologies IV*, IEEE, Piscataway, NJ.

[132] Miller, D., Saenz-Otero, A., Wertz, J., Chen, A., Berkowski, G., Brodel, C., Carlson, A., Carpenter, D., Chen, S., Cheng, S., Feller, D., Jackson, S., Pitts, B., Perez, F., Szuminski, J., and Sell, S., 2000 "SPHERES: A Testbed For Long Duration Satellite Formation Flying In Micro-Gravity Conditions", AAS 00-110, *Proceedings of the AAS/AIAA Space Flight Mechanics Meeting*, Clearwater, FL.

[133] Moseson, W., "Implementation of a FloatCube Video Tracking System," *AIAA Region I 2012 Student Conference*, Syracuse University, Syracuse, NY, 2012.

[134] Chuang, E. S., and Kubala, S. Z., "Data Acquisition and Control for CubeSat Test Modules," *AIAA Region I 2012 Student Conference*, Syracuse University, Syracuse, NY, 2012.

[135] "12mm x 24mm Flat Rectangular Air Bearing Specifications", New Way, http://newwayairbearings.com/Air-Bearings-Flat-Rectangular-12mmx24mm

[136] Sorgenfrei, M., Jones, L., Joshi, S., and Peck, M., "Results from a Reconfigurable Testbed for Dynamics and Control of Flux-Pinned Spacecraft Formations," Journal of Guidance, Control, and Dynamics (to be submitted).

[137] Thuot, P. J., and Harbaugh, G. J., 1995, "Extravehicular Activity Training and Hardware Design Consideration", Acta Astronautica, 36(1), pp. 13-26.

[138] Sharf, I., B. Laumonier, M. Persson, J. Robert, 2008, "Control of a Fully-actuated Airship for Satellite Emulation," Video Proceedings of IEEE International Conference on Robotics and Automation, ICRA2008, Pasadena, CA.

[139] Sunderland, P. B., Axelbaum, R. L., Urban, D. L., Chao, B. H., and Lin, S. "Effects of Structure and Hydrodynamics on the Sooting Behavior of Spherical Microgravity Diffusion Flames," Combustion and Flame, Vol. 132, 2003, pp. 25-33.

[140] Nowierski, S., "Simulated and Experimental Thermal Analysis for the Cooling of a Superconductor in a Flux-Pinned Interface for Spacecraft," AIAA Student Conference, Region I-NE, Syracuse, NY, April 20-21, 2012.

[141] Johnson, D. L., Carrol, B. C., and Leland, R. S., "MSL/CheMin Cryocooler System Requirements and Characterization Tests," Ricor Cryogenic & Vacuum Systems, 2008. [http://www.ricor.com/_Uploads/175RicorICC15609a.pdf. Accessed 6/16/12.]

[142] Pettyjohn, E., "Cryocoolers for Microsatellite Military Applications," 16th International Cryocooler Conference, Atlanta, GA, 2008.

[143] Soucy, M. A., Chateauneuf, F., Deutsch, C., and Etienne, N., "ACE-FTS instrument detailed design," Earth Observing Systems VII. Edited by Barnes, William L. Proceedings of the SPIE, Volume 4814, 2002, pp. 70-81.

[144] Beichman, C., Neugebauer, G., and Chester, T., IRAS Explanatory Supplement. The Joint IRAS Science Working Group, 1988. Available at: < http://irsa.ipac.caltech.edu/IRASdocs/exp.sup/credits.html>

[145] Van Dyk, S., Silberman, N., Spitzer Space Telescope Handbook. Spitzer Heritage Archive Documentation, April 2011. Available at: <http://irsa.ipac.caltech.edu/data/SPITZER/docs/spitzermission/missionoverview/spitzertelescopehandbook/Spitzer_Telescope_Handbook.pdf >

[146] Kelley, R., Mitsuda, K., Allen, C., et. al, "The Suzaku High Resolution X-Ray Spectrometer," Publications of the Astronomical Society of Japan, Vol. 59, No. SP1, Oct. 3 2006, pp 77-112.

[147] Donabedian, M., Gilmore, D., Spacecraft Thermal Control Handbook. The Aerospace Press: El Segundo, CA, 2003.

[148] Grocott, S. C. O., "Modular Attitude Control System for Microsatellites with Stringent Pointing Requirements," 14th AIAA/USU Conference on Small Satellites, 2000.

[149] Mohammed, A., Benyettou, M., Boudjemai, A., Hashida, Y., Sweeting, M., "Yaw Phase Mode Attitude Control Using Z Wheel for LEO Microsatellite," WSEAS Transactions on Communications, Vol. 7, Issue 2, February 2008, pp. 99 – 105.

[150] Laneve, G., and Curti, F., "An Orbit Determination Approach for Small Satellites," Proceedigns of the 12th International Symposium on Space Flight Dynamics, ESOC, Darmstadt, Germany, 1997, pp 275 – 282.

[151] SSBV, "CubeSat Magnetorquer Rod," Ver. 1b datasheet.

[152] SSBV, "Magnetorquer Rod," Ver. 1b datasheet.

[153] Wertz, J., and Larson, W., Space Mission Analysis and Design. Microcosm Press/Springer, Hawthorne, CA and New York, NY, 1999.

[154] Giljarhus, S., AC Losses in MgB2 Superconductors, M.S. Thesis, Norwegian University of Science and Technology, 2007.

[155] Polak, M., Hanic, F., Hlasnik, I., Majoros, M., Chovanec, F., Horvath, I., Krempsky, L., Kottman, P., Kedrova, M., and Galikova, L., "Critical current density, magnetization and AC losses in the YBa2Cu3O6.5+x superconductor," Physica C: Superconductivity, Vol. 156, Issue 1, 1 August 1988, pp. 79-89.

[156] Smolyak, B. M., Babanov, M. V., Ermakov, G. V., Smolyak, I. B., and Naumov, S.V., "The instability of levitation of high-temperature superconductors subject to an alternating magnetic field," Physica C: Superconductivity, Vol. 302, 1998, pp. 23-30

[157] Terentiev, A. N., and Kuznetsov, K. K., "Drift of levitated YBCO superconductor induced by both a variable magnetic field and a vibration," Physica C, Vol 195, 1992, pp. 41-46.

[158]Norman, M., and Peck, M., "Simplified Model of a Flux-Pinned Spacecraft Formation," *Journal of Guidance, Control, and Dynamics*, Vol. 33, No. 3, pp. 814-822, 2010.

[159]Gersh, J., "Architecting the Very-Large-Aperture Flux-Pinned Space Telescope: A Scalable, Modular Optical Array with High Agility and Passively Stable Orbital Dynamics," *AAS/AIAA Astrodynamics Specialst Conference*, Honolulu, HI, Aug 18-21, 2008.

[160]Jones, L., Wilson, W., and Peck, M., "Design Parameters and Validation for a Non-Contacting Flux-Pinned Docking Interface," *AIAA Space 2010 Conference*, Pasadena, CA, Sept. 2010.

[161]Shoer, J. Wilson, W., Jones, L., Knobel, M., and Peck, M., "Microgravity Demonstrations of Flux Pinning for Station-Keeping and Reconfiguration of CubeSat-Sized Spacecraft," *Journal of Spacecraft and Rockets*, Vol. 47, No. 6, 2010.

[162]Jones, L., "Prospects and Challenges of Particulate Solar Sail Propulsion," *AAS/AIAA Astrodynamics Specialst Conference*, Honolulu, HI, Aug 18-21, 2008.

[163]Atchison, J., "A Passive Microscale Solar Sail," AIAA SPACE 2008 Conference & Exposition, San Diego, CA, Sep 9-11, 2008

[164] McInnes, C. R., Solar Sailing: Technology, Dynamics, and Mission Applications, Springer-Praxis, Chichester, UK, 1999.

[165] Gaspar, J., Jones, T., and Murphy, D., "Solar Sail Structural Characterization Test Program." *Journal of Spacecraft and Rockets*, Vol. 44, No. 4, 2007, pp.765.

166 Morrow, E., Scheers D. J., and Lubin D., "Solar Sail Orbit Operations at Asteroids," *Journal of Spacecraft and Rockets*, Vol. 38, No. 2, 2001, pp. 279-286.

167 McInnes, C., "Solar Sailing: Mission Applications and Engineering Challenges," *Philosophical Transactions: Mathematical, Physical and Engineering Sciences*, Vol. 361, No. 1813, 2003, pp. 2989-3008.

168 Johnson, L., Young, R., and Montogmery IV, E., "Status of Solar Sail Propulsion: Moving Toward an Interstellar Probe," *American Institute of Physics Conference Proceedings*, Vol. 886, 2007, pp. 207-214.

169 Swarup, R., Gupta, A. K., and Bansal, M. C., "Effect of sample density on magnetic penetration depth in YBaCuO ceramic superconductors," *Journal of Superconductivity*, Vol. 8, No. 3, 1995, pp. 361-364.

170 Barnhart, D., Vladimirova, T., Sweeting, M., "Very-Small-Satellite Design for Distributed Space Missions," *Journal of Spacecraft and Rockets*, Vol. 44, No. 6, 2007, pp. 1294-1306.

171 Circi, C., "Simple strategy for geostationary stationkeeping maneuvers using solar sails," *Journal of Guidance, Control, and Dynamics*, Vol. 28, No. 2, 2005, pp. 249-253.

172 Nowierski, S., "Simulated and Experimental Thermal Analysis for the Cooling of a Superconductor in a Flux-Pinned Interface for Spacecraft," AIAA Region I-NE Student Conference, Syracuse, NY, April 2012.

173 Jones, L. L., Zeledon, R., A., and Peck, M. A, "A Generalized Framework for Linearly Constrained Control Moment Gyro Steering," Journal of Guidance, Control, and Dynamics, Vol. 35, No. 4, 2012.

174 Schaub, H., and Junkins, J. "Singularity Avoidances Using Null Motion and Variable Speed Control Moment Gyros" *Journal of Guidance Navigation and Control*, Vol. 23, No. 1, Jan.-Feb. 2000, pp. 11-16.

175 Ahmed, J. and Bernstein, D. "Adaptive Control of Double-gimbal Control-Moment Gyro with Unbalanced Rotor" *Journal of Guidance, Control, and Dynamics*, Vol. 25, No. 1, Jan.-Feb. 2002, pp. 105-115.

176 Oh, H., and Vadali, S. "Feedback Control and Steering Laws for Spacecraft Using Single Gimbal Control Moment Gyros" *Journal of the Astronautical Sciences*, Vol 39, No. 2, April-June 1991, pp. 183-203.

177 Hamilton, B. Underhill, B. "Modern Momentum Systems for Spacecraft Attitude Control" *29th AAS Guidance and Control Conference,* Breckenridge, CO, Feb4-8, 2006.

178 Paradiso, J. A., "Global Steering of Single Gimballed Control Moment Gyroscopes Using a Directed Search," *Journal of Guidance, Control, and Dynamics*, Vol. 15, No. 6, 1992, pp. 1236–1244.

179 M. Peck, B. Hamilton, and B. Underhill, "Method and System for Optimizing Torque in a CMG Array," U.S. Patent 7014150, March 21, 2006.

180 Cunningham D. and Driskill, G. "A Torque Balance Control Moment Gyroscope Assembly for Astronaut Maneuvering" NASA 19720018745, 1972

181 Kurokawa, H. "Constrained Steering Law of Pyramid-Type Control Moment Gyros and Ground Tests" *Journal of Guidance, Control, and Dynamics*, Vol 20, No. 3, May-June 1997, pp. 445-449.

182 Kurokawa, H. "Survey of Theory and Steering Laws of Single-Gimbal Control Moment Gyros" *Journal of Guidance, Control, and Dynamics*, Vol. 30, No. 5, Sept.-Oct. 2007, pp. 1331-1340.

183 NASA Marshall Space Flight Center. A Comparison of CMG steering laws for high energy astronomy observatories (HEAOs), NASA TM X-64727, 1972.

184 Bedrossian, N.H, Paradiso, J., HBergmann, E.H, HRowell, D.H, "Steering Law Design for Redundant Single-Gimbal Control Moment Gyroscopes," *AIAA Journal of Guidance, Control, and Dynamics*, Vol. 3, No. 6, Nov.-Dec. 1990, pp. 1083-1089.

185 Wie, B., Bailey. D., Heiberg. C. "Singularity Robust Steering Logic for Redundant Single-Gimbal Control Moment Gyros," *Journal of Guidance, Control, and Dynamics*, Vol. 24, No. 5, pp 865-872.

186 Cornick, D."Singularity Avoidance Control Laws for Single Gimbal Control Moment Gyros" *Guidance and Control Conference*, Boulder, NASA TM X- 64790, 1979.

187 Ford, K. and Hall, C., "Singular Direction Avoidance Steering for Control-Moment Gyros" *Journal of Guidance, Control and Dynamics*, Vol. 23, No. 4, July – Aug. 2000, pp 648 – 656.

188 Wie, B., "New Singularity Escape/Avoidance Steering Logic for Control Moment Gyro Systems," *Proceedings of the AIAA Guidance, Navigation, and Control Conference*, Austin, TX, 2003.

189 Paradiso, J."Global Steering of Single Gimballed Control Moment Gyroscopes Using a Directed Search" *Journal of Guidance, Control, and Dynamics*, Vol. 15, No. 5, 1992, pp. 1236-1244.

190 Vadali, S. R., Oh, H. S., and Walker, S. R., "Preferred Gimbal Angles for Single Gimbal Control Moment Gyros," Journal of Guidance, Control and Dynamics, Vol. 13, No. 6, 1990, pp. 1090-1095.

191 Hefner, R., and McKenzie, C., "A Technique for Maximizing the Torque Capability of Control Moment Gyro Systems," *Astrodynamics*, Vol. 54, No. AAS 83-387, 1983, pp. 905–920.

192 Yoshikawa, T."Steering Law for Roof Type Configuration Control Moment Gyro System" *Automatica*, Vol. 13, 1979, pp. 359 -368.

193 M. R. Elgersma, D. P. Johnson, M. A. Peck, B. K. Underhill, G. Stein, B. G. Morton, and B. J. Hamilton, "Method and system for controlling sets of collinear control moment gyroscopes," U.S. Patent 20070124032, Nov. 30, 2005.

194 Farmer, J."A Reactive Torque Control Law for Gyroscopically Controlled Space Vehicles" NASA TM X-64790, 1973.

195 Fleming, A., and Ross, M., "Singularity-Free Optimal Steering of Control Moment Gyros," *Proceedings of the AAS/AIAA Astrodynamics Conference*, Tahoe, CA, vol. 123, No. 3, 2006, pp. 2681-2700.

196 Kurokawa, H. "Exact Singularity Avoidance Control of the Pyramid Type CMG System" *Proceedings of the AIAA Guidance, Navigation, and Control Conference*, Washington D.C., 1994, pp. 170-180.

197 Udwadia, F. and Kalaba, R. *Analytical Dynamics*. Cambridge University Press, 1996.

198 Brown, D., and Peck, M., "Scissored-Pair Control Moment Gyros: A Mechanical Constraint Saves Power," *Journal of Guidance, Control, and Dynamics*, vol. 31, No. 6, pp. 1823-1826, 2008.

199 Jones, L., and Peck, M., "A Generalized Framework for Linearly-Constrained Singularity-Free Control Moment Gyro Steering Laws," *AIAA Guidance, Navigation, and Control Conference*, Chicago, IL, Aug 10-13, 2009

200 Zeledon, R. and Peck, M., "Singularity-Free Constrained Steering Law for Triplet Control Moment Gyros," *AIAA Guidance, Navigation, and Control Conference*, Toronto, ON, Aug 2-5, 2010.

201 Peck, M., "Uncertainty Models for Physically Realizable Inertia Dyadics" *Journal of Astronautical Sciences*, Vol. 54, No. 1 2006